University of Glasgow

Lee, James M. K. Y (2024) *Advances in laser-free topographic control of the scanning thermal microscope.* PhD thesis.

https://theses.gla.ac.uk/84746/

Copyright and moral rights for this work are retained by the author

A copy can be downloaded for personal non-commercial research or study, without prior permission or charge

This work cannot be reproduced or quoted extensively from without first obtaining permission in writing from the author

The content must not be changed in any way or sold commercially in any format or medium without the formal permission of the author

When referring to this work, full bibliographic details including the author, title, awarding institution and date of the thesis must be given

Enlighten: Theses
https://theses.gla.ac.uk/
research-enlighten@glasgow.ac.uk



University of Glasgow

DOCTORAL THESIS

Advances in Laser-free Topographic Control of the Scanning Thermal Microscope

Author:
James M.K.Y Lee

Supervisors:
Dr. Phillip S. Dobson
Prof. Jonathan M.R Weaver

A thesis submitted in fulfilment of the requirements
for the degree of Doctor of Philosophy
at the

University of Glasgow
James Watt School of Engineering

October 2024

"Thoroughly conscious ignorance is the prelude to every real advance in science."

JAMES CLERK MAXWELL

Abstract

Scanning thermal microscopes typically employ the 'beam bounce' optical lever method to measure nano-scale deflection in their probes. This is a robust and simple approach for many experiments and has been the primary form of deflection measurement of atomic force microscope cantilevers since the 1980's. However, illumination can have a significant impact on the behaviour of the probe or sample being studied. Examples include materials that have light-sensitive behaviour (e.g. semiconductors), and laser illumination creating an additional heat flux to the probe. The measurement of microstructures deflecting without employing optical methods has been addressed in commercial micro-electro-mechanical systems (MEMS) sensors, that typically employ strain gauges or capacitive approaches to measure the deflection of their mechanical sensing elements. This thesis looks to investigate the integration of self-deflection sensing into the SThM system for the purposes of topographic control. The inclusion of strain sensors, based on the electron tunnelling effect, onto the cantilever was explored using high-accuracy overlay alignment techniques developed in this work through novel iterations of the Penrose marker. This work also explores the already available SThM thermal signal as a means of "thermal feedback" topographic control of the microscope. Through the development of custom electronics and control techniques, combined thermal and topographic scans of topographic, thin film, and active semiconductor samples have been presented in air, under liquid, and in vacuum environments without cantilever illumination from an optical lever laser, showing vertical topographic resolutions greater than 5nm.

Acknowledgements

This work could not have been completed without the support, advice, and collective thought of many individuals. Support can come in many forms, be it professional, financial, technical, or emotional and as such I would like to show my particular appreciation to the following people.

I am immensely grateful to my first supervisor, Dr Phil Dobson, whose contributions to this project's success are paramount. Your creativity and insight into any of my problems presented to you proved crucial to the completion of every chapter in this thesis. Your mentorship and encouragement are influential far beyond the ideas in this thesis, allowing me to develop, not only as an effective researcher but on a personal level as well. Thank you for taking me under your wing and entrusting me with this project, and for allowing me the freedom to explore my inquisitiveness.

I would also like to extend my gratitude to my second supervisor, Professor John Weaver. Thank you for allowing me to tap into your unfathomable wealth of knowledge and experience. Your humour and downright wizardry encourage me to believe that anything is possible, no matter how mad it seems.

I would like to thank the JWNC and EPSRC for providing the resources and funding for carrying out this work, the engineers at KNT for providing countless SThM probes for experimentation, and the technical staff at JWNC for their input, advice, training, and support on microfabrication and inspection matters. In particular, I'd like to thank Dr Paul Reynolds, whose input was instrumental to all things relating to E-beam lithography in this thesis. I'm also thankful for the University of Glasgow electronics workshop and their team of technicians who have supported this work. In particular, Andrew Phillips whose advice on PCB design and mechanical setups made the creation of a custom SThM setup possible.

Within the AFM and hyper lithography group, a special thanks goes to Yuan Zhang, whose extensive expertise in all things thermal, AFM, and nanofabrication has helped to narrow down and resolve many hiccups in this work. To past members of the group who set the groundwork for this thesis; Rory, Francesca, Lukas, Chris, and Hao - thank you for providing such detailed and meticulous theses, without which, this work would not have been possible. To those still present, David and Sixuan, thanks for the camaraderie and humour over the years, it has been great to work alongside you through the high points and low points of scientific research.

Of all the staff members within the James Watt School of Engineering, my utmost appreciation goes to Dr Nick Bailey. Your influence on students should not be underestimated or go unappreciated. During my undergraduate years, your support and unique style of teaching made solving any problem, no matter how small, interesting and enjoyable. I will forever be grateful for your friendly support and many cups of coffee over my 9-year journey at the University of Glasgow. I wish you the best of joy in your upcoming retirement, you deserve a rest after all that hard work. You are a true inspiration to many.

To my family - Elsie, Mei lin, and Mum, thank you for encouraging me to take opportunities where I didn't believe I could, and for enabling me to explore my passion for electronics and music from a young age. I would never have even thought about pursuing a doctorate if it weren't for your encouragement and support.

Last but not least, to Cara - you have listened to my nonsense through the years and provided unwavering support beyond what can be expressed in words. I would never have come close to completing this work without you being by my side. Thank you for always being there for me and for making me a better person.

Declaration of Authorship

I, James M.K.Y Lee, declare that this thesis titled, "Advances in Laser-free Topographic Control of the Scanning Thermal Microscope" and the work presented in it are my own. I confirm that:

- This work was done wholly or mainly while in candidature for a research degree at this University.
- Where any part of this thesis has previously been submitted for a degree or any other qualification at this University or any other institution, this has been clearly stated.
- Where I have consulted the published work of others, this is always clearly attributed.
- Where I have quoted from the work of others, the source is always given. With the exception of such quotations, this thesis is entirely my own work.
- I have acknowledged all main sources of help.
- Where the thesis is based on work done by myself jointly with others, I have made clear exactly what was done by others and what I have contributed myself.

Signed: _____

Date: _____

Contents

Abstract ii

Acknowledgements iii

Declaration of Authorship v

1 Introduction 1
- 1.1 Research goals . . . 2
- 1.2 Thesis structure . . . 3

2 Literature Review 5
- 2.1 Evolution of microscopy . . . 5
  - 2.1.1 Scanning Probe Microscopy (SPM) . . . 6
  - 2.1.2 Scanning tunnelling microscope (STM) . . . 6
  - 2.1.3 Atomic Force Microscopy (AFM) . . . 7
  - 2.1.4 Functionalised SPM . . . 10
- 2.2 Thermal measurements at the micro-scale . . . 10
  - 2.2.1 Optical methods . . . 11
  - 2.2.2 Electrical methods . . . 12
- 2.3 Scanning Thermal Microscopy (SThM) . . . 15
- 2.4 Alternative height control systems . . . 22
  - 2.4.1 Scanning Thermal Profiler (STP) . . . 22
  - 2.4.2 Quartz tuning fork . . . 23
  - 2.4.3 Capacitive sensing . . . 24
  - 2.4.4 Resistive . . . 27

3 Microfabrication methods 32
- 3.1 Photolithography . . . 32
- 3.2 Electron Beam Lithography (EBL) . . . 35

3.2.1 Electron sensitive resists . . . 36
3.3 Pattern transfer . . . 38
3.3.1 Metal deposition . . . 38
3.3.2 Thin film growth mechanisms . . . 42
3.3.3 Etch . . . 43
3.4 Multi layer pattern alignment . . . 48
3.4.1 Edge detection based . . . 49
3.4.2 Image correlation based . . . 50
3.4.3 Methods for measuring sub-pixel alignment . . . 53
3.5 Metrology methods . . . 55
3.5.1 Optical microscopy . . . 55
3.5.2 Scanning Electron Microscopy . . . 56

4 SThM topographic control through the 3ω signal 59
4.1 Introduction . . . 59
4.1.1 Requirements to compete with optical methods . . . 59
4.1.2 Sample-environment thermal interactions . . . 60
4.1.3 Thermal Artefacts . . . 65
4.2 SThM approach curve analysis in air . . . 67
4.3 Experimental design . . . 69
4.3.1 Electrical setup . . . 69
4.3.2 Mechanical and environmental setup . . . 77
4.3.3 Probe movement paths . . . 81
4.3.4 Control software development . . . 87
4.4 Experimental . . . 89
4.4.1 Noise analysis of system . . . 89
4.4.2 Single point measurements . . . 101
4.5 Thermal curves as measure of topography . . . 107
4.5.1 Scanning thermal profiler method . . . 108
4.5.2 Thermal discontinuity . . . 110
4.5.3 Thermal contact limit . . . 110
4.5.4 Ramp through contact . . . 111
4.6 Sensitivity analysis . . . 113
4.6.1 STP method . . . 113
4.6.2 Thermal discontinuity . . . 115
4.6.3 Thermal contact limit . . . 118
4.6.4 Ramp method . . . 121
4.7 Discussion . . . 123

5 Topographic scanning using the 3ω signal in air 126
5.1 Introduction . . . 126
5.2 Silicon flat . . . 128
5.3 Silicon pillar . . . 131
5.4 Step edge . . . 145
5.5 Micro heater . . . 160
5.6 Vertical Cavity Surface Emitting Laser . . . 168
5.7 Vertical probe mounting . . . 176
5.8 Results discussion . . . 186

6 Topographic scanning using the 3ω signal under liquid and in a vacuum 189
6.1 Introduction . . . 189
6.2 Topographic control under liquid . . . 189
6.2.1 Design . . . 190
6.2.2 Noise analysis . . . 192
6.2.3 Curve analysis . . . 198
6.2.4 Topographic noise . . . 203
6.2.5 Silicon pillar . . . 204
6.2.6 Step edge . . . 211
6.3 Topographic control in vacuum . . . 227
6.3.1 Design . . . 229
6.3.2 Noise analysis . . . 233
6.3.3 Curve analysis . . . 239
6.3.4 Topographic noise . . . 241
6.3.5 Silicon pillar . . . 243
6.4 Discussion . . . 247

7 Quantification of EBL alignment 248
7.1 Introduction . . . 248
7.2 New Penrose markers . . . 250
7.3 Current Penrose implementation on EBPG 5200+ . . . 258
7.3.1 Experimental design . . . 258
7.3.2 Results . . . 261
7.4 Split Penrose . . . 267
7.4.1 Experimental design . . . 267
7.4.2 Results . . . 275
7.5 Misaligned gratings . . . 278

7.5.1 Experimental design . . . 278
7.5.2 Results . . . 287
7.6 Discussion . . . 290

8 Development of Co-planar Strain Sensors 292
8.1 Introduction . . . 292
8.2 Model . . . 296
8.3 Design of nano islands . . . 298
8.3.1 Deposition of nano islands . . . 300
8.3.2 Electrode design . . . 304
8.3.3 Inter-electrode nanoisland metalisation . . . 307
8.3.4 Electrical measurement . . . 309
8.4 Direct write two-step lithographic ramp-edge junctions . . . 314
8.4.1 Electrode design . . . 315
8.4.2 Oxidation of 60/40 NiCr . . . 319
8.4.3 Electrical measurement . . . 324
8.5 Discussion . . . 330

9 Final remarks 332
9.1 Conclusions . . . 332
9.2 Further work . . . 334

Appendices 336

A Thermal feedback control flows 336

List of References 341

List of Figures

2.1 Working principle of a surface profiler. 6
2.2 Working principle of a scanning tunnelling microscope 7
2.3 A standard AFM probe design 7
2.4 Working principle of a tunnelling probe 8
2.5 Working principle of an AFM 9
2.6 Working principle of an SThM 16
2.7 KNT probe 18
2.8 KNT probe - Tip 18
2.9 KNT probe schematic 19
2.10 Effect of cantilever geometry on topography output 20
2.11 Effect of sidewall angle of topography output 20
2.12 Burnt KNT probe 21
2.13 STP working principle 23
2.14 Capacitive MEMS displacement sensors 24
2.15 Comb capacitor under bending 25
2.16 Various Capacitive probe designs from the literature 26
2.17 Strain gauge working principle 27
2.18 Piezoresistive probes from the literature 28
2.19 Working principle of quantum tunnelling strain sensors 29
2.20 Multiple tunnel junction ‘islands’ strain sensors 30
2.21 Two barrier orientations for electron tunnelling 31

3.1 Photolithography exposure process 33
3.2 Generalised photolithography process 34
3.3 Photolithography contact exposure types 34
3.4 PMMA undergoing molecular change during EBL exposure 37
3.5 Resist line collapse 38
3.6 Simplified overview of a metal evaporator 39

3.7 Example of a standard additive BL process . . . 41
3.8 Thin Film growth mechanisms . . . 42
3.9 RIE etching process . . . 44
3.10 Example of a standard etch process . . . 45
3.11 Pyramid etching process . . . 46
3.12 Pyramid patterning process . . . 46
3.13 Pyramid SEM Image . . . 47
3.14 Pyramid patterning process . . . 48
3.15 Square marker showing edge defects . . . 50
3.16 Square marker measurement . . . 50
3.17 A 10um Penrose marker . . . 52
3.18 Offset vernier for measuring sub-pixel alignment in EBL . . . 54
3.19 V Fit vernier for measuring sub-pixel alignment in EBL . . . 55
3.20 Electron beam - atomic interactions, origins . . . 57
3.21 Electron beam - atomic interactions, contrast . . . 57

4.1 Schematic of thermal conduction paths in the KNT probe . . . 60
4.2 Electrical equivalent to thermal transfer paths of the SThM . . . 62
4.3 Asymmetries in thermal profiles - Top down . . . 64
4.4 Asymmetries in thermal profiles - cross-sectional view . . . 65
4.5 Double tip contact-induced thermal artefacts . . . 66
4.6 A typical SThM approach curve . . . 68
4.7 Probe thermal resistance model in air . . . 69
4.8 Electrical block diagram of setup . . . 70
4.9 Wheatstone bridge probe electrical setup . . . 72
4.10 Available probe currents for DC probe bias . . . 72
4.11 Available probe dissipated power for DC probe bias . . . 73
4.12 Available probe currents for AC probe bias . . . 74
4.13 Available probe dissipated power for AC probe bias . . . 74
4.14 Diagram of the custom SThM setup . . . 78
4.15 Stage Axis calibration . . . 78
4.16 Photos of SThM setup . . . 79
4.17 Air handling unit effect on topography . . . 81
4.18 Second order Xue window and it's integral . . . 83
4.19 A single Xue path movement . . . 85
4.20 Xue path Simulation . . . 86
4.21 Thermal Topo application overview . . . 88
4.22 Histogram of measurement in and out of contact . . . 90

4.23 Drift in measurement out of contact ambient atmosphere 91
4.24 Drift in measurement in contact 91
4.25 Histogram of measurement in and out of contact N2 atmosphere . . . 93
4.26 Drift in measurement in contact N2 atmosphere 94
4.27 Coefficient of variation out of contact 95
4.28 Coefficient of variation in contact 3ω 95
4.29 Coefficient of variation in contact 1ω 96
4.30 Thermal response of a KNT probe with respect to drive frequency . . 97
4.31 Thermal response of a KNT probe with respect to drive frequency expressed as a fractional change 97
4.32 Bode plot probe thermal response 98
4.33 Coefficient of variation of $3\omega_{out}$ vs probe drive voltage 99
4.34 Coefficient of variation of $3\omega_{in}$ vs probe drive voltage 99
4.35 3ω probe response std dev vs probe drive voltage 100
4.36 3ω probe response vs probe drive voltage 101
4.37 A 3ω approach curve 102
4.38 3ω land and retract curves 102
4.39 Histogram of contact point over 60 land and retract cycles 103
4.40 pull-in point over 60 land and retracts vs oscillator voltage 104
4.41 Change in pull in point with probe voltage 105
4.42 Standard deviation of pull in point with probe voltage 105
4.43 3ω response from repeated land and retracts 106
4.44 3ω response from repeated land and retracts aligned by mean 106
4.45 Diagram of typical approaching probe 107
4.46 Probe thermal resistance model STP 108
4.47 Out of contact 3ω amplitude with sample separation 109
4.48 Thermal discontinuity approach 110
4.49 Thermal contact limit approach 111
4.50 Ramp method for measuring sample topography in 3 acquisition cycles 111
4.51 256-pixel single point scan using STP method 114
4.52 256-pixel single point scan using STP method 115
4.53 256-pixel single point scan using Thermal discontinuity method . . . 116
4.54 256-pixel single point scan using thermal discontinuity method 117
4.55 256-pixel single point scan using Thermal contact limit method . . . 118
4.56 256-pixel single point scan using thermal discontinuity method 119
4.57 256-pixel single point scan using ramp method 121

5.1 Diagram of probe scan and mounting directions 127

5.2 Topographic artefact asymmetries . . . 127
5.3 Comparison of topography outputs . . . 129
5.4 Height distribution of Si flat scans . . . 129
5.5 Images of Si pillar sample . . . 131
5.6 AFM of Si pillar sample - pillar heights . . . 131
5.7 Height distribution of Scan . . . 132
5.8 SThM scan of Si pillar sample . . . 133
5.9 Height distribution of Scan . . . 134
5.10 Height distribution of Scan . . . 135
5.11 Digital zoom of two pillars . . . 136
5.12 Radial measurement of pillar topography . . . 137
5.13 Radial measurement of pillar topography . . . 137
5.14 Radial measurement of pillar topography . . . 138
5.15 Line extract from simultaneous topography and 3ω . . . 139
5.16 Schematic of thermal influences during scanning of silicon pillars . . . 140
5.17 Thermal resistance network of interactions . . . 140
5.18 SThM scan of Si pillar sample STP . . . 142
5.19 SThM scan of 600 nm Si pillars . . . 143
5.20 Radial measurement of 600 nm pillar topography . . . 144
5.21 Line extract from simultaneous topography and 3ω . . . 144
5.22 Example of DektakXT step height measurement . . . 145
5.23 Histogram of repeated DektakXT step height measurements . . . 146
5.24 SThM scan of step edge sample . . . 147
5.25 Good mean profile of Topography channel of step edge . . . 147
5.26 Good mean profile of 3ωchannel of step edge . . . 148
5.27 Histogram of topography channel of step edge . . . 148
5.28 Comparison of landing curve on Au and SiNx . . . 149
5.29 Comparison of out of contact portion of 3ω landing curve . . . 150
5.30 STP scan of step edge at DDSN4 - Topography output . . . 151
5.31 STP scan of step edge at DDSN4 - Good mean profile . . . 151
5.32 STP scan of step edge at DDSN4 - Histogram . . . 152
5.33 SThM scan of step edge sample . . . 153
5.34 Good mean profile of Topography channel of step edge . . . 153
5.35 Histogram of Topography channel of step edge . . . 154
5.36 SThM scan of step edge sample . . . 155
5.37 Line extracted from topography and probe response . . . 156
5.38 Good mean topography profile - Contact limit method in nitrogen . . . 157

5.39 Good mean 3ω probe response profile - Contact limit method in nitrogen 157
5.40 SEM image of gold surface . . . 158
5.41 Height distribution of Step edge scan . . . 159
5.42 Distribution of probe thermal response of Step edge scan . . . 159
5.43 Response distribution probe thermal response of Step edge scan. Split by height . . . 160
5.44 Micro heater optical image . . . 162
5.45 Diagram of Experimental procedure . . . 163
5.46 SThM scanning the heater optical image . . . 163
5.47 Methodology to calculate the effect of temperature on topography scans . . . 164
5.48 Topography temperature relation - Thermal discontinuity method . . . 165
5.49 Topography temperature relation varying heater power - Thermal discontinuity method . . . 165
5.50 Contact limit temperature effect on topography . . . 166
5.51 Topography temperature relation - Thermal limit method . . . 166
5.52 Circuit diagram of VSCEL control electronics . . . 169
5.53 Microscope image of VCSEL scan cavity . . . 169
5.54 Microscope image of probe scanning VCSEL . . . 170
5.55 Topography comparison of . . . 171
5.56 Asymmetric tip convolution with side wall . . . 171
5.57 Thermography of active VCSEL device . . . 173
5.58 Thermography of active VCSEL device . . . 173
5.59 Thermography of active VCSEL device: ΔK map . . . 174
5.60 SThM ω optical output of VCSEL - High/low subtracting LED . . . 175
5.61 SThM ω optical output - VCSEL High subtracting low . . . 175
5.62 Vertically mounted probe schematic . . . 176
5.63 Vertically mounted probe image . . . 177
5.64 Vertically mounted probe approach and retract curve . . . 177
5.65 Vertically mounted probe Step Edge - Thermal discontinuity . . . 178
5.66 Vertically mounted probe Step Edge - Thermal discontinuity extracted line . . . 179
5.67 Vertically mounted probe Step Edge - Thermal discontinuity Topographic histogram . . . 179
5.68 Vertically mounted probe Step Edge - Thermal discontinuity Topographic good mean profile . . . 180

5.69 Vertically mounted probe Step Edge - Thermal discontinuity probe response good mean profile . . . 180
5.70 Vertically mounted probe Step Edge - STP . . . 181
5.71 Vertically mounted probe Step Edge - STP extracted line . . . 181
5.72 Vertically mounted probe Step Edge - STP Topographic histogram . 182
5.73 Vertically mounted probe Step Edge - STP Topographic good mean profile . . . 182
5.74 Vertically mounted probe Step Edge - STP probe response good mean profile . . . 183
5.75 Vertically mounted probe Step Edge - Ramp . . . 184
5.76 Vertically mounted probe Step Edge - Ramp extracted line . . . 184
5.77 Vertically mounted probe Step Edge - Ramp Topographic histogram . 185
5.78 Vertically mounted probe Step Edge - Ramp Topographic good mean profile . . . 185
5.79 Vertically mounted probe Step Edge - Ramp probe response good mean profile . . . 186

6.1 Thermal resistance network in liquid . . . 190
6.2 Diagram of liquid setup . . . 191
6.3 Photo of liquid setup - Top view . . . 191
6.4 Photo of liquid setup - Side view . . . 192
6.5 Histogram of measurement in and out of contact . . . 193
6.6 Drift in contact under liquid . . . 194
6.7 3ω coefficient of variation out of contact . . . 195
6.8 3ω coefficient of variation in contact . . . 195
6.9 3ω coefficient of variation in contact - Reduced set . . . 196
6.10 Probe frequency response in liquid . . . 196
6.11 Probe frequency response in liquid . . . 197
6.12 Probe frequency response in liquid as bode plot . . . 197
6.13 112 Hz landing curve in Flutec PP3 . . . 199
6.14 1 kHz landing curve in Flutec PP3 . . . 200
6.15 1.6 kHz landing curve in Flutec PP3 . . . 201
6.16 112 Hz landing curve in Flutec PP3 - gradient and contact . . . 202
6.17 1 kHz landing curve in Flutec PP3 - gradient and contact . . . 202
6.18 5.5 kHz landing curve in Flutec PP3 - gradient and contact . . . 203
6.19 Single point Topographic noise analysis . . . 203
6.20 Histogram of Figure 6.19a . . . 204
6.21 Silicon Pillar sample under Flutec . . . 205

6.22 Histogram of topography data . . . 205
6.23 Radial measurement of 600 nm pillar topography . . . 206
6.24 Radial measurement of 600 nm pillar topography . . . 206
6.25 Radial measurement of 600 nm pillar topography . . . 207
6.26 Radial measurement of pillar topography . . . 207
6.27 Radial measurement of pillar topography . . . 208
6.28 Radial measurement of 300nm pillar 1 topography . . . 208
6.29 Radial measurement of 300 nm pillar 2 topography . . . 209
6.30 Radial measurement of 300 nm pillar 3 topography . . . 209
6.31 3D image of Si pillar . . . 210
6.32 Schematic of frequency dependency of pillars . . . 211
6.33 Silicon Pillar sample under Flutec . . . 212
6.34 Step edge scan under liquid . . . 213
6.35 3D image of gold step height . . . 213
6.36 Histogram of topography data points in Figure 6.34a . . . 214
6.37 line trace of step edge sample . . . 214
6.38 Good mean profile of topography scan in Figure 6.34a . . . 215
6.39 Good mean profile of 2.24 kHz 3ω scan in Figure 6.34e . . . 215
6.40 Topography channel for step edge sample . . . 216
6.41 Thermometry channels . . . 216
6.42 Double tip contact artefact . . . 217
6.43 Step edge scan under liquid . . . 218
6.44 Histogram of topography data points in Figure 6.43a . . . 219
6.46 Good mean profile of topography scan in Figure 6.43 . . . 219
6.45 line trace of step edge sample . . . 220
6.47 Good mean profile of 2.24 kHz 3ω scan in Figure 6.43d . . . 221
6.48 Histogram of 3ω probe response at 448Hz split my height data . . . 221
6.49 Ridgeline plot of 3ω probe response at various frequencies split my height data . . . 222
6.50 Coefficient of variation of 3ω response at various frequencies split by height data . . . 223
6.51 3ω probe response gradient . . . 223
6.52 In-contact topography and 3ω measurement . . . 224
6.53 In-contact 3ω Good mean profile . . . 224
6.54 Out-of-contact 3ω measurement . . . 225
6.55 Out-of-contact 3ω measurement good mean profiles . . . 226
6.56 Thermal resistance network of vacuum system . . . 228

6.57 Image of the vacuum setup . . . 229
6.58 SEM image of the probe in vacuum system . . . 230
6.59 SEM image of the probe tip in vacuum system . . . 231
6.60 Optical microscope image of the probe in vacuum system . . . 232
6.61 Diagram of probe mounting . . . 233
6.62 Histogram of measurement in and out of contact . . . 234
6.63 Drift in contact under Vacuum . . . 235
6.64 Drift in contact under Vacuum . . . 236
6.65 3ω coefficient of variation out of contact . . . 236
6.66 3ω coefficient of variation in contact . . . 237
6.67 Probe frequency response in vacuum . . . 237
6.68 Probe frequency response in vacuum . . . 238
6.69 Probe frequency response in vacuum as bode plot . . . 238
6.70 112 Hz landing curve in vacuum . . . 239
6.71 112 Hz landing curve in vacuum - Zoomed . . . 240
6.72 3ω gradient approach in vacuum . . . 241
6.73 Topographic drift seen upon startup . . . 242
6.74 Single point Topographic noise analysis . . . 242
6.75 Histogram of topographic data points in Figure 6.74a . . . 243
6.76 Silicon Pillar sample in Vacuum . . . 244
6.77 Silicon Pillar sample in Vacuum . . . 244
6.78 Individual silicon Pillar sample in Vacuum . . . 245
6.79 Line traces of silicon pillar . . . 246
6.80 Diagram showing tip switching artefact . . . 246

7.1 A 9 μm^2 Penrose marker design . . . 249
7.2 A 9 μm^2 Penrose marker microfabricated . . . 249
7.3 Penrose marker designs . . . 251
7.4 Penrose marker dewetting after thermal treatment . . . 253
7.5 Marker fabricated from platinum . . . 253
7.6 Dosage of 8 layer marker . . . 254
7.7 Penrose marker contamination after lift-off . . . 255
7.8 SEM gallery - standard Penrose . . . 256
7.9 SEM gallery - 4 μm^2 Penrose with 6 layers . . . 256
7.10 SEM gallery - 4 μm^2 Penrose with 7 layers . . . 257
7.11 SEM gallery - 4μm^2 Penrose with 8 layers . . . 257
7.12 Set of 6 layer markers with reduced polygon numbers . . . 259
7.13 Polygon removal set 1 . . . 260

7.14 Layout of Penrose remove cell . . . 260
7.15 Violinplot of measured offset from log file analysis . . . 261
7.16 Point plot of measured offset from Set1 . . . 262
7.17 Point plot of measured offset from Set2 . . . 262
7.18 Point plot of measured offset from Set3 . . . 262
7.19 Point plot of measured offset from Set4 . . . 263
7.20 Point plot of measured offset from Set5 . . . 263
7.21 Scatter plot of standard deviation in measurement . . . 264
7.22 Penrose set 3 . . . 265
7.23 Split Penrose . . . 268
7.24 Layout of split Penrose cell . . . 270
7.25 Penrose pattern for testing methodology . . . 271
7.26 Split Penrose Correlation search resolution - one alignment . . . 272
7.27 Penrose pattern for testing methodology . . . 273
7.28 Penrose pattern for testing methodology - Zoom . . . 273
7.29 Split Penrose Correlation search resolution - two alignments . . . 274
7.30 Histogram measure of repeatability . . . 275
7.31 Split Penrose spread of alignment . . . 276
7.32 Split Penrose spread of alignment split by type . . . 277
7.33 Split Penrose Euclidean distance from centre - ridgeline plot . . . 277
7.34 Misaligned grating halves . . . 279
7.35 Misaligned grating cell layout . . . 280
7.36 Fabricated offset vernier showing line-width collapse . . . 280
7.37 Fabricated Offset vernier for measuring sub-pixel alignment in EBL . 281
7.38 Fabricated Offset vernier for measuring sub-pixel alignment in EBL - zoom of Figure 7.37 . . . 282
7.39 Process flow for analysis of grating structures . . . 282
7.40 Analysis grating power spectrum . . . 283
7.41 Overlaid f/2 peak . . . 284
7.42 V-fit to plot of peak f/2 magnitudes vs designed offset . . . 285
7.43 V-fit to the plot of peak f/2 magnitudes vs designed offset - an example to real alignment . . . 286
7.44 Histogram of repeatability measurement . . . 286
7.45 Misaligned gratings spread of alignment . . . 288
7.46 Misaligned gratings spread of alignment split by type . . . 289
7.47 Misaligned gratings Euclidean distance from centre - ridgeline plot . . 289

8.1 Ramp edge tunnel junction . . . 292

8.2 crack junctions . . . 293
8.3 Metal island junctions . . . 294
8.4 Direct write junctions . . . 295
8.5 Energy diagram for an MIM junction . . . 296
8.6 Exponential relationship between transmission coefficient and electrode separations . . . 297
8.7 Tunnelling coefficient change for given cantilever deflections . . . 298
8.8 Fabrication steps of co-planer nanoisland junction device (a) through (d) . . . 300
8.9 Discontinuous Au film on SiNx. . . . 301
8.10 Diagram of core-shell approach using NiCr and Au . . . 301
8.11 SEM images of EBPVD discontinuous NiCr and Au on SiNx substrate, showing Au anchored to NiCr islands. . . . 302
8.12 Result from Core-Shell TMAH release experiment . . . 303
8.13 Thin discontinuous film deposition of NiCr . . . 304
8.14 Dose test result for electrode separation study . . . 306
8.15 Electrode design . . . 307
8.16 SEM imaging of line metallisation dose test . . . 308
8.17 Dose test of thin line lift off . . . 309
8.18 SEM imaging of inter-electrode metalisation. . . . 310
8.19 Failed junction - short circuit . . . 311
8.20 Two failed junctions - open circuit . . . 312
8.21 Failed junction - open circuit . . . 312
8.22 Failed junction - open circuit . . . 313
8.23 Failed junction - short circuit . . . 313
8.24 750 nm electrode separation - open circuit . . . 314
8.25 Fabrication steps of co-planer MIM junction (a) through (e) . . . 315
8.26 Deposition of two electrodes . . . 317
8.27 Deposition of centre electrode . . . 317
8.28 Cross section of junction . . . 318
8.29 SEM images of a single junction showing non-contact of electrodes . . . 319
8.30 SEM images of a single junction showing oxidation of electrode 1 . . . 320
8.31 SEM image of 500 °C Oxidised NiCr surface . . . 321
8.32 SEM image of 700 °C Oxidised NiCr surface . . . 322
8.33 SEM image of 400 °C Oxidised NiCr two junction device . . . 322
8.34 SEM image of 480 °C Oxidised NiCr two junction device . . . 323
8.35 SEM image of 600 °C Oxidised NiCr one junction device . . . 323

8.36 SEM image of 600 °C Oxidised NiCr one junction device 324
8.37 IV curve of 200 °C, 15 minute oxidation junction 325
8.38 IV curve of 300 °C, 15 minute oxidation junction 325
8.39 IV curve of 400 °C, 15 minute oxidation junction 326
8.40 IV curve of 500 °C, 15 minute oxidation junction 326
8.41 Released cantilever beam 328
8.42 200 °C 15 min oxidation 328
8.43 200 °C 15 min oxidation 329
8.44 200 °C 1 hr oxidation 329
8.45 200 °C 1 hr oxidation 330

A.1 STP method flow diagram 337
A.2 Discontinuity method flow diagram 338
A.3 Contact limit method flow diagram 339
A.4 Ramp through contact method flow diagram 340

List of Tables

4.1 Tabulated phase increment versus output frequency of the DDS . . . 76
4.2 Tabulated measurement times available per DDSN 76
4.3 Tabulated statistical results from 1000 measurements of the 1ω and 3ω signals 90
4.4 Measured surface roughness from probe drive frequency 114
4.5 Measured surface roughness from probe drive frequency 115
4.6 Measured surface roughness from probe drive frequency Thermal discontinuity method 116
4.7 Measured surface roughness from step size Thermal discontinuity method 117
4.8 Measured surface characteristics from varying DDSN Thermal discontinuity 118
4.9 Measured surface roughness from probe drive frequency thermal contact limit method 119
4.10 Measured surface roughness from step size thermal contact limit method 120
4.11 Measured surface characteristics from varying DDSN Thermal limit . 120
4.12 Measured surface roughness from drive frequency Ramp method . . . 121
4.13 Measured surface roughness from ramp length Ramp method 122
4.14 Measured surface roughness from ramp time Ramp method 123

5.1 Comparison of topography output from custom SThM and commercial AFM, table of statistical quantities 129
5.2 Silicon pillar distribution fitting parameters 132
5.3 Silicon pillar distribution fitting parameters in Figure 5.9 134
5.4 Silicon pillar distribution fitting parameters in Figure 5.10 135
5.5 Tabulated results of radially averaged pillar heights 138
5.6 Table of available VCSEL states 168

6.1 Tabulated statistical results from 1000 measurements of the 1ω and 3ω signals . . . 193
6.2 Tabulated results of terrace fitting to radially averaged 600 nm pillars 207
6.3 Tabulated results of terrace fitting to radially averaged 300 nm pillars 210
6.4 Tabulated statistical results from 250 measurements of the 1ω and 3ω signals . . . 235

7.1 Penrose patterns fabrication steps . . . 252
7.2 Penrose patterns and their associated abbreviations . . . 254
7.3 Penrose set 2,3, and 4 compared . . . 266
7.4 split Penrose patterns fabrication steps . . . 269

8.1 Electrode fabrication steps . . . 305
8.2 Ramp-style MIM fabrication steps . . . 316
8.3 Tabulated results of junction repeatability . . . 327

Introduction

The work undertaken in this thesis concerns advancements in laser-free topographic control of the scanning thermal microscope (SThM). Typically the optical lever, or 'beam bounce', method is used to maintain consistent tip-sample contact allowing for thermometry measurements to be taken. The optical lever technique has been synonymous with atomic force microscope (AFM) techniques since its incorporation into the AFM system in the late 1980s[1]. The use of the laser in an SThM system has been reported to be the critical contributor to thermometry errors, this has been reported to be up to 37%[2], and the cause of a large reduction in measurement repeatability[3, 4]. Laser-induced heating of the probe can also cause alterations in AFM probe stiffness, leading to errors in the topography[5]. Laser positioning on the cantilever body can also produce topography errors on thermally active samples by up to 250%. This is due to the thermally induced bend of the bi-material probes commonly used in SThM studies[6, 7]. At the very least, accurate laser positioning on the cantilever is needed to minimise measurement variability caused by these effects, requiring highly skilled tool operators. The temperature rise from the laser also depends strongly on the position of the laser on the cantilever, since heat is largely dissipated through thermal conduction through the cantilever. As a result, the calibration of the SThM as a thermometer will change every time the beam deflection laser is adjusted. In short, the use of a laser to measure topography in SThM is undesirable as it induces a change in the overall thermal and mechanical configuration of the microscope (which is neither constant nor geometrically stable). Although careful operation can help achieve consistent data, these errors can only be eradicated by the complete removal of the laser itself from the SThM system.

Ramiandrisoa et al. [2] and Spiece et al. [3] proposed solutions to this problem by first landing the SThM probe with the laser on, before turning off the laser and conducting thermometry measurements of the surface. However, these solutions

are only suitable for single-point measurements and do not provide for the three-dimensional simultaneous thermal and topographic mapping of a sample surface, a key feature for accurate surface characterisation through AFM techniques.

This thesis looks to explore avenues of topographic control of the SThM that would permit three-dimensional AFM-like scanning of surfaces without the use of the optical lever. Two possible solutions to this problem have been investigated. The first investigated method is based on "thermal feedback" of the available SThM signals for the determination of tip-sample contact in space. This required the creation of a custom SThM setup to allow raster scanning of samples. The second is the integration of novel microfabricated self-deflection sensing elements based on the tunnel effect into the SThM cantilever body. This required studies into the feasibility of modifying current SThM probe designs to incorporate suitably sensitive self-sensing elements. As part of this, investigations into overlay alignment capabilities in the James Watt nanofabrication centre (JWNC) were required to improve yield of microfabricated devices.

1.1 Research goals

- Investigate high sensitivity strain sensing elements in the available literature for sensing the deflection of micro cantilevers.
- Develop a custom SThM setup allowing for complete mechanical and electrical control of the probe and stage.
- Investigate the feasibility of using existing thermal signals from the SThM as a means of "thermal feedback" to gain topographical control of the SThM.
- Quantify the noise levels in the system and optimise for best performance.
- Demonstrate the ability of the system to measure thermometry and topography accurately in three environmental domains; in air, under liquid, and in a vacuum.
- Improve the electron beam lithography alignment capabilities of the JWNC lab through novel iterations of the Penrose marker.
- Develop high gauge factor strain sensing elements using standard SThM cantilever fabrication processes compatible materials and techniques.

1.2 Thesis structure

This thesis is organised into 9 chapters. Each chapter will provide a brief introduction to the chapter with reasoning and motivation behind the work carried out.

Chapter 2 looks to provide a brief contextual history of SThM and an explanation of its working principles. It will also provide a review of the available literature surrounding the outlined research goals and techniques used in this work.

Chapter 3 will present the methods used throughout this work in the microfabrication of samples used for SThM scanning, as well as for Penrose markers and developed strain-sensing elements in later chapters.

Chapter 4 describes the development of instrumentation for the topographic control of SThM using thermal feedback electronics. Analysis of system noise and sensitivity will be provided. Control of tip-sample contact is discussed through analysis of the thermal approach curve of the SThM. Various methodologies for topographic thermal feedback control will be presented, implemented, and characterised for single-point measurements.

Chapter 5 uses the techniques in Chapter 4 to perform three-dimensional raster scanning of samples without the use of the optical lever in an air environment. A variety of fabricated and commercial samples are scanned to analyse each methodology's response to topographic, material, and thermal changes.

Chapter 6 continues this analysis, presenting similar studies carried out under liquid and vacuum environmental conditions. First, the noise levels in each environment will be quantified for the purposes of optimisation of the scanning conditions required, before analysing scans acquired on topographic and thin film samples.

Chapter 7 presents a study into the current electron beam lithography alignment capabilities in the JWNC, with the aim of improving upon the available overlay accuracy through novel iterations of the Penrose marker. Automation of high-accuracy overlay metrology has been developed as a means to increase the repeatability of measurement of these structures.

Chapter 8 presents a study into the fabrication of high-sensitivity strain gauges based on the electron tunnelling probability of mechanically deformed tunnel junctions, along with the challenges associated with incorporating such elements using standard SThM fabrication-compatible techniques.

Chapter 9 will then discuss the overall outcomes of work carried out in this thesis, before looking to discuss possible further avenues of research to further extend and improve upon laser-free scanning in SThM.

Literature Review

This chapter looks to provide a brief history of the evolution of microscopy over the years and the context in which SThM sits within the field. This chapter also looks to collate and review the current state of literature available concerning the work carried out in this thesis.

Firstly, the evolution of scanning probe techniques leading up to the atomic force microscope will be presented. This will feed into a discussion regarding thermal measurements at the micro and nano scale. Combining scanning probe techniques and the pursuit of higher resolution thermal imaging requirements leads to discussions on thermally functionalised atomic force microscopy. Detrimental influences of the laser in the optical lever lead to the requirement of self-deflection sensing of the SThM compliant structures and as such, a discussion on alternative height control systems is then presented.

2.1 Evolution of microscopy

Microscopy has been used in the labs of many scientists and engineers over the last two centuries to try to understand the properties of materials and samples on the micro-scale. However, the development of optical microscopy had reached its resolution limit by the late 1880's [8]. Abbe [9] explained that this limit was fundamentally due to the use of visible light, which cannot easily resolve features lower than 200 nm without the use of interferometric techniques [10]. The push for higher-resolution microscopy led to the invention of the electron microscope by Knoll and Ruska at the Technical University of Berlin [11] in 1931. Electron microscopy soon became widely adopted and further developments of the electron microscope eventually pushed the microscopy resolution limit down to 1 nm by 1990. Soon after the electron microscope, the first scanning transmission electron microscope

(STEM) was invented by Ardenne [12], and by the 1990s atomic resolution of less than 2Å had been achieved by Shin et al. [13] of some materials using annular dark field (ADF) imaging modes. The desire to understand the micro and nano world in greater detail has pushed scientists and engineers to develop techniques to image, quantitatively measure, and characterise the various phenomena that occur on these length scales.

2.1.1 Scanning Probe Microscopy (SPM)

Scanning probe microscopy (SPM) techniques have become a widespread microscopy tool in the labs of many scientists. From the mid-20th century, mechanical profilers have been utilised for measuring the roughness of surfaces or the heights of topographic elements on a given surface. These instruments typically to use sharp, diamond-tipped styli to trace over a surface while recording its deflection to extract the surface profile. The working principle and image of a stylus profiler can be viewed in Figure 2.1. However, due to requirement of stylus contact with the sample surface, soft materials can easily be damaged or scratched by the stylus. Contamination pickup by the probe can also vastly reduce the resolution of this technique.

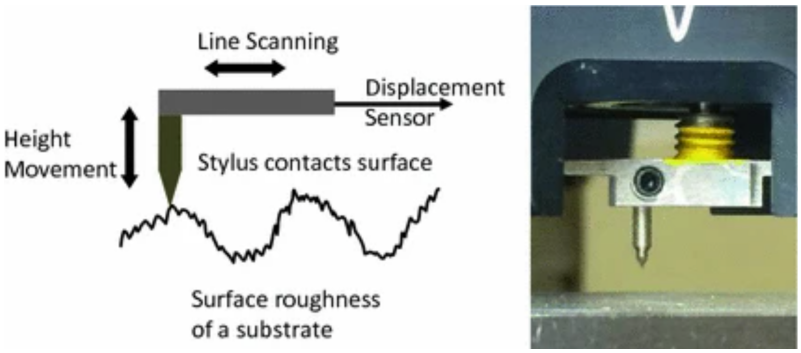


Figure 2.1: Working principle and photograph of a surface profiler. A sharp stylus is placed in contact with the sample surface, it is then scanned along the surface recording its displacement. (From [14])

2.1.2 Scanning tunnelling microscope (STM)

To address limitations of contact measurements, Binnig and Rohrer invented the scanning tunnelling microscope (STM) at IBM in the early 1980s [15], atomic resolution had been achieved for the first time. The schematic of their microscope is shown in Figure 2.2. Their invention led to them being awarded the 1986 Nobel Prize for physics along with Ruska. STMs function by scanning a sharp probe in near contact with a sample surface, while the tunnelling current between the sample and

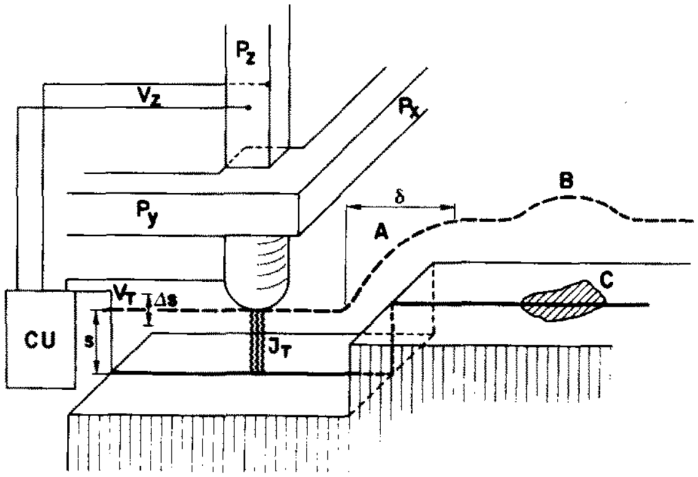


Figure 2.2: Working principle of the scanning tunnelling microscope. Piezo actuators (P_x,P_y,P_z) are used to position a sharp probe above the sample surface within electron tunnelling distance (s). The actuators are then used to raster scan the probe tip across the sample (Dashed line). Contamination on the sample surface at C causes a change in the tunnelling current (J_T) and therefore erroneous topography measurement (B). (From Binnig and Rohrer [15])

the probe is measured (J_T in Figure 2.2), providing resolution down to the atomic scale. SPM and its derivative techniques provided not only atomic-scale images of surfaces but provided quantitative measurements of the atomic interactions of the probe and sample. However, there were still many limitations associated with STM, such as its high sensitivity to contamination, only being able to scan conductive samples, and usually requiring operation in vacuum environments [16].

2.1.3 Atomic Force Microscopy (AFM)

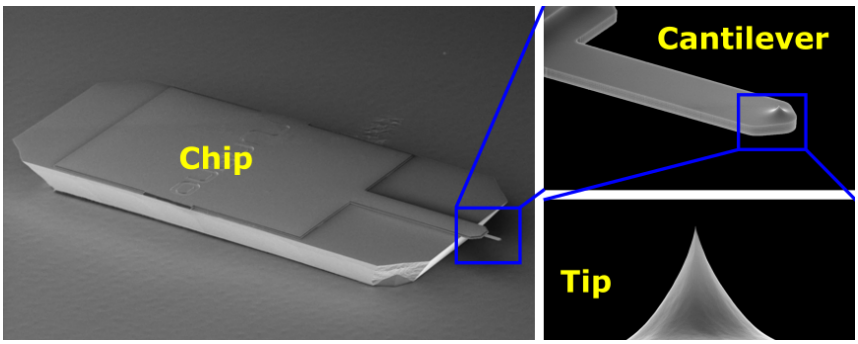


Figure 2.3: A modern AFM probe with a conical tip placed at the extremity of a microcantilever. The cantilever is placed at the end of the chip body, allowing the AFM probe to be handled and attached to a probe holder. (from [17]).

Soon after the invention of STM, Binnig and Rohrer invented Atomic Force Microscope (AFM) in 1986 [19]. The AFM consists of a sharp tip on the free end of

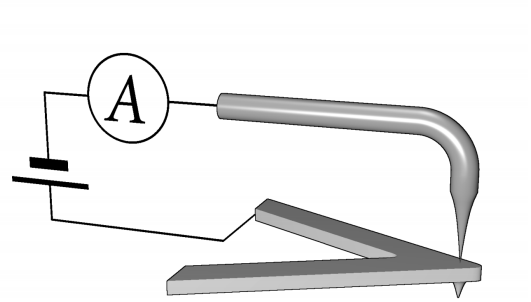


Figure 2.4: Tunneling probe, showing an STM probe detecting the vertical deflections of the AFM cantilever below it. (From [18])

a cantilevered beam as seen in Figure 2.3. It uses piezoelectric actuators to move the tip across a sample while measuring the forces seen by the cantilever. The original AFM probe design by Binnig and Rohrer used an STM to measure the deflection of a conductive cantilever (Figure 2.4). This opened up the possibility to scan non-conductive samples. However, the technique still suffered from similar constraints as the classical STM technique, as the probes had a high sensitivity to surface contamination and required vacuum scanning conditions [19]. To overcome the limitations imposed by of using the STM to measure the cantilever deflections alternative techniques were required, the most common of which today is the optical lever. [20]

The optical lever was first incorporated into AFM systems by Meyer and Amer [1] in 1989. It works on the principle that a laser is reflected off the cantilever surface onto a position-sensitive photodetector, its angle of incidence will change for a given cantilever deflection and the laser spot will move on the photodetector as in Figure 2.5. Cantilever motion due to tip-sample interactions can be recorded by the movement of the reflected laser on the quadrant detector. Sample topography or the measurement of tip-sample forces is recorded by measuring the piezo actuator control signals needed to maintain a constant force on the probe. This technique allows for inexpensive, high-resolution topography measurements to be taken. However, highly skilled operators are required to obtain reliable results, as lengthy setup processes and frequent laser alignment are common drawbacks of this technique. Some samples also exhibit light-sensitive behaviour that cannot be reliably measured via the optical beam method, in particular, active semiconductor materials that are sensitive to photo-electric effects as well as highly reflective metrological samples that produce imaging artefacts due to stray light reflected by the sample surface [21].

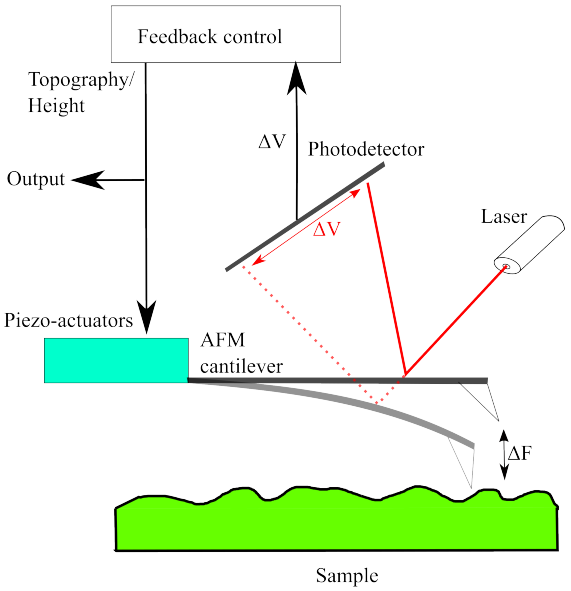


Figure 2.5: Diagram depicting the typical operating principle of AFM, deflection of the cantilever is read out using the optical lever technique, where a laser is reflected off the cantilever surface and aimed at a quadrant photodetector. Any movement of the spot on the photodetector can be read as a deflection of the cantilever due to tip-sample attractive forces.

There are three primary modes in which the AFM can operate; contact, non-contact, and tapping mode. In contact mode, the tip is placed in contact with the sample surface and scanned. Physical forces such as mechanical contact, Van der Waals, and electrostatic forces between the tip and sample can be measured through the deflection of the cantilever according to Hooke's Law ($F = -kx$). This deflection signal is then fed into a feedback loop to keep the probe at a constant force against sample. The deflection is monitored while scanning and reconstructed to provide topographical measurements of the sample. To get the best sensitivity, the most deflection for a given force is required, therefore scanning is best performed with a soft cantilever with a low spring constant. However, at the same time, a high resonance frequency (stiff cantilever) is required to minimise noise from the environment [19]. In contact mode, the tip dragging along the surface can cause a significant shear force. This can cause damage to the probe and sample, as well as possibly picking up contamination which can result in imaging artefacts [22].

In non-contact mode, the cantilever is held at a fixed distance above the sample surface and oscillates at, or near, its resonance frequency. As the probe is brought into near contact with the surface, near field attractive forces induce phase and amplitude shifts in the cantilever resonance. Monitoring of these signals in a feedback loop allow for the reconstruction of the sample topography. This removes the shear

force from dragging the tip along the sample surface and significantly reduces tip wear and sample damage. However, this technique is difficult to use in liquid [22]. In contrast, Tapping mode is a hybrid of contact and non-contact AFM, as reflected in its alternative name 'Intermittent contact'. The tip is oscillated above the sample surface and intermittently brought into contact on the peaks of each oscillation; this takes the best aspects of the other two modes. Reduced contact with the sample significantly reduces the shear force as well as contact with the sample also allows for its use in liquids [22].

In any mode of AFM operation, the deflection mechanics of the cantilever must be accurately known. Many micro-cantilever deflection measuring systems have been developed over the years in an attempt to achieve higher-resolution results.

In addition to advanced detection of cantilever deflection, another area of innovation within the field of AFM is the development of functionalisation of the AFM. Functionalisation of the AFM comes in the form of creating integrated sensors on the tips of the AFM probes, allowing more than just mechanical properties of a sample to be measured. These types of sensors can include, but are not limited to: electrical (KPFM), optical (SNOM), electro-chemical (EC-AFM), capacitive (SCM), and thermal (SThM). With this work particularly concerned with thermally functionalised probes.

2.1.4 Functionalised SPM

The functionalisation of SPM techniques has been explored by many scientists since the invention of the STM by Binning and Rohrer, with the goal of acquiring simultaneous combinations of data, such as combined topographic - electrical/thermal, opening up many other avenues of exploration of materials or microdevices. In particular, these measurements can be crucial to the semiconductor research industry for the electrical evaluation of device designs and/or exploring new materials for the thermal management of next-generation silicon chips, a critical consideration as transistor densities of silicon chips increase according to Moor's law.

2.2 Thermal measurements at the micro-scale

Within the general field of micro-scale metrology, many techniques have been proposed for the measurement of thermal properties. These can be categorised into either optical or electrical techniques. Optical techniques utilise thermal radiation

or scattering of light on a surface to infer thermal properties. Such methods include infrared thermography, thermoreflectance, and Raman scattering, and allow non-contact and non-destructive thermal measurements to be taken. However, optical techniques tend to lack spatial resolution or have poor sample compatibility. Electrical thermal characterisation techniques measure resistances or voltages to determine material thermal properties. Examples include thermovoltaic and resistance thermometers (RTDs). Such sensors mostly have to be placed in contact with or close to contact with the sample being measured. This comes with access requirements that may not be easily available. However, if implemented correctly, they allow greater spatial resolutions over optical techniques.

2.2.1 Optical methods

Infrared Thermography

Infrared thermography is a well-established commercial technique for the remote measurement of the temperature of a given sample surface. It uses the principle of Planck blackbody emission [23, 24], where the spectral radiance of a body is a function of its temperature and can be expressed through Plank's law. A blackbody can be described as an idealised body that has an emissivity of 1, i.e a body that absorbs all incident electromagnetic radiation and emits a spectrum determined by its temperature alone.

However, the concept of a blackbody is purely an idealisation, and cannot exist in nature [24]. Therefore, the blackbody assumption does not hold true during quantitative measurement of surfaces of many materials, and prior knowledge of a material's emissivity is required. As all bodies with non-zero temperatures emit thermal radiation, it can be difficult to abstract the measurand from other background sources of thermal radiation without careful setup. In addition, the long wavelengths of thermal radiation (infrared region) emitted by all but the hottest surfaces limit the spatial resolution of this technique according to the Rayleigh criterion (discussed later in Eq 3.1 in section 3.1 - page 35) to around 10 µm [25]. However, this technique has the advantage of being a purely passive and inexpensive measurement as no sample excitation is required to measure its temperature.

Thermoreflectance

The probability of a photon either reflecting, absorbing or transmitting when it impinges on a surface is known as the material's reflectivity. It has been found that

the reflectivity of a material is weakly dependent on its temperature [26]. Scanning a monochromatic laser across a surface and measuring the reflectivity of the sample surface allows accurate thermometry measurements to be taken, with measurements as low as 10 mK achievable with spatial resolutions of around 100 nm as shown by Lüerßen et al. [27]. Inaccuracies can arise from textures/topography on a sample surface. Thin films, either from contamination or intentionally deposited thin films, can cause significant interference with the light, and small errors in the measurement of high reflectance metals that cause large uncertainties [28].

Raman scattering

Raman spectroscopy examines photon-phonon inelastic scattering in a crystal structure. Incident photons scattering by phonons in a crystal shifts the energies of out scattered photons, showing a spectral shift [29, 30]. This inelastic scattering phenomenon has been shown to have a temperature dependent probability and therefore can be used as a thermometry method by measuring this spectral shift [31]. However, the Raman signal that is emitted is only a small fraction of the overall scattered photons, as the majority of scattered photons occur through elastic Rayleigh scattering where scattered photons have the same energies as incident photons. Despite the small signal, temperature resolutions of around 100 mK are readily available with laser spot size limiting the spatial resolution, with Brugger and Epperlein [32] showing resolutions lower than 1 µm.

However, the acquisition of thermal properties using the Raman spectroscopy is slow and can be around 0.5 s per acquisition point [25], as well as suffering from inaccuracies that can arise due to any mechanical strain or thermal expansion of the materials investigated [33].

Although optical methods can be used to measure thermal phenomena, they either suffer from poor resolution, slow acquisition times, or exhibit large measurement uncertainties which make them difficult to use in a quantifiable manner.

2.2.2 Electrical methods

Electrical methods to measure temperature typically involve sensors that change their electrical properties in response to temperature variations. These sensors can either exist as patterned sensors directly on a sample surface where measurement is required or as a discrete free sensor placed in direct contact with the surface to be measured. An example of the former can be integrated temperature sensors

on microfabricated silicon chips to monitor and manage thermal heat spots. An example of the latter can a thermometer used by a medical professional to monitor the temperature of a patient.

Thermocouples

Thermocouples are commonly utilised for the measurement of temperature. It is an inexpensive and simple approach based on the Seebeck effect, which describes the migration of electrons along a conductor due to a temperature gradient. Every material has a unique Seebeck coefficient, meaning that differing materials will display a different voltage gradient in response to the same temperature gradient [34–36]. To create a thermocouple, two lengths of dissimilar materials are joined together at a junction (the thermocouple junction) and are forced to the same electric potential. The free ends of each conductor will then show non-equal potentials as a result of the difference in their Seebeck coefficient [36, 37]. The generated potential difference can then be measured which will be proportional to the temperature of the junction and the difference in the Seebeck coefficient and is typically measured in µV/K [36]. For the highest sensitivity, thermocouples should be created with materials with a large difference in their Seebeck coefficient [38].

Resistive

Resistance thermometers (RTDs) operate on the principle that many materials exhibit a temperature coefficient of resistance (TCR), meaning that the resistance of a length of material will change proportionally to the temperature of the resistor itself [39]. Materials can either show a positive TCR, such as platinum, palladium, gold and many other metals, or a negative TCR, such as silicon, germanium, and other semiconductor materials.

The interaction of electron flow and the thermal vibrations associated with phonons is the primary driver for materials exhibiting a positive TCR. The increase in thermal vibration caused by the increase in temperature increases the probability of electron-phonon collisions, reducing the mean free path of the electron and resulting in increased electrical resistance. This resistance change is generally linear with temperature [36]. Platinum is particularly useful as an RTD as it can be made pure, remain stable, and not oxidise easily. It also has a very high melting point of over 1700 °C with an operating range between 10-1200 K. Platinum RTDs also show a far higher sensitivity than thermocouple junctions with measurements typically around 3.75-4 mΩ/K [36]. Due to their simplicity and compatibility with semiconductor

fabrication techniques, RTDs are a popular approach to thermal monitoring and characterisation of integrated circuits.

In the case of negative TCR materials, as in semiconductor materials, electrons are excited from the valence to conduction band as temperature increases. This increases the available charge carriers and lowers the overall electrical resistance of the material. However, this temperature-dependent effect is highly nonlinear and has narrower operating temperatures, typically between −100 and 150 °C [36]. Their low cost makes them an attractive choice for low-accuracy applications.

Joule heating

Biasing an RTD above a threshold current will induce Joule heating in the resistive elements [40]. This is where electron bombardment of the atomic lattice increases phonon generation and thus increases its temperature. This allows for RTDs to be used as a heat source by controlling the current through its resistive elements, allowing it to be both a heat generation and measurement element. This can be a particularly useful method for measuring the thermal conductance of materials. One can heat the device to a set temperature by passing current through the sensor before bringing the sensor into contact with a surface. Monitoring the change in resistance upon contact can then be used as a measurement of the efficiency of heat abstraction by the sample. However, simple DC current passing through the device can lead to inaccuracies in the measurement. If the sample and sensor are at the same absolute temperature, there will be no thermal transfer upon contact and no induced change in resistance.

An advanced method to address this issue is through the three-omega (3ω) technique and is commonly used in the thermal measurement of materials [41–46]. It allows for accurate measurements, not just of a sample's absolute temperature, but also of the thermal conductance of materials. It uses a thermally resistive sensor element driven by a sinusoidal current (AC) of the form $I = cos(\omega t)$.

Due to Joule heating, the probe temperature will oscillate at 2ω as $P = I^2R$. and its change in temperature (ΔT) can be expressed as the sum of the steady state temperature (T_{rms}) of the element and this 2ω oscillation as seen in Eq 2.1.

$$\Delta T(t) = T_{rms} + T_{2\omega} \cdot \cos(2\omega t + \phi_{2\omega}) \qquad \text{(Eq 2.1)}$$

A phase delay, $\phi_{2\omega}$, must be added to account for the delay in the thermal response of the sensing element. The sensor will exhibit some temperature coefficient of

resistance and will vary as $R(T) = R_0(1 + \alpha T)$, where R_0 is the resistance of the element at a reference temperature, and α is the first order temperature coefficient. This can assumed to be linear for moderate changes in temperature ($\alpha T \ll 1$). A general expression for the resistance of the sensing element can then be expressed as Eq 2.2.

$$R(t) = R_0 + R_{rms} + R_{2\omega} \cdot \cos(2\omega t + \phi_{2\omega}) \quad \text{(Eq 2.2)}$$

where R_{rms} is the resistance change due to T_{rms}. Using Ohm's law and the definition of resistance from Eq 2.2, the voltage with respect to time across the sensing element,$V(t)$, can be expressed as Equation Eq 2.3.

$$V(t) = (R_0 + R_{rms})I \cdot \cos(\omega t) + \frac{R_{2\omega}I}{2} \cdot \cos(\omega t + \phi_{2\omega}) + \frac{R_{2\omega}I}{2} \cdot \cos(3\omega t + \phi_{2\omega}) \quad \text{(Eq 2.3)}$$

It can be seen that the signal $V(t)$ at ω has a dependence on R_{rms}, and ultimately T_{rms}. Whereas the signal at 3ω only depends on the resistance change due to joule heating, $R_{2\omega}$. Therefore, the third harmonic signal can be used as a method for measuring the temperature change of thermal fluctuations created by the heater itself, without respect to any electrical drift in R_0.

When such RTD sensors are patterned onto device surfaces they are limited to a static thermal measurement at the point that get are patterned. This may be all that is required in some cases such as for the thermal measurement of known hotspots on a fabricated silicon chip. However, the ability to combine the high thermal sensitivity of RTDs and SPM techniques to precisely position a thermal probe at will on any point of a sample surface provides an attractive metrological capability for material studies [43].

2.3 Scanning Thermal Microscopy (SThM)

Scanning Thermal Microscopy (SThM) has emerged as a powerful tool for investigating thermal properties at the nanoscale. A schematic of a typical setup in SThM is available in Figure 2.6. Most SThM setups make use of the popular beam bounce optical lever for topographic control during sample scanning as in normal AFM operation. Other techniques of deflection sensing of the cantilever exist such as pla-

cing the probe on a quartz tuning fork [47], but such techniques require the creation of stiffer hand-crafted tips, leading to potential issues of measurement repeatability.

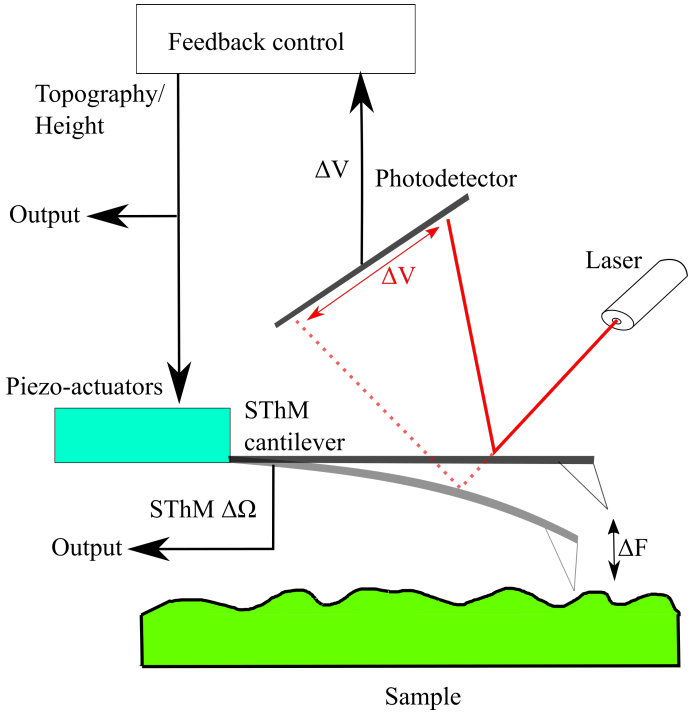


Figure 2.6: Diagram depicting the typical operating principle of the SThM, deflection of the cantilever is still read out using the optical lever technique. But additional signals from a temperature dependant resistor located at the extremity of the tip are also recorded

Two main categories of probes can be utilised for SThM measurements: thermocouple and resistive. The spatial resolution of probes is limited only by the interaction area of the sensor and the sample [48].

Thermocouple

As discussed earlier, the electrical properties of thermocouples can be utilised for highly localised temperature measurements. Mills [49] fabricated thermocouple junctions on the apex of an AFM cantilever, temperature fluctuations at the tip can be monitored through the small voltage that will appear across the junction due to the Seeback effect. SThM thermocouple junctions that have been reported include gold-palladium [49], gold-chromium [50] and gold-platinum [51]. Such probes, however, show poor sensitivity compared to resistive probes and careful consideration of the compatibility of materials and fabrication steps must be taken to ensure adhesion of the materials across the junction as well as to the substrate. Materials such as gold and platinum typically require the deposition of adhesion layers before the target

metal as will be discussed later in section 3.3.1. This adhesion layer may not be compatible with the thermocouple junction limiting material choices of thermocouple junctions.

Resistive probes

Resistive probes in the literature can be divided into two types; thin metal resistive probes and doped silicon probes.

Doped silicon probes can be created by connecting two highly doped, low-resistance silicon legs and a low-doped, high-resistance silicon area near the AFM tip. An example of such a probe is the NanoTA-200[1]. Passing current through the legs results in joule heating of the tip. Although sharp tips (≈10 nm) can be created using traditional AFM cantilever fabrication techniques showing that these probes will have a high topographic spatial resolution, these types of probes have a low thermal spatial resolution and response time as the heater is recessed from the tip with high contact thermal resistances from the sharp tip. Doped silicon probes can also sustain relatively high-temperature operating conditions with the NanoTA-200 probe having a manufacturer-stated reliability up to 350 °C.

Thin metal film resistive probes offer greater thermal spatial resolution and faster response times. They consist of palladium resistors at the tip extremity allowing direct contact of the heated element with the sample and operation in ambient conditions. An example of such probes is the commercially available Kelvin Nanotechnology thermosensitive probe[2] (KNT-SThM-2an) as seen in Figure 2.7 and 2.8, and schematically in Figure 2.9, this probe type is hereon in referred to the KNT, or KNT-SThM probe, and are a popular choice within the SThM community [2, 3, 6, 52–61]. These probes are the main probe types used in this work. Other materials, such as platinum [62], can also be used as the tip resistor.

[1] https://www.brukerafmprobes.com/p-3699-vita-mm-nanota-200.aspx
[2] https://kntnano.com/probes

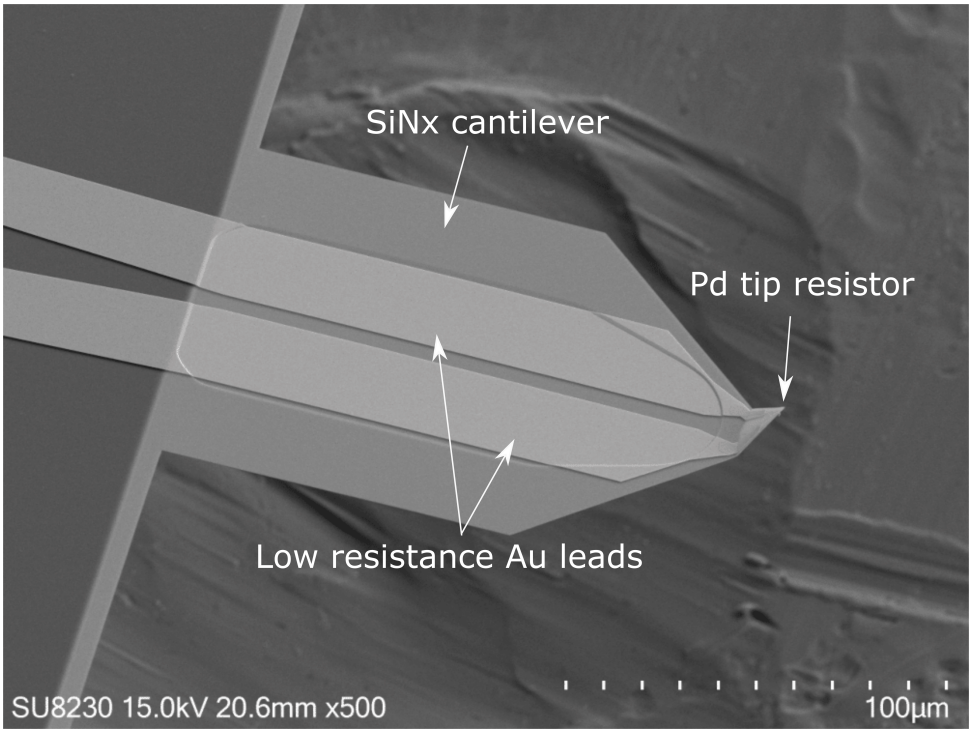


Figure 2.7: A SEM image of the KNT probe. A thin film palladium resistor at the probe apex, allows for high-resolution thermal characterisation of samples.

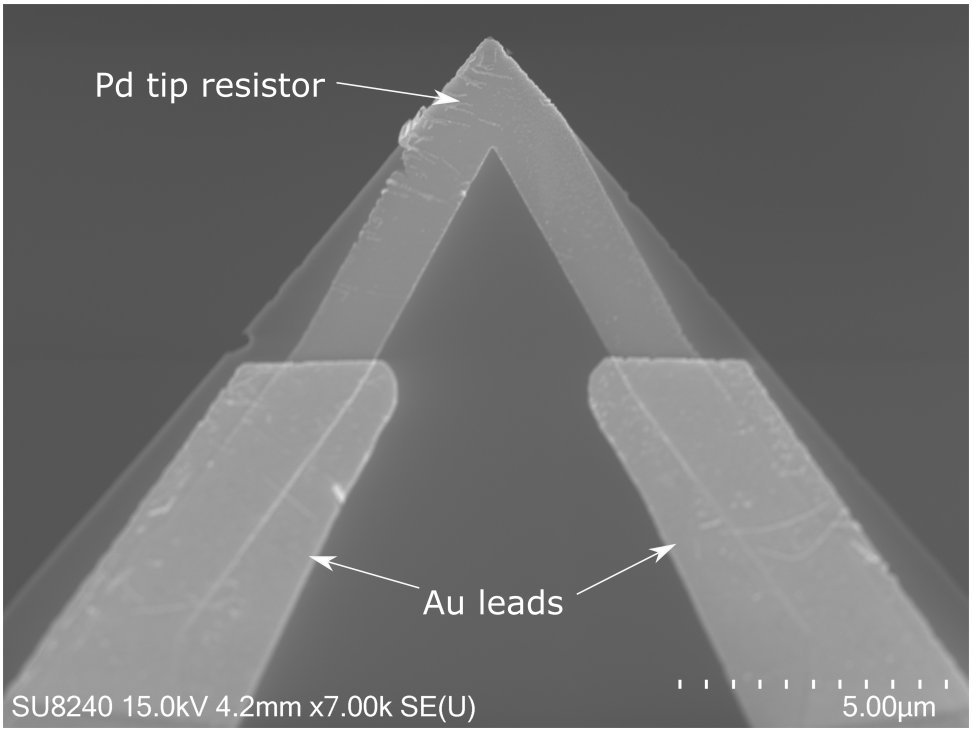


Figure 2.8: A SEM image of the KNT probe tip. The thin film palladium resistor can be seen at the probe apex.

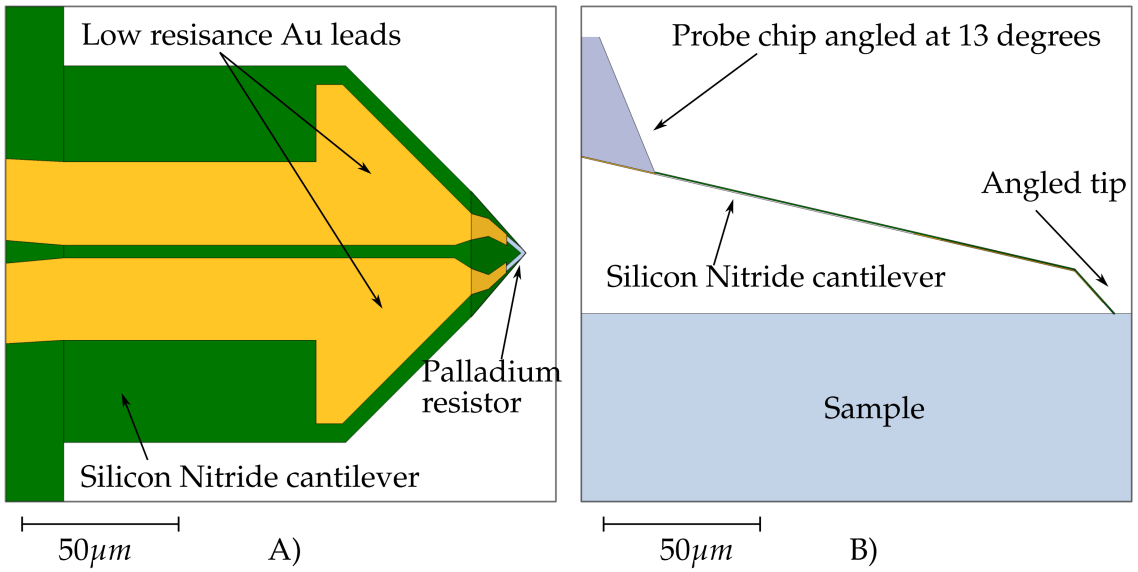


Figure 2.9: Schematic of the KNT probe showing A) a top-down view of the probe, showing the relatively wide cantilever body and tip angle. B) a side view of the probe scanning a sample, the extremity of the tip is angled and nominally makes contact with the sample between 50°-60°. (from ref. [63])

It has been shown by Tovee et al. [54] and Ge [62] that KNT probes have an interaction area of approximately 50 nm. Although this higher tip radius shows that topographic spatial resolution will be lower than doped silicon probes, they offer a high thermal spatial resolution [64]. The rest of the probe geometry and angle also affect the topographic resolution and have been schematically shown in Figure 2.10. To make matters worse, the tip of the KNT probe has a relatively wide sidewall angle in one axis which makes access to trenches and a measurement of sidewalls on the wide axis difficult. This has again been shown schematically in Figure 2.11, and is also visible in the SEM image in Figure 2.8.

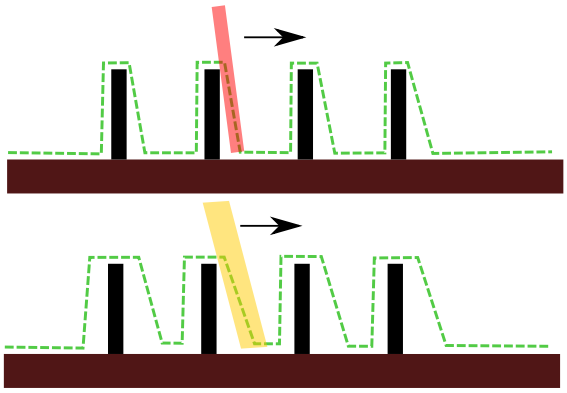


Figure 2.10: Schematic showing the effect of cantilever geometry (cantilever thickness) on an AFM measurement of topographic pillars (black) with an angled probe. A tip with a thin geometry (red - top) shows a greater spatially resolved topographic output (green) than a relatively larger thickness (yellow - bottom). Depending on the angle of the probe tip to the sample there may be an asymmetric profile to the pillars. This can occur due to the angle of contact in the probe design, or from uneven loading of the sample into the AFM.

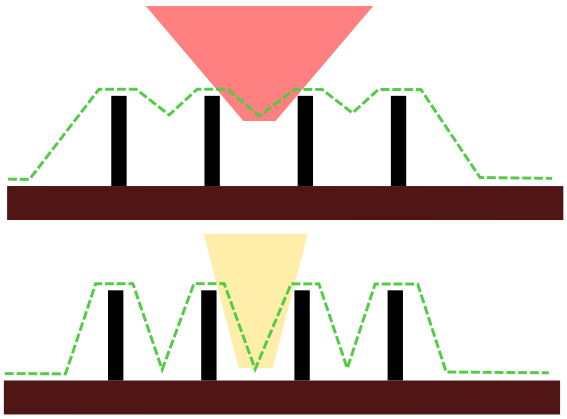


Figure 2.11: Schematic showing the effect of tip sidewall angle on an AFM measurement of topographic pillars. Tips that have a wide opening angle (red - top) won't be able to reach as far into the areas between the pillars, compared to a tip with a narrower opening angle to the tip (yellow - bottom). Although both probes have the same tip radius, the narrower opening angle of the bottom tip shows better topographic resolution.

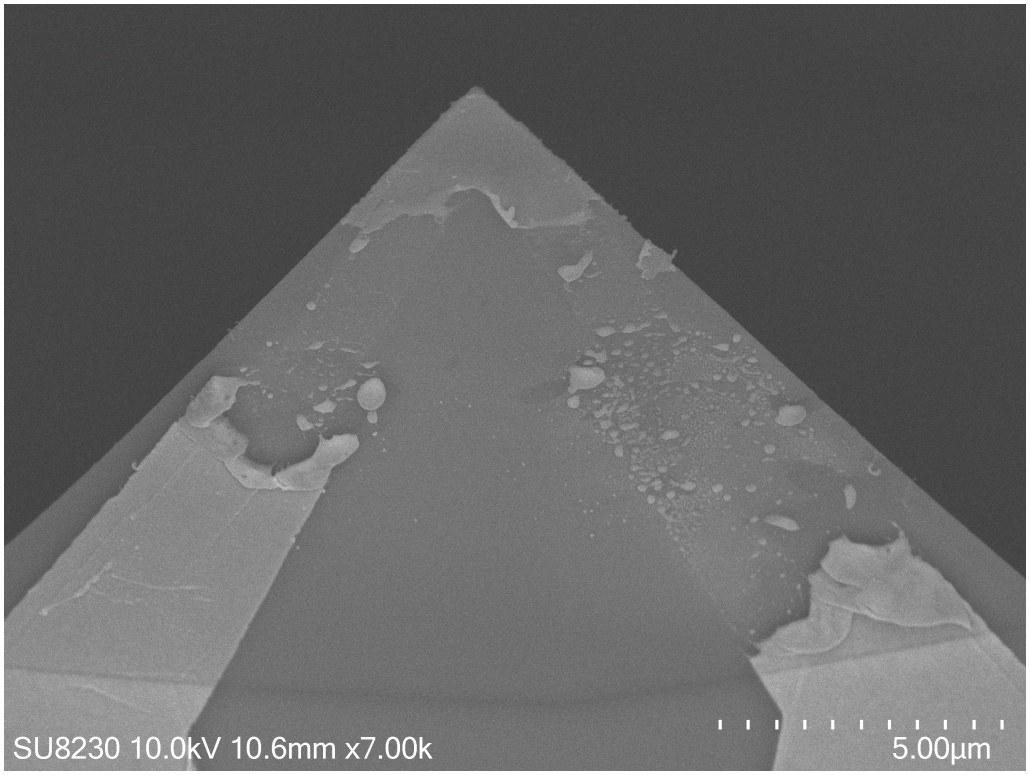


Figure 2.12: A SEM image of a burnt KNT probe tip. High current passed through the tip, in this case by ESD, can cause the tip to become non-functional.

High current in the KNT probe can cause damage to the tip resistor. Figure 2.12 shows a burnt KNT probe tip. In this particular case, high voltage, caused by electrostatic discharge (ESD) across the Pd resistor, has resulted in the vaporisation of the tip resistor. Electromigration [65] is another failure mechanism that these probes are sensitive to [62], and manifests itself as a small, localised break in the tip resistor. Although all the materials in the probe construction are compatible with high-temperature operation, self-heating of the probe is limited by the maximum current density for the device before electromigration effects take place [62, 66]. Therefore these probes have a limited temperature operation window with a manufacturer-stated maximum of 160 °C, far lower than doped silicon probes.

In the literature, many have presented difficulties in gaining quantifiable results utilising the KNT probe. Mordue et al. [6] has shown that thermally induced topography errors of upwards of 100 nm/K can emerge from incorrect placement of the optical lever laser due to the bi-material nature of the probe. Spièce [4] had shown that the laser can also cause instability in the thermal measurement with Ramiandrisoa et al. [2] showing that errors of up to 37% can be seen. Therefore, for accurate thermometry and topography measurements, the laser must be removed

from the SThM system and alternate systems for maintaining tip-sample contact must be investigated.

2.4 Alternative height control systems

Although cantilever deflection is detected traditionally through the optical lever-/beam bounce mechanism, other mechanisms exist for the determination of the tip's position in space as a means to control the tip-sample separation and contact. Methods such as the Scanning Thermal Profiler (STP) utilise the thermal signal of thermocouple probes to determine tip-sample distances, or quartz tuning forks that utilise the resonance frequency of a quartz crystal for height control. Other methods such as capacitive or strain sensing require dedicated, fabricated deflection sensing elements that must be placed on the area or in close proximity to the area to be interrogated.

This section looks to explore the literature for potential avenues for non-laser-based deflection sensing of thermal probes.

2.4.1 Scanning Thermal Profiler (STP)

The scanning thermal profiler was first devised as a technique to measure a sample's topography by Williams and Wickramasinghe [67] in 1986. This method of surface profiling uses the near-field thermal interactions of a stiff, heated thermocouple probe and a given sample. A schematic of its working principle is available in Figure 2.13. The technique works on the basis that the thermal loading on the tip will change as it moves closer to a surface driven by a DC temperature difference between the probe and the sample. By feedback of the thermal signal into the Z-axis servo control, Williams and Wickramasinghe [67] found the lateral resolution to be approximately equal to that of the probe fly height. If the heated probe can be flown close to the sample surface it can be used as a non-contact method for the measurement of topography with high sub 100 nm lateral resolution [68].

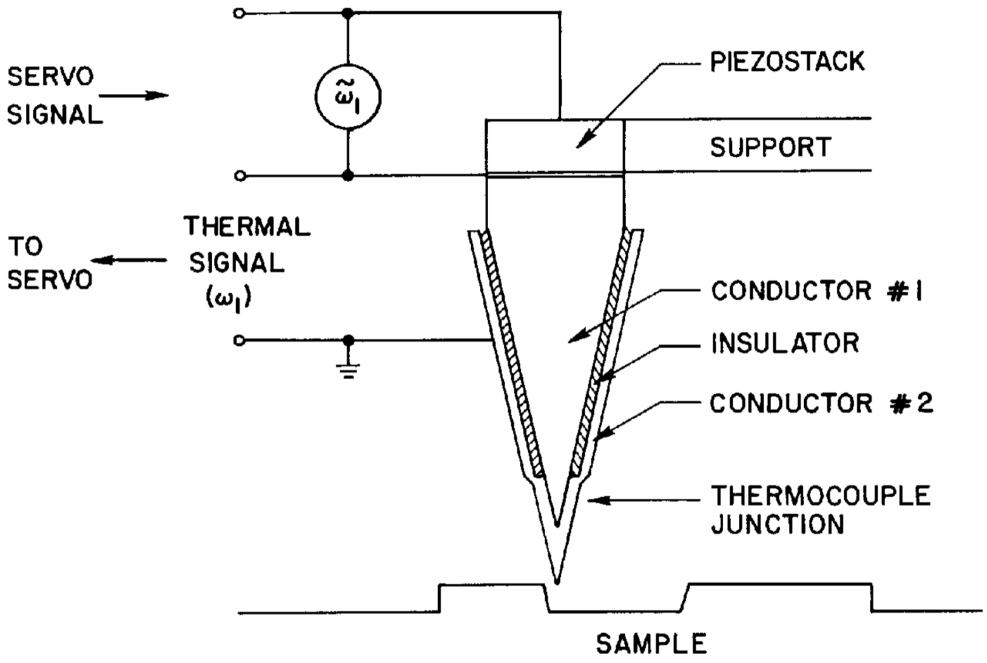


Figure 2.13: Schematic showing the working principle of the STP. A thermocouple probe is attached to a piezo stack, the probe is modulated at a frequency ω, and the resulting signal at ω is measured and utilised to control the average tip-sample spacing. (from ref. [68])

2.4.2 Quartz tuning fork

Quartz tuning forks have emerged as a valuable method for height control in AFM since first being reported by Karrai and Grober [69] due to their mechanical stability and well-defined resonance characteristics [47, 70]. As the tip interacts with the surface, the attractive forces between the tip and sample induce changes in the resonance frequency of the tuning fork. By monitoring these frequency shifts through phase-locked loop circuits, tip-sample separation can be accurately controlled. Edwards et al. [71] had shown that sub-nanometer vertical resolution imaging is possible with this technique. However, both Karrai and Grober [69] and Edwards et al. [71] utilised relatively stiff hand-crafted wire probes in their tuning fork setups. Bontempi et al. [47] functionalised this method by attaching Wollaston wire thermal sensor to the tuning fork, realising thermal measurements using this technique. FIB processing of the Wollaston wire is required for high spatial resolution scanning and as such is not a routine measurement. Additional issues of repeatability can also be associated with hand-crafted probes.

2.4.3 Capacitive sensing

Capacitive elements are common for sensing the deflecting components of highly compliant and sensitive devices, such as microphones, gyroscopes, accelerometers, and pressure sensors. Microphone and pressure sensors usually consist of a metalised rigid back plate and flexible membrane that moves in response to applied pressure. The change in distance between the back plate and membrane changes the capacitance of the device according to Eq 2.4. Elements like these have been developed to measure micro-cantilever deflections [72].

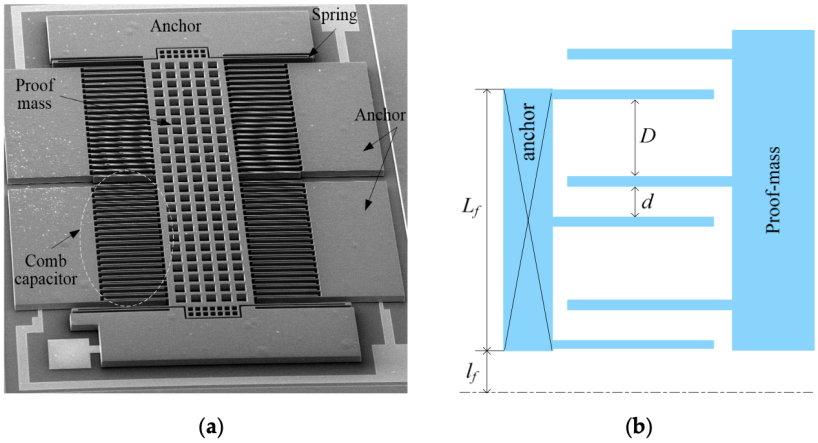


Figure 2.14: a) SEM image of MEMS accelerometers sensing element, b) a schematic showing the interdigitated electrodes and proof mass (From [73])

Microfabricated gyroscopes and accelerometers (Figure 2.14) usually employ suspended interdigitated electrodes (IDE) that move in response to a given force (gravitational or acceleration), providing a capacitive readout proportional to the given force. These are highly sensitive devices, however complex fabrication techniques would be required to realise these structures on top of released cantilevers.

Fully rigid comb (IDE) capacitors are of interest in the field of flexible and printable electronics, due to their simple design. It has been shown in the literature that such capacitors can be calibrated to act as strain sensors [74–77]. The deformation of the comb structure under an applied strain (Figure 2.15) results in a change in the separation between the comb capacitor fingers and therefore capacitance of the device. These structures have been shown to be moderately sensitive, with a gauge factor of up to 6.

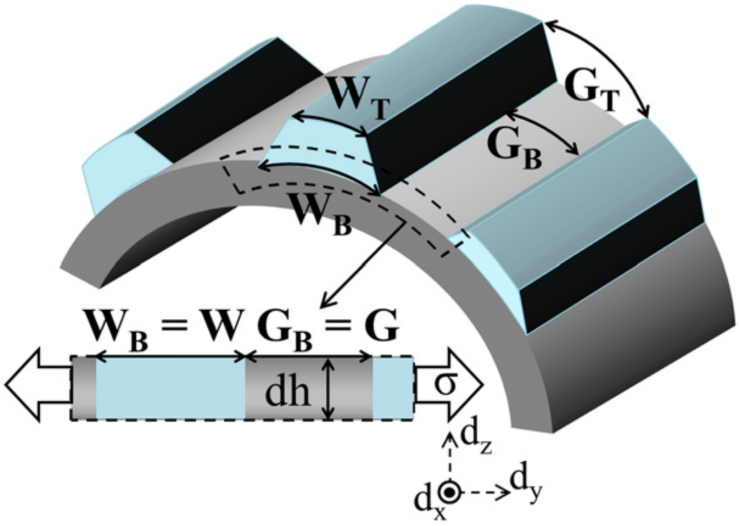
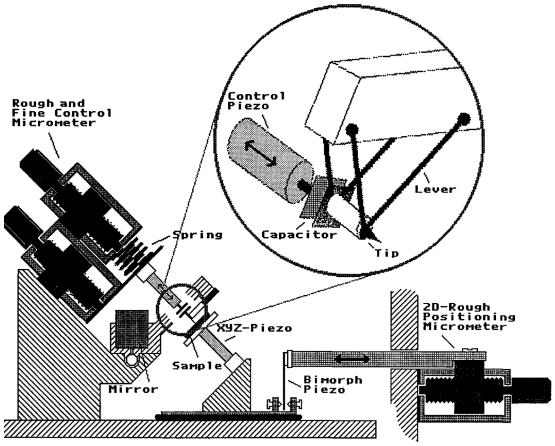


Figure 2.15: Schematic showing a comb capacitor structure under bending conditions (from Molina-Lopez et al. [74]). Deformation of the capacitor structure changes the capacitance between the electrodes, which can be read out electronically

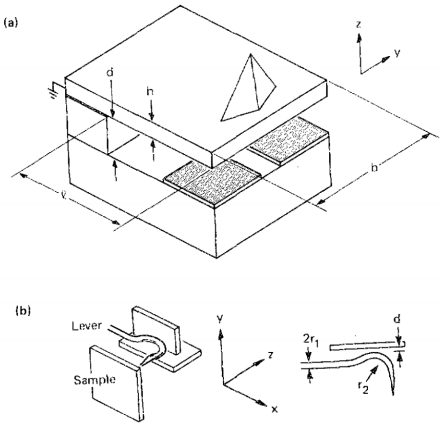
Capacitive probes have been proposed as a high sensitivity solution by Göddenhenrich *et al.* [78] and Neubauer *et al.*[79] in 1990 (Figures 2.16a, 2.16b), with later improvements by Shiba *et al.* in 1998 [72]. All these designs incorporate a flat plate capacitor, of which their capacitance value, C, can be determined by Eq 2.4.

$$C = \frac{\varepsilon A}{d} \qquad \text{(Eq 2.4)}$$

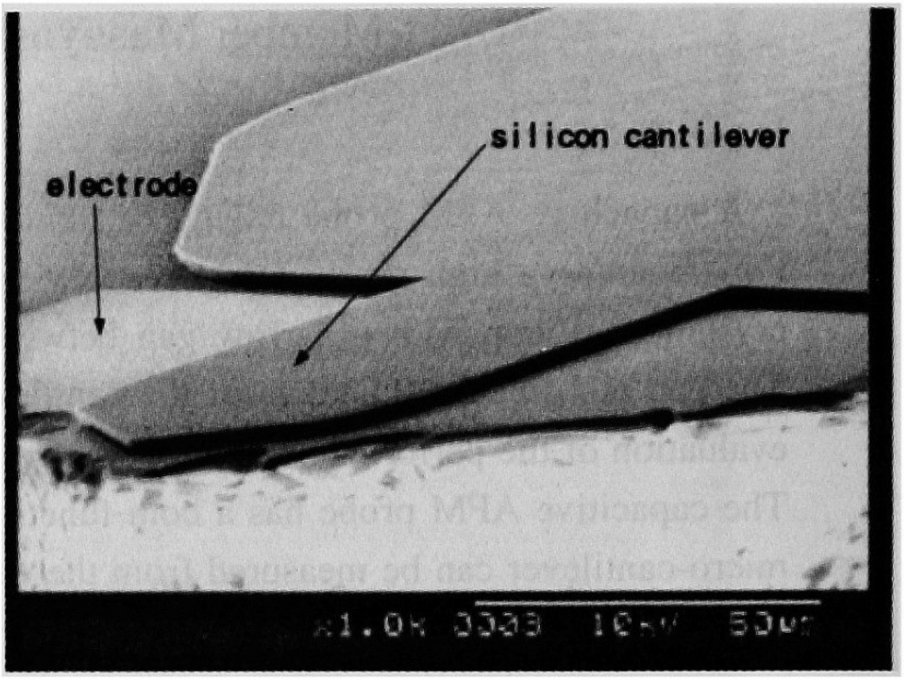
Where ε, is the dielectric constant of the material between the two electrode plates, A is the overlapping sensor area, and d is the distance between the two plates which changes with cantilever deflection. As seen in Eq 2.4, extremely sensitive detection can be achieved with very narrow gaps [80]. There are practical limits to the fabrication and use of the probe design by Shiba et al. [72]. Released structures with narrow gaps can suffer from adhesion [81]. This occurs when inter-atomic forces (Van der Waals, electrostatic, capillary etc.) cause the released structure to 'stick' to the stiff electrode backplate. An external and opposite force is then required to overcome the adhesion forces to return the device to normal operation [81].



(a) Göddenhenrich *et al.* AFM design. (From [78])



(b) Two designs by Neubauer *et al.* (From [79])



(c) Improved capacitive probe by Shiba *et al.* (From [72])

Figure 2.16: Evolution of capacitive deflection sensing AFM probes. (a) Göddenhenrich *et al.* introduced capacitive sensing as a method in SPM for detecting probe-sample interactions. (b) Neubauer *et al.* introduced a smaller cantilever design using microfabrication techniques. (c) Shiba et al. later batch fabricated high-speed probes using wafer bonding techniques to achieve a plate separations of 1 µm showing vastly improved deflection sensitivity.

Although capacitive sensing has been shown to be a highly sensitive avenue in the literature, complex fabrication is required to prevent adhesion of highly compliant elements. Full rigid comb structures could be utilised to reduce the requirements for complex release mechanisms. However, these large and dense structures would require high-density lines that would be prone to defects that would lower yield.

2.4.4 Resistive

Thin film

Metal film strain gauges are another popular avenue to monitor strain in the deflection of compliant structures [39, 82, 83]. Typically, they work on the principle that a material's absolute resistivity is dependent on the cross-sectional area and length. Geometric changes that occur where the strain gauge is placed proportionally deforms the strain gauge geometry itself. This results in a change in the resistivity of the material that can be measured. This concept has been shown in the schematic in Figure 2.17.

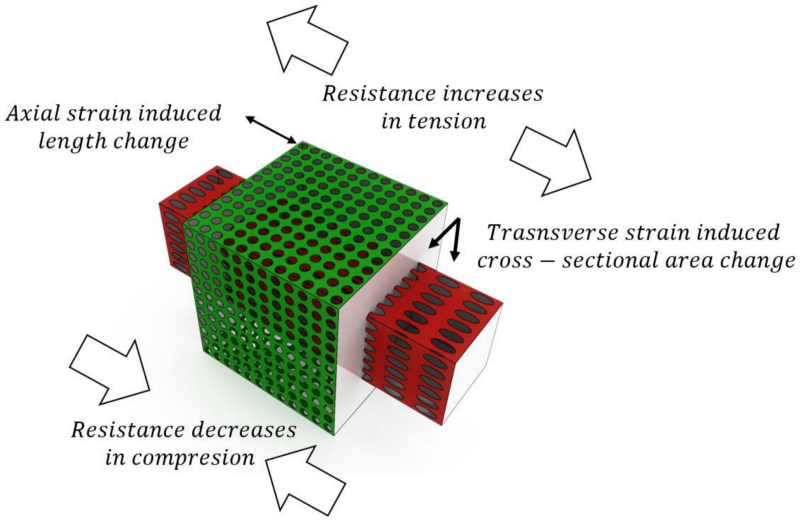
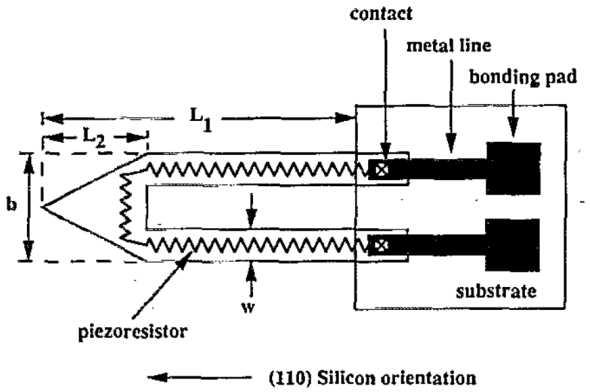


Figure 2.17: The working principle of a resistive strain gauge. Strained geometry in the conducting element can cause a change in the material resistivity. (from Avilovas [39])

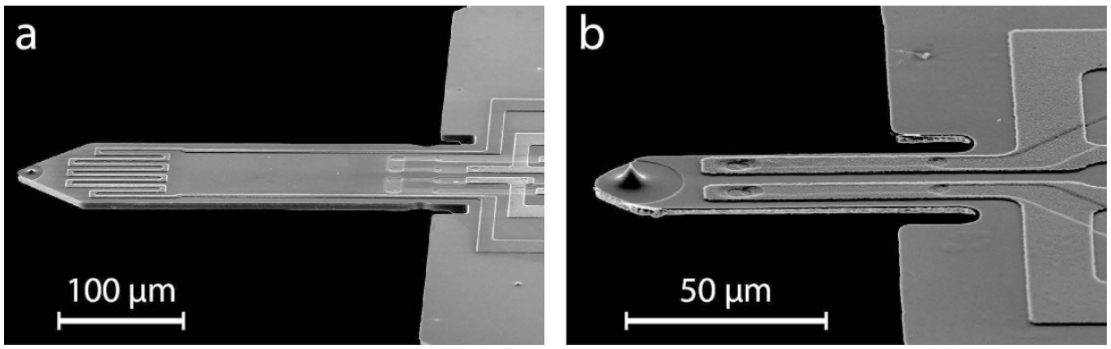
They can be fabricated on cantilevers to measure strain with gauge factors in the region of 2 to 2.5, utilising materials such as nichrome that also show low temperature TCRs of 85 ppm/°C [84, 85], ideal for use in environments that have fluctuating temperature profiles, such as an active SThM cantilever. A practical disadvantage to this approach is the requirement that the strain sensor must be placed at the very base of the cantilever and cover a large area to gain sufficient sensitivity. This in turn can cause vast cantilever bends from deposition-induced stress in the materials used [39], making the sensors impractical for use in AFM cantilevers.

Piezoresistive

The first piezoresistive cantilevers were developed by Tortonese et al. [86] in 1993 using doped silicon resistors (Figure 2.18a). Piezoresistive elements detect deflection by measuring the strain-induced band gap changes in the compliant material, which



(a) Schematic of Tortonese *et al.* first piezoresistive probe. (From [86])



(b) SEM images of piezoresistive cantilevers. (From [21])

Figure 2.18: Piezoresistive deflection sensing cantilevers. (a) Tortonese *et al.* designed the first piezoresistive probes, achieving vertical resolution in the 10 pm region. (b) Improvements on the piezoresistive design by Dukic *et al.* resistors in a Wheatstone bridge configuration and built in thermal actuation of the tip. Dukic *et al.* also shortened the cantilever length to increase the resonant frequency of cantilever, improving on the scanning speed of the probe.

is read through a change in the material resistivity. These probes present many advantages over the more common optical lever probes. They require very little setup as well as their ability to measure light-sensitive samples in dark conditions. Light can actually be detrimental to doped silicon cantilevers as they exhibit a degree of sensitivity to light illumination that can cause issues in some laboratory setups [87].

The probes are also very scaleable, allowing increased acquisition speeds when multiple cantilevers are incorporated into large arrays [88]. With the reduction in cantilever size (Figure 2.18b), the sensitivity of the probe can be drastically increased [21].

Piezo-resistive elements are an attractive choice for cantilever deflection sensing as they show high sensitivity [39, 86]. However, they suffer from a high sensitivity to thermal effects showing a TCR upwards of 1000 ppm/°C [89], so are not suited for

measuring deflections in thermally active environments, such as SThM.

Electron Tunnelling

In classical mechanics, a charge carrier at a potential barrier would require an energy higher than the barrier to pass through it. However, quantum mechanics states that charge carriers have both particle and wave-like properties [90]. Quantum tunnelling is a well-known phenomenon where the wave function of a charge carrier has a non-zero probability of tunnelling through a sufficiently thin potential barrier (as long as the barrier is shorter than the wave's evanescent decay through the barrier). This tunnelling probability depends exponentially on the width and height of the potential barrier and is therefore incredibly sensitive to changes in distance. This was the working principle behind the original STM by Binnig and Rohrer in the early 1980s [15].

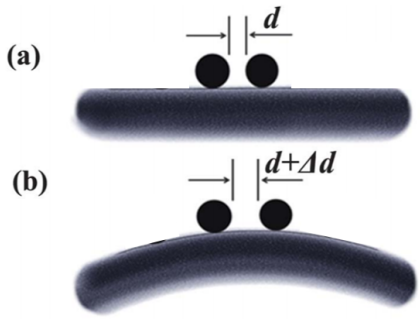


Figure 2.19: Working principle behind quantum tunnelling strain sensors. (a) the un-deformed geometry with electrode separation, d. (b) Deformation of the substrate causes a change in electrode separation (Δd), producing a proportional change in the device conductance (adapted from [91])

Tunnelling strain sensors have a similar operation principle to capacitive IDE sensors where the strain in the cantilever surface causes a deformation in the gap between electrodes (Figure 2.19). This change in the electrode separation will cause a change in the tunnelling probability and therefore device conductance. It has been shown in the literature to be a very sensitive method for strain sensing (gauge factors of over 100) [91–93].

Kulkarni et al. [92] proposed such a sensor for magnetostriction measurements. This was achieved by slowly sputtering gold on the sample until nanoparticles accumulated on the surface with tunnelling distance gaps between them (Figure 2.20). Kulkarni also showed that such a sensor would work for sensing the deflection of a cantilever.

Dukic et al. [93] integrated these sensors into AFM nano-cantilevers by depositing

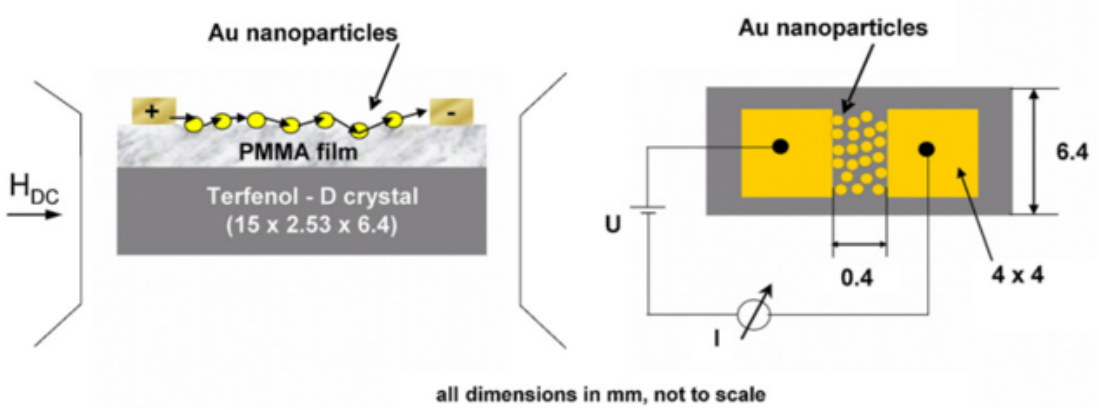


Figure 2.20: Tunneling strain sensor by Kulkarni et al. [92] for magnetostriction measurements. Strain changes in the crystal change the inter nanoparticle distances, altering the conduction through the nanoparticle chain. (from [92])

nanogranular metal via focused electron-beam-induced deposition (FEBID) to create a chain of metal islands with tunnelling distance gaps between them.

The two types of junction orientations have been drawn schematically in Figure 2.21 with the electron transport across the barrier (red) shown with a back arrow. Classical tunnel junctions are most commonly created through the stacking of grown or deposited layers of an electrode material, barrier material and then counter-electrode material, where the majority of the electron transport occurs perpendicular to the substrate (i.e the barrier is parallel to the surface). Such barriers have been deposited on suspended compliant structures by Koppinen et al. [94], and show relatively high gauge factors upwards of 30 utilising Al-AlOx-Al barriers.

Co-planar junctions are considered so when the barrier is perpendicular to the substrate material, i.e the direction of electron transport is parallel to the substrate. An example of these types of junctions are ones fabricated by Kulkarni et al. [92] and Dukic et al. [93].

The ability to incorporate any of the aforementioned alternate height control elements into the SThM cantilever requires an intimate understanding of the microfabrication process. Understanding the tools and processes' capabilities and limitations allows for realistic device design that will show a high yield during manufacture.

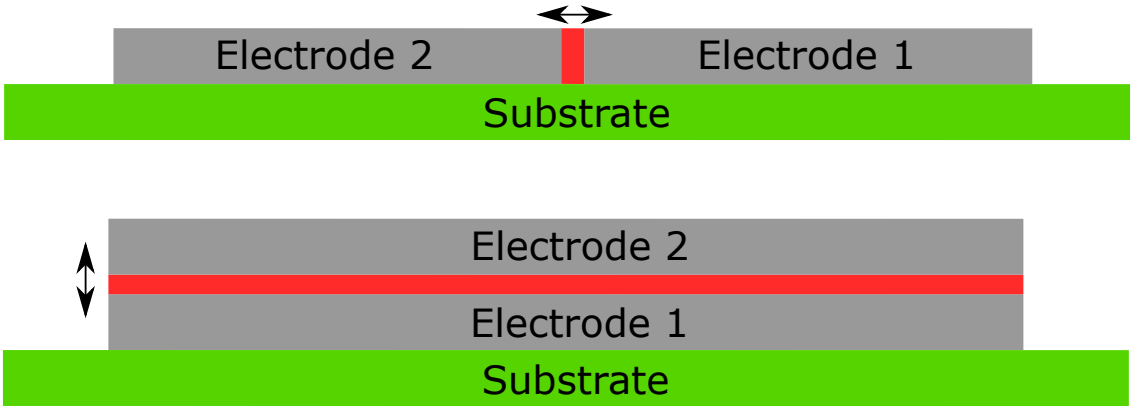


Figure 2.21: Two orientations of junctions are possible. Planar junctions (bottom) where electron transport (black arrows) occurs through the barrier (red) between the electrodes perpendicular to the substrate as opposed to co-planar junctions (top), where the direction of electron transport is parallel to the substrate surface

Microfabrication methods

Batch fabrication of SThM probes, and microdevices more generally, heavily rely on the ability to construct features on a substrate using both additive (deposition) and subtractive (etching) processes in a reliable and accurate fashion. This chapter looks to briefly introduce the concepts behind microfabrication processes used for the production of SThM probes, and devices created in this work with discussions on the challenges of batch fabrication on the micro and nanoscale.

The SThM fabrication process utilises the strengths of various methods for defining its lithographic features, such as UV lithography and electron beam lithography. They are used for the definition of mask patterns for either etching or metallisation to create probe elements such as the cantilever shape, thermally sensitive tip resistor, or for the inclusion of current limiting resistors.

3.1 Photolithography

Photolithography is a widely employed technique in semiconductor facilities to fabricate microdevices [95]. The process typically results in the creation of topographic features in a resist on a substrate that can be used as a mask for further processing, such as etching or metal deposition. Photolithography starts with the production of a mask plate that showcases the desired characteristics of the pattern to be printed. These mask plates depict features as metallic films covering specific areas on a transparent substrate and typically are chromium-plated quartz. Masks are then placed in the path of UV light to allow light passage only in the intended exposure regions.

Many UV exposure tools fall under two main categories; projection, or contact exposure tools. Projection tools place an objective lens between the mask and the

sample as shown in Figure 3.1. This lens collects the diffracted light and projects it onto a sample surface. An advantage of this technique is that the pattern features on the mask can be created larger than the final desired pattern size. This is possible as the lens system can be used to shrink the size of the projected patterns on the wafer. This comes with an additional advantage that any contamination, such as particles or mask defects will also be reduced in size when projected onto the wafer. The throughput of these tools is limited by the number of dies required on a given wafer, as each die must be exposed sequentially.

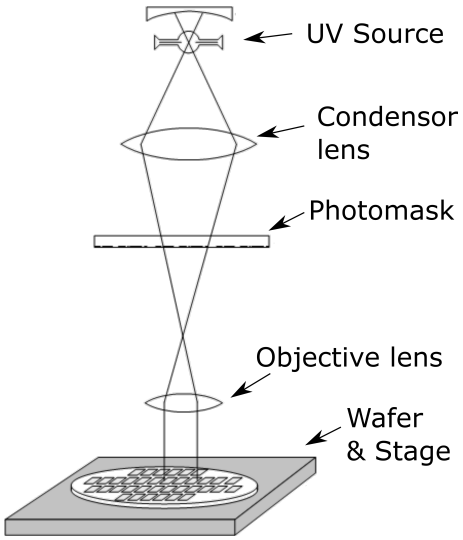


Figure 3.1: Diagram of a generic projection photolithography tool. (Adapted from [96])

Alternatively, as with photolithography conducted in the JWNC, contact exposure tools can be used. This is where a photo mask with the desired pattern is placed in direct contact, or in close proximity with, the sample. Features to be printed must be written the same size on the mask as would be desired on the sample. The procedure to pattern a sample starts with coating the sample with a photosensitive film, known as photoresist. Subsequently, the photo mask is placed in contact (or close to contact) with the photoresist-coated sample. UV radiation is then applied through the photomask. After exposure, the solubility of the photoresist in a developer changes. In positive resists, exposed areas become more soluble, while in negative resists, exposed areas become crosslinked and insoluble. This allows for a large area of different features and multiple dies to be exposed at the same time, allowing for a large throughput of devices through the tool. A generalised photolithography process flow is shown in Figure 3.2.

Various modes of exposure can occur during Figure 3.2c, which arises from varying the gap between the mask and resist in the case of proximity exposures (Figure 3.3)

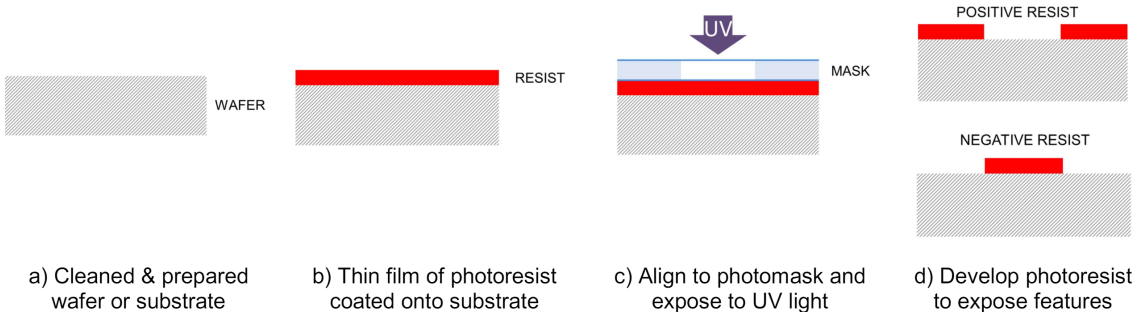


Figure 3.2: Simplified photolithography process showing the steps from (a) clean wafer through (b) photoresist coating, to (c) exposure and (d) development. (from [97])

or, in the case of contact exposures, by varying the contact force between the mask and sample.

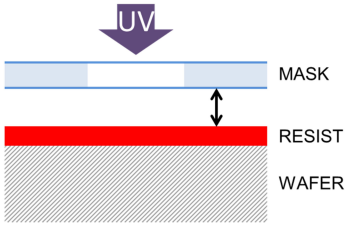


Figure 3.3: Typical exposure of resist in a photolithography process. The exposure gap (Black arrow) or contact force between the mask and resist can be altered to expose in different modes. (from [98])

Contact exposures can generally be split into four modes; Proximity, where the mask and wafer are held slightly apart with an exposure gap of a few microns to a few hundred microns. Soft contact, where the mask and wafer are only just brought into contact with one another and very little force is applied. Hard contact, where the mask and wafer are brought into contact, and further pressure is applied as specified by the tool operator. Vacuum contact, where the mask and wafer are brought into hard contact, and a vacuum is then used to pull them even together. Generally speaking, a greater resolution is achieved through harder mask-wafer contact, with vacuum contact yielding the highest resolutions as diffractive effects are minimised [98]. However, harder contact comes with its disadvantages, contamination can more easily be transferred between the mask and wafer, as well as repeated contact can cause damage to the mask, resulting in decreasing pattern fidelity and lowering yield over time.

The conventional approach for achieving a consistent thickness of resist covering a substrate is through spin coating. Resists are formulated with specific viscosities to ensure well-defined thicknesses when applied through the spinning process onto a sample [99]. Typically, the resist datasheet provides a table indicating the necessary

spin speeds and times to achieve specified thicknesses.

The MA6 (Karl Suss) tool is used within the JWNC to expose the photoresist to UV light. It allows for the sample to be translationally aligned to previous lithography layers using manual micrometres located on the side of the wafer stage. Alignment accuracy is ultimately determined by the skill of the operator and requires well-defined markers for high-accuracy alignment. During exposure the tool emits broadband UV in the 230 to 450 nm wavelength region. However, this wavelength of UV light limits the feature sizes available to pattern due to the Rayleigh criterion [100] as described by Eq 3.1 and Eq 3.2.

$$Resolution = \frac{k_1 \lambda}{NA} \tag{Eq 3.1}$$

$$Depth\ of\ focus = \frac{k_2 \lambda}{NA^2} \tag{Eq 3.2}$$

Where λ is the wavelength of light used and NA the numerical aperture. k_1 and k_2 are coefficients dependent on multiple factors, such as projection optics or the inclusion of reticle enhancement techniques including phase-shift masks, or proximity error correction (PEC) techniques. These coefficients are believed to have a physical limit of 0.25 due to diffraction theory [101].

To reduce the pattern size beyond what UV photolithography allows, one must either decrease the wavelength of light or increase the numerical aperture. However, as indicated in equation Eq 3.2, increasing the numerical aperture significantly reduces the depth of focus, impacting exposure uniformity across a wafer, lowering process latitude, and, consequently, device yield [95].

In areas that require lower-resolution lithography, such as the definition of the pyramid or the SThM chip pop-out mechanism, UV photolithography is used.

3.2 Electron Beam Lithography (EBL)

EBL, or E-beam, is capable of a much higher depth of focus and resolution of features than the more traditional photolithography techniques as its resolution is not limited by the wavelength of electrons ($\lambda \approx 4$ pm at 100 kV), but rather limited by source size, electron optic aberrations [95], as well as resist limitations [102]. EBL also has the capability of adjusting the focal point during the writing of patterns, allowing for fine corrections that may be needed due to writing on highly topographic substrates, such as that used in the microfabrication of the SThM cantilevers.

High-resolution, discrete feature sizes in the sub 10 nm range are regularly available to pattern. Feature sizes down to 2 nm have been reported using aberration-corrected scanning transmission electron microscopes (STEM) [103, 104]. However, using STEM as a means to define EBL is incompatible with regular substrates and requires patterning electron transparent substrates such as thin ($\lessapprox$50 nm) membranes.

Although there is a drastic increase in resolution available from EBL over more conventional UV photolithography, writing is a slow, serial process, making wafer throughput considerably lower. Patterns that require high electron dosages, or small beam step sizes for good pattern fidelity, can drastically reduce the throughput of devices on the tool.

For the fabrication of SThM probes, EBL is used for defining elements that require high overlay accuracy, small exposure areas, high resolution, and high depth of focus. Such a use case would be in the definition of current limiting resistors, or for the definition of the thermally sensitive tip resistor.

3.2.1 Electron sensitive resists

Pattern definition in EBL follows a similar principle to photolithography. However, the sample is covered in an electron beam-sensitive resist layer, typically polymethyl methacrylate (PMMA), which is then subsequently patterned by an electron beam. PMMA has been extensively used as an electron beam resist for over 55 years [105].

The resist starts out compromising as long polymer chains. When electrons impinge on the resist molecules, this causes localised changes to the molecular structure of the resist. In the case of positive tone resits, this selectively causes chain scissions, drastically increasing its solubility in a developer only in the exposed regions. In the case of negative tone resists, this causes crosslinks, decreasing its solubility. A visual representation of this is available in Figure 3.4.

As in UV photolithography, the patterned sample is then developed in a solvent such as MIBK:IPA to create a high-resolution mask of the pattern on the substrate for further processing. The temperature, development time, and concentration of MIBK:IPA used while developing EBL resists all make a contribution to the final developed feature geometry [102].

However, unlike photolithography, EBL is a serial process. The electron beam must

be raster or vector scanned across the sample by deflection coils in the E-Beam column.

Isolated line widths of better than 20 nm can regularly be obtained and can easily be removed in acetone with little residue. These properties make it ideal for use in research laboratories.

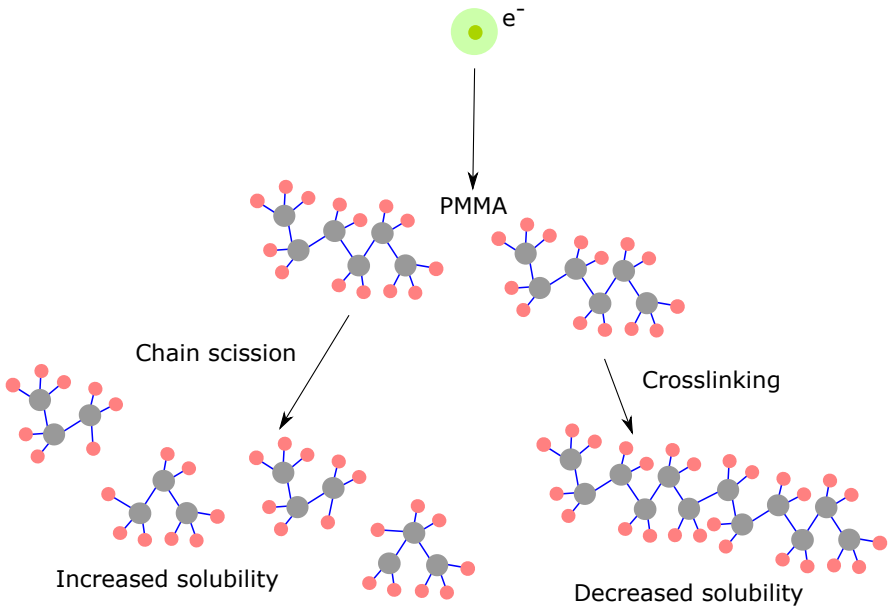


Figure 3.4: Simplified, visual representation of molecular structural change when electron sensitive resist is exposed to an electron beam. Electron interaction with the resist can cause either chain scission or crosslinking of the long chain polymer resist, resulting in increased or decreased solubility local to the area of electron bombardment

Resist limitations

The thickness of the resist and the substrate being patterned also can have a great impact on the final feature size of EBL [102]. As resist film thickness is increased, secondary electron scattering and backscatter electron events can cause an effective increase in the resist-electron interaction area, reducing the resolution available [106].

A primary feature resolution limiting factor is due to resist collapse, a common problem when writing nanogaps with high aspect ratios. Such resist collapse can be seen in Figure 3.5. This primarily happens due to capillary forces acting on the resist features that have low mechanical stiffness during drying after resist development.

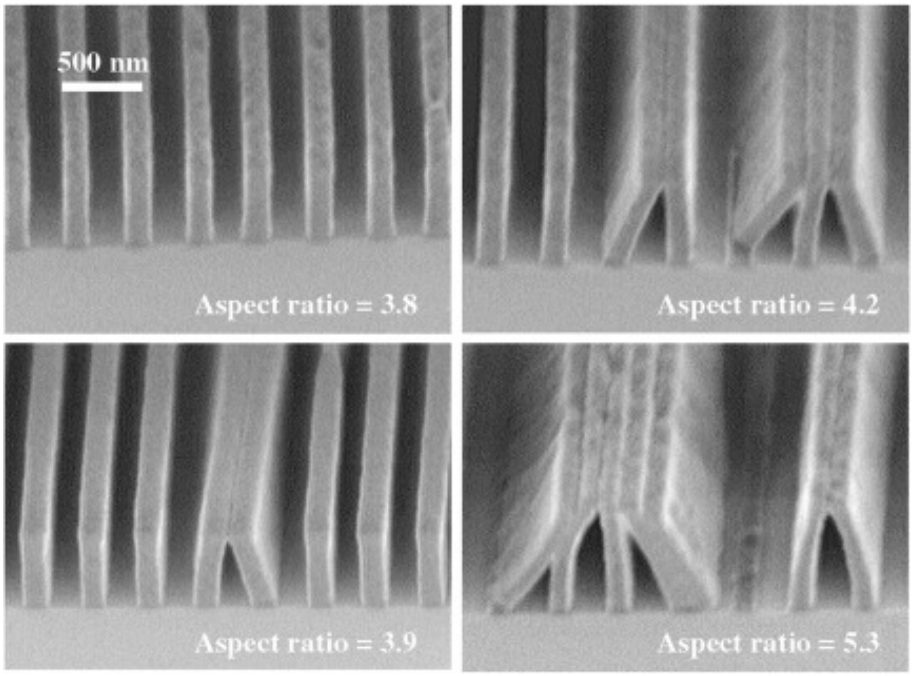


Figure 3.5: Resist line collapse - a common issue in high aspect ratio PMMA structures. This is caused by capillary forces pulling the structures together when the sample is dried after development. (from Nealey et al. [107])

In this work, positive tone PMMA from AllResist[1] has been exclusively used as an electron beam-sensitive resist.

3.3 Pattern transfer

Transferring a designed pattern into a structure on the substrate is a crucial part of microfabrication. The available manufacturing processes can be split into two main categories, additive (deposition and doping) and subtractive (etch). Combining multiple subsequent layers of these process types allows the creation of highly complex devices.

3.3.1 Metal deposition

Metal deposition can be used for the creation of electrical and optical components of SThM probes after the appropriate mask has been defined through EBL or UV photolithography. The regions of removed photoresist can be metalised using evaporation. Metalisation can be used to create pads and tracks of gold to allow electrical connections to the thermally sensitive palladium tip resistor, or to create sheets of

[1] https://www.allresist.com/products/e-beam-resist/

reflective gold on an optically transparent silicon nitride cantilever body to permit the functionality of the AFM's optical lever mechanism [108].

Physical vapour deposition (PVD) is a standard additive process used extensively in the fabrication of nanodevices. Electron beam physical vapour deposition (EBPVD) is a common subset of PVD for the deposition of metals (Figure 3.6). A crucible of source material is bombarded with electrons from an electron gun, causing atoms of the material to transition to a gaseous phase in the high vacuum. Evaporated atoms from the source material can then travel and precipitate in a film on the target sample. A rotating carousel of crucibles within the chamber allows for multiple layers of differing materials to be deposited sequentially, without breaking the high vacuum. If the vacuum is broken between deposited layers, contamination can be introduced or oxidation of the deposited metal can occur in the ambient atmosphere [109–112]. This can be highly problematic in the case of metals used as adhesion layers [113, 114], or when the contamination of metals leads to device failure [115].

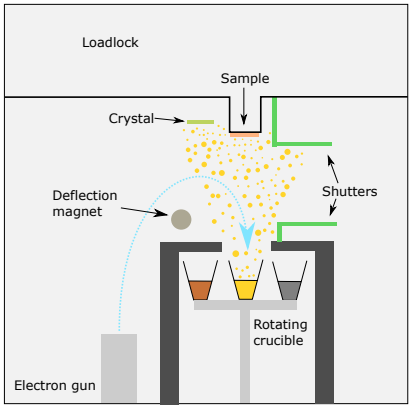


Figure 3.6: Simplified working principle of a metal evaporator. An electron gun is used to impinge electrons on a crucible of material, causing it to vaporise and deposit on the target

The thickness of deposited metals must be accurately controlled and monitored during depositions. Quartz crystals are used as a method of *in situ* deposition thickness monitoring. The resonant frequency of the crystal is primarily dependent on its dimensions and density. The introduction of additional mass through a deposited thin film reduces the resonant frequency of the crystal. If the density of the material is known then the thickness of the deposited material can be easily determined [116, 117]. The use of shutters to block the line of sight from the crucible to the sample allows for the deposition rate to be finely tuned before any deposition occurs on the sample, as well as allowing for quick stoppage of deposition once the required deposition thickness has been achieved. Monitoring of deposition rates upwards of 25 µm per second [118] or as low as 10 nm per minute [119] can be achieved in the high vacuum of EBPVD systems.

Typically, in an additive pattern transfer process, a bi-layer of PMMA resist is used for EBL patterning to prevent liftoff defects such as flagging metal and create a clean liftoff profile. This bi-layer consists of a lower layer of PMMA dissolved in

an anisole solvent that has a lower molecular weight than that of the upper layer of PMMA dissolved in an ethyl lactate solvent. Due to the higher solubility of the lower molecular weight resist in developer compared to the higher weight resist when exposed to the same dose of electrons, this creates an overhang or 'undercut' resist profile (Figure 3.7c) once developed. Allowing the metal to be cleanly lifted off with significantly reduced ripping or flagging. A standard fabrication of metallic features is presented in Figure 3.7.

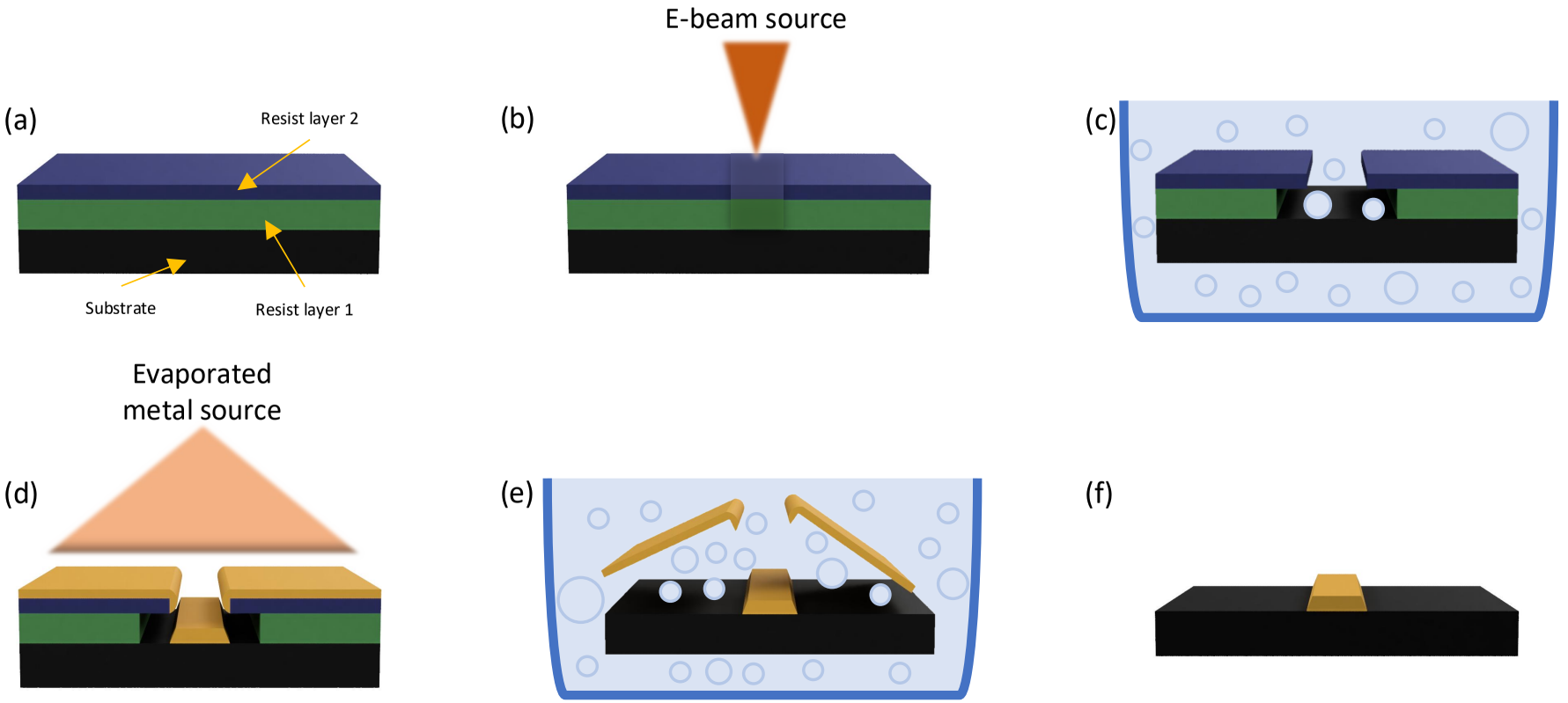


Figure 3.7: A standard additive process utilising a resist bi-layer and electron beam lithography to pattern high-resolution features. A bi-layer of electron-sensitive resist is spun onto the sample in (a) and the desired pattern is exposed from an electron beam in (b). The exposed regions are then developed in solution as in (c) to the point where the top layer produces an overhang due to its higher molecular weight. Material is then deposited on the surface through the resist mask in (d). (e)-(f) The resist layers are then removed to lift off the metal on masked areas in solution to leave behind the metalised geometry of the desired pattern

3.3.2 Thin film growth mechanisms

The growth mechanics of grown thin films depend strongly on the bonding strength of the films adatoms and the surface. There are 3 modes of growth associated when depositing materials on the surface of a sample (Figure 3.8).

Volmer-Weber

Where the cohesive force between deposited adatoms is stronger than their adhesive force to the substrate, Volmer-Weber growth occurs. This causes the deposited film to preferentially bond together and form three-dimensional discrete islands. Growth then continues from these nucleation islands into thin films. The higher the adatom cohesive forces, the larger the discrete islands and subsequent percolation thicknesses. This is the generally accepted growth mechanism for metal deposition on insulating surfaces [121].

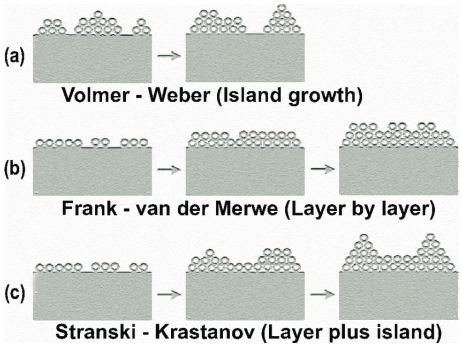


Figure 3.8: Cross-sectional view of primary growth modes of thin films. Each mode is shown in terms of increasing surface coverage from left to right. (from [120])

Frank-van der Merwe

In Frank-Van der Merwe growth, the bonding strength between the deposited film atoms is smaller than their bonding strength to the substrate. This causes the first atoms to deposit as two-dimensional atomic monolayers on the substrate. Subsequent layers then decrease in binding energy towards the bulk crystal value of the material deposited. This growth mode is seen in many metal-on-metal and semiconductor-on-semiconductor depositions.

Stranski–Krastanov

Stranski–Krastanov growth occurs when discrete islands form on top of initial monolayers of deposited material as seen in both Frank-van der Merwe and Volmer-Weber growth. This can be attributed to lattice mismatching between the deposited material and substrate causing strained film deposition. However, the formation of islands is energetically favourable, as it causes a reduction in the strain energy in the crystal. Island formation occurs after a given critical thickness (usually measured in monolayers) which is strongly dependent on the lattice mismatching between the materials. [122]

To reliably deposit inert metals such as gold or platinum to a silicon substrate, an adhesive layer is required due to the low bonding strength between these metals and oxide layers which would typically cause film delamination [113, 114]. Titanium, chromium, and nickel-chromium are commonly used as an adhesive layer due to their strong Ti-O and Cr-O bonding strengths, which are comparable to the Si-O bonding strength. This adhesion layer in effect creates a stable connecting bridge between the substrate and the metal layer.

Schwartzkopf et al. [123] investigated controlling the metal layer morphology during deposition by varying the deposition rate and effective thickness. It was found that higher deposition rates induced smaller particle sizes with smaller inter-island gaps. However, higher deposition rates also lead to an earlier onset of the percolation threshold. The substrate temperature also plays a role in the distribution of island and gap sizes during PVD. At low substrate temperatures, reduced surface diffusion of atoms as they hit the surface [117] cause smaller islands with smaller inter-island gaps to form.

3.3.3 Etch

The fabrication of cantilevers, and MEMS devices more generally, makes particular use of subtractive processes to create complex, physical sensors and actuators at the micro and nanoscale. Etching is required to create voids in structures or to release the compliant structures. Etching can generally be split into two categories; dry etching and wet etching. The former uses gases in plasma to etch material away, whereas the latter submerges the sample in a selective etch solution to remove material.

Dry etch

Primarily for the fabrication of SThM probes and in this project, reactive ion etching (RIE) is used to define cantilever shapes before wet etching of the underlying silicon. This process works by process gasses being broken down into chemically reactive species in a plasma, which then diffuse onto the target substrate surface. The reactive species then react with the sample substrate and eventually desorb from the surface (Figure 3.9). Depending on the etching conditions, RIE etching can have a high selectivity and produce highly anisotropic etches. Dry etching is used extensively in the creation of MEMS devices for defining etch pits for the release of suspended structures.

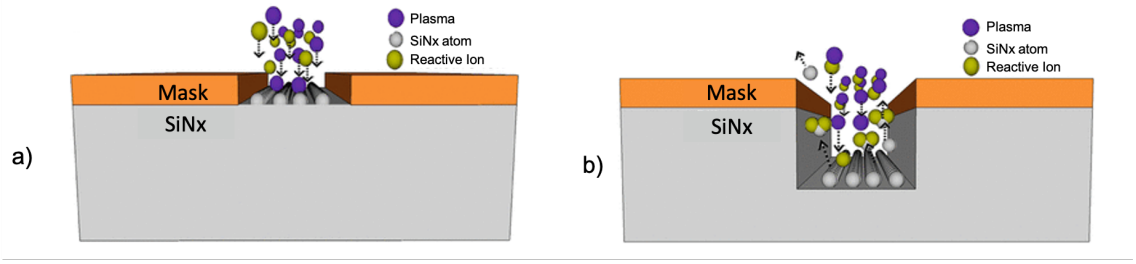


Figure 3.9: RIE process diagram. (a) A mask is patterned on the substrate with areas to be etched left exposed. (b) process gasses in plasma react with surface atoms to selectively etch substrate (adapted from Nayak et al. [124])

Wet etch

Microfabricated cantilevers make use of the etching properties of silicon to release suspended structures. Due to the single crystal nature of silicon substrates, they can be anisotropically etched in strong alkaline hydroxide solutions, such as potassium hydroxide (KOH) or tetramethylammonium hydroxide (TMAH)[125], through the reaction described in Eq 3.3 and Figure 3.10f. Due to the varied number of inter-atomic bonds on each crystal plane, which require different activation energies for the reaction to occur, the solution will etch each crystal plane at a different rate. Using Miller index naming conventions, the (100) crystal plane will etch significantly faster, approximately an order of magnitude faster [126], than the (111) plane (at a 54.7° angle from the (100) plane). This results in controllable etched geometric features which align to the crystal planes [127]. Due to this etching alignment to the crystal plane, it is crucial that the crystal orientation of the substrate is always kept in mind during lithography steps.

$$Si + 2OH^- + 2H_2O \rightarrow SiO_2(OH)_2^{-2} + H_2 \qquad \text{(Eq 3.3)}$$

The success of releasing cantilevers relies heavily on the spring constant (stiffness) of the designed cantilever and the materials used. Cantilevers that are designed to be too soft will suffer from adhesion effects where the inter-atomic forces, such as electrostatic, capillary, and Van der Walls forces, overcome the cantilever restoring force (i.e its spring constant) causing the cantilever to 'stick' to the etch pit [81].

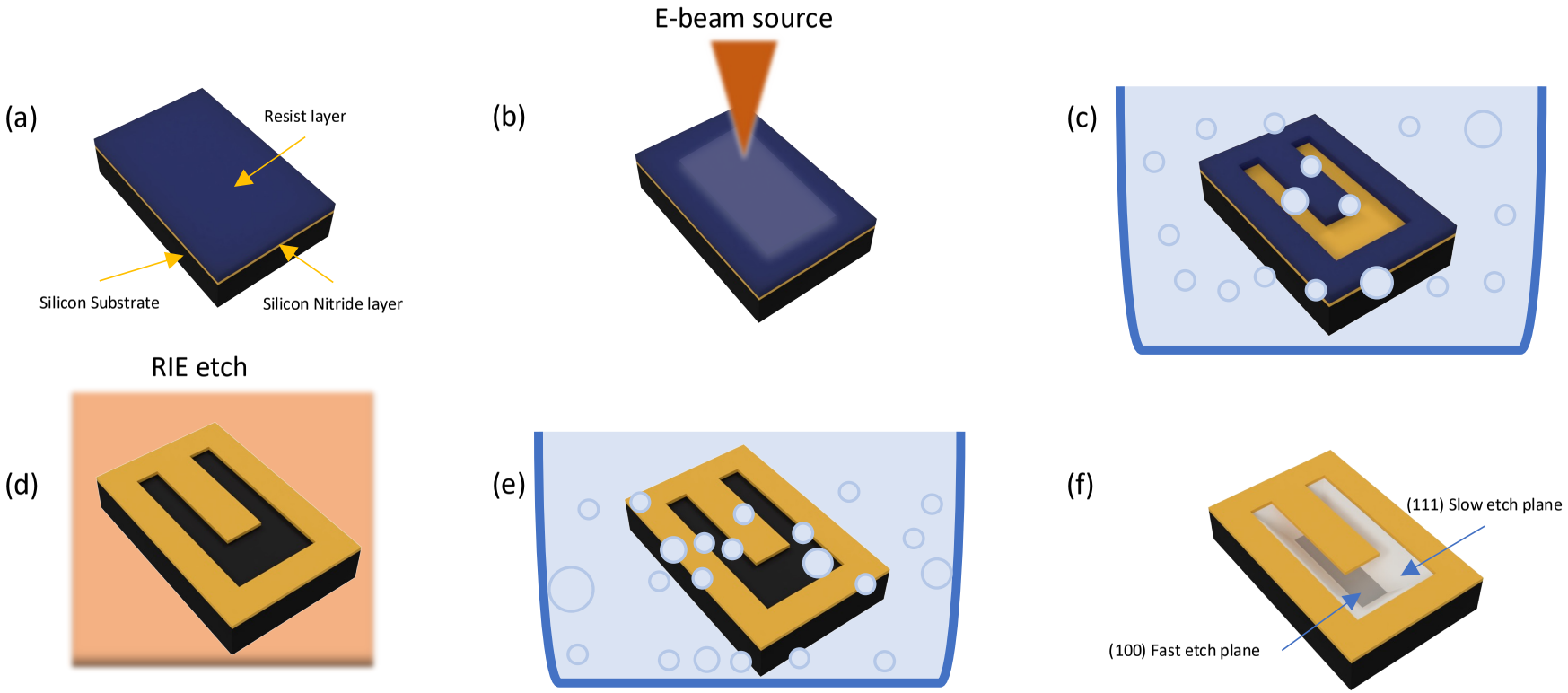


Figure 3.10: Etch process for cantilever fabrication. (a) Substrate with released layer and resist mask. (b) - (c) Mask is lithographically patterned and developed. (d) RIE etching of compliant layers structure through the developed mask. (e)-(f) Anisotropic wet etching of bulk substrate to release cantilever.

Wet etching can be used not only to create etch pits on the substrate, but also can be used to create positive topographic features, such as pyramids and bars [128]. The fabrication steps to create a pyramid through dry and wet etching are shown in Figure 3.11. In SThM probe fabrication, a cantilever can then be constructed against the angled pyramid side wall, this is shown in the diagram in Figure 3.12 and in a SEM of the fabricated structure in Figure 3.13.

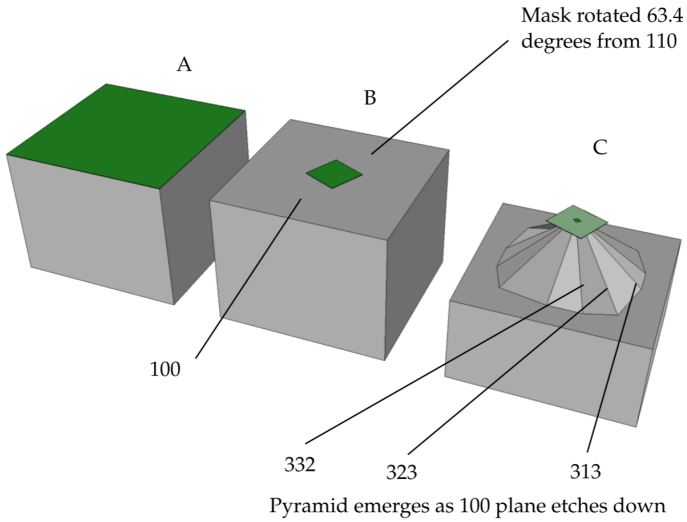


Figure 3.11: Drawing showing the creation of a pyramid structure on the silicon substrate through etching of the crystal planes. This is used as a method of tip formation in SThM fabrication. (A) A silicon nitride layer is deposited on a blank silicon substrate. (B) The silicon nitride layer is patterned and dry etched to form a hard mask rotated 63.4°to the 110 plane. (C) The silicon is wet etched in an alkaline solution to form a pyramid structure. The hard mask will eventually fall off from the pyramid tip if the etch is taken through to completion. (from Lambert [63])

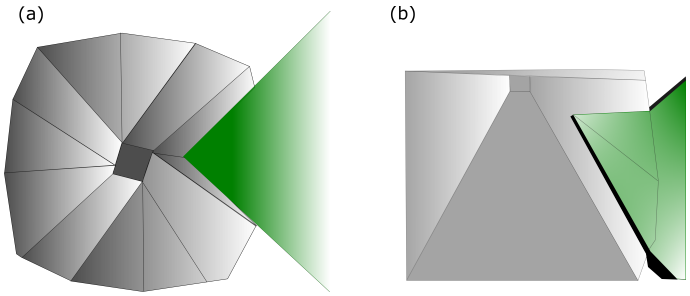


Figure 3.12: Diagram of the (A) Top view and (B) side view of a cantilever tip (green) fabricated against a wet etched pyramid (grey). *(Diagram courtesy of David Atkins of the AFM and Hyper-lithography group, University of Glasgow)*

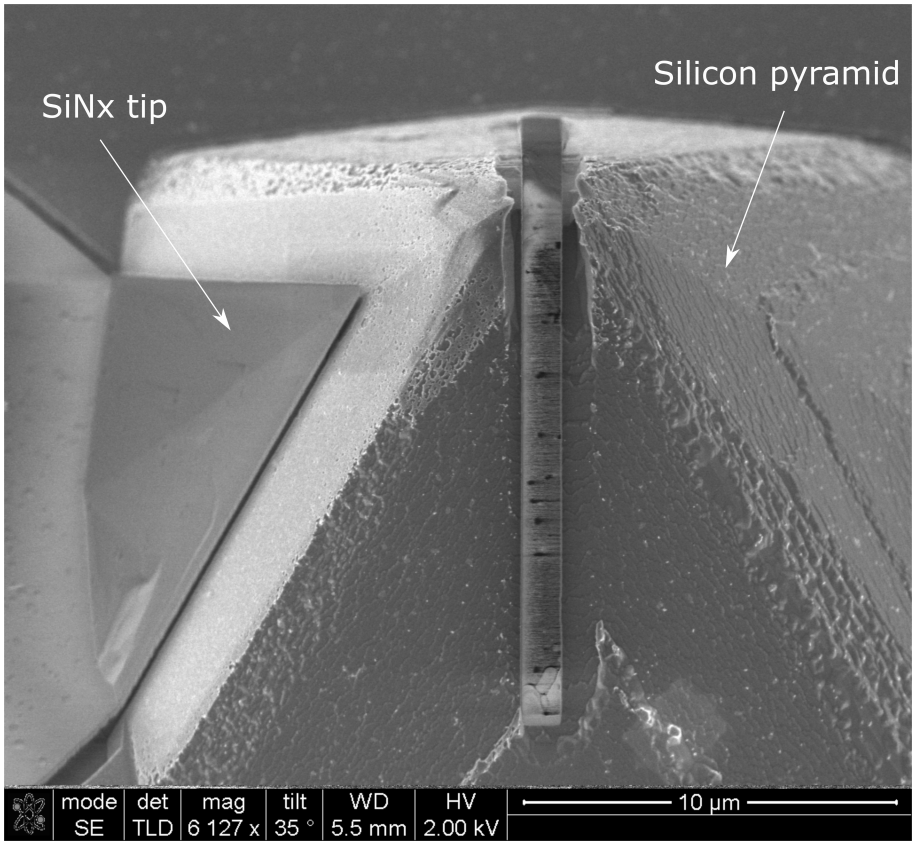


Figure 3.13: SEM image of a fabricated SiNx cantilever against a pyramid structure. *(SEM image courtesy of David Atkins of the AFM and Hyper-lithography group, University of Glasgow)*

Utilising EBL's large depth of focus allows for high-resolution patterning of the tip sensor at the pyramid apex [128–131], shown schematically in Figure 3.14. The creation of an angled probe structure allows for the tip sensor to be in contact with the sample while keeping the majority of the cantilever body far from the sample, reducing the cantilever-sample thermal coupling, which will be discussed in detail in section 4.1.2.

The reliable removal of pyramids and the release of cantilevers, once the cantilever body and tip/resistor have been defined, necessitates additional wet etching. This procedure constitutes the final step in the SThM fabrication process. Given that a wet-release etch is the concluding step, any materials that must remain on the cantilever post-release etch, such as tip resistors or other sensing elements, must be compatible with the etchant used. In the JWNC, this release step is executed using either KOH or TMAH. Consequently, this imposes restrictions on the metals that can be deposited onto cantilevers, limiting them to gold, palladium, platinum, and nichrome.

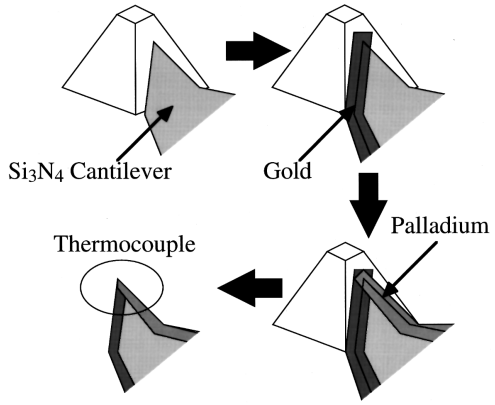


Figure 3.14: Drawing showing the creation of a silicon nitride cantilever and tip sensor (thermocouple) against a topographic silicon pyramid. A recessed cantilever body allows for improved thermal isolation between the body and sample, while the angled tip allows for the tip sensor to be placed in direct contact with the sample. (from Mills et al. [129])

3.4 Multi layer pattern alignment

An advantage of EBL over standard manual UV photolithography is the ability to have automatic computer-aided alignment. As an electron beam is already present in the tool, EBL tools contain electron sensors at various angles that allow the monitoring of backscattered and secondary electron signals (as in SEM). This allows the tool to 'see' the sample surface and take measurements of existing features. Alignments typically involve monitoring the backscattered electron signal to determine the location of features on a substrate.

The ability to layer multiple steps of lithography accurately on top of one other is of great importance to the fabrication of complex devices. This allows multiple successive processes to be applied to the same sample. For example, successive metalisation steps with metals of differing types or thicknesses, or aligning etches to previously defined metalisation steps. In many cases, the functionality, yield, and quality of fabricated devices will depend greatly on the precision to which multiple layers can be aligned on a wafer.

In the case of SThM probes, the thermally sensitive resistor will need to be accurately aligned with the cantilever tip to ensure direct thermal contact between it and the sample being interrogated during scanning.

Due to the small feature sizes written by EBL, slight distortions in the substrate topography either from defined topographic features on the sample, previous lithography step inaccuracies, or from substrate or stage tilt/drift when loading the

sample into the machine, can cause fabrication defects that lead to low device yield [102]. It is therefore greatly important to account for and adjust for these distortions. This can be achieved through the use of alignment markers.

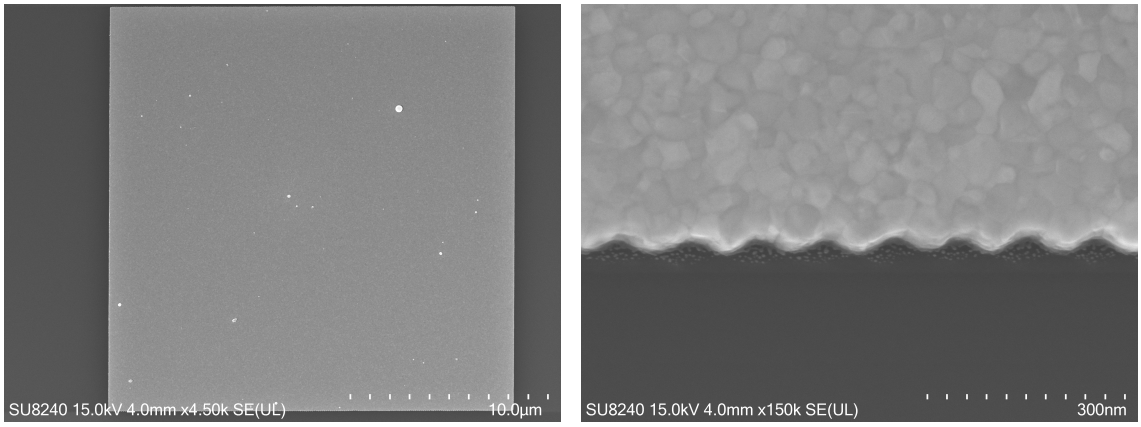
Markers are typically placed in four corners of a design to provide a known reference location on the substrate. This allows the position of subsequent lithography layers to be adjusted not just laterally and rotationally, but also correcting for any scale and keystone effects, to accurately align the new pattern to already existing patterns.

Markers must be made in such a way that there is sufficient contrast in the signal from the marker and the background [132]. This can be achieved by a combination of metalising with sufficient thickness and/or using metals with atoms of a large difference in size (larger atomic number) to that of the substrate material. For example, markers constructed with 50 nm of gold will give much greater contrast in the video signal as opposed to 70 nm of aluminium on a silicon substrate.

3.4.1 Edge detection based

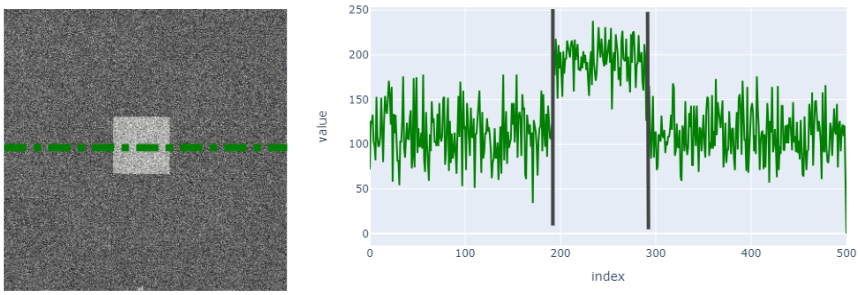
Due to its ease of fabrication, one of the most common markers used for alignments is the square marker (Figure 3.15). Simply, squares of known dimensions are either metalised, or etched onto the substrate at known locations. These marker types provide good alignment placement of features for most semiconductor fabrication processes, with work done internally in the JWNC showing that well defined 20 µm gold squares can provide overlay with an accuracy greater than 20 nm. The location of square markers are determined by measuring the locations of the edge step in the line signal to calculate the centre of the marker, making it a fast and simple measurement, taking less than 1 second to capture and calculate the pattern centre as only a few scan lines are required in each axis as seen in Figure 3.16. However, it makes these markers highly susceptible to edge defects [133] (such as Figure 3.15b) and can lead to alignment errors upwards of 100's of nanometers [134].

In the case of additive processes. Any layers of resist must be spun thick enough to cover the marker, as well as any existing features on the substrate as to not cause accidental 'capping' where material is unintentionally deposited on features. Resist and other contamination build-up on the edges of large square markers can also cause addition errors on the edge detection in the video signal after multiple uses.



(a) (b)

Figure 3.15: (a) Typical 20 µm square used for alignment in electron beam lithography, with (b) showing a close-up of the south edge of a square containing a roughness defect, caused by over-exposure and a large electron beam step size during marker fabrication.



(a) (b)

Figure 3.16: (a) Video image of Square marker with overlaid signal line (green dash) as seen by the e-beam tool. (b) Extracted line shows two steps in video signal at square edges (grey lines) allowing the centre point of the square to be calculated.

3.4.2 Image correlation based

Correlation-based alignment uses a scanned image and a reference image, which are compared to calculate the translational shift between them. This provides a highly accurate method of determining the centre of a surface pattern with alignments better than 50 nm regularly reported [135, 136]. As image correlation does not rely on just a few edge measurements and takes the whole image of a structure into account, it is less susceptible to fabrication defects visible on structure edges. However, as a whole image of the structure is required (typically 4-5 s capture time), this method can significantly slow down throughput of an E-Beam tool.

The correlation of a function with itself can be described as an autocorrelation. The peak sharpness of which can represent a function's sensitivity to any shift in its position in space [137]. Wiener–Khintchine theorem states that the autocorrelation of a function and its power spectral density (PSD) are a Fourier transform pair. It

follows that to gain a sharp autocorrelation, one must use a marker that contains a broad PSD, with a uniform and frequency-rich Fourier transform, such as patterns that have highly complex geometry [138]. Image correlation using patterns with complex geometries are also far less susceptible to marker fabrication defects. As positional data is stored in the many edges of a complex geometry rather than a single edge (such as in a square marker) edge roughness and edge defects are far less influential to the overall alignment accuracy.

In particular, Penrose patterns (Figure 3.17) consisting of two fundamental tiles (derived from tiling by Roger Penrose [139] type P2 'kites' and 'darts'), have shown to be highly effective marker with high accuracy in the sub-nanometer range [138]. The rules set out by Penrose for the tilings are such that every point in the pattern is surrounded by a differing and unique pattern using the two same fundamental tiles. This creates a translationally aperiodic pattern that can be extended infinitely on a 2D plan. The translational aperiodicity with approximately 50% fill ratio of Penrose patterns gives them an advantage as a marker as every part of the pattern is unique, giving it high spatial frequency components, allowing the centre of the pattern to be determined with high sub-pixel accuracy.

An appropriate metric to measure the sharpness of a patterns correlation peak is to compare the primary correlation peak to secondary peaks, which can be expressed through it's peak-to-correlation energy ratio (PCE). The ideal pattern would be a delta function which shows a PCE of 1. Work done previously by Docherty [138] had shown that for square patterns as seen in Figure 3.15, $PCE = 2.2 \times 10^{-4}$; and for Penrose patterns $PCE = 2.2 \times 10^{-3}$, showing an order of magnitude increase in image correlation marker quality when using Penrose patterns.

A disadvantage to using Penrose tiling is its potentially complex fabrication, as features can be close to the resolution limit of many electron beam patterning processes. However, Docherty et al. [140] have shown that even severely degraded Penrose markers can still be used for accurate placements down to the single-digit nanometer range.

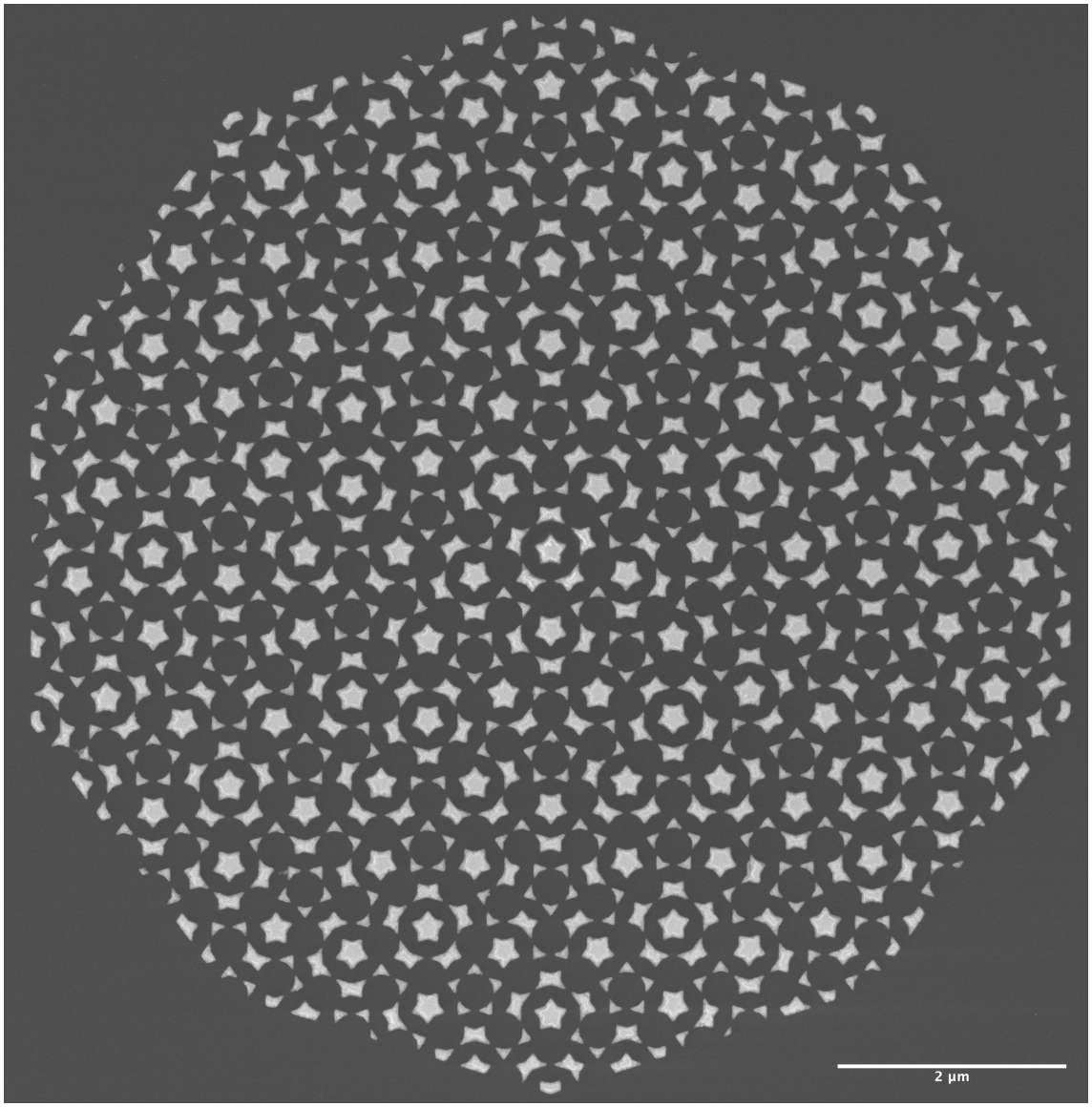


Figure 3.17: A Penrose marker, used for highly accurate image correlation-based alignments.

In this work, three alignment strategies have been employed to create multi-layer devices.

- **Pre-markers** - Two square markers on the substrate that are visible under a standard optical microscope that allow the tool operator to load the sample and coarsely adjust for sample rotation to within approximately 0.2°. This also serves as a starting registration coordinates for the tool to locate the next layer of global alignment markers.
- **Global alignment** - Four square markers placed at the four corners of the substrate. A large area is used to search for these markers as their locations are

only roughly known. The resulting measurement of these markers is sufficient to account for the relative offset, tilt and fine rotational adjustment of the patterns over the whole substrate. This also serves to allow the finding of cell markers without having to search over large areas. This is beneficial to avoid unnecessary exposure of any areas that are to be written with device features.

- **Cell markers** - Four Penrose markers placed in the corners of each repetition of the pattern to be drawn. This accounts for any required local variations in alignment; which could be due to stage drift that occurred in either the writing of previous layers or during the current layer.

3.4.3 Methods for measuring sub-pixel alignment

The measurement of sub-pixel alignment accuracy is a non-trivial matter and requires techniques beyond those that simply measure the distance between two shapes. Vernier structures can be used to gain highly accurate measurements of displacement [63, 140–142]. However, their sensitivity to fabrication defects (such as over/under exposure or development) shows that they can have a very narrow processing window for accurate measurements. Moreover, the manual reading and interpretation of some methods make quantitative comparisons between data sets difficult.

Docherty et al. [141] proposed a technique that proves immune to resist exposure conditions by measuring the frequency of overlaid gratings written in two steps, with each half written with a period of $\frac{2}{f}$ and offset by $\frac{1}{f}$ from each other. Fourier analysis of a grating when perfectly aligned shows that only the fundamental frequency of the grating f is present. Fourier analysis of a grating that contains any misalignment of the grating halves shows that there will be a spectral component at $\frac{f}{2}$ proportional to the severity of the grating misalignment as shown schematically in Figure 3.18.

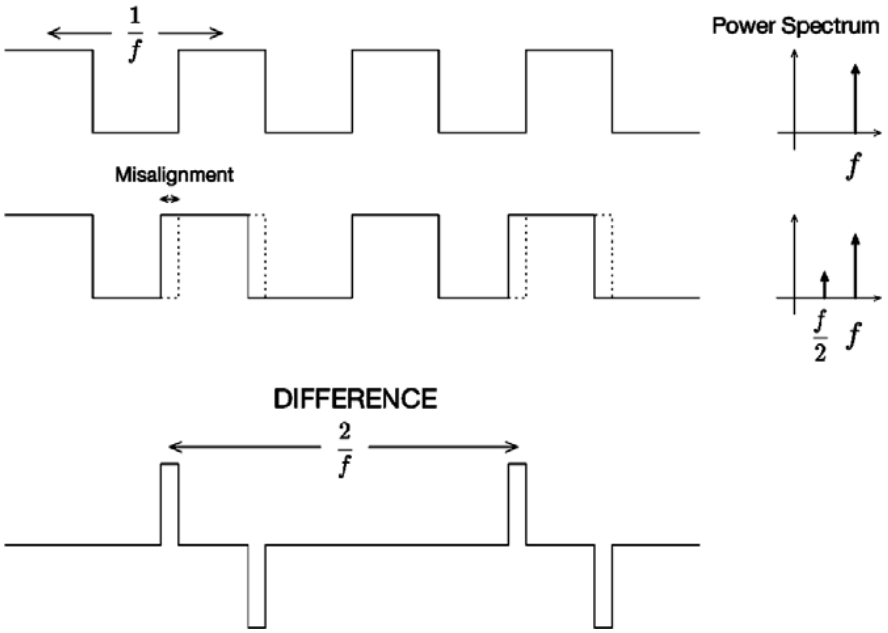


Figure 3.18: Schematic depicting methodology for using the power spectrum of misaligned gratings to determine the offset between alignment maps (From [141])

By creating structures of these gratings, with purposeful misalignments between -6 nm and +6 nm in steps of 1 nm, and fitting a 'V-shape fit' to a plot of the amplitude of the half grating frequency peak against the designed misalignment of each grating, Docherty et al. [141] had shown that sub-nanometer measurements of alignments could be made in Figure 3.19.

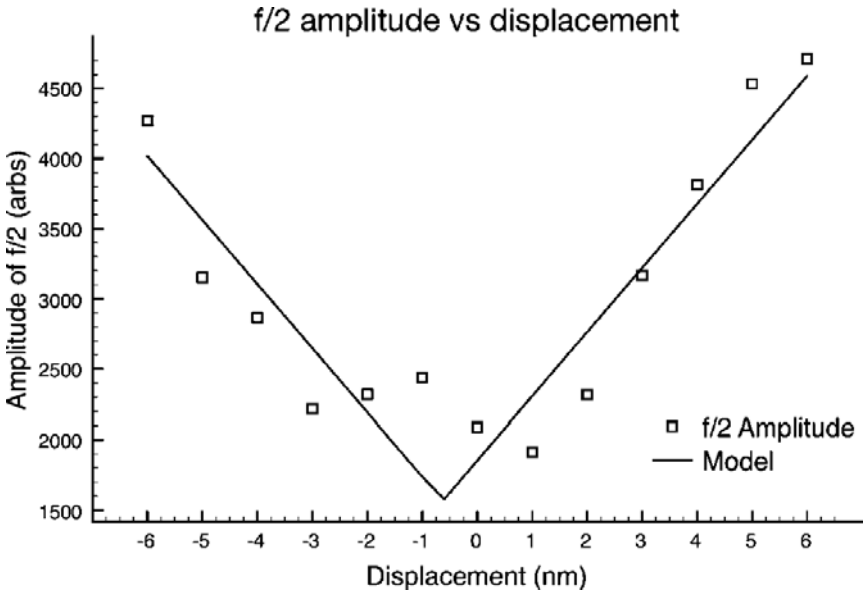


Figure 3.19: V-Shape model fit to misalignment, showing a sub-nanometer measure of alignment accuracy of 0.63nm (From [141])

The benefit of this method of vernier fabrication is that it can be written in the same EBL step, with the same exposure and resist conditions, but with each half aligned to different markers. Therefore the only variant in the measurand is the set of markers that have been aligned to, as well as any possible stage drift that may have occurred during the writing of the grating. However, with a write time of approximately 20 seconds this stage drift should be minimal.

3.5 Metrology methods

The ability to create micro and nano functionalised surfaces and devices requires accurate inspection and characterisation, not only of the final fabricated device, but also of the fabrication process steps. The multitude of characterisation tools used by microscopists vary depending on size, resolution, as well as the required information from the device or fabrication step being examined.

3.5.1 Optical microscopy

The optical microscope is the first port of call for inspecting samples during each step of the fabrication process. It allows quick imaging of large features (such as square markers) in a non-invasive manner. It also allows for the quick inspecting of spun EBL resists for debris or 'comets' that could potentially affect the resulting

EBL quality before exposure, or inspecting the development progress after exposure. However, quantitative measurements of features in the sub-micron region are difficult due to the previously mentioned Rayleigh criterion and diffraction limits of the visible wavelength light used.

3.5.2 Scanning Electron Microscopy

Scanning Electron Microscopy (SEM) is an invaluable tool used for high-resolution inspection of micro and nanostructures. It can be used to quantify the size of fabricated features on the order of nanometers. The SEMs used throughout this work are the Hitachi Su8240, Hitachi Su8230, and the FEI Novasem.

SEMs are able to resolve such small features due to electrons having very small wavelengths as described in detail by de Broglie [143]. In summary, An electron exhibits a wavelength inversely proportional to its momentum. This is called the de Broglie wavelength and can be described through Eq 3.4.

$$\begin{aligned} \lambda &= \frac{h}{p} \\ &= \frac{h}{\sqrt{2m_0 eU}} \end{aligned} \tag{Eq 3.4}$$

Where h is planks constant, m_0 an electron rest mass, e electron charge and U is the potential difference. It can be seen for an electron potential of 10 kV, the de Broglie wavelength can be determined to be 10 pm. Substituting the de Broglie wavelength into the Rayleigh criterion (Eq 3.1) shows that very high resolutions are possible.

The SEM has two primary modes of detecting electron sample interactions, through its secondary electron detector, and its back scattered electron detectors. The secondary electron signal is generated from the inelastic scatter of a primary electron with an electron orbiting a sample atom. These signals generally have a lower energy and leave the sample at an angle from the surface. By contrast, the back scattered electron signal arises from the elastic interaction of a primary electron and the nucleus of an atom, generally having higher energies and coming from deeper within the sample. These interactions with the sample surface have been depicted in Figure 3.20.

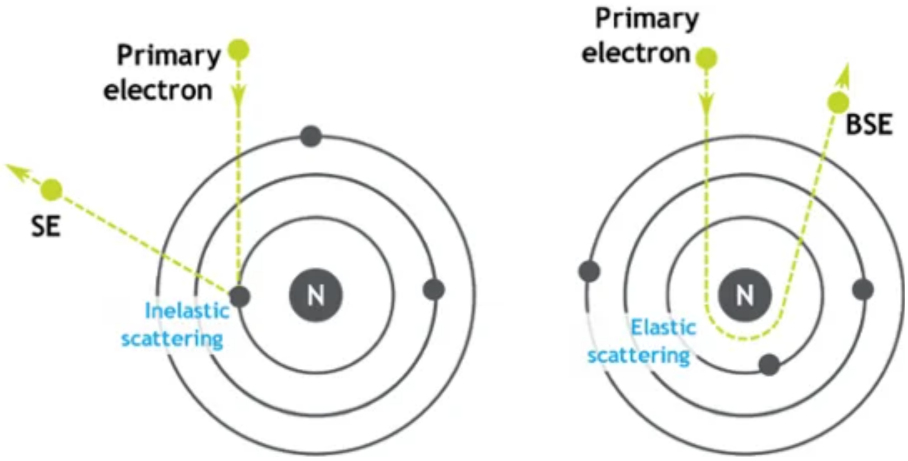


Figure 3.20: Primary electron beam interactions with an atom in a sample. LHS - The formation of secondary electrons formed from inelastic scattering. RHS - Back scattered electrons formed from elastic scattering (from AZO Materials [144])

Secondary electrons can be useful for the detection of edges in a topographic sample. This is due to more electrons being emitted out the side of a feature according to Figure 3.21 showing greater contrast. In the case of the back scattered electron interactions with surface atom nuclei, the signal strength (depicted as contrast) at the back scatter detector can also provide information regarding the elemental make-up of surfaces. Sample atoms that have a higher atomic mass have a greater interaction with the primary electron beam.

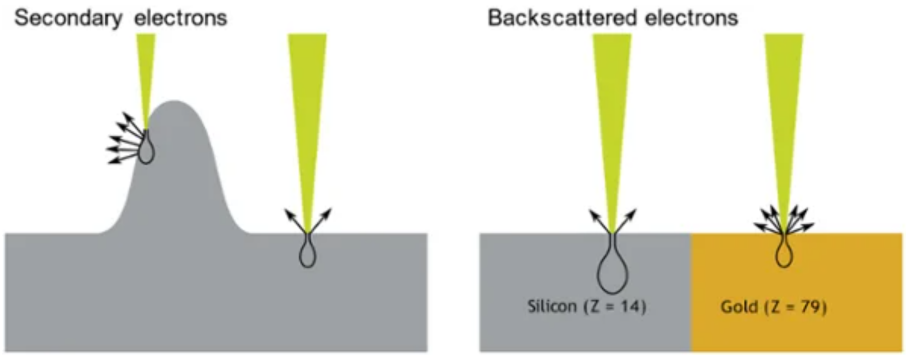


Figure 3.21: Electron beam interaction with topographic and material differences. LHS - more secondary electrons are emitted from topographic edges, showing a change in image contrast. RHS- material atomic number effects the yield of back scattered electrons. (from AZO Materials [144])

Having considered this background information, it is possible to fabricate samples to characterise the custom built SThM in chapter 4, as well as experimentally explore patterns and structures for improving upon the overlay alignment capabilities of the EBPG5200+ EBL tool within the JWNC. Improved alignment capabilities will

increase the yield of devices that rely on small overlaps of electron tunnelling sensors described in section 2.4. Additional techniques discussed in this chapter, such as wet/dry etching and thin film growth mechanisms, will be relevant in chapter 8 during the fabrication of designed strain sensing elements.

SThM topographic control through the 3ω signal

4.1 Introduction

In this chapter topographic control of the SThM has been addressed in dark conditions, without the use of a laser, in ambient air conditions using the concept of "thermal feedback". This is achieved through monitoring of the probe's resistive elements when driven in AC mode.

Commercially available KNT probes were used in this work[1]. As referenced in section 2.3, these consist of a thermo-resistive palladium tip (radius of approximately 50-100 nm [53, 54, 62]), at the end of a soft SiNx cantilever allowing for high-resolution topography and temperature mapping. Typically they have electrical resistances between 300-400 Ωwith a sensitivity of $\sim$ 0.1 - 1 Ω/K [62].

4.1.1 Requirements to compete with optical methods

One of the main advantages of the optical lever system is that the thermal measurement is separated out from the cantilever deflection measurement. Meaning that measurements of deflection can be taken quickly, and in real-time due to the fast response times of the photodiode with signal detection bandwidths upwards of 5 MHz [145]. The thermal signal can be slow compared to the optical lever, with thermal bandwidths between 1-2 kHz available from KNT-SThM probes [58, 63].

Any method developed must balance resolution, either topographic or thermographic, with scanning speed dependent on the experimental context. One may not require high topographic resolution but require high-resolution thermography data,

[1] https://kntnano.com/probes

for example in bulk materials studies [60], or one may require both high-resolution topography and thermography [53, 62].

Any system created must have the ability for flexibility to balance the pixel capture speeds, preventing any possible drift artefacts, and having appropriate resolution for the scan required.

4.1.2 Sample-environment thermal interactions

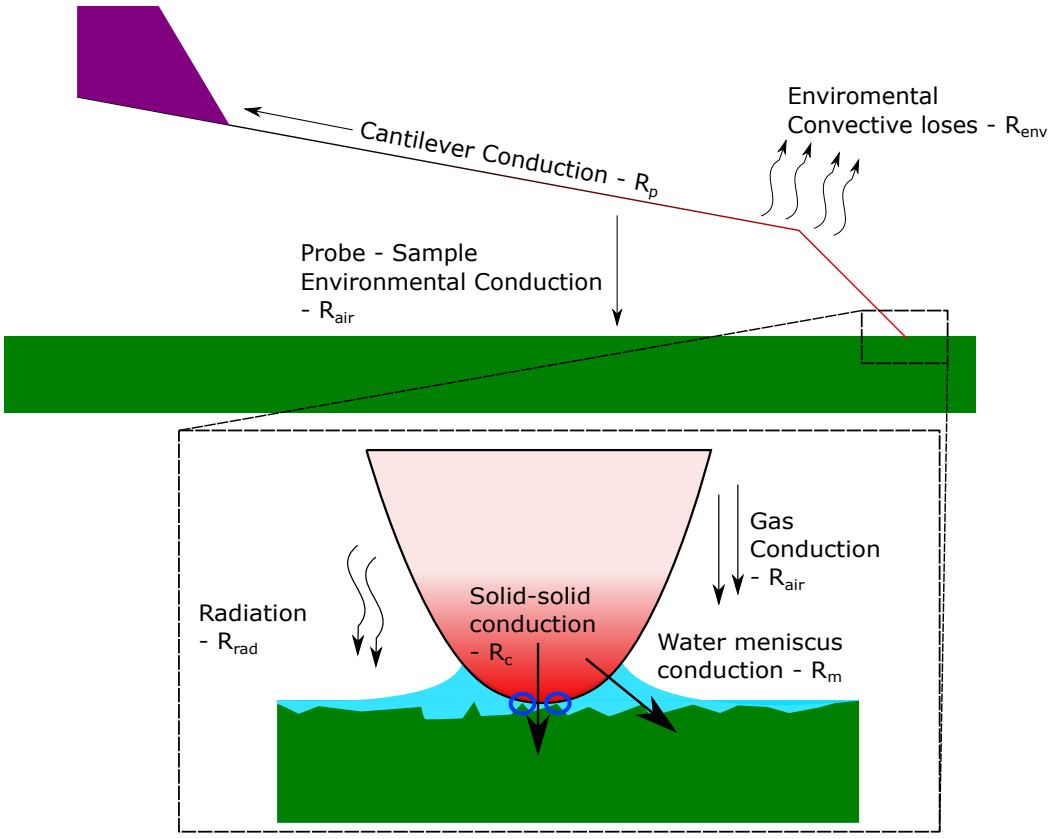


Figure 4.1: Schematic showing thermal transfer paths of the SThM between the probe, sample, and environment while scanning in ambient air. Probe tip conduction paths include primarily, solid-solid conduction at mechanical contact points (dark blue circles), water meniscus conduction through hydration or contamination films, gas conduction, and radiation. However, the effects of radiation are minimal. Cantilever heat transfer paths include solid conduction to the probe base, general probe-sample environmental conduction, and convective losses to the environment.

The schematic in Figure 4.1 presents the multiple heat transfer paths that the SThM system has between the probe tip, the sample, and the ambient air environment. The heat flux for each can be dependent on many factors, such as probe design, tip shape, and environmental conditions. For example, it is reasonable when scanning in vacuum conditions to disregard gas conduction, water meniscus conduction,

cantilever-sample environmental conduction, as well as convective losses to the environment.

Thermal resistance networks are commonly utilised to describe these various heat transfer mechanisms, by equating heat sources, sinks, and flux to electrical elements in a circuit. In these models, current represents heat flow, voltage represents a temperature change, and resistors represent thermal resistances. Many SThM studies present different networks dependent on the study and environment of concern [3, 48, 51, 146].

A complete model proposed by Lambert [63] describes the SThM in any operating environment, utilising switches to include or isolate heat transfer paths associated with environmental or contact conditions. An adaptation of the model has been provided in Figure 4.2.

The circuit in Figure 4.2 can be split into four distinct sections. These are; elements that describe the probe interactions with itself (red), elements that describe probe-sample interactions (green), elements related to the sample (blue), and environmental dependant elements (purple).

Switches

An important inclusion of switches in the model allows for direct control of the thermal transfer paths in the circuit equivalent. In the case of the lack of a surrounding gas or liquid, i.e in a vacuum, S_{env} will remain open. One can see that the only form of thermal transfer between the sample and probe is through R_{rad} until the closure of S_c, placing R_c in parallel, which occurs only when mechanical contact has been made.

In an example of STP scanning conditions, as briefly touched on while discussing the functional principle of STP in section 2.4.1, thermal loading on the tip of a cantilever will change as the thermal heat transfer paths to its environment changes, but contact is never made. S_c remains open throughout, and S_{env} remains closed. It can then be seen that R_{air} and R_{rad} are the only thermal transfer paths between the sample and probe.

Temperature nodes

Nodes of importance have been highlighted in a red circle, labelled T_p and T_s, signifying the probe tip temperature and sample temperature respectively. These

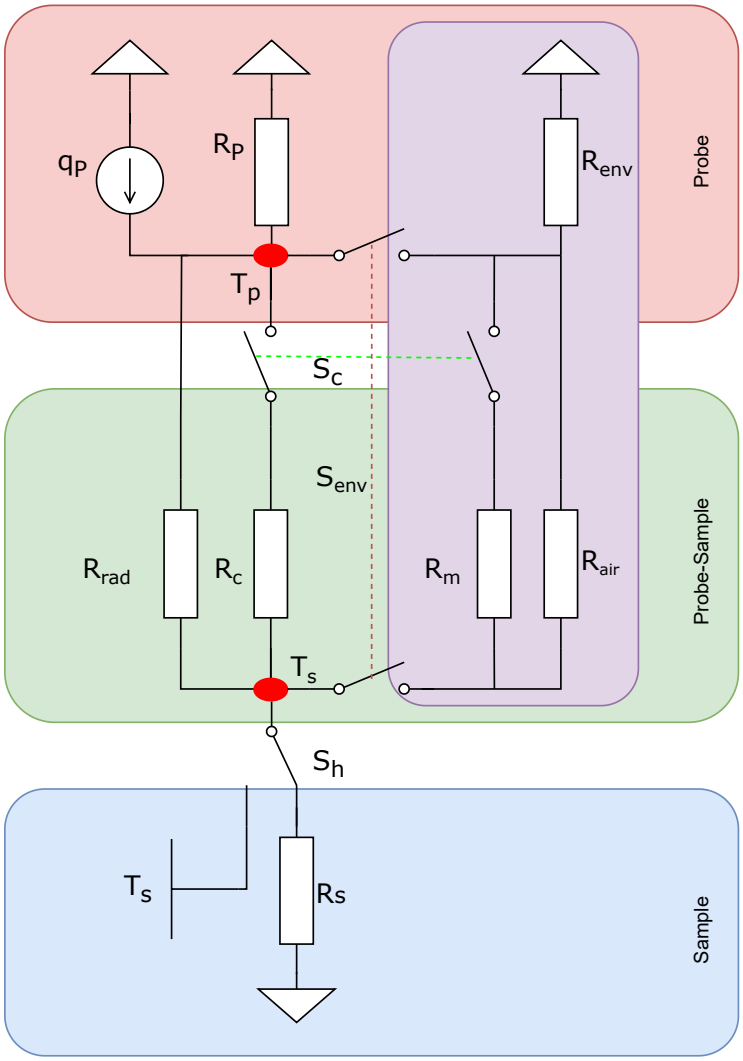


Figure 4.2: Thermal-electrical equivalent resistance network, used to describe the SThM probe-sample interactions in any environment and operating conditions. The network is split by colour, indicating elements that describe the probe interactions with itself (red), elements that describe probe-sample interactions (green), elements related to the sample (blue), and environmental dependant elements (purple). (adapted from Lambert [63])

can be thought of analogously to voltage nodes in an electrical circuit.

The probe tip temperature node, T_p, can be dependent on the mode of operation of the SThM. In passive SThM studies, the node T_p can be described by the probe's ambient temperature, and effects of the probe temperature coefficient of resistance (TCR) as influenced by the sample temperature, T_s, through the resistance network. In active operation, T_p is heated to above ambient temperature by applied current flow, q_p. The measure of T_p is then a function of the efficacy of thermal heat abstraction by the sample, which is a function of the thermal conductivity of the sample, R_s.

The sample temperature node, T_s, can be at ambient temperature or in the case of an active device measurement, elevated above ambient by closing the switch, S_h, to the voltage source T_s. This node can also be affected T_p through contact with the probe or conduction through the air.

Sources and sinks

In active operation, probe joule heating can be represented by q_p, this raises the temperature of node T_p. In purely resistive materials, such as the SThM probe tip resistor, it can be assumed that electrical power is dissipated as heat according to the Joule-Lenz law, $P = I^2R$, where I is the applied current, and R is the probe electrical resistance.

Another source is in the case of an active sample, or a device at a raised temperature above ambient such as in the case of a micro heater device. As stated previously, this is represented by switching S_h and the node T_s is driven to a stable temperature by the voltage source T_s.

Ground potentials in the electrical equivalent represent heat sinks in the setup where the temperature is that of the overall setup and ambient environment. These sinks can be assumed to be large in size, compared to the heat generated by either the probe or sample (typically on the order of µW to mW), to the extent that temperature fluctuations of sinks, due to probe-sample temperature changes, is negligible.

Resistances

R_{env} and R_p are convective losses from the probe tip to the environment and solid conduction to the probe chip base respectively. In the absence of surrounding gas or liquid, such as when in a vacuum, R_p is the only method of heat abstraction from the probe until contact can be made.

R_c is representative of the interfacial thermal resistances that arise from mechanical solid-solid contact between the probe tip (approx. 50 nm radius) and sample. Due to the nanometer length scales of these contacts in SThM, any changes in this mechanical contact can cause large variations in this contact resistance.

Radiative heat transfer between the probe and sample, R_{rad}, occurs regardless of the environment that is scanned. However, its effects are negligible and are never regarded as a dominant heat transfer mechanism in many studies [62]. R_m represents

conduction through the water meniscus that forms between the probe tip and thin hydration films on the sample due to ambient humidity in the environment. It has been reported that R_m can be a considerable contributor to probe-sample coupling [51]. However, investigations by Assy [147] disprove this claim and solid-solid contact remains the primary factor for thermal transfer.

R_{air} describes the conduction between the probe and sample through environmental gases or liquids. As long as a surrounding liquid or gas is present, this probe-sample heat transfer path is present regardless of contact conditions. The magnitude of this resistance is proportional to the separation distance of the probe elements to the sample. Conduction between the probe through R_{air} can occur locally through the tip apex to the sample as well as through the cantilever body to the sample. The slip regime, considered to be roughly the area from the tip extremity to 7 µm along the cantilever, has a significant contribution to the overall probe coupling [62]. This region can cause significant asymmetries in the obtained scans that align with the probe mounting direction. This has been shown schematically in Figure 4.3 and 4.4.

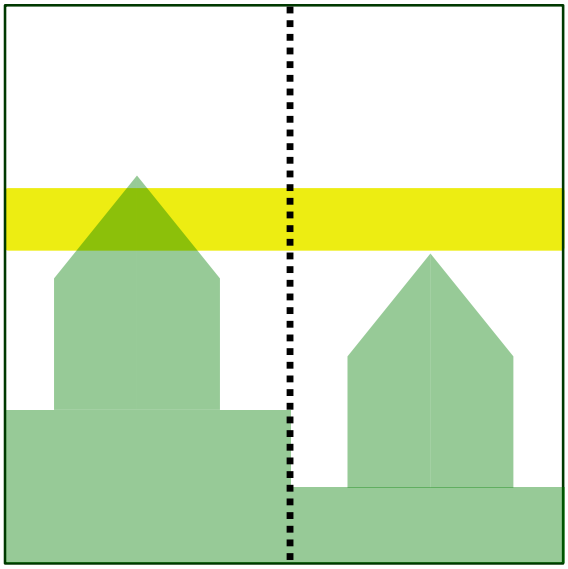


Figure 4.3: Top down diagram of conduction through R_{air} when the probe overhangs the feature shows asymmetries in thermal profiles. The thermometry profile around the yellow feature would expected to be symmetrical. However, the overhanging cantilever (LHS) would show a greater response to that of the cantilever with no overhang of the feature (RHS)

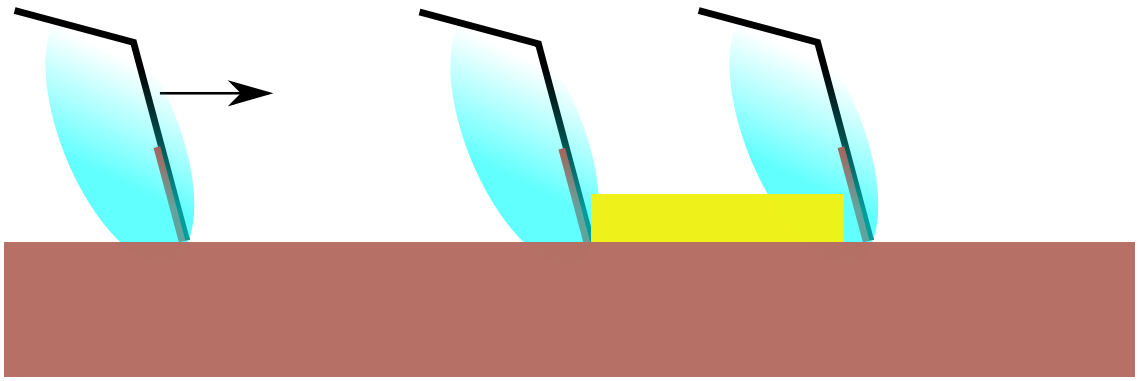


Figure 4.4: Cross sectional diagram of conduction through R_{air} when the probe overhangs the feature. It can be seen that conduction through R_{air} (light blue area) is greater when the probe overhangs the feature. (Features not to scale)

4.1.3 Thermal Artefacts

Contact Artefacts

Multiple or reduced contact artefacts are a common issue in SThM [148–150]. They arise from the increase or decrease in the interaction area of the probe with the sample due to changes in the sample topography, as shown in Figure 4.5. In terms of the thermal resistance network, increased thermal contact from two distinct contact points (Figure 4.5b) will decrease the thermal resistance, as multiple R_c impedance elements are placed in parallel. In the case Figure 4.5c, reduced thermal contact with the very edge of a topographic feature will cause an increase in thermal resistance, and increase the R_c impedance in the thermal resistance network.

This makes quantitative SThM on samples with complex geometries difficult. Work done by Martinek et al. [149] and Klapetek et al. [150] attempt to compensate for these thermal artefacts by post-processing the thermal signal with consideration to its topography signal. This has been implemented using neural networks or finite element methods.

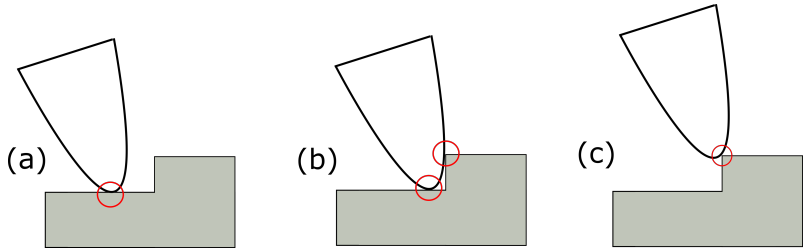


Figure 4.5: Diagram showing topographically induced thermal artefacts. Points of tip-sample contact are circled in red. (a) Shows a general single point of contact during a scan on a flat surface. (b) Due to a second general point of contact introduced by the base of sample topography, the tip-sample interaction increases, this equates to an increase in conduction between the tip and sample. (c) A point of contact with the very top edge of a topographic feature decreases the contact area between the tip and sample, increasing the thermal resistance, and decreasing conduction. Both conditions (b) and (c) both result in artefacts in the resultant thermal image.

Laser Induced Artefacts

Accurate, quantitative thermometry measurements of a sample can also be prohibited by influences to the measurement that are not directly related to the thermal interactions of the tip and sample. In many SThM studies, the use of a laser for deflection sensing has been shown to increase the probe temperature adding a significant source of uncertainty to the measurement [2, 3, 52, 151–153].

The extent of temperature rise depends strongly on the position of the laser on the cantilever [3] since the heat is largely dissipated through thermal conduction through the cantilever, and can have a significant impact on thermometry measurements in vacuum. As a result, the calibration of the SThM as a thermometer will change every time the beam deflection laser is adjusted or moved. Making matters worse, the power deposited into the cantilever will be affected by laser reflections from the sample as the probe is scanned, resulting in a significant interferometric component to the heating. In terms of the thermal resistance network discussed earlier. The addition of the laser into the SThM system is equivalent to adding an unknown and variable current noise source to the T_p node.

Many functionalised AFM probes are also constructed of multilayers of materials, with differing thermal expansion coefficients, causing thermo-mechanical bending [154, 155]. The optical lever can misinterpret this thermal bending, resulting in an entirely incorrect value for the cantilever bend being reported by the feedback loop, and therefore producing erroneous topographic information [6, 156].

It has been observed that the implementation of a laser alone can introduce errors of up to 37% [2] in temperature measurements. To address this issue, some re-

searchers have proposed the utilisation of 'Dark mode' techniques [2], involving the landing of the probe using the optical lever method with laser assistance, followed by its deactivation during thermometry measurements[2, 3]. Alternatively, another approach involves the incorporation of fabricating dedicated elements to facilitate laser heat abstraction from the cantilever to the chip base, thus reducing the adverse effects [153, 157]. However, the use of dedicated elements, although effective in reducing the problem, adds complications to the fabrication of the probes as explored in chapter 8. It should also be noted that their inclusion only reduces the laser influence and does not necessarily eliminate the thermal measurement uncertainty [153], and does not account for laser-induced topography artefacts as described by Mordue et al. [6].

4.2 SThM approach curve analysis in air

Before looking to use the thermal signals as a means to gain topographic control in SThM, we must first analyse the relationship of the simultaneous force-thermal with distance curve relationship. An example of a typical SThM approach and retract curve is shown in Figure 4.6. The thermal resistance network for out-of-contact and in-contact air operation of the SThM can be seen in Figure 4.7.

In active mode, the current passed through the SThM sensor is sufficient to induce significant self-heating of the probe [7, 63]. The temperature rise depends on the total thermal impedance from the sensor to the environment and solid conduction to the probe base (R_{env}, R_p respectively). In air, this impedance varies smoothly over long distances as the sample approaches a surface due to air conduction to the sample (R_{air}), with a sudden rise in conduction seen on the achievement of solid-solid contact (S_c closing) and solid-solid tip-sample conduction (R_c), as well as water meniscus conduction (R_m).

When the probe base is extended further towards the surface after the initial tip-sample contact point, the sensor-sample distance remains constant. Further motions of the microscope are accommodated by the flexure of the soft probe cantilever and an increase in compressive force between the sensor and sample. Past the initial surface contact point (0 point in Figure 4.6) little change in contact thermal signal is seen for moderate compressive forces due to slight changes in R_{air}. Upon retraction of the probe, tip-sample adhesion generally leads to significant hysteresis in the thermal-distance relationship, so that the solid–solid contact is sudden, and maintained, until the probe is explicitly removed, or forced away from the surface.

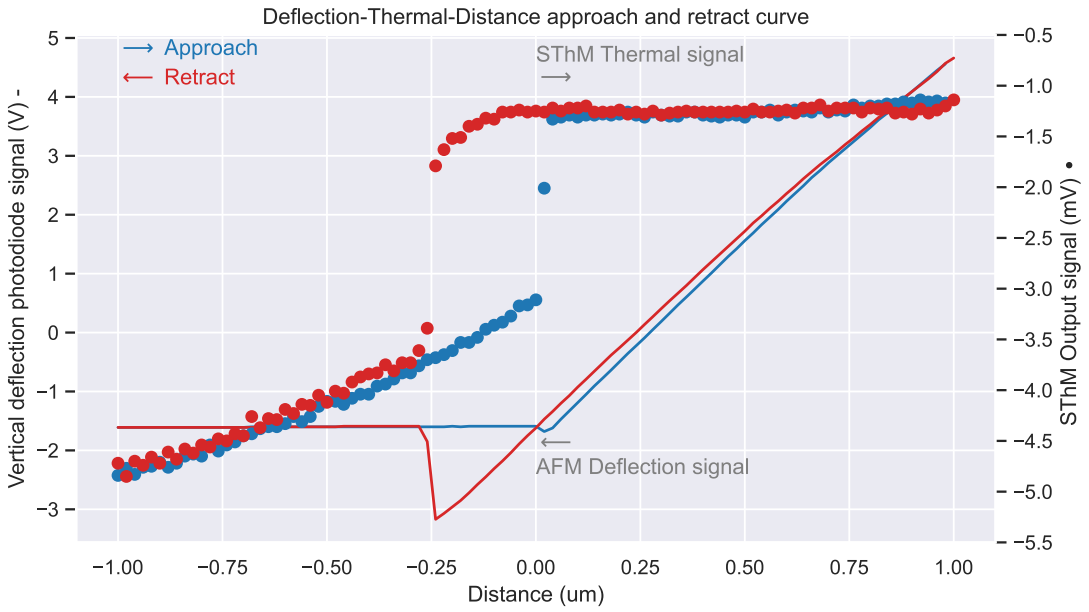
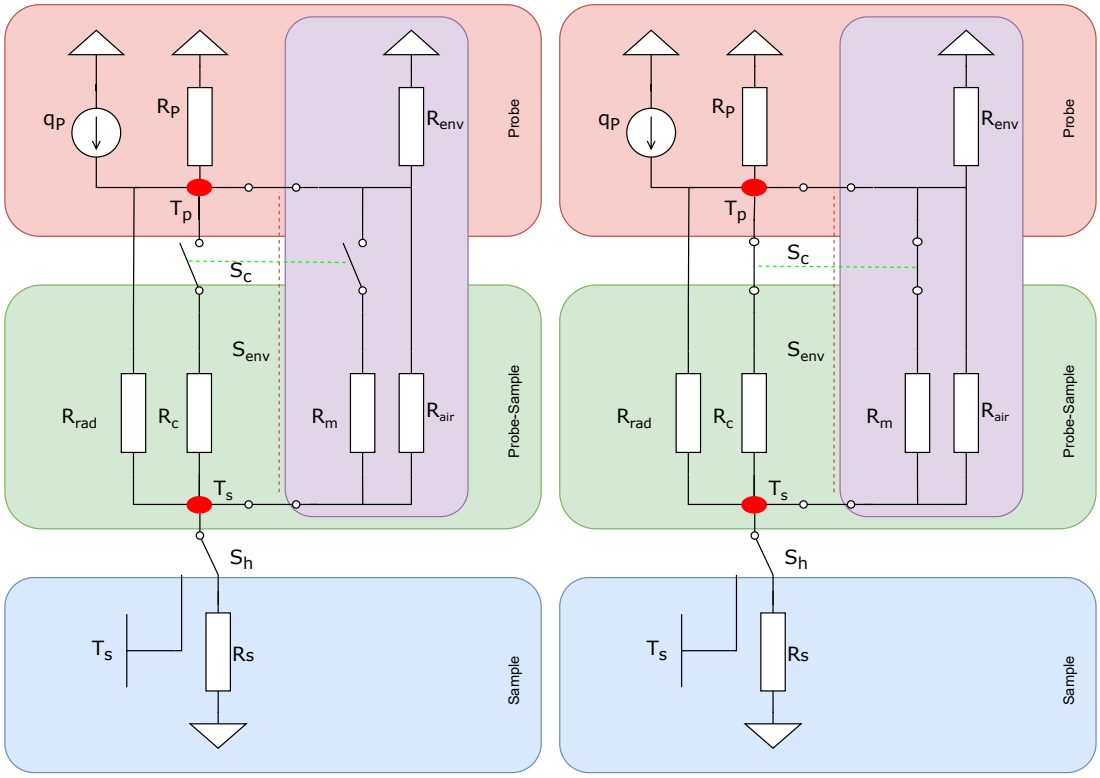


Figure 4.6: A typical approach and retract curve showing the output of the thermal and photodiode signals when driven in DC mode. The 0 distance point is the initial contact point of the probe with the surface. Significant hysteresis can seen upon retracting the probe from the surface, due to the soft cantilever spring constant. It can also be noted that for moderate distances into the surface, there is little to no observable change in the SThM output. *Data courtesy of Dr. Christopher Mordue of the AFM and Hyper-lithography group, University of Glasgow*

This behaviour of the SThM provides a convenient method for controlling the tip height and hence for topographic control of the microscope. One simply approaches the sample until the self-heating of the sensor is observed to drop indicating that the probe has made contact with the surface, the piezo extension at which the signal drops is then a measure of the sample topography. Due to the stability of the probe's thermal signal beyond contact (as seen in Figure 4.6), for moderate cantilever force there should be minimal effect on the thermometry measurement taken. Since the temperature of the sample may be non-uniform, a simple DC measure of probe temperature, such as that in Figure 4.6, is not an appropriate metric. In the case that the sample, environment, and tip are at the same temperature then there is no increase in heat conduction upon contact.

Driving the probe with an AC current and using the "3-omega" (3ω) measurement technique can overcome problems presented by simple DC measurement of probe temperature. This comes with the disadvantage that the measurement of the thermal signal is no longer one that can happen in the time domain, and must be measured in the frequency domain or through more complex signal processing techniques. This adds compromises on pixel capture times and resolution of the thermal



(a) Out of contact (b) In contact

Figure 4.7: Thermal resistance model of probe operation in air. As S_{env} remains closed, there will always be a thermal transfer path through R_{air}.

signal. However, AC measurement comes with many advantages as it avoids interference from sample temperature measurements, as well as allowied for signal-to-noise improvements by bandwidth narrowing.

4.3 Experimental design

Before utilising any of the methods for the determination of sample topography. We must first describe the setup, both electrically and mechanically, to allow accurate interpretation and quantification of results and scans obtained.

4.3.1 Electrical setup

As mentioned in section 4.2, to monitor the probe's thermal conductivity to its environment we must drive the probe with an AC bias. Figure 4.8 shows a simplified block diagram of the electrical architecture used to achieve this. A microcontroller development board featuring an overclocked MIMXRT1062 ARM Cortex-M7[2] was

[2]Teensy 4.1 : https://www.pjrc.com/store/teensy41.html

used to provide low latency interrupt-driven processing of data.

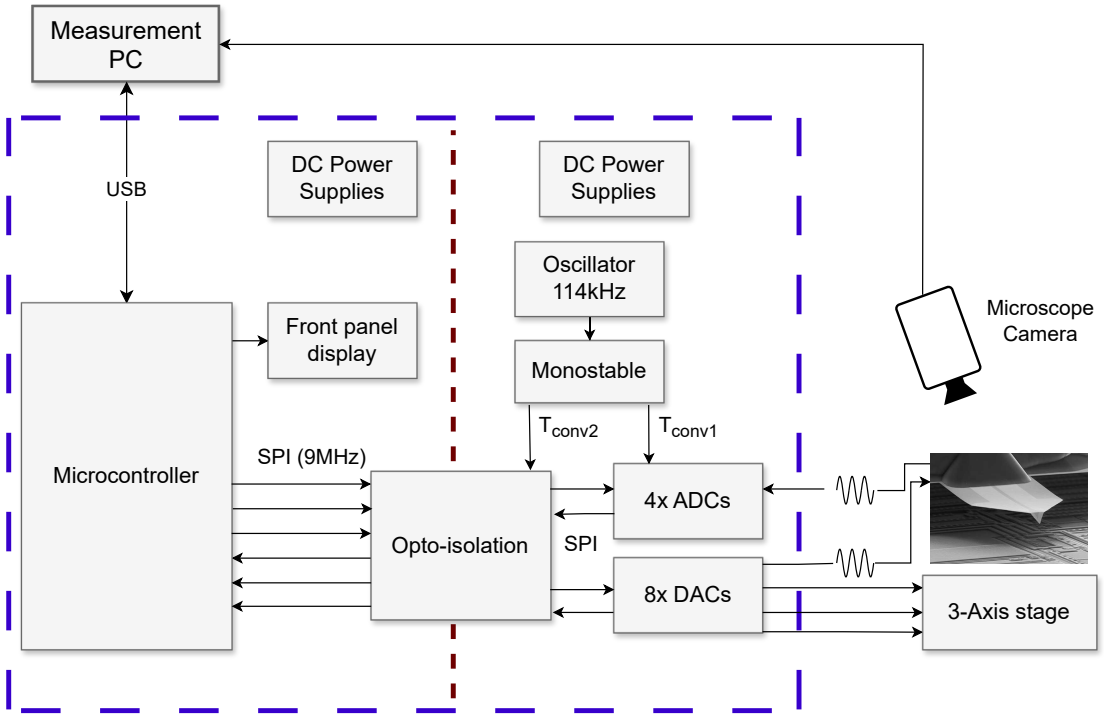


Figure 4.8: Simplified block diagram of the feedback electronics box, dashed brown line shows electrically isolated components via opto-isolation. The Blue dashed line indicates components internal to feedback electronics, and external devices.

An oscillator providing a stable clock reference was utilised to which we can drive a 16-bit digital-to-analogue converter (DAC) and analogue-to-digital converter (ADC) in an interrupt-driven fashion to bias and monitor the probe output. This allowed the probe to be continually AC biased when moving the probe through space, negating any thermalisation time that may be required to get the probe into thermal equilibrium with its environment. To achieve low phase noise and low jitter acquisition, convert lines of the ADC and DAC were directly linked to the oscillator through a monostable, allowing for a convert signal to be sent to the ADC and a subsequent interrupt signal to the microcontroller after the ADC conversion completion time.

Opto-isolation of the microcontroller and analogue measurement components allowed for low interference between the two sides. However, such architecture severely limits the communication speed between the microcontroller and the ADCs/DACs. The SPI communication bus between them was experimentally found to be reliable up to a maximum speed of 9 MHz through the opto-isolator utilised. This was lim-

ited by the slew rate and propagation delay of the opto-isolaters. The ADC/DAC setup was designed such that the MOSI of the DAC for biasing the probe and the MISO of the ADC for measuring the probe response, are written and read on the same clock edges. This allowed for efficient data transfer across the isolation barrier in only 3 bytes, with an extra 3 bytes per movement of each axis of the stage. In reality, on a probe approach to the surface, one would only require movement of the Z axis of the stage, so approaches can occur in as little as 6-byte transfers.

The probe was configured in a balanced Wheatstone bridge configuration as shown in a simplified diagram in Figure 4.9. When the Wheatstone bridge was balanced, small variations in the thermally dependant resistance of the probe were measured with a large gain ($\times$101), low noise amplifier. Current limiting resistors were chosen to limit the current through the probe to within safe operating limits. Literature studies of SThM probes of a similar type to KNT probes, tend to use probe currents of between 300 µA and 2 mA to acquire an appropriate signal-to-noise ratio as well as prevent damage to the probe tip [3, 53, 57, 62, 63, 158]. The manufacturer's website[3] states a recommended maximum DC probe current of 2.5 mA. Probe resistances of between 300 and 400 Ω with a typical resistance of around 350 Ω were used in this work. Therefore, 0.1% 2 kΩ resistors were chosen to limit the current through the probe to a maximum of around 1.4 mA when driven by the maximum available DC voltage from the control instrumentation. Probe currents and power dissipated through the tip resistor were available up to the 3.4 V maximum and have been graphed in Figure 4.10 and 4.11.

[3] https://kntnano.com/probes

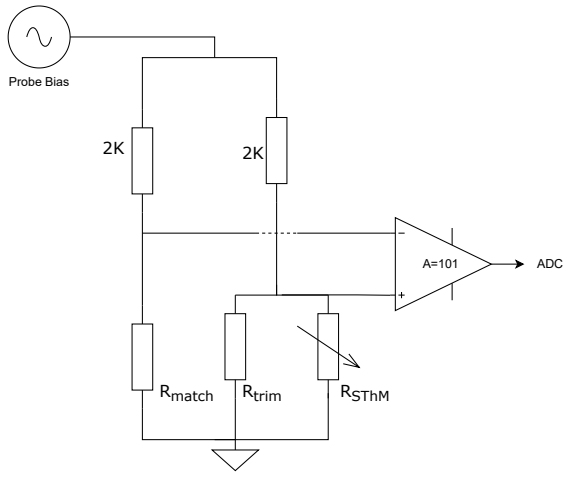


Figure 4.9: Simplified circuit diagram used to bias and measure SThM probes in this work. The probe is placed in a Wheatstone bridge configuration. R_{match} is chosen to be a high tolerance resistor with the nearest standard value below the resistance of the probe at room temperature. R_{trim} is then selected to bring the parallel resistance of R_{trim} and R_{SThM} down to match R_{match} as close as possible. This balances the bridge and allows for high sensitivity to changes in R_{SThM}

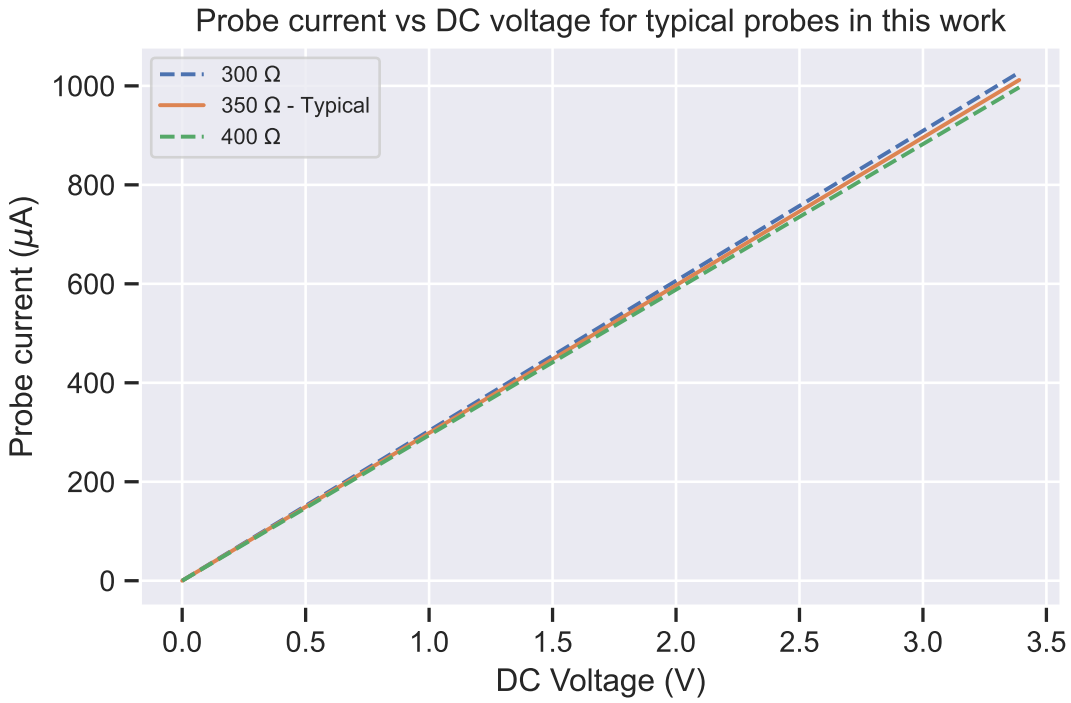


Figure 4.10: Probe DC currents available to bias the probe in the measurement setup, 2kΩ limiting resistors are employed to limit the probe current to 1.4mA for probes used in this work

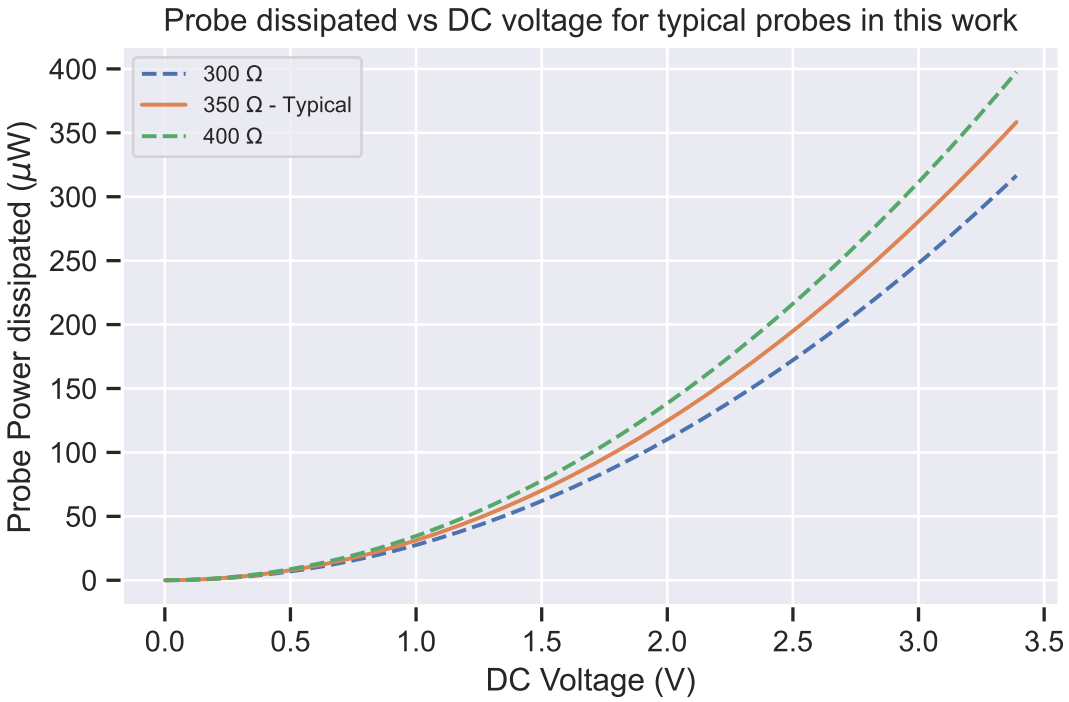


Figure 4.11: Probe dissipated power from DC voltage available to bias the probe in the measurement setup, limiting resistors are employed to limit the probe power to 800µW for probes used in this work

One should note that in experimentation we require AC probe excitation, therefor we take the RMS of the voltage amplitude to obtain the current through R_{SThM} and power. Graphs for the available RMS current and power can be seen in Figure 4.12 and 4.13.

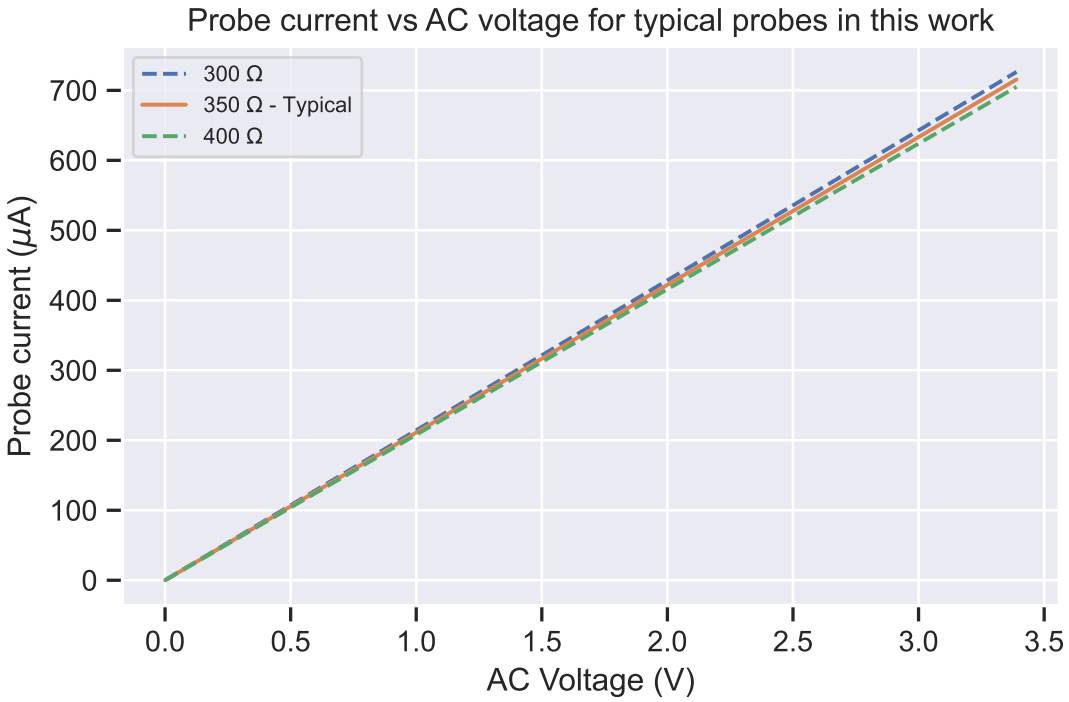


Figure 4.12: Probe DC currents available to bias the probe in the measurement setup, limiting resistors limit the probe current to approximately 1mA for probes used in this work

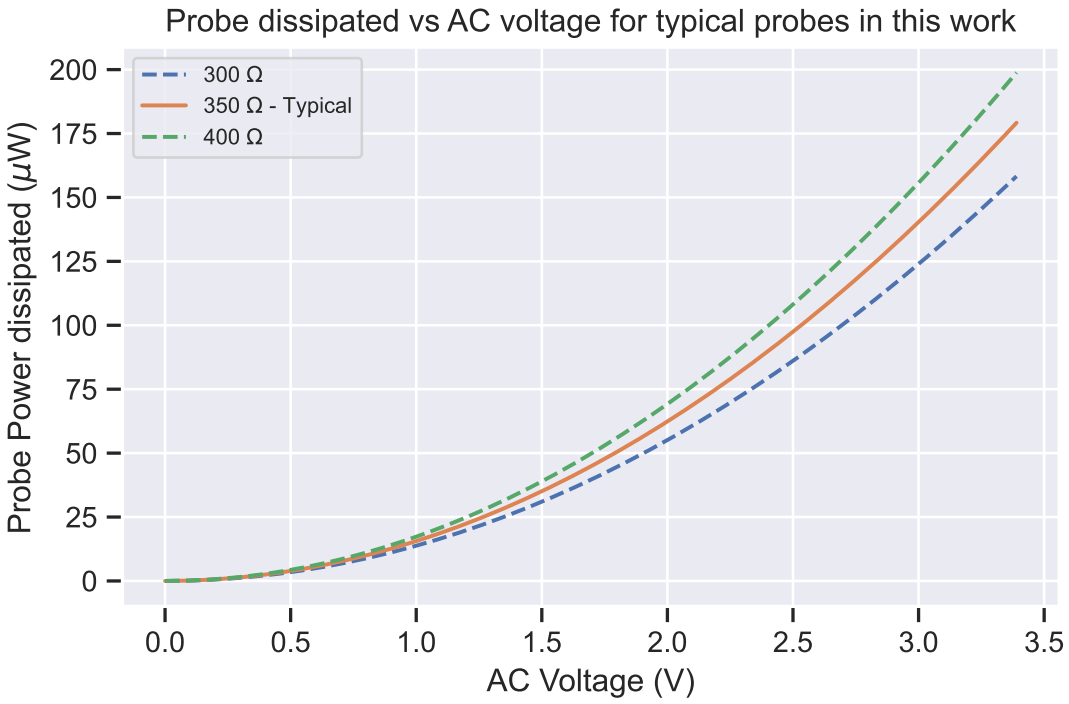


Figure 4.13: Probe dissipated power from AC voltage Source, limiting resistors are employed to limit the probe power to 400µW for probes used in this work

We can also estimate the temperature change experienced by the probe by reading the RMS bridge imbalance while the probe is biased. Assuming a perfectly balanced bridge, such that R_{match} and R_{SThM} are perfectly matched (and R_{trim} is left open circuit). It follows that any change in voltage seen at the ADC (ΔV_{out}) will take the form of the voltage divider formulation in Eq 4.1.

$$\Delta V_{out} = A \times V_{Bias} \times \frac{\Delta R_{SThM}}{R_T} \tag{Eq 4.1}$$

Where R_T is the total series resistance of the 2k limiting resistors and R_{SThM}, and A the amplifier gain (A=101). Substituting ΔR_{SThM} with the TCR equation and rearranging for ΔK we obtain the following Eq 4.2

$$\Delta K = \frac{\Delta V_{out} \times R_T}{V_{Bias} \times A \times R_{SThM} \times \alpha} \tag{Eq 4.2}$$

Where α is the TCR of R_{SThM}. Of the KNT probes used in this work values of α are reported in the literature to be 1.17x10^{-3} K^{-1} [62], 1.2x10^{-3} K^{-1} [158] and, 1.37x10^{-3} K^{-1} [56].

Direct Digital Synthesis

Direct Digital Synthesis (DDS) is a fast method for the creation of cyclical analogue signals from a DAC and a reference clock using look-up tables stored in memory[159]. It is realised by first creating a lookup table of DAC values for a single sine wave, which can be incremented through on each edge of the reference clock, once the table has been fully incremented through, the next increment can be wrapped around to the beginning of the table, and the cycle repeats.

The number of table elements that are incremented, σ_{inc}, on each reference clock edge will determine the frequency output of the DDS and will follow $f_{out} = \frac{f_{clk}}{N/\sigma_{inc}}$, where f_{out} the output frequency, f_{clk} the reference clock frequency, and N is the length of the lookup table. Due to the output frequency being a fraction of the reference clock frequency, any jitter or phase noise associated with the reference clock is reduced by $\frac{f_{clk}}{f_{out}}$.

f_{clk} and N were chosen carefully to avoid f_{out} from aligning with known interference frequencies and their associated harmonics, in particular mains 50Hz and computer screen refresh rates of 60 Hz. Frequencies that are multiples of 16Hz, conveniently

miss these interference frequencies and their harmonics. For a N of 1024, f_{clk} frequencies that are multiples of 16.384 kHz will provide DDS frequencies that avoid 50 Hz and 60 Hz harmonics. Therefore, f_{clk} was set to 114.688 kHz, the fastest clock rate multiple of 16.384 kHz achieved through microcontroller code optimisations before interrupts were missed.

A sample table of phase increments and their associated output frequencies can be seen in Table 4.1.

Table 4.1: Tabulated sample of output frequencies available from the DDS at a f_{clk} of 114.688 kHz and N = 1024

σ_{inc}	f_{out}
1	112 Hz
2	224 Hz
3	336 Hz
4	448 Hz
5	560 Hz
10	1.12 kHz
20	2.24 kHz
50	5.60 kHz

To increase the sensitivity of the measurements by averaging out jitter and other measurement effects, as well as to account for any thermalisation effects, it was decided to include functionality to change the time over which measurements were taken. This has aptly been named DDS-number, or DDSN. It is an exponential number of the form $l = N * 2^{DDSN}$, where $DDSN$ is a non-negative integer value, N the size of the DDS lookup table, and l the number of samples acquired during the measurement. This allows for measurements of various lengths to be taken, Table 4.2 shows tabulated measurement times available.

Table 4.2: Tabulated measurement times available per DDSN with the DDS at a f_{clk} of 114.688kHz and N = 1024

DDSN	No. samples	Measurement time
0	1024	8.93 ms
1	2048	17.8 ms
2	4096	35.7 ms
3	8192	71.4 ms
4	16384	143 ms
5	32768	285 ms
6	65536	571 ms
7	131072	1.14 s
8	262144	2.3 s

Synchronous ADC/DAC control

Any clock oscillator will have some error associated with its output frequency and may drift with temperature or other factors. To determine the 3ω and 1ω signals reliably we must simultaneously read from the ADC on the same clock edge as writing to the DAC. This means that any uncertainties in jitter or drift of the measured signals are at least identical to the generated signal. Simultaneous ADC and DAC control also permit methods that move the stage synchronously with probe driving and measurement, such as the ramp method as described later in section 4.5.4. The electronic design of the data acquisition board is such that writing to the DAC via the MOSI SPI line and receiving from the ADC via the MISO, happen on the opposite SPI clock edge, allowing faster data transfer times, and therefore increased reference clock speeds.

A 2nd order Bessel filter in a Sallen-Key topology was placed on the ADC input with a cutoff frequency of 15 kHz, far above the 1 to 2 kHz bandwidth of the probes used in this work [58, 63, 158, 160]. This reduces aliasing effects of RF interference as well as reducing interference from the closed loop stage piezo's drive signal.

4.3.2 Mechanical and environmental setup

Commercial AFMs tend not to allow direct closed-loop access to the full range of the Z axis of the stage without the optical lever laser being active. Therefore it was decided to create a custom SThM setup in a sample scan configuration, allowing unfettered access to the thermometry signals as well as custom closed loops driving of the 3-axis stage signals. Realisation of this setup was found through the use of a Thorlabs 3-Axis NanoMax™ Flexure Stage[4] combined with a Mellis Griot BPC103 piezo controller and custom in-house built thermal feedback electronics. Images of the physical set-up are shown in Figure 4.14. The use of this flexure stage allowed for 20 µm of closed-loop piezo movement in all axes, but this was practically limited by the DAC output to approximately 10 µm. Such setups have been used in the literature for high-precision positioning monitoring [161, 162]. Thorlabs [163] have stated a closed loop resolution of approximately 20 nm for this setup combination with a stated closed loop repeatability of 50 nm.

[4] https://www.thorlabs.com/thorproduct.cfm?partnumber=MAX301

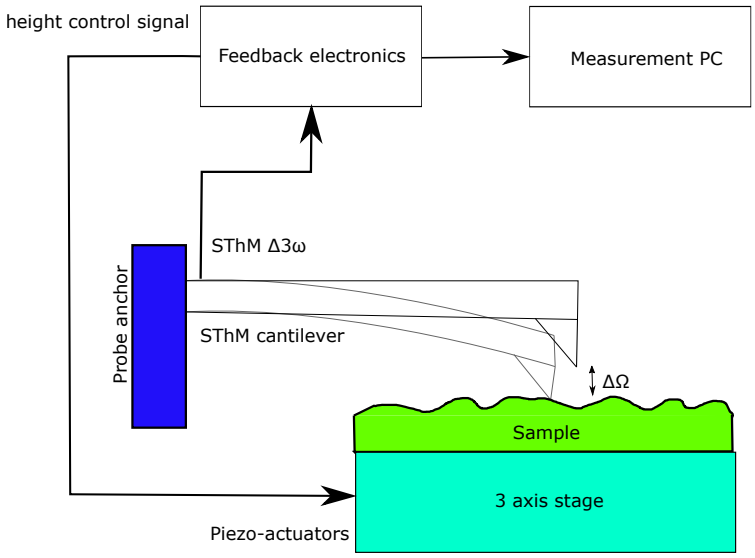


Figure 4.14: Simplified diagram of the SThM setup showing topographic feedback from the SThM thermometry signals. One should note the absence of any optical lever laser and photodiode. Diagram elements are not to scale

It was first important to calibrate the conversion from applied voltage to measured displacement of the stage axis. This was be achieved through applying voltages from the feedback electronics to the stage controller and reading out the calculated displacement from the piezo controller software[5]. This provided a conversion factor that allows any applied voltage to be converted to a reading of piezo extension. The result of this calibration can be seen in Figure 4.15, and shows good linearity of the closed loop stage.

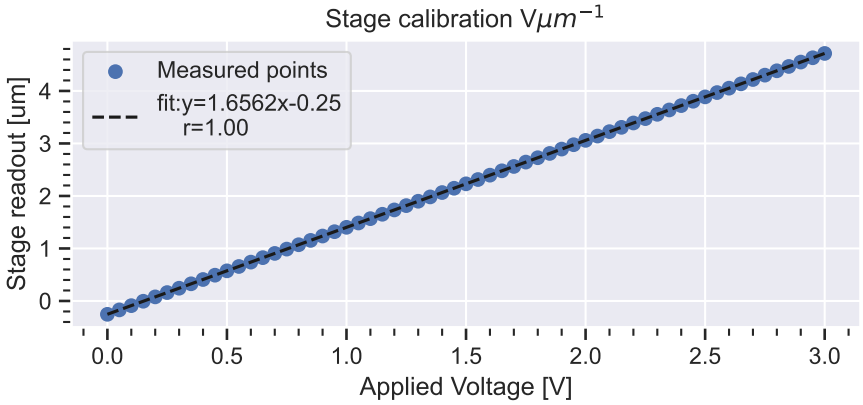
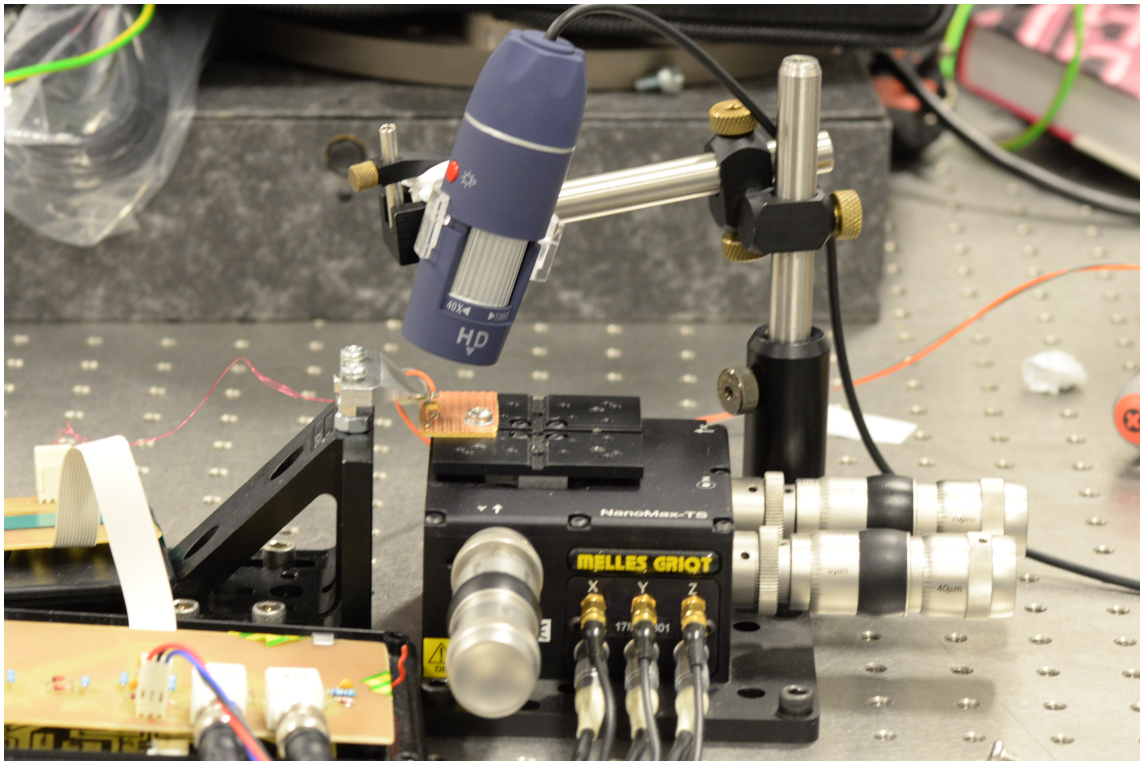
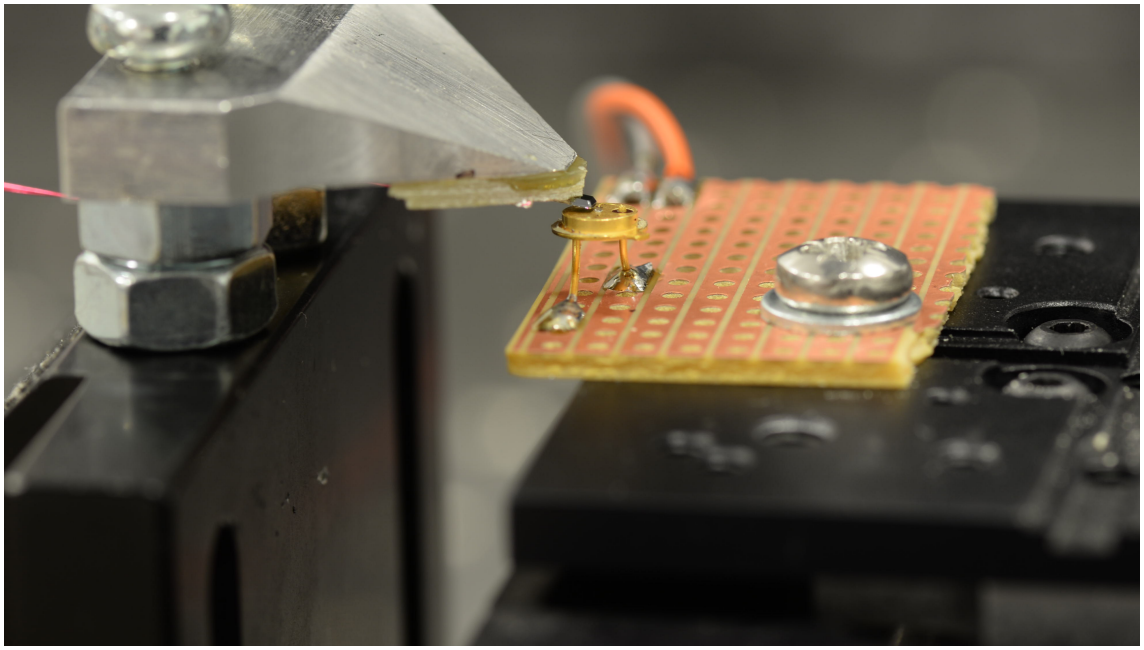


Figure 4.15: Stage axis calibration, showing a good linear fit to the measured points.

[5]Thorlabs' APT software



(a) Wide angle photo of SThM setup showing sample mounted to three-axis stage, probe mounting with microscope camera above, control electronics out of view.



(b) Photo of cantilever and sample setup, showing probe mounting above the surface of a sample.

Figure 4.16: Photos of SThM setup showing mechanical setup.

Thermal expansion of the parts can manifest as errors in the topographic measurement. Although the stage has internally thermally compensated closed-loop piezo actuators, the probe anchor that was mounted separately to the optical stage does not. As the anchor was constructed from aluminium, there exists a temperature expansion coefficient of 23 µm/m °C. With an approximately 8 cm anchor mounting height, a 0.1 K increase in the anchor temperature would cause thermal expansions in the hundreds of nanometres.

As such the setup was enclosed in a box lined with thermally insulating material to reduce the effects of sudden changes in environment, temperature, or air movement that could occur when someone enters a room. As discussed, these types of environmental changes could manifest themselves as errors in the topography measurement due to thermal expansions.

An example of such changes in the environment is air handling units in the room that periodically turn on and off to maintain steady room temperatures and airflow. An experiment was conducted to quantify this effect using methods described later in section 4.5. Figure 4.17 shows repeated single-point measurements of one pixel. The first measurement was taken with the room air handling unit active. The air handling unit was then turned off, with the setup allowed to drift in temperature with the room over a weekend before repeating the experiment. Clear changes in the measured pull-in point can be seen at regular intervals with the air handling unit active, that are no longer present once it has been disabled.

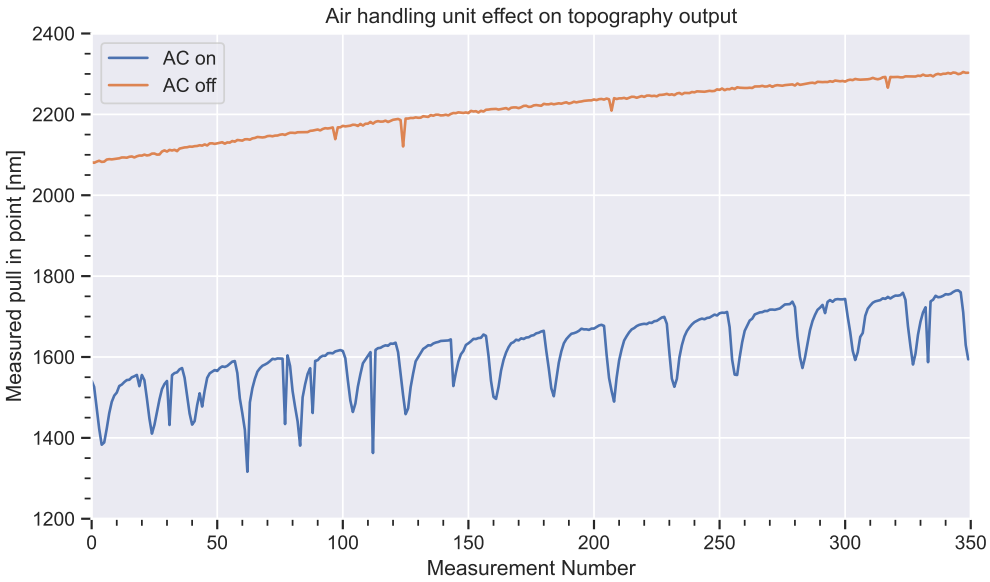


Figure 4.17: Repeated measurements of a single point with the air handling unit on and off, clear changes in the measured tip-sample contact point can be seen at regular intervals when the AC unit turns on and off. This is most likely due to slight thermal expansions of the materials as cool air is released into the room for a short duration of time at periodic intervals.

A solution to this could be to actively monitor the temperature of all components used in the mechanical design and compensate for expansions *a posteriori*, or implement active heating elements into the SThM setup to keep the setup components at a reasonable setpoint [3]. However, the implementation of such methods is not the primary focus of this work and the air handling unit was disabled for all measurements.

4.3.3 Probe movement paths

Thermometry measurements are required to be taken in and out of contact with the sample at each pixel in a reliable fashion without exciting any stage resonances. Typically the SThM is primarily a contact measurement with the contact kept through use of the optical lever technique. However, in our case, the probe must be retracted far enough away from the sample surface to break attractive forces that hold the tip in contact, before beginning the approach to the next pixel for measurement. This must be done quickly as to not unnecessarily increase the time spent moving the probe at the expense of time spent acquiring thermometry data, as well as avoiding resonant excitation of the stage piezo. The probe must follow a curve that retracts from the sample surface to a required height that breaks these adhesion forces and returns the probe to the sample just above the surface for the next measurement,

all while minimising the time spent moving and high-frequency energy as much as possible.

Xue and Yang [164] describes in detail a set of optimal raised cosine window functions used for DFT. The Xue formulations mimic features of the Hanning window, such as having finite width and sinc x roll off out of band. These functions aim to minimise this out-of-band behaviour by ensuring that the energy is predominantly contained within the frequencies of the cosine curves. This is achieved by setting the gradient and higher derivatives at the window's ends to zero. Consequently, the Xue window functions are zero at their ends and rise to a peak in the middle.

For our case, we may require a different starting and ending position, and we are therefore required to add an anti-symmetric element to these functions. This can be achieved through the integration of the second order Xue functions as in Eq 4.3 and Eq 4.4, scaled to a range of 0 to 1.

$$X_2(n) = \frac{3}{8} - \frac{\cos(\frac{2\pi n}{N})}{2} + \frac{\cos(\frac{4\pi n}{N})}{8} \tag{Eq 4.3}$$

$$\int X_2(n) \equiv \Sigma_2(n) = \frac{n}{N} - \frac{2\sin(\frac{2\pi n}{N})}{3\pi} + \frac{\sin(\frac{4\pi n}{N})}{12\pi} \tag{Eq 4.4}$$

Where n is the discrete time variable and N is the number of samples in a given window. It can be seen in Eq 4.3 that $X_2(0, N) = 0$, and $X_2(\frac{N}{2}) = 1$. For the integrated Xue function, Eq 4.4, it can be seen that $\Sigma_2(0) = 0$, $\Sigma_2(N) = 1$, and $\Sigma_2(\frac{N}{2}) = 0.5$. These functions have been graphed for N=1024 in Figure 4.18.

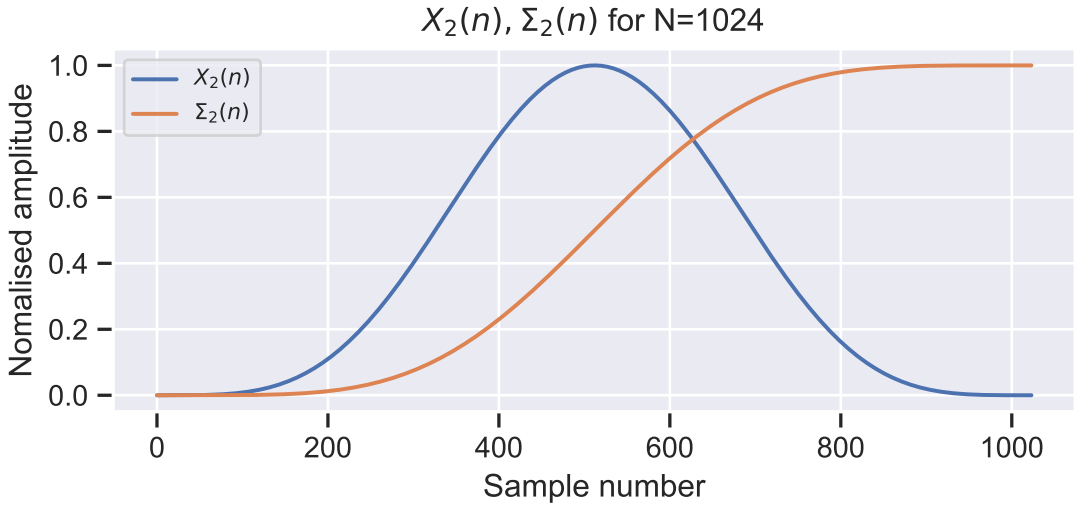


Figure 4.18: Scaled second order Xue window ($X_2(n)$) and it's integral ($\Sigma_2(n)$).

Using a combination of the second-order Xue function and its integral, we can create a movement path function (referred to hereon as a Xue path or Xpath) of the form $Xue\ path = A + BX + C\Sigma$ through any three, start (y_0), mid (y_1), and end (y_2) points.

Since $X_2(0, N) = 0$ and $\Sigma_2(0) = 0$, we have that $A = y_0$, and $C = y_2 - y_0$. If the mid point peak of our Xue path where $X_2(\frac{N}{2}) = 1$ and $\Sigma_2(\frac{N}{2}) = 0.5$, then $B = y_1 - \frac{y_2+y_0}{2}$. However, we have actually shifted the peak due to the asymmetry of the Xue path, where the solution to B requires the solution of complex transcendental equations not suited to implementation in a fast microcontroller loop. In practice, the maximum peak of the curve will be very near to the midpoint if C is relatively small. Polynomial expansion of the sin and cosine terms around the peak position and the maximum value may then be solved analytically to form an approximate solution. To maintain the low maximum frequency of the sine and cosine terms, we can use the second order Xue path function, $Xpath_2(n) = A + BX_2(n) + C\Sigma_2(n)$.

$$Xpath_2(n) = A + B\left(\frac{3}{8} - \frac{\cos(\frac{2\pi n}{N})}{2} + \frac{\cos(\frac{4\pi n}{N})}{8}\right) + C\left(\frac{n}{N} - \frac{2\sin(\frac{2\pi n}{N})}{3\pi} + \frac{\sin(\frac{4\pi n}{N})}{12\pi}\right) \quad \text{(Eq 4.5)}$$

Expanding Eq 4.5 around $n = N/2$, and letting $\eta \equiv n - N/2$ shows

$$Xpath_2(n) = A + B\left(\frac{3}{8} - \frac{\cos(\frac{2\pi\eta}{N})}{2} + \frac{\cos(\frac{4\pi\eta}{N})}{8}\right) + C\left(\frac{n}{N} - \frac{2\sin(\frac{2\pi\eta}{N})}{3\pi} + \frac{\sin(\frac{4\pi\eta}{N})}{12\pi}\right) \quad \text{(Eq 4.6)}$$

Expanding around $\eta = 0$

$$\cos\left(\frac{2\pi\eta}{N}\right) \approx 1 - 2\left(\frac{\pi\eta}{N}\right)^2; \qquad \cos\left(\frac{4\pi\eta}{N}\right) \approx 1 - 8\left(\frac{\pi\eta}{N}\right)^2;$$
$$\sin\left(\frac{2\pi\eta}{N}\right) \approx \frac{2\pi\eta}{N}; \qquad \sin\left(\frac{4\pi\eta}{N}\right) \approx \frac{4\pi\eta}{N}$$

$$\begin{aligned} Xpath_2(\eta) &\approx A + B\left(\frac{3}{8} + \frac{1}{2} - \left(\frac{\pi\eta}{N}\right)^2 + \frac{1}{8} - \left(\frac{\pi\eta}{N}\right)^2\right) \\ &\quad + C\left(\frac{\eta + \frac{N}{2}}{N} + \frac{4\eta}{3N} + \frac{\eta}{3N}\right) \\ &\approx A + B\left(1 - 2\left(\frac{\pi\eta}{N}\right)^2\right) + C\left(\frac{1}{2} + \frac{8\eta}{3N}\right) \end{aligned} \quad \text{(Eq 4.7)}$$

We now have a fairly good approximation of the Xue path, even for large values of C. and can create an algorithm to gain an approximate calculation of B.

1. Estimate value of B using $B \approx y_1 - \frac{y_2+y_0}{2} \equiv B^*$
2. Determine value of n giving the maximum of the Xue path such that $\frac{dXpath_2(n)}{dn} = 0 \therefore \frac{-4\pi B^* \eta_{max}}{N^2} + \frac{8C}{3N} = 0 \therefore \eta_{max} = \frac{2CN}{3\pi^2 B^*}$
3. Determine the values of $X(\eta_{max})$ and $\Sigma(\eta_{max})$ using Eq 4.7
4. Determine a best estimate of B from $A + BX(\eta_{max}) + C\Sigma(\eta_{max}) = y_1 \therefore B = \frac{y_1 - A - C\Sigma(\eta_{max})}{X(\eta_{max})}$

Using these algorithm steps we can create Xue paths starting from one point to another through a midpoint as shown in Figure 4.19.

A simulation of a path through 500 arbitrary positions in space was carried out to

compare the frequencies each path would exhibit. The set path was followed through space using both linear and Xue paths, with 0.5s of these simulated movements displayed in Figure 4.20a, and frequency domain analysis presented in Figure 4.20b. A comparison of the two movement strategies shows that by using these Xue paths over linear movements, we can vastly reduce the higher frequency components generated by moving the stage in space, allowing quick movements without exciting any resonances of the stage. For a lightly loaded Thorlabs NanoMax^{TM} stage, piezo resonances lie around 300 Hz. A reduction in power of around 20 dB around this region is observed.

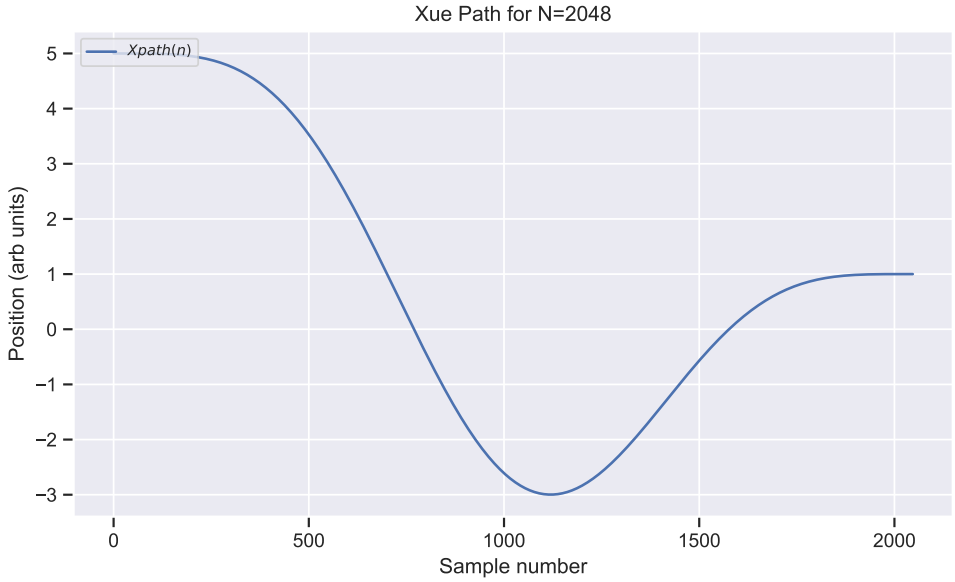
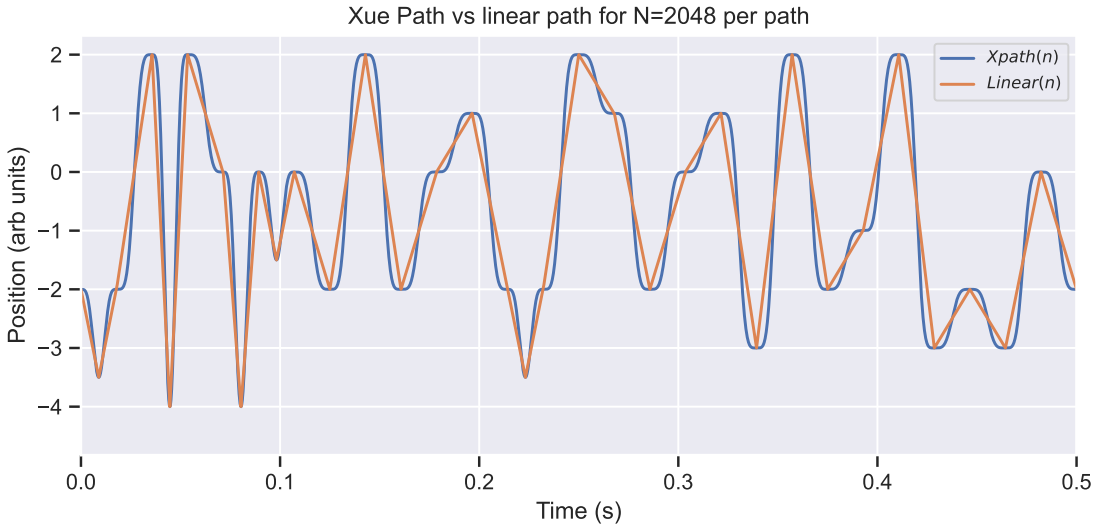
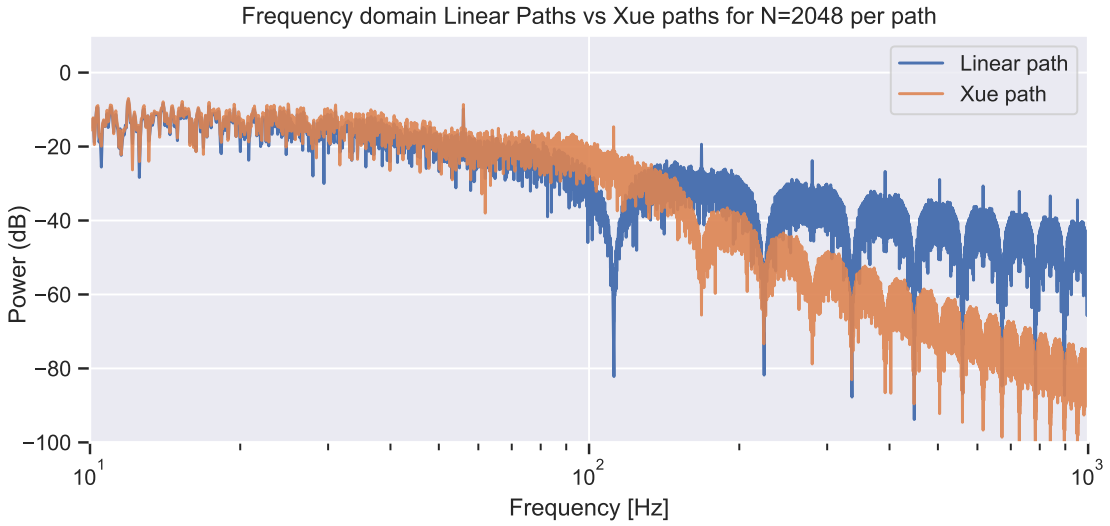


Figure 4.19: A single Xue path movement from 5 to 1 with a midpoint at -3.

These movement paths can be extended to all three axes of the stage, allowing movement to any arbitrary location in 3D space, through any middle point quickly without exciting stage resonances.



(a) First 0.5 seconds of a simulation of 1000 sequential linear and Xue path movements



(b) FFT of linear vs Xue Path, showing a large decrease in higher frequency power.

Figure 4.20: Xue path simulation of 1000 movement, time domain movements and their associated frequency spectrum.

4.3.4 Control software development

Custom computer software, named 'Thermal-Topo', was created for the real-time monitoring of thermometry signals on the measurement PC, written in Python using the open-sourced Qt framework[6]. This allowed for remote connection to the SThM, allowing remote starting and monitoring of scans, as well as microcontroller code reprogramming when necessary. An overview of the control software can be seen in Figure 4.21. Any raw or derived value that is available from the SThM measurement or stage control signals can be viewed in the software.

Once a scan or series of scans had been completed, the software automatically gathered the relevant data, split it up into the types of scans acquired and ran analysis scripts on the individual scans. This allowed multiple scans of different capture techniques with the same sample parameters to be acquired sequentially without the need for interaction with the setup. Scans were automatically output in a raw format via the use of log files. Automated scripts had been written to convert the signal channels and their derivatives into the Gwyddion native (.gwy) file format[7] that can be readily opened in Gwyddion [165] for analysis as if it were acquired on a commercial AFM.

[6] https://www.qt.io/
[7] http://gwyddion.net/documentation/user-guide-en/gwyfile-format.html

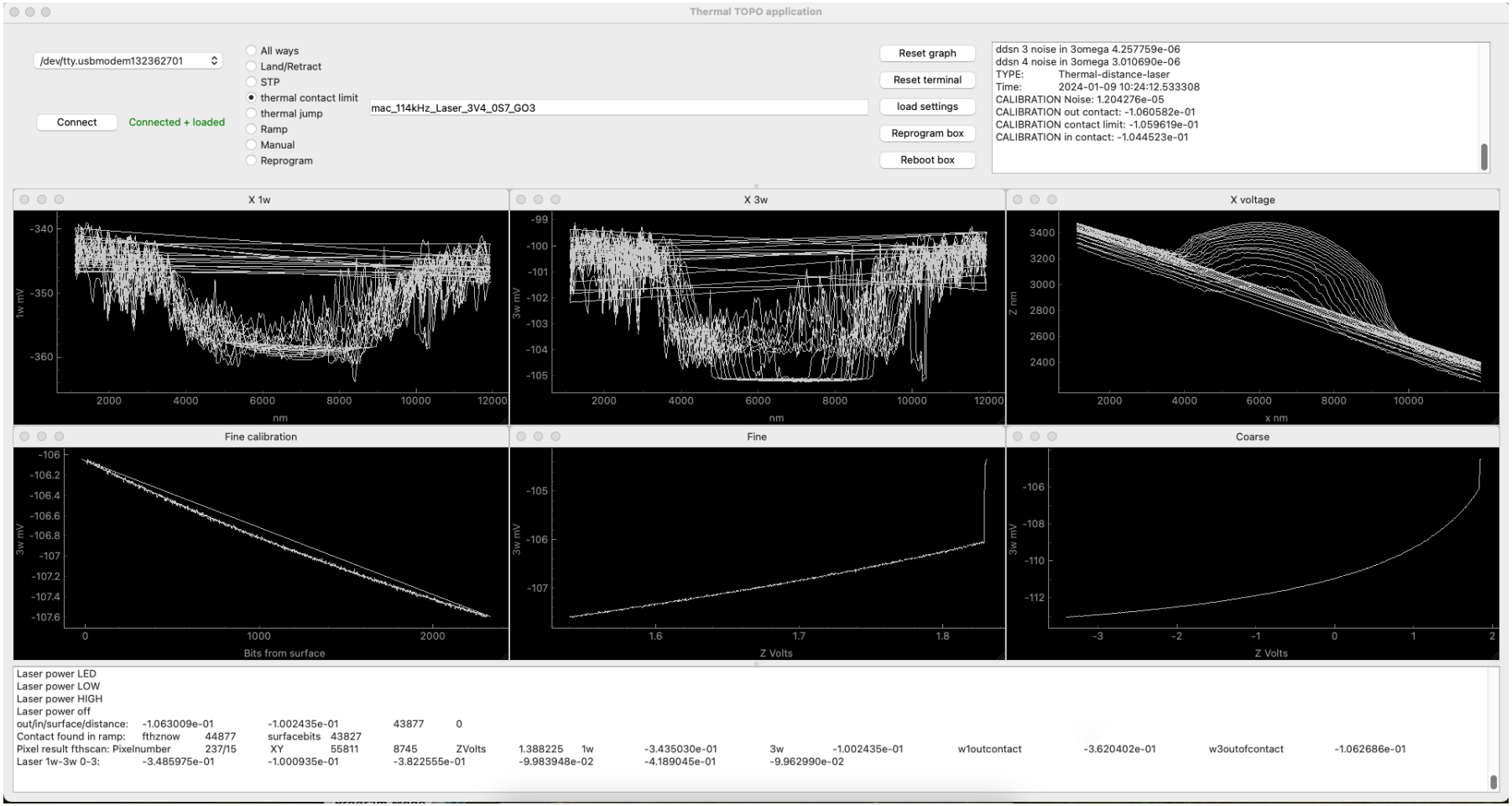


Figure 4.21: Screenshot of the thermal topo application during scan of VCSEL device, designed to give real-time monitoring and control over the SThM signals. Signals currently visible on the top row from left to right 1ω, 3ω and topography. On the bottom, calibration landing curves are visible: STP calibration, fine calibration and coarse calibration.

4.4 Experimental

This instrumentation provided all the elements needed to move the probe in space without exciting stage resonances as well as the ability to bias the probe, move the stage and take measurements synchronously. However, the performance of the setup required characterisation as well as the ability of surface detection quantified. Without the need to go through the complex probe response calibration procedure to obtain an absolute temperature from a given probe resistance, a common method to express the response of SThM probe is in the form of a fractional change in a given signal from out-of-contact to in-contact [3, 57, 63, 166]. As we are concerned with the 3ω signal, a useful comparison would be $\Delta 3\omega/3\omega_{out}$ where $\Delta 3\omega \equiv 3\omega_{in}\text{-}3\omega_{out}$

4.4.1 Noise analysis of system

To understand the topographic output of the system, the measurement noise in the thermometry signals required quantification. A convenient method of comparing the stability of the measurement signals with varying mean values can be to express each measurement as a ratio of it's standard deviation to the mean as a percentage. This is known as a coefficient of variation (CV). To analyse the noise of the system 1000 measurements were taken at least 5µm out of contact, and moved into contact at the base frequency of 112 Hz, and a bias current of 900 µA, the results of which can be seen in Figure 4.22, with measurements of mean, standard deviation, and coefficient of variation tabulated in Table 4.3.

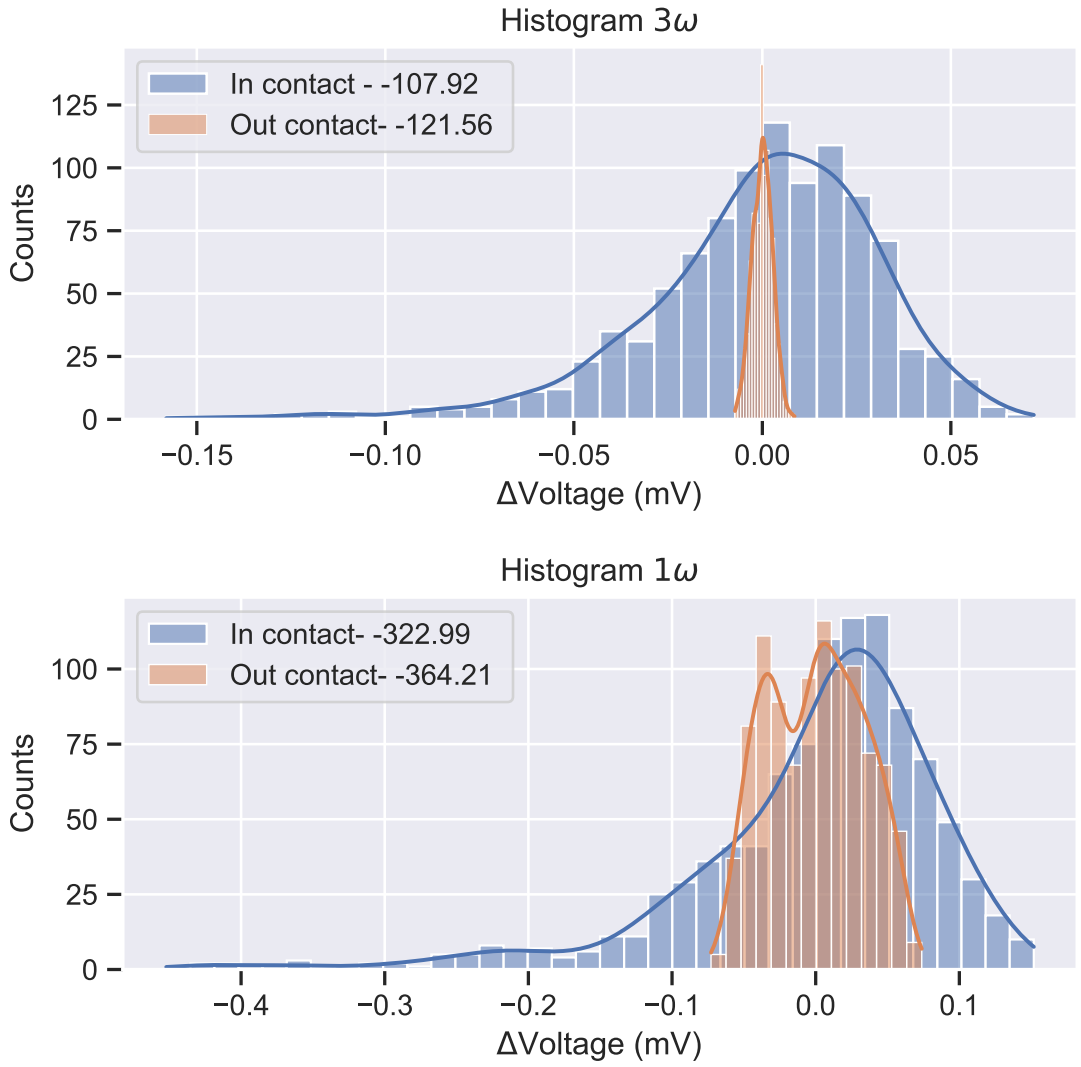


Figure 4.22: Histogram of 1000 sequential measurements at a ddsn of 4 at 112 Hz in and out of contact (Top) showing 3ω signal (Bottom) 1ω signal.

Table 4.3: Tabulated statistical results from 1000 measurements of the 1ω and 3ω signals in and out of contact

Signal	Mean [mV]	pk-pk [µV]	Std Dev [µV]	CV [%]
$3\omega_{out}$	-121.56	15.7	2.65	0.002
$3\omega_{in}$	-107.92	230.1	30.7	0.028
$1\omega_{out}$	-364.21	146.6	32.96	0.009
$1\omega_{in}$	-322.98	603.9	87.67	0.027

As seen in Figure 4.22 and Table 4.3, 3ω thermometry signals show an approximately Gaussian distribution with an approximate 10% change in mean value from out of contact into contact. This signal is very stable in air (Figure 4.23) with a CV of 0.002% over the measurement period, making it an ideal candidate for positional

sensing. Such small variations in the out of contact measurement are negligible when detecting a change in magnitude on the order of 10%. A slight drift on the order of 0.1% of the in contact measurement can be seen in the raw data over the first few measurements in contact Figure 4.24, which equates to approximately 5 seconds.

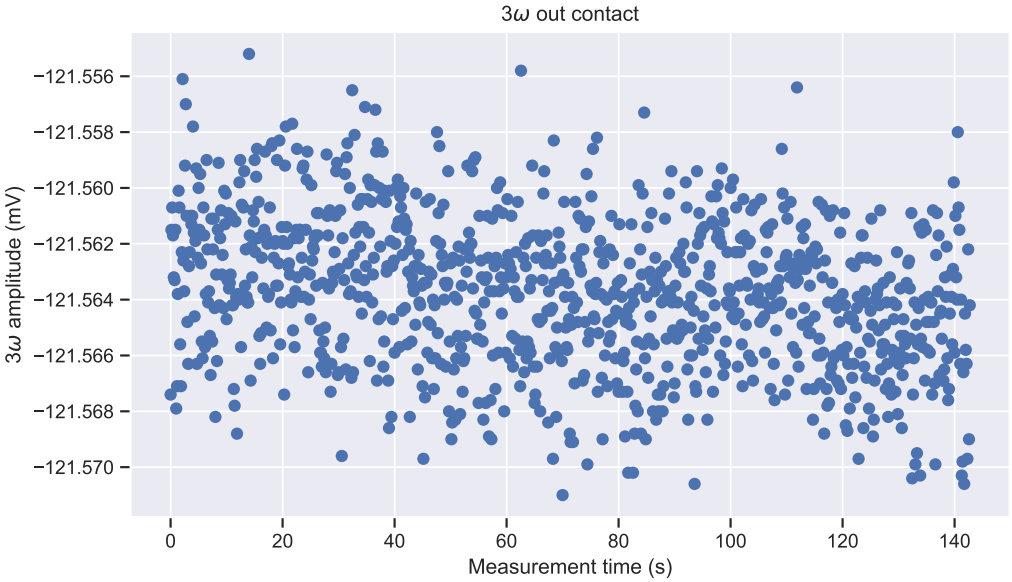


Figure 4.23: Drift over measurement of 3ω at ddsn of 4 at 112 Hz out of contact

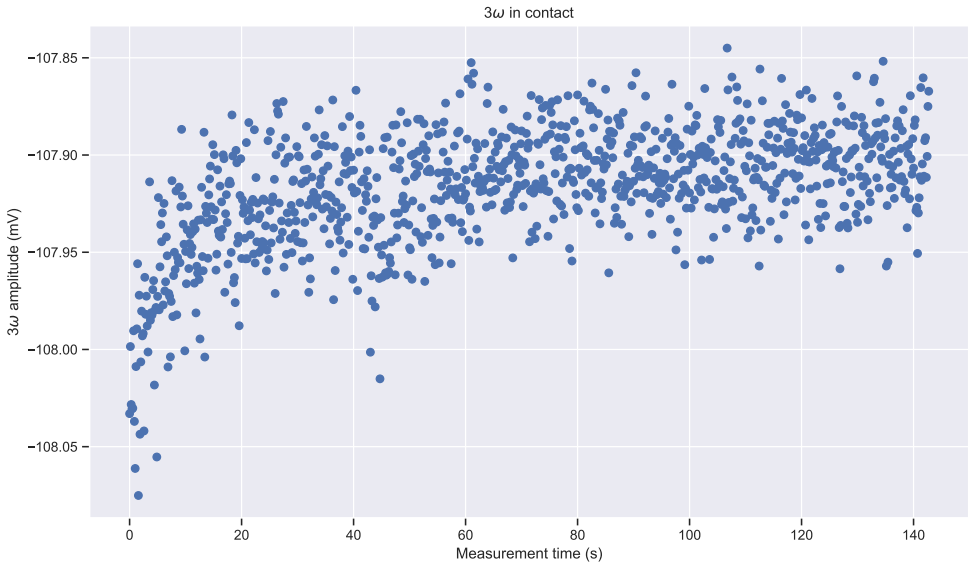


Figure 4.24: Drift over measurement of 3ω at ddsn of 4 at 112 Hz in contact

This drift in the contact probe response is hypothesised to be due to capillary forces taking effect, and meniscus formation around the probe tip. The meniscus possibly also includes some contamination from the sample surface. Literature studies by Vitorino et al. [167] and Szoszkiewicz and Riedo [168] have shown that AFM probes with a tip radius of approximately 25 nm have shown nanobridges of water meniscus occurring in under 10 ms. Studies by Wei and Zhao [169] had shown that although the water meniscus forms relatively quickly, the adhesion force of the liquid bridge increases with contact time reaching a force equilibrium at around four seconds of contact at a relative humidity of 65%. However, with the complex construction of the KNT SThM probe, with multiple heat transfer routes, as well as taking into account the conduction change due to these events, it is not implausible that such events may happen on a much longer timescale in this setup. Wei and Zhao [169] had shown that the effect can be vastly reduced by lowering the relative humidity of their AFM setup.

To verify this hypothesis (and ensure this artefact does not derive from the measurement electronics) the housing of the microscope was flooded with dry nitrogen to reduce the humidity levels around the sample and probe, which in turn should reduce the effect of water meniscus forming when the probe tip makes contact with the sample. Repeating this experiment in a dry nitrogen-rich atmosphere showed similar overall trends as before, shown in Figure 4.25. However, there was significantly less drift in the probe response in contact. Figure 4.26 shows that the measurement stabilised after only 3 to 4 measurement points, or in approximately 500 ms. Although this shows a tenfold reduction in stabilisation time, it is still at least an order of magnitude away from meniscus formation times observed by Vitorino et al. [167] and Szoszkiewicz and Riedo [168].

It should be noted however, that it is only the time constant of the measurement that is affected, the overall drift of approximately 100-150 µV from the first measurement to stabilisation is the same in ambient and nitrogen-rich atmosphere.

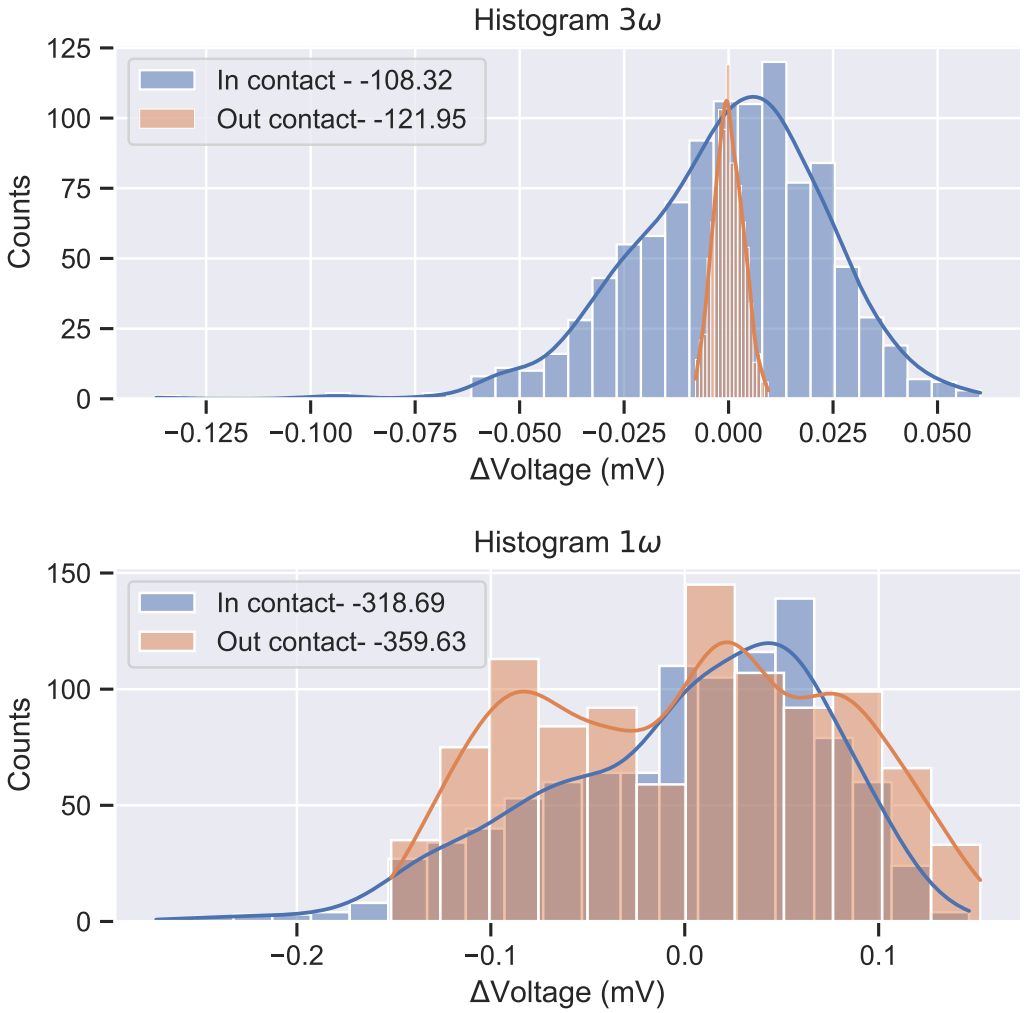


Figure 4.25: Histogram of 1000 sequential measurements at a ddsn of 4 at 112 Hz in and out of contact in nitrogen-rich atmosphere. (Top) showing 3ω signal (Bottom) 1ω signal

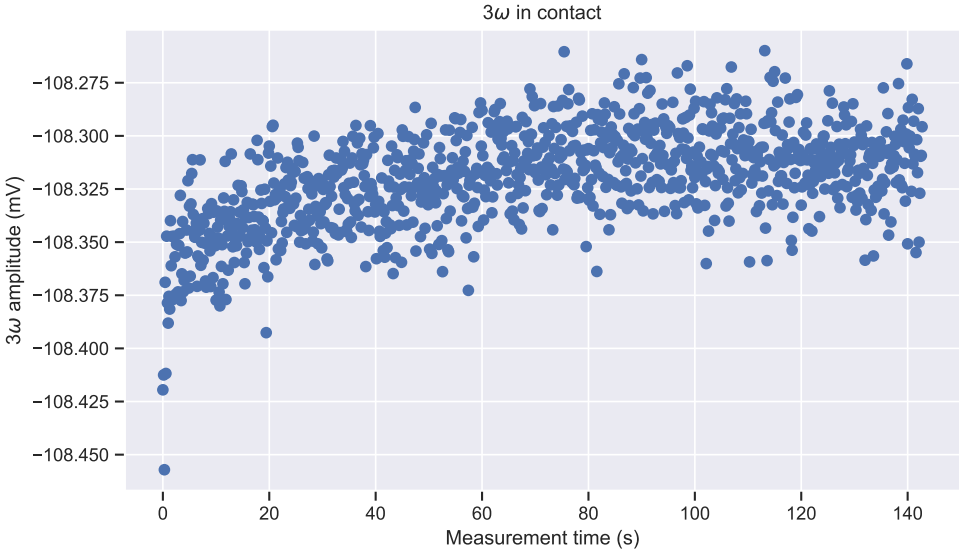


Figure 4.26: Drift in measurement of 3ω in contact in nitrogen-rich atmosphere, significantly less drift visible over measurement

As the setup was not in a hermetically sealed environment, there was a large amount of nitrogen leakage from the setup. It would be impractical and expensive to continuously flood the setup with dry nitrogen for long periods of time. Although part of the origin of these artefacts has been identified, they are not accounted for in further measurements unless stated. However, the observed effect must be considered when interpreting further thermal measurement data.

Repeating noise measurements in and out of contact at the frequencies available from the DDS up to 7 kHz showed relative stability in the out of contact 3ω signal across all measurement frequencies (Figure 4.27), with a rise around the 3 kHz region. In contact measurements (Figure 4.28) show in rise in the noise levels at a probe drive frequency in the 1 kHz range. This could potentially be due to USB packet frames (125 µs bursts a 1 ms intervals [170], 8 kHz and 1 kHz respectively) and their associated harmonics. Or possibly other electrical noise at, or at the 3rd harmonic of, the drive frequency being the capacitively coupled from either the stage, measurement PC, or control electronics through the sample. Noise in the 1ω measurement (Figure 4.29) shows a similar profile around the 2 kHz range, showing that this noise most definitely must be due to the probe driving frequency, but its origins remain unclear.

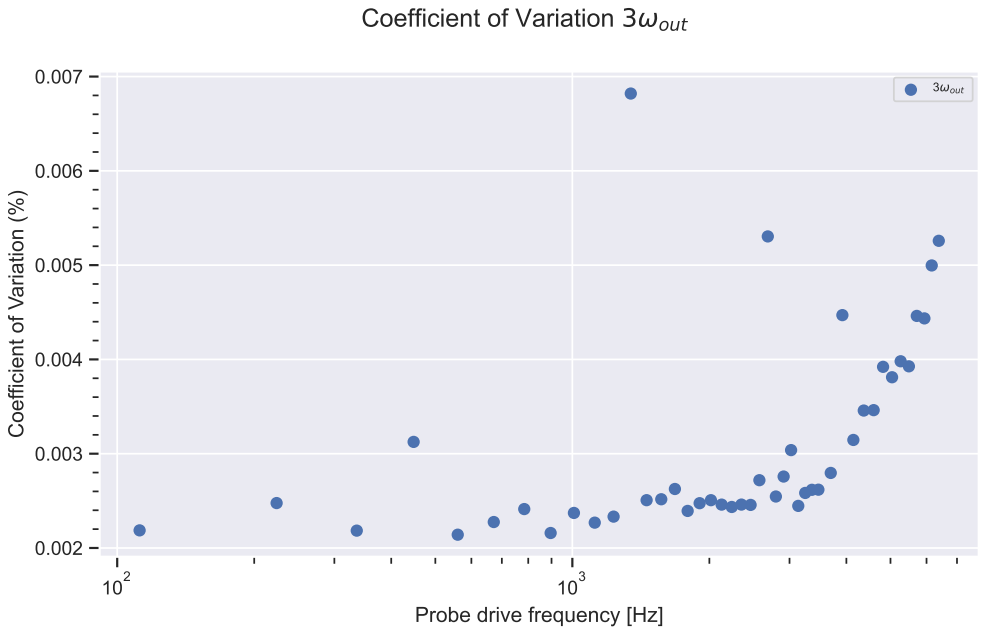


Figure 4.27: 3ω coefficient of variation values (expressed as a percentage) for out of contact across available frequencies

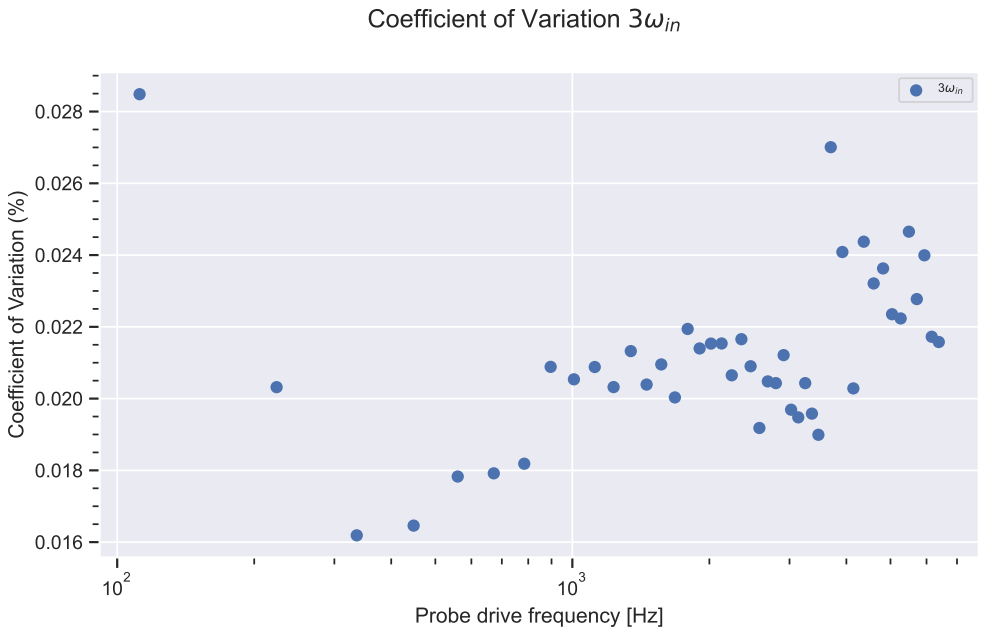


Figure 4.28: 3ω coefficient of variation values (expressed as a percentage) for in contact across available frequencies

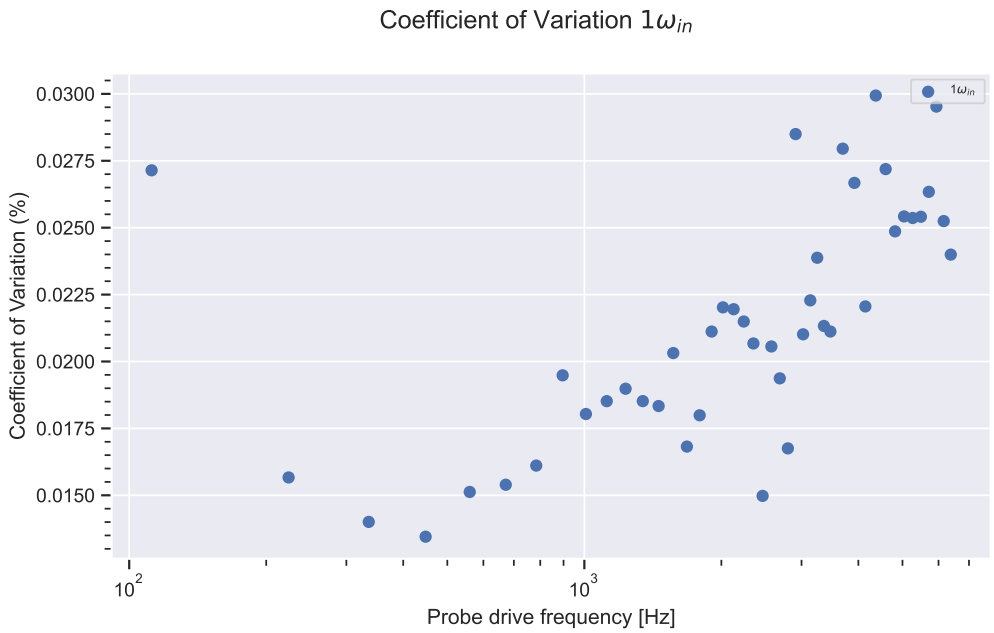


Figure 4.29: 1ω coefficient of variation values (expressed as a percentage) for in contact across available frequencies

Probe Frequency Response

The probes used for this work when driven with AC bias are known to have a cut-off (-6 dB) frequency of its thermal response that lies in the kHz region [58, 63, 158, 160]. Therefore an upper limit of 3 kHz during the taking of thermal measurements was placed to maximise the setup sensitivity. To verify this in our system, the probe 3ω signal was measured in air at various frequencies for 1000 measurements at a DDSN of 4 as done previously. In the experiment, the probe started at least 5µm out of contact of the sample, before being approached to the surface and measurements taken in contact with the sample. Measurement results can be seen in Figure 4.30. Expressing the in-contact measurement as a fractional change of the out-of-contact measurement shows Figure 4.31, and can be expressed in dB in Figure 4.32.

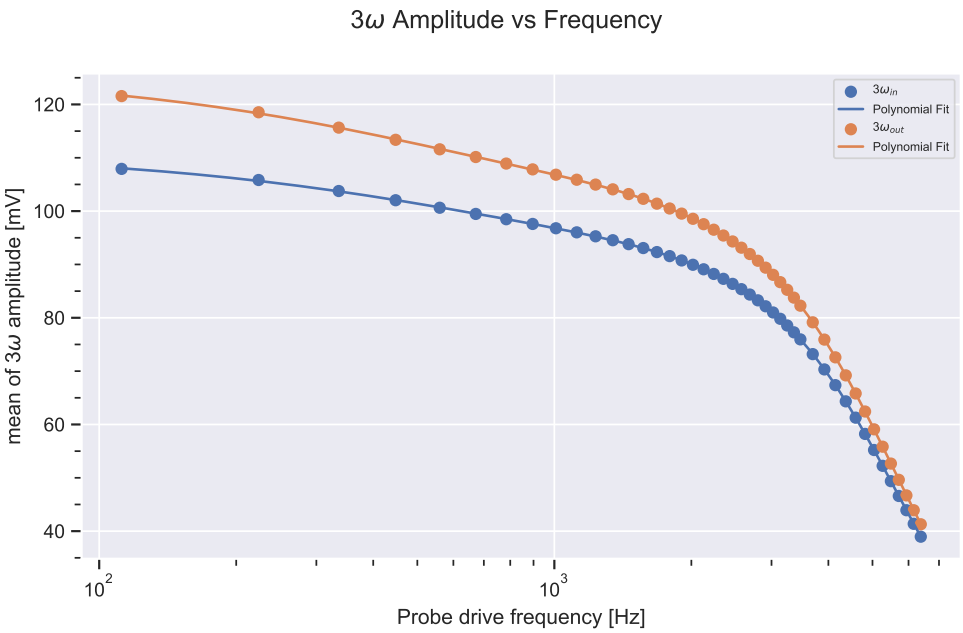


Figure 4.30: Frequency response of a KNT probe. Mean 3ω values in and out of contact for various probe drive frequencies

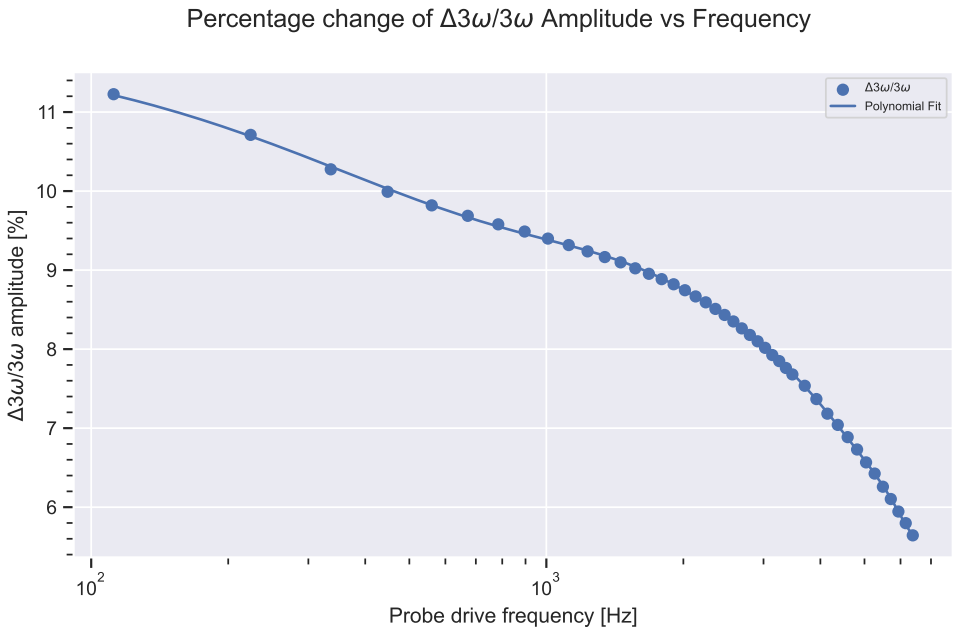


Figure 4.31: Frequency response of a KNT probe. Expressed as a fractional percentage change from it's out of contact measurement

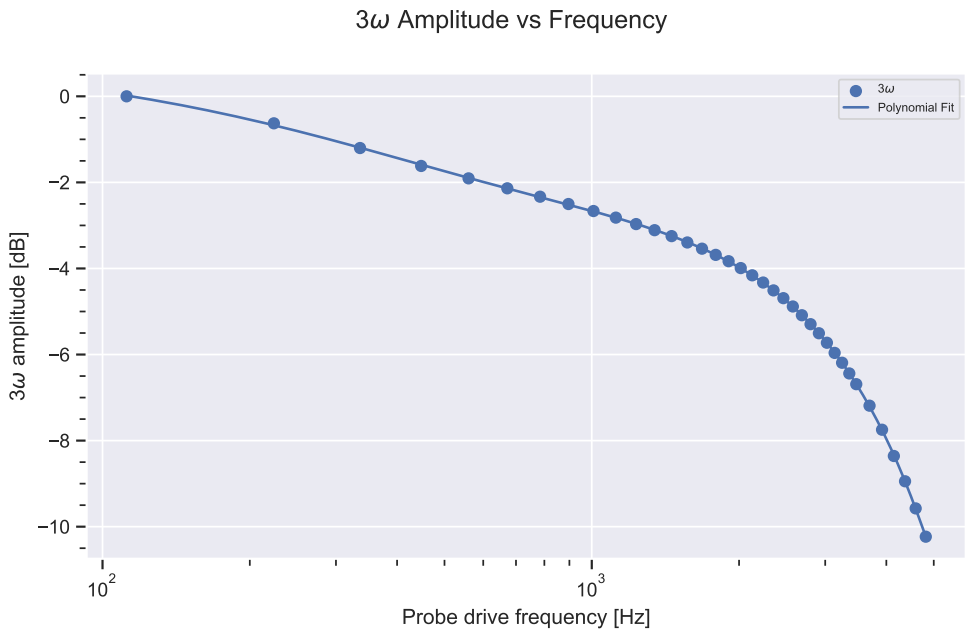


Figure 4.32: Fractional change of probe thermal response expressed as a Bode plot, 0 dB point is the response of the lowest frequency available from the DDS output.

It can be seen from Figure 4.32, that the -6 dB point in the system occurs just above 3 kHz, with a sharp roll-off thereafter. This bandwidth is slightly lower, and roll-off steeper, than reported in the literature [58, 63, 158, 160]. However, due to the inclusion of the 2nd order filter on the ADC input with a cutoff frequency of 15 kHz, a steeper roll-off in the 3rd harmonic in the 5 kHz region is expected.

Figure 4.31 and 4.32 show a slight 'scalloping' profile between 100 Hz and 2 kHz. This profile has been observed in literature by Bodzenta et al. [58] and Puyoo et al. [158], and cannot be described by first-order thermal low pass filter mechanics. Bodzenta et al. [58] state that this profile may be due to heat transfer through the complex geometry of the KNT probe. This is further confirmed by Lambert [63], where microfabricated SThM probes of similar structure and fabrication to commercial KNT probes, but with tips thermally isolated from the cantilever body, do not exhibit as significant a scalloping profile and therefore pushes the probe bandwidth to around 8 kHz.

Probe Voltage

Previous work by Lambert [63] had shown that probe bias had little to no discernible difference in the thermal response of the SThM probe. As the commercial system used by Lambert included the use of a laser, noise dependence on probe voltage was investigated again as part of this work.

A drive frequency of 448 Hz was selected to compare the probe voltage effect on the measurement noise. The probe was measured 1000 times in and out of contact in a similar manner to Figure 4.22. Figure 4.33 and 4.34 show the noise levels, expressed as a coefficient of variation, at each measured voltage in and out of contact respectively.

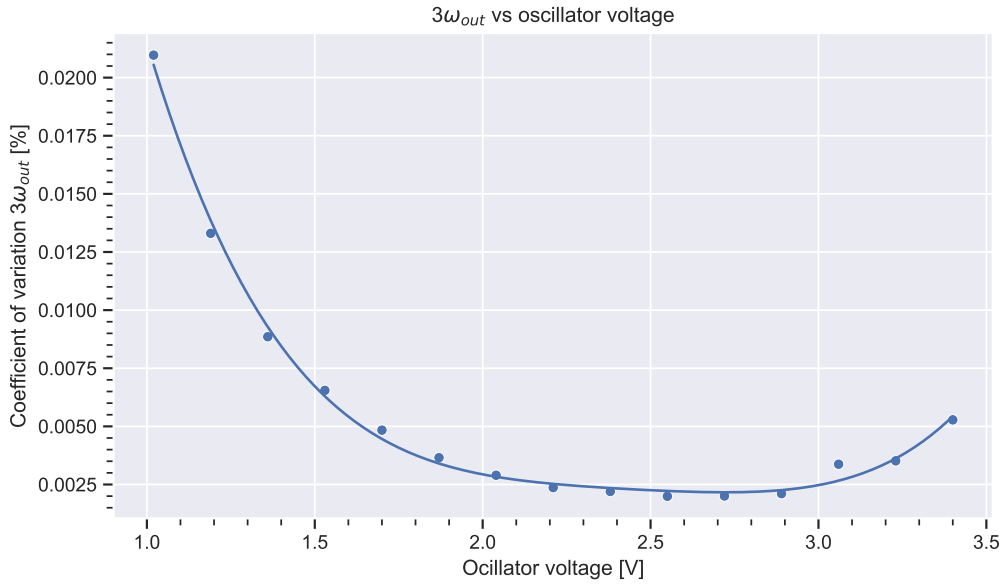


Figure 4.33: Coefficient of variation of out-of-contact 3ω $3\omega_{out}$ vs probe drive voltage. 1000 points at a drive frequency of 448 Hz and DDSN of 4

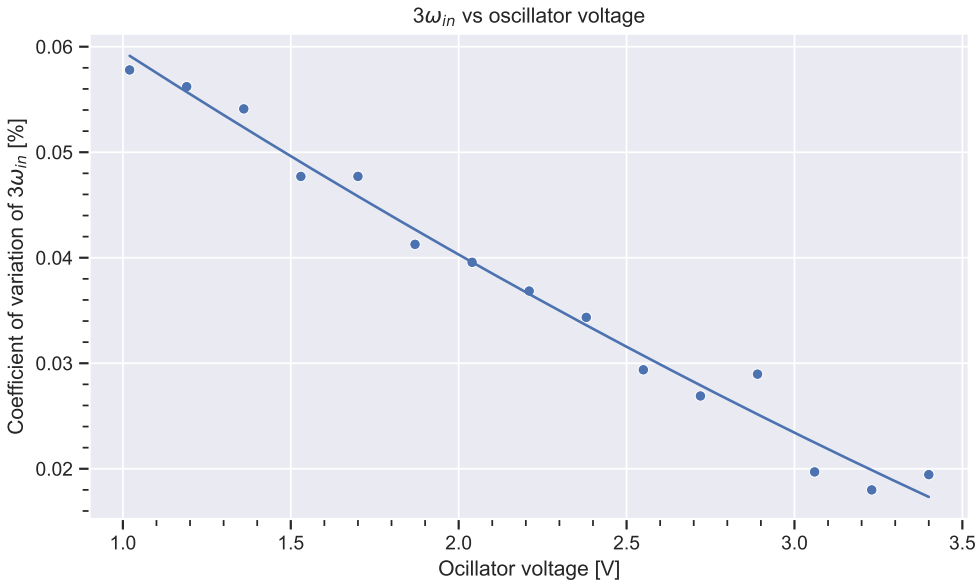


Figure 4.34: Coefficient of variation of in-contact 3ω ($3\omega_{in}$) vs probe drive voltage, 1000 points at a drive frequency of 448 Hz and DDSN of 4.

Many SThM studies tend to keep probe currents below 2 mA to achieve a good signal-to-noise ratio without causing damage to the sensor [2, 3, 52, 53, 62, 158]. Figure 4.33 shows a clear minimum in the noise measurement between 2 and 3 V, corresponding to a probe current between approximately 600 and 800 µA (Figure 4.12). The higher noise seen at lower voltages can be attributed to the very low mean signal levels in the system at these probe currents. In the upper region, the rise can be attributed to an observed exponential increase in the standard deviation of the noise with probe current as seen in Figure 4.35. This could likely be due to the increased effect of thermal actuation of the tip [171], or possible heating of the tip causing thermal instability of the sensor metallisation causing it to creep, exciting 1/f noise in the probe resistance value.

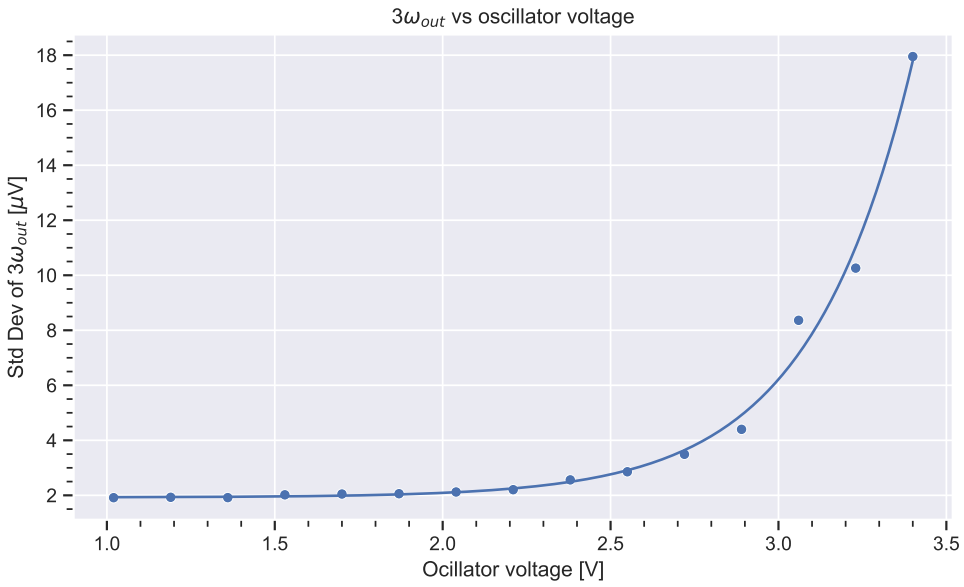


Figure 4.35: Std Dev of probe 3ω response vs probe drive voltage, 1000 ddsn 4 points at 448 Hz drive frequency. showing a large increase in the out-of-contact noise above 3 V.

Plotting the response of the probe changing from out of contact to in contact leads to a slight voltage dependence of the probe as seen in Figure 4.36. This contradicts Lambert [63], who noted that probe bias has little to no effect on the probe response. However, with signal changes of over 10% across the voltage ranges measured, and very low measurement noise, there is ample scope to use the 3ω signal as a means to gain topographic control of the SThM.

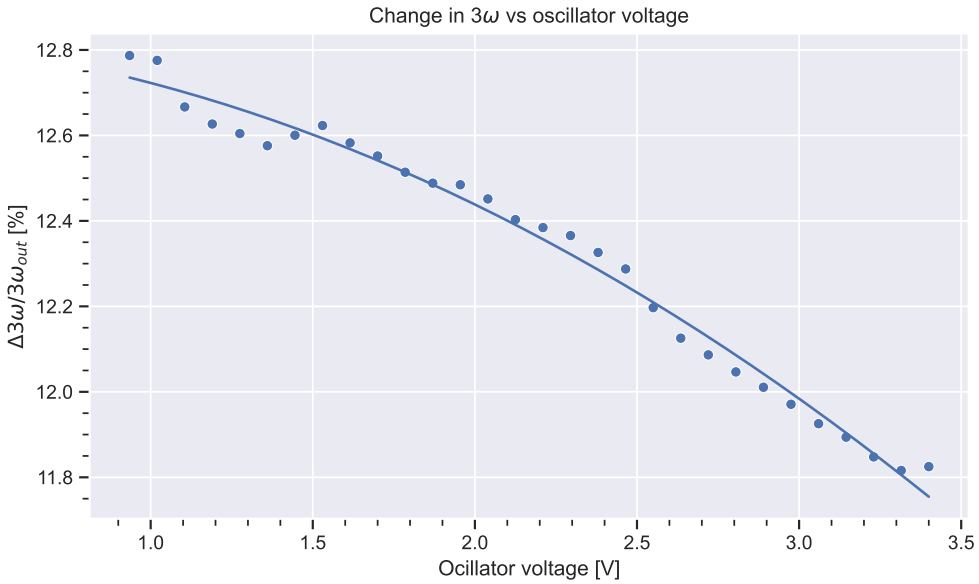


Figure 4.36: Change of probe 3ω response vs probe drive voltage expressed as a percentage of its out of contact response, 1000 points at a 448 Hz drive frequency and DDSN 4.

4.4.2 Single point measurements

As the noise levels of the in-contact and out-of-contact measurements, as well as probe voltage response, had now been qualified in the system, the appropriate next step was to determine how these parameters affected the ability of the system to detect a surface. The Z piezo of the stage was extended and retracted to engage and disengage the probe from the sample surface. Figure 4.37 shows the point of contact can be easily identified as a sharp decrease in the 3ω signal. This was repeated multiple times on the sample surface while monitoring the point of contact, three of these land and retracts are shown in Figure 4.38.

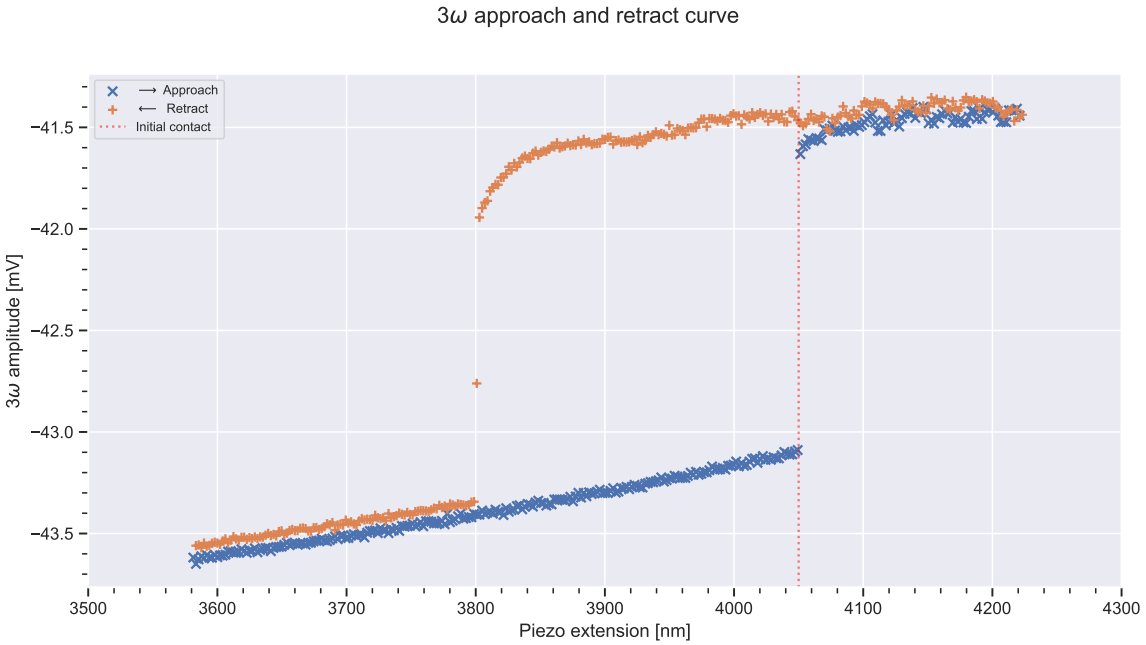


Figure 4.37: A typical approach and retract curve showing the 3ω signal when driven in AC mode. Significant hysteresis can be seen upon retracting the probe from the surface, due to the soft cantilever spring constant. It can also be noted that for moderate distances into the surface, there is little to no observable change in the SThM output.

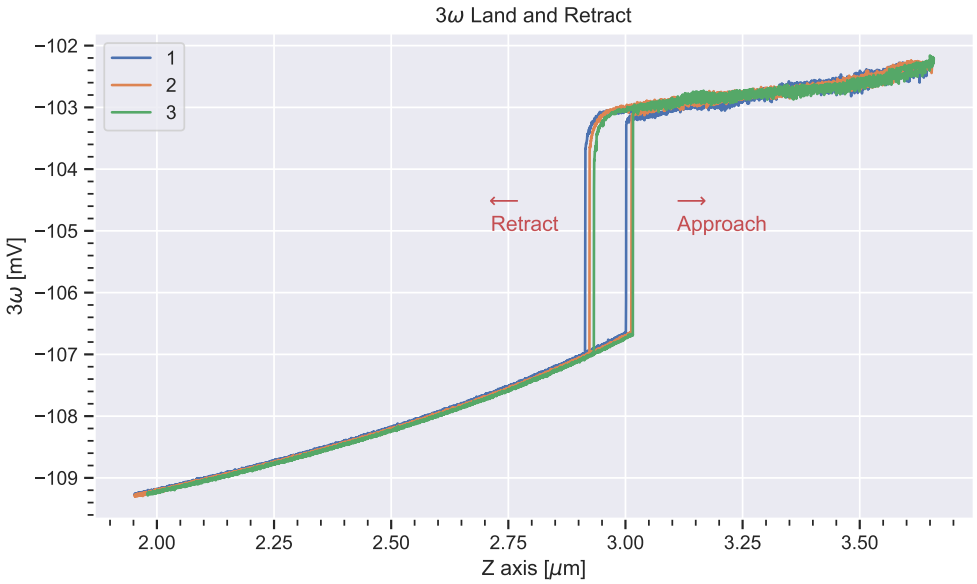


Figure 4.38: Monitoring the 3ω response as the probe is approached and retracted from the surface (Three cycles shown). Slight change in the 3ω signal can be seen past contact, this can possibly be attributed to slight changes in the contact area or contamination layers of the sample surface.

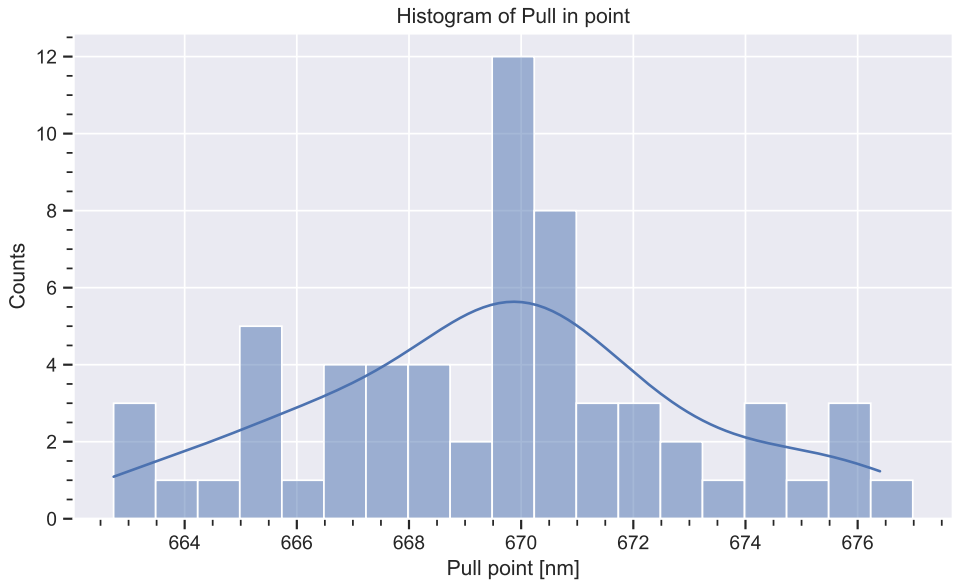


Figure 4.39: Histogram of pull-in point (calculate point that 3ω snaps into contact) over 60 land and retract cycles. Mean of 669.60 nm, standard deviation of 3.355 nm and pk-pk of 13.665 nm

A histogram of the measured point at which the 3ω jumps into contact (pull-in point) over 60 land and retract cycles can be seen in Figure 4.39 showing that a standard deviation of the noise measurement was below the stated closed-loop resolution of the stage. There was a relatively large spread of pull-in points over the distribution, however, they remain within the resolution of the stage.

It should be noted that for cantilevers of this type, with a soft spring constant in the 0.2 Nm^{-1} to 0.4 Nm^{-1} range, errors of 14 nm in the topography readout will correspond to maximum uncertainties in the tip-sample contact force of between 2.8 nN and 5 nN. It can also be seen in Figure 4.37 that once in contact, a 14 nm error in the sample contact measurement has little to no discernible effect on the thermal measurement taken. Errors in topography at this scale are common in AFM due to the thermal bend of the cantilever [6], sample bow, or laser artefacts [172].

To determine the root cause of these topography errors, Figure 4.40 shows the results of the experiment repeated with the probe biased at various oscillator voltages. It can be seen that there was a slight drift in the pull-in point up to 2.6 V, with the mean of each sequential measurement within a standard deviation of the previous measurement, this drift is most likely due to thermal expansion of mechanical components. A large change in the pull-in point is seen above 2.6 V. This change could be due to many factors. Thermal noise or thermal bending could play a part due

to the large temperature rise of the probe tip at these probe currents above 1mA (>50 °C [63]), which can cause upwards of 100's of nm deflection per degree Kelvin [6]. A similar trend above 2.6 V in the data is seen in Figure 4.35 and are most likely related.

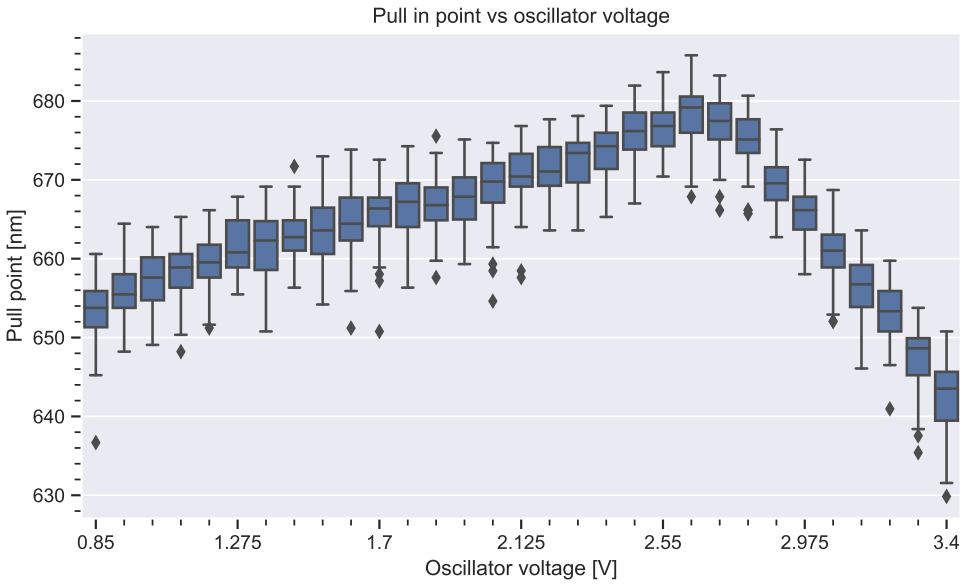


Figure 4.40: Probe voltage dependence on the measured pull-in point, There is a slight trend in the mean pull-in point as the voltage is increased, possibly due to mechanical setup expansion due to room temperature drift, with a sharp change around 2.6 V (∼1.1 mA)

Comparison of the pull-in points though Figure 4.40 proves difficult due to the drift in the pull-in point. Aligning the ranges of the data in terms of a change from mean value can be seen in Figure 4.41, and standard deviations in Figure 4.35. This shows that there is little discernible effect of the probe voltage (and therefore thermal vibration from probe tip temperature) on the ability to determine the probe pull-in point, at least for the mechanical setup used in the project. If a higher resolution stage were to be used, trends in the data may emerge.

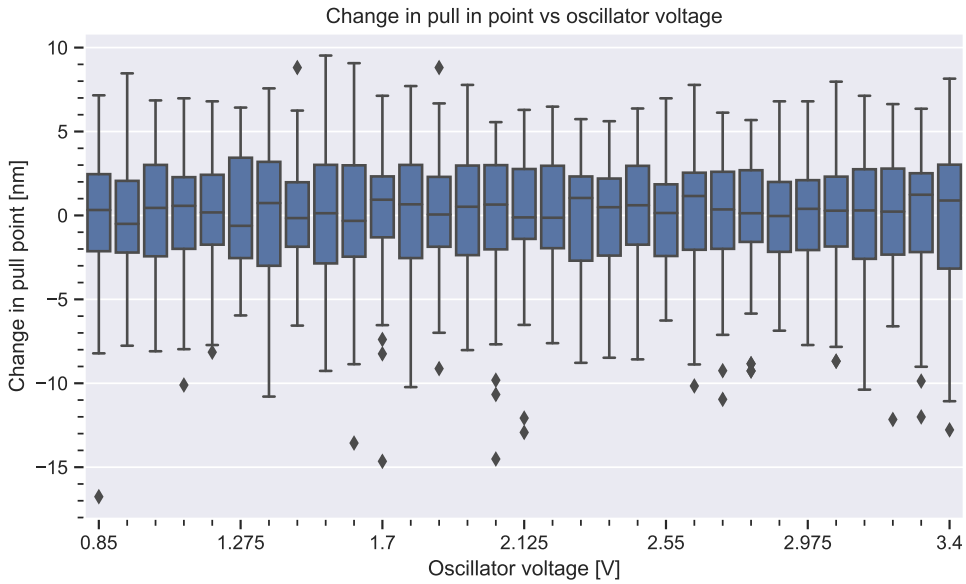


Figure 4.41: Changes in determined pull in point with probe oscillator voltage, no discernible trend is seen in statistical metrics of the measured pull-in point.

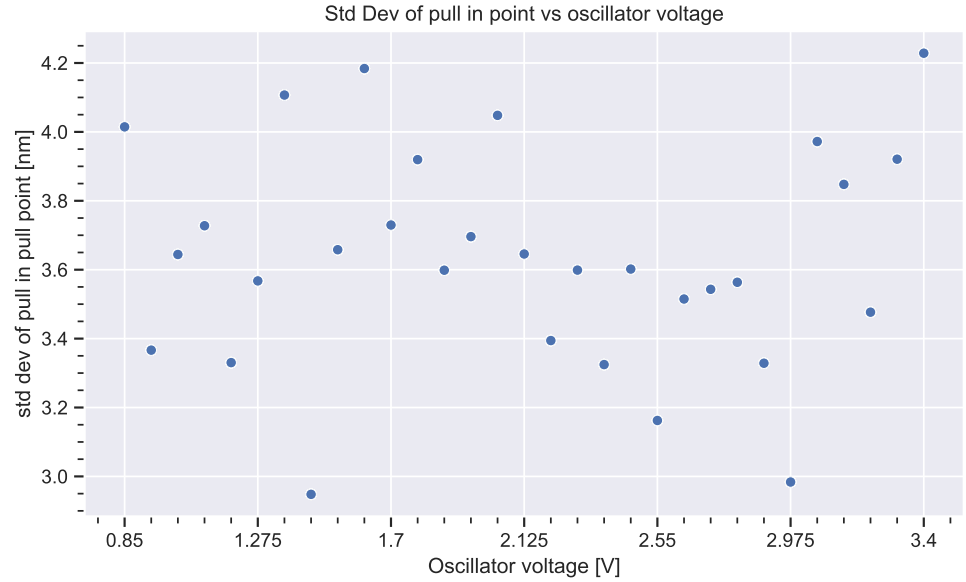


Figure 4.42: Standard deviation of pull in point with probe voltage. The topographic noise in the system appears independent of probe voltage.

Although quantitative thermal measurement in air proves difficult [3, 173], we can compare how the spread of topography determination affects the spread of 3ω values obtained from the surface measurement with probe voltage as seen in Figure 4.43, and again expressed as a change in mean value in Figure 4.44.

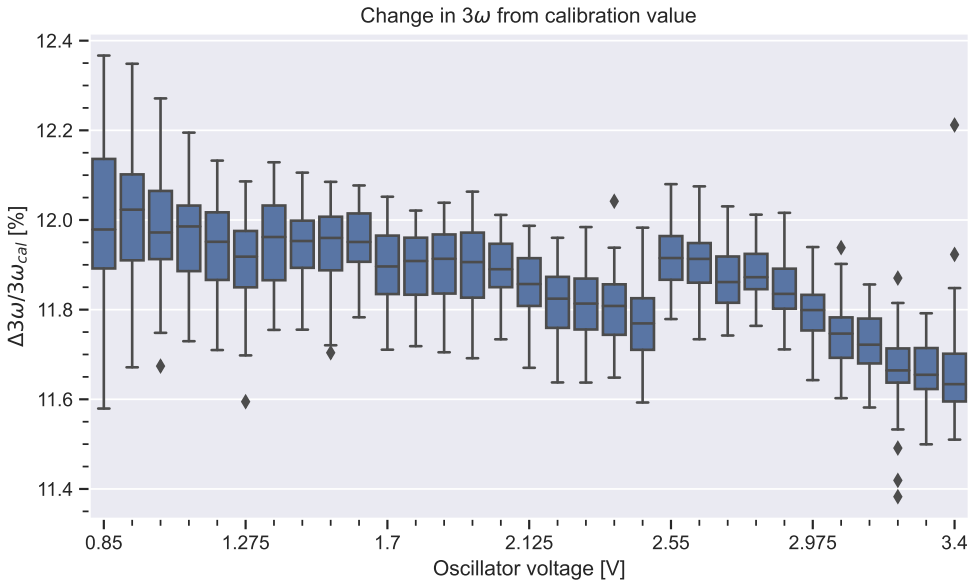


Figure 4.43: Probe 3ω response with probe voltage from repeated land and retracts.

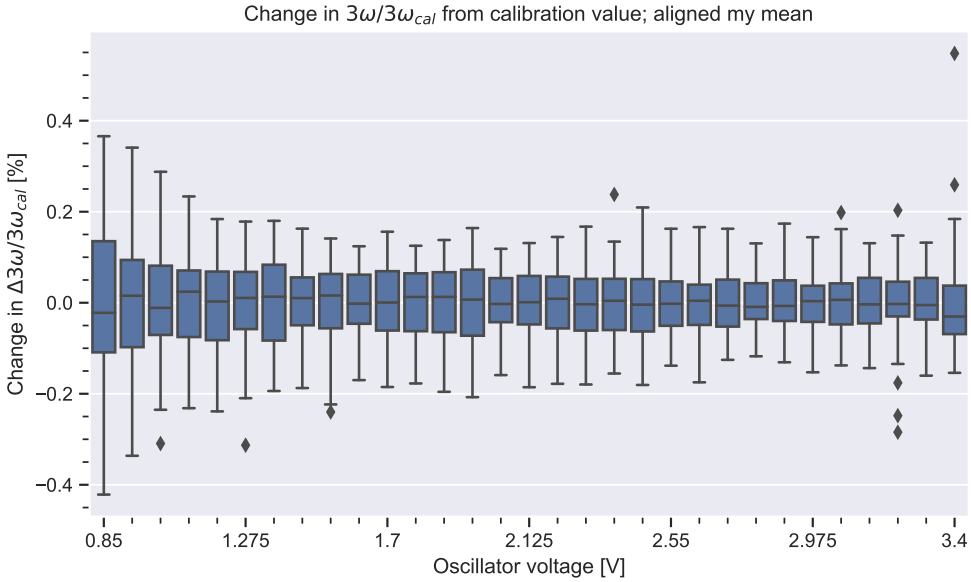


Figure 4.44: Change in surface 3ω response with probe voltage from repeated land and retracts. A larger spread in values can be seen at lower voltages, with no discernible change in noise above 1.2 V

It can be seen that Figure 4.43 follows a similar trend to Figure 4.36, and shows a slight decrease in probe response at higher probe voltages. Comparing the change in probe response with probe voltage shows an initial decreasing spread in the surface 3ω measurement up to approximately 1.2 V, above which there is little to no change in the spread of the probe response.

4.5 Thermal curves as measure of topography

By analysing the typical approach curves in Figure 4.37 and 4.38, three distinct types of measurement of 3ω can be made, shown in Figure 4.45. In the moving section (yellow) of Figure 4.45, it can be seen that the tip loading and 3ω measurement varies smoothly, decreasing with tip-sample distance until an abrupt change upon tip-sample contact.

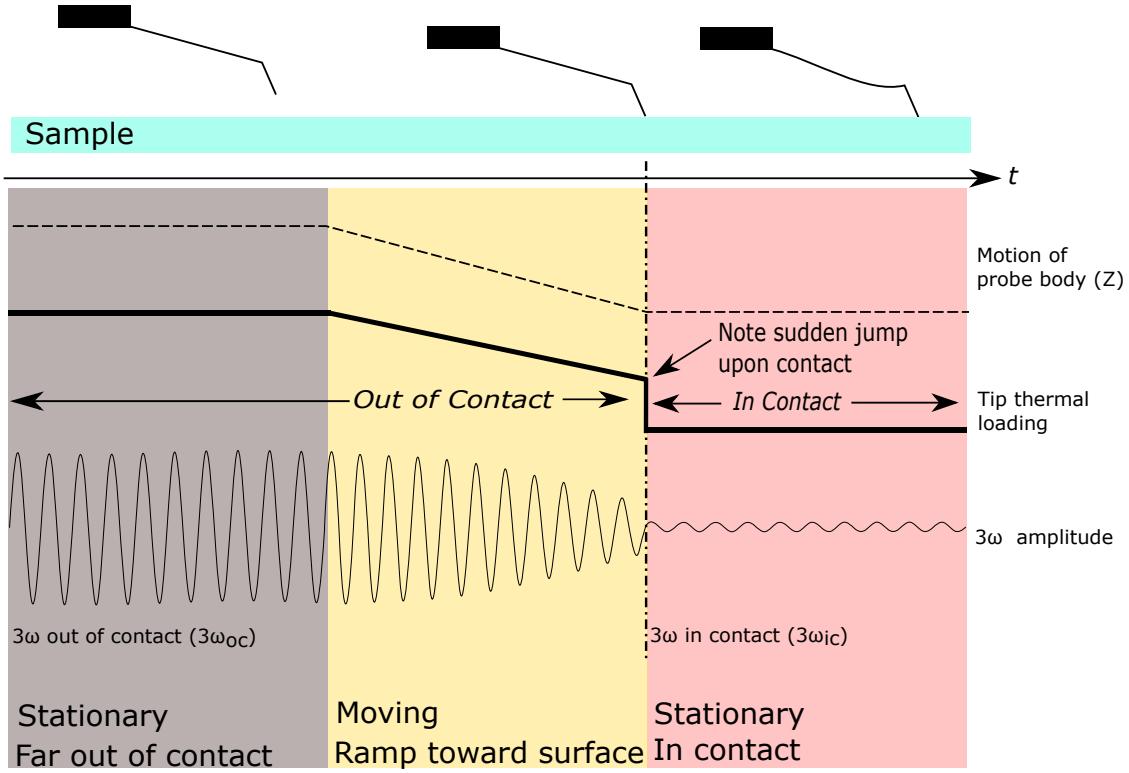


Figure 4.45: The three distinct areas of 3ω can be seen: (grey) stationary far out of contact, (yellow) moving in space towards the surface, and (red) stationary in contact.

By combining these measurements in different ways, methods to determine the sample surface were derived. Four distinct methods were designed and characterised for important scanning parameters, including topographic resolution, thermal measurement spread, and control loop speed. All methods must start with a calibration land and retract to acquire appropriate values to determine when contact has been made. Flow diagrams of each method are available to view in Appendix A.

4.5.1 Scanning thermal profiler method

Taking inspiration from the original scanning thermal profilers (STP) by Williams and Wickramasinghe [67], one can use the out of contact thermal signal as a measure of sample topography. Referring back to the thermal resistance networks in section 4.1.2, the thermal transport mechanisms of the STP method can be described through Figure 4.46. Although mechanical contact between the probe and sample has not been made. In the presence of of a gas or liquid (S_{env} closed), there is a thermal transfer path present though R_{air} which is proportional to the probe-sample separation distance. This transfer path can be seen when the probe is positioned just above the sample surface in Figure 4.37 and 4.38.

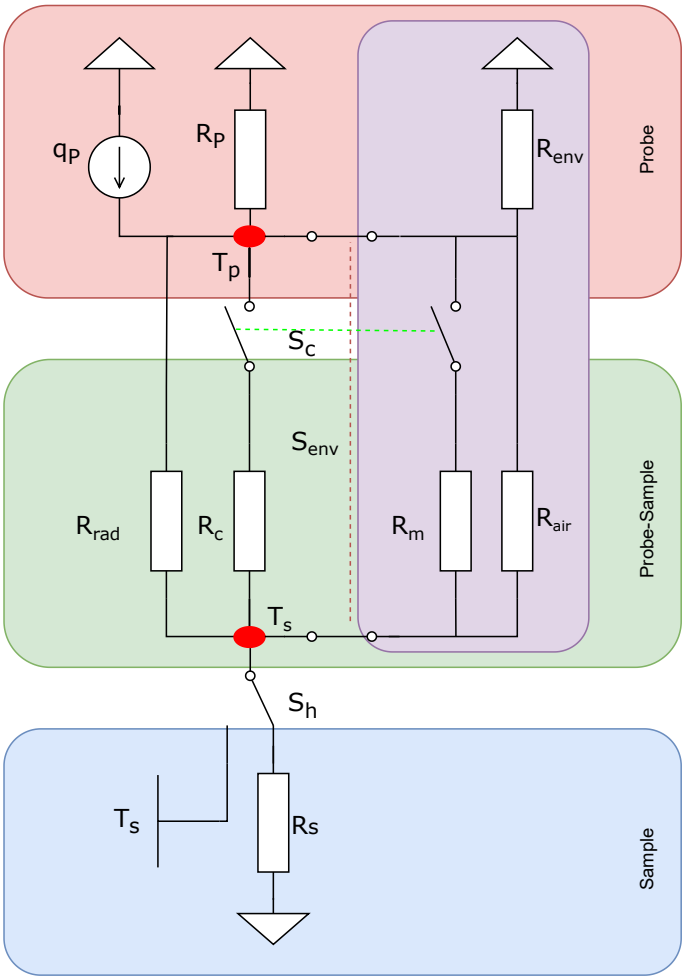


Figure 4.46: Thermal resistance model of probe in STP operation. As S_{env} remains closed, there will be a thermal transfer path through R_{air}, which is proportional to tip-sample separation

Examining only the out-of-contact portion of an approach curve leads to Figure 4.47. Fitting a polynomial to this portion of the signal (captured during a calibration land

and retract) allowed the probe and control electronics to act as an STP [67] for a non-contact measurement of sample topography with a programmable fly height. The probe could then be moved a set distance into the surface making tip-sample contact for surface thermometry measurements.

As the probes used in this work had a relatively soft cantilever, the probe needs to be flown at a relatively higher height than that of the original STP by Williams and Wickramasinghe [67] to avoid any adhesion to the sample. This led to the imaging of topographic samples suffering from significant smoothing of edges as an artefact. This can partly be attributed to an increase in the interrogation area the tip has over the sample, changing the out-of-contact thermal loading and showing very low spatial resolution. However, this technique can be useful in finding the general surface of the sample, or in samples that have minimal topography (such as 2D samples).

If this method is used to calculate the tip-surface distance before moving the tip into contact for thermal measurements, as stated previously in section 4.2, as long as contact between the tip and sample has been made, there will be little to no difference in the thermal signal unless the probe is compressed into the surface such that deformation of the probe tip occurs.

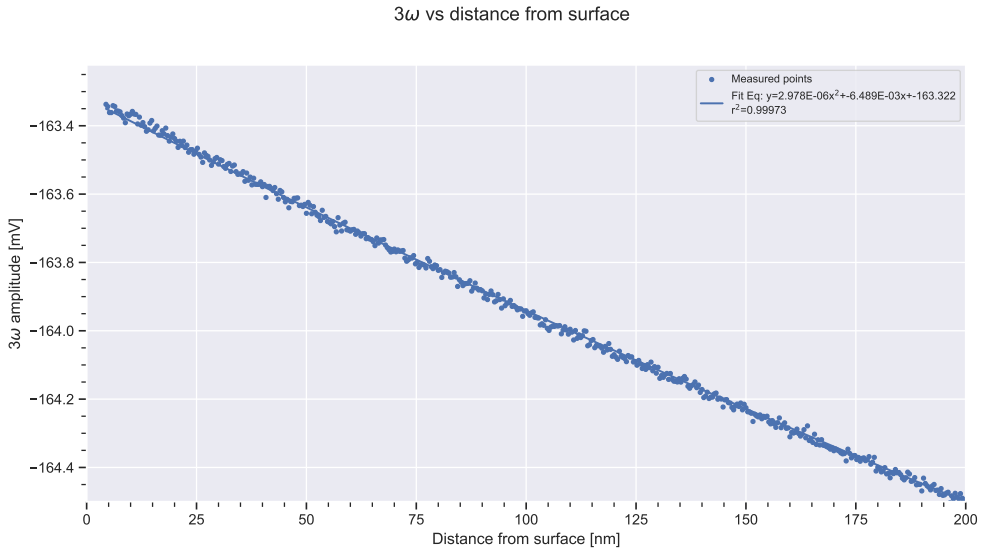


Figure 4.47: Out of contact 3ω amplitude varying with probe-sample distance. Fitting a second-order polynomial shows a good fit with r = 0.999

4.5.2 Thermal discontinuity

As seen in Figure 4.37, 4.38 and 4.47, the out-of-contact 3ω signal varied smoothly with distance from the sample surface. It can then be determined that any abrupt interruption to this smooth signal as the probe approaches the surface can be a measurement of the sample topography. In terms of the thermal resistance network, this abrupt change occurs due to the immediate closure of S_c and the immediate inclusion of R_c and R_m.

A discontinuity of the signal can either be determined through monitoring the gradient of the 3ω signal as it moves in space as shown in Figure 4.48, or through placing some limit on the allowable percentage change of consecutive measurements of the 3ω signal.

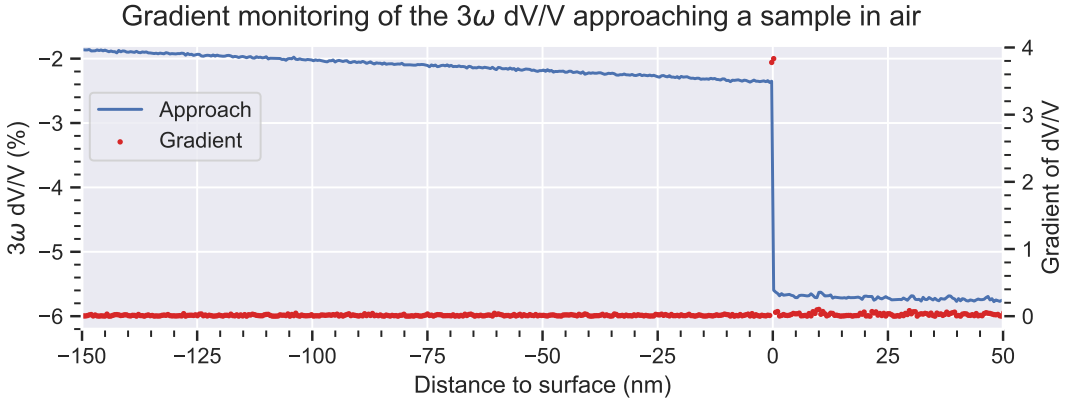


Figure 4.48: Monitoring the gradient in the 3ω signal upon an approach in air, shows a large spike at the point of contact.

4.5.3 Thermal contact limit

Due to the inherent stability of the 3ω signal and relative immunity to thermal and electrical drift, a threshold value (chosen to be 6 std deviations of measured noise in the system) was placed on the closest out-of-contact measurement of 3ω to the surface as measured from a calibration land and retract cycle where the surface is determined from the gradient monitoring method. This has been shown in Figure 4.49. It can be deduced that any 3ω signal that crosses this threshold is a measurement of contact with the sample surface. Recording the Z piezo extension at this point can be used to infer topography at the pixel. The probe can then be moved a set distance into the surface making reliable tip-sample contact for thermometry measurements. Although this simplifies the measurement comparatively to the thermal discontinuity method, one should note that the 3ω signal has a slight

temperature dependence. If temperature-induced changes to the 3ω signal change out with this chosen calibration value, this method will show erroneous topographic control.

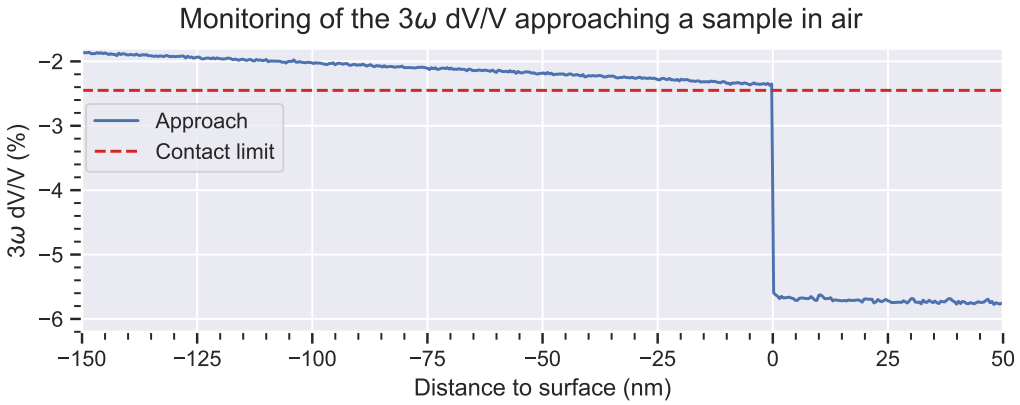


Figure 4.49: Monitoring the 3ω signal upon an approach in air, if the signal were to drop below a set value, it can be inferred to be a measurement in contact.

4.5.4 Ramp through contact

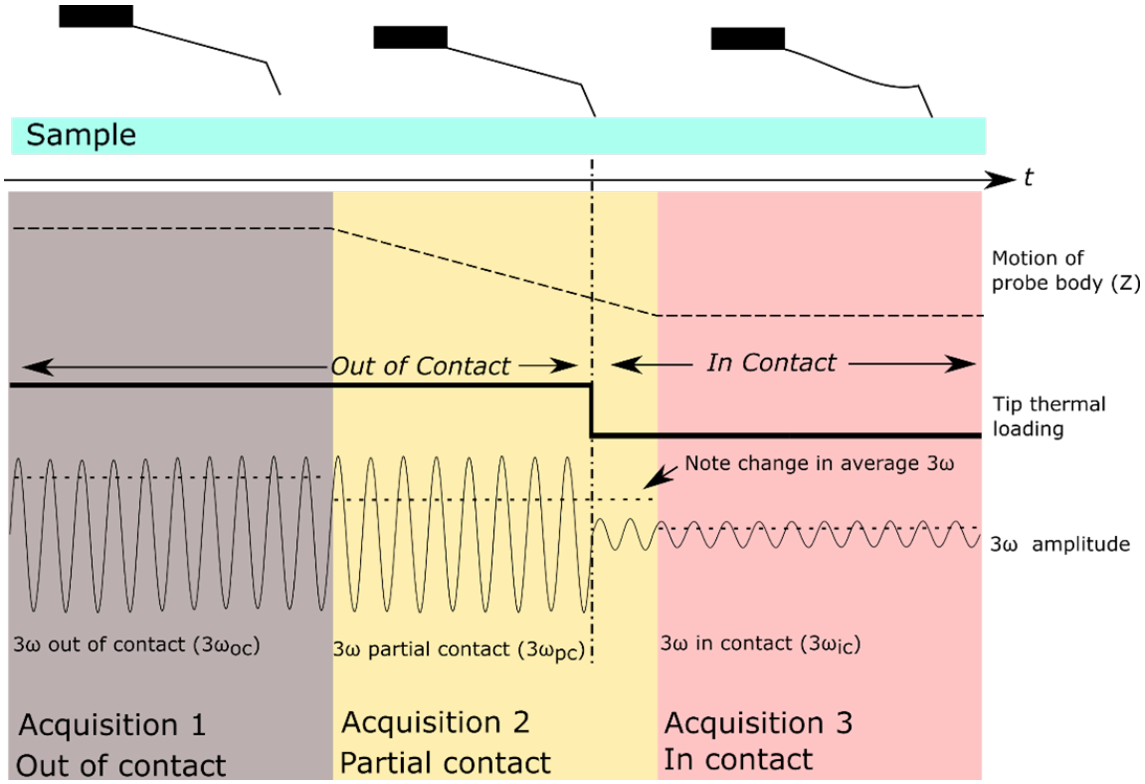


Figure 4.50: The three acquisition cycles required to calculate the sample topography from the ramp through contact method.

Another fast method of capture is one where the probe is ramped towards the sample surface by a given distance per clock cycle during sampling (as opposed to a discrete measurement at each step). If the sample contact occurs during a uniform linear ramp in time, from an initial height above the surface to a notional distance below the surface (Figure 4.50), then the time at which this occurs will be a measure of the moment of tip-sample contact. This can be calculated in a minimum of three acquisition cycles set out in Figure 4.50. From the three measurements of 3ω amplitude, the time of contact during acquisition 2 can be calculated as a percentage ($3\omega_t$) according to Eq 4.8

$$3\omega_t = \frac{3\omega_{oc} - 3\omega_{pc}}{3\omega_{oc} - 3\omega_{ic}} \qquad \text{(Eq 4.8)}$$

$3\omega_t$ being a value between 0 and 1 with 0 showing the probe barely touching during acquisition (i.e towards the end of acquisition 2), and 1 being touched immediately during acquisition 2. The surface location can then be found by applying Eq 4.9.

$$Surface = Z_{a3} + (N \cdot 3\omega_t) \qquad \text{(Eq 4.9)}$$

Where Z_{a3} is the probe height at the start of acquisition 3, N is the length of the probe ramp per acquisition cycle. However, this method assumes 3ω is constant for all distances above the surface. This is true in vacuum but can be approximated in air for sufficiently small N.

This method requires very low noise in the measurements of 3ω. Noise reduction in the 3ω measurement can be achieved by increasing the time for each acquisition (higher resolution FFT), i.e. slowing the ramp down and increasing the capture time at each step of N. However, doing so comes at a pixel capture time disadvantage, which will result in slower scans that are more susceptible to mechanical and thermal drift. This technique also suffered from the same issue as the thermal contact limit method due to its reliance on a stable out-of-contact 3ω for the detection of contact, which may not be the case due to slight temperature dependences.

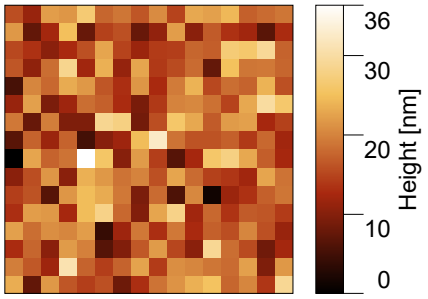
4.6 Sensitivity analysis

To compare each method's control loop on its ability to quickly attain a reliable measurement of topography, single point measurements were carried out while varying parameters of the control loop that may influence the measured topography. The probe drive frequency, number of DAC steps and DDSN used approaching the surface, and in the case of the ramping method, the size of the ramp were chosen as appropriate metrics to investigate.

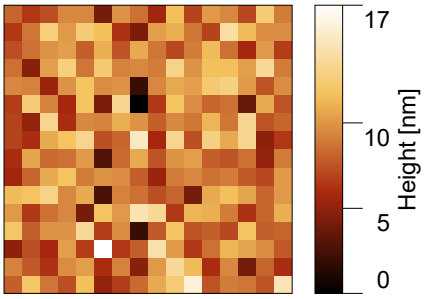
In each case, topography was measured of a single point on 400 nm silicon nitride on bulk silicon before moving the probe into firm contact (10 nm distance ≡ 2-4 nN force) for a thermometry measurement, then retracted from the surface for the next pixel using the Xue path movements as described in section 4.3.3. This was repeated 256 times to obtain statistical measurements of the ability of each method to detect the surface. Topography noise was quantified through a standard deviation and pk-pk of a single point as measured in each scan. The effect on the thermometry measurements was quantified for given parameter changes, expressed through the standard deviation of the probe response as well as the coefficient of variation (CV) of the probe response. The effects of thermal drift over the 256 pixels are assumed to be minimal over the short acquisition time so are not taken into account when comparing parameters unless stated otherwise.

4.6.1 STP method

The control loop was set to servo the probe's fly height to remain below 50nm as measured from a calibration land and retract. An example of an obtained single-point scan can be seen in Figure 4.51. For convenience, the results are displayed in a 16x16 grid pattern as if it were a typical AFM scan, with the pixel order starting from left to right, and top to bottom. Investigating the effects of probe drive frequency on the measured topography has been tabulated in Table 4.4



(a) Probe drive frequency of 224 Hz - Measured standard deviation of 5.9 nm and a pk-pk measurement of 36.3 nm



(b) Probe drive frequency of 1008 Hz - Measured standard deviation of 2.6 nm and a pk-pk measurement of 16.9 nm

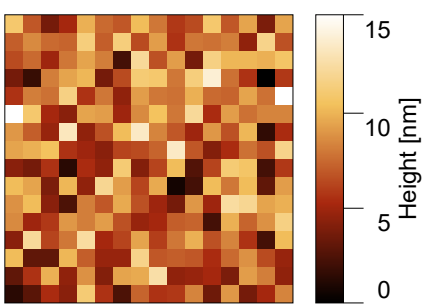
Figure 4.51: Example of 256-pixel single point scan using the STP method for measuring sample topography.

Table 4.4: Tabulated results of measured topography of single point, while increasing the probe drive frequency

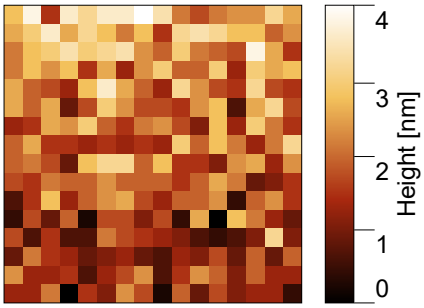
Frequency [Hz]	Z Std Dev [nm]	Z Pk-Pk [nm]	$\Delta 3\omega/3\omega_{cal}$ Std Dev [%]	$\Delta 3\omega/3\omega_{cal}$ CV [%]	Pixel rate [Hz]
224	5.89	36.29	0.0183	0.169	2.136
336	4.08	24.55	0.0207	0.198	2.135
448	2.59	15.80	0.0197	0.195	2.135
560	2.68	15.15	0.0186	0.188	2.134
672	2.64	16.44	0.0170	0.175	2.134
784	2.67	14.52	0.0170	0.178	2.134
896	2.58	15.16	0.0178	0.188	2.135
1008	2.61	16.87	0.0193	0.205	2.135
1120	2.84	16.23	0.0206	0.220	2.134

It can be seen that increases in the probe drive frequency come with a reduction in standard deviation and Pk-Pk surface topographic noice until 448 Hz. There is no effect on the pixel capture rate with an average pixel taking 460 ms, the majority of which comes from the move into contact, thermal measurement at a DDSN of 4, and subsequent move back out of contact for the next pixel; which totals approximately 215 ms (Table 4.2). If this method were solely to be used for the determination of topography with surface thermometry disabled, speeds of upwards of twice this rate are available.

Measurement noise may also be a limiting factor in the resolution available. Using a probe drive frequency of 448 Hz, this was investigated by comparing scans using a DDSN of 0 to 4 during the measurement to determine the tip-sample separation, results are displayed in Figure 4.52 and tabulated in Table 4.5.



(a) DDSN 0 - Measured standard deviation of 2.9nm and a pk-pk measurement of 15.1nm



(b) DDSN 4 - showing measured standard deviation of 820pm and a pk-pk measurement of 4nm, the slight drift with temperature can be seen over the course of the measurement

Figure 4.52: Example of 256-pixel single point scan using the STP method for measuring sample topography.

Table 4.5: Tabulated results of comparing measured topography of single point using DDSN from 0 to 4

DDSN	Z Std Dev [nm]	Z Pk-Pk [nm]	$\Delta 3\omega/3\omega_{cal}$ Std Dev [%]	$\Delta 3\omega/3\omega_{cal}$ CV [%]	Pixel rate [Hz]
0	2.87	15.15	0.0171	0.172	2.135
1	1.80	9.82	0.0199	0.199	2.088
2	1.23	8.11	0.0162	0.162	2.000
3	0.98	5.34	0.0167	0.167	1.845
4	0.82	4.06	0.0223	0.221	1.598

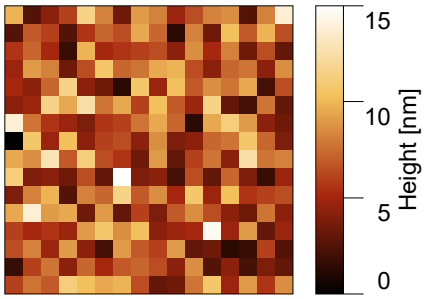
A vast improvement in the single-point topography resolution can be seen when using higher DDSN values. However, this comes at a pixel capture rate disadvantage. When considering a 128x128 scan of a topographic sample, before considering any readjustments of the stage due to changes in the topography, this can easily increase the scan times upwards of 30%.

It should be noted that these measurements of the topography are not of the true surface location at each pixel. Williams and Wickramasinghe [67] [68] have shown that there is a large interaction area when the probe is flown above the surface, so spatial resolution is very much limited, and the measurement is of the general surface around that location.

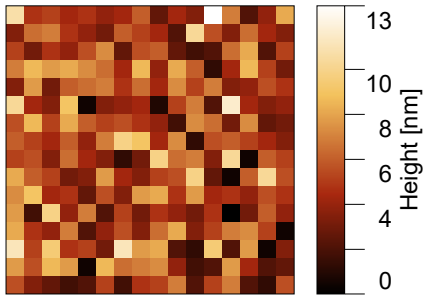
4.6.2 Thermal discontinuity

Characterisation of the thermal discontinuity method primarily focused on the probe drive frequency and probe Z-axis step size used in the approach. As with the STP method, its ability to determine the sample topography is read through a standard

deviation of multiple measurements of a single point on a surface, as if it were an AFM scan of a flat surface. Scans acquired by varying the probe drive frequency are displayed in Figure 4.53 as well as tabulated results in Table 4.6 using an approach step size of 6 DAC values (approximately 1.2nm step size)



(a) Probe drive frequency of 224 Hz - Measured standard deviation of 2.9 nm and a pk-pk of 14.9 nm



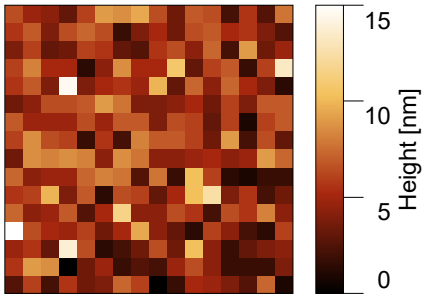
(b) Probe drive frequency of 1008 Hz - Measured standard deviation of 2.4 nm and a pk-pk of 12.8 nm

Figure 4.53: Example of 256-pixel single point scan using the Thermal discontinuity method for measuring sample topography. No discernible effect can be seen when varying probe drive frequency

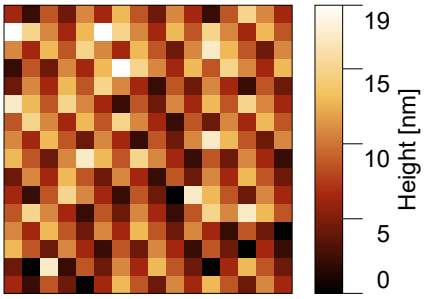
Table 4.6: Tabulated results of measured topography of single point using the thermal discontinuity method, while increasing the probe drive frequency

Frequency [Hz]	Z Std Dev [nm]	Z Pk-Pk [nm]	$\Delta 3\omega/3\omega_{cal}$ Std Dev [%]	$\Delta 3\omega/3\omega_{cal}$ CV [%]	Pixel rate [Hz]
224	2.87	14.94	0.0187	0.173	1.274
336	2.45	13.67	0.0165	0.159	1.276
448	2.43	13.24	0.0175	0.173	1.272
560	2.45	13.67	0.0166	0.168	1.272
672	2.26	11.10	0.0182	0.187	1.259
784	2.49	15.37	0.0205	0.214	1.273
896	2.58	15.37	0.0209	0.221	1.261
1008	2.40	12.81	0.0216	0.229	1.270
1120	2.46	14.52	0.0198	0.212	1.274

As can be seen, unlike the STP method, there is little to no effect of varying the probe drive frequency when using the thermal discontinuity method as a means to determine sample topography. A more appropriate parameter to investigate this method was to vary the step size of the probe approach which has been displayed in Figure 4.54 and Table 4.7.



(a) 0.4 nm approach step size - Measured standard deviation of 2.5 nm and a pk-pk of 14.9 nm.



(b) 10 nm approach step size - Measured standard deviation of 4.15 nm and a pk-pk of 19.2 nm. The quantisation of the sample surface can be seen.

Figure 4.54: Example of 256-pixel single point scan using the thermal discontinuity method for measuring sample topography.

Table 4.7: Tabulated results of measured topography of single point using the thermal discontinuity method, while increasing the probe approach step size

Step size [nm]	Z Std Dev [nm]	Z Pk-Pk [nm]	$\Delta 3\omega/3\omega_{cal}$ Std Dev [%]	$\Delta 3\omega/3\omega_{cal}$ CV [%]	Pixel rate [Hz]
0.2	2.82	25.20	0.0112	0.111	0.414
0.4	2.53	14.95	0.0128	0.126	0.739
0.6	2.27	16.87	0.014	0.138	0.935
0.8	2.39	16.23	0.0147	0.145	1.08
1.0	2.62	17.08	0.0150	0.148	1.185
2.0	2.72	12.81	0.0179	0.177	1.47
3.0	2.76	16.01	0.0185	0.182	1.402
4.0	2.60	17.08	0.0213	0.210	0.837
5.0	3.56	18.15	0.0192	0.190	0.520
6.0	4.05	21.35	0.0193	0.191	0.379
7.0	4.42	24.56	0.0193	0.190	0.368
8.0	4.43	25.62	0.0243	0.241	0.334
9.0	3.74	24.56	0.0191	0.190	0.328
10.0	4.15	19.22	0.0241	0.238	0.332

Step sizes smaller than 4 nm show no increase in the topography resolution of a single-pixel capture. However, it does show a slight improvement in repeatability of the probe response ($\Delta 3\omega/3\omega_{cal}$). The slower capture rates at higher step sizes were due to the re-measurement of the pixels when the control loop did not detect the surface. This was due to the control loop being optimised for step sizes under 2 nm. Adjustments could be made to reliably monitor larger step sizes, but it can be assumed to facilitate faster pixel rate captures at these higher step sizes.

The DDSN used to capture the approach curve was adjusted to determine if improvements to the pixel capture time could be made without a reduction in probe

response repeatability.

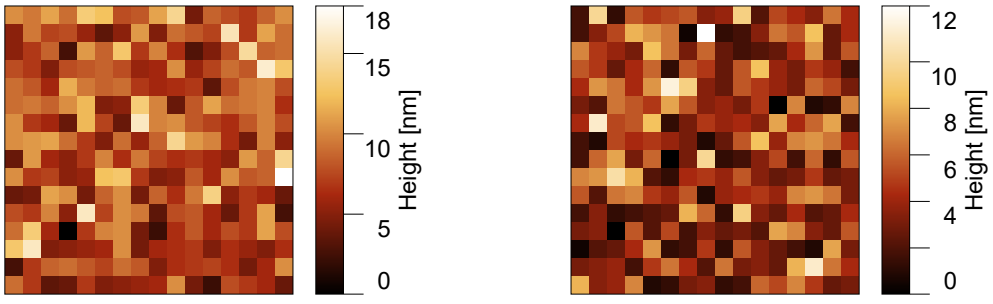
Table 4.8: Tabulated results of comparing measured topography of single point using DDSN of 0 to 4

DDSN	Z Std Dev [nm]	Z Pk-Pk [nm]	$\Delta 3\omega/3\omega_{cal}$ Std Dev [%]	$\Delta 3\omega/3\omega_{cal}$ CV [%]	Pixel rate [Hz]
0	2.45	12.81	0.0156	0.157	1.274
1	2.55	12.81	0.0164	0.164	1.043
2	2.50	17.94	0.0130	0.130	0.766
3	2.55	12.38	0.0189	0.189	0.501
4	3.16	16.65	0.0167	0.119	0.295

It can be seen that the speed of the approach measurement has very little effect on the surface sensing capabilities of this method, and the fastest approach should be used to minimise pixel capture time.

4.6.3 Thermal contact limit

The thermal contact limit's characterisation also focused on the probe drive frequency and probe Z-axis step size used in the approach. As with the previous methods, its ability to determine the sample topography was read through a standard deviation of multiple measurements of a single point on a surface. Scans acquired by varying the probe drive frequency are displayed in Figure 4.55 as well as tabulated results in Table 4.9 using a step size of 6 DAC values (approximately 1.2 nm step size)



(a) Probe drive frequency of 224 Hz - Measured standard deviation of 2.89 nm and a pk-pk of 17.94 nm

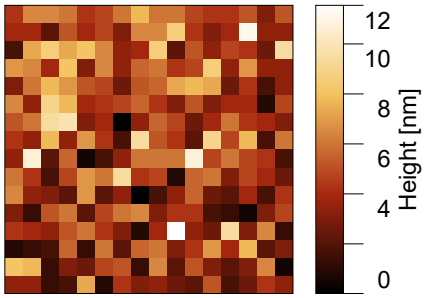
(b) Probe drive frequency of 1008 Hz - Measured standard deviation of 2.6 nm and a pk-pk of 12.38 nm

Figure 4.55: Example of 256-pixel single point scan using the Thermal contact limit method for measuring sample topography. No discernible effect can be seen when varying probe drive frequency

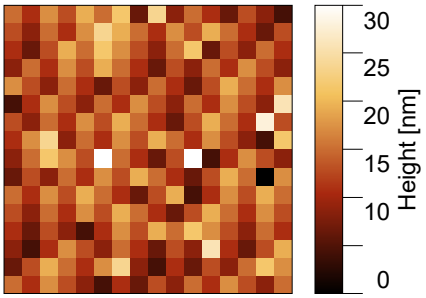
Table 4.9: Tabulated results of measured topography of single point using the thermal contact limit method, while increasing the probe drive frequency

Frequency [Hz]	Z Std Dev [nm]	Z Pk-Pk [nm]	$\Delta 3\omega/3\omega_{cal}$ Std Dev [%]	$\Delta 3\omega/3\omega_{cal}$ CV [%]	Pixel rate [Hz]
224	2.89	17.94	0.0186	0.172	1.264
336	2.43	14.95	0.0163	0.157	1.264
448	2.59	17.94	0.0189	0.187	1.265
560	2.80	16.23	0.0172	0.174	1.266
672	2.46	14.52	0.0182	0.188	1.265
784	2.32	12.38	0.0193	0.202	1.265
896	2.38	12.38	0.0180	0.190	1.265
1008	2.36	12.38	0.0203	0.215	1.265
1120	2.38	16.23	0.0205	0.219	1.265

As expected and similar to the thermal discontinuity method, there is little to no change in the topography output with drive frequency, with no change in the pixel capture speed. Again, sensitivity to step size has been investigated as a potential route of optimisation, as displayed in Figure 4.56 and Table 4.10.



(a) 0.4 nm approach step size - Measured standard deviation of 2.2 nm and a pk-pk of 11.5 nm.



(b) 10 nm approach step size - Measured standard deviation of 4.83 nm and a pk-pk of 29.89 nm. Again, the quantisation of the sample surface can be seen.

Figure 4.56: Example of 256-pixel single point scan using the thermal discontinuity method for measuring sample topography.

Table 4.10: Tabulated results of measured topography of single point using the thermal discontinuity method, while increasing the probe approach step size

Step size [nm]	Z Std Dev [nm]	Z Pk-Pk [nm]	$\Delta 3\omega/3\omega_{cal}$ Std Dev [%]	$\Delta 3\omega/3\omega_{cal}$ CV [%]	Pixel rate [Hz]
0.2	2.39	14.52	0.0118	0.116	0.457
0.4	2.22	11.53	0.0140	0.138	0.741
0.6	2.38	14.52	0.0141	0.139	0.934
0.8	2.92	24.77	0.0152	0.150	1.075
1.0	2.41	16.01	0.0156	0.154	1.181
2.0	2.52	10.68	0.0174	0.172	1.473
3.0	2.98	16.01	0.0181	0.179	1.606
4.0	3.29	21.35	0.0188	0.186	1.682
5.0	3.26	18.15	0.0176	0.174	1.728
6.0	3.90	23.49	0.0176	0.174	1.759
7.0	4.21	23.49	0.0174	0.173	1.778
8.0	3.87	21.35	0.0186	0.184	1.787
9.0	4.31	21.35	0.0171	0.170	1.803
10.0	4.83	29.89	0.0192	0.190	1.797

Again, although only a small change in the standard deviation of the measured topography is observed, a slight improvement in both topography and probe response can be seen for lower step sizes.

DDSN was increased from 0 to 4 to slow the approach down, but simultaneously improve the noise of each measurement the probe approaches.

Table 4.11: Tabulated results of comparing measured topography of single point using DDSN of 0 to 4

DDSN	Z Std Dev [nm]	Z Pk-Pk [nm]	$\Delta 3\omega/3\omega_{cal}$ Std Dev [%]	$\Delta 3\omega/3\omega_{cal}$ CV [%]	Pixel rate [Hz]
0	2.55	12.38	0.0164	0.166	1.262
1	2.66	16.23	0.0190	0.190	1.039
2	2.46	15.37	0.0159	0.159	0.765
3	2.46	12.81	0.0150	0.150	0.502
4	3.12	14.09	0.0198	0.197	0.297

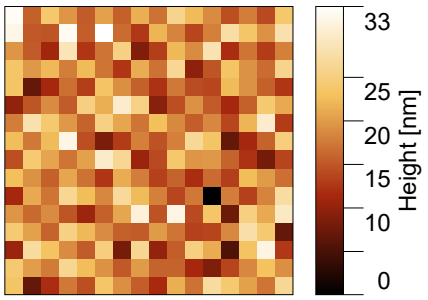
Similarly to the thermal discontinuity method, the faster the approach the higher the increase in repeatability, with the bonus of decreased pixel capture time.

4.6.4 Ramp method

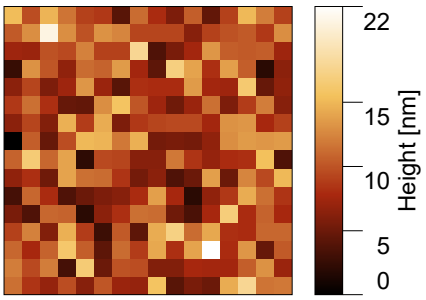
Characterisation of the ramp method was predominantly carried out by varying three parameters: the probe drive frequency, the ramp length, and the ramp time. One would think that decreasing the ramp length and increasing the ramp time would increase the surface detection ability of the control loop. This is true in theory, however, they potentially come at a vast time disadvantage, particularly if there are large jumps in sample topography, which could negate the pixel rate advantage that this method holds.

Unless stated otherwise an initial ramp length of 51.2 nm, ramp time of DDSN 2 and drive frequency of 448 Hz were used to allow qualitative comparisons between scans.

As with the other proposed methods, the probe drive frequency was varied to quantify its effect on the resolution available. Figure 4.57 shows examples of single-point scans obtained, with tabulated results in Table 4.12



(a) 224 Hz Drive frequency - Measured standard deviation of 5.8 nm and a pk-pk of 33.1 nm.



(b) 1008 Hz Drive frequency - Measured standard deviation of 3.7 nm and a pk-pk of 22.4 nm

Figure 4.57: Example of 256-pixel single point scan using the ramp method for measuring sample topography while varying the probe drive frequency.

Table 4.12: Tabulated results of measured topography of single point using the ramp method, while increasing the probe drive frequency

Frequency [Hz]	Z Std Dev [nm]	Z Pk-Pk [nm]	$\Delta 3\omega/3\omega_{cal}$ Std Dev [%]	$\Delta 3\omega/3\omega_{cal}$ CV [%]	Pixel rate [Hz]
224	5.78	33.10	0.0269	0.310	1.742
336	5.05	27.97	0.0274	0.317	1.705
448	4.49	23.91	0.0191	0.22	1.68
560	4.20	23.70	0.0192	0.222	1.681
672	3.61	19.64	0.0219	0.251	1.672
784	3.84	19.86	0.028	0.321	1.707
896	3.90	24.56	0.0299	0.344	1.673
1008	3.71	22.42	0.0270	0.310	1.702
1120	3.75	18.58	0.0232	0.150	1.724

It can be seen from Table 4.12 that probe drive frequencies above 448 Hz show an improvement in the topography and probe response repeatability with no effect on the pixel capture rate.

The next parameter investigated was the ramp length. Ramp lengths were chosen to be powers of 2 divisions of DDSN 0, so for example, in a ramp acquisition of 1024 clock cycles, the ramp would move 1024 or 512 DAC bits (i.e. a DAC bit per 1 or 2 clock cycles). Results have been tabulated in Table 4.13.

Table 4.13: Tabulated results of measured topography of single point using the ramp method, while decreasing the acquisition ramp length

Ramp length [nm]	Z Std Dev [nm]	Z Pk-Pk [nm]	$\Delta 3\omega/3\omega_{cal}$ Std Dev [%]	$\Delta 3\omega/3\omega_{cal}$ CV [%]	Pixel rate [Hz]
204.8	5.25	29.25	0.0271	0.267	1.083
102.4	3.82	20.50	0.0186	0.184	1.112
51.2	3.07	16.65	0.0152	0.151	1.535
25.6	3.38	19.64	0.0136	0.134	1.094
12.8	2.46	15.16	0.0138	0.137	0.865

From Table 4.13, although improvements in resolution can be seen when decreasing the ramp length, this comes at a large disadvantage in pixel capture rate as there is a need to constantly readjust the probe at such short ramp lengths, each time retaking the three acquisitions needed to calculate the surface. This is also before considering the slow slew rate that would occur when the probe encounters topographic features above the size of the ramp length. If there is no topography present on a sample, in this experimental setup a ramp height of 51.2 nm seems the optimal choice.

The resolution of the stage used may also be a factor for the slow pixel capture rate. When attempts are made to position the probe 13nm above the surface, with a stage resolution of around 15nm, inaccuracies in the stage positioning may cause premature probe contact. Increasing the time taken over the ramp acquisition is also a parameter that can be optimised for, having the advantage that this does not require the constant probe readjustment as mentioned previously.

Table 4.14: Tabulated results of measured topography of single point using the ramp method, while increasing the acquisition ramp time

Ramp time [DDSN]	Z Std Dev [nm]	Z Pk-Pk [nm]	$\Delta 3\omega/3\omega_{cal}$ Std Dev [%]	$\Delta 3\omega/3\omega_{cal}$ CV [%]	Pixel rate [Hz]
0	4.60	22.21	0.0151	0.152	1.695
1	3.44	20.50	0.0150	0.151	1.694
2	3.24	16.65	0.0154	0.154	1.524
3	2.96	16.23	0.0169	0.170	1.245
4	2.75	15.37	0.0195	0.195	0.920

Again, increasing the acquisition time of the ramp increases resolution, but at an expected pixel capture rate disadvantage. Increasing the DDSN past 4 for this method would prove inhibitively slow, thermal drifts in the setup would most likely show. Although there is an improvement in the topographic repeatability, the thermal repeatability goes down slightly, which may be due to slight thermal drifts.

4.7 Discussion

The noise levels of the thermometry signals in the setup have been characterised, and generally show a very low noise level in the system. When adjusting probe settings such as drive frequency and amplitude, variations in the signals can be seen. However, these tend to be negligible in magnitude, with the coefficient of variations staying in the 0.01% region and peaking at 0.1% in the worst of cases. A drift on order of 5 seconds in the contact thermal measurements can be seen before stabilisation, hypothesised to be due to the meniscus formation of contamination layers. This can be reduced by flooding the setup with dry nitrogen and shows a vast improvement in the stabilisation time.

Four methodologies for determining topographic control of the SThM have been addressed using solely the thermometry signals from the tip sensor, single point measurements for each method have been carried out and an evaluation of their sensitivity to control loop parameters presented. However, determining the optimal method for topographic control is a complex endeavour, necessitating a careful balance of compromises between acquisition speed, both XY, and Z resolutions, and thermal response repeatability.

The STP method emerges as a favourable choice for swiftly capturing sample topography with relatively low spatial resolution. This capability could prove valuable for preliminary scanning across extensive areas, identifying key features, before con-

ducting more intricate scans for in-depth inspection using another proposed method. Furthermore, its relevance extends to scenarios where large topographic features are predominant, and the focus is concentrated on thermometric scanning without much concern for topographic resolution.

The thermal discontinuity and thermal contact limit methods exhibit similar performance. The thermal contact limit method introduces a potential drawback if the probe tip were to collect contamination or alter its shape during a scan. Contamination could alter the thermal loading seen by the tip and potentially disrupt the calibration of the control loop. In contrast, the discontinuity method, while exhibiting a marginal reduction in scanning speed, focuses on abrupt changes in the 3ω signal, presenting a more robust resistance to probe contamination and alterations in probe shape during scanning.

The thermal discontinuity method would therefore prove useful for single point measurements in material studies in the dark, or where laser illumination is detrimental, and may provide a solution to problems encountered in studies presented by Ramiandrisoa et al. [2] and Spiece et al. [3].

The ramp during acquisition method proves to be a well-balanced compromise, offering a blend of speed and resolution while demonstrating a certain level of immunity to probe contamination.

Overall, with the exception of the STP method, the probe drive frequency has minimal impact on the monitoring of surface location. There is a slight variance in the thermometric measurement taken. However, this is most likely due to noise in the 3ω signal itself rather than being due to changes in contact force from errors in topography.

In all cases and methods, the effect on probe response ($\Delta 3\omega / 3\omega_{cal}$) is marginal, with the majority of standard deviations in the 0.01 - 0.03% range and CV values in the 0.1-0.3% range. This low scatter in the probe response aligns with studies by Ramiandrisoa et al. [2] and Spiece et al. [3] that both showed laser illumination as a large influence on the scatter of thermal measurements; up to 37% in some cases. It is thought that a remainder of the CV may be due to slight differences in the probe landing shape upon repeated landings, or be due to uncontrolled microscope and sample temperatures, a solution to which is presented by Spiece et al. [3] showing a 5 to 10 fold increase in measurement repeatability when temperature drift is accounted for.

Overall, CV values obtained from repeated probe landings tend to stay within an order of magnitude of the CV obtained from repeated measurements with contact held, showing that the system has excellent overall stability.

Topographic scanning using the 3ω signal in air

5.1 Introduction

Using the techniques and methods described in section 4.5, while raster scanning the X and Y axis of the sample stage, one can use the 3ω signal as a method to create topographical and thermometric maps of samples in complete dark conditions. As discussed in section 4.4.1, although issues of water meniscus formation around the tip can cause issues in the measurement, scanning in an air environment remains a popular choice within the SThM community [2, 3, 6, 52, 53, 57–61, 174] due to the ease of measurement setup.

For accurate interpretation of scans obtained it is important to first define the probe mounting direction and scanning axis. Asymmetries in thermal measurements (discussed in section 4.1.2), as well as drift artefacts can vary depending on the probe mounting direction and probe fast/slow scanning axis. As such, in scans obtained in this work in the custom SThM, the probe is mounted according to Figure 5.1 with the tip pointing to the right-hand side of the scans along the X axis, with this axis also being the fast scan axis. Due to this mounting and scanning direction, thermal profiles of features scanned will show asymmetries in the X-axis from probe overhang, as well as slight asymmetries from the probe-sample contact angle. The Y axis is always scanned as the slow axis and will be more prone to ambient thermal drifts of the setup. This axis will also show greater tip convolution with the side wall of the wider section of the probe on this axis. The topographic asymmetries from the probe scanning in each axis have been shown in Figure 5.2.

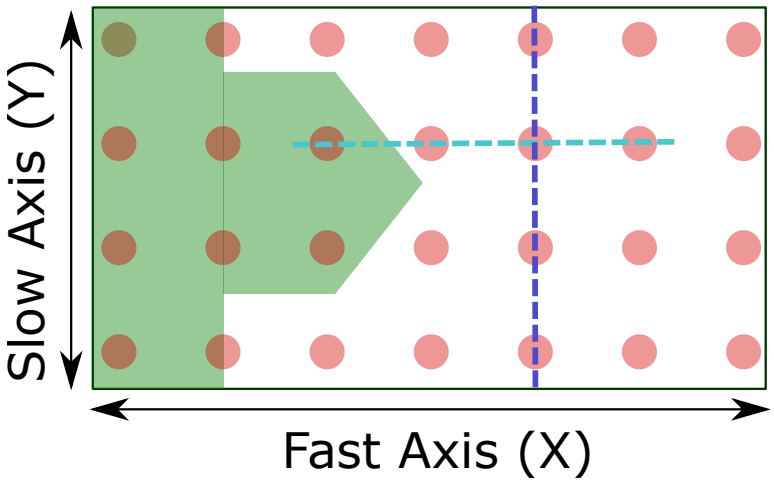


Figure 5.1: Diagram of probe scan and mounting directions. The X and Y axes are chosen as the fast and slow axes respectively. The probe (green) is mounted with the tip pointing and advancing in the fast axis. In this example, pillars (red) are being scanned. While scanning a given pillar from left and right, an asymmetric thermal profile is to be expected due to pillar overhang

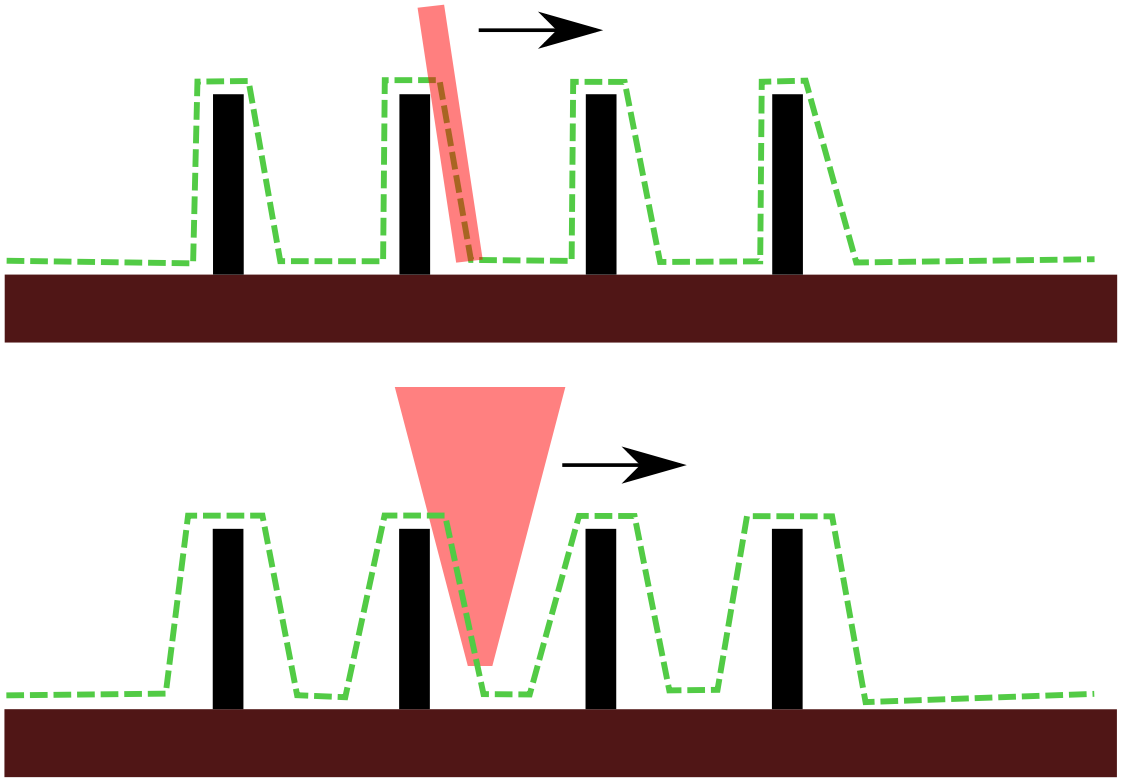


Figure 5.2: Topographic asymmetries that can occur on each scanning axis. Advancing in the fast axis direction (top - light blue line in Figure 5.1 may show slight topographic artefacts due to either probe sample contact angle or uneven sample loading. Advancing in the slow axis (bottom - dark blue line in Figure 5.1) can show more convolution of the wide probe opening angle with the pillars.

Samples were scanned using the various methods described in section 4.5 to asses each technique's performance to a variety of changes in topography, temperature and material. First, a topographic sample consisting of etched silicon pillars of approximately 48 nm height developed for the QUANTIHEAT[1] project was scanned using all techniques previously described. A gold step edge sample of an 80nm lithographic step from SiNx to evaporated NiCr/Au (10 nm/70 nm) was then scanned to determine the material dependency measurement capabilities of the system.

An experiment to determine the ability of each technique to control topography while experiencing a change in sample temperature was also carried out. This involved the scanning of an area approaching a microheater, at various microheater power outputs.

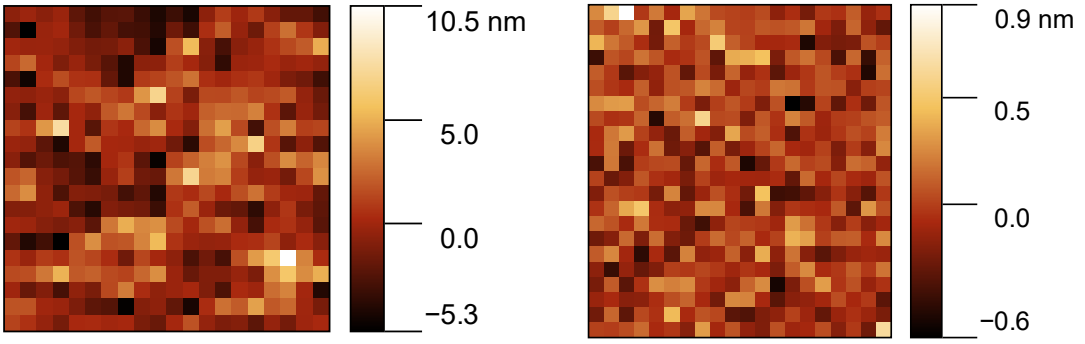
An active laser device, a Firecomms vertical cavity surface emitting laser (VCSEL), was also scanned as a proof of concept. Previously, these sorts of SThM studies would have been impracticable to carry out, particularly due to the need for blanking of the optical lever laser and photodiode mechanism during measurement.

As the requirement for access to the probe's reflective elements has been eased, this also opens up avenues to explore alternative mounting of the SThM probes. As a proof of concept, the mechanical setup was changed to point the probe perpendicular towards the sample and samples were remeasured.

5.2 Silicon flat

Flat areas from a scan utilising the thermal discontinuity method in the SThM setup and a scan of the same silicon measured on a Bruker Dimension Icon (OSTEPA-R4 probe) were compared to determine the difference in topography output. Scanned areas of comparable size (approx. 1 µm^2) from both systems can be seen in Figure 5.3 with histograms and statistical quantities in Figure 5.4 and Table 5.1. It should be noted that the probes used between the two SPM systems are not the same probe, with the commercial setup utilising OSTEPA-R4 probes designed for topography measurements with a tip radius of approximately 7 nm, unlike the custom setup where probes are first and foremost designed for thermal acquisition with a comparatively larger tip radius of approximately 50 nm[53, 63]

[1]European Union Seventh Framework Program FP7-NMP-2013-LARGE-7 under GA N°604668 Project "QUANTIHEAT"



(a) Custom SThM

(b) Commercial AFM (Bruker Dimension Icon)

Figure 5.3: Comparison of topography output acquired from custom SThM setup and commercial AFM

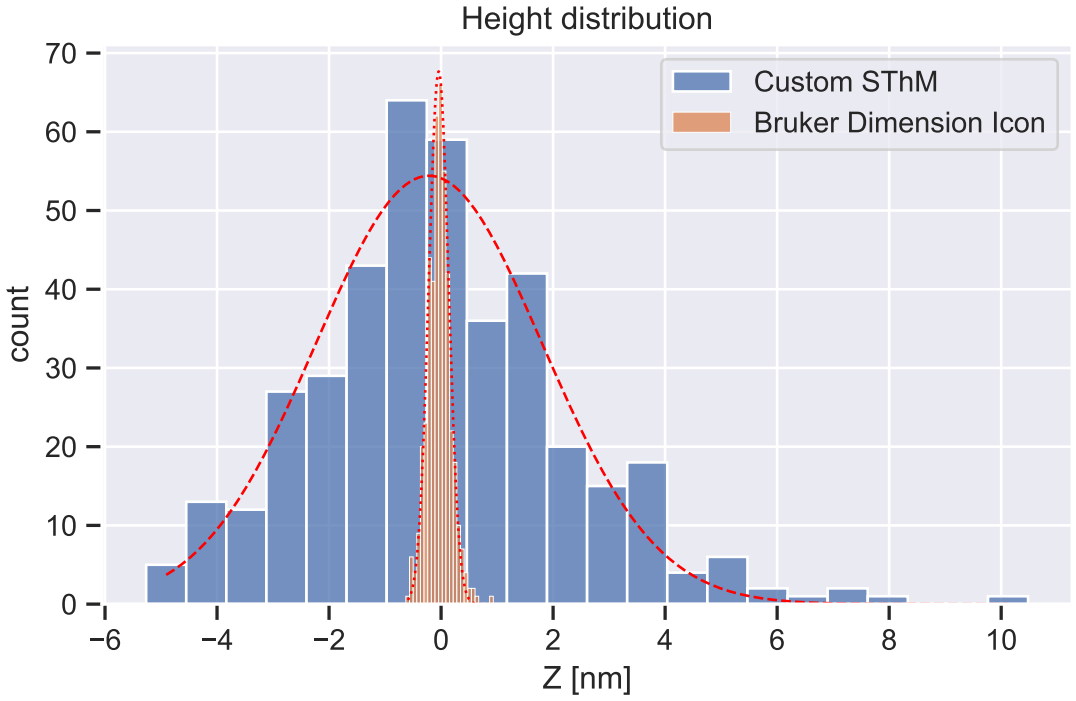


Figure 5.4: Overlaid height distributions of Figure 5.3, with Gaussian fits to both distributions (red).

Table 5.1: Comparison of topography output from custom SThM and commercial AFM, table of statistical values

Quantity	Custom SThM	Commercial AFM
Std Dev (σ) [nm]	2.309	0.205
Pk-pk [nm]	15.75	1.560

It can be seen that the custom setup has approximately an order of magnitude

higher noise levels in measurements when compared to the commercial AFM. Analysis of the distributions in Figure 5.4 show an approximate Gaussian distribution for both sets of results. The limiting factor in AFM Z height measurement is generally accepted to be shot noise in the photodetector and thermal vibration of the cantilever, both of which will show Gaussian noise profile [175, 176]. Studies by Butt and Jaschke [177] have shown that thermal noise, Δz, in an AFM cantilever can be calculated through Eq 5.1 when no optical lever laser is present and Eq 5.2 in the case of the optical lever.

$$\Delta z = \sqrt{k_b T / k} \tag{Eq 5.1}$$

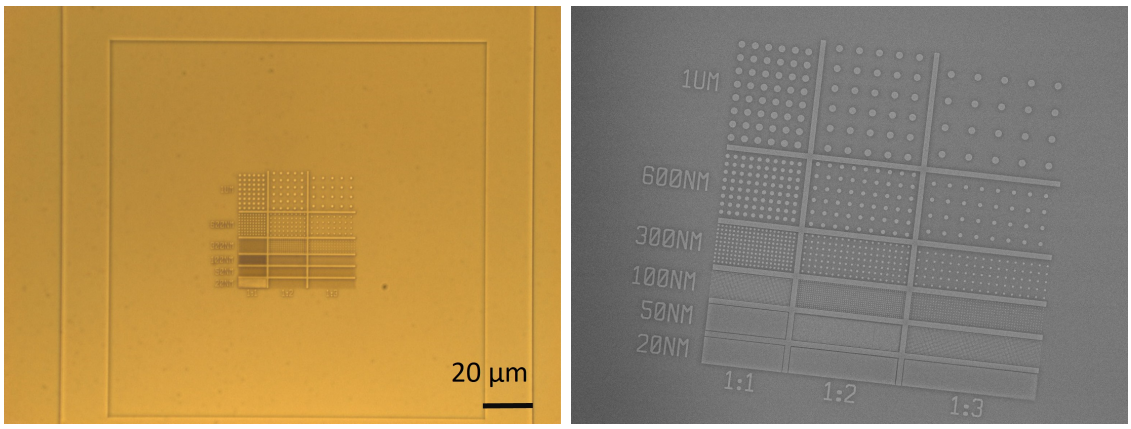
$$\Delta z = \sqrt{4 k_b T / 3k} \tag{Eq 5.2}$$

Where k_b is the Boltzmann constant, T is the operating temperature of the cantilever, and k is the spring constant of the cantilever. In the case of the OSTEPA-R4 AFM probe utilised in the commercial system with a nominal spring constant of 26 Nm^{-1} and operating at room temperature (22 °C), solving Eq 5.2 shows a Δz of 14.5 pm. In the case of the KNT probe utilising Eq 5.1, with a spring constant of 0.2-0.4 Nm^{-1}, we can calculate a Δz of 100.9 pm to 142.7 pm at room temperature. Raising the temperature to an operating temperature of the SThM of 100 °C, this maximum thermal vibration raises to 160.4 pm. Although this shows a theoretical order of magnitude higher thermal actuation than the OSTEPA-R4 probe, the thermal vibration of the KNT cantilever, even at higher operating temperatures, is not the root cause of the observed higher noise levels in the system. One might expect that thermal oscillations caused by electrical oscillations of the probe tip at 2ω may be the cause of this increase in noise, however, as was previously discussed in section 4.4.2, upon changing the amplitude of the drive frequency no observable change was observed.

More likely the reasoning for the discrepancy between systems is that they utilise different stages, with the Bruker Dimension Icon having a closed loop Z axis with an RMS noise level of 50 pm compared to the custom SThM stage only having a manufacturer-specified closed-loop resolution of 20 nm [163]. The comparatively low accuracy stage and possible unintentional excitation of piezo resonances may be the origin of the higher noise levels.

5.3 Silicon pillar

A sample of etched pillars in silicon was chosen as a topography standard sample. This sample consists of many pillars of different diameters and pitches. As there are many topographic edges in the sample of the same material, it will show many double-contact thermal edge artefacts but no material contrast. An optical microscope and SEM image of the sample are available in Figure 5.5a and 5.5b.

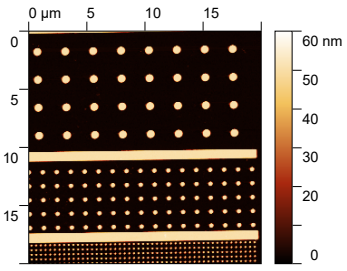


(a) Bench top microscope image

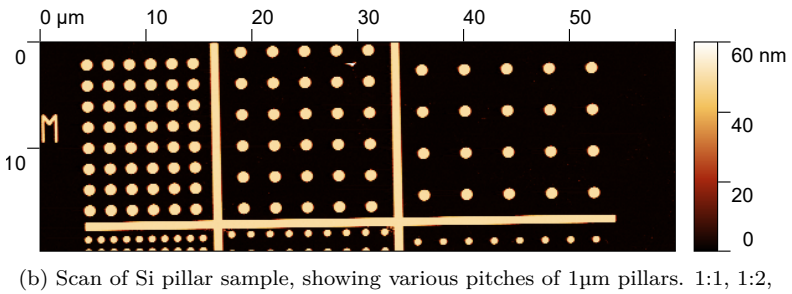
(b) SEM image

Figure 5.5: Images of Si pillar sample layout, pillar diameters are displayed on the Y axis and pitch variations on the X

Before placing the sample in the custom SThM setup, it was scanned in a commercial AFM (Bruker Dimension Icon OSTEPA-R4 probe). This provided an accurate topography scan to assess the performance of the custom topography loops. Results of scans are visible in Figure 5.6.



(a) Scan showing various diameters of the pillar. 600 nm, 300 nm, and 100 nm diameters at a 1:3 pitch.



(b) Scan of Si pillar sample, showing various pitches of 1µm pillars. 1:1, 1:2, 1:3 pitches

Figure 5.6: Tapping mode AFM topography scans of Si pillar sample to measure pillar height.

The calculation of pillar heights can be achieved though analysis of the height distribution data acquired in Figure 5.6. Least squares fitting two Gaussian distributions to the data, one for the base of the pillars and one for the apex of the pillars as in

Figure 5.7, allows a measurement of their location in space to be obtained. Fitting parameters and associated error (taken as 1 σ from each) for the two distributions are available in Table 5.2.

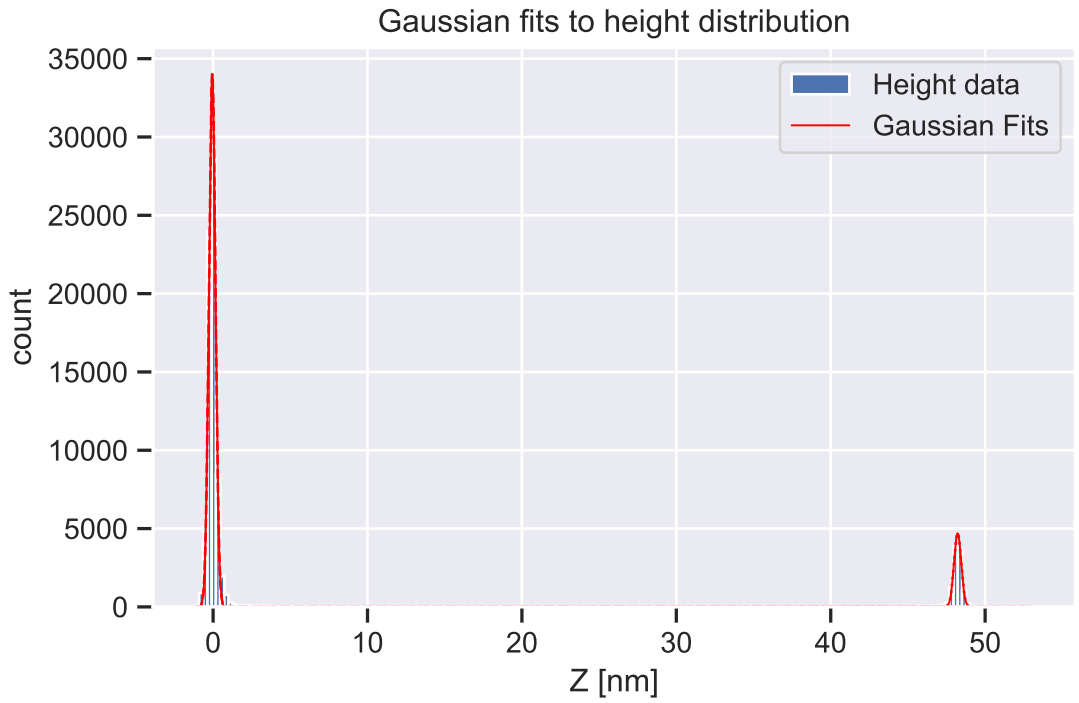


Figure 5.7: Height distribution of Figure 5.6b. By taking the difference of the two means in the height distribution, we can determine a pillar height of 48.27 ± 0.443 nm

Table 5.2: Silicon pillar Gaussian distribution fitting parameters

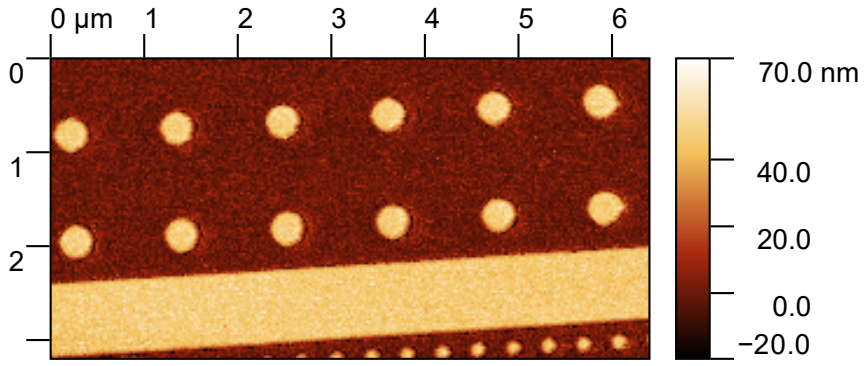
Distribution	A	Mean (μ) [nm]	Std dev (σ) [nm]
Base	34010	-0.056	0.212
Apex	4702	48.220	0.231

By analysis of Gaussian fit parameters in Table 5.2 and subtracting the mean (μ) values and adding the error terms, we obtained a pillar height measurement of 48.27 ± 0.443 nm.

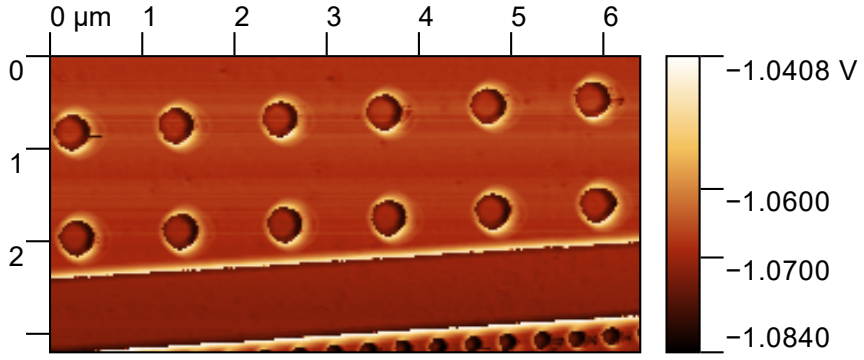
Ramp through contact

The sample was then inserted into the custom SThM setup. Using the devised ramp technique for topographical feedback control, a simultaneous topographic and thermal contact measurement was taken and displayed in Figure 5.8. Due to inaccuracies in the level loading of samples into the custom SThM, they have been

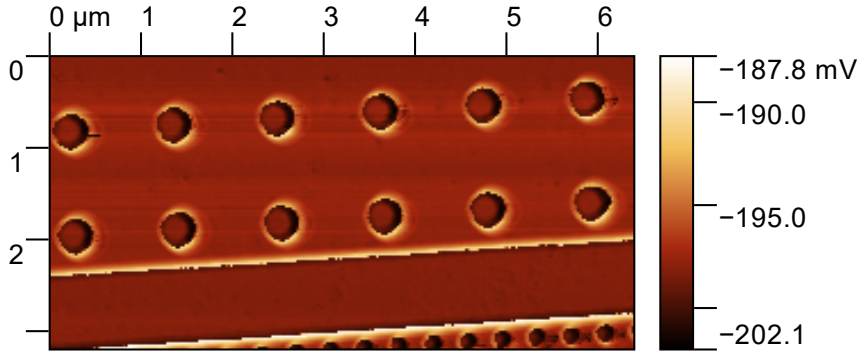
artificially levelled in Gwyddion using the flatten base and path levelling functionalities[2].



(a) Z topography channel



(b) 1ω thermometry channel



(c) 3ω thermometry channel

Figure 5.8: SThM scan using the ramp method of 300 nm diameter Si pillars using the ramp method.

Following the same procedure in Figure 5.7, Figure 5.9 and Table 5.3 shows a calculated pillar height of 45.7 ± 8.5nm.

[2] http://gwyddion.net/documentation/user-guide-en/leveling-and-background.html

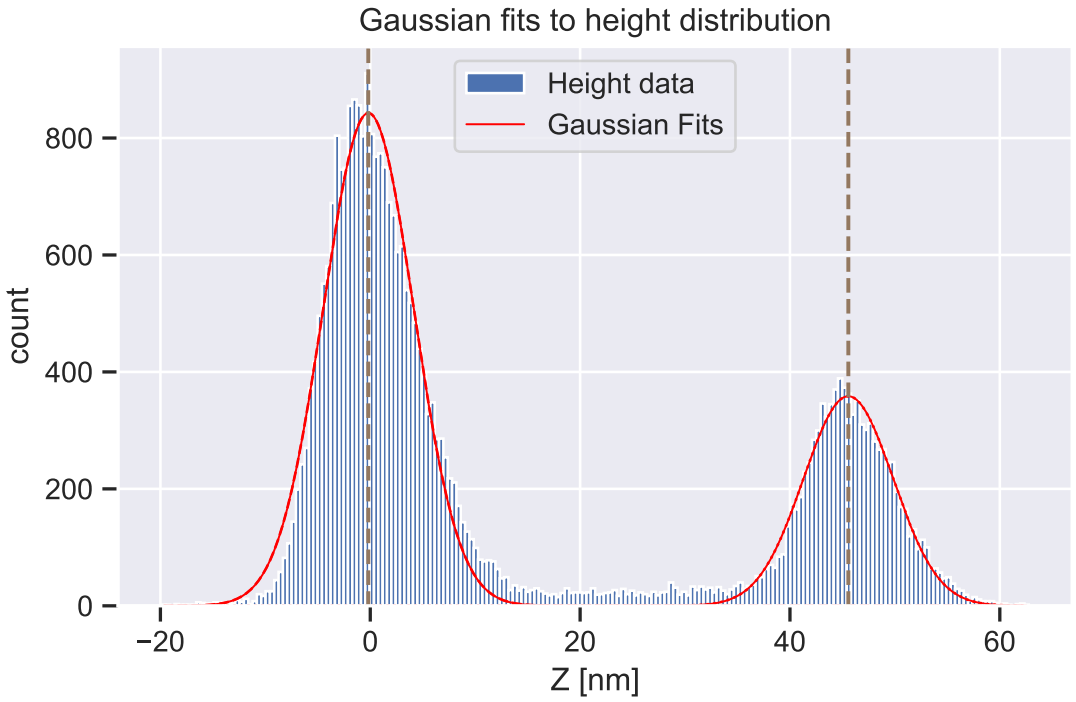


Figure 5.9: Height distribution of Figure 5.8a. By taking the difference of the two Gaussian fit means in the height distribution, we can determine a pillar height of 45.7 ± 8.5nm

Table 5.3: Silicon pillar Gaussian distribution fitting parameters for Figure 5.9

Distribution	A	Mean (μ) [nm]	Std dev (σ) [nm]
Base	814	-0.180	4.290
Apex	346	45.56	4.263

Measures of the standard deviation of the two peaks match closely to that obtained utilising this method in previous single point measurements in section 4.6.4. However, it can be seen that a Gaussian distribution does not fit the measured height data well. It should be noted that there is an intermediate distribution between the two peaks, values in this region can be assumed to come from the large physical probe tip radius of the KNT probe. Accounting for this transition period we can fit skewed Gaussian distributions to the data, which visually appear to fit the data better in Figure 5.10 with tabulated fit values in Table 5.4.

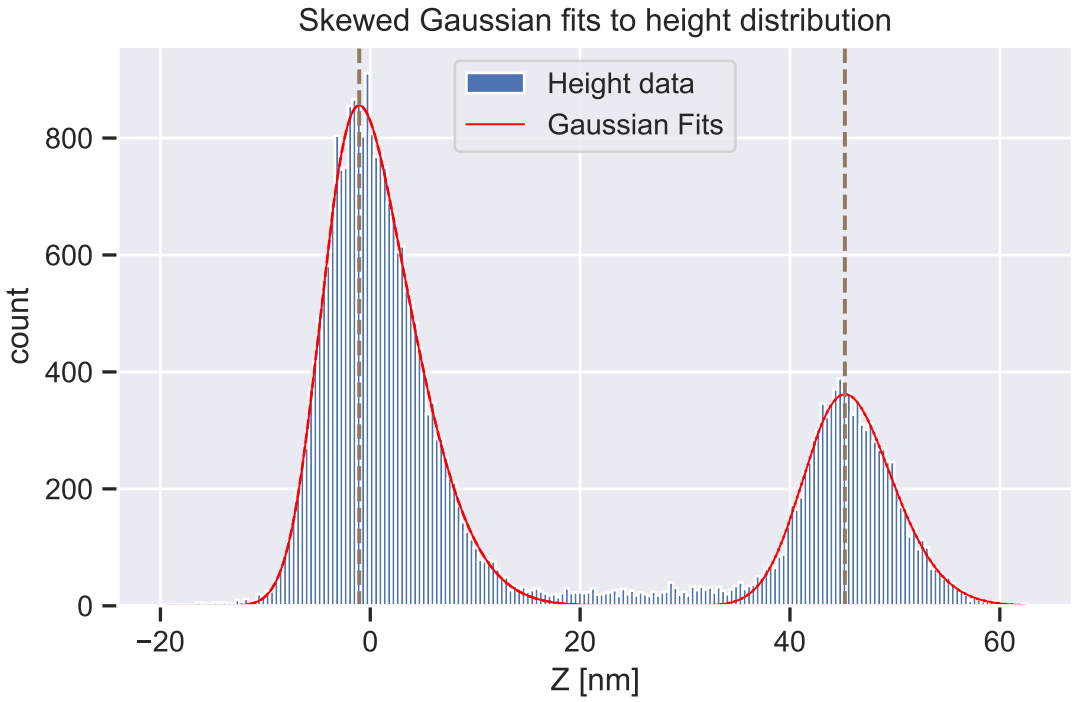


Figure 5.10: Height distribution of Figure 5.8a. By taking the difference of the two skewed Gaussian fit means in the height distribution, we can determine a pillar height of 46.6 ± 12.45nm

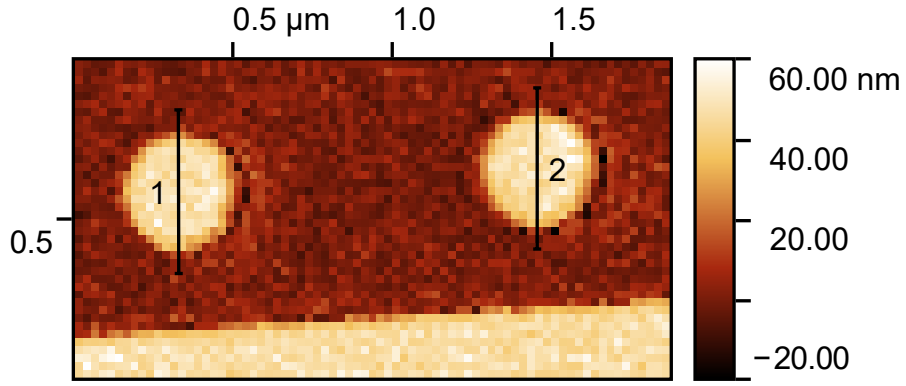
Table 5.4: Silicon pillar Gaussian distribution fitting parameters for Figure 5.10

Distribution	A	Mean (μ) [nm]	Std dev (σ) [nm]
Base	836	-4.461	6.77
Apex	349	42.17	5.68

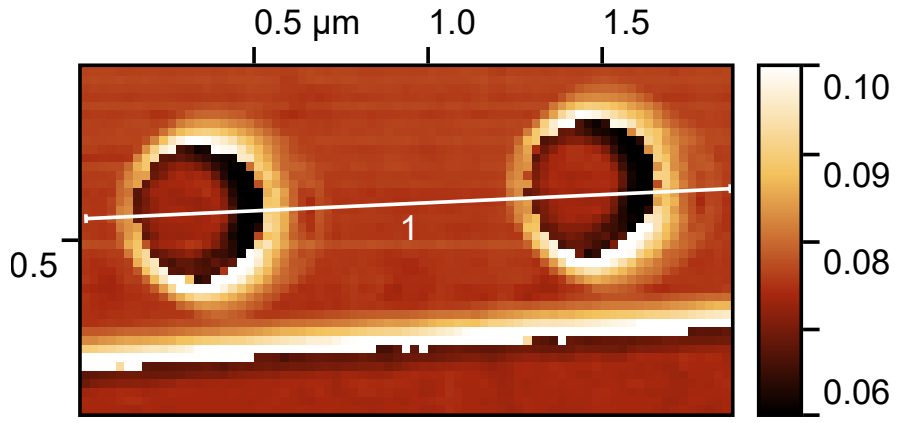
Although there is now a better fit to the data, and a measured mean value that is closer to that as measured on the commercial AFM, we still have quite a large random error due to the large standard deviations of the Gaussian distributions. A more meaningful way to measure the pillar height could come from radial topographic analysis of the pillars. This aims to angularly average a feature of a scan line centred on the pillar apex. To exclude this transition region from the measurement completely, we can fit terraces to radially averaged measurements of the pillars utalising Gwyddion's 'Fit terraces' functionality[3].

The height of the pillars can then be extracted from the scans, examples of two pillar measurements in Figure 5.11a have been shown in Figure 5.12 and 5.13. This measurement shows a smoothing of the what should be relatively vertical pillar

[3] https://gwyddion.net/documentation/user-guide-en/feature-measurement.html



(a) Little effect of edge artefacts present in the topography output. Perhaps a slight halo is visible to the right of the pillars



(b) Double contact (bright) and reduced contact (dark) artefacts are visible in the 3ω signal around the pillar. Contrast is plotted as a fractional change of probe response ($\Delta 3\omega/3\omega_{cal}$).

Figure 5.11: Digital zoom of middle pillars of Figure 5.8: (a) Topography and (b) 3ω channels

edges, over a lateral range of approximately 70 nm. This is a known topography artefact relating to probe tip shape [178], and aligns with many reports of KNT SThM probe apex dimensions presented in the literature [48, 54, 56, 147]. This most likely is the reason behind the skew of the distributions and the transition period between the peaks.

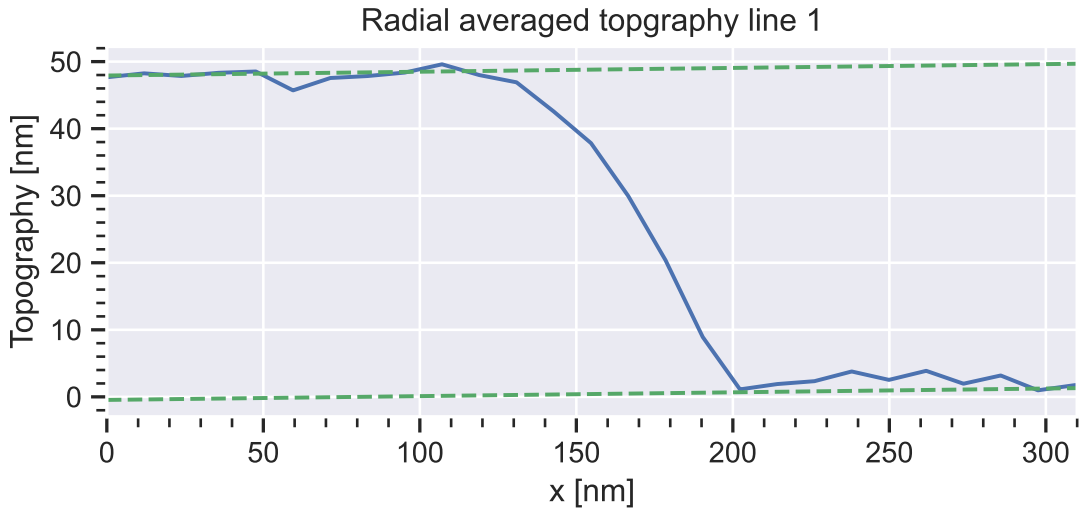


Figure 5.12: Radially averaged measurement of scan line 1 from Figure 5.11a. 0 nm on the X-axis indicates centre of the pillar. 300 nm diameter pillars appear slightly larger than designed. This is an artefact of pillar convolution with a relatively large tip apex of around 50-100 nm. Green dashed lines show fitted terraces showing a measurement of 48.38 ± 3.49nm

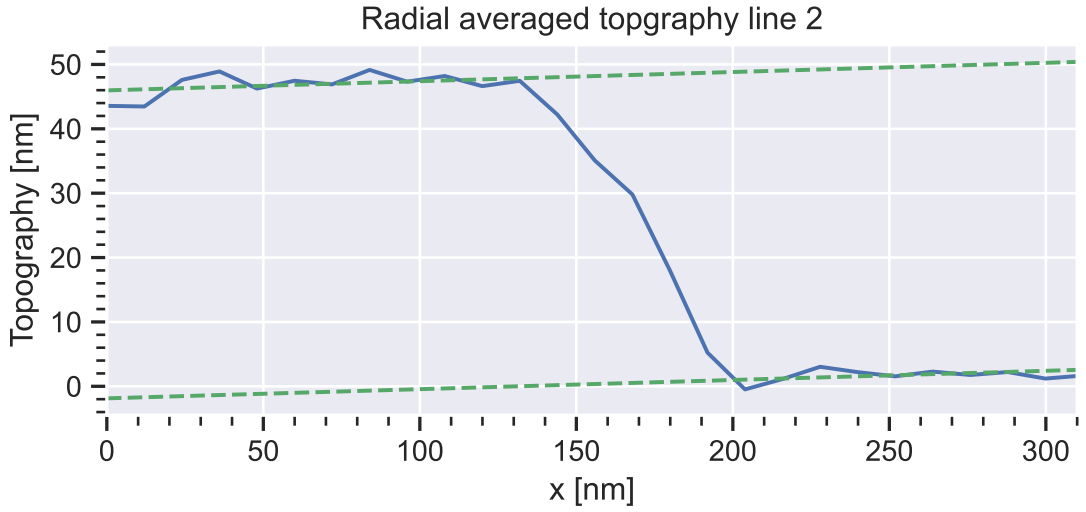


Figure 5.13: Radially averaged measurement of scan line 2 from Figure 5.11a. 0 nm on the X-axis indicates centre of the pillar. Again, the 300 nm diameter pillars appear slightly larger than designed. Green dashed lines show fitted terraces showing a measurement of 47.84 ± 1.54nm

This measurement of fitting terraces shows a similar pillar height to that acquired through the commercial AFM, and can be repeated for all 300 nm pillars in Figure 5.8a. Radial averaged lines of all the pillars, numbered from top left in a clockwise manner, are shown in Figure 5.14. Results from fitting terraces to each step can be found in Table 5.5, and shows a mean calculated pillar height of

Table 5.5: Tabulated results of radially averaged pillar heights

Pillar No	Height [nm]
1	47.39 ± 1.66
2	46.30 ± 2.56
3	46.10 ± 1.89
4	47.73 ± 1.02
5	46.67 ± 1.73
6	47.36 ± 2.47
7	47.93 ± 1.68
8	47.23 ± 1.44
9	46.66 ± 1.56
10	46.53 ± 2.34
11	46.80 ± 1.79
12	48.58 ± 2.31

47.10 ± 6.63nm.

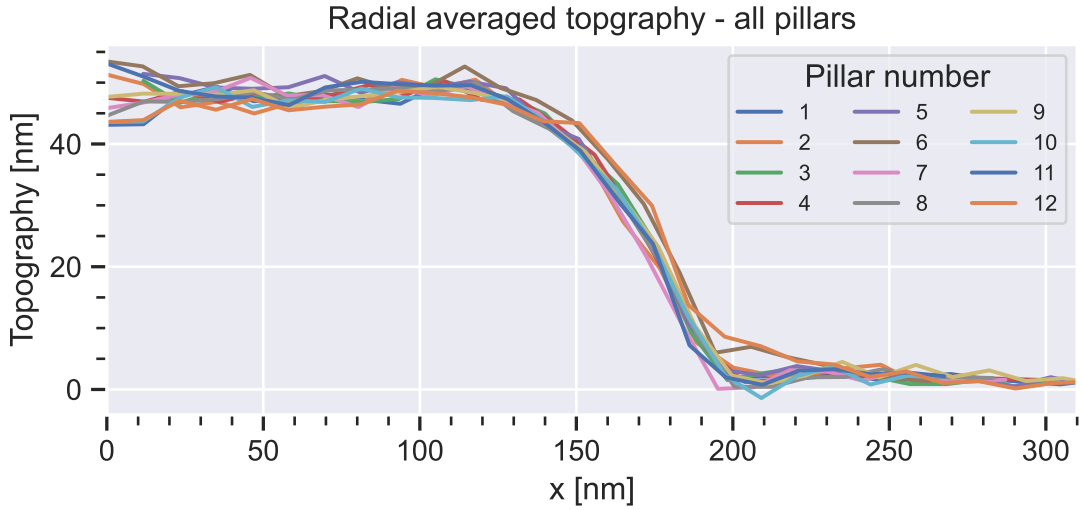


Figure 5.14: Radially averaged measurement of scan all pillars from Figure 5.11a, numbered from the top left pillar in a clockwise manner. 0 nm on the X-axis indicates centre of the pillar.

It can be seen that this methodology for the calculation of pillar height can be useful for the interpretation of topographic results obtained from the SThM. As we only utilise the apex and the base of the pillars, the effects of tip convolution are reduced. Comparatively to Gaussian fitting, the mean measured pillar height through step fitting matches closer, and with a lower error, to the measurements made by the commercial AFM

In terms of the probe thermal response, Figure 5.11b shows the slight asymmetry

in the contrast of the thermal edge artefacts that can be seen between the left and right sides of each pillar. As the probe was scanned left to right, with the tip of the probe pointing to the right-hand side as previously shown in Figure 5.1, this asymmetry is due to a slight increase in air conduction between the cantilever and the sample as the cantilever body overhangs the pillar as discussed previously in section 4.1.2.

An extracted line, labelled 1 in Figure 5.11b, has been graphed in Figure 5.15. The same line in the topography image has also been provided as a reference. This shows a clear correlation between double contact artefacts (green dashes) and increased probe response, as well as partial probe contact (red dashes) and decreases in the probe response. The effects of the probe overhang effect are clearly visible on the right hand section of each pillar

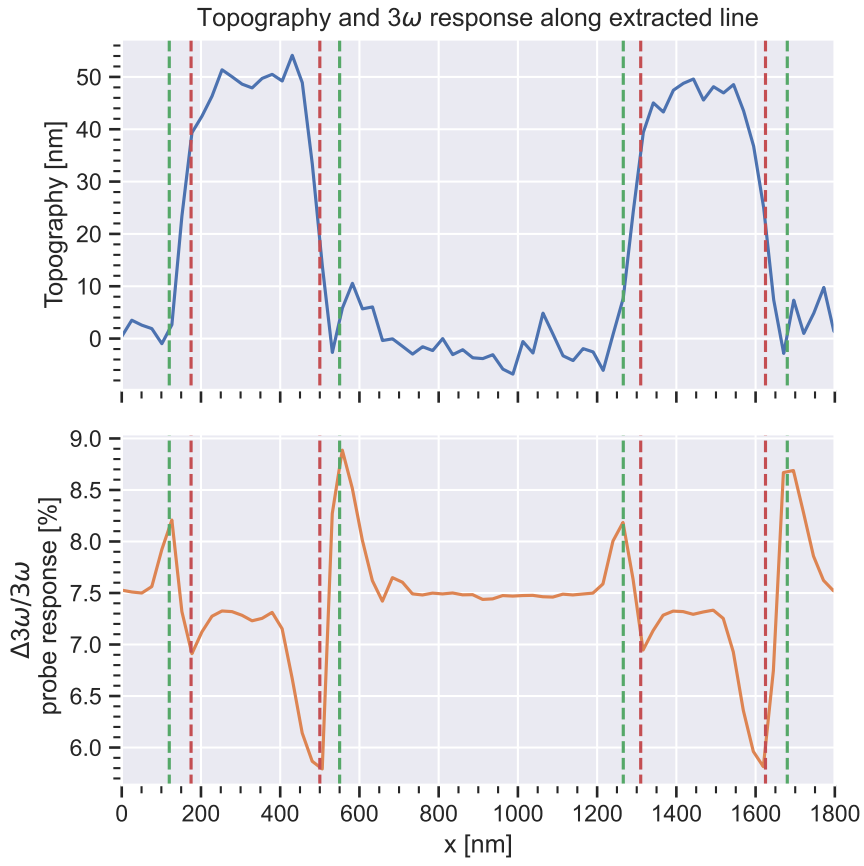


Figure 5.15: Line extracted from Figure 5.11b with the same line path extracted from the topography. Showing a clear correlation between thermal artefacts and sample topography. An increase in 3ω occurs at base of pillar where double contact occurs (green dashed lines). Decrease in 3ω occurs when only partial contact of the tip is made with the sample (red dashed lines)

A difference of 0.2% in the 3ω probe response signal changing from 7.53% to 7.3%

can be seen between the bottom and top of the pillars respectively. This difference is most likely due to the slight reduction in the amount of silicon interrogated by the probe at the pillar apex as depicted schematically in Figure 5.16. Referring to the thermal resistance model of the thermal impedance paths in Figure 5.17. Although R_c will remain somewhat constant between the centre of the apex tip and base, probe-sample coupling through R_{air} can change due to the slight changes in probe bulk sample separation.

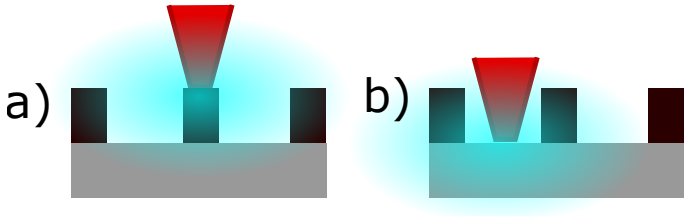


Figure 5.16: Change in thermal interactions from measuring the silicon pillar apexes and base. The SThM tip (Red) interaction area (blue) has less coupling to the base silicon (grey) and surrounding pillars (black) when measuring at the apex of the pillar (a) compared to the base of the pillars (b)

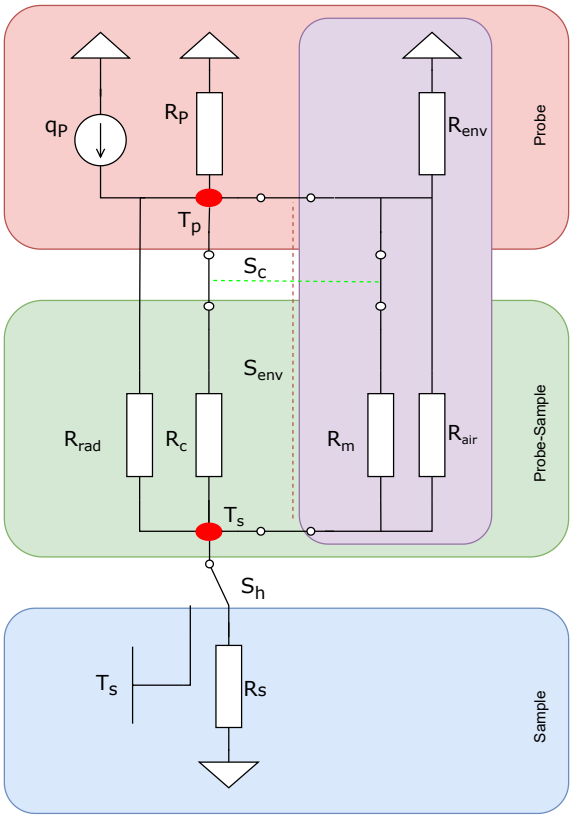


Figure 5.17: Thermal resistance network during contact measurements in air.

Another hypothesis for the change in thermal measurement of the pillar apex and

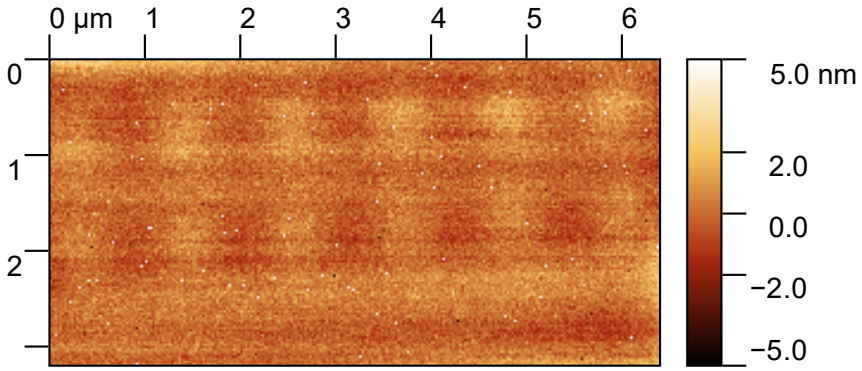
underlying silicon base is the potential inconsistency of water meniscus formation in either location. Wicking of hydration and contamination layers to the probe could be less at the pillar apex due to there being less volume of the layer in the immediate surroundings of the contact area, showing a lesser probe response. This can be seen as a variation in R_m between locations in the thermal resistance model in Figure 5.17

Most likely, this change in the measured value of the tip apex has contributions from both effects, as both thermal transfer paths can contribute significantly to the measured 3ω value.

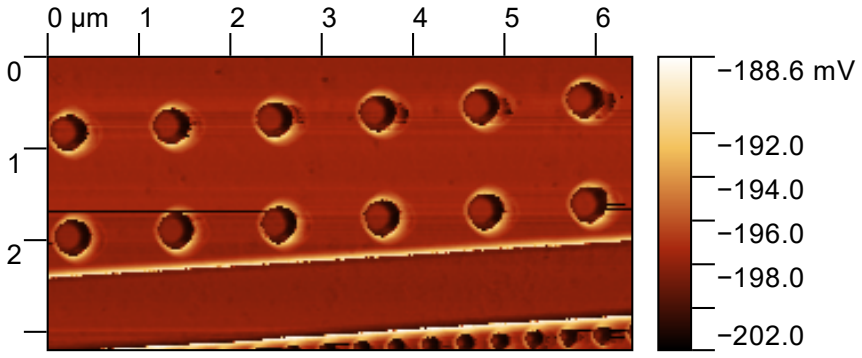
STP

Measurement of the same area using the STP method shows very little in terms of topography output (Figure 5.18a). Only slight changes in the topography output on the order of 5-10 nm can be seen between the pillar apex and base. This aligns with initial STP studies by Williams and Wickramasinghe [68] who had shown that when scanning features that are comparable in size to the tip, a reduction of measured topography variation is to be expected. The assumption of the STP is that the initial calibration land and retract is on a flat plane with no surrounding topography. However, in our case, the minimum X and Y piezo extensions for the scan (top left-hand corner of image) is where the calibration is taken, topographical influences will effect the calibrated 3ω Vm^{-1} conversion. This effect has been shown previously for in-contact measurements in Figure 5.16 and the same effects apply when only considering the out-of-contact measurement (before contact has been made). Due to the small volume of each silicon pillar in comparison to the bulk silicon, contributions of the pillar conductivity (pillar's R_s in the thermal resistance network - Figure 5.17) in the out of contact measurement will be minimal.

If we increase the distance the probe travels past the measured surface location to take a thermometry measurement to 50 nm (approximately 10-20 nN force), contact of the probe and sample can still be achieved as in Figure 5.18b, but we have significantly changed the error in applied force for the measurement. It should be noted that the resultant 3ω surface measurement in Figure 5.18b remains essentially unchanged when comparing it to the ramp method in Figure 5.8c. This shows that for unheated samples this method still provides a fast method for acquiring surface measurements and the 0.2% change in 3ω signal can still be seen from the apex of the pillar to the base.



(a) Z topography channel - calculated from out-of-contact thermal distance measurement

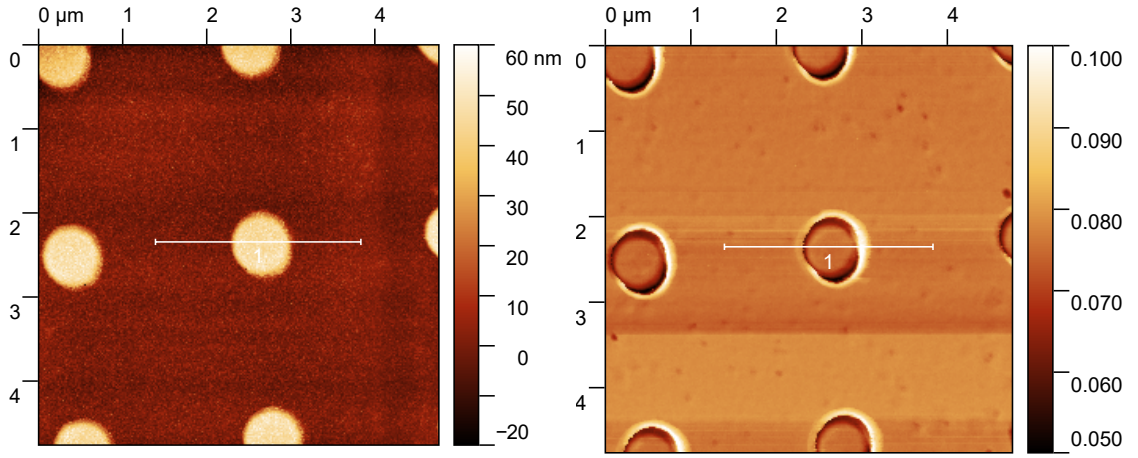


(b) 3ω thermometry channel - Probe is moved into contact to make surface measurement

Figure 5.18: SThM scan using the STP method of 300 nm diameter Si pillars using the STP method. Average pixel capture rate: 2.65 Hz

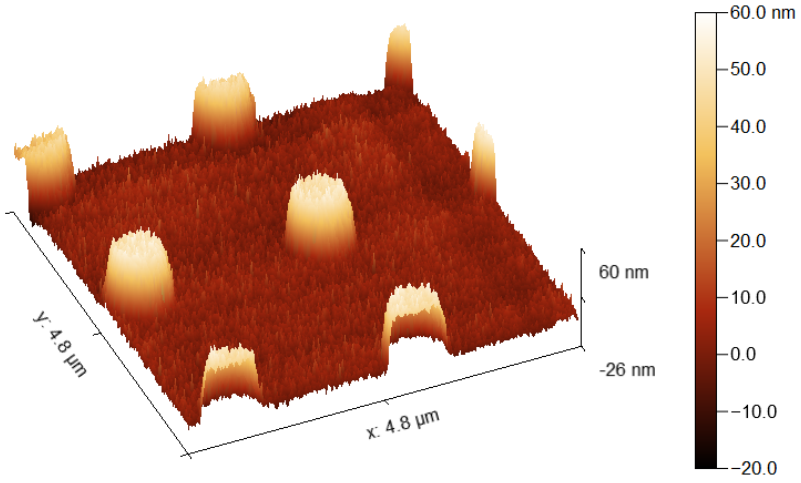
Thermal discontinuity

Similarly, the thermal discontinuity method was used to interrogate the 600 nm pillars and can be seen in Figure 5.19. Similar topographic analysis to the 300 nm pillars was undertaken of the pillar labelled 1 in Figure 5.19a, showing a radial profile with a transition period on the order of the probe tip radius in Figure 5.20 and a fitted height step height of 48.31 ± 0.49 nm. However, when comparing the change in probe response of the 600 nm pillars, we note that there is no significant change in the response from the base to the apex of the pillars as we had observed previously for the 300 nm pillars, remaining at a constant 7.5% with the exception of the known thermal artefacts. This is possibly due to the larger distances between the pillars, showing decreased interaction with neighbouring pillars, or more consistent formation of water meniscus between scanning the pillar apex and bases.



(a) Z topography channel

(b) $\Delta 3\omega/3\omega_{cal}$ thermometry channel



(c) 3D rendering of Z topography channel

Figure 5.19: SThM scan using the thermal discontinuity method of 600 nm diameter Si pillars.

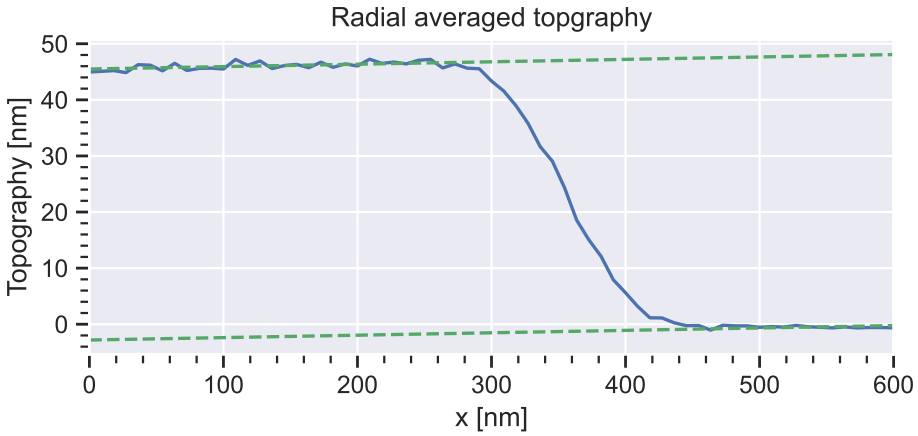


Figure 5.20: Radially averaged measurement of scan lines 1 from Figure 5.19a. 0 nm on the X-axis indicates the centre of the pillar. 600 nm diameter pillars appear slightly larger than designed. Showing tip convolution of around 100 nm. Green dashed line shows fitted terraces measuring 48.31 ± 0.49 nm.

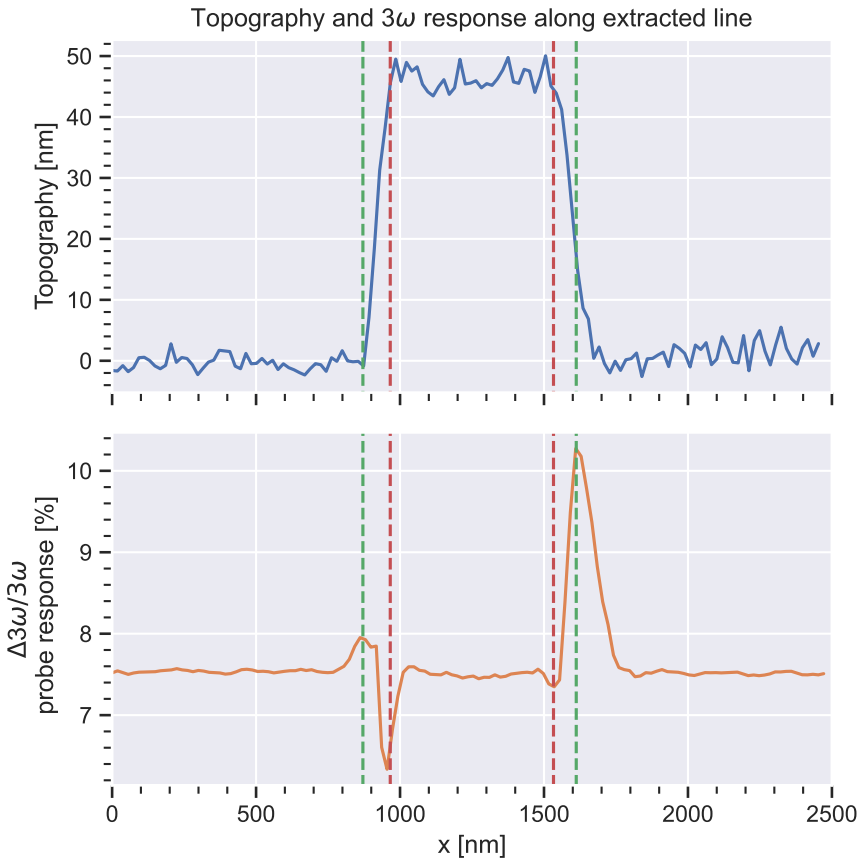


Figure 5.21: Line extracted from Figure 5.19 with the same line path extracted from the topography. Showing a clear correlation between thermal artefacts and sample topography edges.

5.4 Step edge

To analyse the effect of material and topographic changes, a step-edge sample was micro-fabricated. It consists of an 80 nm thick lithographic step from SiNx to evaporated NiCr/Au (10 nm/70 nm). When depositing materials in the metal evaporator, an overshoot of around 10% is expected. As such, the sample was first measured by stylus profilometry on a Bruker DektakXT as seen in Figure 5.22. To obtain a step height across the sample, DektakXT scans were repeated across the sample at multiple random locations to obtain a mean step height and associated error in the step height. A histogram of the measured step heights from 68 measurements can be seen in Figure 5.23, measuring a mean step height of 90.8 ± 1.87 nm.

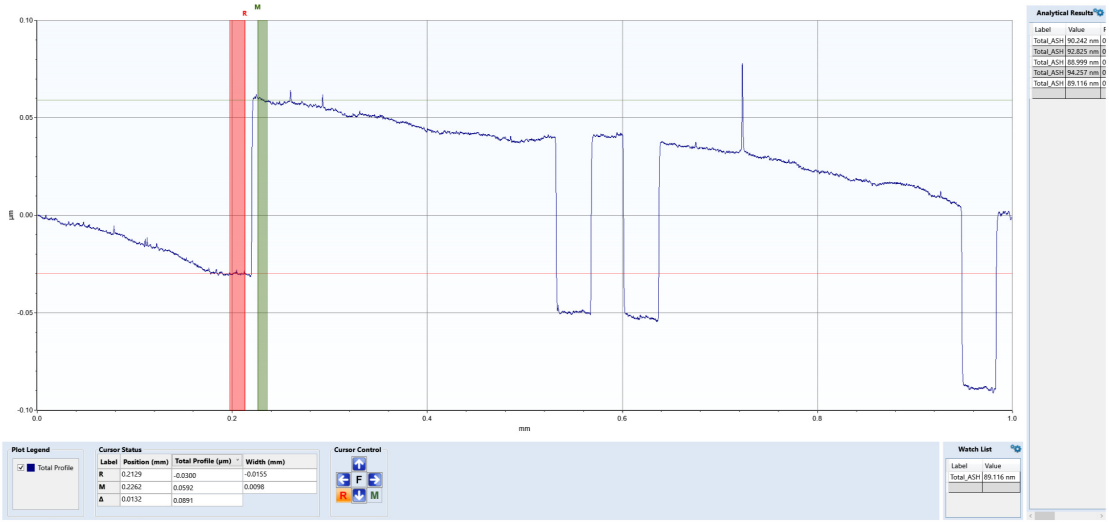


Figure 5.22: Example of DektakXT step height measurement. The difference in the green and red shaded area is taken as a height measurement

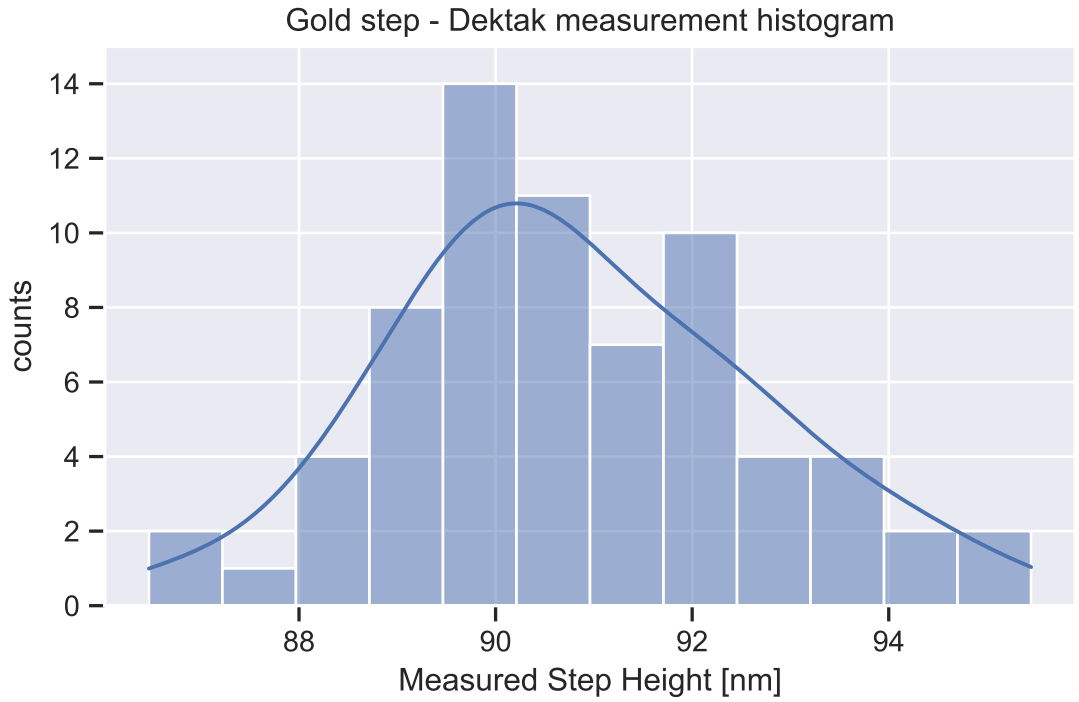
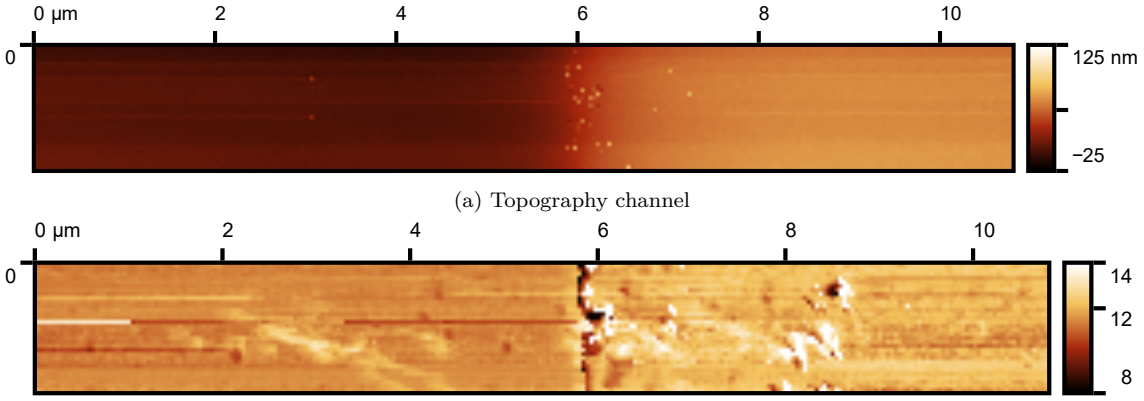


Figure 5.23: Histogram of repeated step height measurements across the sample. A mean step height of 90.8 nm and a standard deviation in the measurement of 1.87 nm.

In SThM scans presented in this section, scale bars have been kept constant between scans where appropriate. This allows for better visual comparisons of the spatial differences of the methods presented.

The scan obtained by employing the STP method with (plane fitting) data levelling on the left-hand (lower) plane can be seen in Figure 5.24. Good mean profile of the topography and probe 3ω response can be seen in Figure 5.25 and Figure 5.26 respectively. The height measurement histogram is also shown in Figure 5.27.



(a) Topography channel

(b) $\Delta 3\omega/3\omega_{cal}$ channel showing probe response as a percentage change from calibration.

Figure 5.24: SThM scan using the STP method of stepping from SiNx (LHS) to 80 nm NiCr/Au (RHS).

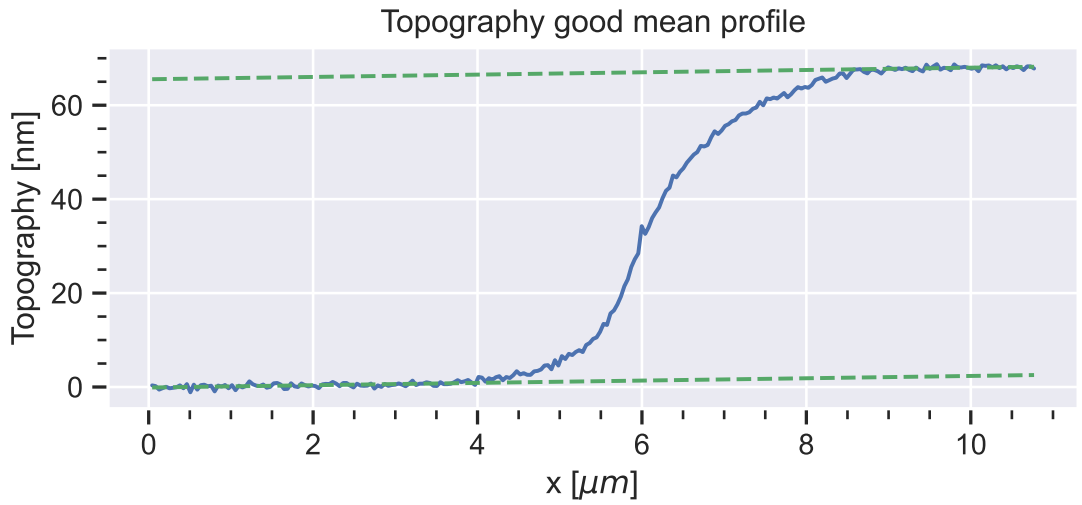


Figure 5.25: Good mean profile of Figure 5.24a. Showing significant smoothing of the step edge over the scan, green dashed lines are fitted terraces, measuring 65.64 ± 0.75nm.

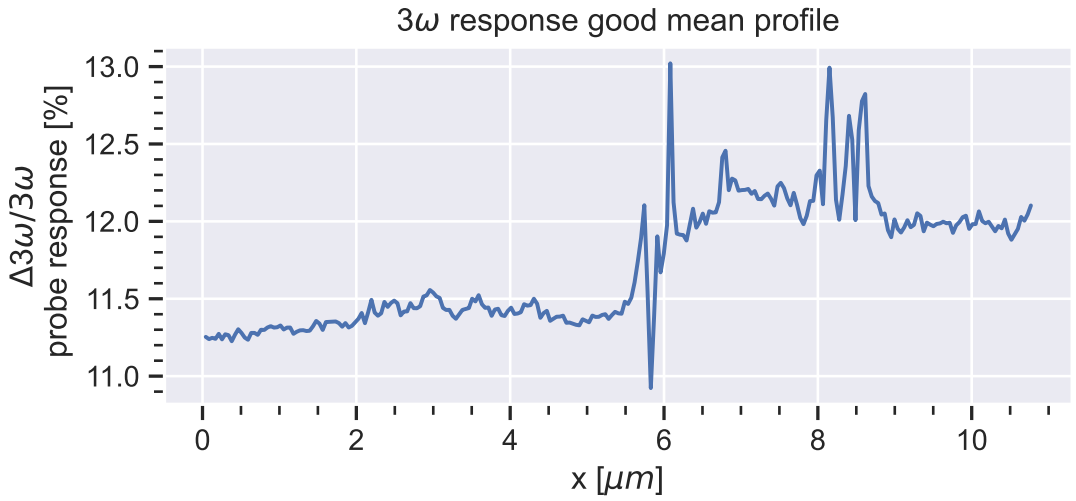


Figure 5.26: Good mean profile of Figure 5.24b. A change in probe response from approximately 11.4% to 12% can be seen when stepping to the step edge.

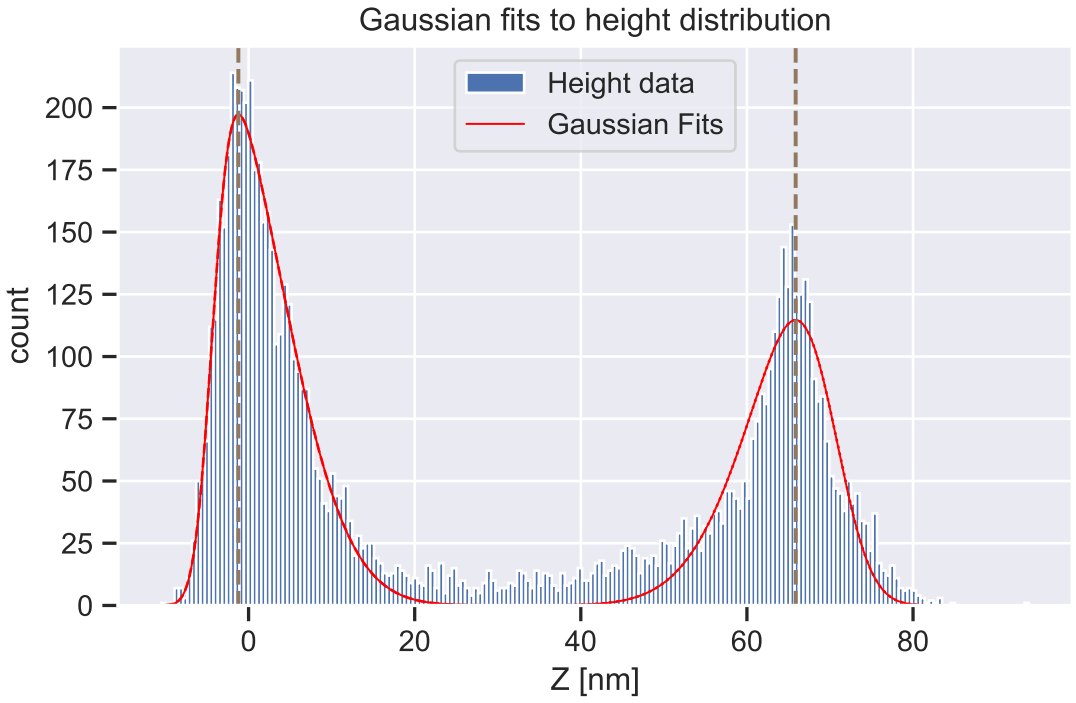


Figure 5.27: Histogram of Topography channel of step edge in Figure 5.24a. A measured step height of 67.1nm can be calculated by the difference of the two modes.

We can see significant smoothing of the step edge in Figure 5.24a and Figure 5.25. This is to be expected due to the increased conduction in the out-of-contact measurement with the edge distorting the approach curve. However, the measurement

of the height at 67 nm is significantly different in Figure 5.27 compared to other measurements of the step height. Gwyddion's fitted step height can be seen as green dashed lines in Figure 5.25 and measured to be 65.64 ± 0.75 nm, showing that there is a large systematic error in the measurement.

One might expect that the differences in material may be the cause for the lower measure of step height when utilising the STP method to measure topography in this sample. Gold has a higher thermal conductivity than silicon nitride [179, 180]. If the influence of material conductivity is the driver for the step height discrepancy, referring in terms of the thermal resistance network, a reduction in impedance of R_s would imply a larger R_{air} is required to maintain the control loop out of contact '3ω distance' set point. In other words, one would assume the probe must be positioned further away from the true surface when located above the gold compared to when above the silicon nitride. This would make for a larger than mechanical step height measurement, which is the opposite of what is observed.

Literature studies show that out-of-contact measurement will be practically material independent due to the large differences in thermal properties of ambient air and any solid [67, 68]. This can be confirmed by overlaying 3ω landing curves on the same sample of the two materials, one on the silicon nitride, and one on gold, as shown in Figure 5.28.

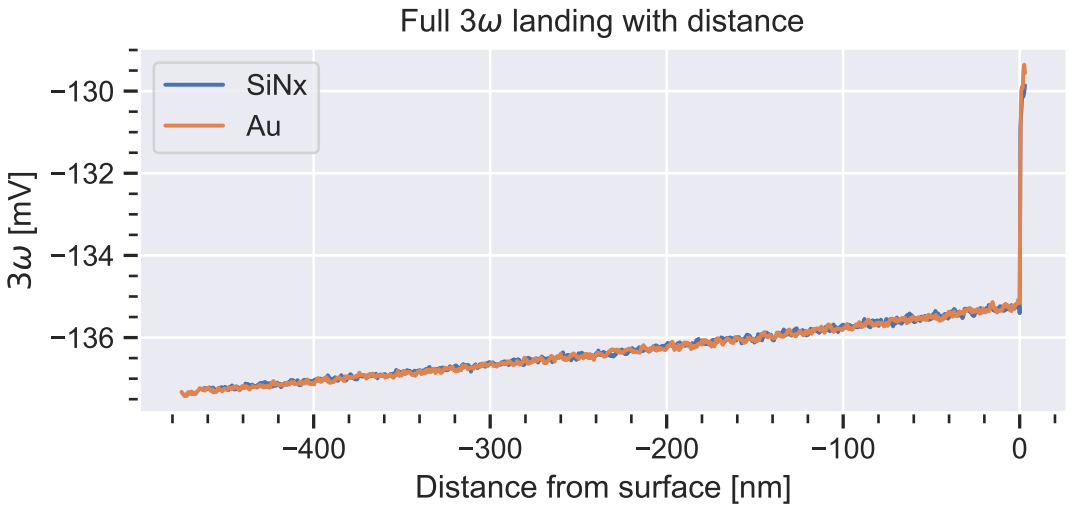


Figure 5.28: Comparison of landing curves on Au and SiNx. Data aligned in X by pull-in point where 0 in X is representative of the calculated pull-in point.

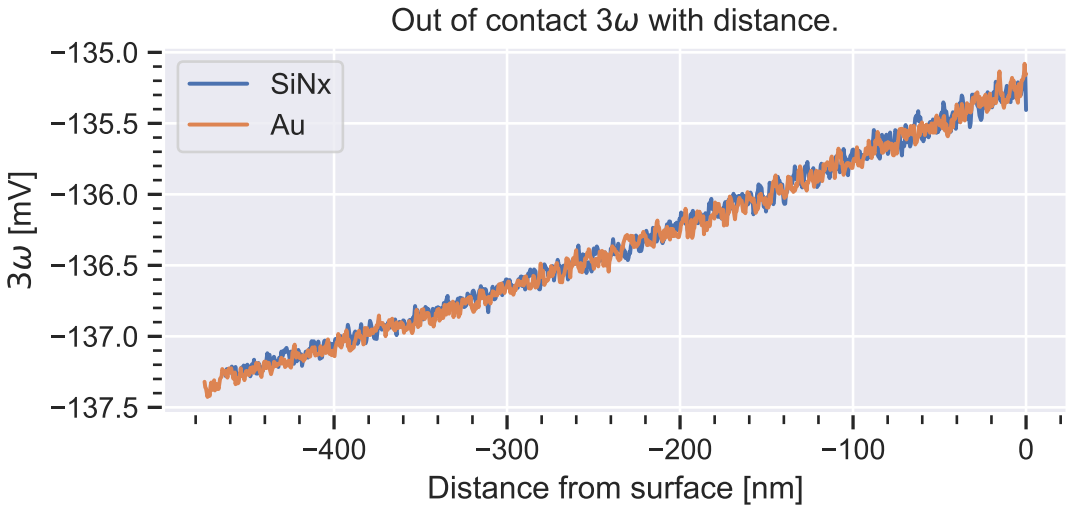


Figure 5.29: Comparison of out of contact portion of landing curve in Figure 5.28. Data aligned in X by detected surface point where 0 in X is representative of the calculated pull-in point.

Analysis of Figure 5.28 and in particular Figure 5.29, shows that there is no observed difference in the out of contact 3ω approach for landing on both materials. Material differences cannot be the cause of this discrepancy.

What is most likely the cause of the step height measurement discrepancy is the relatively high fly height of the probe (>80 nm required to avoid accidental collision with step edge). In the original STP studies by Williams and Wickramasinghe [67] resolution was found to be proportional to the tip fly height, with a best depth resolution of just below 10 nm for the lowest fly heights. It is also quite possible the control loop had a poor calibration in this scan.

Despite this difference in step height measurement, we can see from Figure 5.24 and Figure 5.26 that we still see a moderate 3ω probe response from the step of around 0.6%.

From previous experimentation in section 4.6.1, increasing the DDSN from zero to four in the control loop had shown a reduction in the standard deviation of the calculated surface location, due to improved signal noise averaging, at the expense of scan times. Topographic output, good mean profile, and histogram plot of the edge measured with a DDSN of 4, can be seen in Figure 5.30, 5.31 and 5.32

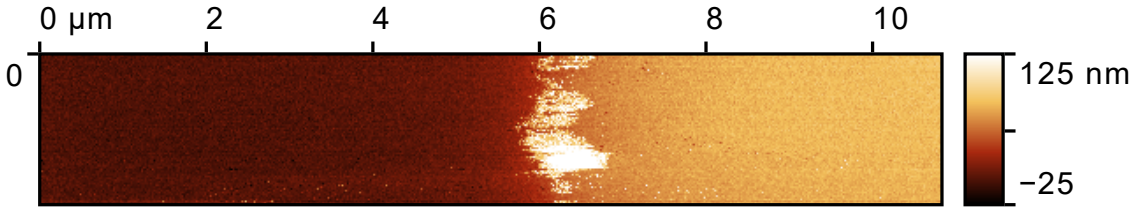


Figure 5.30: Topography output of scan from the STP method with a DDSN of 4 utilised in the control loop for probe fly height control

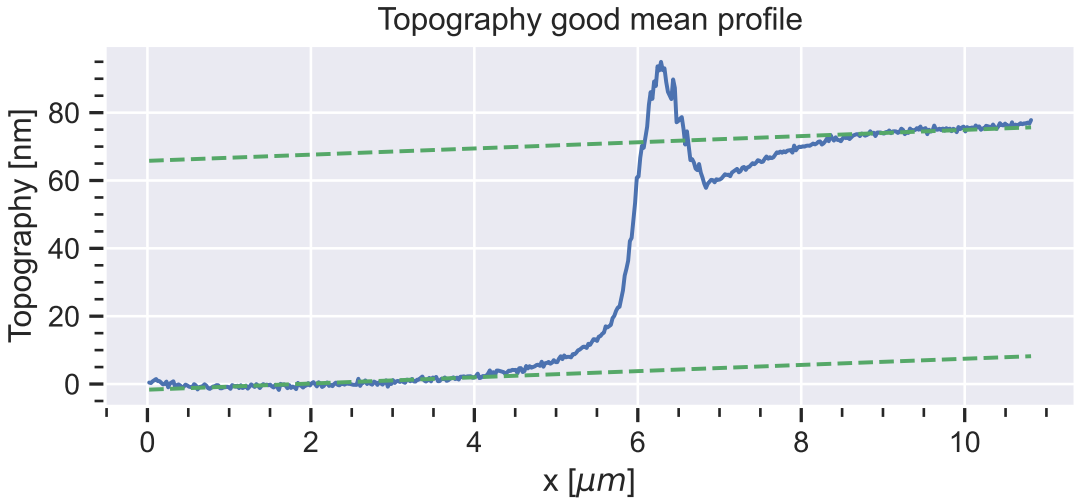


Figure 5.31: Good mean profile of step edge in Figure 5.30, fitted step height shown in green dashed lines, measuring 67.46 ± 0.38 nm

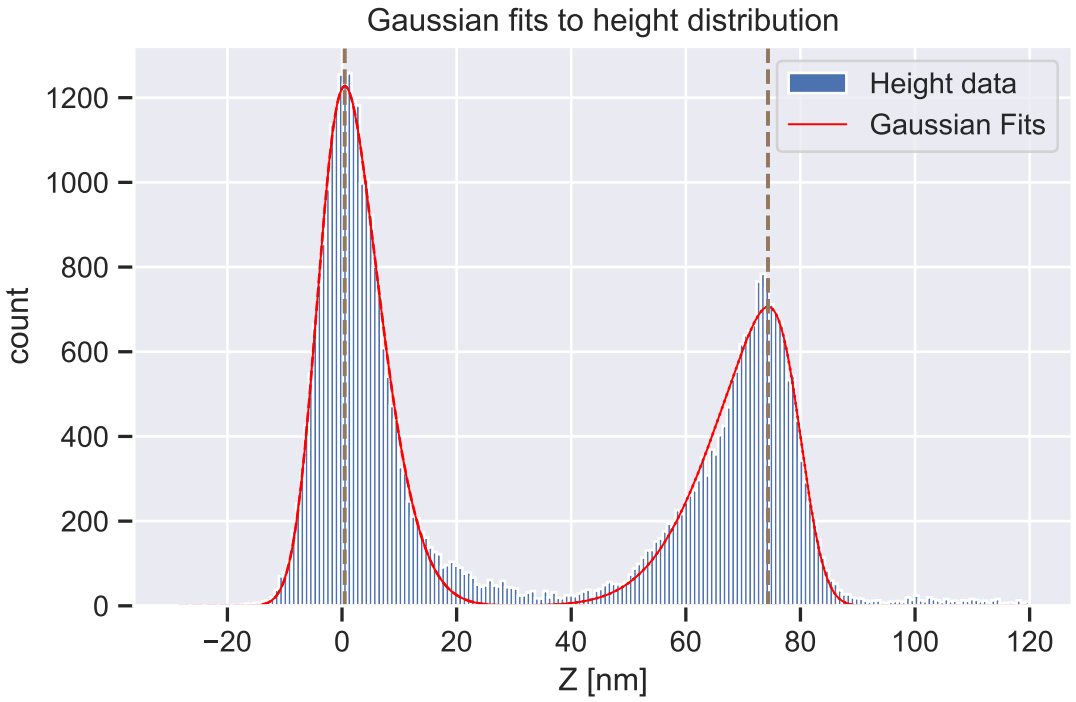
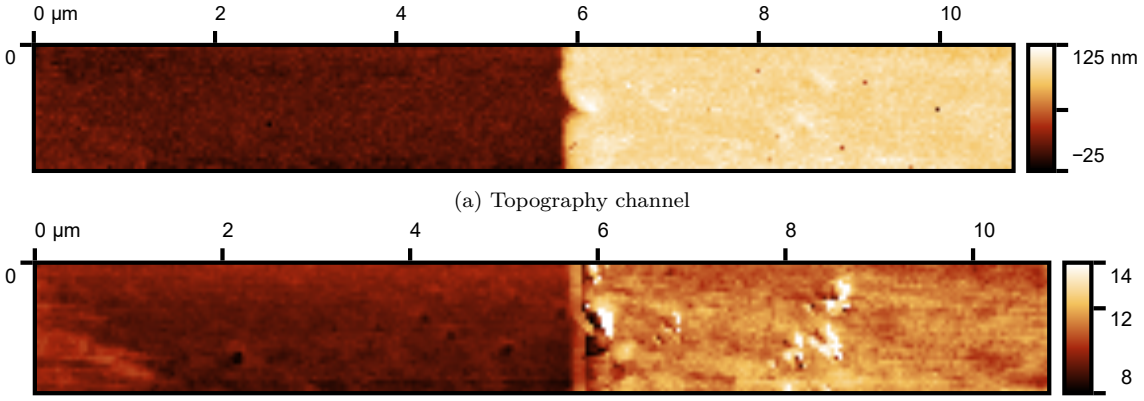


Figure 5.32: Histogram measurement of step edge in Figure 5.30 showing a measurement of 73.8 nm

It can be seen from Figure 5.30 that there are bad pixels in the topography output around the step edge. This is most likely due to contact of the probe with the edge during the controlling of the probe fly height. Similar behaviour was seen by Williams and Wickramasinghe [67] during the original STP studies. We can also note that both calculated step heights through Gwyddion's step height fitting functionality and histogram measurement show slightly higher measurements at 67 nm and 73 nm respectively for a DDSN of 4, compared to the 65 nm and 67 nm measured utilising a DDSN of 0. This points to noise in the measurement possibly being an significant contributing factor in the fly height calcualtions.

Using a more reliable method of topographic measurement, such as the thermal discontinuity method, a scan stepping over the same area of the edge was obtained again and can be seen in Figure 5.33, with good mean profile and topography histogram available in Figure 5.34 and 5.35 respectively.



(a) Topography channel

(b) $\Delta 3\omega/3\omega_{cal}$ channel showing probe response as a percentage change from calibration.

Figure 5.33: SThM scan using the thermal contact limit method of stepping from SiNx (LHS) to 80 nm NiCr/Au (RHS).

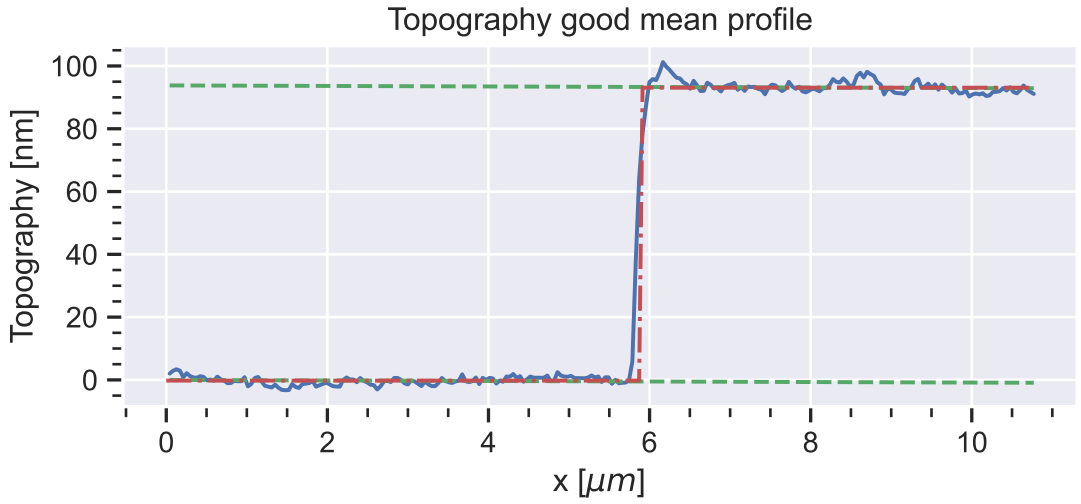


Figure 5.34: Good mean profile of step edge in Figure 5.33a. Showing a measured height of 93.82 ± 0.54 nm through terrace fitting (green dashed line). As we have a sharp edge in the mean profile, we can utilise Gwyddion's Edge height functionality to measure a step edge of 93.31 ± 2.2 nm (red dashed.)

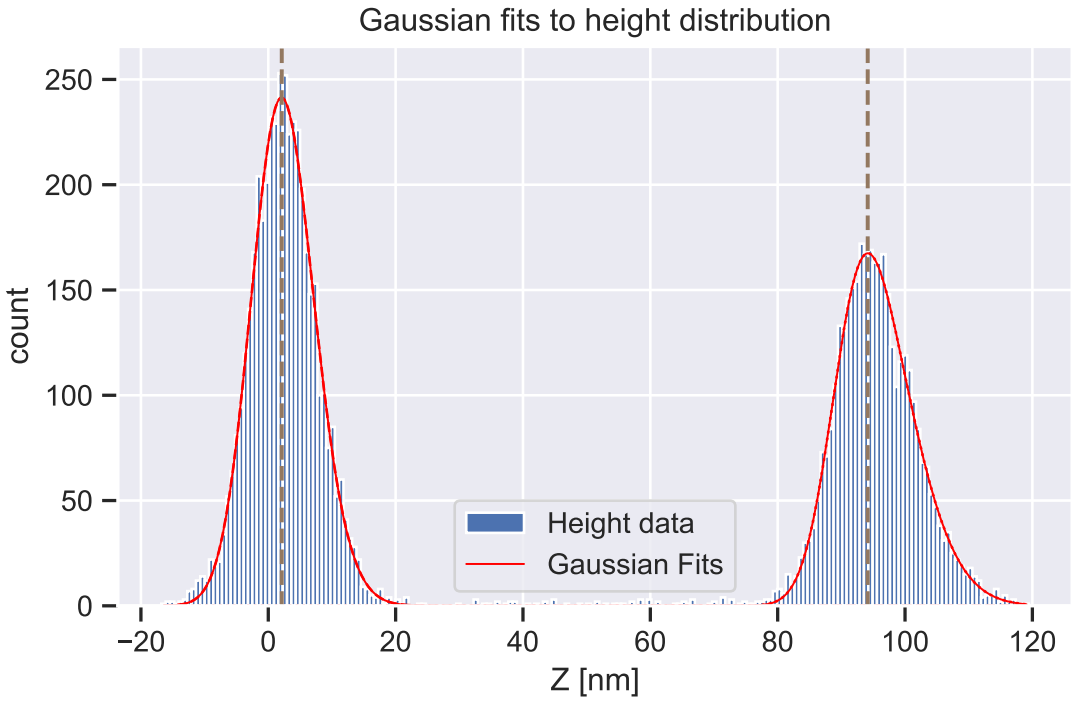


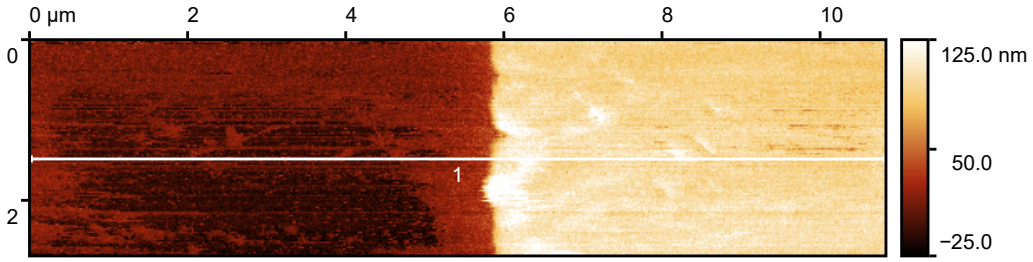
Figure 5.35: Histogram of Topography channel of step edge in Figure 5.33a. A measured step height of 92.02 nm can be calculated by difference of the two modes.

As we have a sharp transition on the step edge, we can utilise Gwyddion's edge height measurement functionality, shown as a red dashed line in Figure 5.34 which measures to be 93.31 ± 2.2 nm. This agrees with the measure through terrace fitting (green dashed line) of 93.82 ± 0.54 nm. The step edge height can be measured to be 92 nm from Figure 5.35. These measures are significantly higher than those measured by the STP method and closely match measurements of the step height on the Bruker DektakXT. One should also note the vastly reduced transition region between the two peaks in this scan compared to the silicon pillar scan in section 5.3. As we only have a few pixels at the edge of a topographic feature in the step-edge sample compared to the silicon pillar sample, this further suggests that the transition region seen in the silicon pillar sample was in fact due to tip convolution.

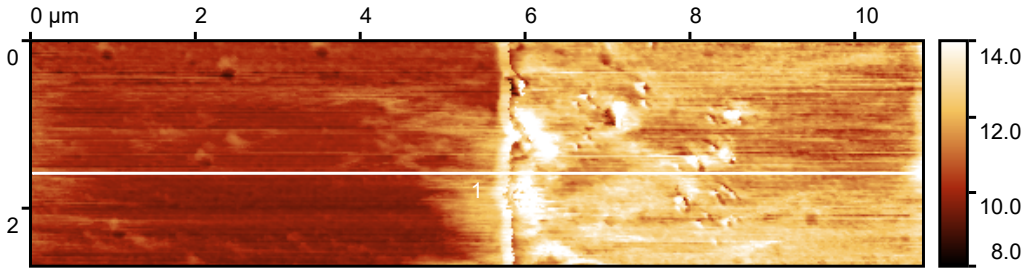
Better contrast in the 3ω probe response scan can also be seen in Figure 5.33b, with an approximate probe response change of 1.3%. As discussed previously in section 4.4, there can be a drift in probe response once contact has been made due to hydration and contamination layers forming nano-bridges between the probe and and sample.

Therefore, the measurement was repeated, while continuously flooding the meas-

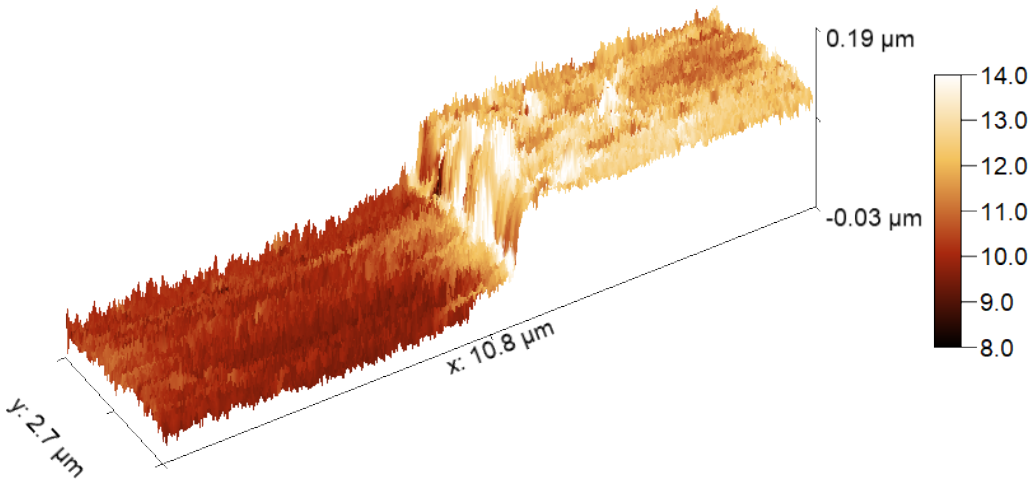
urement setup with dry nitrogen to reduce the effects of meniscus formation on the sample. In terms of the thermal resistance model, by measuring in dry nitrogen atmosphere the impedance of R_m will increase, decreasing it as a thermal transfer path and hopefully reducing the variability of the measurement. The scan obtained can be seen in Figure 5.36 with an extracted line plotted in Figure 5.37, where improved contrast in the probe 3ω probe response can be observed.



(a) Topography channel



(b) $\Delta 3\omega/3\omega_{cal}$ channel showing probe response as a percentage change from calibration.



(c) $\Delta 3\omega/3\omega_{cal}$ overlaid on topography output, showing alignment of response with with topographic features

Figure 5.36: SThM scan using the thermal contact limit method of stepping from SiNx (LHS) to 88 nm NiCr/Au (RHS).

As expected, a clear double contact thermal artefact is visible along the step edge as seen in Figure 5.37. As heat transfer occurs primarily through point contact when scanning in air, there are also additional double-contact thermal artefacts visible on

the gold surface.

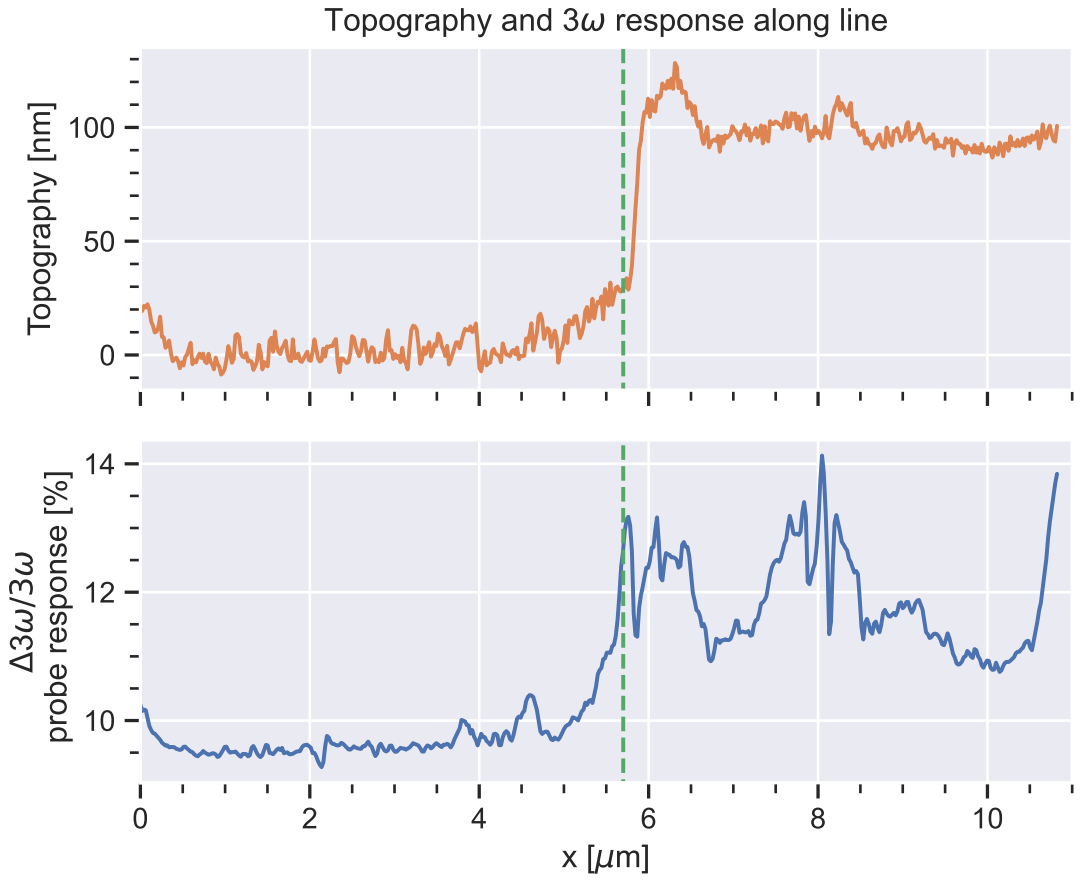


Figure 5.37: Line extracted from Figure 5.36. Double contact artefact with the step edge has been marked by the green dashed line. A large variation in the probe response can be seen on the gold surface.

As with previous measurements, the noise seen in the measurement of step height can be reduced by conducting a good mean topography profile of the topography channel (Figure 5.36a) before terrace fitting in Figure 5.38. A good mean profile of the probe response of Figure 5.36b has also been carried out in Figure 5.39.

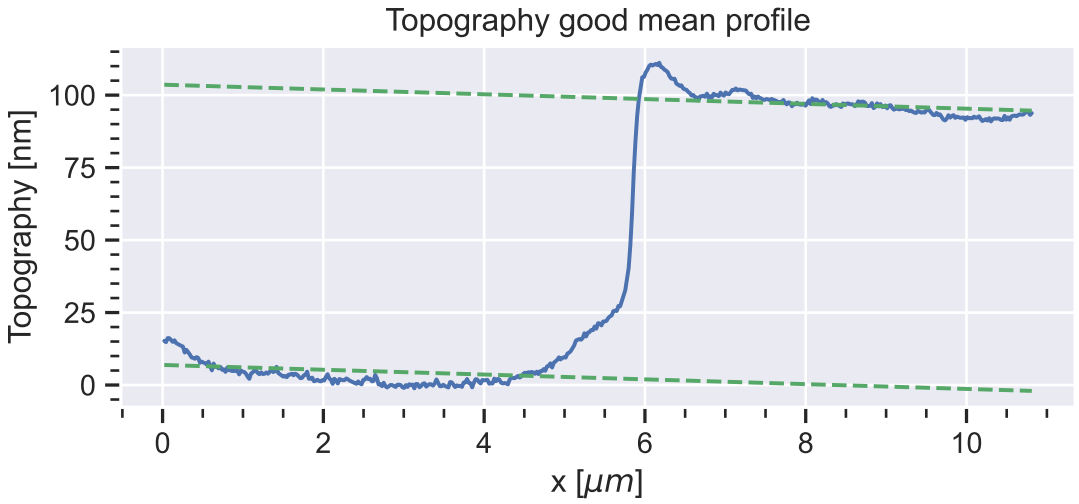


Figure 5.38: Good mean topography profile of step edge in Figure 5.36a, fitted step height shown in green dashed lines, measuring 101.0 ± 0.8 nm

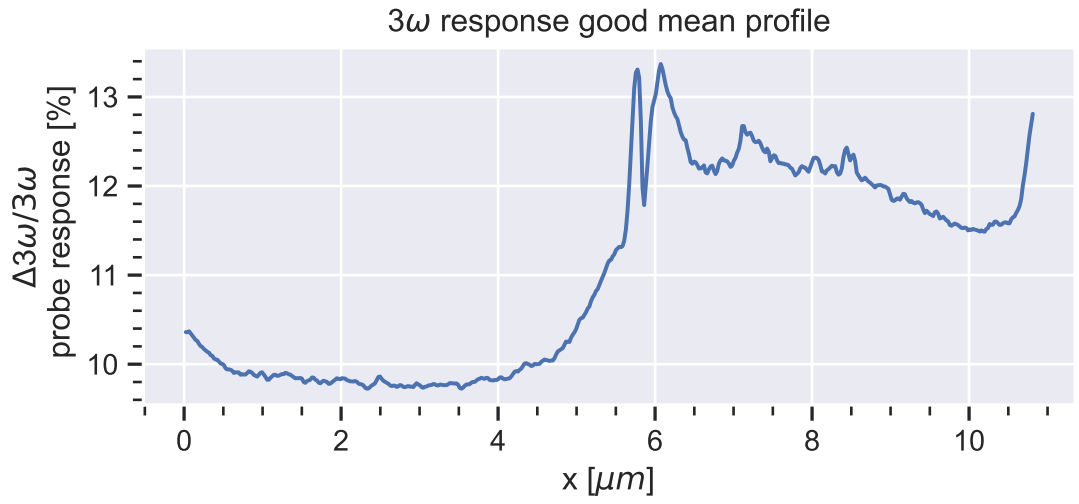


Figure 5.39: Good mean 3ω probe response profile of step edge in Figure 5.36b.

These large spikes in the probe response from double contact artefacts on the gold surface are most likely due to surface roughness from of the evaporated metal either through contamination present under the film or granularity of the film. An example SEM image of the granular nature of gold as well as contamination under the film is presented in Figure 5.40

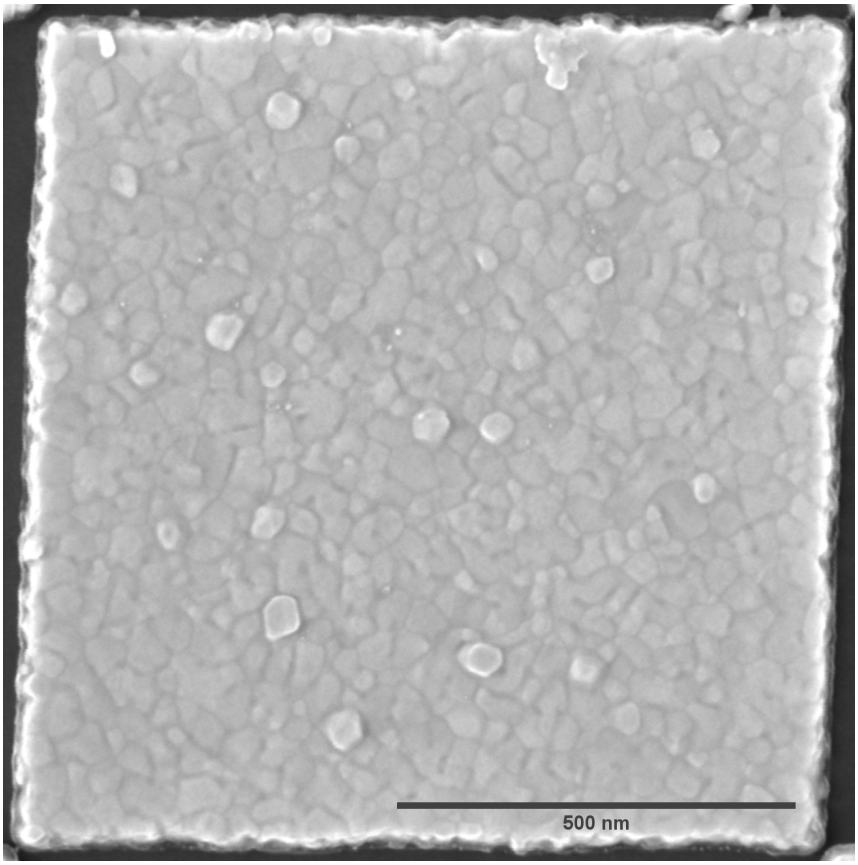


Figure 5.40: SEM image of a 1µm^2 gold square showing the granular nature of the sold surface. Grains can be seen protruding from the surface due to metal evaporation atop contamination.

As with Figure 5.9 we can determine the step edge height from the topography image (Figure 5.36a) by means of the difference in modes as in Figure 5.41, showing a step height measurement of 105 nm and 83 nm, dependant on which peak measured. These two distinct peaks can be seen in the slight contrast in colour on the topography channel in Figure 5.36a, it can be seen that there are clear patches of contrast that cannot be explained by effects such as particulate pickup. Contamination on the SiNx surface may be the cause of there being two discrete levels. In previous scans, these patches may have been hidden by other contamination or hydration layers that have now dried off in the dry nitrogen atmosphere.

A similar approach can be taken for the probe response and is shown in Figure 5.42. This shows a clear change in probe response ($\Delta 3\omega/3\omega_{cal}$) from 9.9% on the silicon nitride, and increasing to approximately 11.9% on the NiCr/Au step.

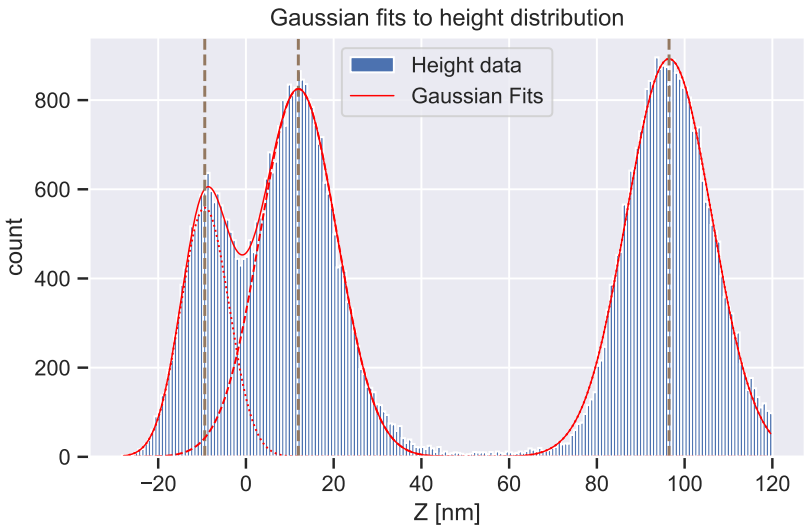


Figure 5.41: Height distribution of Figure 5.36a. By taking the difference between the two outer modes (purple lines) in the height distribution, we can determine a measured step edge height of 105 nm. It can be seen that an extra distribution appears between the peaks, take the difference in the middle and right peak, a measure of 84.5 nm can be made.

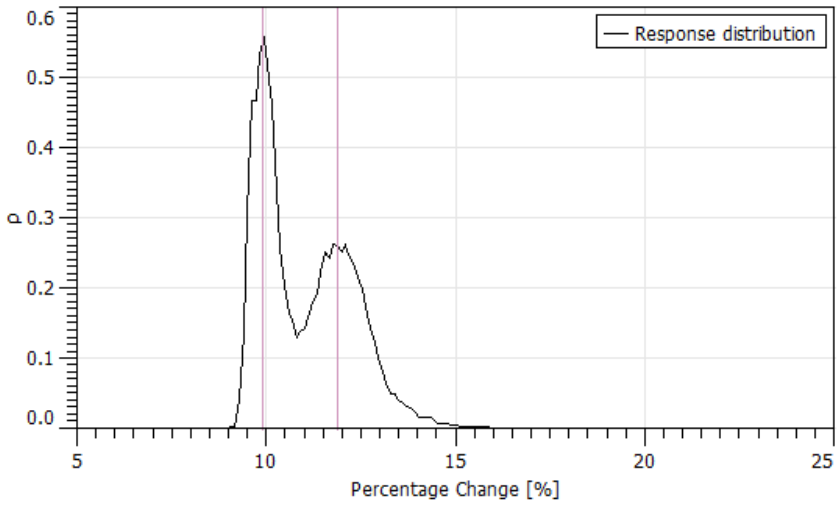


Figure 5.42: Probe $\Delta 3\omega/3\omega_{cal}$ distribution of Figure 5.36b as a percentage. By taking the difference between the two modes (purple lines) in the distribution, we can determine a measured fraction change in probe response from 9.9% on SiNx to around 11.9%. A change of 2%.

Analysis of the differences in probe response from the variation in material can be easier to interpret by combining the two images. One can use the height data to determine if a given pixel is on the gold step or on the silicon nitride substrate. The probe response can then be split along this line and the distribution of each area compared (Figure 5.43). It can be seen that there are overlaps in the response between the silicon nitride and gold measurements which skews interpretation of the

results slightly.

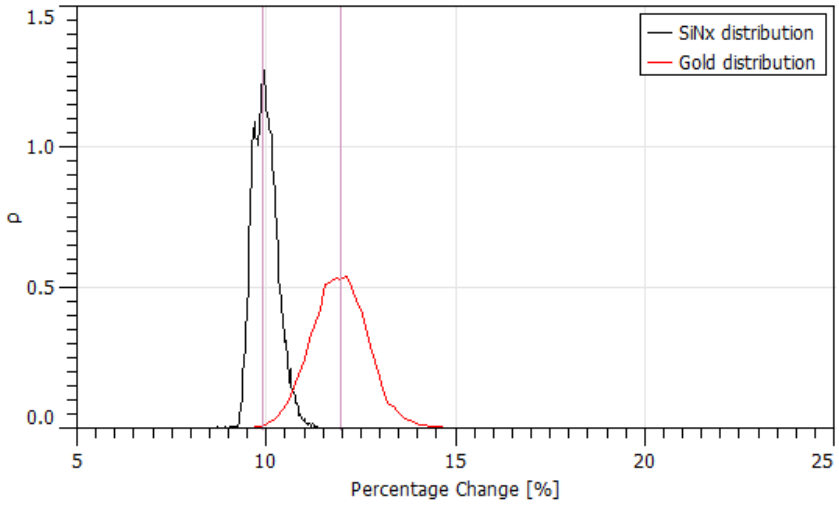


Figure 5.43: Response distribution of Figure 5.36b, split by the gold step edge.

However, it can be seen that there is a larger spread in probe response when scanning the gold step, making material properties investigations difficult to quantify. This is most likely due to large variations in contact shape and thermal resistances from the granularity of the EBPVD deposited gold (as seen previously in Figure 5.40), or from mono/multi-layers of contamination that may be present on the sample or tip. To perform materials characterisation one must move to liquid where contact area is less of a contributing factor [173], or move to vacuum where spreading resistances have less effect.

Studies by Ftouni et al. [179] show silicon nitride with a thermal conductivity around 3 W/mK, Zhang et al. [180] shows the conductivity of thin film gold in the 150 W/mK region. Although there is a clear increase in the thermal conductivity in the gold region compared to the silicon nitride region, studies by Lambert [63] had shown that in air, KNT probe response saturates at around 80 W/mK. This equates to around 12% changes in probe response in their study using probes of the same type. This is due to the probe already distributing as much heat as it can into the sample due to contact resistances. This again makes quantitative analysis of the material properties difficult in air [3, 173].

5.5 Micro heater

The results above indicate that material variation does not have a significant effect on the topography output and material differences can be handled well. However,

as SThM is primarily a thermal measurement system, the ability of surface determination of each method in the presence of temperature gradients across a scan must also be quantified.

To measure any effect of temperature on the topography, the flat plane around an active micro heater, described in detail by Dobson et al. [181] and shown in Figure 5.44 and 5.46, was scanned with the heater off and at various heater powers. To avoid thermal bend of the cantilever body while the heater was active [6] the probe was positioned pointing towards the heater as shown in Figure 5.45.

The bulk silicon surface of the sample acts as a heatsink when the nichrome heater is active and will exhibit minimal temperature rise. Therefore the probe tip was kept on the silicon and not advanced onto the membrane. However, the active heater will conduct heat into the air above it and show a temperature gradient according to the inverse square law. Advancing the tip in and out of this temperature gradient while monitoring both the thermometry and topography signals allows for each topography measurement method's sensitivity to tip temperature to be quantified.

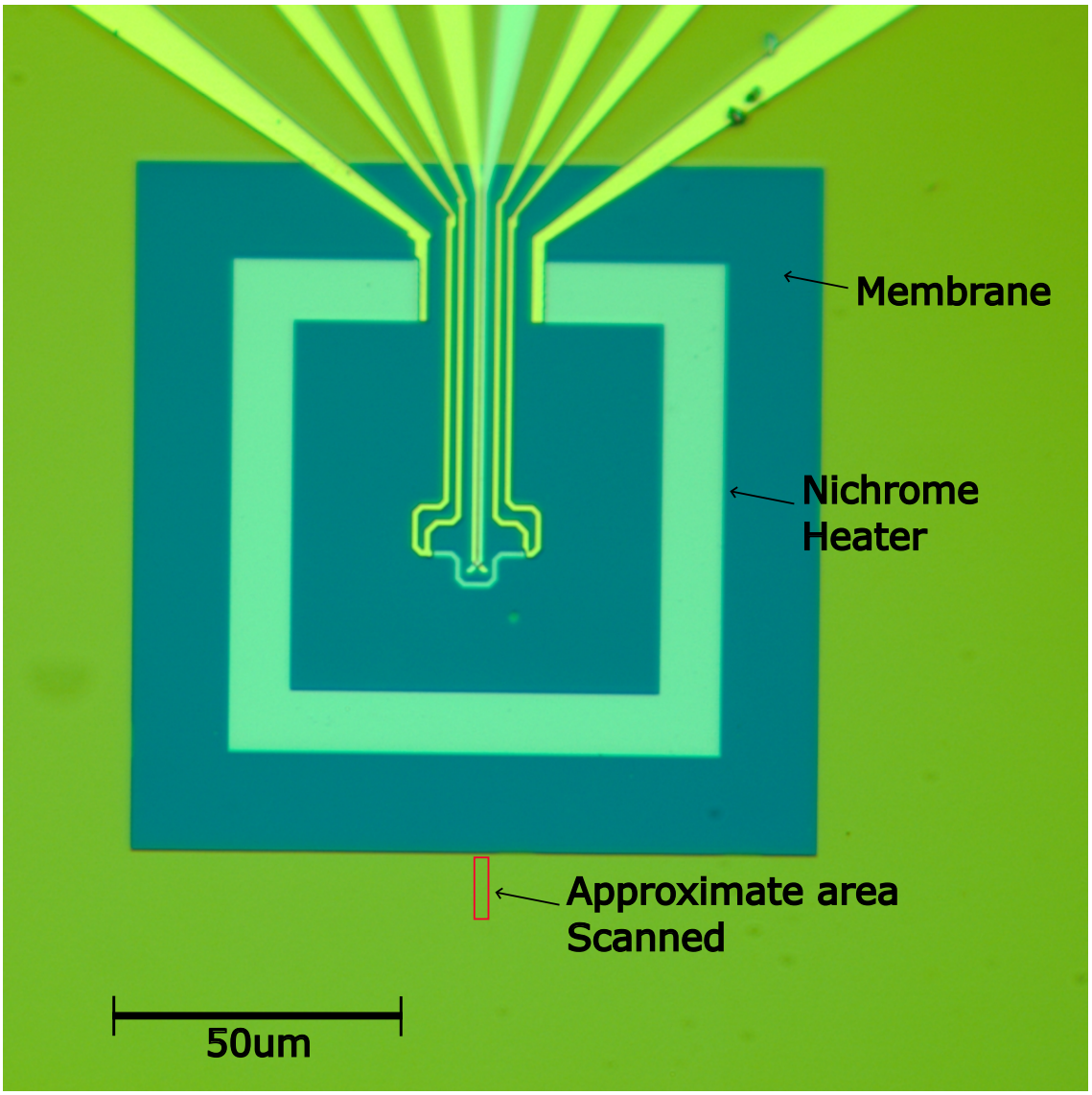


Figure 5.44: Optical image of micro heater, showing nichrome heater on silicon nitride membrane.

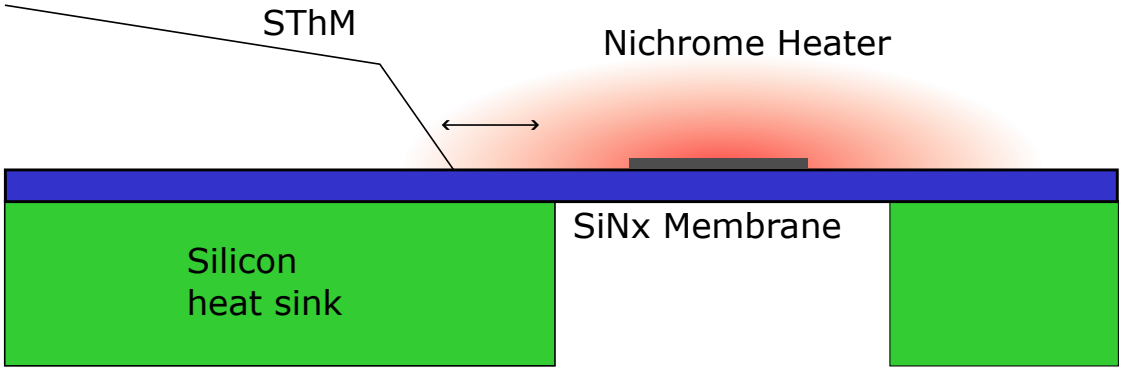


Figure 5.45: Diagram of experimental procedure. The probe is advanced towards and retracted from the nichrome heater. The SThM body is kept on the area above the silicon heat sink to keep the thermal bend of the cantilever to a minimum [6]. As the probe tip approaches the heater it advances through the thermal gradient in the air due to the heater.

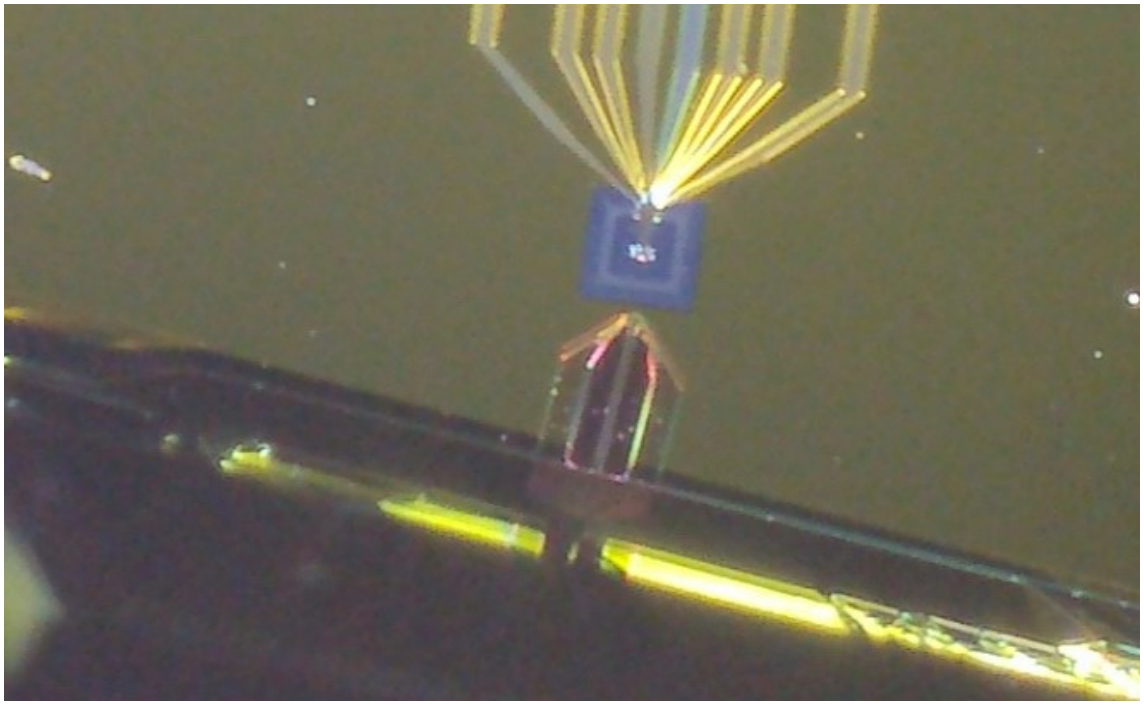
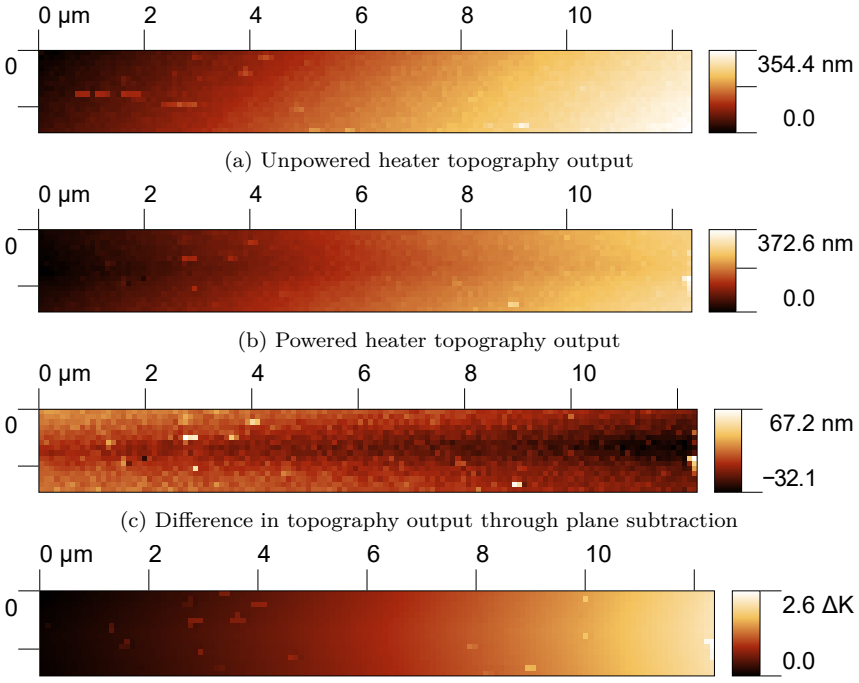


Figure 5.46: Optical image of SThM scanning the micro heater

The area was first scanned using each method with the heater powered off (Figure 5.47a). This allowed the topographic tilt of the surface to be determined. Fitting a plane to this surface allowed for the natural surface tilt to be accounted for in consequent scans. This was achieved by subtracting this plane from any powered heater scan's topography, allowing for the determination of slight changes in the topography output (Figure 5.47c) that may appear from tip temperature rises. Plotting

the estimated tip temperature rise, derived from the 1ω signal magnitude, versus topography difference (Figure 5.48) shows a correlation of -13.6 ± 0.3 nm/K.

This experiment was then repeated at various heater powers and shown in Figure 5.49. All values for the estimated change in tip temperature rise (ΔK), are referenced to the first pixel of each scan being '0'.



(a) Unpowered heater topography output

(b) Powered heater topography output

(c) Difference in topography output through plane subtraction

(d) Estimation of tip temperature rise.

Figure 5.47: Methodology to calculate the effect of temperature on topography. Fitting a plane to the unpowered scan in (a), and subtracting that plane from a powered scan in (b), results in (c) showing any change in the topography output as a result of temperature changes. (d) Showing estimated change in tip temperature.

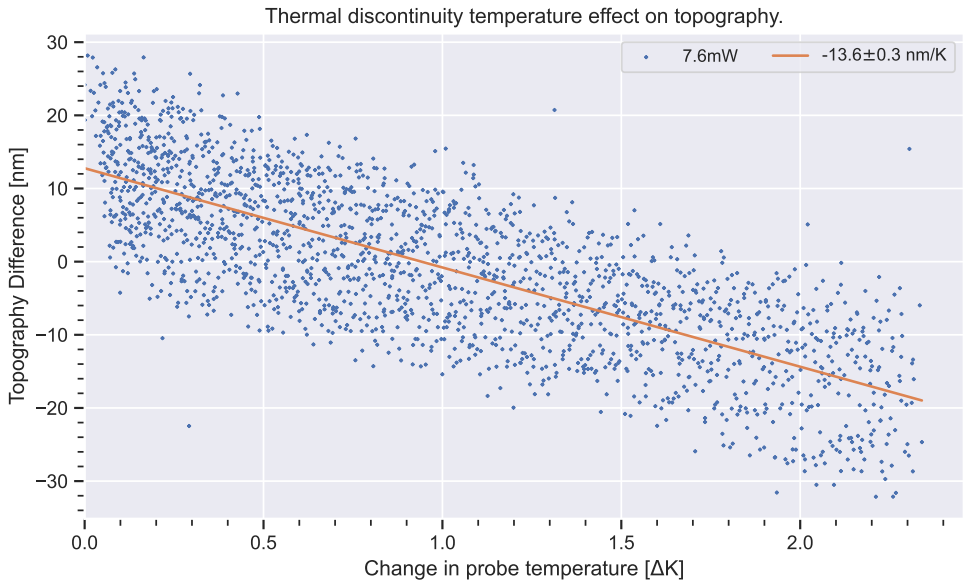


Figure 5.48: A straight line fit of 5.47c and 5.47d, showing a line fit with a slight gradient of approximately -13.6 nm/K with a heater power of 7.6 mW. Sample contamination shows outliers in 5.47c and 5.47d that have been masked for the calculation.

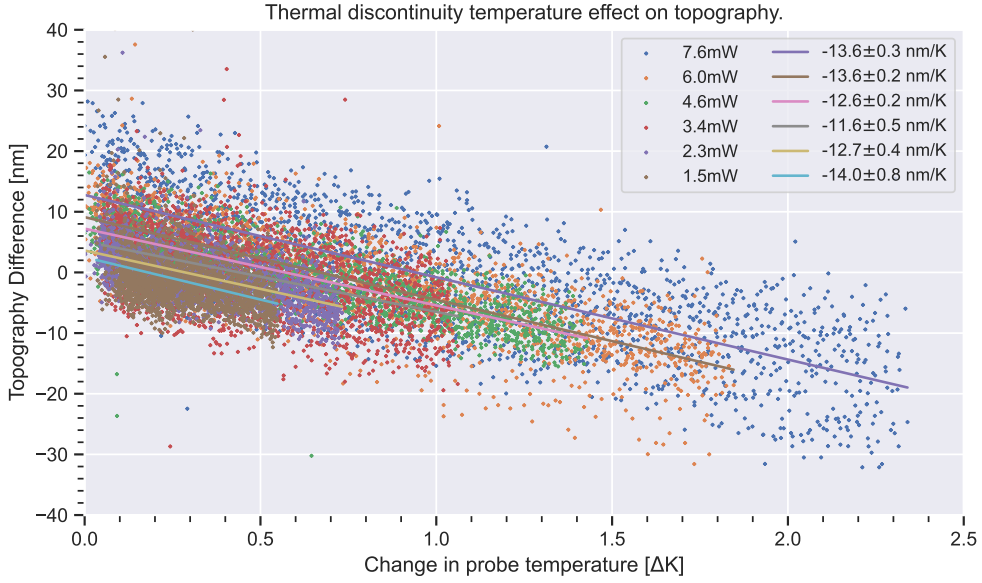
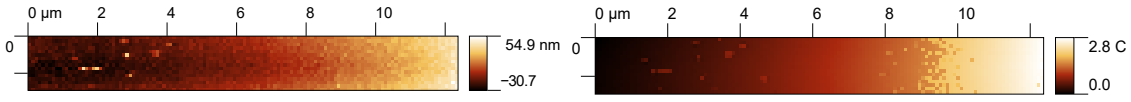


Figure 5.49: Overlay of all heater powers experiments and gradient calculations for each. Showing a gradient of topography with temperature of -13.012 ± 0.8 nm/K

Results from scans at various heater powers agree with one another and show a gradient of -13.012 ± 0.8 nm/K. The consistent residual gradient that is visible across all heater powers could be attributed to the slight thermal bending of the cantilever as the tip temperature rises [6, 7]. Mordue et al. [6] have shown that

the bi-material design of the KNT probe can cause thermal bend of the cantilever upwards of 200 nm/K when a uniform temperature heats the whole probe. Modelling by Mordue [7] and Lambert [63] has previously shown that cantilevers of the KNT type will have an inherent tip deflection of around 17 nm/K from tip heating. As in this experiment, only the tip is influenced by approaching the heater out of contact, the results obtained in these scans confirm this model.

Repeating the experimental procedure using the thermal contact limit method shows Figure 5.50 and Figure 5.51.



(a) Difference in heater topography output

(b) Powered heater change in temperature output

Figure 5.50: 7.6 mW scans obtained through the contact limit method

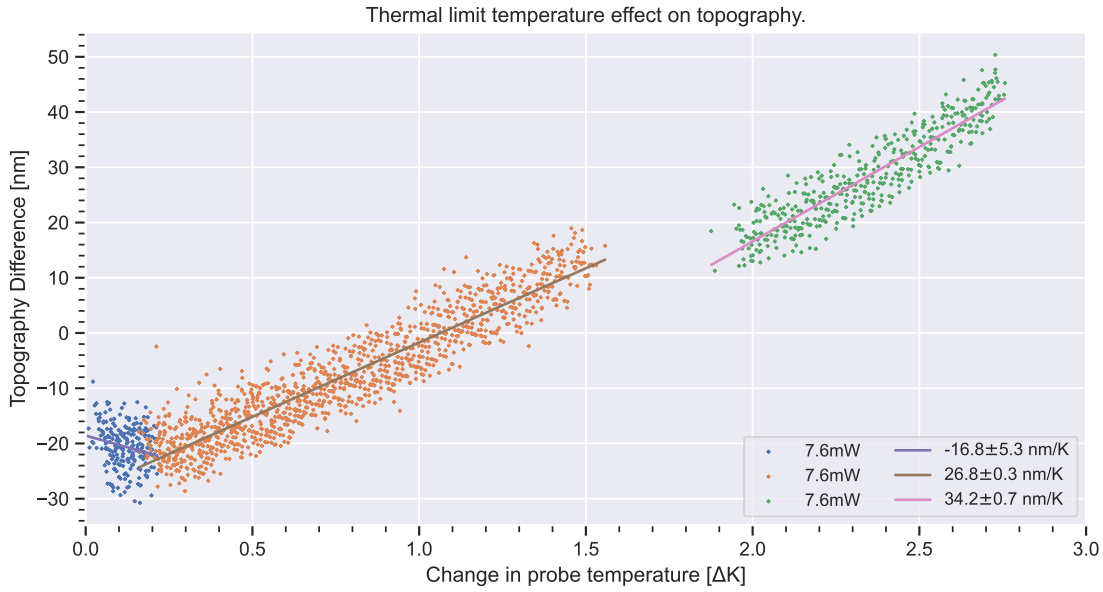


Figure 5.51: Straight line fits showing three distinct areas with gradients of -17 nm/K, 27 nm/K, and 34.2 nm/K, with a heater power of 7.6 mW. For small temperature changes (<0.2 °C) The measurement shows little change compared to the thermal discontinuity. The middle and right sections show a change in sign and a larger gradient. Disconnected measurements on the right-hand side are due to contact not being made with the surface and are measurements of temperature above the surface.

As can be seen from Figure 5.51 the measured topographic change per degree is vastly different to previous measurements. Except for small temperature changes, a change in sign and a positive gradient of 26.8 nm/K and 34.2 nm/K are measured. The positive gradient in the measurements can be explained by the slight temperature dependence that the 3ω signal has, due to the TCR of the probe resistor.

This causes the control loop to cross the calibrated threshold value of 'contact' 3ω when no contact has been made. For all scans in this experiment, the probe was advanced past the detected surface by 10 nm (approx. 2-4 nN of force) for surface thermometry measurements. Moving the probe past this measured contact point by 10 nm still allowed for contact to be made up until topography differences were greater than this setpoint, if the detected surface was above this point, no contact between the probe and sample has been made during measurement, and the 'in contact' measurement was actually a measure of above the surface. As the silicon cannot act as a heatsink for the probe due to lack of tip-sample contact, the jump in ΔK between the middle and right areas of Figure 5.51 appears.

It is clear that methods of surface detection that rely solely on calibrated values of 3ω will show some temperature-dependent artefacts and should be avoided when scanning at non-uniform out-of-contact temperatures. However, one can still measure using the thermal discontinuity methodology as this does not rely on any calibration threshold value of 3ω, the only topography-temperature artefact that is visible in such methods are one of the cantilever bend due to the bimetallic nature of the probe construction.

5.6 Vertical Cavity Surface Emitting Laser

One of the limiting factors to the performance of vertical cavity surface emitting lasers (or VCSELs) is the heat generated in the cavity during lasing [182]. This can cause spectral misalignment of the cavity resonance [183, 184] as well as increasing the threshold current and reducing output efficiency [184]. As such, thermometry studies of VCSELs are important to their continued development. SThM measurements of a VCSEL cavity would prove difficult if an optical lever were to be employed. For accurate measurement, the optical lever would be required to be blanked or turned off during the thermal measurement to avoid any interference with surface thermal measurements. Stray light emitted from the VCSEL may also interfere with the optical lever photodiode, causing erroneous measurements in the feedback system. Luo et al. [185] have shown that SThM measurement of VCSELs cross sections to map the temperature distribution around the active region using a thermocouple probe at various biases. However, the authors did not account for the optical lever laser influence on the measurement, which adds a significant additional heat source to the measurement [2, 3]. Other methods, such as thermoreflectance have also been used to measure the operating temperature of VCSELs [186]. As a proof of concept, a multi-mode 665 nm VCSEL (Firecomms - RVM665T [187]) with its cap removed was placed into the custom SThM and scanned while at a variety of laser bias states.

The VCSEL was wired up according to Figure 5.52, allowing for a controlled current through the VCSEL in four states according to Table 5.6. The LED state (at 0.5 mA bias) is just below the threshold current of the laser (0.6 mA) where no lasing occurs [187], but light is still emitted, while the low and high lase are above the threshold current where lasing of the device occurs. The switches (S1 and S2) were implemented via relays to allow for automated control of the VCSEL states from the feedback electronics box.

Table 5.6: Available VCSEL states

S1/S2	Bias	Power	State
Off/Off	0 mA	0 mW	Off
Off/On	0.5 mA	1.0 5mW	LED
On/Off	1.5 mA	3.15 mW	Low lase
On/On	2 mA	4.2 mW	High lase

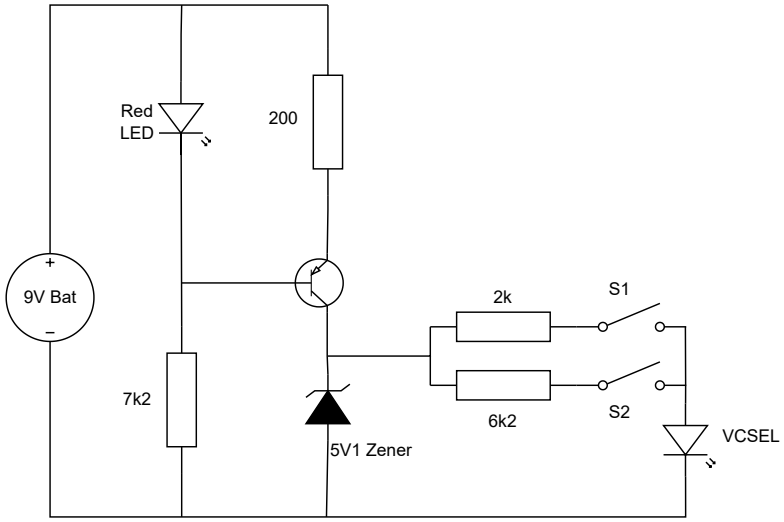


Figure 5.52: Control electronics to switch current through VCSEL

An optical image of the scanned area is shown in Figure 5.53, with an image of the scan taking place in Figure 5.54.

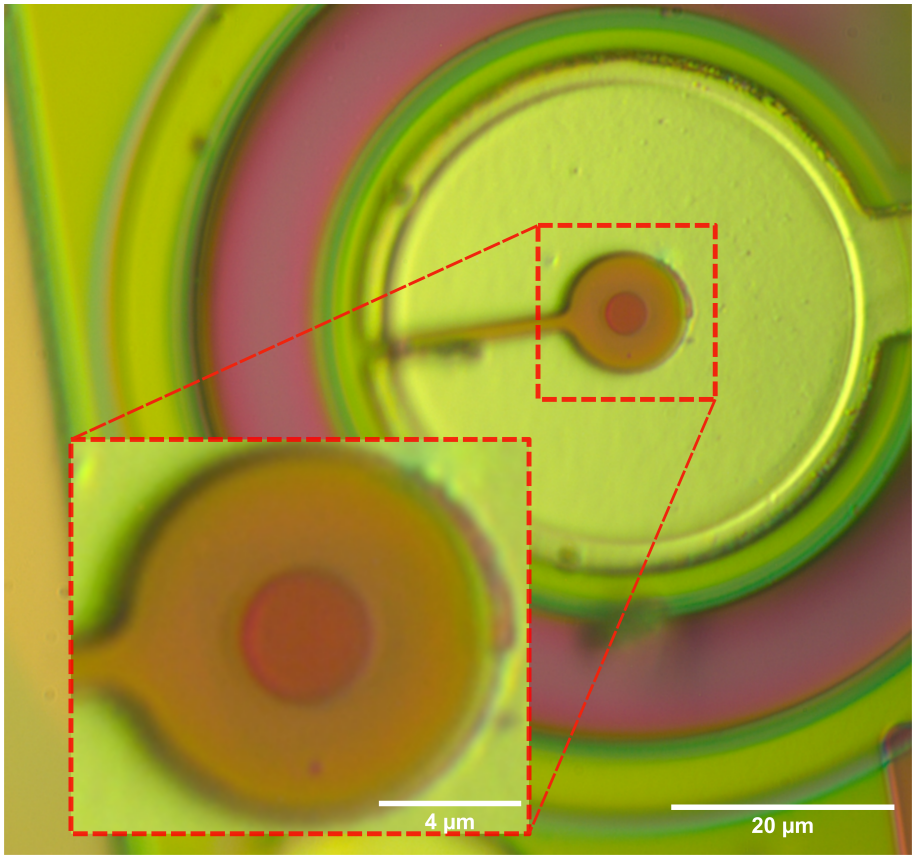


Figure 5.53: Microscope image of VCSEL cavity, with a zoomed section of the approximate area scanned.

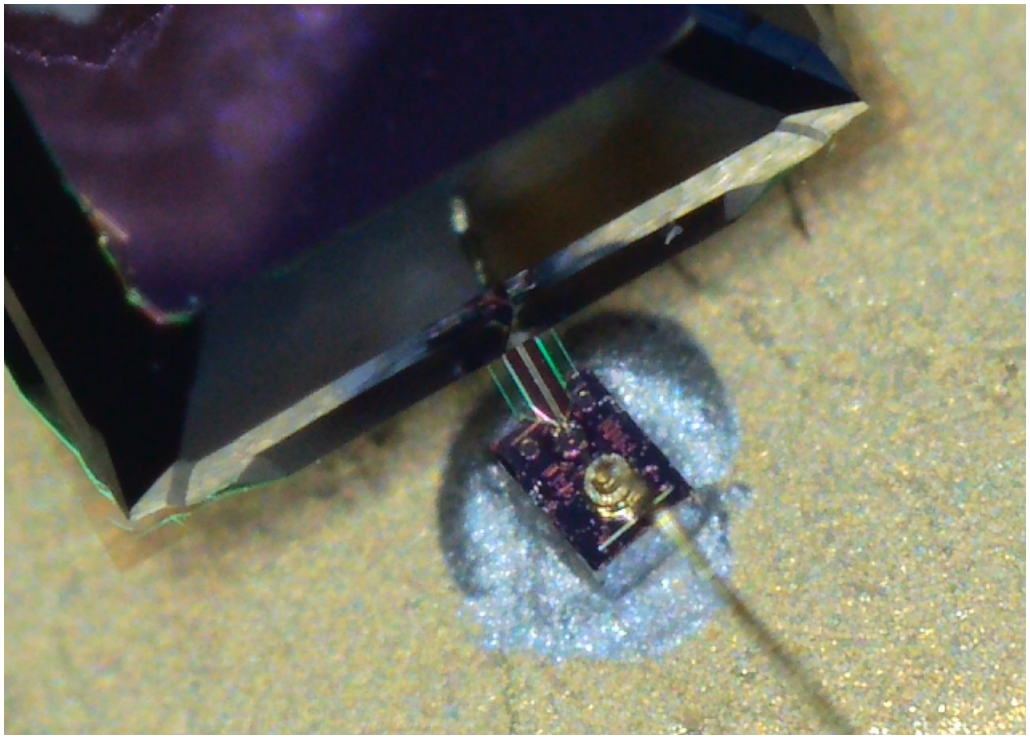
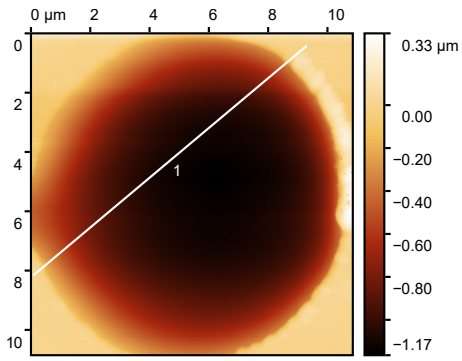
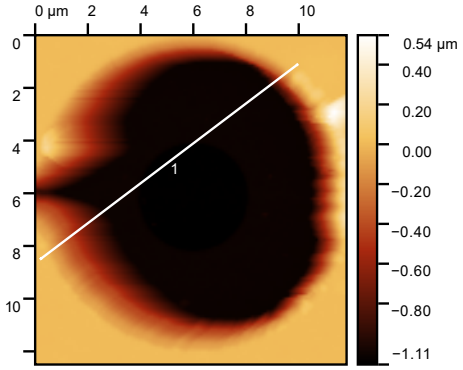


Figure 5.54: Microscope image of VCSEL scan

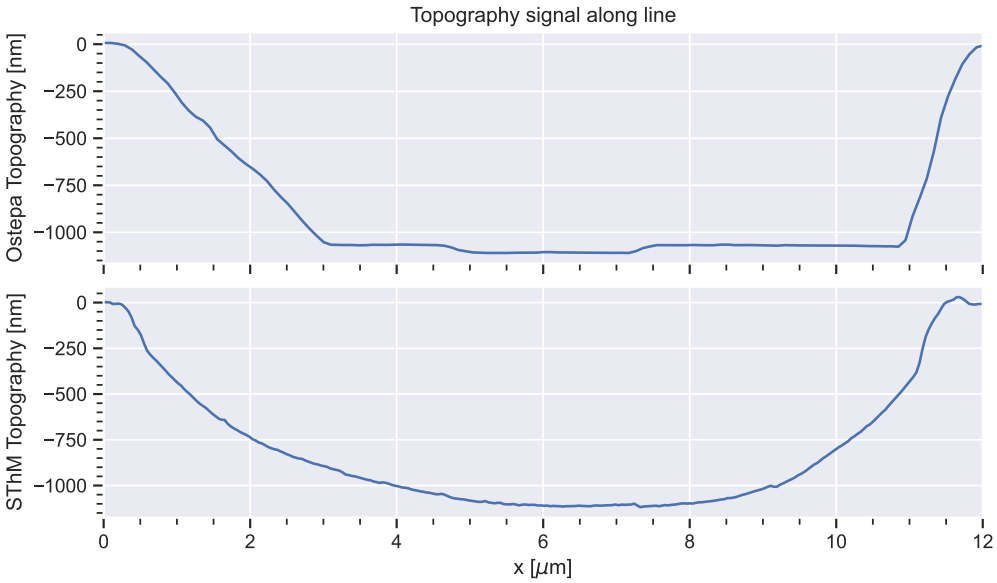
Each pixel of the scan can be landed and topography measured with the VCSEL off, then switched through each active VCSEL state while thermometry measurements are taken. Figure 5.55 shows the topography measurement from both the custom SThM setup as well as one obtained on a commercial AFM after data levelling in Gwyddion. It can be seen from Figure 5.55c that in both scans the VCSEL may not be loaded square to the probe and sample tilt is present causing an asymmetry in the side wall profile. As expected, tip convolution with the side wall is again greater with the KNT SThM probe when compared to an AFM tip designed for topographic imaging. this has been shown schematically in Figure 5.56.



(a) SThM topography output of VCSEL



(b) OSTEPA-R4 topography output of VCSEL



(c) Comparison of topography lines labelled 1 in (a-b); showing tip convolution in the SThM topography output in the large side walls

Figure 5.55: Topography comparison of VCSEL device

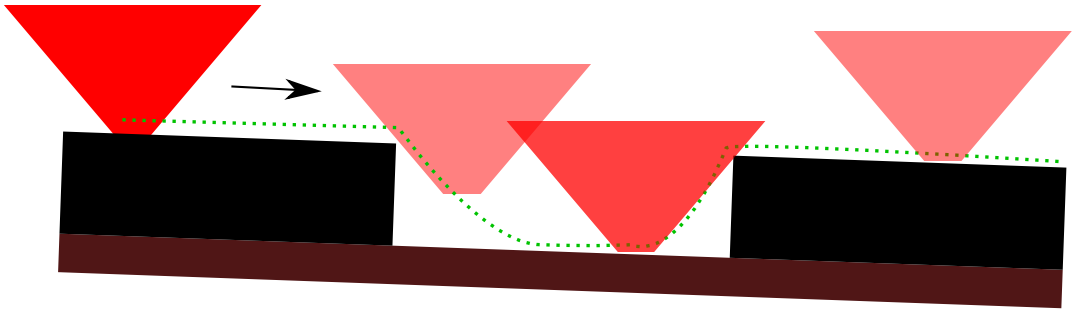


Figure 5.56: Schematic of tip convolution of large KNT probe (red) with side walls (black). There is an asymmetry in the probe path (green) as it scans due to the uneven loading of the VCSEL on the sample stage.

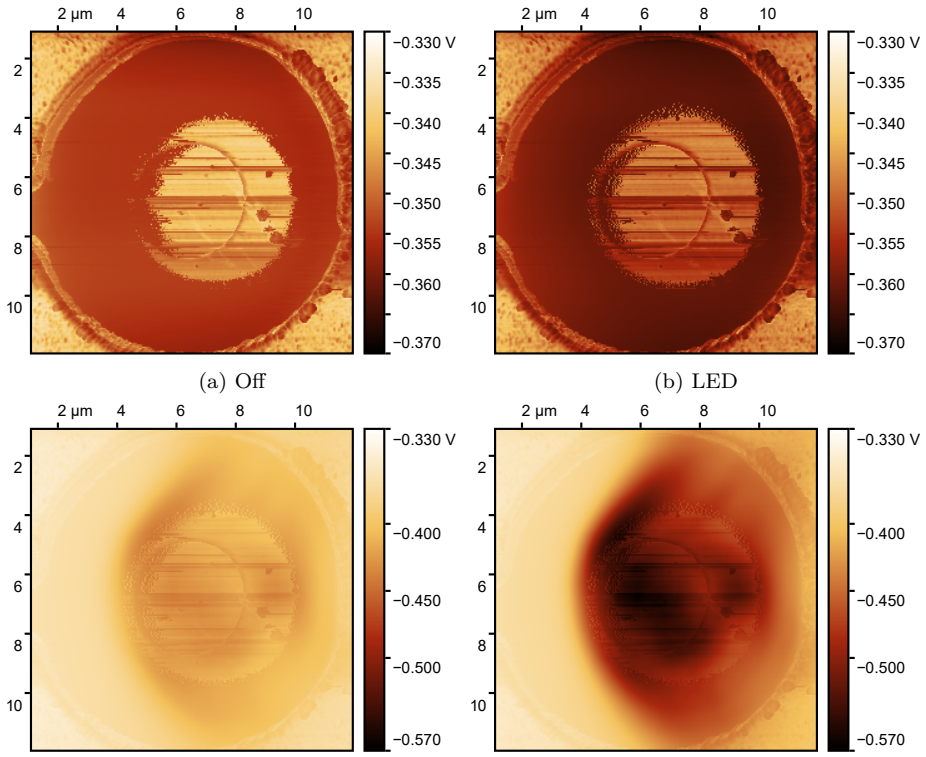
The effects of tip convolution with the side wall are visible in the thermometric output of the SThM at each state and can be seen in Figure 5.57 for the 1ω channel and Figure 5.58 for the 3ω channel. As shown in Figure 5.56, during periods of side wall contact with the probe body, the most sensitive area of the probe (the metalised tip) is not in contact with any surface, so the probe will show very little contact response. However, there will still exist some contact thermal transfer through the silicon nitride along the edge of the probe and will be sufficient to trigger the control loop acquisition of contact.

A clear change in the 1ω channel signal can be seen in Figure 5.57 in the low and high states. Vertical symmetry in the scans can be seen due to the probe probe pointing towards the right-hand side of the image. This also creates a lateral asymmetry in the response with the right-hand side of the image showing a greater response than the left-hand side due to the cantilever overhanging the laser cavity as it passes to the right-hand side. This results in laser heating of the cantilever body, which transfers as an artefact in the measurement. This also acts as a reminder of the issues that cantilever laser illumination can cause.

Such changes are not observable in the 3ω response in Figure 5.58, as this signal is generally immune to slight changes in temperature.

As we have point measurements of the VCSEL states at each pixel, we can create maps of changes in thermometry signals at each VCSEL state. For example, if we subtract the 'off' VCSEL states from each 'on' VCSEL state we can also approximate the change in SThM tip temperature of the probe through the change in 1ω signal. This leads to the creation of maps in terms of ΔK for each VCSEL state in Figure 5.59.

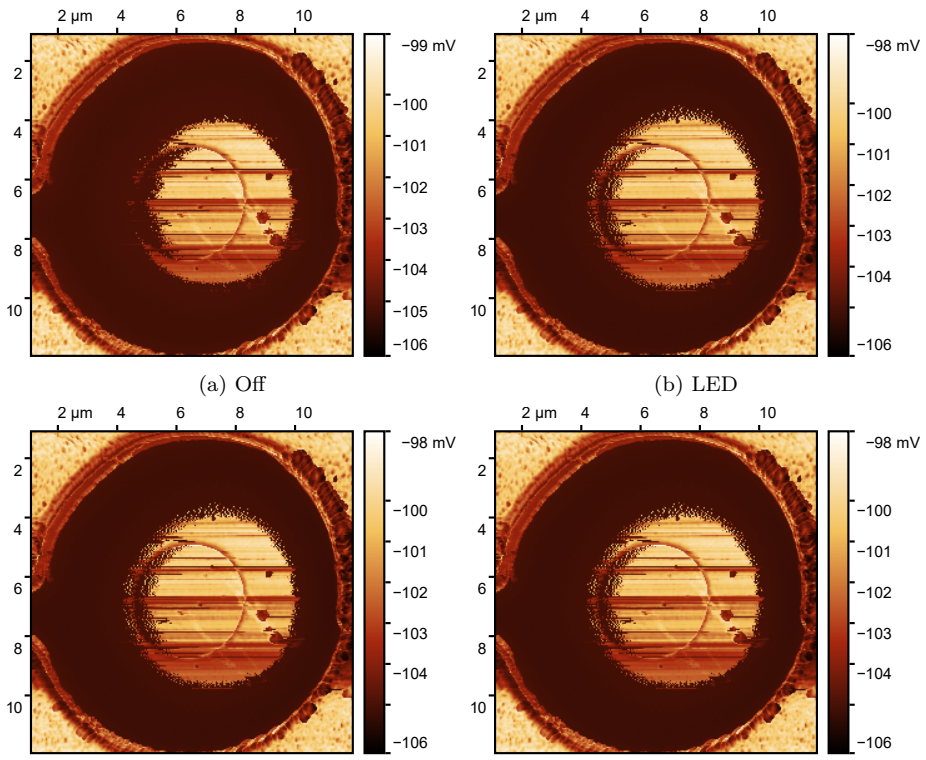
Figure 5.59a shows that when switching to the LED state, there is a temperature change in the SThM tip resistor in the order of tens of mK. Using a typical TCR value of the tip resistor (taken as the mean of 1.17×10^{-3} K^{-1} [62] and 1.2×10^{-3} K^{-1} [158]), the tip temperature rise can be estimated to be 0.2 ± 0.0098 K at the centre of the cavity. Once lasing has commenced in Figure 5.59b and 5.59c, this rise increases to upwards of 2.6 ± 0.12 K and 5.9 ± 0.34 K for low and for high lasing respectively. Slight changes in thermal artefacts, particularly in Figure 5.59a, can be seen around areas of potential double contact. This could be due to the engaging or disengaging of double contact from the off state to any on state due to the thermal bend of the cantilever as it heats up. Studies by Mordue et al. [6] as well as previous experimentation in section 5.5 have shown even slight changes in the probe



(a) Off (b) LED

(c) Low (d) High

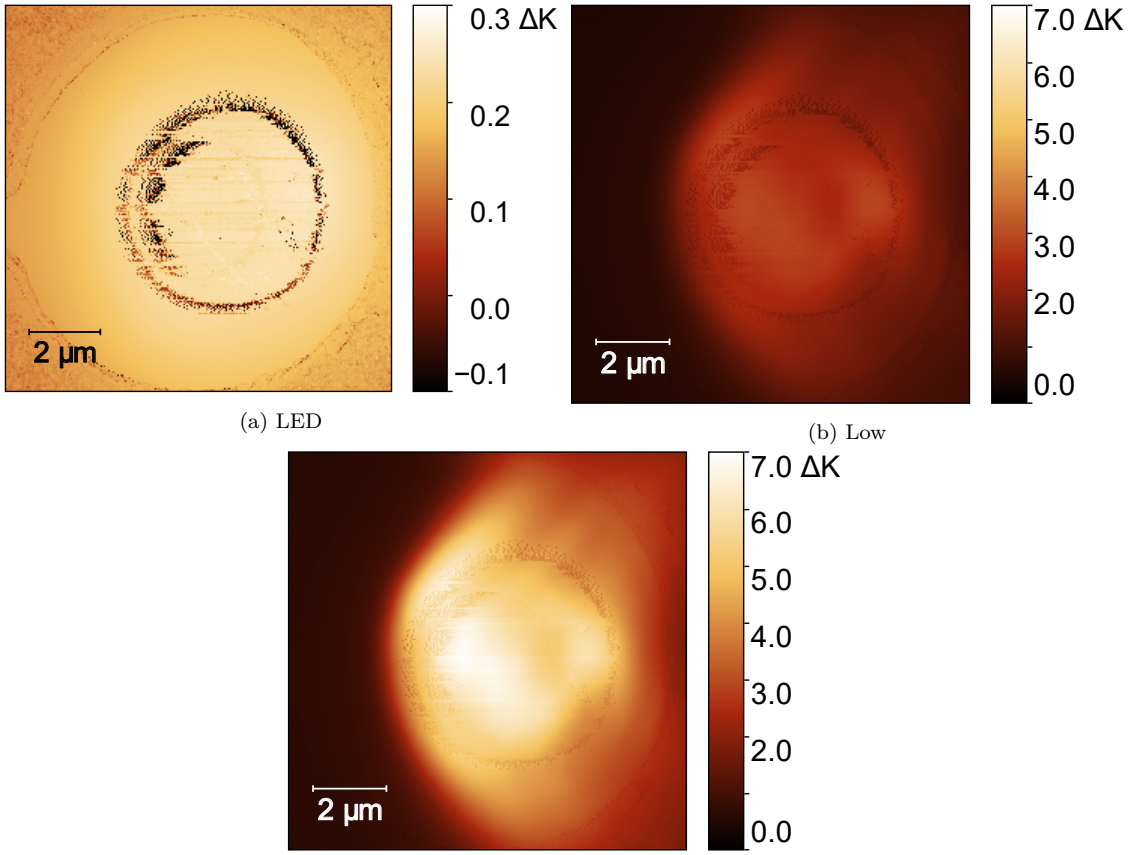
Figure 5.57: SThM 1ω channel of each VCSEL state.



(a) Off (b) LED

(c) Low (d) High

Figure 5.58: SThM 3ω channel of each VCSEL state.



(a) LED

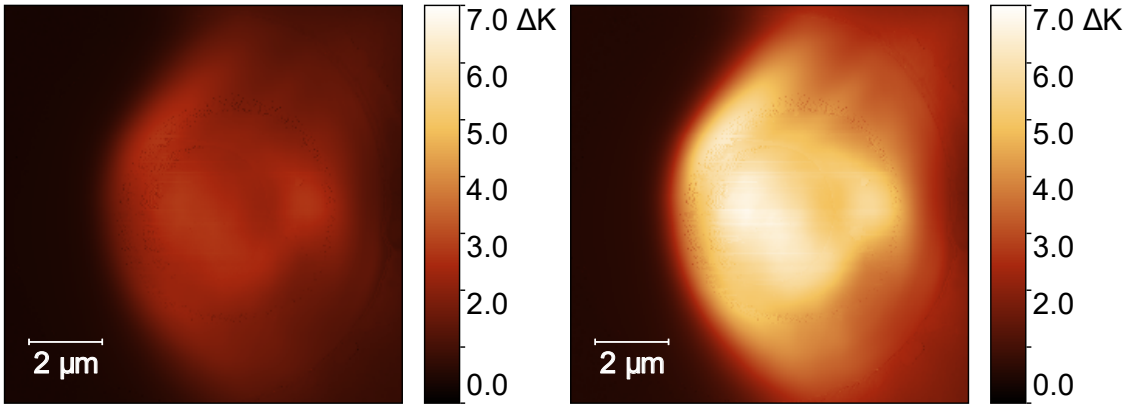
(b) Low

(c) High

Figure 5.59: SThM estimated ΔK of each VCSEL state.

temperature can cause significant bend of the cantilever.

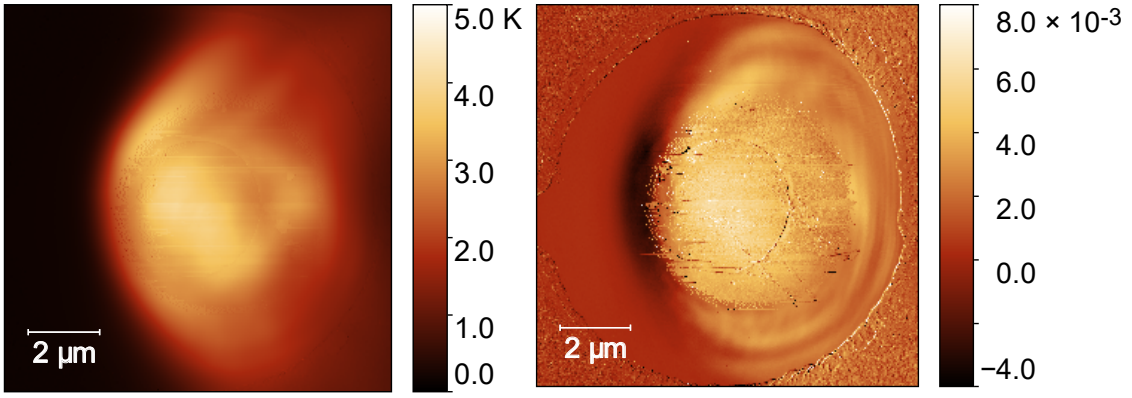
We can also obtain maps of the probe response change with respect to changes in lasing bias by subtracting the high/low state from the LED state, or the high state from the low state. This should remove the effects of surface artefacts and show only the change in response due to an increase in lasing power. High and low states subtracting the LED state can be seen in Figure 5.60. Measuring the cavity temperature in low bias minus LED state (Figure 5.60a) shows a 3.5 ± 0.13 K temperature increase given a change in dissipated VCSEL power of 2.1 mW. This corresponds to a measured temperature dependence of 1.6 °K/mW. This rises to 1.9 °K/mW when the same analysis is applied to the high minus LED scan as shown in Figure 5.60b. These measurements are in line with other low-power VCSEL thermal impedance measurements as reported in the literature [186, 188]. Results of subtracting the high from the low state can be seen in Figure 5.61. The fractional response of the 3ω signal is less obvious. However, there still exists a change in signal in the cavity and most likely arises from the slight 3ω temperature dependence.



(a) Low bias minus LED

(b) High bias minus LED

Figure 5.60: Thermometry output from subtraction of 1ω channels



(a) Estimated change in ΔK derived from 1ω channel

(b) Fractional change in 3ω channel

Figure 5.61: Thermometry output (High-Low) from subtraction of ω channels

Near-field in-contact direct absorption and far-field laser heating influences on the tip temperature are difficult to separate in the acquired images. During lasing, it can be assumed that the beam is Gaussian. Using the typical beam divergence from the VCSEL datasheet [187], $\Theta = 14°$, along with its wavelength, $\lambda = 665$ nm, one can approximate the size of the beam waist according to $\omega_0 = \frac{\lambda}{\pi n \theta}$ [189, 190], where $n = 1$ in air, and $\Theta = 2\theta$. This shows an approximate beam waist size of 1.7 µm. However, this beam waist may be located within the VCSEL, assuming a Bragg reflector pair thickness of around 150nm per pair and 35 pairs in total [191], this places the VCSEL aperture at approximately 5 µm from this beam waist, which would add approximately 2.4 µm (2θ) to the beam diameter due to beam divergence. According to these calculations, approximately 4.1 µm diameter circle could be considered the limit of the near field in contact absorption. This rough calculation matches the measured diameter of the VCSEL aperture of 4 µm. As the cantilever body is recessed approximately 10 µm from the probe tip, the limit of the

far-field laser heating can be calculated to be an additional 2.4 µm radius on top of the near-field limit.

5.7 Vertical probe mounting

An interesting benefit to decoupling the contact measurement from the optical lever is of probe access and positioning. As laser access to the cantilever is no longer a requirement, the position of the probe can be placed in any arbitrary orientation desired to allow differing scanning conditions or to allow improved access to measure awkward places, such as the potential scanning of sidewalls of deep etch trenches. One such positioning could be to mount the probe vertically in an attempt to artificially stiffen the cantilever as shown schematically in Figure 5.62 with an optical photo of the probe mounting in Figure 5.63. Such mounting positions could potentially avoid premature pull-in of the cantilever and reduce adhesion effects. Increasing the separation of the probe cantilever from the sample also has its benefits from a thermal standpoint as it reduces cantilever-sample coupling through the air, effectively increasing R_{air} in the thermal resistance model.

In the mechanical setup used, accurate placement of probe angle with the sample is difficult. In this section, through visual inspection of images similar to Figure 5.63 and scans obtained with the probe in this position, the mounting angle is assumed to be in the region between 60° and 85° normal to the sample.

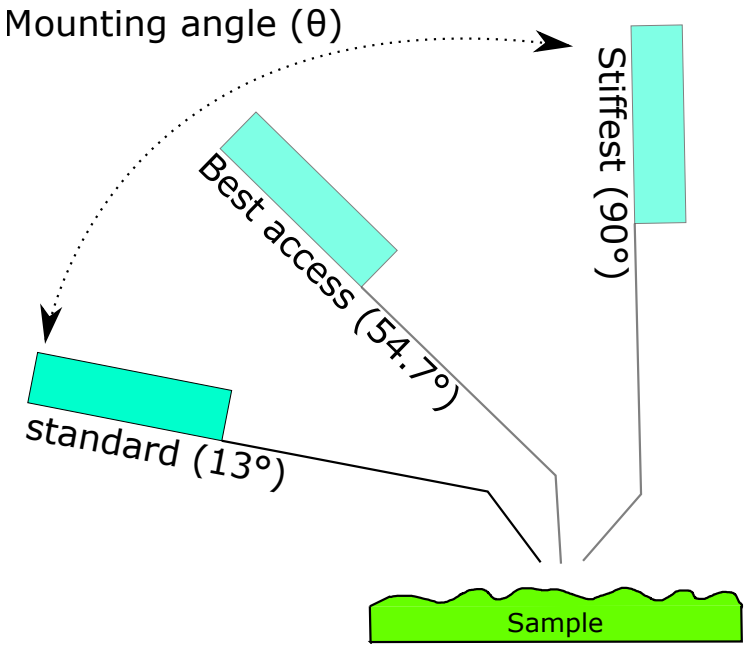


Figure 5.62: Changing the probe mounting angle could lead to interesting scanning conditions

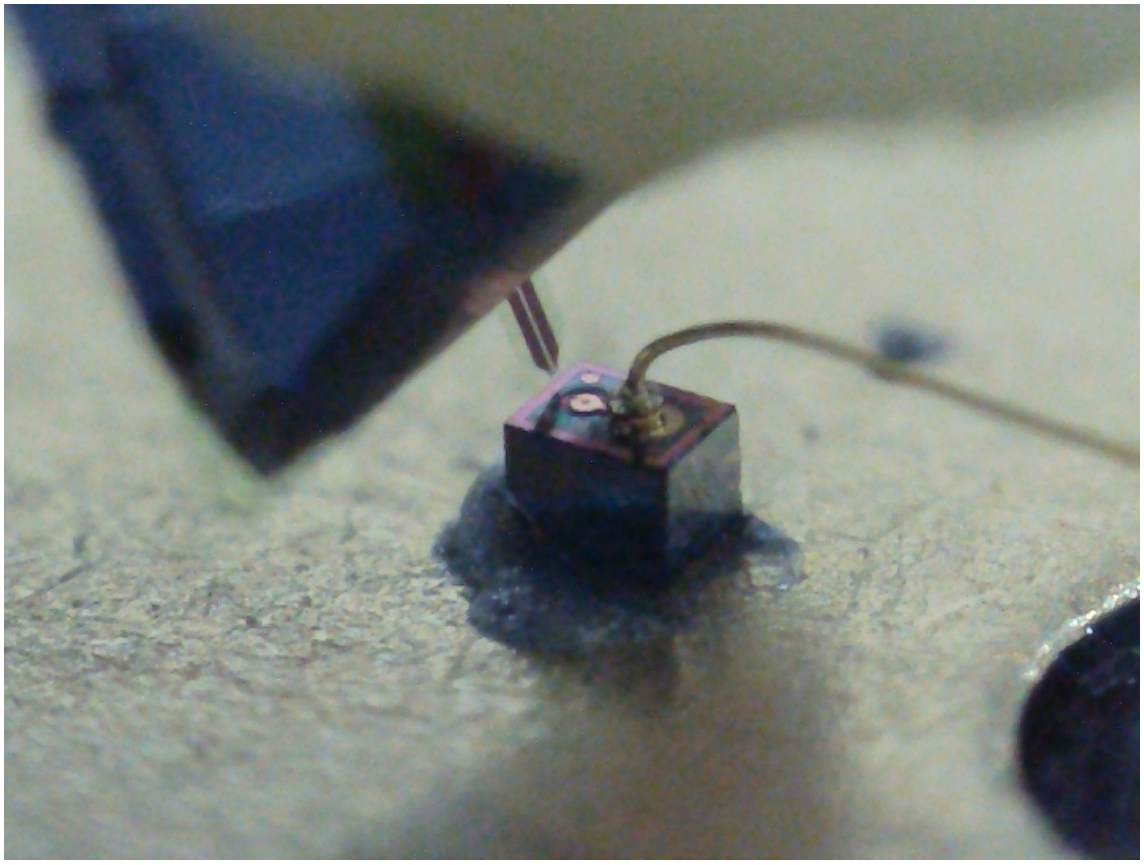


Figure 5.63: Vertically mounted probe measuring a VCSEL device.

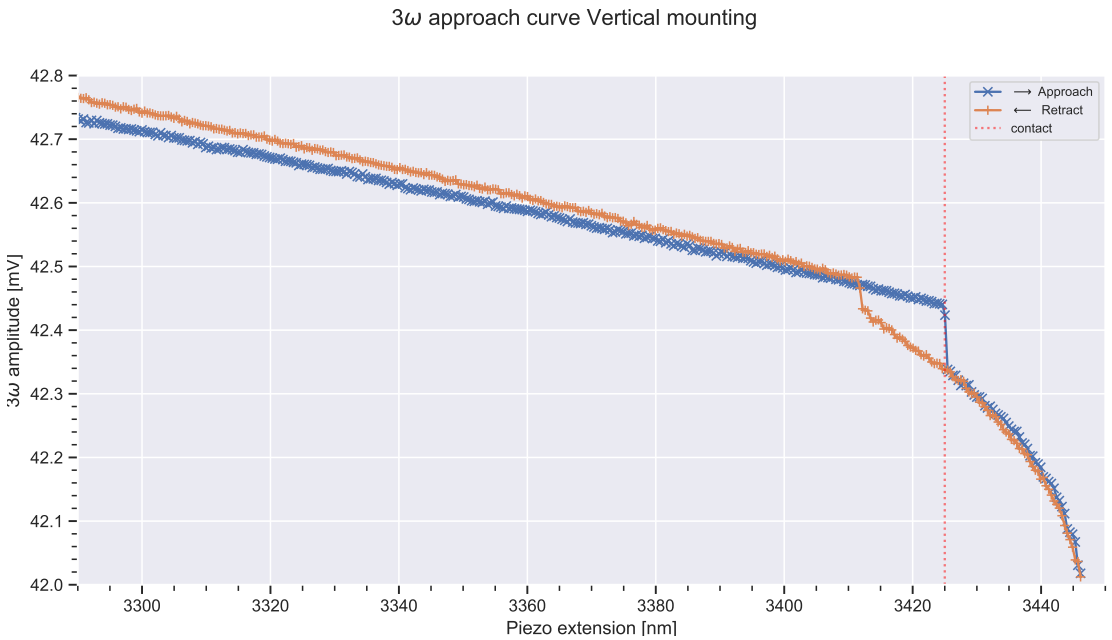


Figure 5.64: Vertically mounted probe approach and retract curve. Initial contact has been marked in red. It can be seen that tip resistor deformation occurs, causing large changes in the 3ω measurement past contact.

Visually analysing Figure 5.64, we can we can see a similar out-of-contact approach curve as with standard probe mounting. However, once contact has been made, 3ω amplitude continues to decrease, potentially due to increased probe tip/cantilever deformation from increased Z-axis stiffness. This hypothesis is supported by the reduction in hysteresis in the approach/retract curve that has been reduced to approximately 20 nm, from upwards of 100's of nanometres as seen previously in section 4.2.

Step edge

The step edge sample from section 5.4 was scanned again with the probe now in a vertical mounting position as described schematically in Figure 5.62. Initially utilising the thermal discontinuity method for topographic control, scans of the sample are visible in Figure 5.65, with extracted lines in Figure 5.66, histogram height measurement of the step edge in Figure 5.67, and mean profiles of topography and 3ω probe response in Figure 5.68 and 5.69.

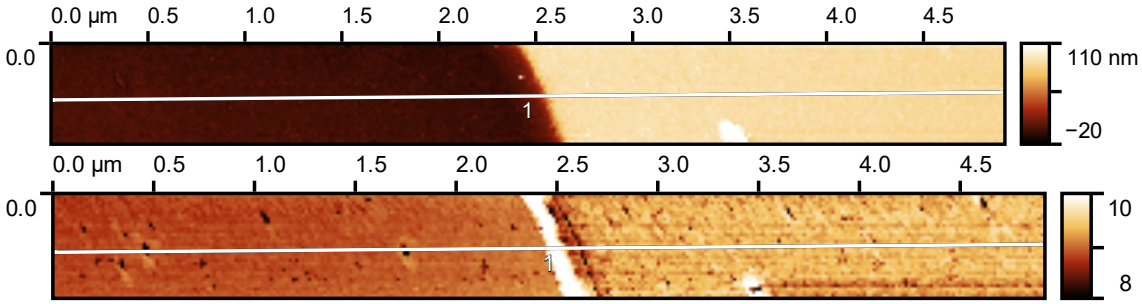


Figure 5.65: Vertically mounted probe scan of step edge sample using the thermal discontinuity method. Topographic output (Top) and 3ω probe response as a percentage (Bottom).

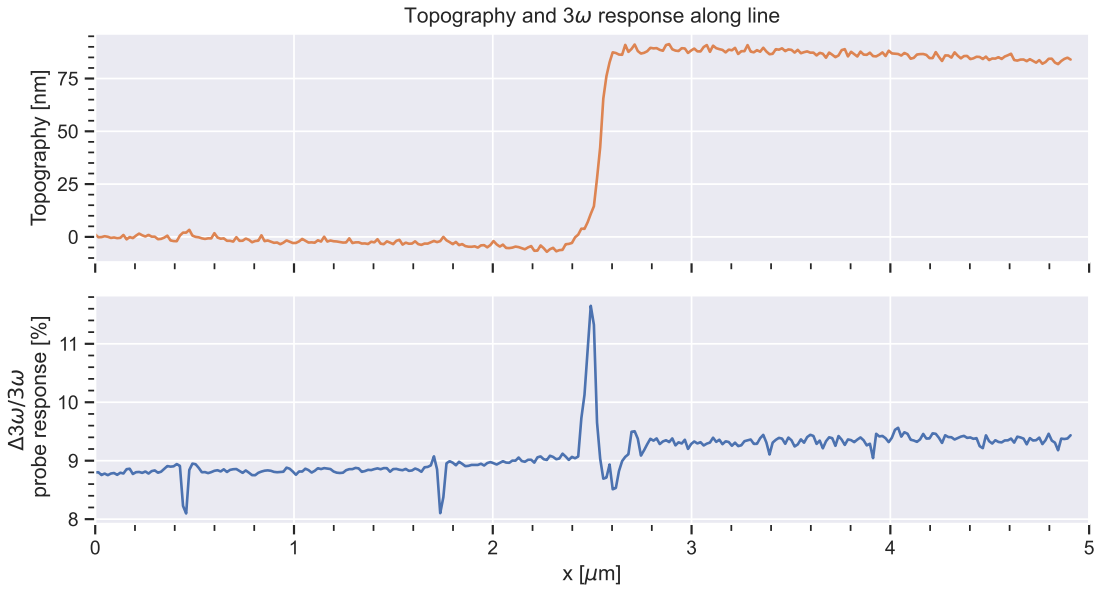


Figure 5.66: Extracted lines from Figure 5.65

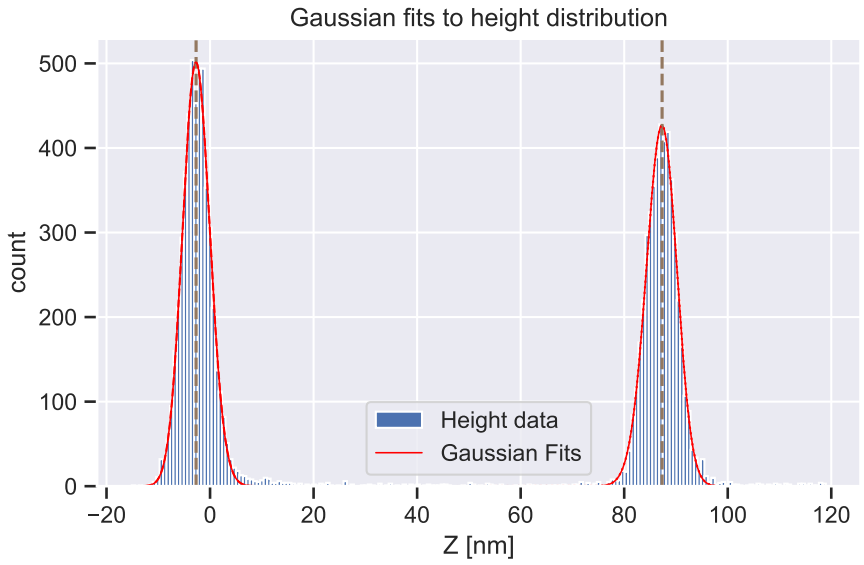


Figure 5.67: Histogram of topographic scan in Figure 5.65, showing a measured step height of 90.01 ± 13.02 nm

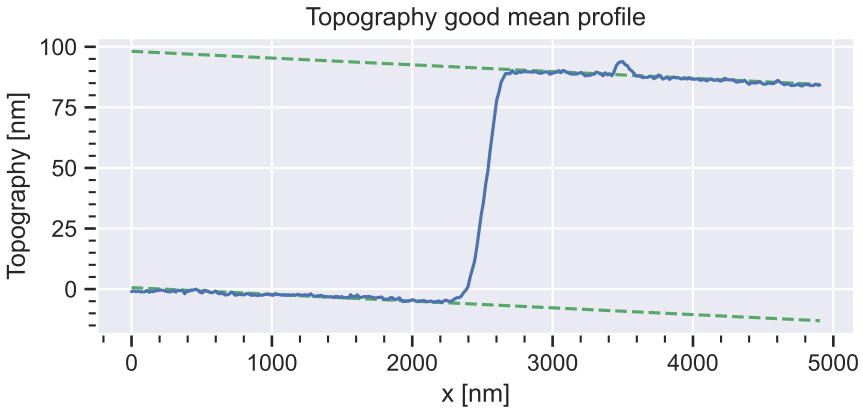


Figure 5.68: Good mean profile of topography channel of Figure 5.65, showing a fitted step height of 97.52 ± 0.4nm

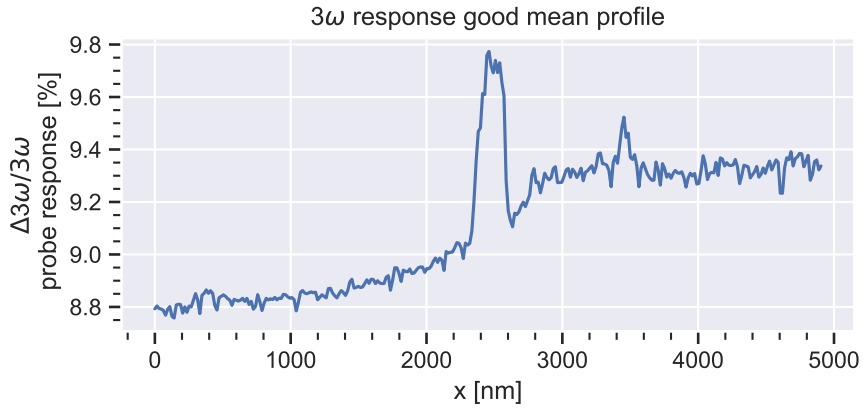


Figure 5.69: Good mean profile of 3ω channel of Figure 5.65

Analysis of the extracted lines in Figure 5.66 shows that double contact and reduced contact artefacts are visible as expected, and we observe a slight rise in the probe response from 8.8% to 9.3%, an approximately 0.5% rise. Figure 5.67 shows that the measured height of the step edge of 90 nm, and is comparable with previous measurements of the step height in section 5.4.

Similar analysis can be carried out for the same area scanned utilising the STP method in Figure 5.70 through 5.74.

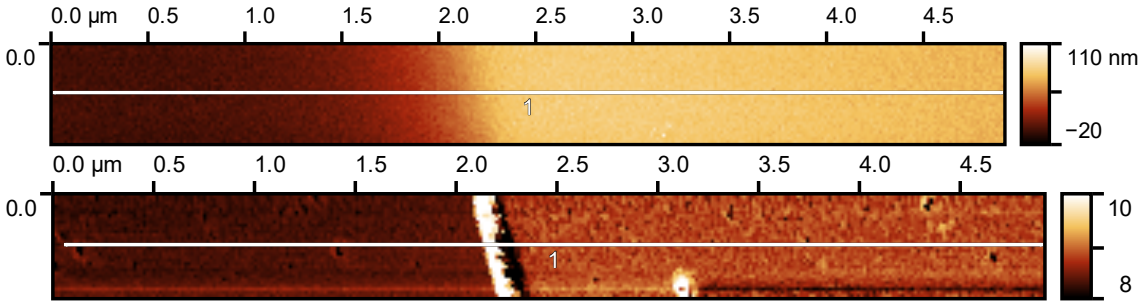


Figure 5.70: Vertically mounted probe scan of step edge sample using the STP method. Topographic output (Top) and 3ω probe response as a percentage (Bottom).

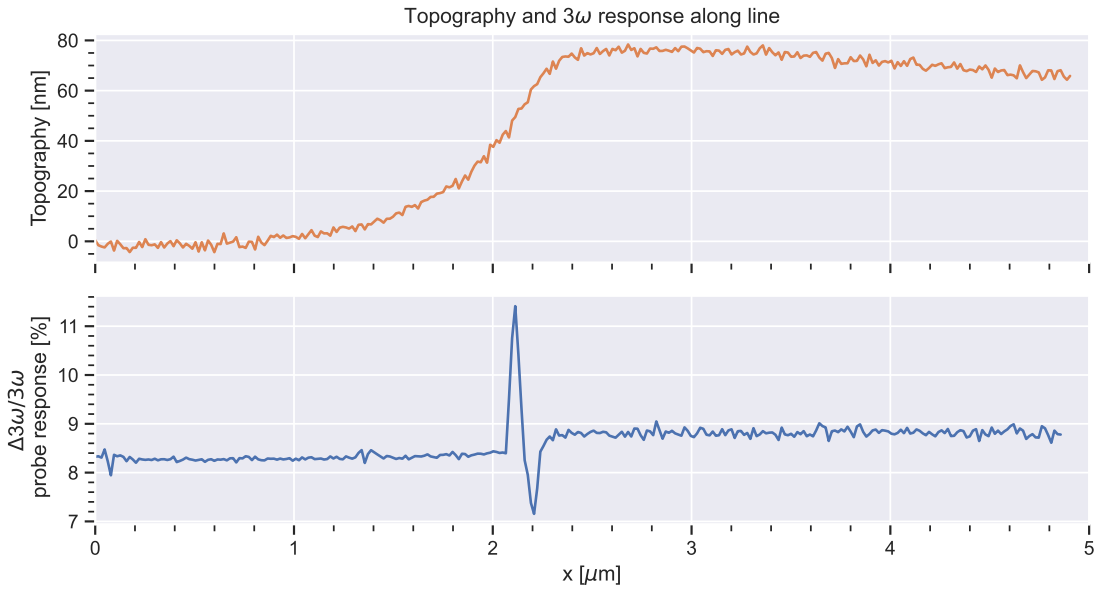


Figure 5.71: Extracted lines from Figure 5.70

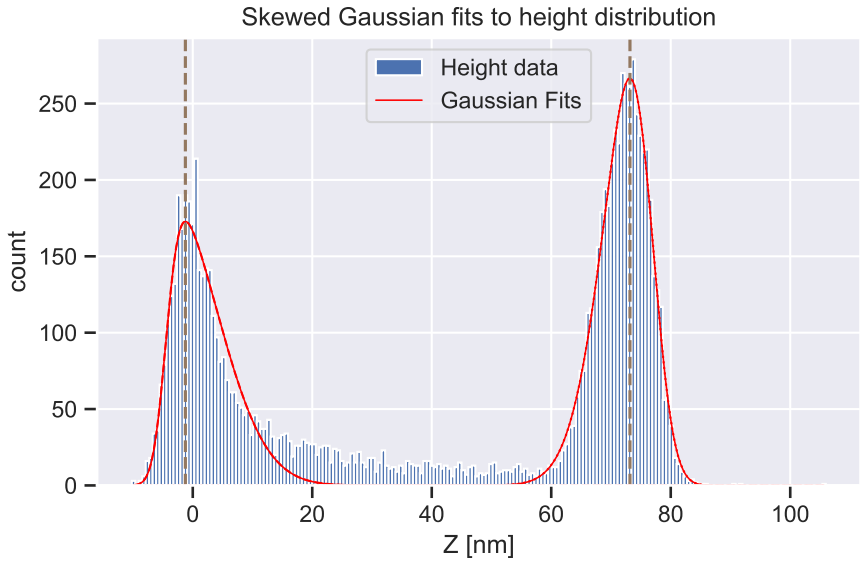


Figure 5.72: Histogram of topographic scan in Figure 5.70, showing a measured step height of 74.4 ± 29.49 nm

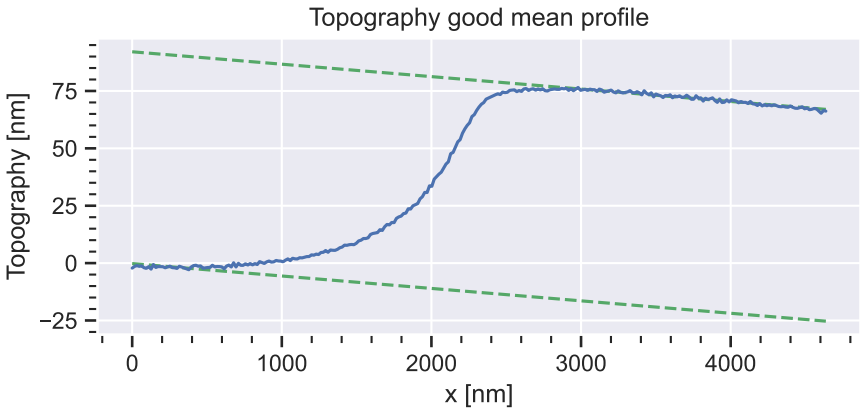


Figure 5.73: Good mean profile of topography channel of Figure 5.70, showing a fitted step height of 92 ± 0.42 nm. Green dashed lines show fitted terraces.

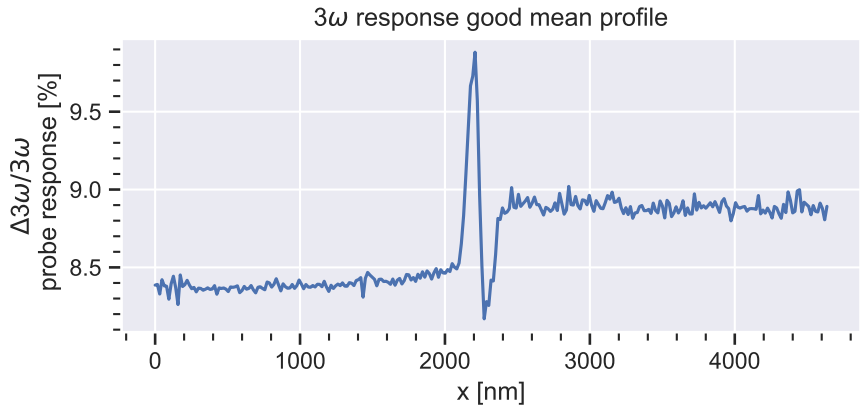


Figure 5.74: Good mean profile of 3ω channel of Figure 5.70

We can see from the topography scan in Figure 5.70, the extracted line in Figure 5.71 and good mean profile in Figure 5.73, that utilising the STP method shows significant smoothing of the step edge over micron distances. Measurement of the step edge height through analysis of the topographic scan's histogram (Figure 5.72) shows a step height of 74 nm, lower than the expected 80-100 nm measurement. However, this disagrees somewhat with the step height measured through terrace fitting in Figure 5.73. It is possible that the start of the scan in this measurement is too close to the step edge to achieve a good fit of the terraces and suffers from not enough data points being on the SiNx to an appropriately sharp peak for accurate measurement.

Smoothing of the edges is expected in the topography scan due to the long-range effects of side coupling of the probe tip to the step edge as it approaches the edge. It can be seen that there is a slight asymmetry to the topography edge, upon approach to the edge there is a smaller. This is indicative of increased coupling of the probe to the step edge due to the higher landing angle of the probe. As there is now less bulk cantilever coupling to the sample, the response settles quickly.

Looking at the probe's 3ω response in Figure 5.71 and 5.74, we still see the expected edge artefacts that were present in the thermal discontinuity method. The same 0.5% rise in response from 8.4% to 8.9% is observed.

The step edge was also scanned utilising the ramp method with acquired data visible in Figure 5.75 through 5.79.

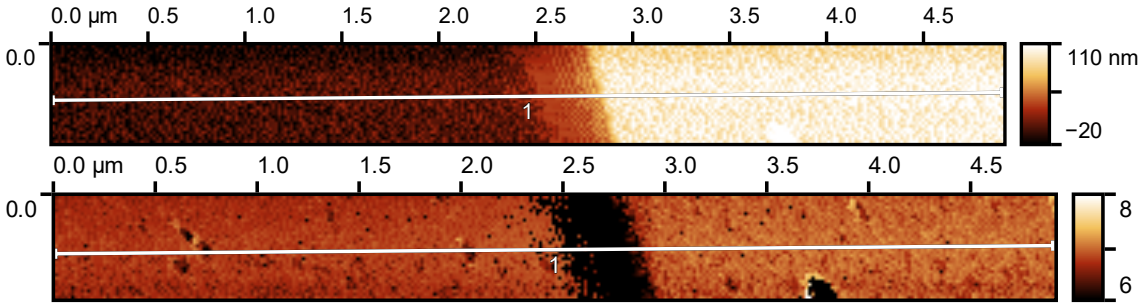


Figure 5.75: Vertically mounted probe scan of step edge sample using the ramping method. Topographic output (Top) and 3ω probe response as a percentage (Bottom).

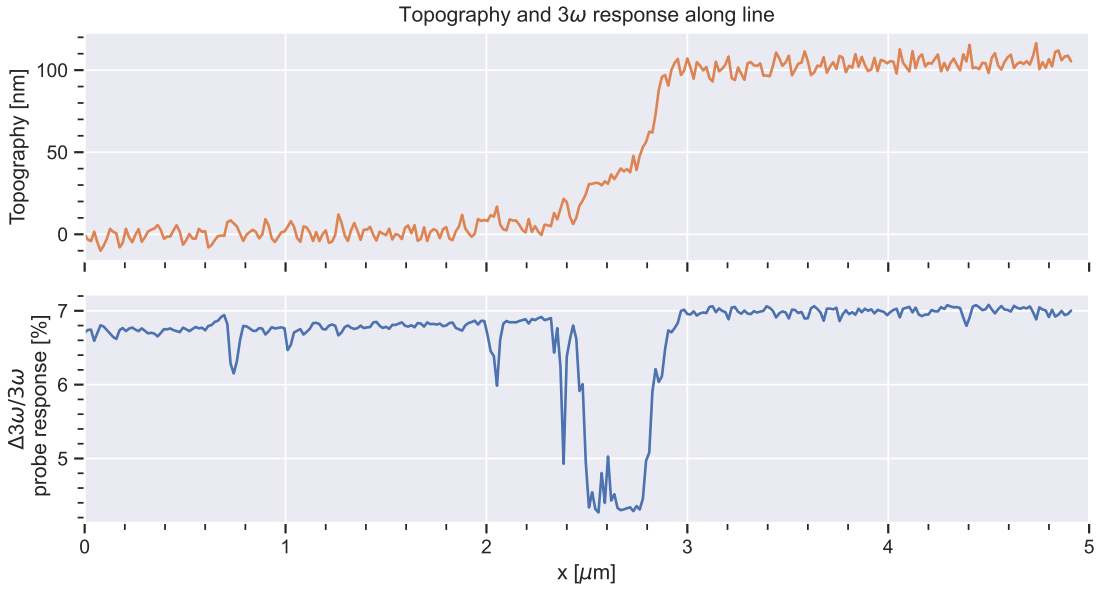


Figure 5.76: Extracted lines from Figure 5.75

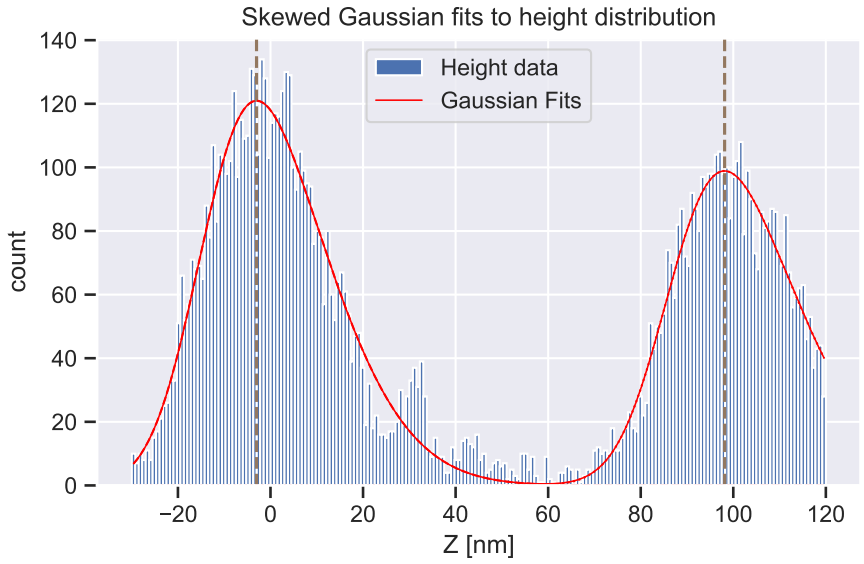


Figure 5.77: Histogram of topographic scan in Figure 5.75, showing a measured step height of 100.89 ± 41.97 nm

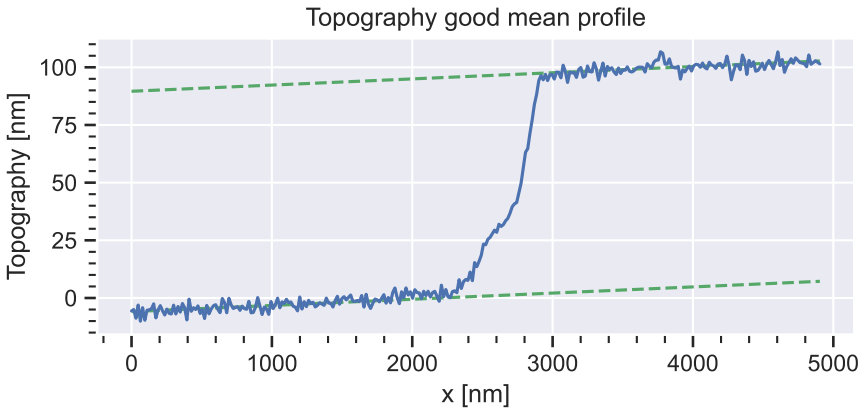


Figure 5.78: Good mean profile of topography channel of Figure 5.75, showing a fitted step height of 95.52 ± 0.93 nm. Green dashed lines show fitted terraces.



Figure 5.79: Good mean profile of 3ω channel of Figure 5.75

As seen in Figure 5.75, 5.76, and 5.79, the probe 3ω response is somewhat minimal with a general lower mean in the probe response by roughly 1%, as well as a lower change in probe response of 0.2% when atop the gold step when compared to other methods utilised. The root cause of this is most likely due to miss-calculation of the 3ω calibration values required in this method and/ or change in this value over the scan due to potential sensor damage from tip rolling.

Noise levels in the topography channel of the scan in Figure 5.75 can be visually seen to increase slightly, analysing the histogram of the topography scan in Figure 5.77, shows a larger spread in the two peaks from this increased topographic noise. Increased noise levels using this method is expected as previously described in section 4.5.4. However, the measured step height from this method can be determined to be 101 nm, far above what is expected.

Interestingly, the area around the edge shows very low little to no response. It's been hypothesised that this edge artefact arises from actuation of the probe, causing premature contact of the probe with the step edge during an approach. This causes the control loop to think it is in contact when it is hovering just above the surface.

5.8 Results discussion

Using techniques described in chapter 4 to capture the point of contact between the probe tip and sample, various samples were scanned to determine the thermal feedback SThM's measurement capabilities in various conditions.

All techniques were utilised for scanning a topographic mono-material sample consisting of anisotropicly etched silicon pillars. Topographic analysis of the pillars was carried out using the ramp and thermal discontinuity techniques and showed typical artefacts of the probe shape to that reported in the literature. With the exception of the STP technique of determination of the sample topography, all pillar heights agree to topography measurements taken of the sample by a commercial AFM. However, it has been shown that sample roughness measurements could be an order of magnitude higher than that obtained on a commercial AFM. This can be a result of the probe technology platform not being optimised for topography measurements, unlike the probe used in the commercial system, and the use of a piezo stage, with only a stated closed-loop resolution of around 20 nm. As expected, all methods show typical thermal artefacts near pillar edges.

The STP technique does show very low-resolution topography, but it remains a fast technique for quick measurements. For instance, one could potentially use it as a coarse measurement over a large area to find the relevant scan area, before moving to a slower, higher resolution, method for a more accurate topographic and thermometry study.

The techniques presented also work on multi-material samples, such as a lithographically defined step from SiNx to NiCr/Au (10 nm/70 nm). Again, typical thermal artefacts are again visible in the scans obtained. An increase in 3ω probe response can be seen upon stepping up onto the NiCr/Au. However, thermometry measurements of both the silicon nitride surface and the gold surface show a large spread of values, with overlaps in the probe response histogram visible.

As SThM is primarily utilised as a method to measure the thermal properties of a sample, an experiment involving a microheater was carried out. This was to determine the effect of sample temperature on each topography measuring technique. It was found, due to the slight temperature dependence of 3ω that methods that rely on an initial calibration value of 3ω unsurprisingly also show temperature-dependant artefacts in the topography output, in some cases, this leads to incorrect measurement of the sample surface location in space and "in contact" thermographic measurements actually being taken out of contact.

Utilising a method that does not rely on calibration values of 3ω, such as the thermal discontinuity method, shows temperature dependence in the topography output in the order of expected cantilever bend due to the bi-material nature of the KNT probes used.

As a proof of concept measurement, a VCSEL was scanned in the system. Such measurements are not routinely available in optical lever systems, due to interference of the optical lever laser, as well as possible illumination of the quadrant photodetector by the VCSEL. Comparing the topography of the sample to that obtained in a commercial AFM, we see similar results of the cavity depth of around 1 µm. However, we see significant smoothing of the sidewalls from the convolution of the relatively wide tip of the KNT probe.

Due to the temperature dependence of the methods and probe, the device topography was determined at each pixel with the laser off, before switching through various laser states for temperature measurements. The thermal bend of the cantilever was observed to engage/disengage at points of double contact in the cavity. As we have measurements of the laser states at each pixel, we can determine the purely optical change in probe response due to increases in the laser power.

Finally, alternative probe mounting positions were examined to artificially change the probe parameters. It was shown to artificially stiffen the cantilever in the approach axis, reducing adhesion effects, and possibly enabling the improved access to deep trenches. Stiffening of the cantilever still shows significant smoothing of the edge when scanning utilising the STP method, as well as introducing extra edge artefacts when utilising the ramp method.

To summarise the experiments presented and discussed in this chapter, topographic control of the SThM has been achieved in ambient air conditions for the purposes of raster scanning samples while collecting topography and thermography measurements. The strengths and weaknesses of all methods proposed have been discussed. However, measurements with respect to material studies have proven difficult to characterise in air. Air is not the only environment that SThM studies are carried out in, other common environments that SThM measurements are carried out in include in vacuum and under liquid. Reliable topographic control utilising thermal feedback of the SThM must also be achieved in these environments.

Topographic scanning using the 3ω signal under liquid and in a vacuum

6.1 Introduction

As stated previously in section 5.4, materials characterisation using SThM in air is limited. This is primarily due to inconsistencies in the surface contact area and influences of contamination/hydration layers culminating in a large spread in the 3ω values [180]. Materials characterisation is best suited to either vacuum conditions where point contact is the primary mode of heat transfer and air conduction is zero [3, 56, 61, 157, 192], or liquid where tip and contact shape artefacts are less influential as most of the heat transfer occurs through liquid conduction [3, 173, 193, 194]. Therefore it is important to evaluate the self-sensing capabilities of the probe tip-sample contact point in these environments.

This chapter has been split into measurements first taken in liquid, before moving on to measurements taken in vacuum.

6.2 Topographic control under liquid

Liquid SThM (sometimes referred to as immersion SThM or iSThM) has been recently developed to provide a means of accurate materials characterisation [4, 54, 173, 193, 194]. The thermal resistance network for liquid operation is available in Figure 6.1, noting that R_{air} has now been modified to R_{liquid}. Due to the nature of most liquids having a greater thermal conductivity than gases, R_{liquid} and R_{env} have a much smaller thermal impedance. This reduces the parallel effects of R_c and R_p

from the measurement.

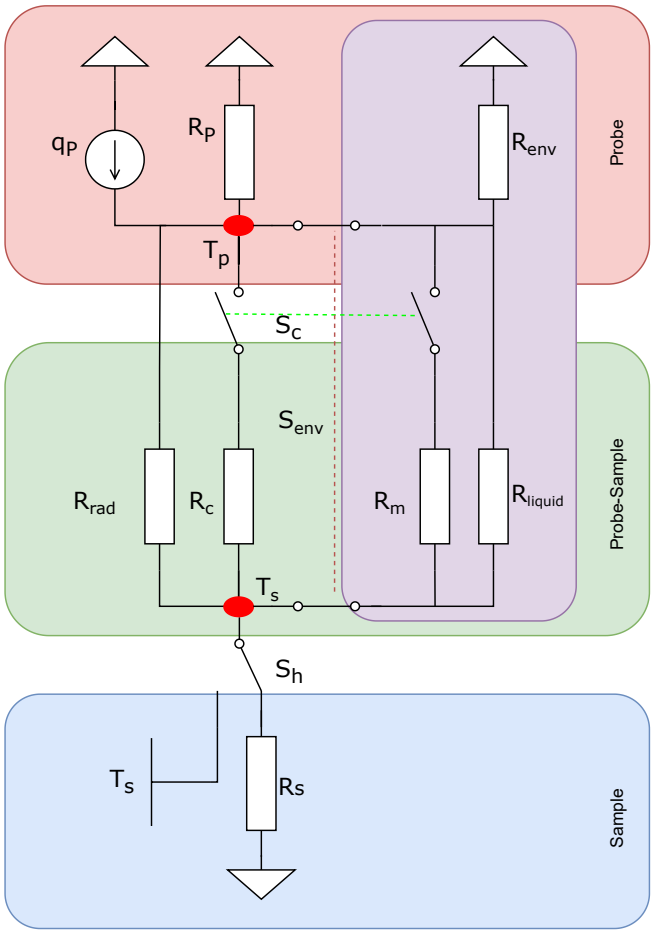


Figure 6.1: Thermal resistance model in liquid. Note, the change from R_{air} to R_{liquid}

6.2.1 Design

This section looks to acquire topographic control of the SThM while immersed in liquid conditions under perfluoro-1,3-dimethylcyclohexane, sold commercially as Flutec PP3[1] by F2 chemicals (Lea town, UK). Flutec is a non-flammable, electrically inert liquid with a low surface tension. This allows enhanced liquid coupling between the probe to the sample without complicated transformer-isolated probes that would be required if immersed in water, such as those utilised by Dobson et al. [195] and Tofani [173].

The surrounding setup remains the same as scans conducted in air. A container was constructed out of epoxy resin on the sample stage so that samples could be easily inserted/removed and flooded with Flutec PP3, while allowing probe access to the

[1] https://www.f2chemicals.com/perfluoro-1,3-dimethylcyclohexane.html

sample. The probe was placed on an extended probe arm constructed from FR4 as seen in Figure 6.2, 6.3 and 6.4. During scanning, cling film was wrapped around the container opening in an attempt to reduce the rate of Flutec evaporation.

The inclusion of the extended probe arm slightly increased the thermal instability of the setup, slight drifts of the X and Z axis were introduced to the scans with temperature. This was primarily due to the cantilevering effect of the FR4 expanding with temperature. However, the control loops utilised accommodated expansions in Z fairly robustly. Artefacts of Z drift with temperature in the resulting scan images were compensated for by post-processing in Gwyddion through path levelling.

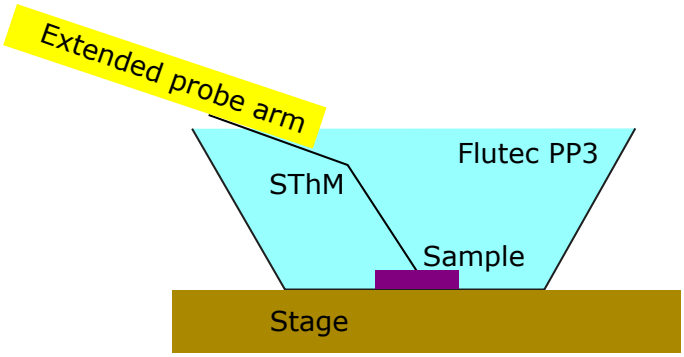


Figure 6.2: Simplified diagram of SThM liquid setup. A container made from epoxy is constructed on the stage and the sample is affixed to the bottom and contained filled with Flutec PP3. The probe is placed on an extended arm to allow better access to the submerged sample.

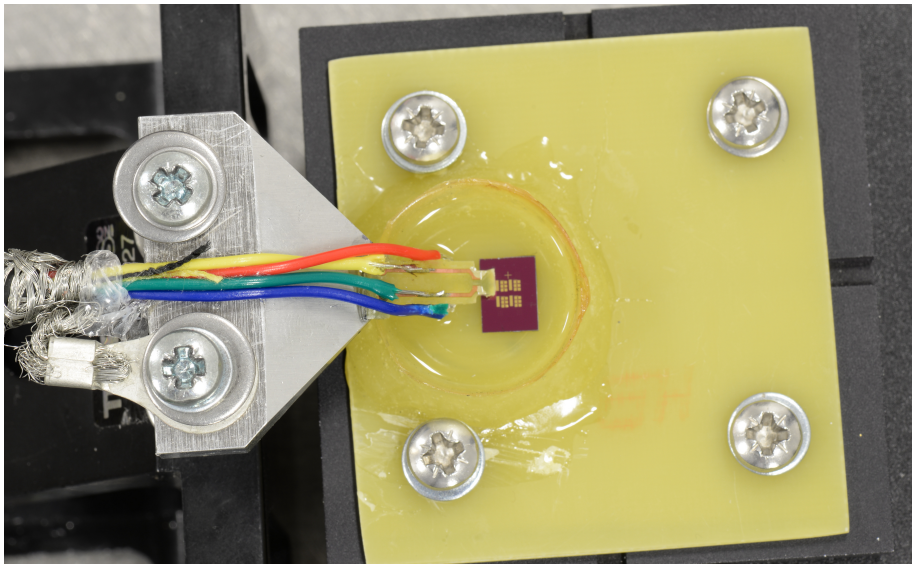


Figure 6.3: Top down photo of the liquid SThM setup, A well is created out of epoxy where the sample is placed inside and flooded with Flutec PP3.

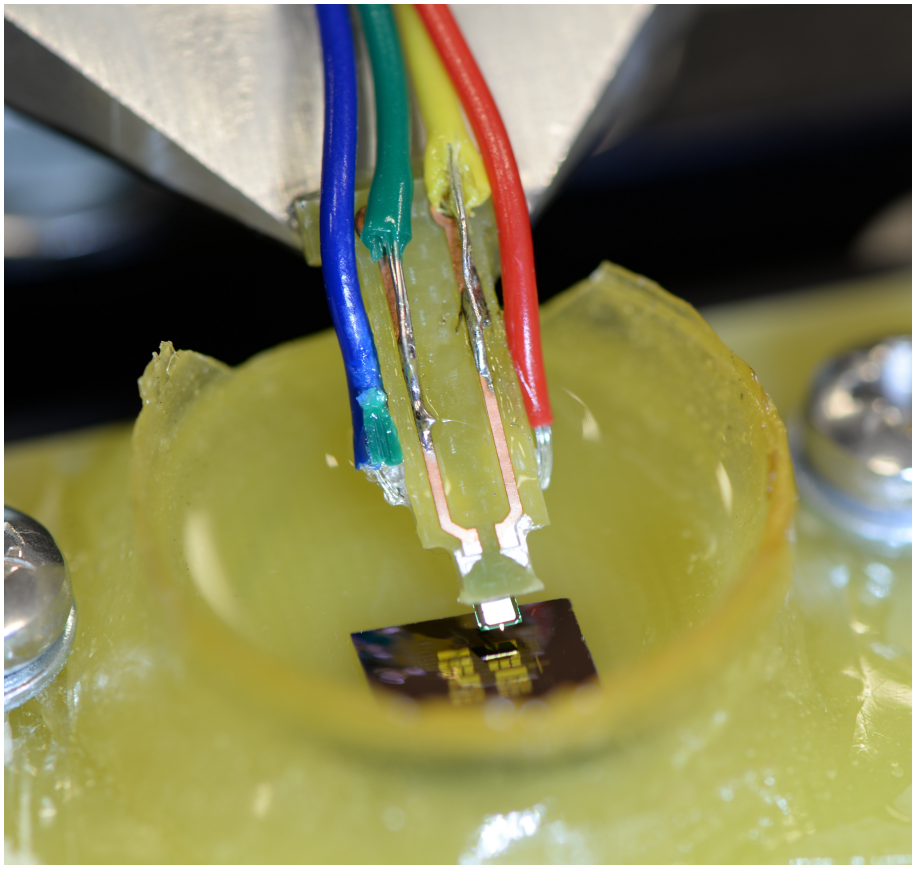


Figure 6.4: Side view photo of the liquid SThM setup, Showing probe extension arm and probe mounting.

6.2.2 Noise analysis

Similarly to measurements in air, one must quantify the noise levels in the system under liquid conditions to allow for an accurate interpretation of the results obtained.

To analyse the noise of the system 1000 measurements were taken at least 5µm out of contact, and moved into contact at a frequency of 336 Hz, and a probe power of 80 µW. Results of which can be seen in Figure 6.5 with measurements of mean, standard deviation, and coefficient of variation tabulated in Table 6.1.

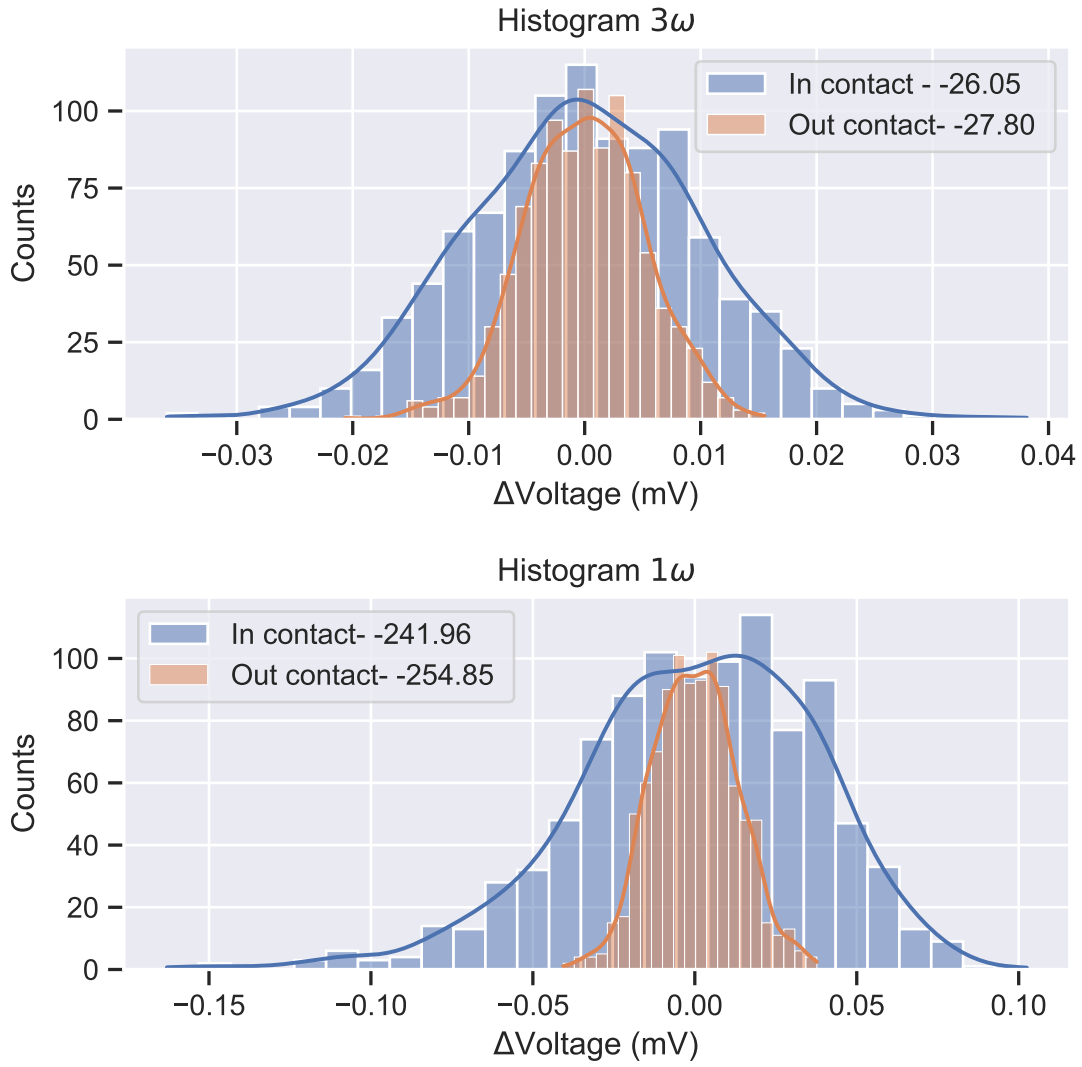


Figure 6.5: Histogram of 1000 sequential measurements at a ddsn of 4 at 336 Hz in and out of contact

Table 6.1: Tabulated statistical results from 1000 measurements of the 1ω and 3ω signals in and out of contact

Signal	Mean [mV]	pk-pk [µV]	Std Dev [µV]	CV [%]
$3\omega_{out}$	-27.79	78	5.1	0.018
$3\omega_{in}$	-26.04	265	10.09	0.038
$1\omega_{out}$	-254.8	36	32.96	0.005
$1\omega_{in}$	-241.95	74	37.24	0.015

In common with SThM in air, 3ω thermometry signals show approximately Gaussian distribution with an approximate 6% change in mean value from out of contact into contact. This signal is also still very stable in liquid with a CV of 0.04% over the measurement period.

Interestingly, looking at the in-contact measurements of 3ω in Figure 6.6, no drift in the measurement is visible during the measurement time period. Either the previously seen drift observed in the contact measurements in air (section 4.4.1) is below the noise floor in the liquid setup, or this acts as further confirmation of the hypothesis in that these drifts in the contact measurement in air were a result of nano-bridges of liquid changing the conduction of the probe to the sample.

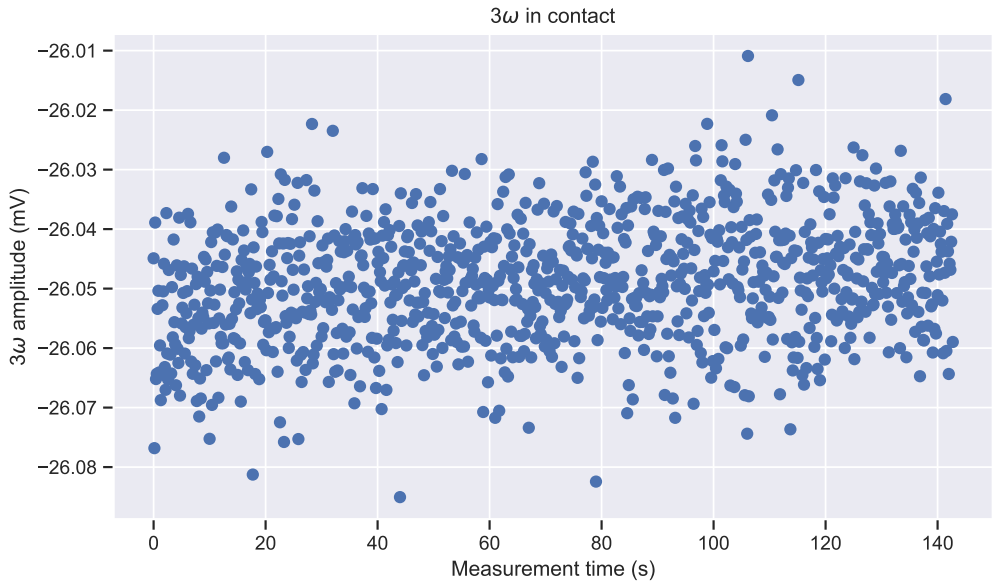


Figure 6.6: No drift over measurement of 3ω at ddsn of 4 at 336 Hz in contact observed.

Repeating these noise measurements in and out of contact while increasing the DDS up to approximately 3 kHz shows stability in the out-of-contact 3ω signal across all frequencies and shows a similar profile to that obtained in air in section 4.4.1. Coefficients of variation for the 3ω signal are available in Figure 6.7 and Figure 6.8. A large noise profile is visible in the noise spectrum at 112 Hz and 224 Hz in the contact measurement in Figure 6.8, which shows a vaguely similar profile to the in contact 3ω measurements in air and vacuum. The increased coupling of the probe to the sample shows an increase in the lower frequency noise. The mechanisms for this increased noise level at lower frequencies still remain unclear. It is possible that thermal bending caused by joule heating could potentially cause self-actuation of the probe at these frequencies in such a way as to move air or liquid around the probe tip resulting in increased noise. Removing these outliers shows Figure 6.9, where a clear minimum can be seen in the measurement around 1 kHz.

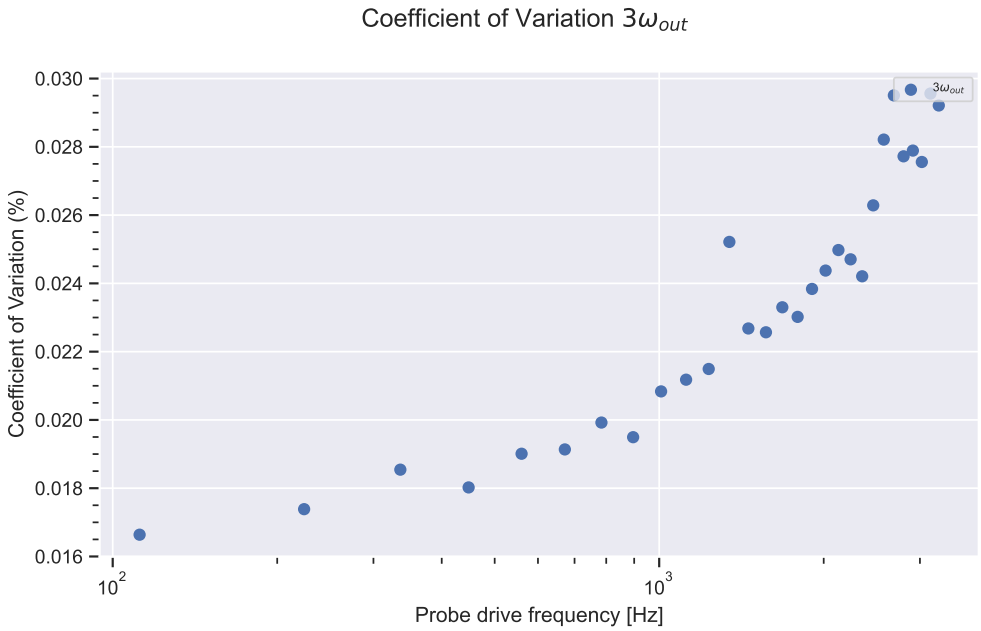


Figure 6.7: 3ω coefficient of variation values (expressed as a percentage) for out of contact across available frequencies

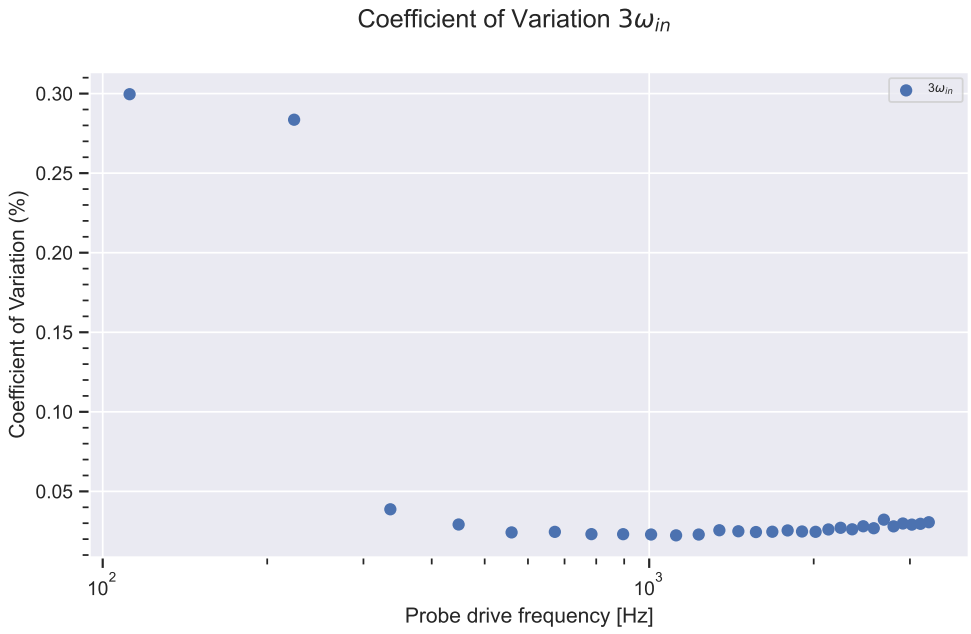


Figure 6.8: 3ω coefficient of variation values (expressed as a percentage) for in contact across available frequencies

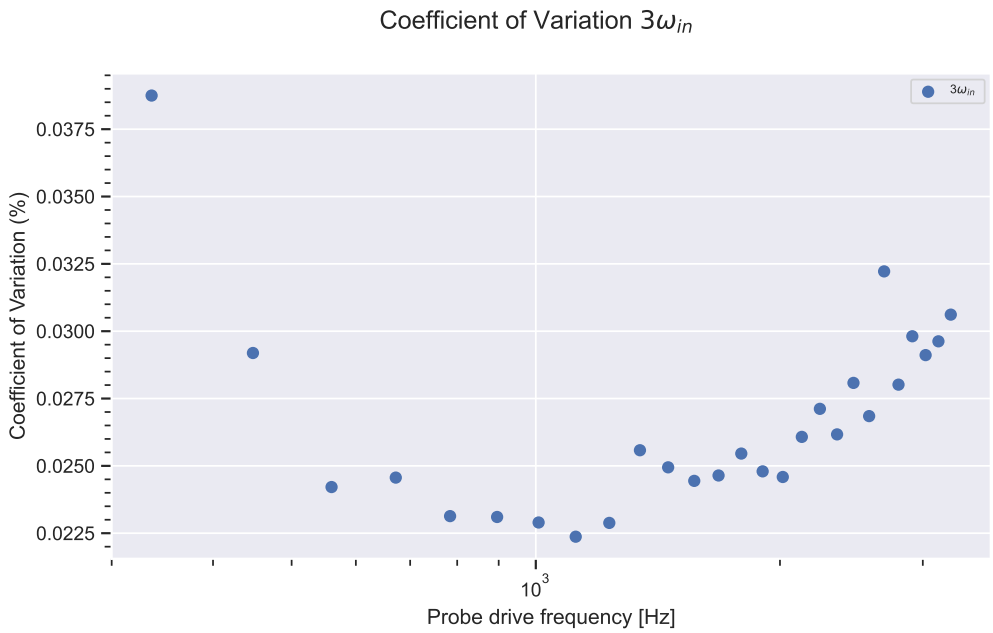


Figure 6.9: Reduced set of 3ω coefficient of variation values (expressed as a percentage) for in contact measurements

As described in Figure 6.1, heat transfer paths have significantly changed when immersed in liquid, therefore the probe frequency response must also be qualified. Measuring the probe frequency response from the out-of-contact to in-contact measurement we can see the relation in Figure 6.10 and Figure 6.11.

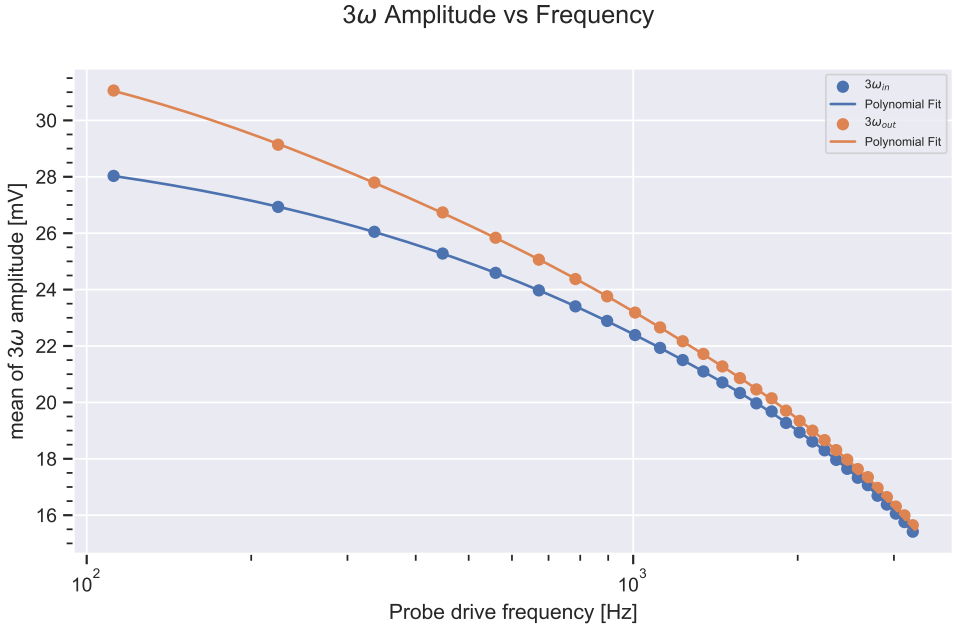


Figure 6.10: Mean 3ω values in and out of contact for various probe drive frequencies in liquid

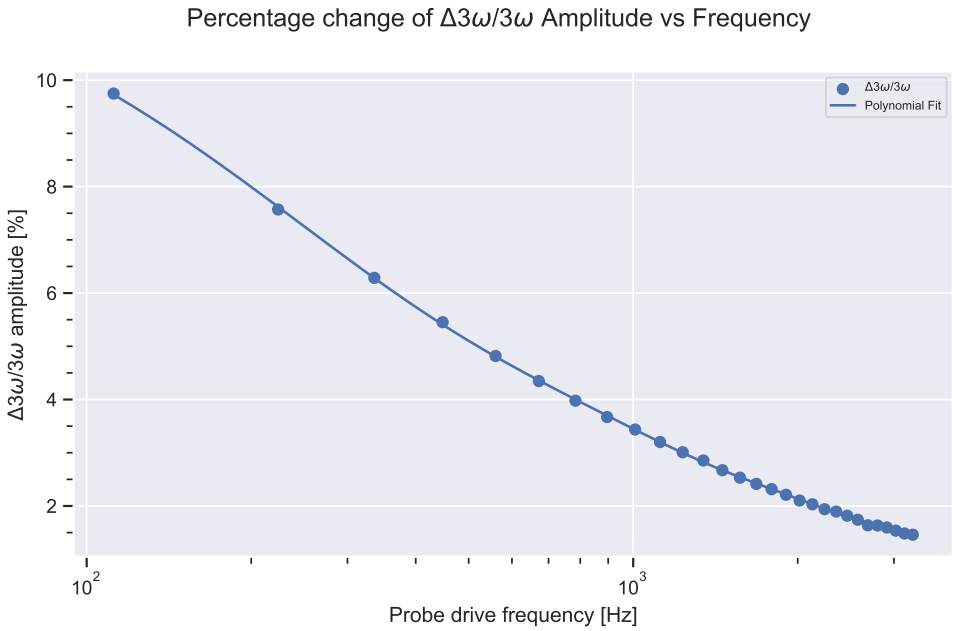


Figure 6.11: Mean 3ω values in and out of contact for various probe drive frequencies in liquid expressed as a fractional percentage change from its out-of-contact measurement

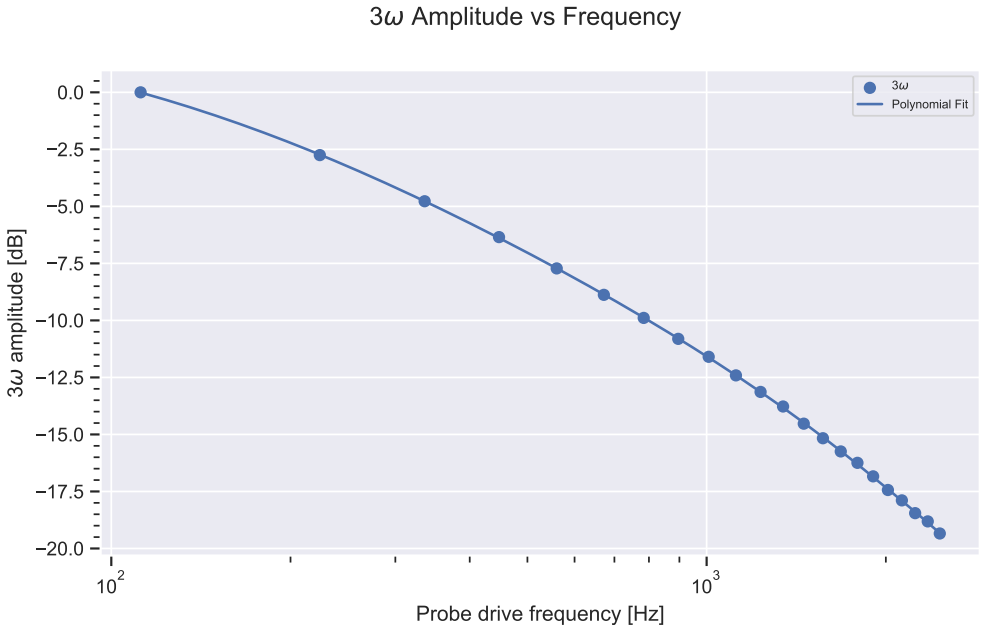


Figure 6.12: Fractional change of probe thermal response expressed as a Bode plot, 0dB point is the response of the lowest frequency available from the DDS output.

It is clear that the probe 'scalloping' profile that was seen with probe responses in air is no longer in effect. Primarily this can be attributed to the change in thermal heat extraction paths, in particular, heat extraction through liquid to the environment is now the primary source of heat loss, so geometric effects of the probe are less influential.

6.2.3 Curve analysis

Probe land and retract curves were taken at various drive frequencies to analyse the requirements for surface detection in a control loop. Figure 6.13 shows the change in the 3ω signal as the probe approaches the surface at a probe drive frequency of 112 Hz. The low noise level of the out-of-contact 3ω is clearly visible. Once contact is made the noise level of the signal can be seen to increase slightly. As discussed previously in the thermal resistance model under liquid, R_{liquid} is now the dominant thermal transfer mechanism between the probe and sample. When the probe body is advanced past tip-sample contact, even to extensions of over 2 µm (400-800 nN of force), very little change in the signal can be seen, showing that contact force or shape is not the main mechanism for thermal transport.

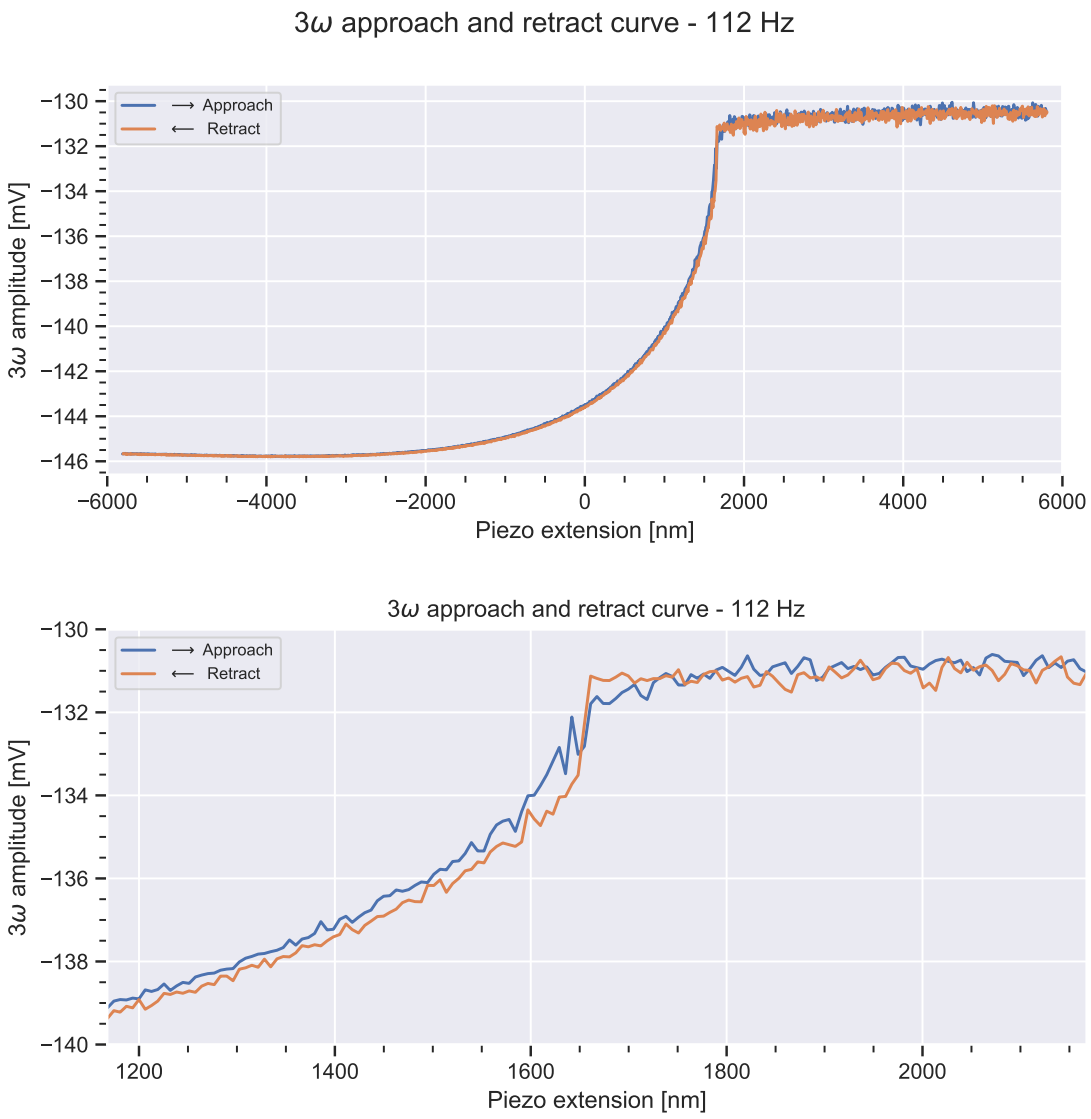


Figure 6.13: Monitoring the 3ω signal as the probe approaches and retracts from the sample surface, at a probe drive frequency of 112 Hz over the full piezo range (Top). With a zoom (bottom) of the contact point.

It can be seen that there is a slight decrease in the 3ω signal on approach before the increase in amplitude towards contact. This is much clearer at higher frequencies such as that in Figure 6.14 and 6.15, and as is most likely related to the diffusivity of Flutec.

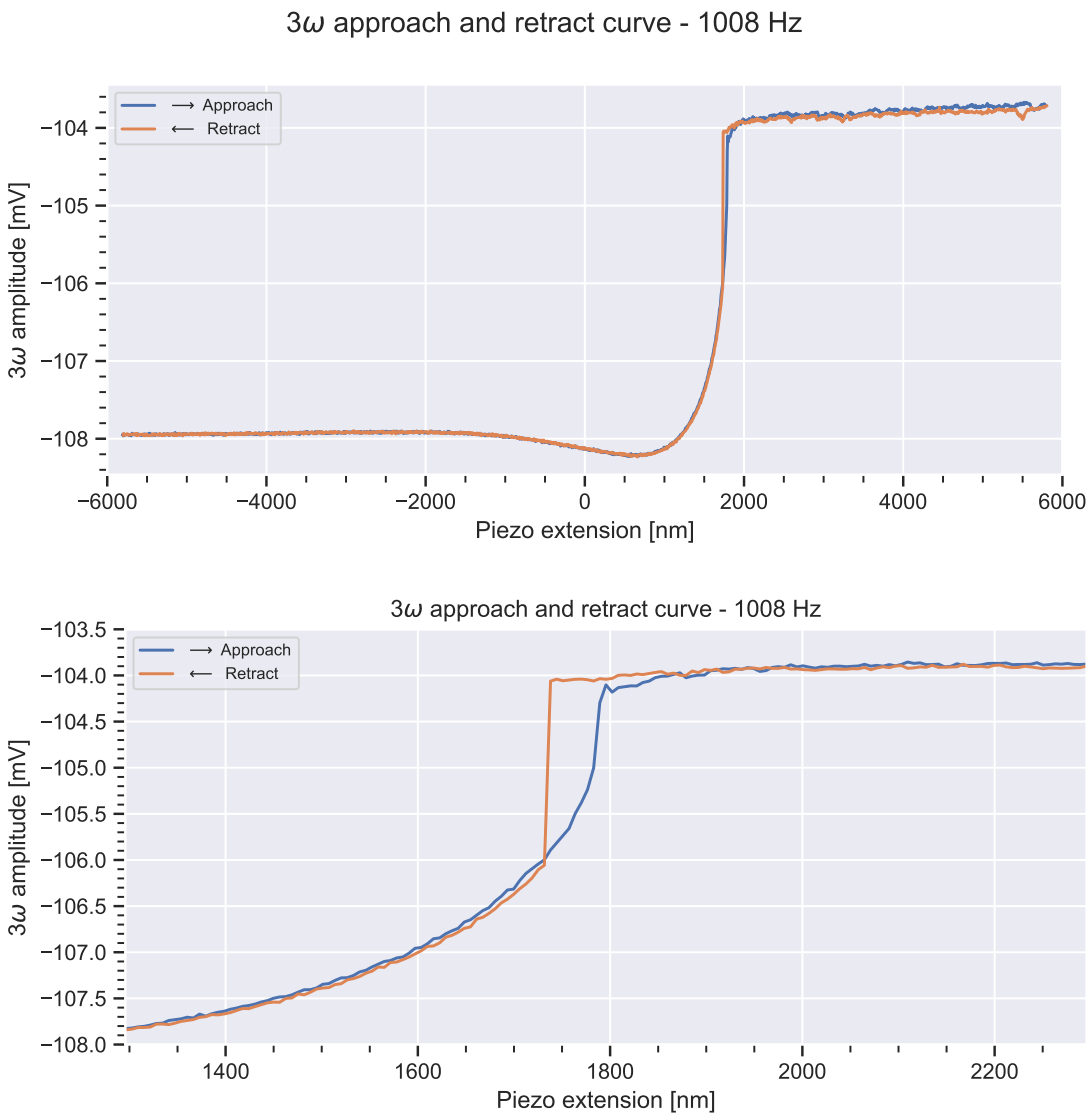


Figure 6.14: Monitoring the 3ω signal as the probe approaches and retracts from the sample surface, at a probe drive frequency of 1 kHz.

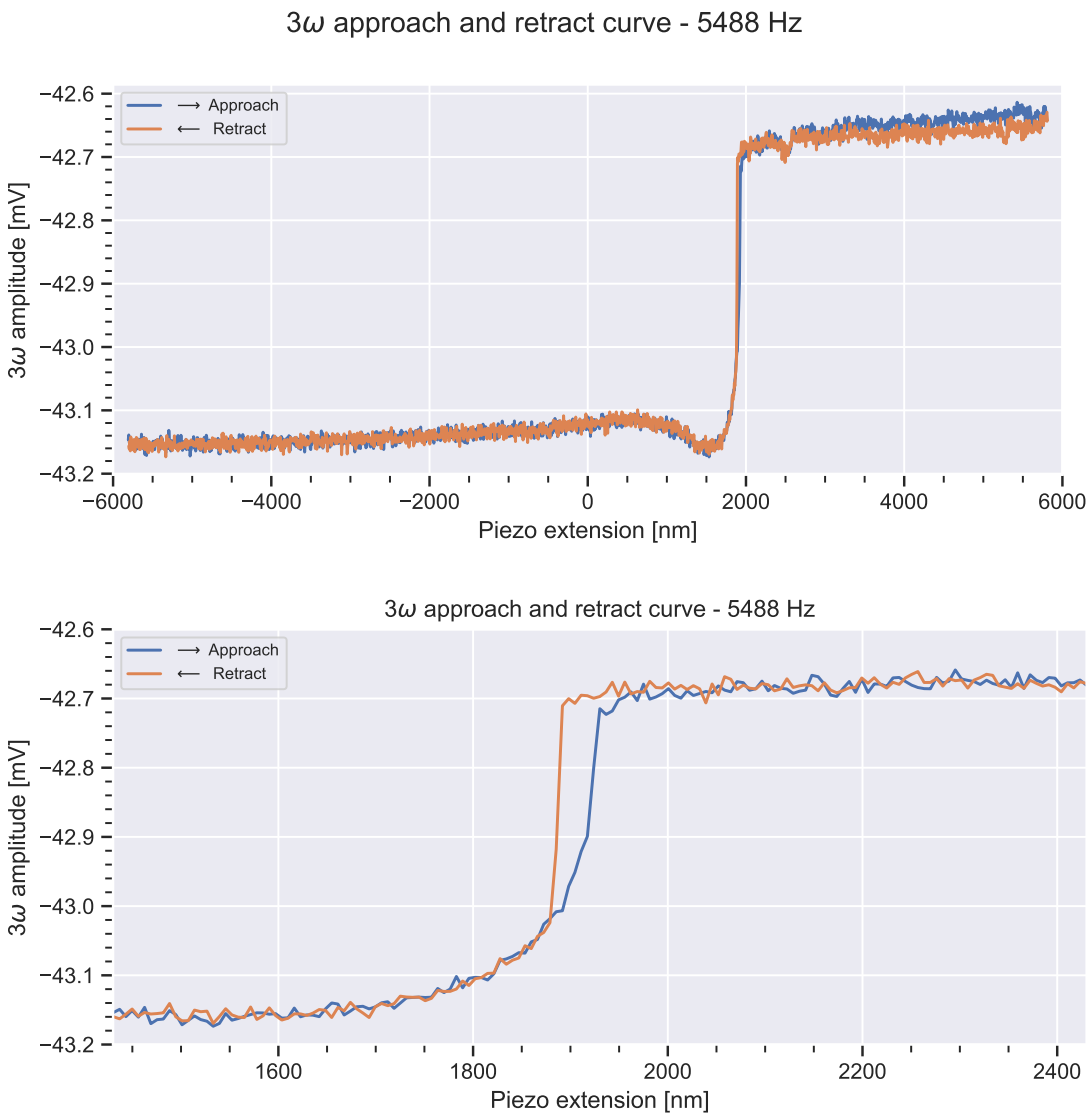


Figure 6.15: Monitoring the 3ω signal as the probe approaches and retracts from the sample surface, at a probe drive frequency of 5.4 kHz.

One should also note the decrease in hysteresis in the approach and retract curve in Figure 6.13 when compared to measurements in air. This is due to the absence of a water meniscus causing adhesion of the probe tip to the surface while under liquid. However, some contamination/hydration layers or electrostatic adhesion may still exist which shows slight hysteresis around the contact point, particularly at higher frequencies.

One can use similar methods to surface detection as that in air through monitoring the gradient of the 3ω signal. To reduce the effect of out-of-contact / in-contact noise on the gradient measurement, it was found that the best practice was to utilise linear regression to fit a gradient line to a rolling window of the eight previous

measurements on an approach, once a peak has been detected and subsequent gradient measurements reduce by a significant factor, one can infer the surface location to be at the location of the peak. Visual analysis of the gradient in the probe response through this method leads to Figure 6.16 through Figure 6.18, where one can see that the spike in the gradient of the signal aligns with the contact point, making surface detection possible, even with high in-contact noise or higher frequencies (Figure 6.16 and 6.18 respectively).

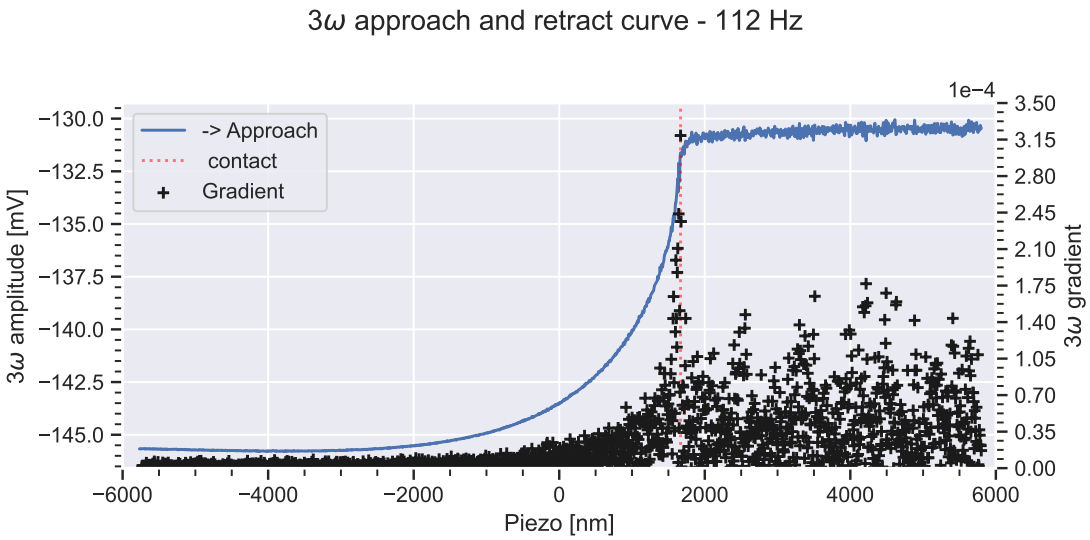


Figure 6.16: Monitoring the gradient of the 3ω signal as the probe approaches the sample surface at 112 Hz

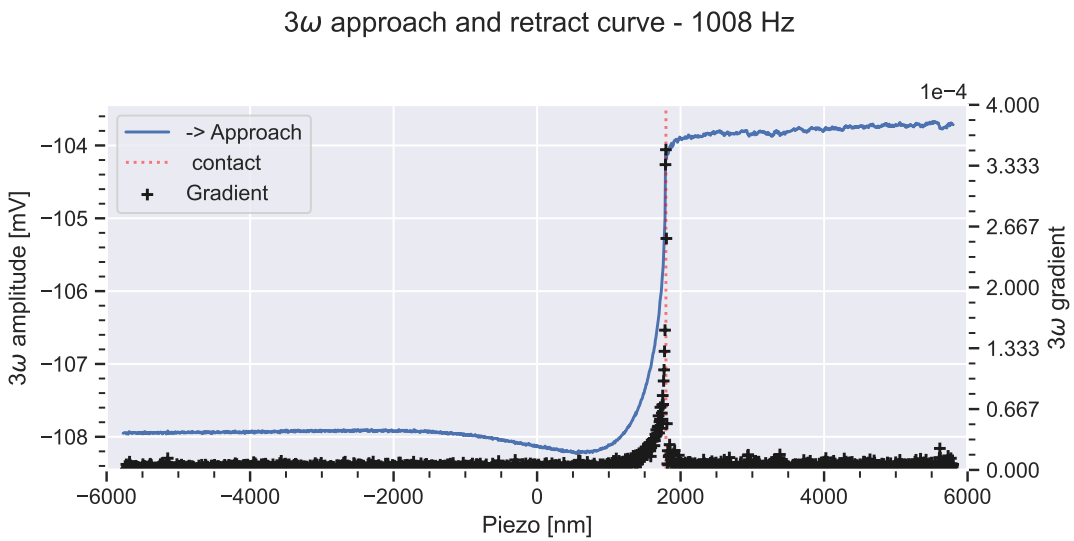


Figure 6.17: Monitoring the gradient of the 3ω signal as the probe approaches the sample surface at 1 kHz

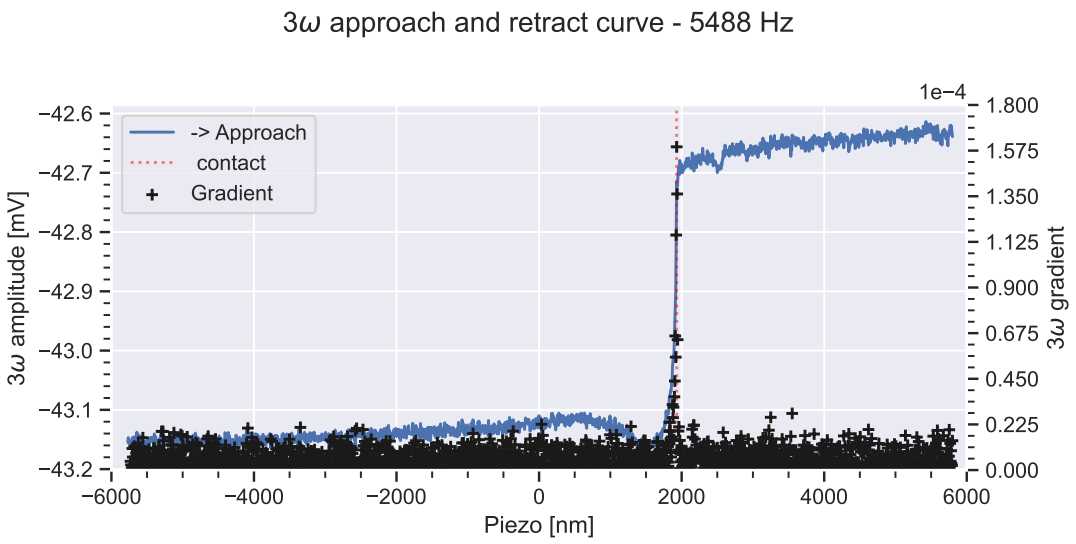
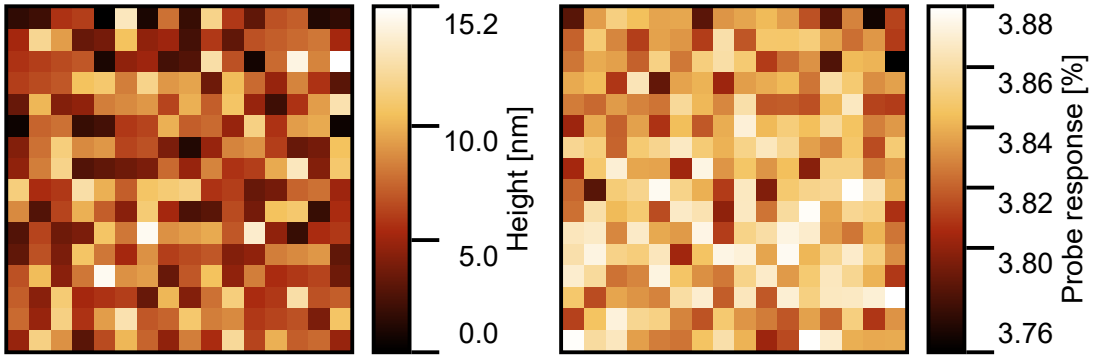


Figure 6.18: Monitoring the gradient of the 3ω signal as the probe approaches the sample surface at 5.5 kHz

6.2.4 Topographic noise

As was done previously with the measurements in air and vacuum, a quick experiment to quantify the ability of the method to detect the surface location by measuring the apparent topographic noise in repeated measurements of a single point was conducted. Utilising a probe drive frequency of 448 Hz and 80 µW probe power, a scan of a single point was obtained utilising the gradient monitoring technique and displayed in a 16x16 grid in Figure 6.19 and histogram in Figure 6.20.



(a) Topographic output of scan showing a Pk-pk noise of 15.2 nm with a standard deviation of 2.94 nm.

(b) 3ω Probe response as a percentage, showing a standard deviation in response 0.022%

Figure 6.19: A single point displayed in a 16x16 pixel grid.

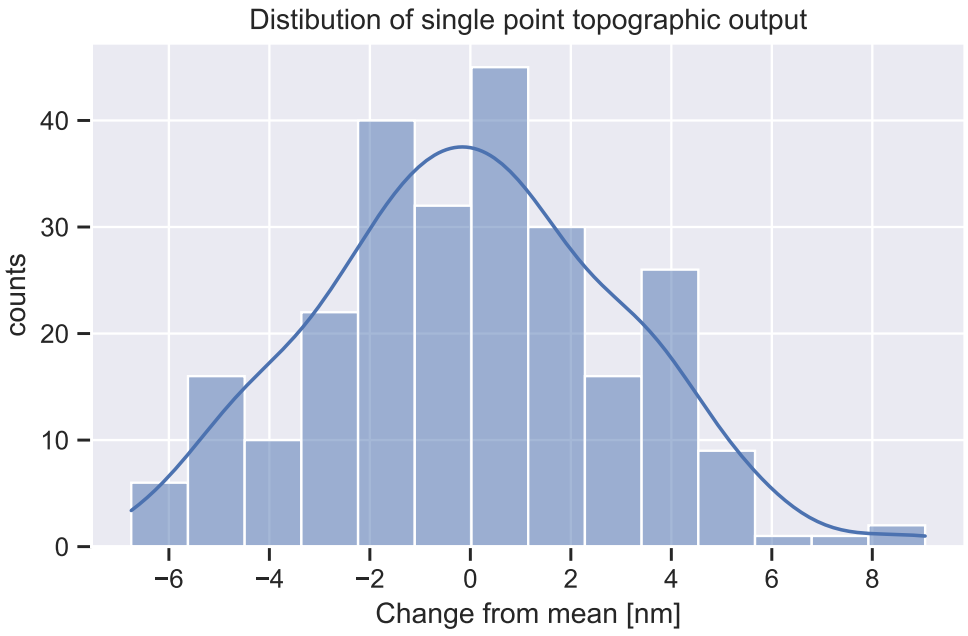


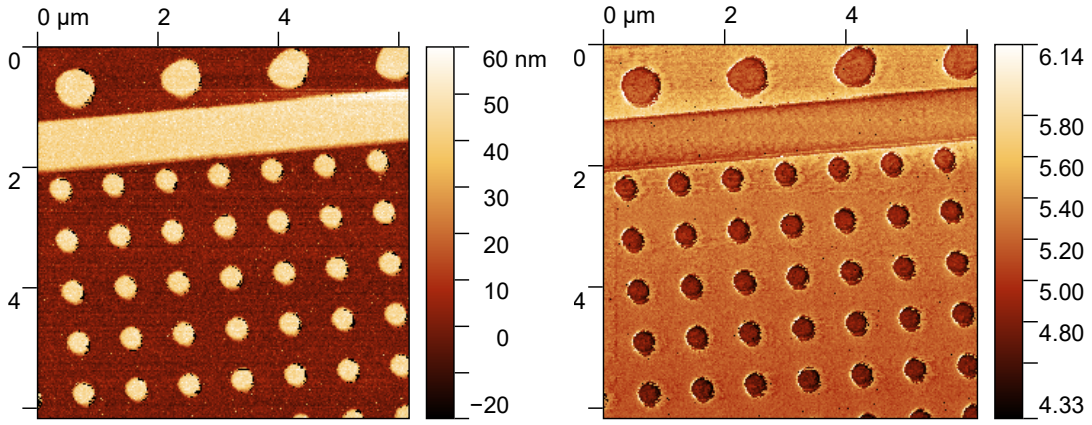
Figure 6.20: Histogram of data points from Figure 6.19a, showing a standard deviation in the topography measurement to be 2.94 nm

It can be seen in Figure 6.19 and 6.20 that the topographic noise of a single point is on par with measurements in air, with an approximately Gaussian distribution in the topography noise. It shows a pk-pk noise of 15 nm with a standard deviation of 3 nm. One can note the very low standard deviation in the thermal measurement of 0.02%, which is on par with measurements taken in air.

6.2.5 Silicon pillar

To compare dark condition liquid topographic control to that obtained air and vacuum, the silicon pillar sample (discussed earlier in section 5.3 and 6.3.5) was scanned under Flutec at a probe drive frequency of 224 Hz using the gradient monitoring method discussed in section 6.2.3. Topographic output can be viewed in Figure 6.21a with 3ω probe response shown in Figure 6.21b.

Displaying the height data of Figure 6.21a as a histogram in Figure 6.22 we can measure a pillar height of 44.3 ± 11.06 nm. However, as with measurements in air, the transition between the two peaks is caused by tip convolution with the pillars which may skew the Gaussian fits.



(a) Topographic output

(b) 3ω probe response output as a percentage

Figure 6.21: Silicon pillar sample scanned under Flutec. The top pillars (above the long bar) are 600 nm diameter pillars, with 300 nm diameter pillars below

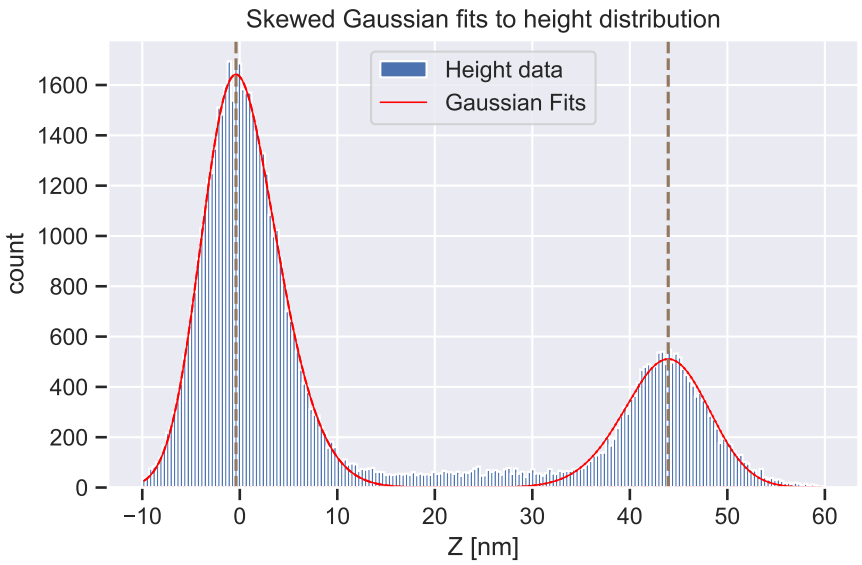


Figure 6.22: Histogram of topography data showing the distribution of height data in Figure 6.21a, Showing a 44.3 ± 11.06 nm pillar height, slightly lower than that measured in air.

To exclude the transition region from the measurement the individual pillar heights can be measured through terrace fitting to radially averaged profiles of the pillars. Figure 6.23 through 6.26 show the pillar profiles and fitted terraces for the 600 nm pillars, with tabulated results in Table 6.2. The results show a mean pillar height of 43.79 ± 2.41 nm.

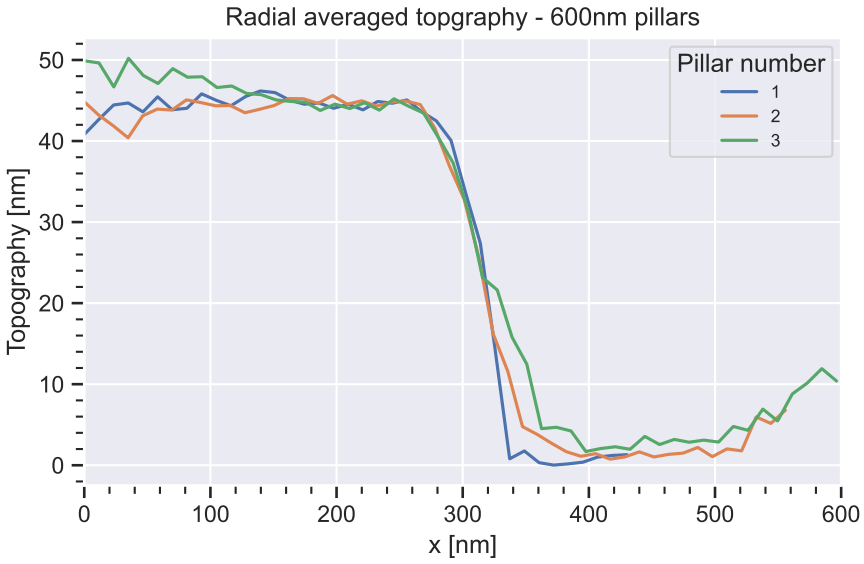


Figure 6.23: Radially averaged measurement of 600 nm pillars scans from Figure 6.21a, numbered from the top left to right. The far right-hand pillar was excluded due to incomplete scanning. 0 nm on the X-axis indicates the centre of the pillar.

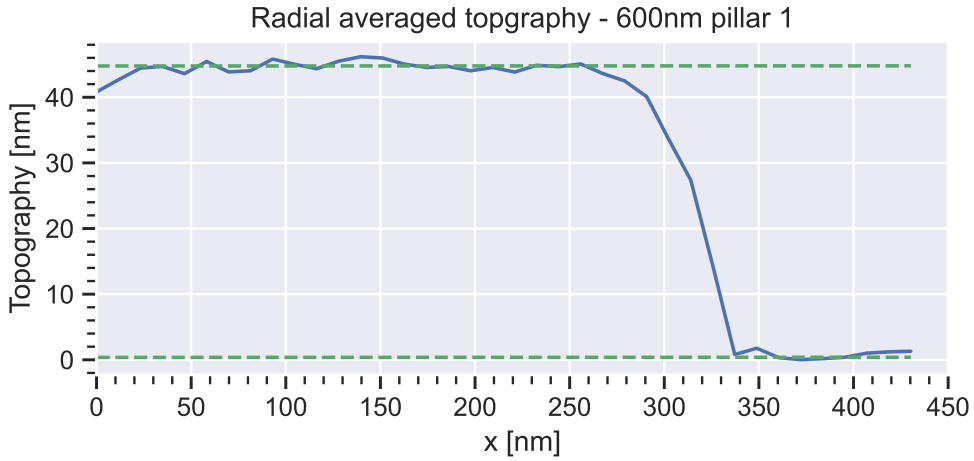


Figure 6.24: Radially averaged measurement of scan 600 nm pillar 1 from Figure 6.21a, measuring 44.4 ± 0.67 nm.

Table 6.2: Tabulated results of terrace fitting to radially averaged 600 nm pillars

Pillar No	Height [nm]
1	44.40 ± 0.67
2	45.07 ± 0.70
3	41.97 ± 2.21

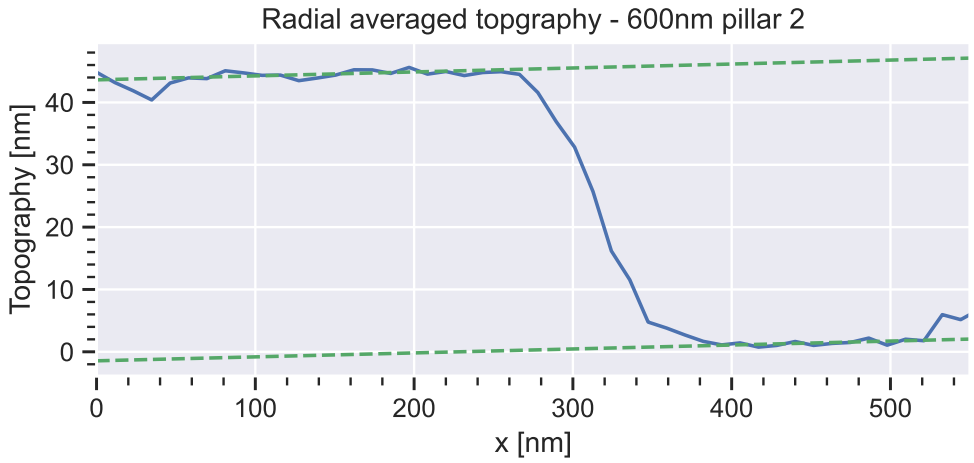


Figure 6.25: Radially averaged measurement of scan 600 nm pillar 2 from Figure 6.21a, measuring 45.07 ± 0.70 nm.

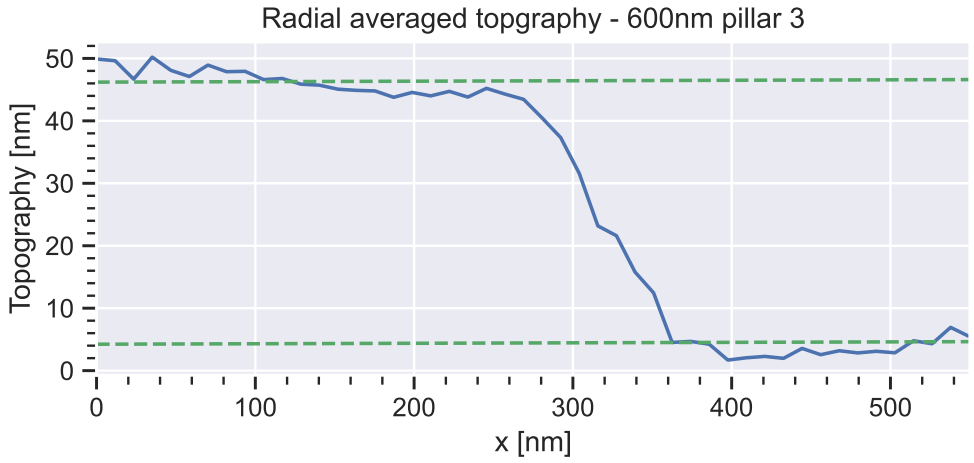


Figure 6.26: Radially averaged measurement of scan 600 nm pillar 3 from Figure 6.21a, measuring 41.97 ± 2.21 nm.

Pillar 3 in Figure 6.23 and 6.26, shows a greater tip convolution than the other pillars. However, the artefact seen is not one of tip convolution, but of slight thermal drift in the X and Y axes of the image (Figure 6.21a) over the first couple of line scans as the stage and setup approaches thermal equilibrium. This greatly distorts the radial

measurement as the circular pillar appears with a slightly elliptical profile.

A similar radial analysis can be carried out for the 300 nm diameter pillars and can be seen in Figure 6.27 through 6.30. Due to the topmost row of pillars being close to the separation bar, they have been excluded from the measurement. The remaining pillars are numbered left to right, top to bottom starting from the second row from the top. Only the first three pillar measurements have been shown, but tabulated results of 20 pillars are available in Table 6.3.

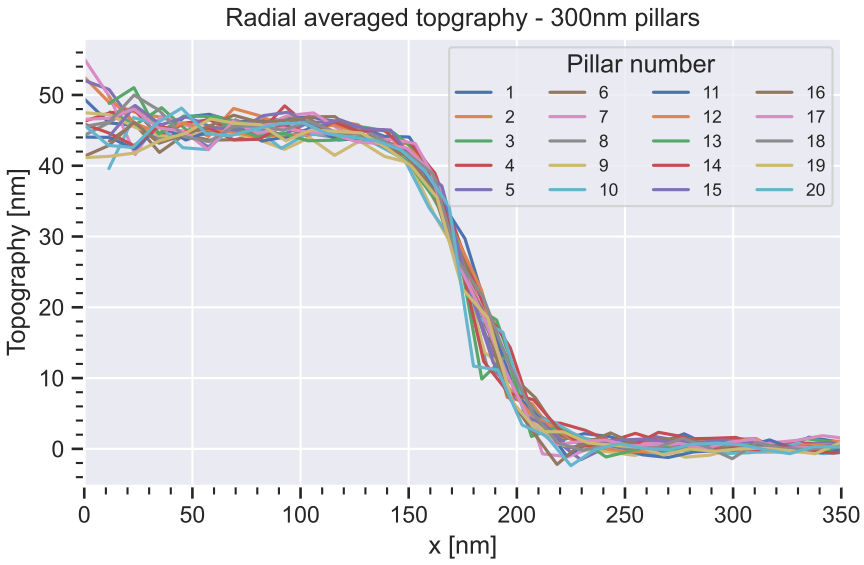


Figure 6.27: Radially averaged measurement of 300 nm pillars scans from Figure 6.21a, numbered from the second row from the top left to right, then top to bottom. Tip convolution in the 50-100 nm range can be seen over the transition region between pillar apex and base.

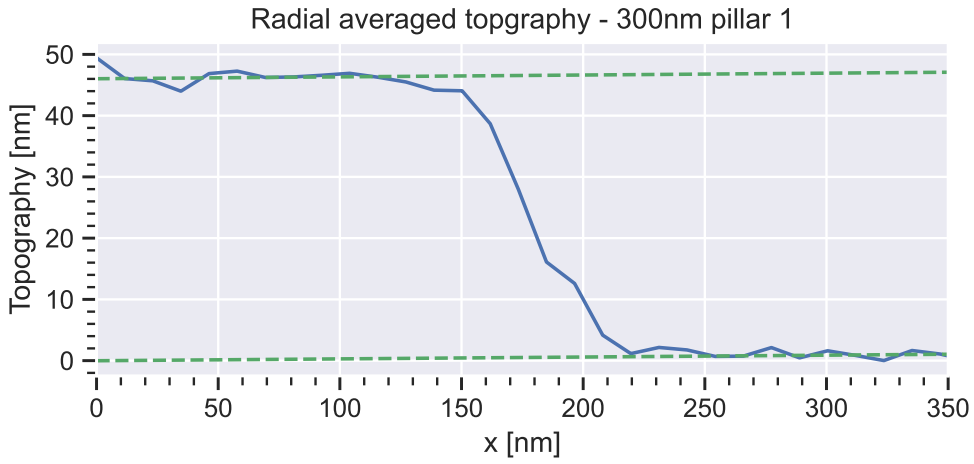


Figure 6.28: Radially averaged measurement of scan 300 nm pillar 1 from Figure 6.21a, measuring 46.04 ± 0.95nm.

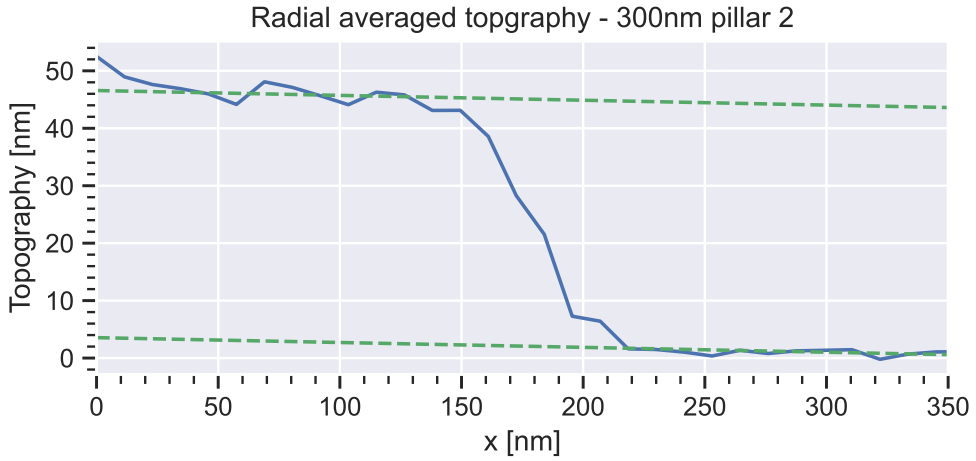


Figure 6.29: Radially averaged measurement of scan 300 nm pillar 2 from Figure 6.21a, measuring 45.22 ± 1.31 nm.

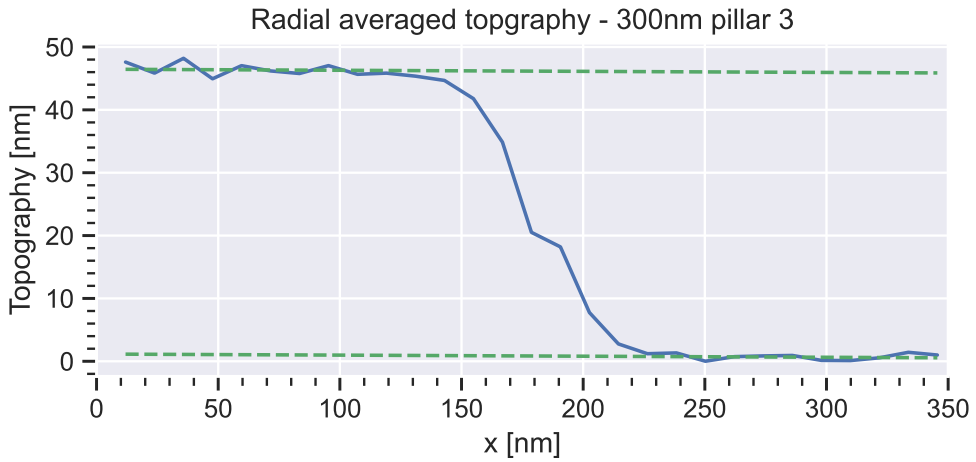


Figure 6.30: Radially averaged measurement of scan 300 nm pillar 3 from Figure 6.21a, measuring 45.31 ± 1.4 nm.

From Table 6.3, we can calculate a mean pillar height of 44.50 ± 6.56 nm. This agrees with the histogram measurement in Figure 6.22, but shows a lower mean pillar height than when measured in air.

Overlaying the probe response on the topography shows Figure 6.31, where clear decreases in the response can be seen at the pillar apexes. Similar to results found in section 5.3, this could potentially be explained by the increase in 'bulk' sample separation. I.e the thermal interaction area is dominated by the Flutec at the apex of the pillars as opposed to the base, where silicon interaction is increased.

Table 6.3: Tabulated results of terrace fitting to radially averaged 300 nm pillars

Pillar No	Height [nm]	Pillar No	Height [nm]
1	46.04 ± 0.95	11	45.94 ± 1.22
2	44.22 ± 1.31	12	43.37 ± 0.71
3	45.31 ± 1.40	13	43.46 ± 1.44
4	43.78 ± 1.49	14	42.00 ± 1.62
5	43.22 ± 1.29	15	44.88 ± 0.93
6	45.22 ± 1.51	16	48.75 ± 1.99
7	46.03 ± 1.85	17	42.07 ± 1.90
8	43.34 ± 1.67	18	43.78 ± 1.92
9	45.00 ± 1.30	19	44.84 ± 1.02
10	44.22 ± 1.65	20	45.03 ± 1.39

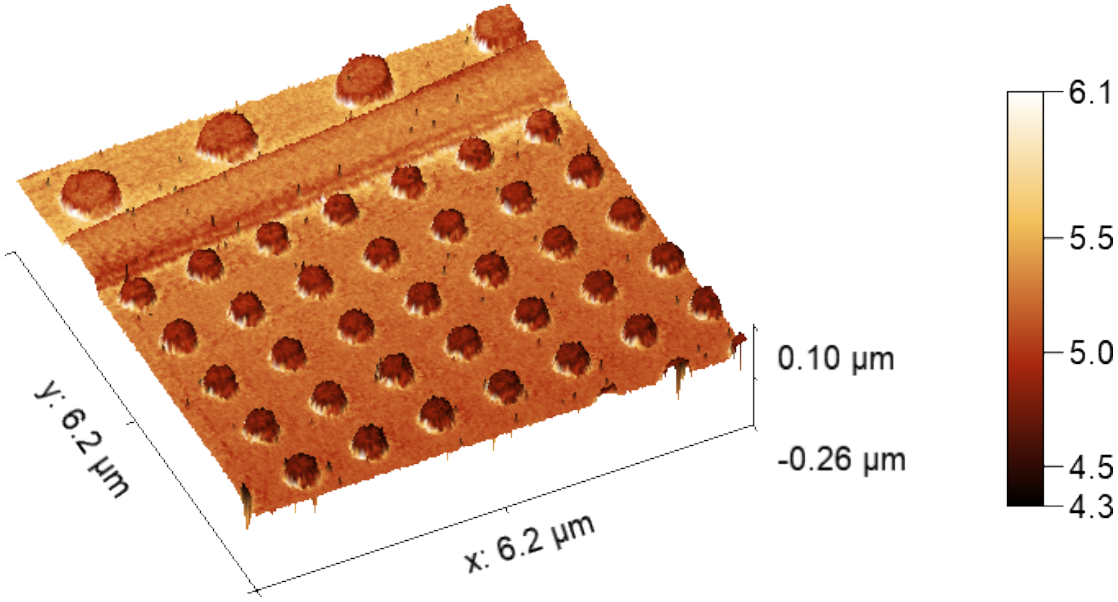


Figure 6.31: 3D representation of silicon pillar sample with probe response coloured (overlaid) on topography

Increasing the measurement frequency may hold clues to the apparent decrease in thermal conduction at the pillar apexes. The penetration depth of the thermal wave decreases as the square root of the drive frequency according to $\delta = \sqrt{\frac{\alpha}{2\omega}}$ where α is the thermal diffusivity of the surrounding material and ω the angular probe drive frequency. However, with thermal diffusion lengths in Flutec of 4.9 µm at a probe drive frequency of 224 Hz and 1.5 µm at 2.24 kHz, its effects will be small.

Visualisation of this effect has been schematically drawn in Figure 6.32 where it can be seen that measurements taken at the apex of a pillar show less interaction with the base silicon and greater interaction with the surrounding medium. The opposite is also visualised in Figure 6.32b/d where differences in the measurement are less

apparent.

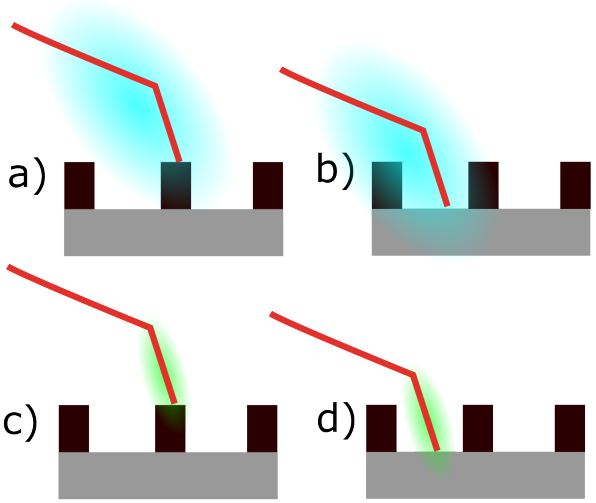


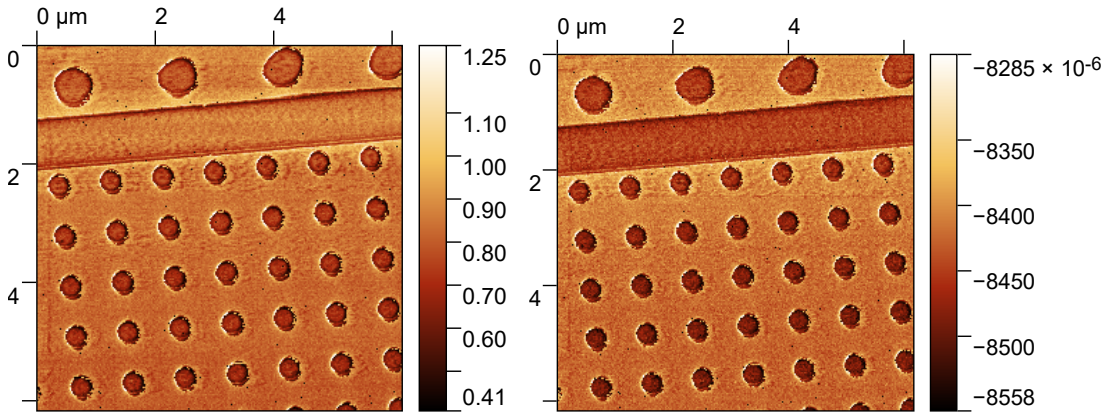
Figure 6.32: Schematic of frequency dependency of AC driven probe (red) measuring the pillar apex (black) vs base (grey). a-b) Lower frequency probe driving shows longer thermal wavelengths (blue) that are able to interact with the substrate from afar, and thus the 3ω has a strong dependency on the topographic structures. c-d) Higher frequencies reduce this effect as the interaction area becomes vastly reduced (green), leading to a greater influence of medium closer to the tip. (Elements and effects vastly exaggerated and not to scale)

As such, the control loop of the system was modified to include a frequency-sweeping capability. This allowed multi-frequency point-by-point measurements of a sample. At each point we change the phase increment of the DDS output, increasing the probe drive frequency up to 2.24 kHz, with a 5 ms settling time of oscillation in contact at each frequency before a measurement is taken. The 3ω response at 2.2 kHz is displayed in Figure 6.33a. We can then fit a gradient to the frequencies measured on a point-by-point basis to get a frequency dependency map as shown in Figure 6.33b.

Comparing Figure 6.33b to Figure 6.33a or Figure 6.21b, we can see the clear frequency dependency of the pillars.

6.2.6 Step edge

A primary advantage of SThM in liquid is the increased coupling of the probe tip to the sample. The reduced influence of contact shape when scanning in liquid proves more appropriate for materials studies [3, 55, 173]. As such, the step edge sample was fabricated utilising the same fabrication process as the one fabricated



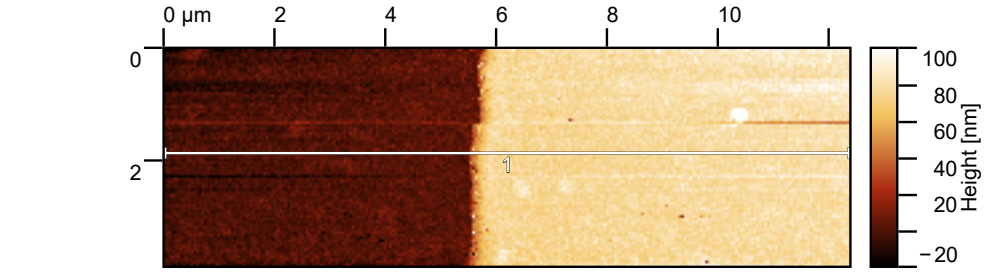
(a) 3ω probe frequency response at 2.24kHz

(b) 3ω probe frequency response gradient

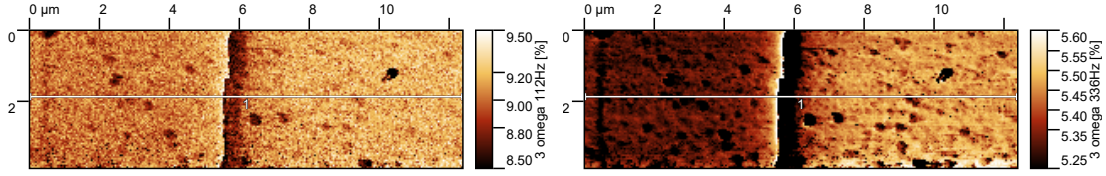
Figure 6.33: 3ω amplitude with log frequency gradient measurement

for measurements in air in section 5.4. this sample was scanned using the multi-frequency technique described previously.

For frequencies under 15 kHz, it is safe to assume that $\lambda \gg h$ where h is the tip resistor width (typically <2 µm), and we are in the regime where log-linear approximation of the probe response with frequency holds true [42, 45]. This had previously been shown to approximately hold true in Figure 6.11 in section 6.2.2. Therefore the slope of the 3ω amplitude against the log of the drive frequency can be an indication of the sample conductivity. It can be seen from Figure 6.34 that the 3ω response from the gold changes as the probe drive frequency increases.

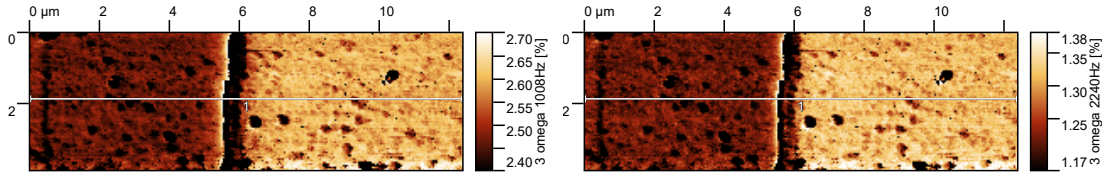


(a) Topographic output



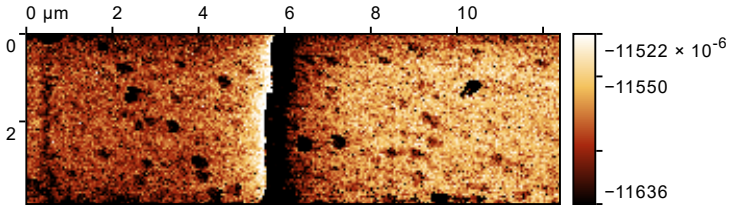
(b) 3ω Probe response at 112 Hz

(c) 3ω Probe response at 336 Hz



(d) 3ω Probe response at 1008 Hz

(e) 3ω Probe response at 2240 Hz



(f) 3ω Probe response gradient

Figure 6.34: Step edge scan from SiNx (LHS) to NiCr/Au (10 nm/70 nm - RHS). (a) showing the topography output. (b) The high contact noise levels are visible in the 112 Hz image and shows poor contrast. However, above this frequency (c-e), clear material dependency of the 3ω signal frequency is visible with the gradient shown in (f). One should also note the frequency dependency of edge defects as seen in the silicon pillar sample.

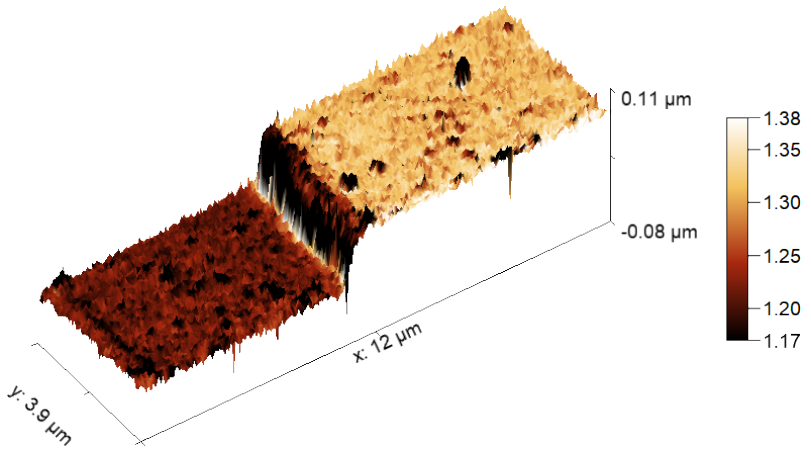


Figure 6.35: 3D representation of gold step sample with probe response at 2.24 kHz coloured (overlaid) on topography. A clear increase in conduction is visible as the probe approaches the base of the step, with a decrease as the probe moves up the edge.

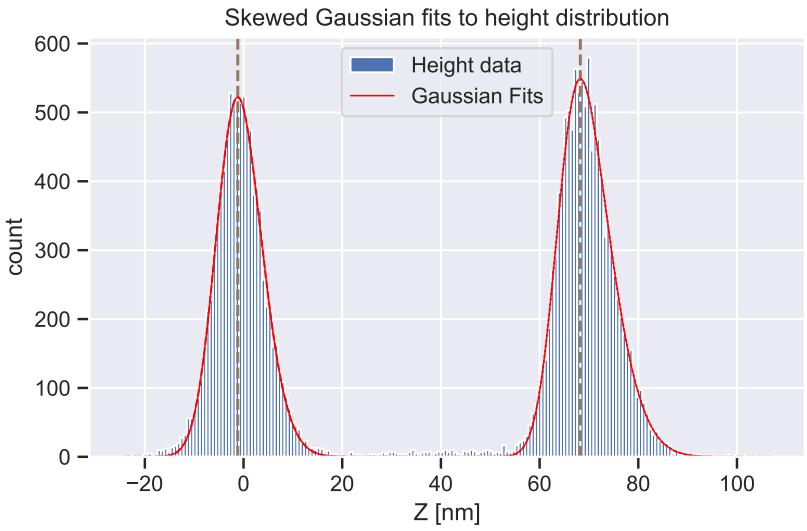


Figure 6.36: Histogram plot of Figure 6.34a showing a measured step height of 69.4 ± 13.8 nm

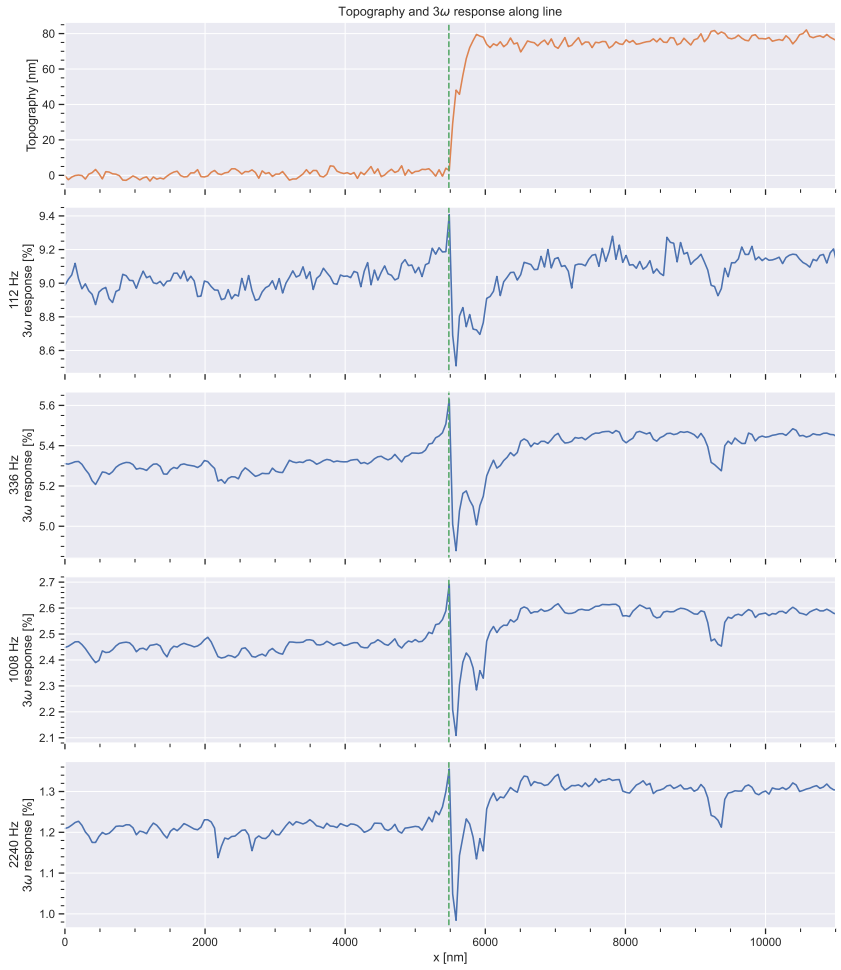


Figure 6.37: Line traces from Figure 6.34, green dashed line marks point of double contact. Top trace showing extracted topography line. second row onwards shows increasing probe drive frequency.

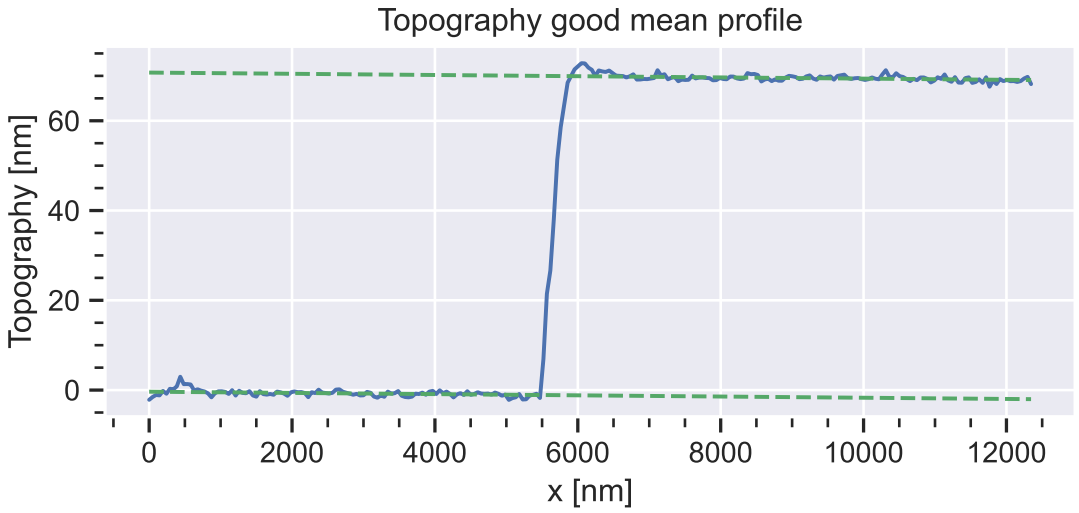


Figure 6.38: Good mean profile of Figure 6.34a. Green dashes show fitted terraces with a calculated step height of 71.10 ± 0.18 nm



Figure 6.39: Good mean profile of probe response at 2.24 kHz in Figure 6.34e. Probe response at this frequency can be seen to be 1.22% on the silicon nitride and 1.31% on the gold step, a change of 0.1%.

However, although contrast was visible in the scans, the material response was still not very strong, as evidenced by the lack of contrast visible in the gradient scan in Figure 6.34f. This could potentially be due to thin film contamination of the sample interfering with the measurement. Particle contamination is visible on the sample, so it is not unreasonable to assume that there may be some film contamination.

The sample was cleaned with multiple washings of IPA and Flutec before being

blown with a dry nitrogen gun. Right before applying Flutec and commencing the scan of the sample, heat was applied in the form of a heat gun to drive away any remaining moisture or contamination. The room temperature control was also temporarily re-established to reduce the rate of Flutec evaporation and allow longer scans before the Flutec drying up. As can be seen in the 1ω channel in Figure 6.41a, this re-introduced noise into the system as the AC cycled on and off to maintain temperatures.

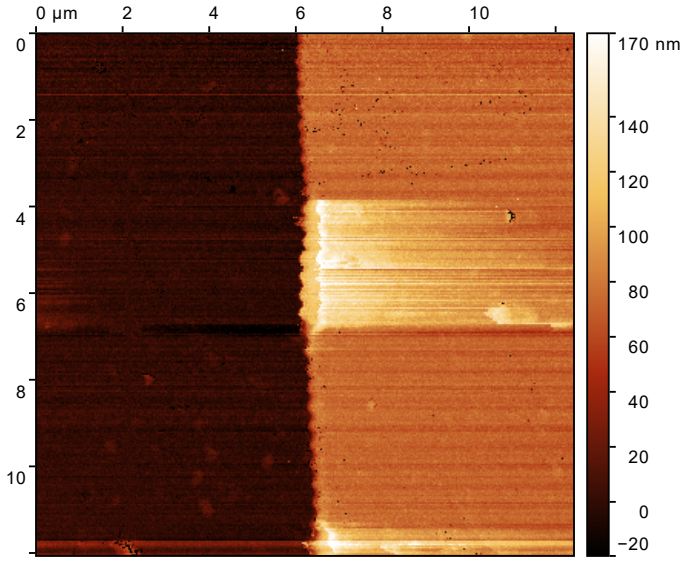
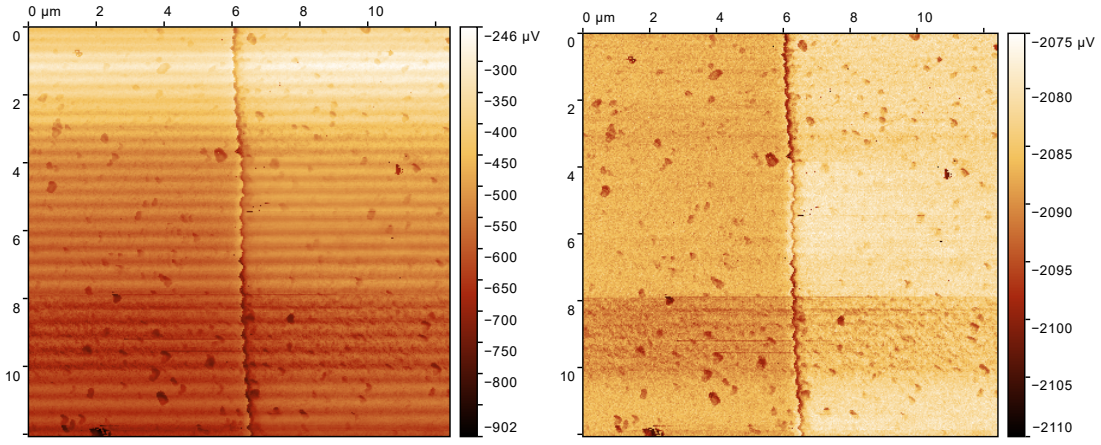


Figure 6.40: Topography channel for step edge sample; Particulate pickup during scanning causes erroneous height measurements, the effects of tip switching can be seen at the step edge



(a) 1ω channel; The cycling of AC is now visible in the measurement, and clearly aligns with the slight lateral shift of the step edge.

(b) 3ω channel; The tip switching has an impact on resulting 3ω values. However, no effect of AC cycling is visible.

Figure 6.41: Raw thermometric signals from scan if step edge sample under Flutec PP3

From Figure 6.40 and 6.41, one can clearly see the effect of particulate pickup or metal flagging of the tip having an impact on height and thermometry measurement.

A zoom of the affected area has been provided in Figure 6.42, where a clear 'double tip' artefact can be seen, causing erroneous height measurements.

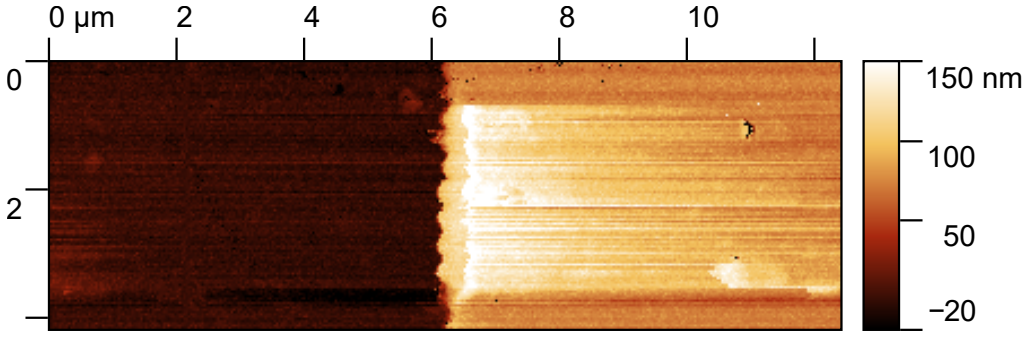
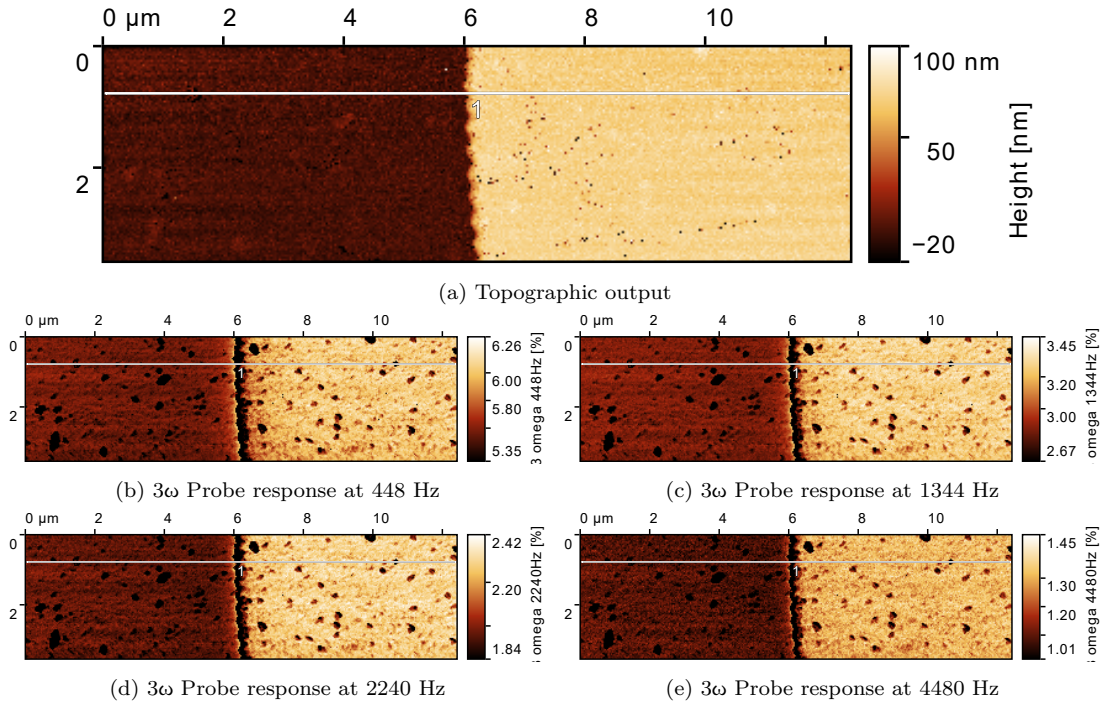


Figure 6.42: Cropped area of Figure 6.40 where metal flagging or particulate pickup or has caused double tip contact artefacts at the step edge.

As such, for accurate measurement and to avoid the influence of the change in tip shape on the measurement, we take the top 3 µm of the scan, as shown in Figure 6.43 where topographic output alongside a selection of frequency responses has been shown. To avoid the influence of high in-contact noise in signals that appear at 112 Hz and 224 Hz, only frequencies available above these have been recorded. Extracted lines have been plotted in Figure 6.45.



(a) Topographic output

(b) 3ω Probe response at 448 Hz

(c) 3ω Probe response at 1344 Hz

(d) 3ω Probe response at 2240 Hz

(e) 3ω Probe response at 4480 Hz

Figure 6.43: Step edge scan from SiNx (LHS) to NiCr/Au (10 nm/70 nm - RHS) after cleaning. (a) Showing the topography output. (b-e) showing the probe responce at various freqneucies, with a clear material dependency of the 3ω signal frequency visible with the gradient shown in (f).

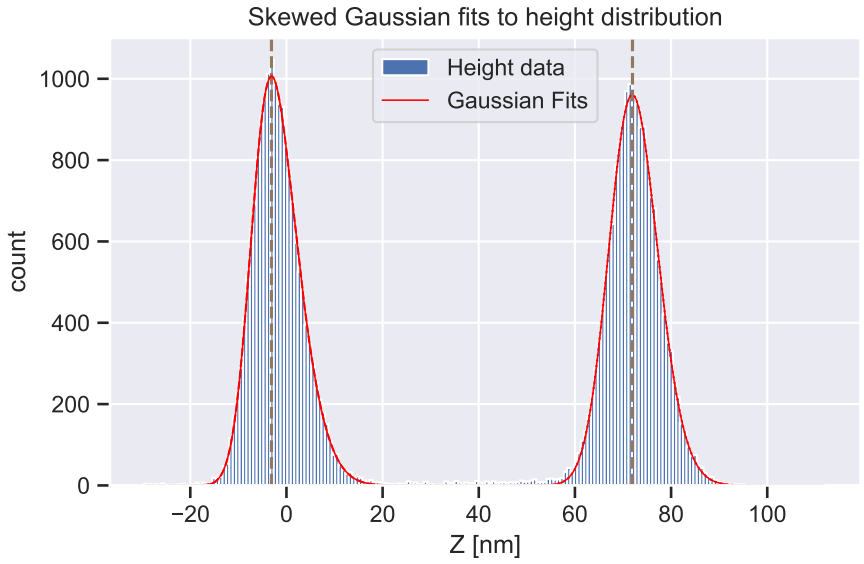


Figure 6.44: Histogram plot of Figure 6.43a showing a measured step height of 75.08 ± 13.52 nm

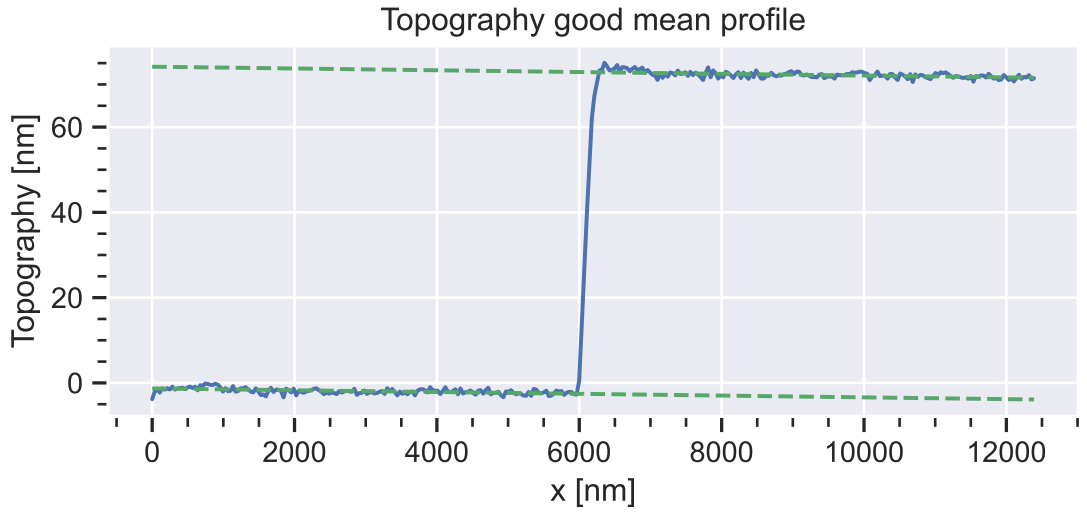


Figure 6.46: Good mean profile of Figure 6.34a. Green dashes show fitted terraces with a calculated step height of 75.46 ± 0.15 nm

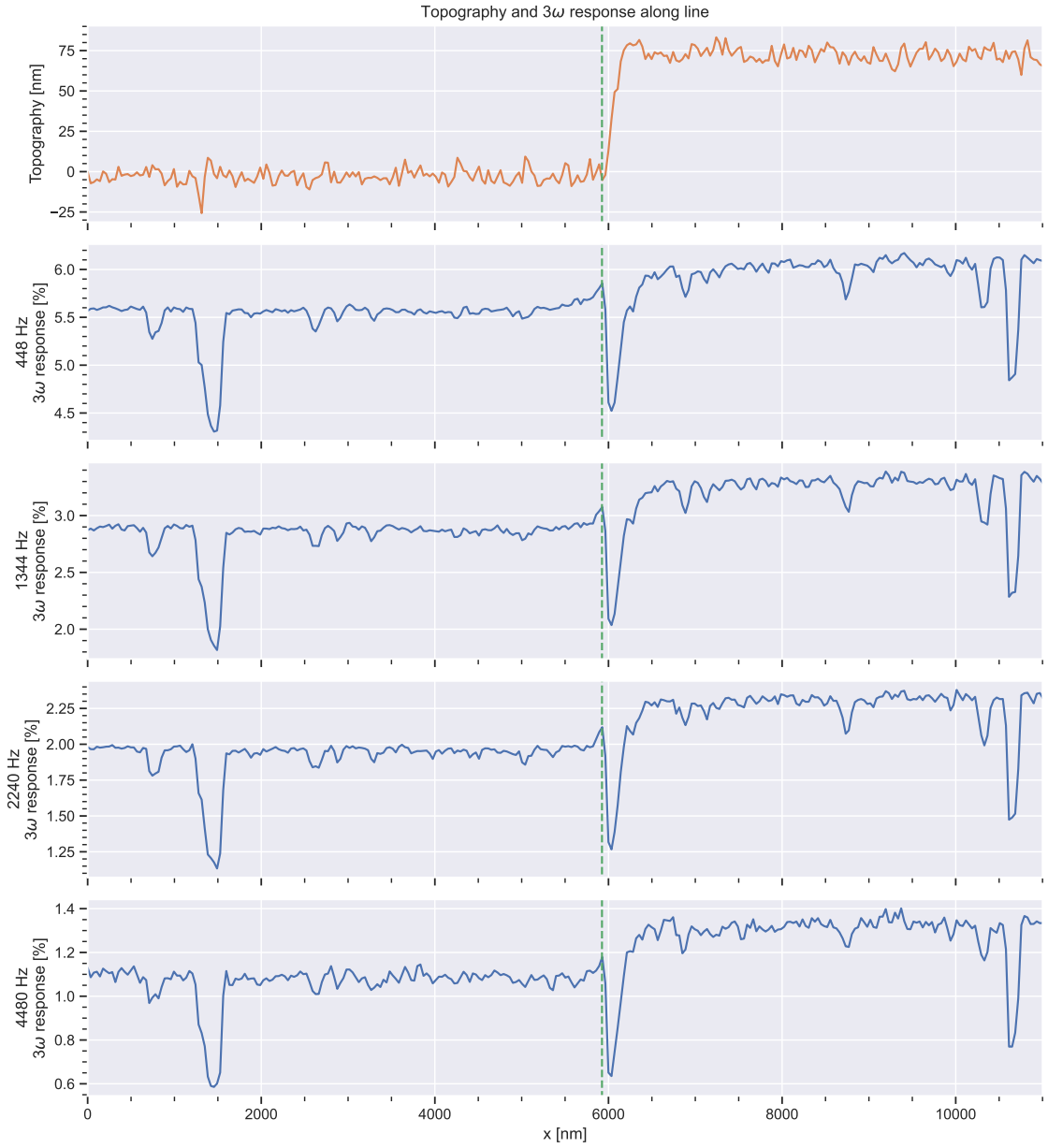


Figure 6.45: Line traces from Figure 6.43, green dashed line marks point of double contact. Top trace showing extracted topography line. second row onwards shows increasing probe drive frequency.



Figure 6.47: Good mean profile of probe response at 2.24 kHz in Figure 6.43d. Probe response at this frequency can be seen to be 1.95% on the silicon nitride and 2.3% on the gold step, a change of 0.3%

As with measurements carried out in air in section 5.4, one can plot a histogram of the probe response at 448 Hz, split using the height data as in Figure 6.48. To reduce the effect of topographic feature influence on the 3ω measurement, it was found best to exclude any data points that were within 1 µm of the edge. A very distinct change in probe response of around 0.45% can be seen. Although the difference in the magnitude of the probe response was smaller compared to air, sharper responses can be seen as the probe-sample coupling is much less dependent on contact shape and variations in conduction through water menisci. Figure 6.49 shows the distributions at various frequencies as a ridgeline plot.

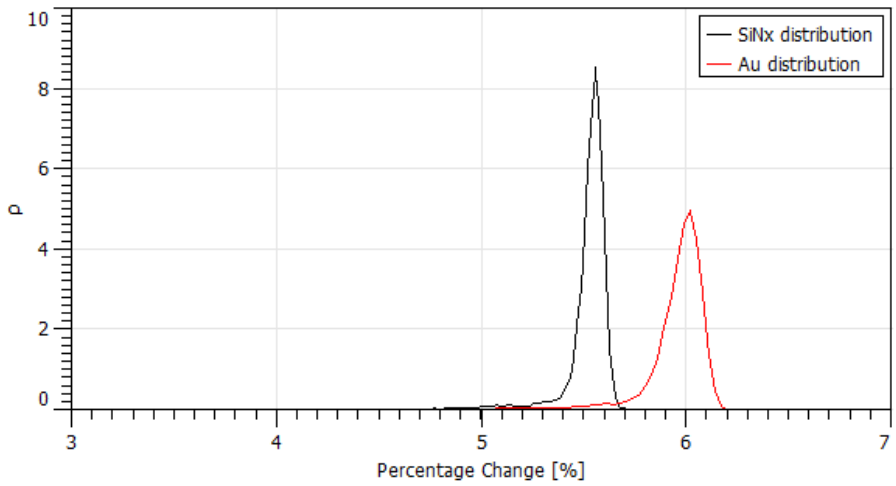


Figure 6.48: Histogram of 3ω Probe response at 448 Hz split by height data. A clear change in probe response of 0.45% is visible from the silicon nitride to gold areas of the scan

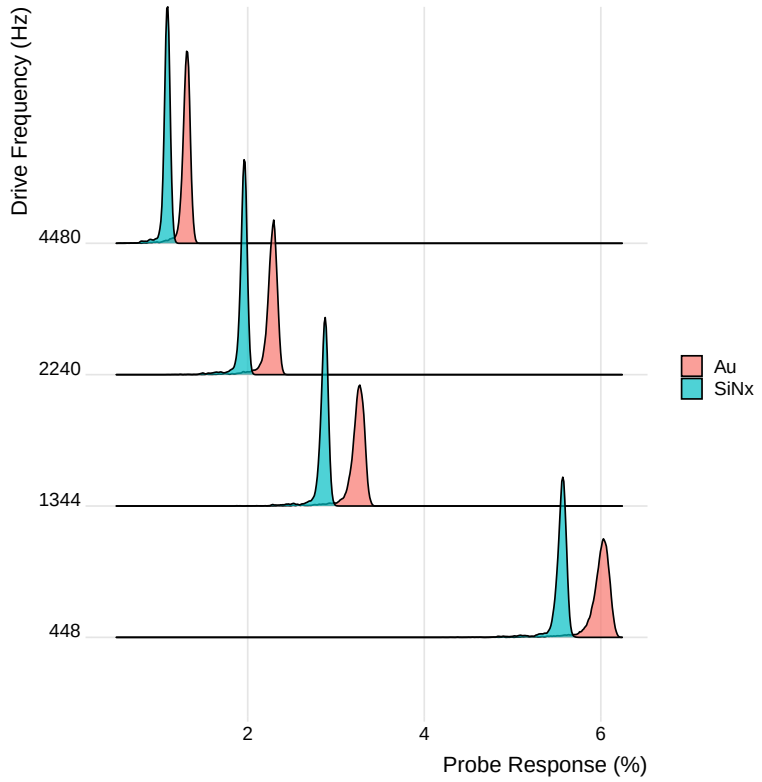


Figure 6.49: Ridgeline of 3ω Probe response at split by height data. Changes in probe response are visible from the silicon nitride to gold at all drive frequencies

From Figure 6.49, it can be seen that although the magnitude change in probe response at lower frequencies is larger (i.e larger separation of peaks), the distribution of measurements is tighter at higher frequencies.

The precision of each measurement can be again described by the coefficient of variation (CV) of each distribution which has been plotted, alongside the magnitude change in response at each frequency, in Figure 6.50. It can be seen that although the precision in the measurement increases with frequency, the magnitude of the response decreases. This would be expected given the limited bandwidth of probes of this type.

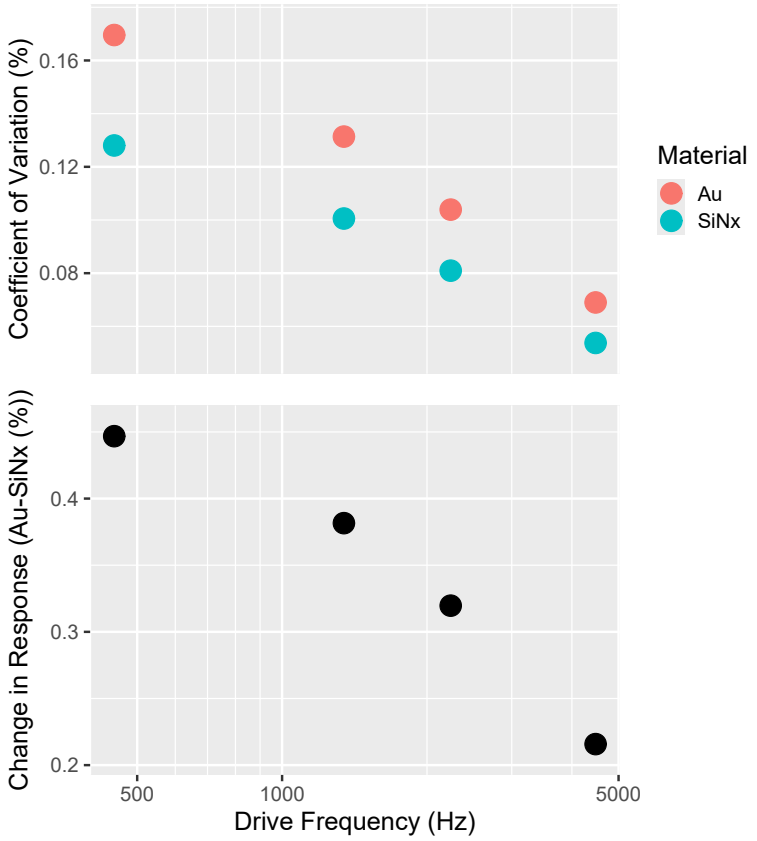


Figure 6.50: Coefficient of variation of 3ω response at various frequencies split my height data (Top), and magnitude of change in response (Bottom)

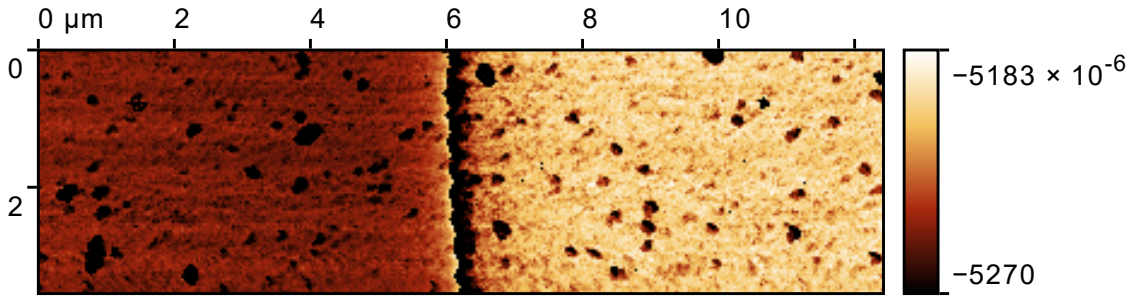


Figure 6.51: 3ω Probe response gradient of thin film gold (RHS) on silicon nitride (LHS)

To see the frequency-dependent response the gradient of the probe response with frequency can be plotted as in Figure 6.51, it can be seen that the gold step has a significant frequency-dependant response, leading to possible extraction of material properties such as thermal conductivity or diffusivity. However, extraction of quantitative results would require highly detailed studies of the particular probe used as well as calibration to conductivity standards, which is beyond the scope of this work.

As there is a strong coupling between the probe and sample without any direct physical contact between them, this opened up the possibility of out-of-contact thermal measurements of samples [55, 173]. One can measure with the probe completely out-of-contact and negate uncertainties derived from solid-solid contact shape. As such, the step edge sample was measured again with a probe drive frequency of 560 Hz and an increased probe power of 200 µW. However, once an in-contact measurement was made at each pixel, the probe was retracted from the surface (via a Xuepath mid-point of >1 µm from the sample surface to break any tip-sample adhesion) to 30 nm, 100 nm, and 200 nm above the surface to take further measurements. The initial acquired topography and in-contact 3ω scan can be seen in Figure 6.52 with an extracted good mean profile of the step response in Figure 6.53.

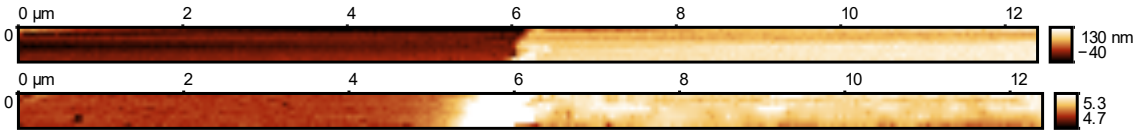


Figure 6.52: Acquired topography (top) and 3ω probe response as a percentage (bottom) in-contact.

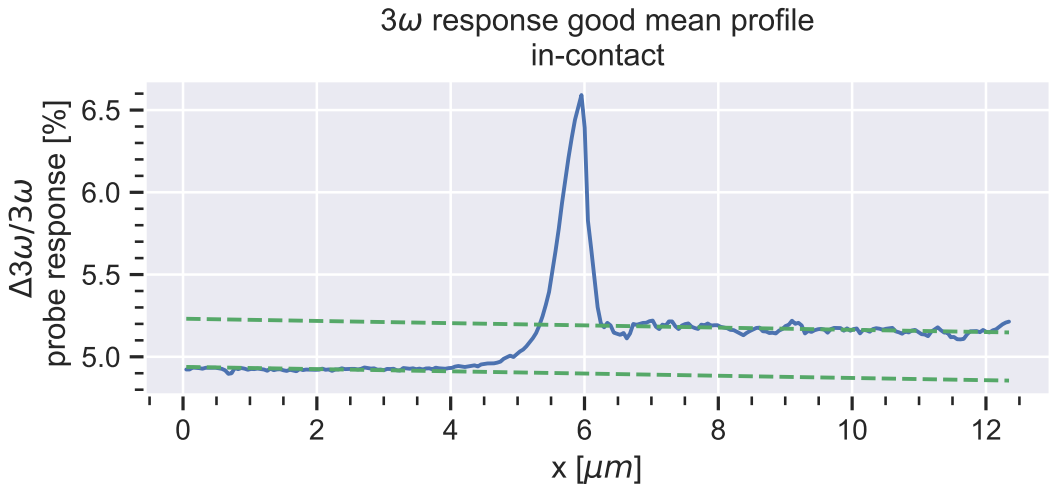


Figure 6.53: Good mean profile of the 3ω probe response in Figure 6.52, showing a change in probe response of 0.2% calculated from terrace fitting.

Figure 6.53 shows a clear contrast between the silicon nitride and gold, with a calculated probe response change of 0.2% when stepping onto the gold for this particular scan. It should be noted that a large double-contact edge artefact can

be seen, possibly due to the higher temperature of the probe tip from the large dissipated probe power, increasing the probe interaction with the step edge. For measurements taken above the sample surface, scans are shown in Figure 6.54 with good mean profiles and terrace-fitted probe responses in Figure 6.55.

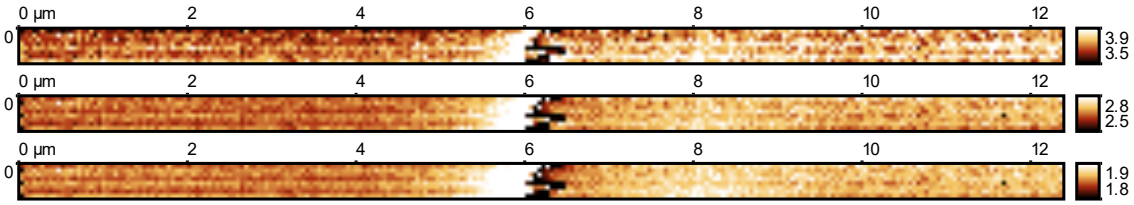


Figure 6.54: Acquired 3ω probe response as a percentage at 30nm, 100nm, and 200nm (Top to bottom) above the sample surface.

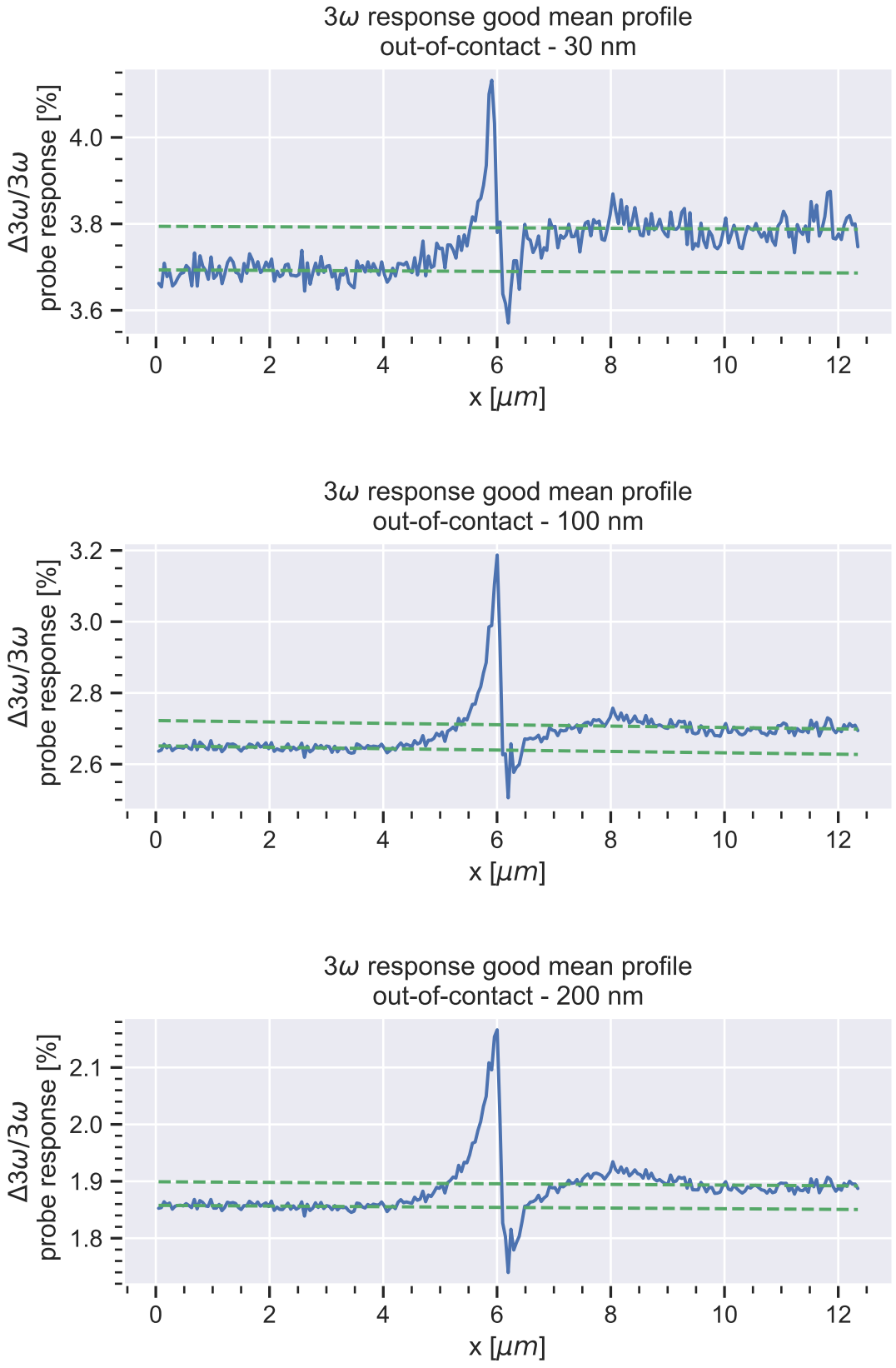


Figure 6.55: Good mean profiles of scans in Figure 6.54 showing fitted changes in probe response of 0.1%, 0.07%, and 0.04% for the 30 nm, 100 nm, and 200 nm scans respectively.

For all measurements taken above the surface, the contrast in the acquired scans in Figure 6.54 is minimal. However, plotting the good mean profiles in Figure 6.55 shows a clear probe response change of 0.1%, 0.07%, and 0.04% for the 30 nm, 100 nm, and 200 nm scans respectively, showing that out-of-contact scanning of material characterisation could be possible if calibrated probes where to be used. The increased noise levels visible in the 30 nm scan may be due to the non-linear relationship of the 3ω signal with distance as shown previously in section 6.2.3, at such small distances from the sample surface, uncertainties in the tip positioning in space would have a significant impact on the measurement.

The increased tip-sample separation should show a reduction in edge artefacts as noted by Tovee and Kolosov [55] and Tofani [173]. However, artefacts are still observed throughout this work under the liquid. It is most likely that the artefacts are observed due to increased probe sensitivity from the long measurement dwell times used in this work.

6.3 Topographic control in vacuum

To assess the ability of these techniques as a method of topographic control in settings when no liquids or gases are present, we conduct SThM measurements in measurements. Vacuum measurements have long been advocated as the best method of quantifiable SThM [3, 43, 48, 56, 61, 157, 192]

In terms of the thermal resistance model, in Figure 6.56 the switch S_{env} is now open and no conduction can occur between the probe and sample without explicit contact, with the exception of radiative heat transfer. However, this thermal transfer path is negligible in most circumstances [48, 53, 56].

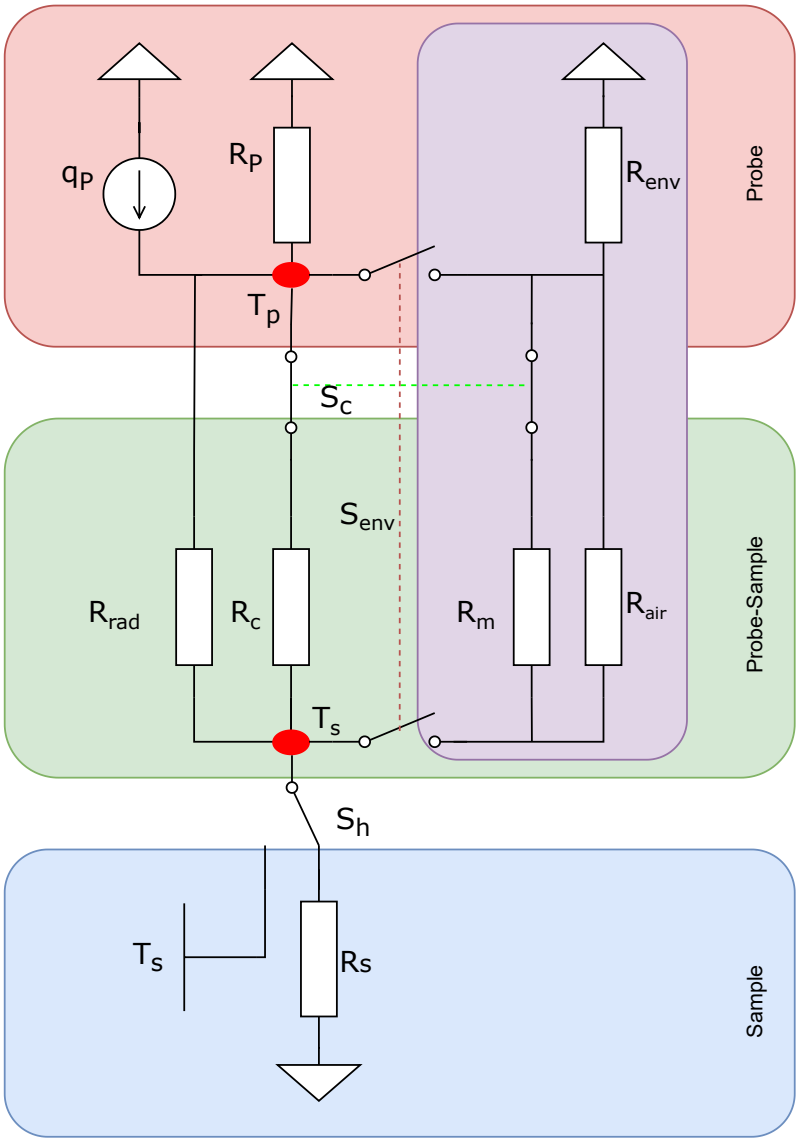


Figure 6.56: Thermal resistance network of vacuum SThM measurements

6.3.1 Design

The electrical setup remained unchanged when scanning in a vacuum and the same control electronics were used as in air and liquid. However, due to the requirement of a vacuum, a Nanomics vacuum SPM system, photographed in Figure 6.57 was utilised.

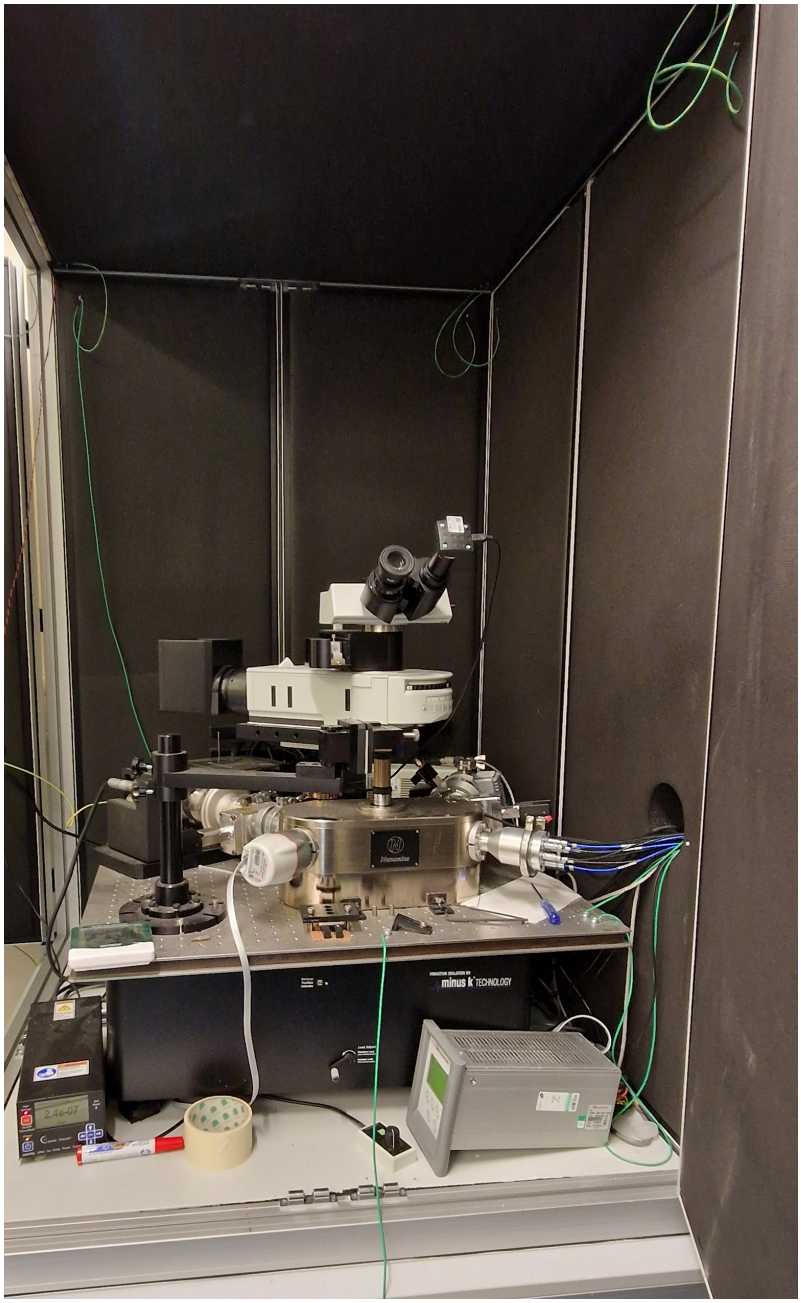


Figure 6.57: Photograph of the SThM in vacuum setup.

For all experiments, the vacuum was held between 2.4-2.8x10^{-7} mbar. Due to other ongoing experiments with this SPM system, and the difficulties associated with

changing the probe and sample in a vacuum, the probe used for vacuum scans is not a KNT probe, but a custom probe designed for other experimental work by Ge et al. [53]. An optical image of this probe scanning can be seen in Figure 6.60, with a SEM image of the overall probe in Figure 6.58, and a close up of the tip in Figure 6.59. The probe is built on the same technology platform as that of the KNT probe, with a similar tip shape and angle, and includes a similar thermally sensitive resistor near the tip with no current series limiting resistors. The probe also has the additional inclusion of a heater element on the cantilever and a thermocouple at the tip extremity. However, these elements were not utilised in this work.

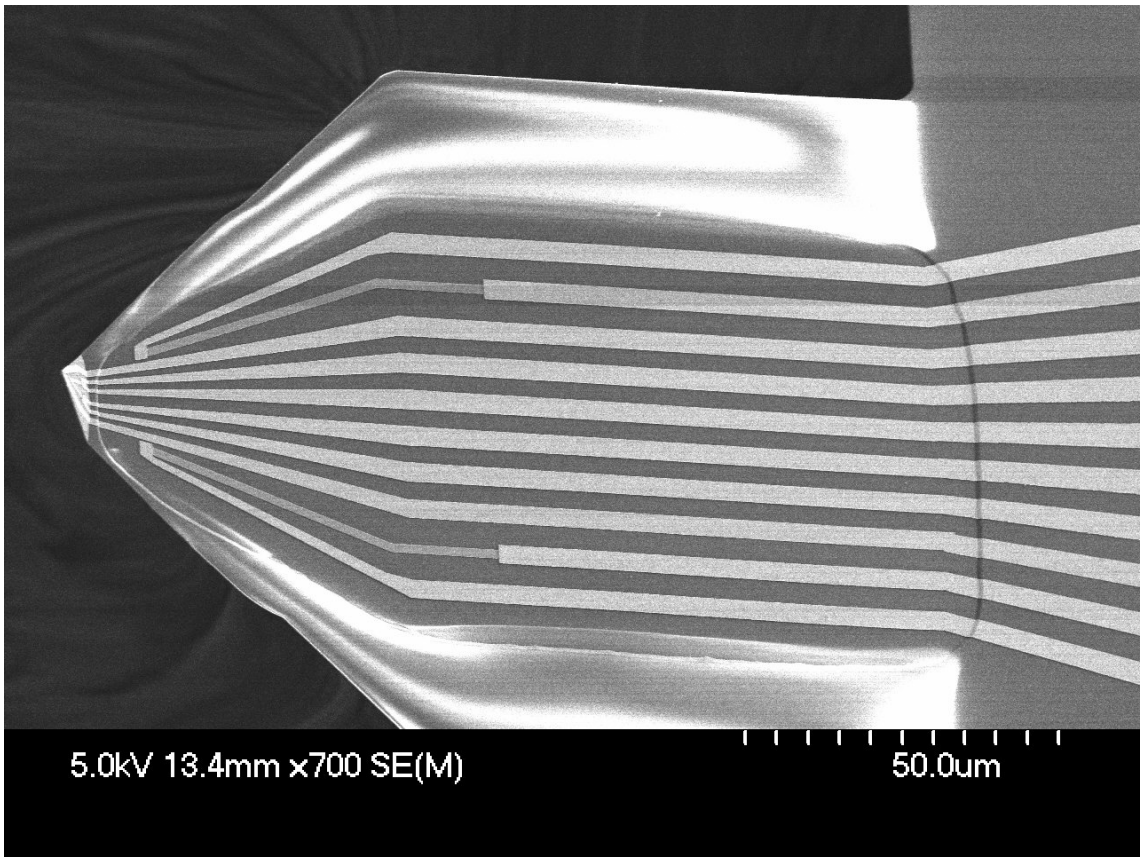


Figure 6.58: SEM image of the probe utilised in vacuum system. *Image courtesy of Prof. Johnathan Weaver of the AFM and Hyper-lithography group, University of Glasgow*

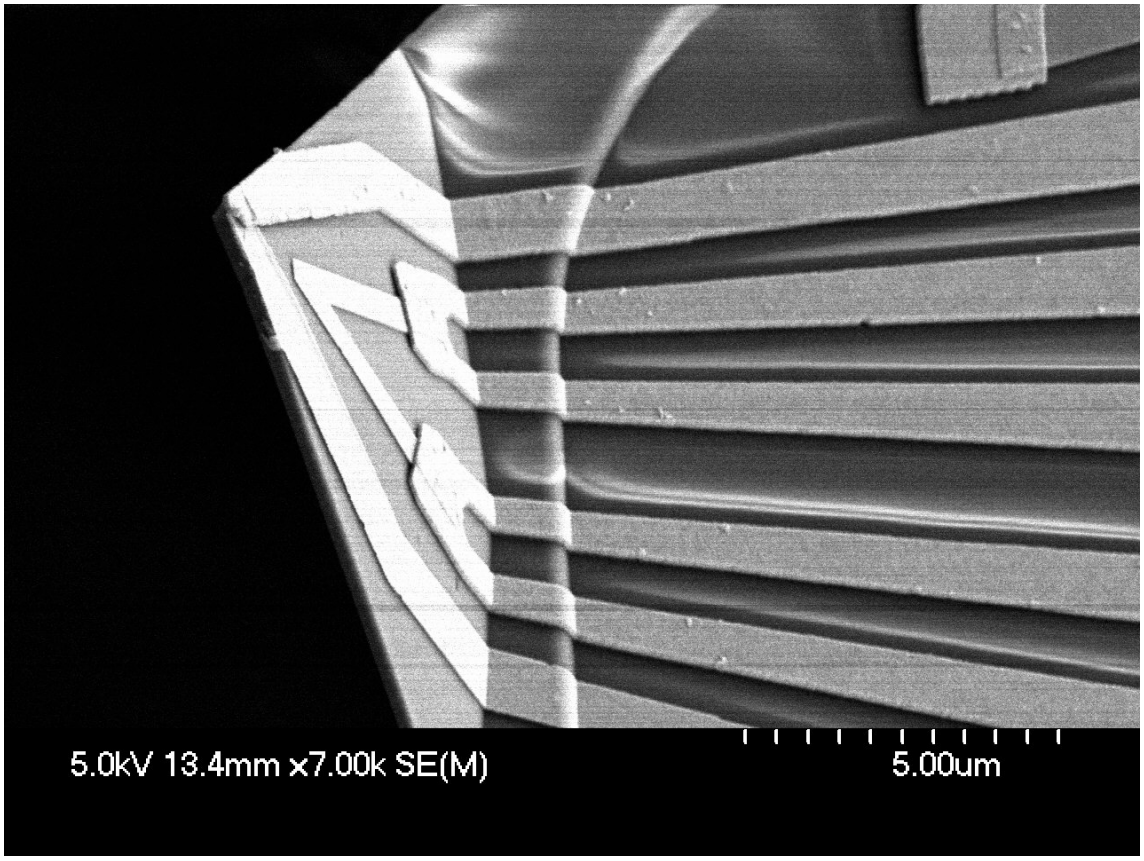


Figure 6.59: SEM close up of probe tip. A thermocouple junction is located at the tip extremity with a recessed Pd resistor. *Image courtesy of Prof. Johnathan Weaver of the AFM and Hyper-lithography group, University of Glasgow*

The inclusion of multiple tracks on the probe cantilever as well as a slightly recessed thermal resistor from the tip of the probe, slightly changes the thermal response of the resistor. Primarily the probe has an ever so slightly slower thermal response time. As vacuum is the surrounding environment, the only method of heat transfer between the probe and sample is that of point contact (Figure 6.56), leading to very small changes in the probe response.

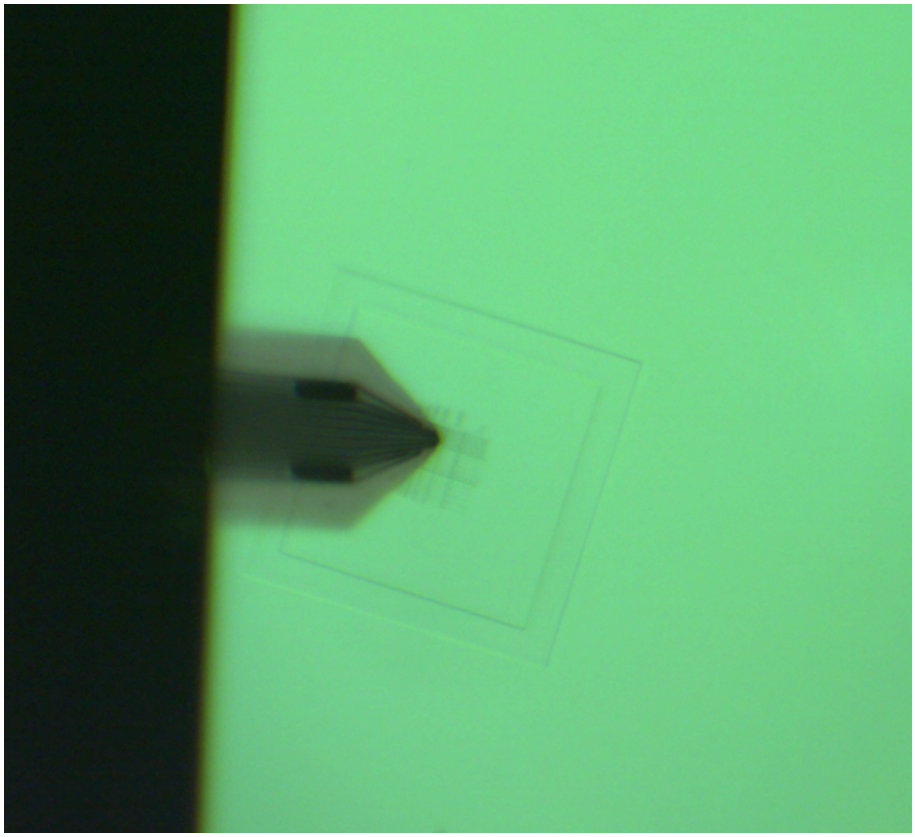


Figure 6.60: Optical microscope image of the probe utilised in vacuum system.

A significant difference in the vacuum setup compared to air and liquid was the use of a bi-morph piezo controlling the Z axis of the system. This operation is depicted in Figure 6.61. The probe attached to this bi-morph did not have the capability to be driven closed loop and had a limited range of approximately 800nm. As we were acquiring topographic control of the probe this was deemed to not be a significant issue.

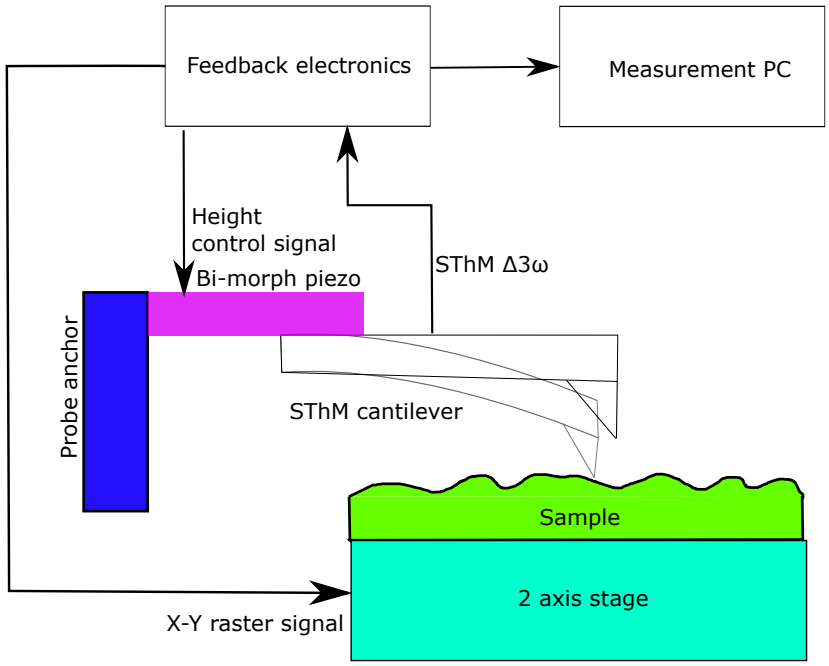


Figure 6.61: Diagram of probe mounting on bi-morph piezo enabling probe actuation in Z axis.

Although the X and Y axes of the sample stage were closed-loop controlled, the stage and probe were attached to components that contained little thermal expansion compensation. These drifts became visible as scan artefacts in scans acquired later in section 6.3.5. Due to the lack of environmental heat dissipation through the environment, mechanical parts will show a greater magnitude of thermal expansion, due to the build-up of heat. All heat generated by the various system parts must transfer through solid conduction to a heat sink through components used to align the sample and probe, causing higher temperatures, and subsequently greater thermal expansion of these parts in all axes in the process.

The limited range of the probe bi-morph piezo also presented issues caused by thermal expansion. If the expansion of parts exceeds the range of the Z piezo, then the probe has no ability to contact the sample and measurements cannot be taken. Many metals such as aluminium have a thermal coefficient of expansions upwards of 10 µm/°C. As a result, even changes in temperature of less than 0.1 °C could potentially cause issues in the setup.

6.3.2 Noise analysis

Similarly to measurements in air, the noise levels in the system under vacuum conditions were first re-qualified to allow for accurate interpretation of results ob-

tained.

To analyse the noise of the system 250 measurements were taken at a probe drive frequency of 448 Hz, at a probe power of 80 µW, and at least 500 nm out of contact, the furthest extension of Z possible in the setup, before being moved into contact. Results of which can be seen in Figure 6.62 with measurements of mean, standard deviation, and coefficient of variation tabulated in Table 6.4.

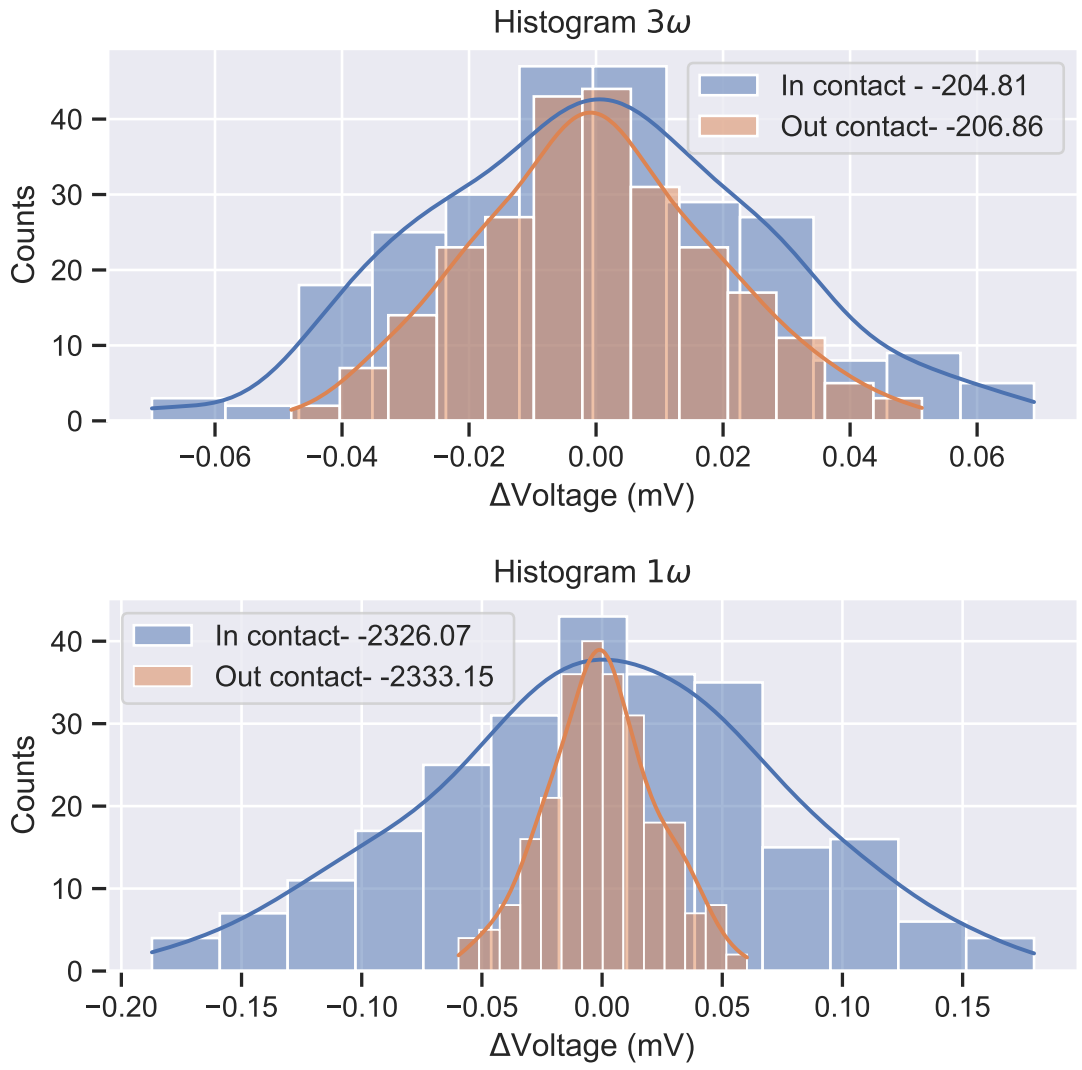


Figure 6.62: Histogram of 1000 sequential measurements at a ddsn of 4 at 448Hz in and out of contact

Similarly with SThM in air, 3ω thermometry signals show an approximately Gaussian distribution with an approximate 0.95% change in mean value from out of contact into contact. This signal is also stable with an out-of-contact CV of 0.001%

Table 6.4: Tabulated statistical results from 250 measurements of the 1ω and 3ω signals in and out of contact in vacuum

Signal	Mean [mV]	pk-pk [µV]	Std Dev [µV]	CV [%]
$3\omega_{out}$	-206.8	99.2	18.7	0.00097
$3\omega_{in}$	-204.8	138	26.1	0.01
$1\omega_{out}$	-2333	119	22.8	0.0009
$1\omega_{in}$	-2326	366	72.2	0.003

over the measurement period for both in-contact and out-of-contact measurements. It can be seen that moving into contact, noise levels increased slightly, but were still far within acceptable margins. A large offset in the 1ω value can be seen, this is most likely due to a mismatch in the resistance of the probe with the matching resistor.

Looking at the in-contact measurements of 3ω in Figure 6.63, a slight drift in the measurement is visible over the measurement time period. It is possible that slight contamination layers exist on the sample and we are seeing the effect of accumulation of this contamination on the probe. However, this theory is unlikely in this environment due to the high vacuum in the system, as little to no moisture should exist inside the system. This drift in measurement could be a result of the drift in 1ω as the probe temperature drifts with the sample temperature, which has been plotted in Figure 6.64.

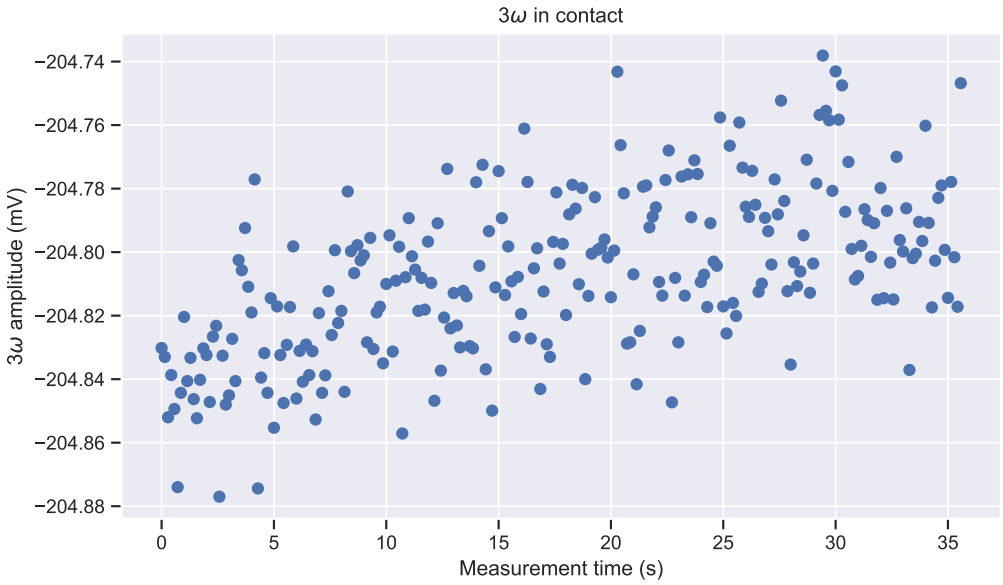


Figure 6.63: Slight drift over measurement of 3ω at ddsn of 4 at 448 Hz in contact observed.

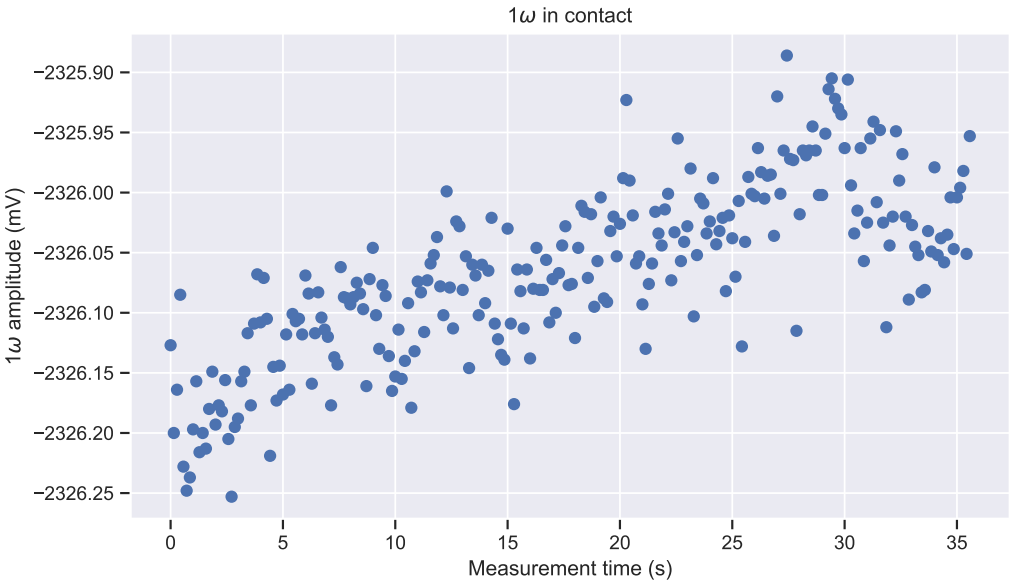


Figure 6.64: Slight drift over measurement of 1ω at ddsn of 4 at 448 Hz in contact with room temperature.

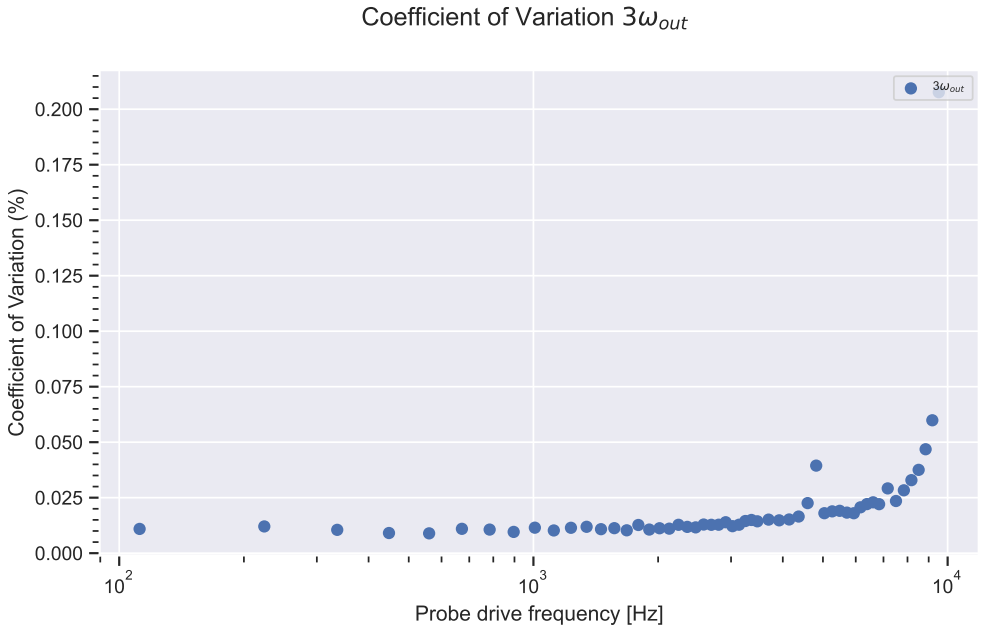


Figure 6.65: 3ω coefficient of variation values (expressed as a percentage) for out of contact across available frequencies

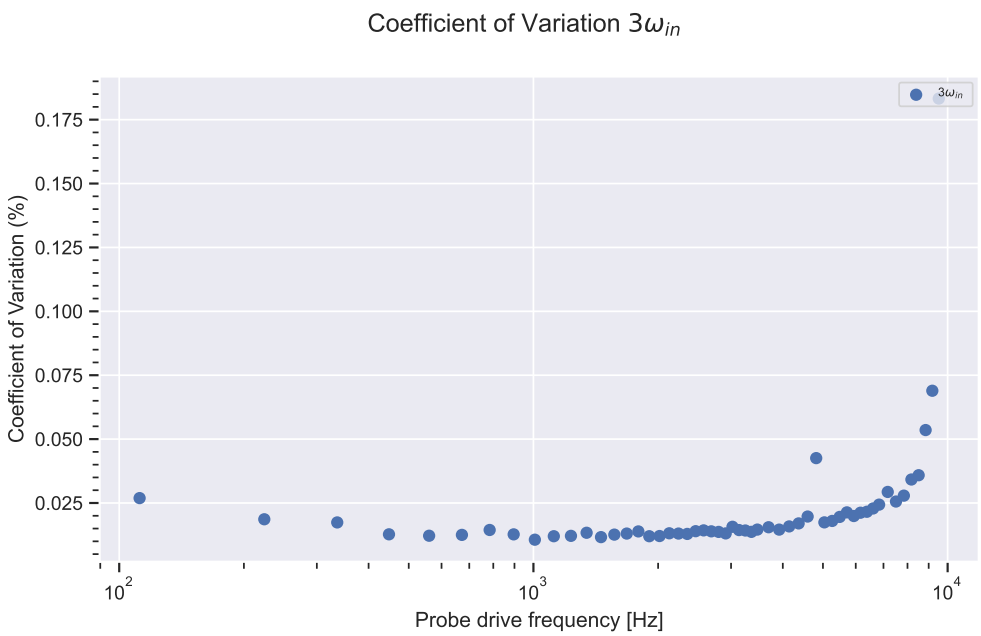


Figure 6.66: 3ω coefficient of variation values (expressed as a percentage) for in contact across available frequencies

As the mechanisms for heat transfer have significantly changed when moving to a vacuum and using a different probe type, the probe frequency response was again also re-qualified. Measuring the probe frequency response from the out-of-contact to in-contact measurement we can see the relation in Figure 6.67 and Figure 6.68.

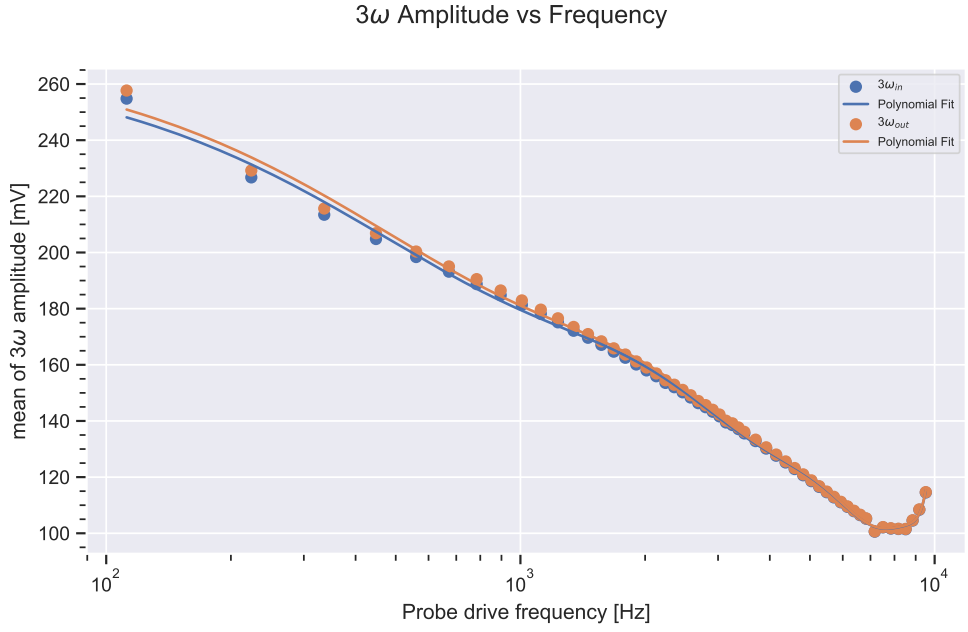


Figure 6.67: Mean 3ω values in and out of contact for various probe drive frequencies in vacuum

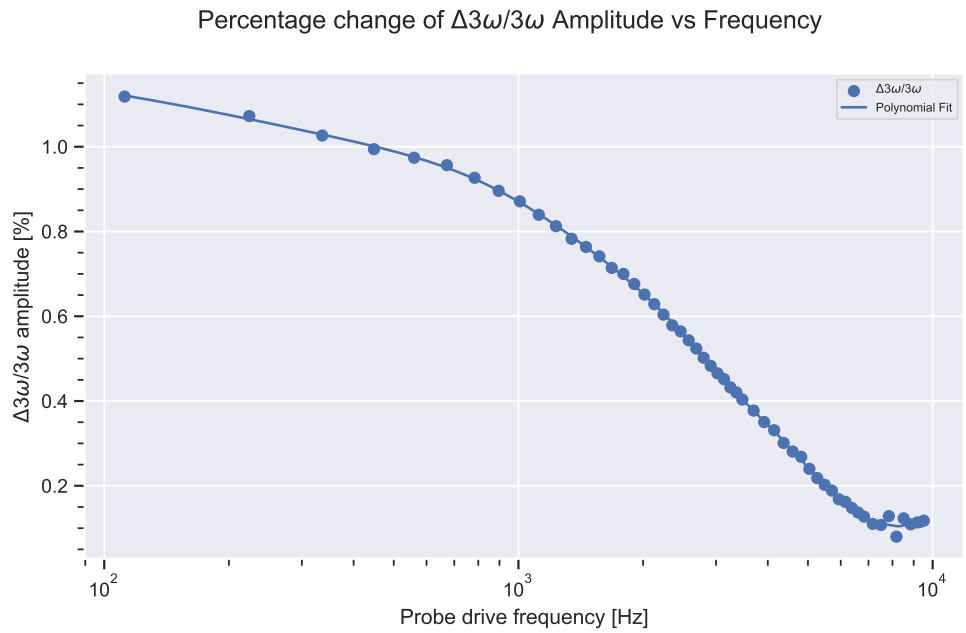


Figure 6.68: Mean 3ω values in and out of contact for various probe drive frequencies in vacuum expressed as a fractional percentage change from it's out of contact measurement

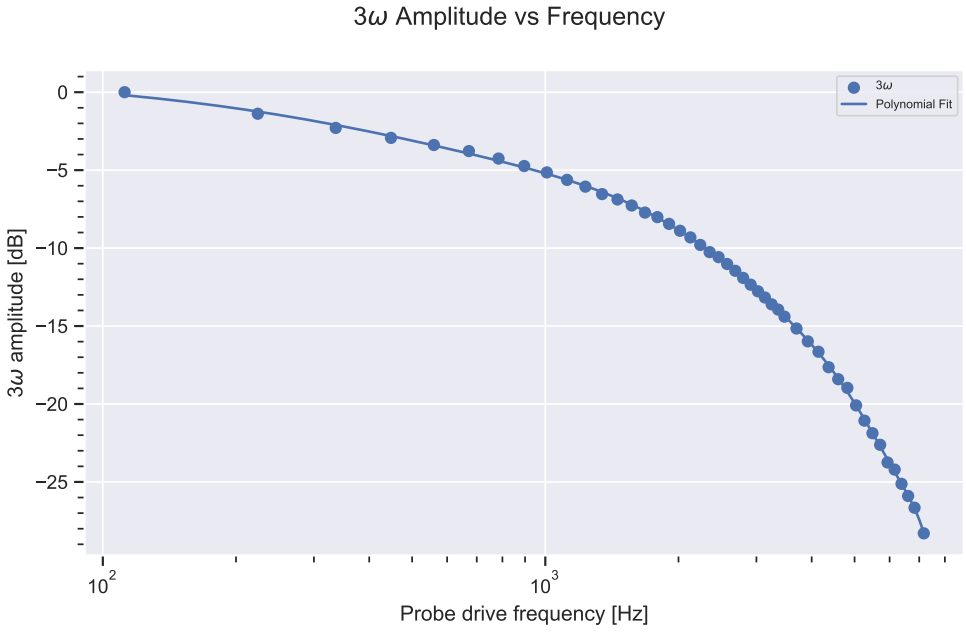


Figure 6.69: Fractional change of probe thermal response expressed as a Bode plot, 0dB point is the response of the lowest frequency available from the DDS output.

The probe's 'scalloping' profile that was seen with probe responses in air are still in effect in a vacuum, confirming that this is an artefact of the probe shape and design, rather than one of its environment. A vast decrease in the magnitude of the probe response was also seen in a vacuum. In air, changes in the 5-10% range

were observed. However, changes in probe response are now in the <1%. This is primarily due to point contact of the probe and sample being the only method of heat transfer, with the exception of radiative effects which in this case will be negligible.

6.3.3 Curve analysis

A typical land and retract curve while monitoring the thermal signals in a vacuum is shown in Figure 6.70. As expected, the out-of-contact signal does not vary with distance from the sample surface due to the lack of a thermal transfer path between the two. Upon contact, the signals showed a large change in 3ω as thermal contact had been made between the probe and sample. Extending the probe past the initial contact point shows increasing conduction between the probe and sample due to increasing contact area that the probe makes with the sample with increasing force. Although capillary action had been reduced to practically zero by moving to a vacuum environment, there still exists adhesion forces such as electrostatic and van der Waals forces that cause approximately 100 nm of hysteresis. This is more clearly shown by zooming in on the measurements around the contact point (Figure 6.71).

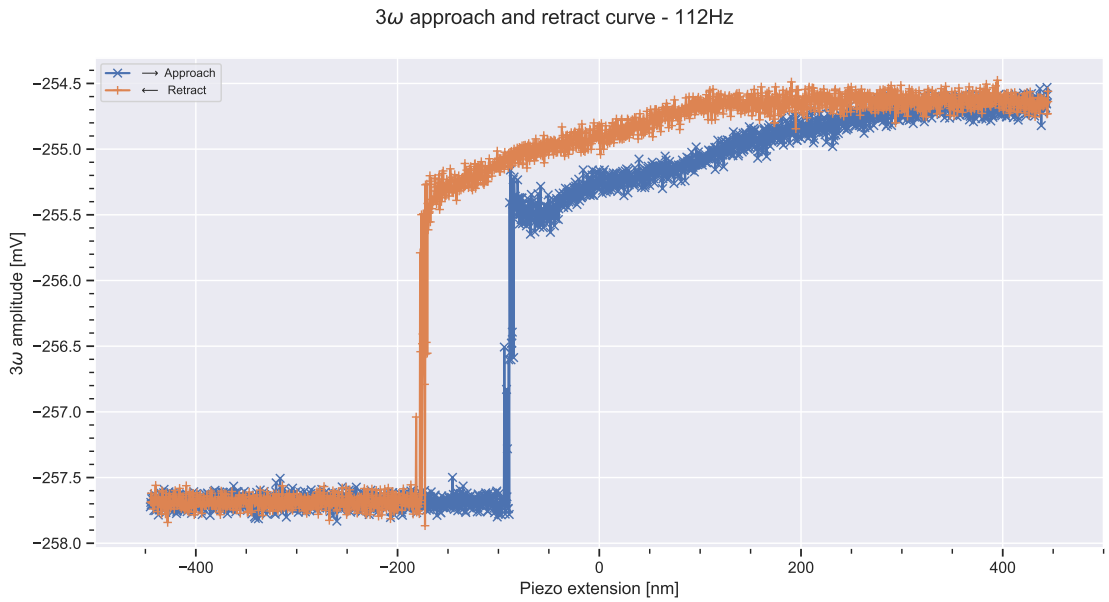


Figure 6.70: Monitoring the 3ω signal as the probe approaches and retracts from the sample surface, at a probe drive frequency of 112 Hz.

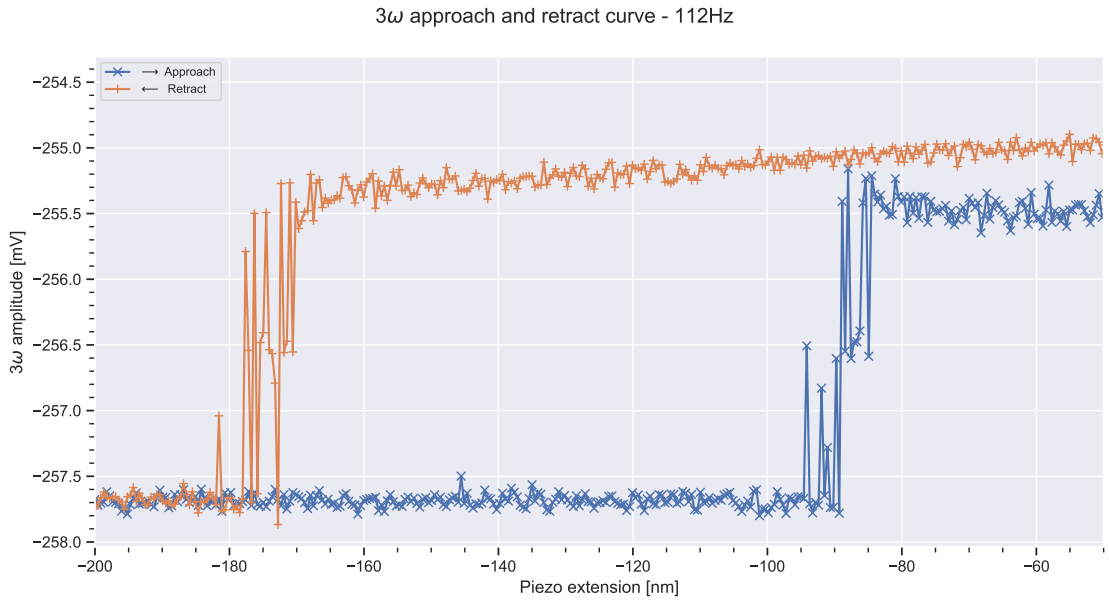


Figure 6.71: Zoomed in to measurements around the contact point while monitoring the 3ω signal as the probe approaches and retracts from the sample surface.

Examining Figure 6.71 it can be seen that at the immediate areas where the probe makes or loses contact, there is a rise in noise in the measurement. As this is on the order of around 10 nm, it could be an artefact of bimetallic thermal bend in the cantilever causing probe actuation, engaging and disengaging the tip with the surface before making firm and sustained contact. However, once sustained contact has been made, there is little to no change in the signal past contact.

The probe cantilever has an approximate spring constant of 0.2-0.4 Nm^{-1}. Extending the probe 500 nm past initial contact (as in Figure 6.70) equates to approximately 100-200 nN of applied force, a far greater force than many SThM studies require. As such, the system was designed to apply a minimal force of between 2 and 4 nN, approximately 10 nm past initial contact, which is comparable to tapping mode AFM forces [196]. However, it can be noted from Figure 6.71 that even upwards of 20 nm past firm contact (4-8 nN of force) no detectable change in the SThM output could be seen.

Similarly to measurements in air, monitoring the gradient of the 3ω signal with distance on an approach allows for the determination of the tip-smaple contact location at the gradient maximum. This has been shown in Figure 6.72. It has been found experimentally that reduction of the probe bouncing effect on the gradient measurement can be achieved by passing gradient measurement through a digital low pass filter. Although this introduces a slight delay in the rise of the gradient signal.

Its time constant is constant for all approaches and can therefore be accounted for.

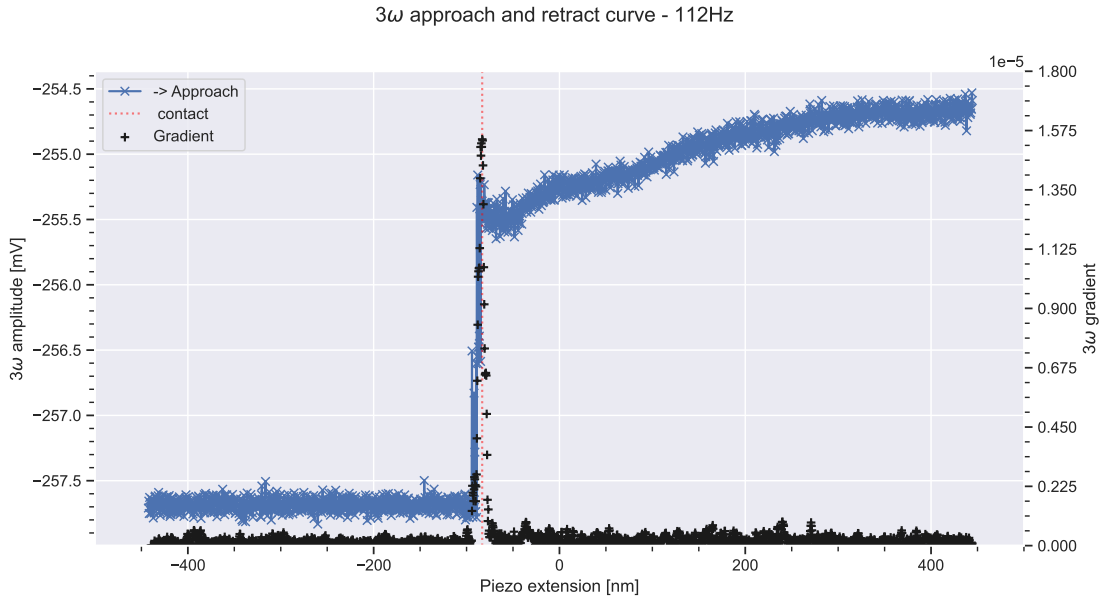


Figure 6.72: Monitoring the gradient of the 3ω signal as the probe approaches the sample surface. calculated contact point marked.

6.3.4 Topographic noise

As was done previously with measurements in air in section 4.4.2, the method's ability to detect the surface location could be quantified by measuring the apparent topographic noise in repeated measurements of a single point. Utilising a probe drive frequency of 448 Hz and 80 µW probe power, a scan of a single point was obtained utilising the gradient monitoring technique has been shown in Figure 6.73. It can be seen that there is a significant drift of over 100 nm before equilibrium had been reached and the measured pull-in point of a single point stabilises. Although this drift is significant given the full range of the Z piezo of approximately 1 µm, it can be corrected for in post-processing by path levelling.

Once the sage had settled and reached equilibrium, the measurements were started and are displayed in a 16x16 grid in Figure 6.74 with a histogram of the topography data points in Figure 6.75.

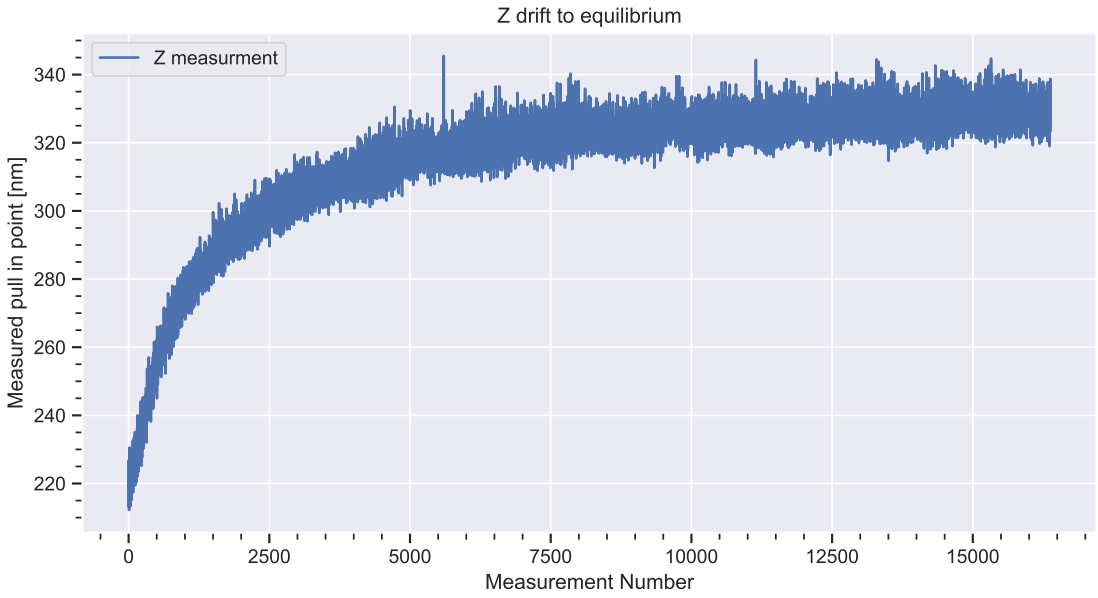
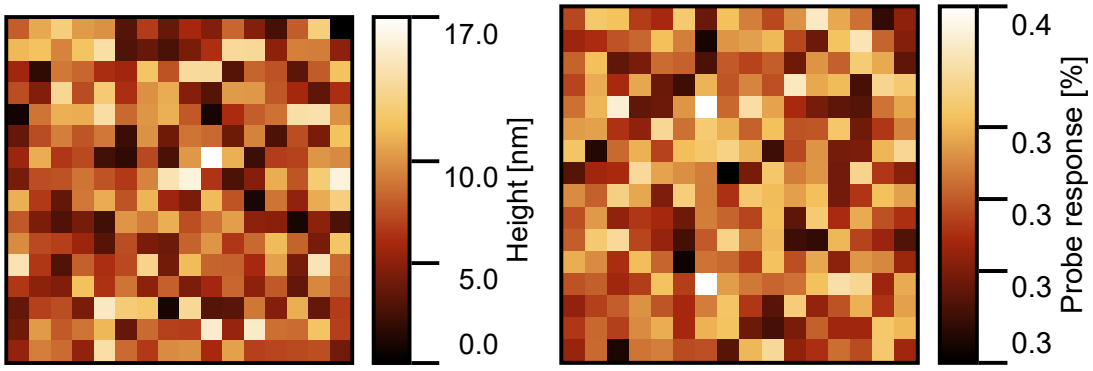


Figure 6.73: Drift in the topographic output can be seen until equilibrium has been reached.



(a) Topographic output of scan showing a Pk-pk noise of 17 nm with a standard deviation of 3.49 nm.

(b) 3ω Probe response as a percentage, showing a standard deviation in response 0.020%

Figure 6.74: A single point displayed in a 16x16 pixel grid.

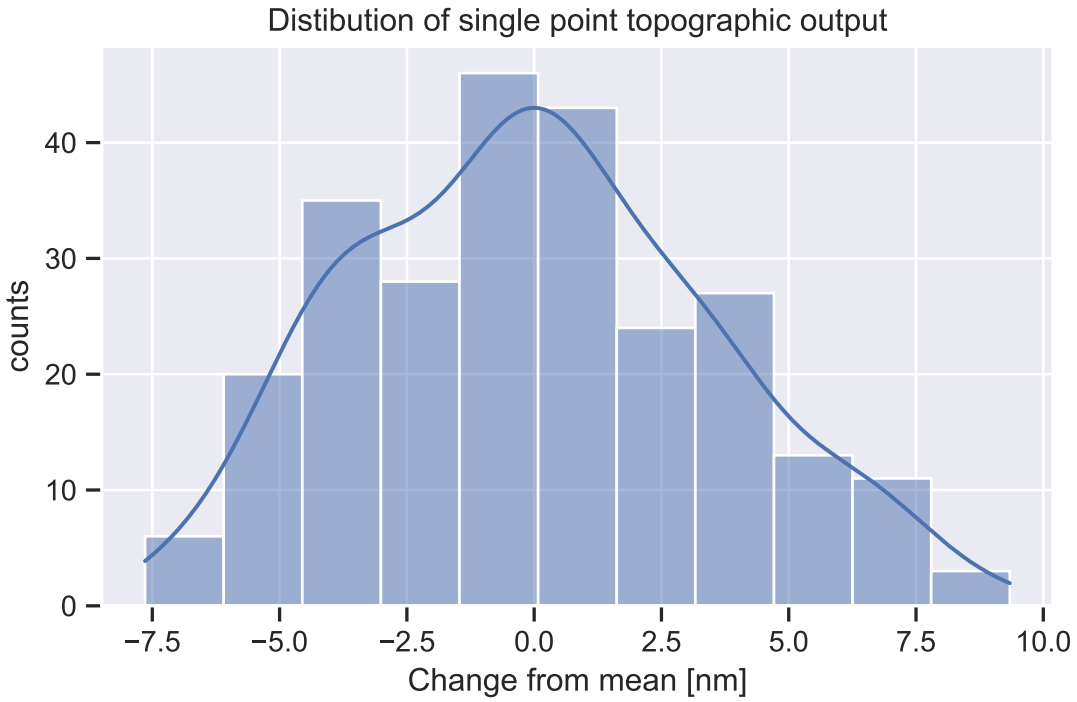


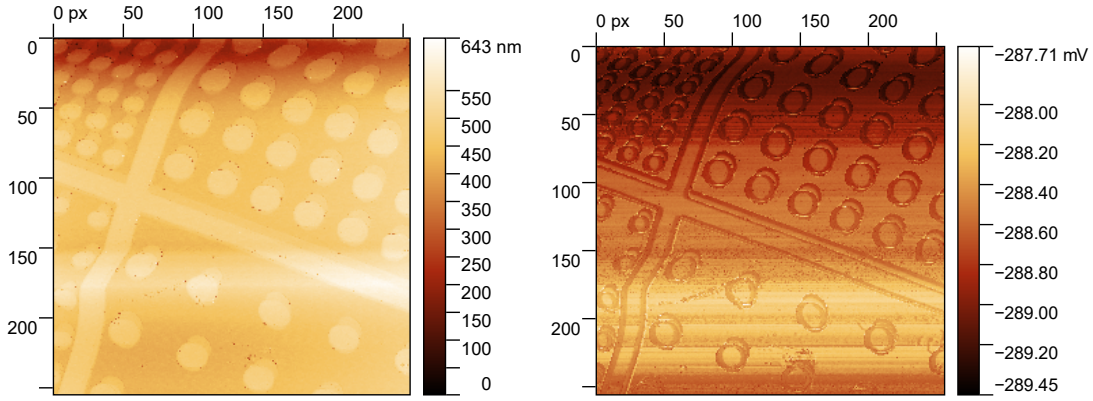
Figure 6.75: Histogram of topographic data points in Figure 6.74a, showing an approximately Gaussian distribution with a standard deviation of 3.49 nm

Pk-pk noise in the topographic output was measured to be 17 nm for the measurement with a standard deviation of 3.5 nm, and is comparable with measurements in air and liquid. The 3ω response of the probe was also stable in a vacuum with a standard deviation in the measurement of 0.02%. However, with the lower mean in the probe response, a large coefficient of variation of 6.5% in the repeated point measurement was present.

6.3.5 Silicon pillar

To compare dark condition topographic control to that obtained in air, the silicon pillar sample (as discussed earlier in section 5.3) was scanned in a vacuum utilising the gradient monitoring method. As discussed in section 6.3.4 topographic drift with temperature is a significant issue for the system utilised as evidenced by comparing the raw topography output and 1ω signals from the measurement in Figure 6.76a and b.

Post-processing of the height channel in Gwyddion though path levelling and base flattening were carried out to account for this thermal drift in Z with the result of this seen in Figure 6.77a. However, drifts in X and Y are more difficult to correct

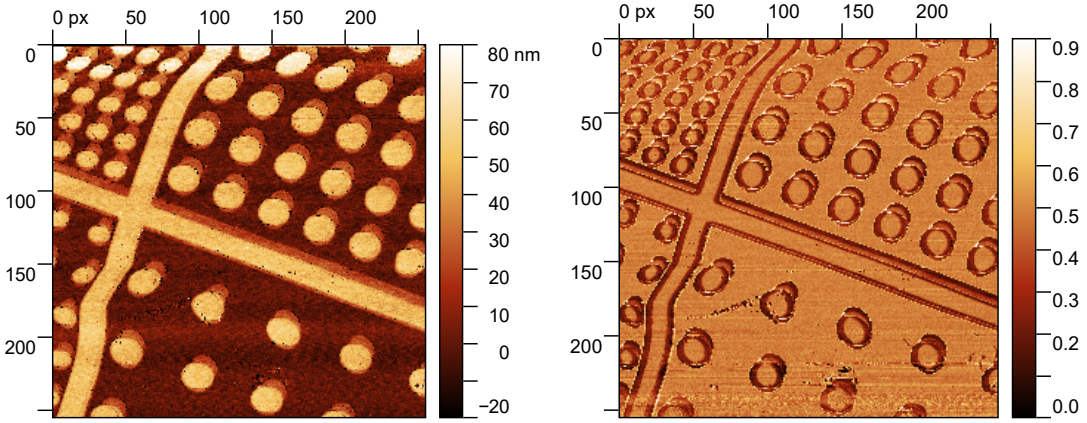


(a) Topographic output

(b) 1ω signal drifting with rooom temperature

Figure 6.76: Raw signals from silicon pillar sample scanned in Vacuum

for. 3ω probe response can be seen in Figure 6.77b. As expected, the 3ω response of the probe is vastly reduced to <1% due to the point nature of conduction.



(a) Topographic output corrected

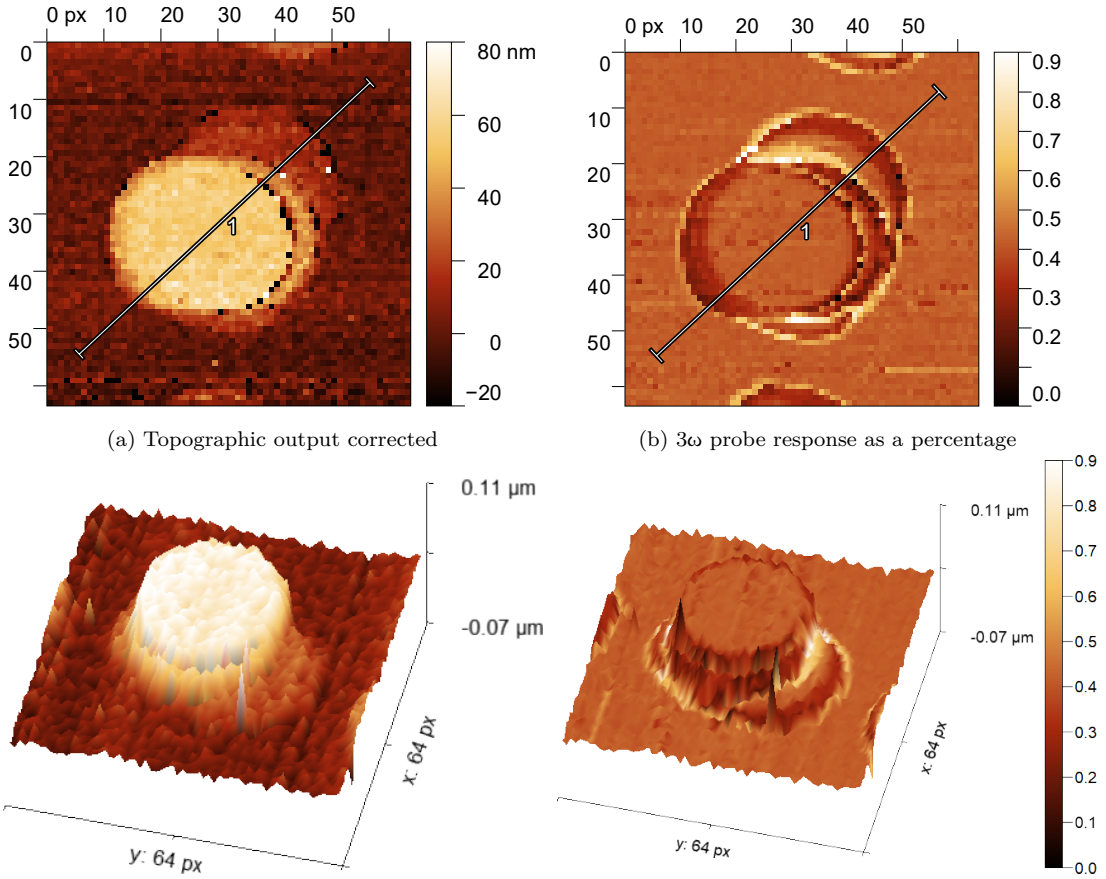
(b) 3ω probe response as a percentage

Figure 6.77: Silicon pillar sample scanned in Vacuum

The sample was re-scanned, focusing on an individual pillar, as shown in Figure 6.78. Corresponding line extractions are provided in Figure 6.79, probe responses are consistent across the flats of the silicon and at the apex of the pillars, with the exception of when the probe contact is reduced around the edges of the pillar apex, visible clearly in Figure 6.78d, primarily this was caused by the reduced area of contact due to the relatively large tip size.

The very small change in signal when the probe makes initial contact with the very edge of the pillar, caused the control loop to push the probe further into the sample until the probe makes better contact, or the probe slips into firmer contact. This artefact of the system is not easily resolvable in the control loop, due to the change in signal being below the noise floor of the system.

In the topographic output in Figure 6.78a and Figure 6.78c, there was a clear tip switching artefact occurring as metal flags or other areas of the probe tip were making contact with the pillar causing multiple 'shadows' to appear. The largest of which can be measured as a secondary tip on the probe occurs approximately 20 nm recessed from the true probe tip apex and can be clearly seen in the extracted line in Figure 6.79. A diagram showing the origin of the tip switching is given in Figure 6.80.



(a) Topographic output corrected

(b) 3ω probe response as a percentage

(c) 3D representation of single pillar

(d) 3ω probe response (colour bar) overlaid on 3D topography

Figure 6.78: Individual silicon pillar sample scanned in Vacuum

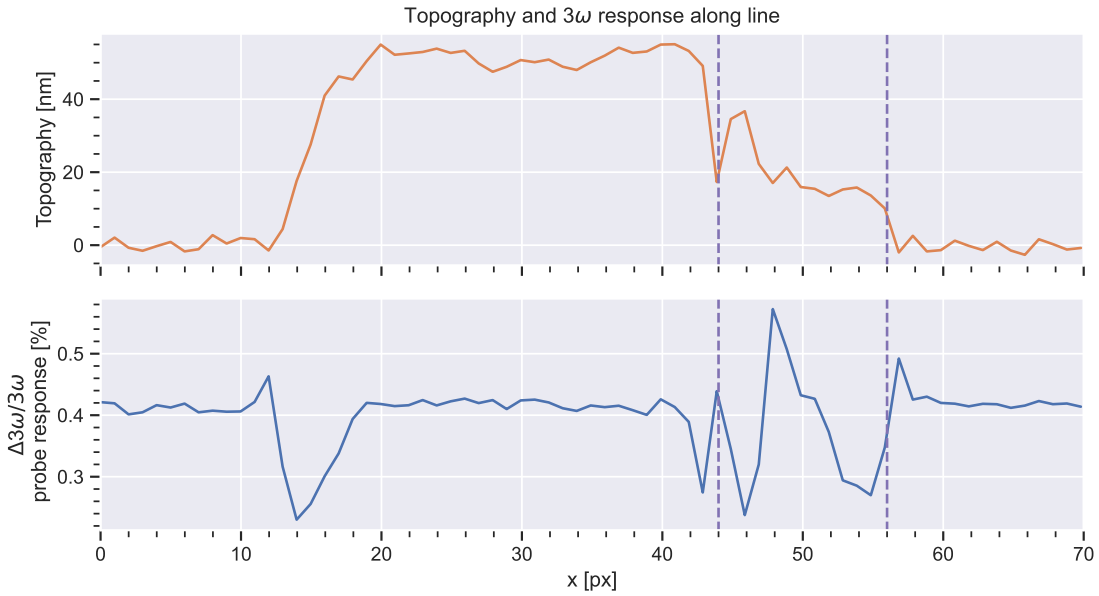


Figure 6.79: Line traces from silicon pillar scan in Figure 6.78a and b. The area highlighted by purple lines denotes the measurement of the probes secondary tip.

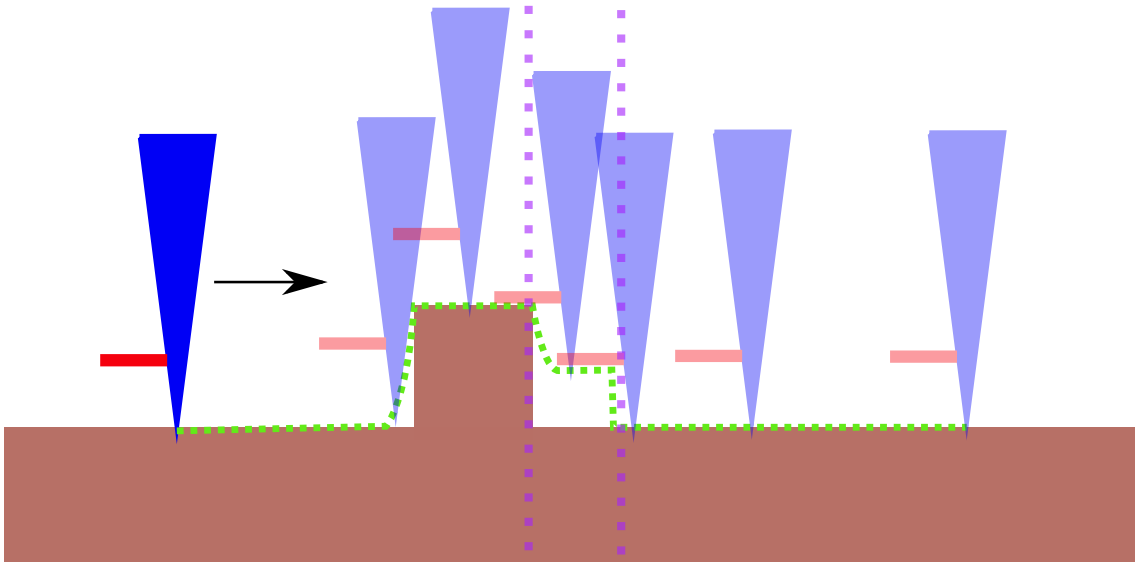


Figure 6.80: Diagram depicting a metal flag (red) on a probe tip (blue) showing a shadow (purple dashed lines) in the topography measurement (green dashed line) as the probe scans over a feature.

Interestingly, double contact artefacts in Figure 6.78b only occur in the immediate pixel at the base of the pillar, or at contact with the secondary tips. This is expected due to the point contact nature of thermal heat transfer in vacuum SThM as described in Figure 6.56.

6.4 Discussion

As shown in this chapter, adaptations of the control loops have been made to provide topographic control of the SThM in both liquid and vacuum environments. The topographic noise in both environments has been characterised, and shown to be comparable to the resolution obtained in air. Results from the vacuum setup show that these techniques of topographic control can be applied to probes of differing construction, with changes in probe response less than 0.1% still being captured by the control loop. It has also been shown that scanning can still be carried out with a probe-scan configuration, a more common setup compared to the sample-scan method used in liquid and air, with minimal alterations to the control loop. The same topographic silicon pillar scanned in air was re-scanned in liquid and vacuum with comparable topographic results. The thin film gold step edge sample was re-scanned in liquid, showing the greater thermal measurement precision that can be achieved from measurement in liquid. The ability to perform out-of-contact surface characterisation allows for reduced effects of inconsistent solid-solid contact as well as the ability to perform frequency sweeps during in-contact thermal measurements open up the possibility for further exploration of SThM for quantifiable measurement of thermal conductivity and diffusivity of scanned materials via the 3ω technique as set out by Cahill [41].

Although it has now been shown that topographic control of the SThM is possible in air, liquid, and vacuum environments using "thermal feedback" techniques, the speed of scanning is limited. As there is a lack of force measurement, the tip-sample contact must be broken for each pixel to be captured, preventing the technique from allowing in-contact raster scanning. To reintroduce this ability back into the SThM, integrated sensors must be developed that can provide the appropriate deflection signals to monitor tip-sample mechanical forces.

Quantification of EBL alignment

7.1 Introduction

To accurately place strain sensing elements on the most sensitive areas of a cantilever, and improve manufacturing yield. We must have a method to align layers of the lithographic process precisely.

As briefly discussed in section 3.4, one of the most common marker types used within the JWNC for the alignment of lithography layers is the square marker. However, they generally have quite a variable alignment accuracy which is dependent on factors such as line edge roughness [133]. As they are large markers, they tend to be written with a large beam spot size and step size to reduce the pattern write time. However, in doing so, line edge roughness is increased and can lead to alignment errors upwards of 100's of nanometres [134].

Salvation can come in the form of correlation-based alignment of Penrose markers [138, 140, 141]. As stated in section 3.4.2, the Penrose pattern (Figure 7.1) consists of two fundamental shapes, 'kites' and 'darts', arranged in such a way to create a translationally aperiodic pattern that can be extended infinitely on a 2D plan. All Penrose tilings used in this work contain 5-fold rotational symmetry. A microfabricated standard Penrose marker used for high accuracy alignment in the JWNC can be seen in Figure 7.2 and takes up an approximately 9 μm^2 area.

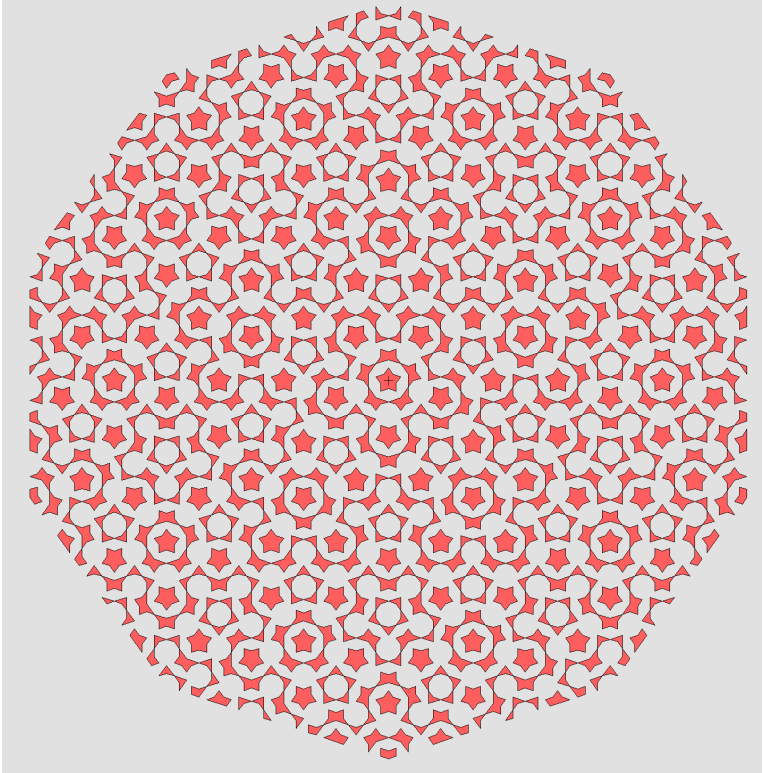


Figure 7.1: GDSII design file of a Penrose marker, consisting of kite and dart shapes arranged in an aperiodic fashion.

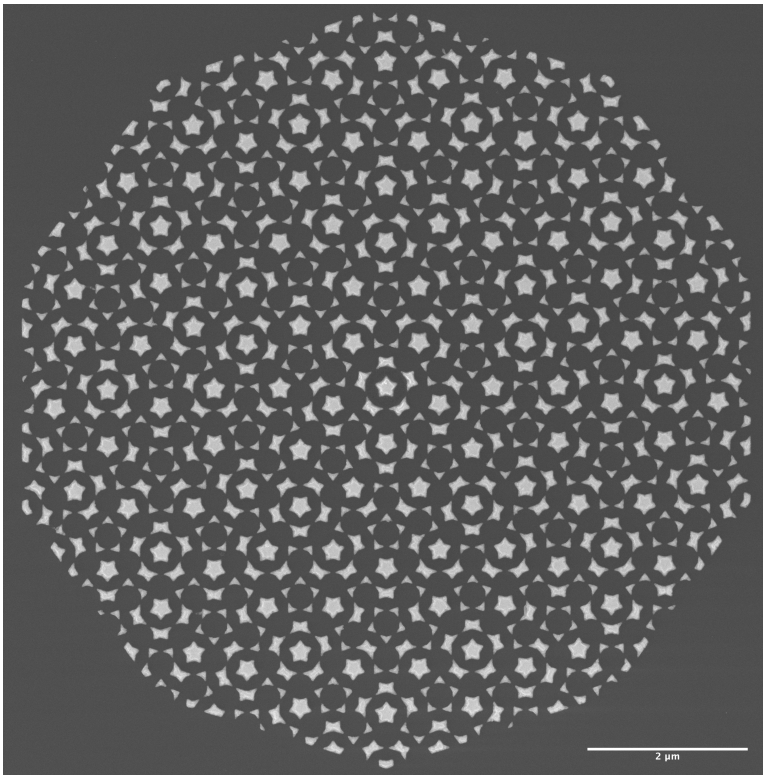


Figure 7.2: A micro fabricated 9 μm^2 Penrose marker.

7.2 New Penrose markers

The standard Penrose marker design (shown in Figure 7.3a) has been created with 8 layers of tiling over 9 µm^2. This has been shown to supply a sufficient number of edges with an appropriate density for accurate alignment to low single-digit nanometer length scales [138] with relative ease in fabrication.

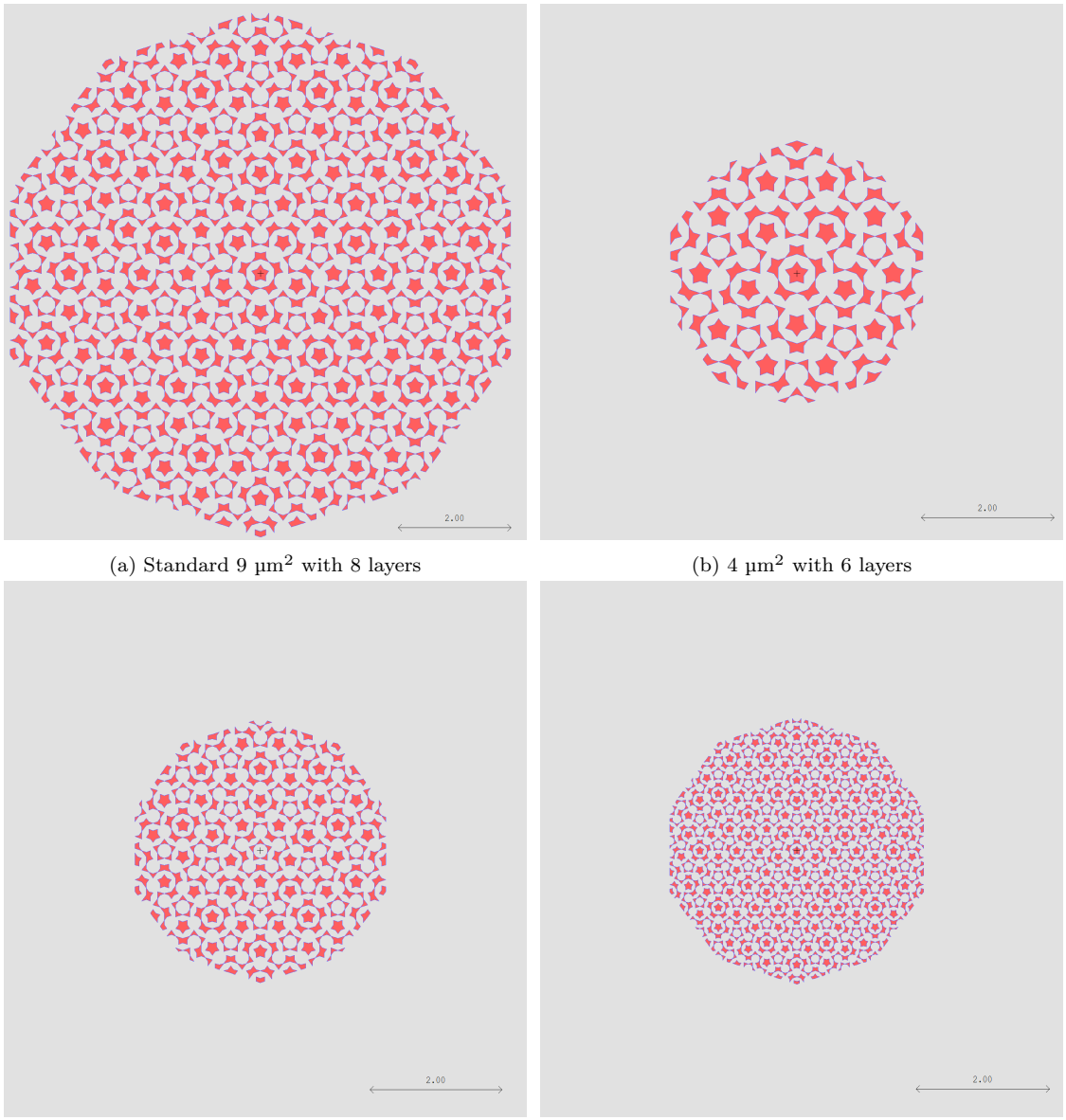
As part of this work, newer, smaller area Penrose markers have been designed and fabricated. These new markers have been designed to take an approximate 4 µm^2 area, a reduction of the area used of over 50%, with 6, 7, and 8 layers of tiling. 4 µm^2 markers with 6 layers of tiles will have similar feature size and density to that of the 9 µm^2 marker but with a smaller interrogation area and more signal averaging. Small markers with 8 layers of tiles should have the same number of shapes as the 9 µm^2 marker but with a higher density of shapes. The design of these various Penrose tiles has been shown in Figure 7.3.

An additional benefit of reduced marker space could be the potential of multiple marker measurements for a cell corner to create a least-squared fitted alignment map, such methods were utilised by Lambert [63] for etched square markers and saw drastic improvements to the alignment capabilities.

Fabrication

To micro-fabricate these patterns, a blank sample of PECVD-grown silicon nitride (400 nm) on silicon (400 µm) was cleaned by sonication for 5 minutes in acetone, methanol, isopropyl alcohol, and RO water sequentially. The sample was then left in running RO water for an extra 5 minutes before blow drying with dry nitrogen to remove any particulate contamination. It was then oxygen plasma ashed for 3 minutes at 150 W power in a barrel asher to further remove thin film contamination.

Before the spinning of PMMA on the sample, it was dehydrated on a 180 °C hotplate for 5 minutes. A bi-layer of fast positive tone resist PMMA was utilised. For pattern fidelity of small structures, thin layers of PMMA are required to avoid resist collapse. As such, 4% 200K molecular weight PMMA dissolved in anisole (AllResist, AR-P 642.04) was used as a bottom layer, with a top layer of 1% 950k molecular weight PMMA dissolved in ethyl-lactate (AllResist, AR-P 679.01). The bottom and top layers were spun at 2000 rpm and 4000 rpm for 60 s, giving layer thicknesses of 150 nm and 30 nm respectively. After spinning each resist layer the sample is baked at 180 °C on a hotplate for 3 minutes to drive out solvent and re-flow the resist.



(a) Standard 9 µm^2 with 8 layers

(b) 4 µm^2 with 6 layers

(c) 4 µm^2 with 7 layers

(d) 4 µm^2 with 8 layers

Figure 7.3: Penrose marker designs with (a) showing a standard Penrose marker for high accuracy alignments, and (b-c) showing new marker types with increasing layers of tiling.

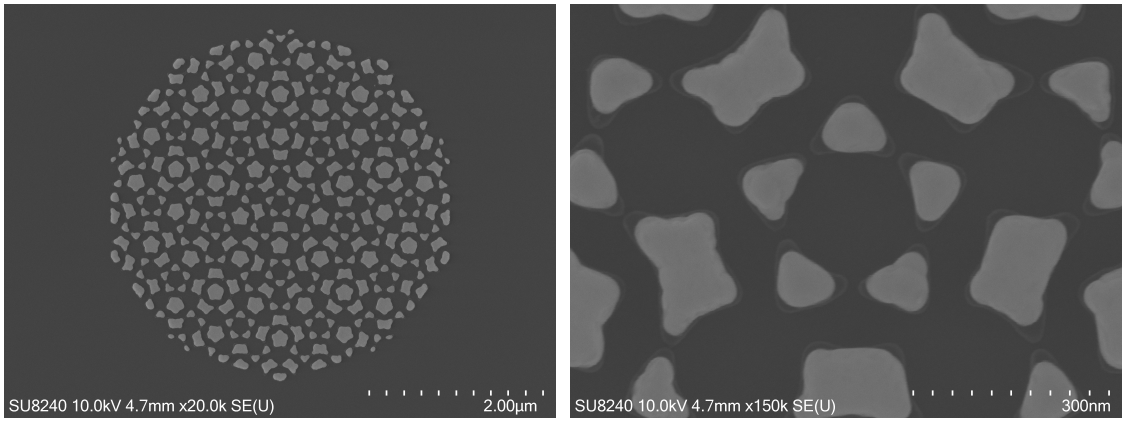
The patterns were then defined in the PMMA on the EBPG 5200+ E-beam writer tool and developed in 23 °C 3:1 MIBK:IPA for 30 seconds before development being stopped in IPA for 30 seconds. The sample was then ashed in the barrel asher for 30 seconds at 80 W power to remove any residual surface PMMA in the areas written. The patterns are then metalised by EBPVD with 5 nm of nichrome as an adhesion layer before the deposition of 70 nm of platinum. The deposited sample was then placed in a bath of 50 °C acetone to lift off the features for a minimum of 2 hours, before quick sonication in acetone, IPA and RO water sequentially for 1 minute each before blow drying with dry nitrogen.

The fabrication steps are best summarised in a process sheet shown in Table 7.1.

Table 7.1: Penrose pattern microfabrication steps.

#	Step	Process
1	Sonication	5 mins, in acetone, methanol, IPA, and RO water, then N2 blow dry.
2	O_2 Ash	3 mins at 150 W.
3	Bake	5 minutes on 180 °C hotplate dehydration.
4	Spin	4% 200K MW Anisole PMMA (AR-P 642.04) at 2000 rpm, 60 s for a 150 nm bottom layer.
5	Bake	3 minutes on 180 °C hotplate PMMA tempering.
6	Spin	1% 950K MW Ethyl-Lactate PMMA (AR-P 679.01) at 4000 rpm, 60 s for a 30 nm top layer.
7	Bake	3 minutes on 180 °C hotplate PMMA tempering.
8	E-Beam	Write Penrose patterns.
9	Develop	23 °C 3:1 MIBK:IPA, 30 s with mild agitation. Stopped in IPA.
10	O_2 Ash	30 s at 80 W.
11	Metalisation	NiCr/Pt (5 nm/70 nm).
12	Lift-off	50 °C acetone bath, 2 hours.
13	Sonication	1 min in acetone, IPA, and RO water, then N2 blow dry.

Typically markers need to be fabricated with a material with a high atomic size, or sufficiently thick to provide contrast in the E-beam tool at 100 kV. Usually, gold is used as marker material. However, in this work, it was found through experimentation that gold markers with features at this length scale deform when exposed to the high temperatures required to dehydrate and re-flow resists for subsequent device lithography layer. An example of gold marker dewetting after hotplate baking can be seen in Figure 7.4. This has been overcome by metalisation of the marker with platinum instead of gold due to the higher bonding strength with the adhesion layer, with a platinum fabricated marker shown in Figure 7.5.



(a) Full marker SEM (b) Zoom of centre

Figure 7.4: (a)SEM image of 4 µm^2 marker with 7 layers metalised with gold, showing significant rounding of the feature edges. (b) Increased magnification at the pattern centre. This is caused by the dewetting of the gold due to the low bonding strength with the lower nichrome layer.

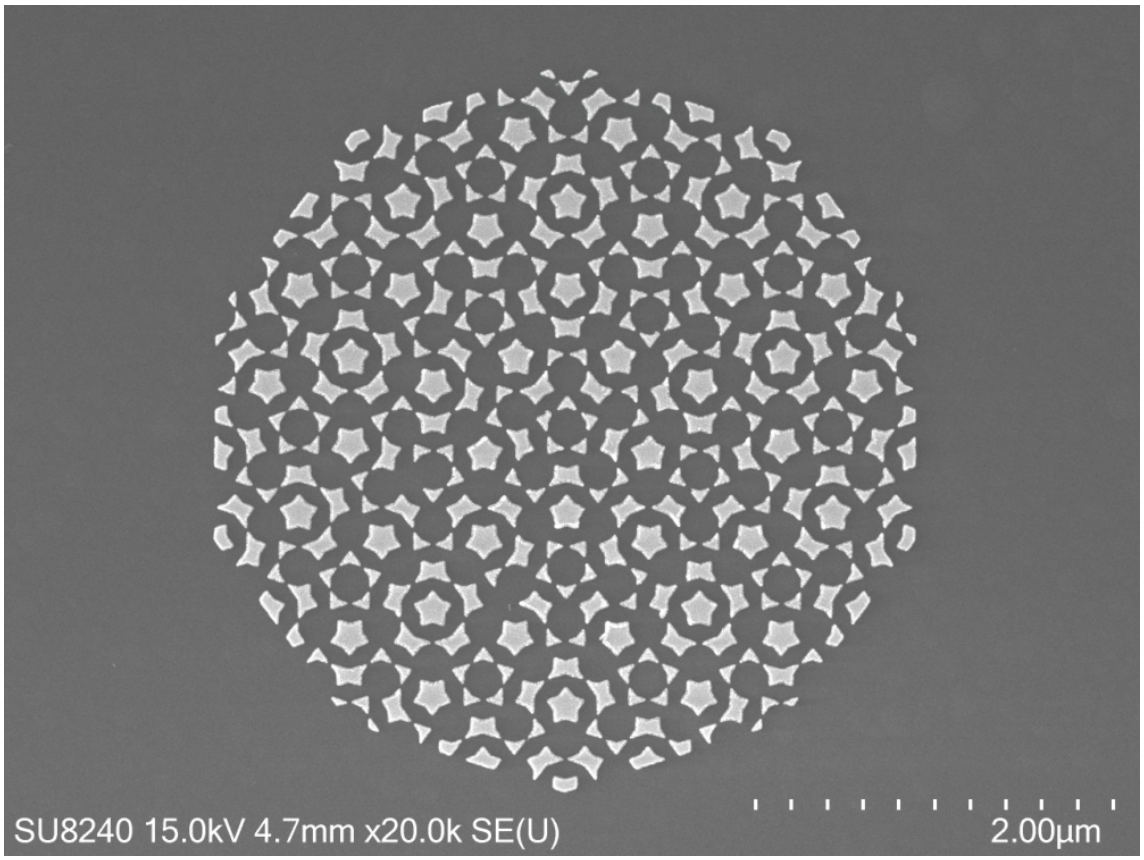
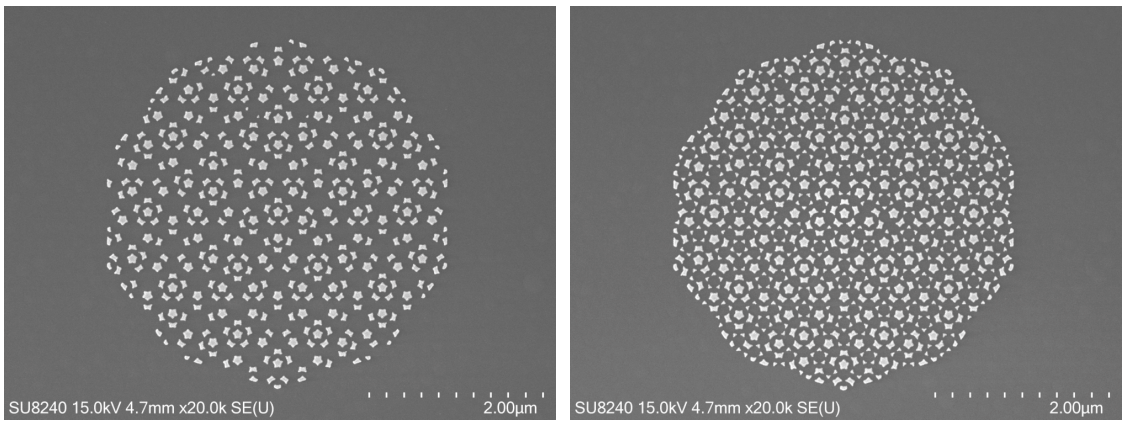


Figure 7.5: A Penrose marker metalised with platinum, showing much better pattern fidelity and increased resistance to thermal processing.

For writing the patterns on the beam writer using the smallest beam step size of 1 nm and a beam current of 1 nA, the required dosage for high pattern fidelity was found to be 840 µC/cm^2 for the 9 µm^2 marker as well as the 6 and 7 layer

4 µm^2 marker. However, the 8 layer 4 µm^2 pattern required a higher dosage for the definition of the smaller features at 972 µC/cm^2 (Figure 7.6).



(a) 840 µC/cm^2 (b) 972 µC/cm^2

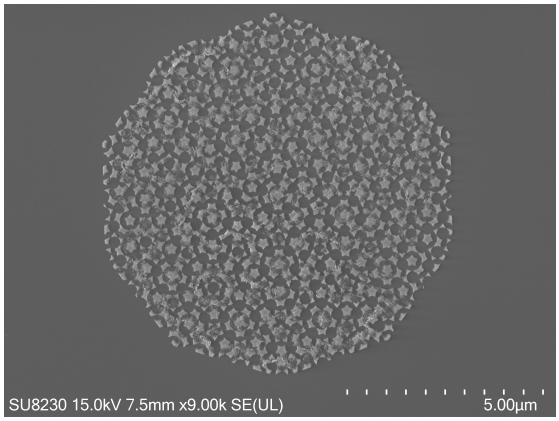
Figure 7.6: SEM images of 4 µm^2 marker with 8 layers. Smaller features in the pattern do not develop appropriately in (a). Increasing the dosage to (b) shows proper development of the pattern.

Although Penrose markers are relatively immune to defects, additive contamination of the features can cause erroneous correlations and an increase in the standard deviation of marker searches [138, 140]. Care must be taken to appropriately clean the sample after metal lift-off to ensure pattern fidelity. An example of additive defects that can occur are drying marks of contamination on the features, obscuring the feature edges as seen in Figure 7.7.

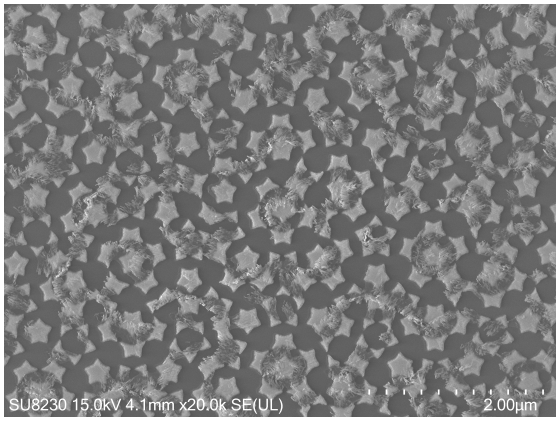
A SEM gallery of Penrose markers fabricated for this work is shown in Figure 7.8 through 7.11. Heron in, each marker type has been given an abbreviated name associated with its area and layers of tiling according to Table 7.2. The marker labelled 'Large 8' is the standard high-accuracy alignment marker utilised within the JWNC. New iterations of the marker are abbreviated to 'Small' and their associated number of tiling layers.

Table 7.2: Table of Penrose patterns investigated in this work

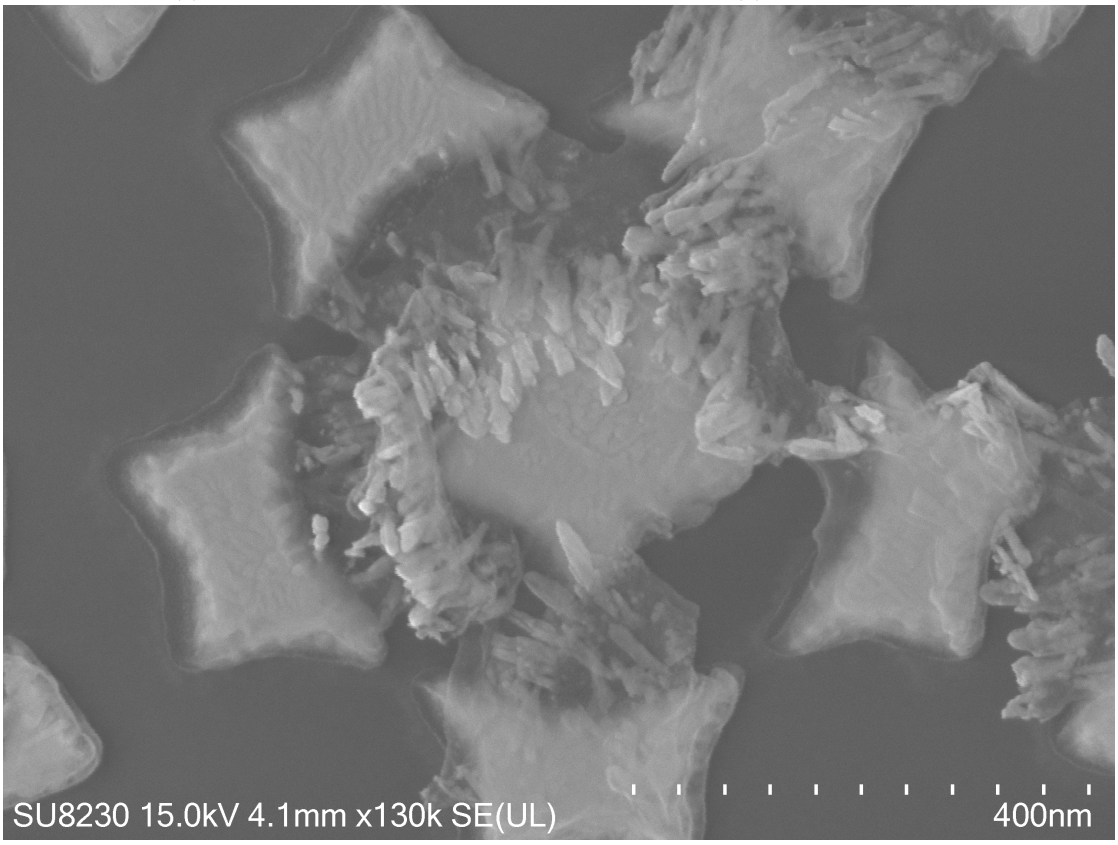
Area [µm^2]	Tiling layers	Abbreviation
9	8	Large 8
4	6	Small 6
4	7	Small 7
4	8	Small 8



(a) Full marker SEM



(b) Close up of centre



(c) Zoom of one feature

Figure 7.7: SEM image of 9 µm^2 marker with 8 layers metalised with platinum. (a) Showing full Penrose image where contamination may not be so obvious. (b) Increased magnification of the pattern features showing significant contamination. (c) close up of single feature suggests possible contamination deposing on of the surface during sample drying after lift-off.

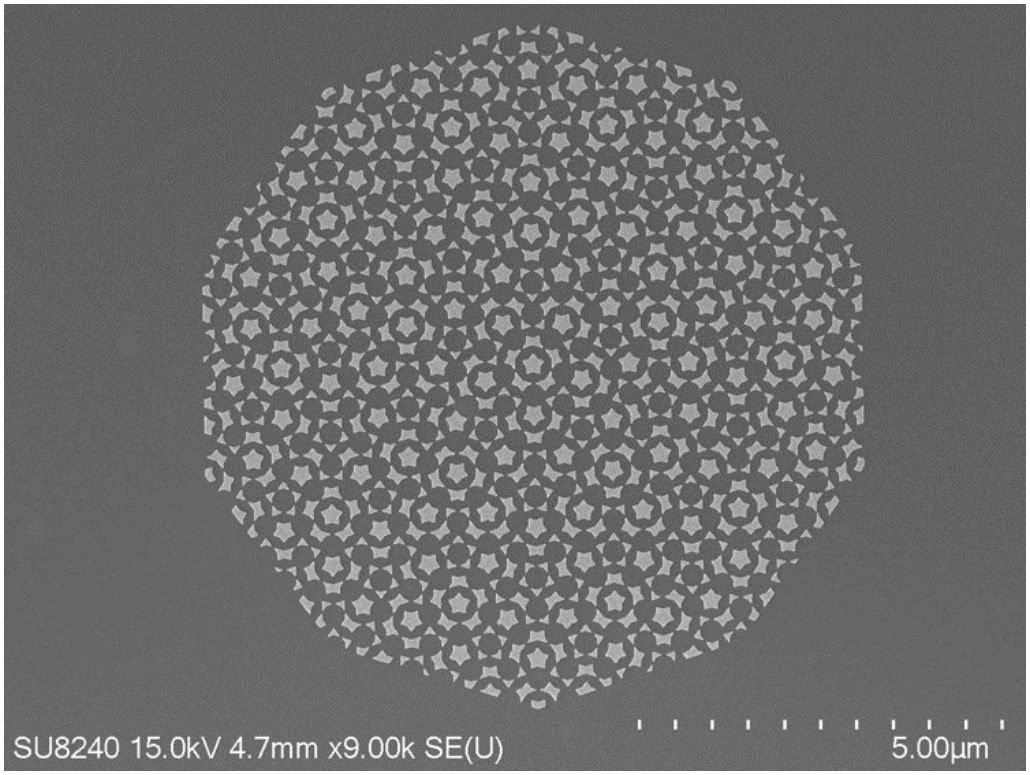


Figure 7.8: Standard 9 µm^2 marker with 8 tiling layers, abbreviated to Large 8

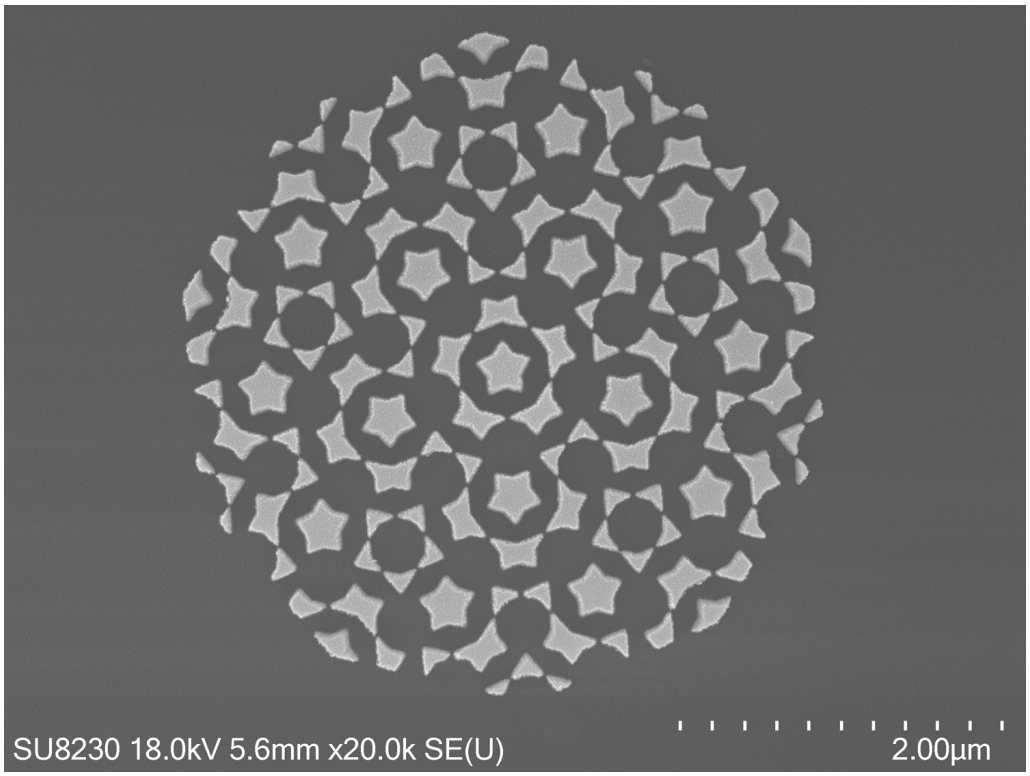


Figure 7.9: 4 µm^2 marker with 6 tiling layers, abbreviated to Small 6

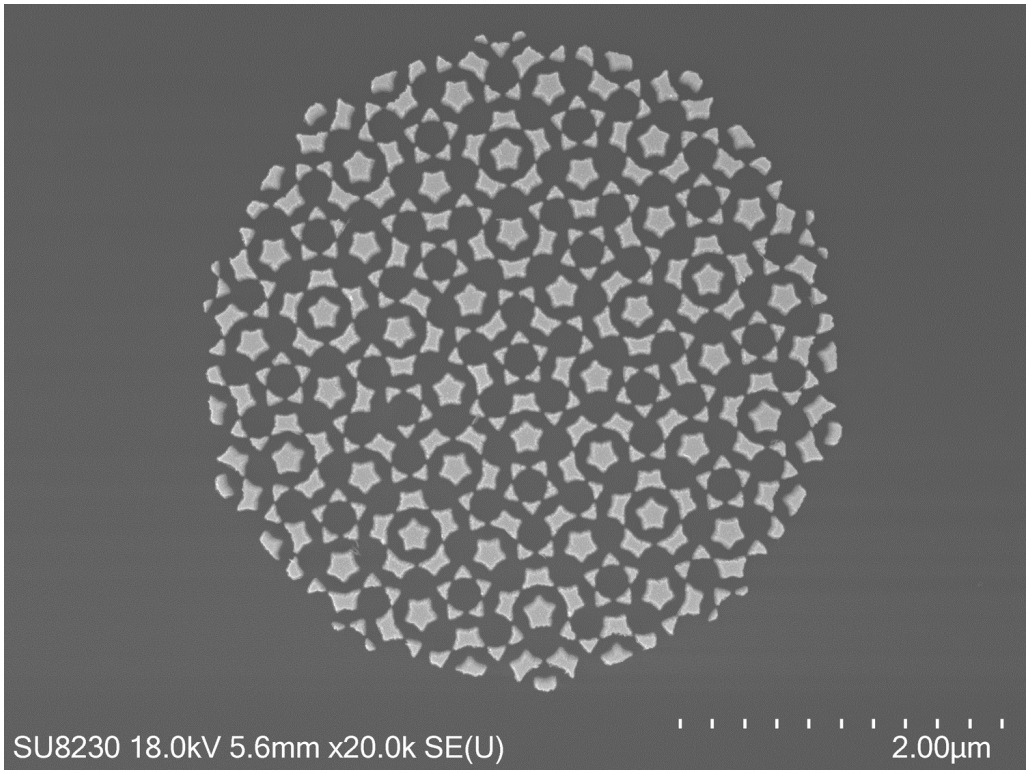


Figure 7.10: 4 µm^2 marker with 7 tiling layers, abbreviated to Small 7

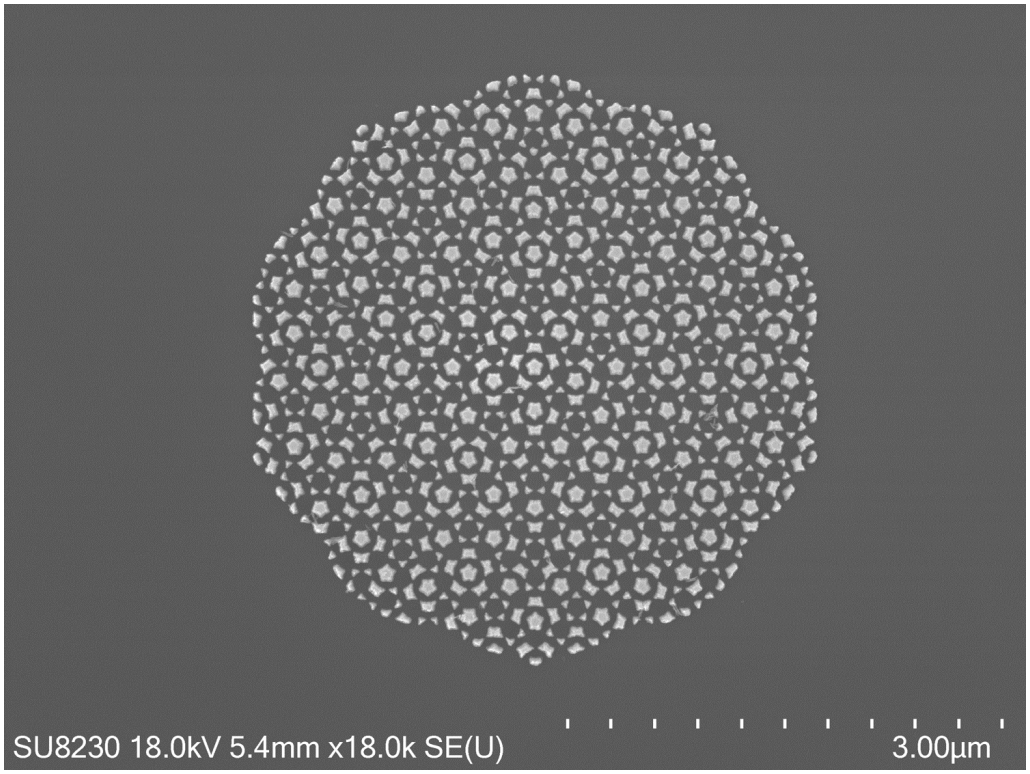


Figure 7.11: 4 µm^2 marker with 8 tiling layers, abbreviated to Small 8

7.3 Current Penrose implementation on EBPG 5200+

As toolsets within the JWNC have changed significantly over the last few years, in particularly the switch of beam writers from the VB6 to the EBPG 5200+. It was necessary to first re-qualify the Penrose tiling performance as an alignment marker. These markers have been shown previously to have a large process window, with high robustness to additive and subtractive marker damage. Docherty et al. [140] had previously shown that markers with approximately 30% of the pattern remaining can still provide single digit nanometer correlation alignments through deliberate under-dosing of the markers.

7.3.1 Experimental design

To re-affirm the Penrose marker's resilience to under dosage, an experiment was devised where the GDSII design files of the 6 layer, 4 μm^2 marker were run through a python script to repeatably and randomly remove a set number of polygons until few remained. This was repeated to obtain 5 differing sets of markers with a decreasing number of polygons to remove any bias to one particular shape type. An example of a set of markers obtained through this method can be seen in Figure 7.12, with a selection of individual markers in Figure 7.13a to 7.13l.

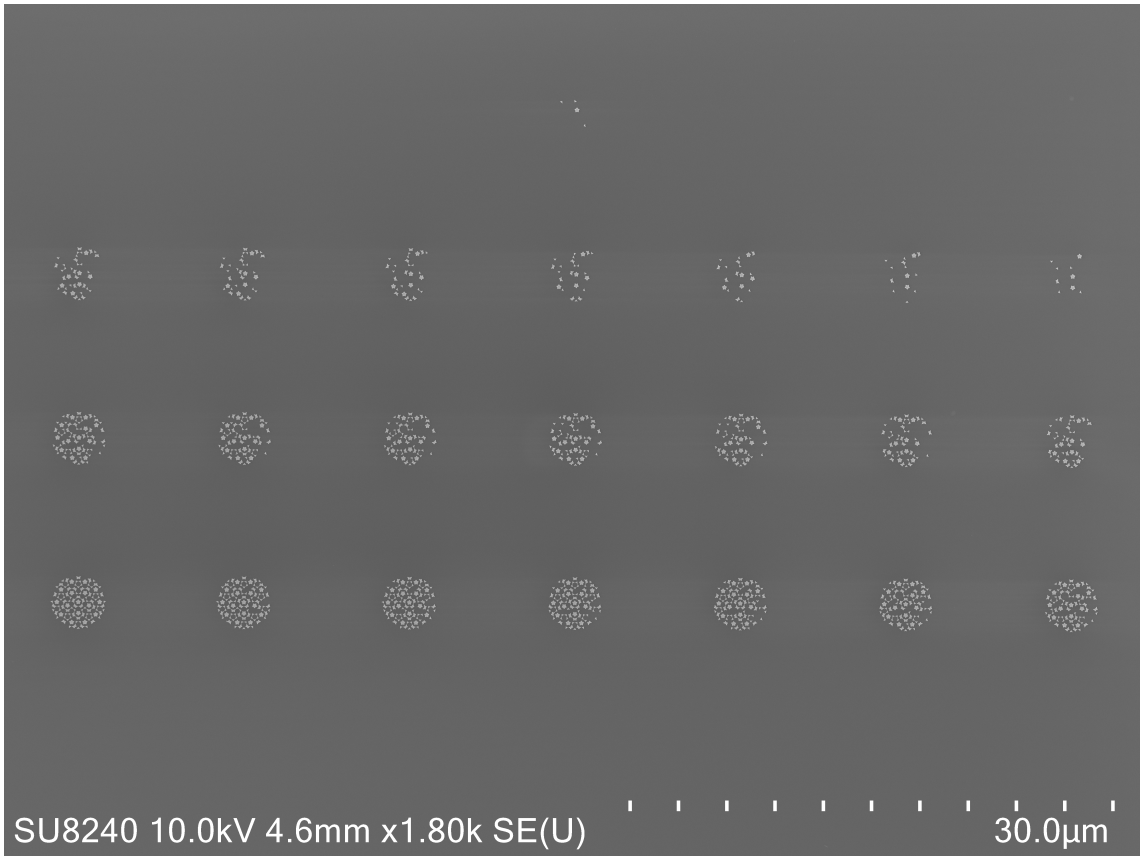
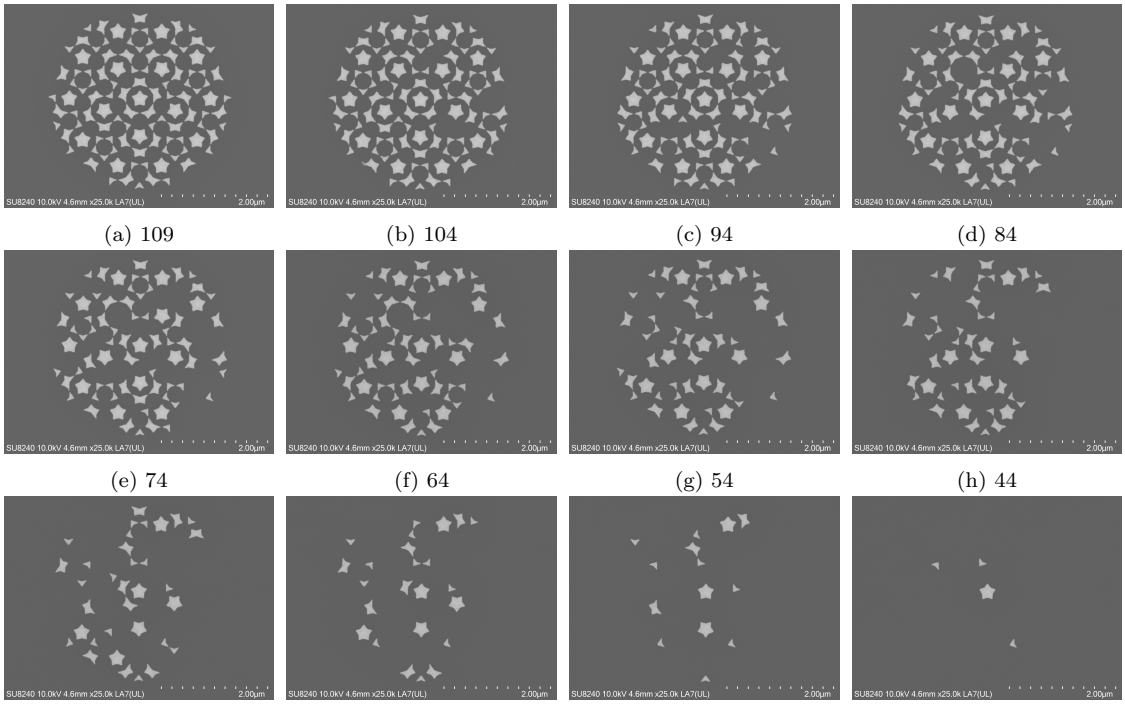


Figure 7.12: Set 1 of 5 from polygon removal experiment - bottom left polygon consists of 109 total shapes, reducing by 5 shapes in subsequent markers to the right and above.

Penrose markers of varying quality were fabricated in the corners of a cell with four known good Penrose markers (9 µm^2, 8 layers) in the centre of the field as shown in Figure 7.14. EBPG5200+ jobs were then created to search for the known good markers in the centre utilising an alignment map calculated from the corner markers of variable quality. We can measure the offset caused by the variable marker by calculating the difference of the expected marker location, with that of the found marker location from each alignment map.

It should be noted that standard 20 µm^2 square markers were utilised as backup markers. If the EBPG5200+ fails to correlate to a variable marker, it falls back onto an alignment map calculated from these squares.



(a) 109 (b) 104 (c) 94 (d) 84

(e) 74 (f) 64 (g) 54 (h) 44

(i) 34 (j) 24 (k) 14 (l) 4

Figure 7.13: Selection of images from set 1 of 4µm^2 markers with 6 layers. Number of polygons indicated for each image with a full marker in (a), and increasing number of polygon removal in (b)-(l)

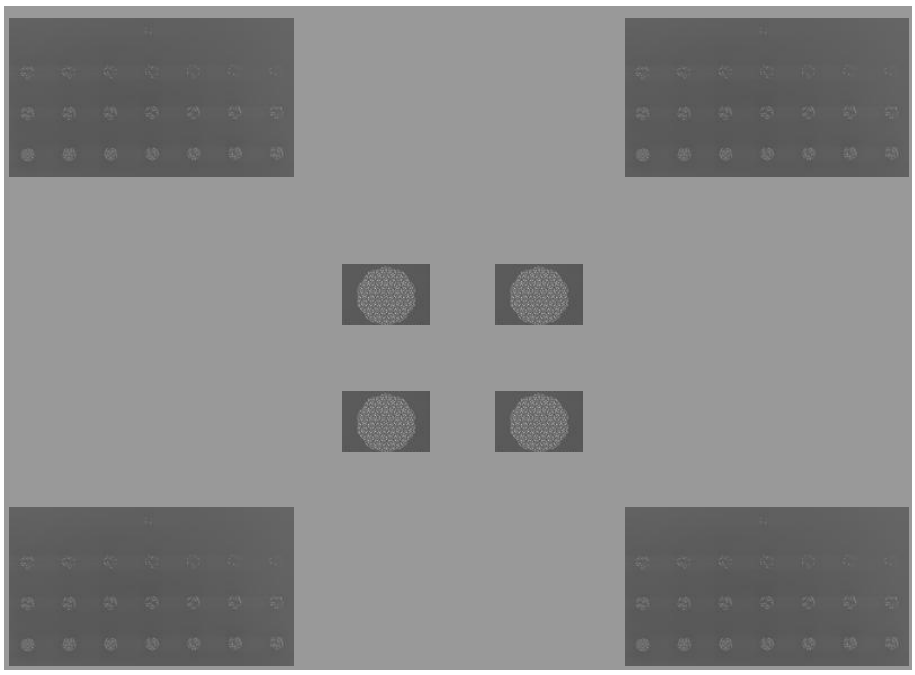


Figure 7.14: Cell layout used in the experimental procedure - Features not to scale. Sets of Penrose with an increasing number of shapes removed are placed in the corner of each cell. Four known good Penroses are placed in the centre at known locations. Aligning to the corner Penrose, then measuring the location of each centre Penrose according to each alignment map, the difference in the found location and the expected location can be an indication of errors in the calculated alignment map.

7.3.2 Results

Scripts were written to analyse the log files from the EBPG5200+ jobs upon completion. Results of the 5 sets have been displayed in a violin plot, split by axis, in Figure 7.15. In this section, we consider 'Good' alignment to occur when the correlation of the Penrose was successful. If the marker failed to correlate within set parameters in the tool, we consider it 'bad' as backup markers must then be aligned to instead. In this case, metalised 20 μm^2 square markers were used as backup markers, where alignment is known to be more variable.

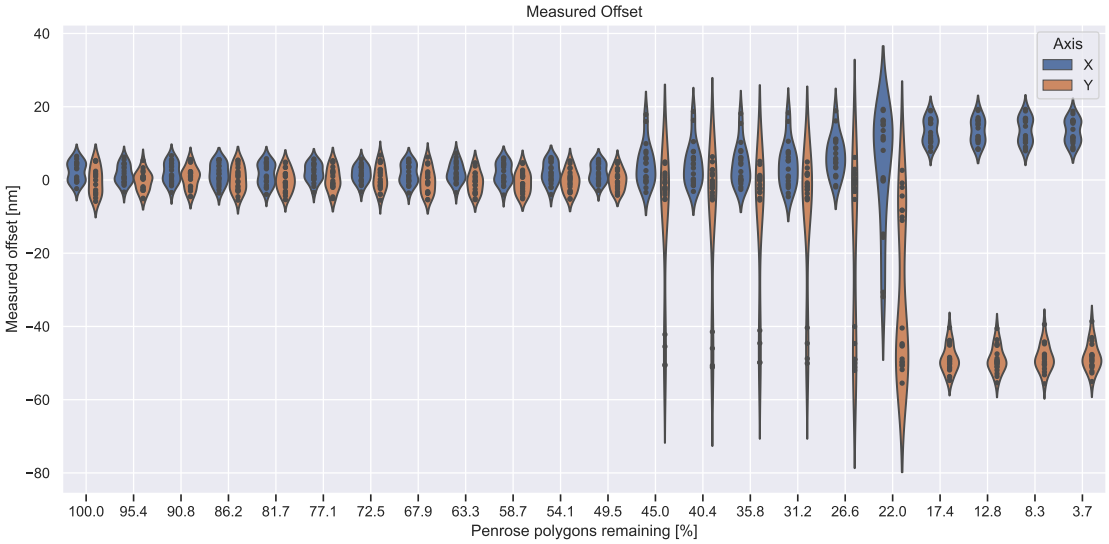


Figure 7.15: Violin plot of the measured offset between expected locations and found locations

From Figure 7.15, we can see that all markers align to within ± 10 nm until approximately 50% of the pattern remains. The alignment then gradually fails back to the square markers until around 20% when no high accuracy alignment remains. Splitting the dataset up by set of polygon removal leads to better analysis of this transition period in Figure 7.16 through 7.20 and standard deviations in the measurement plotted in Figure 7.21.

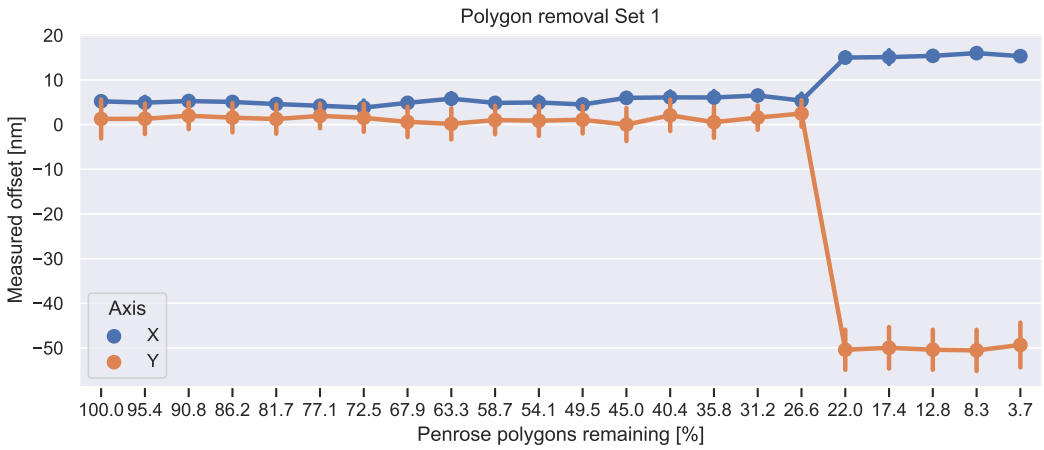


Figure 7.16: Point plot of measured offset from Set 1

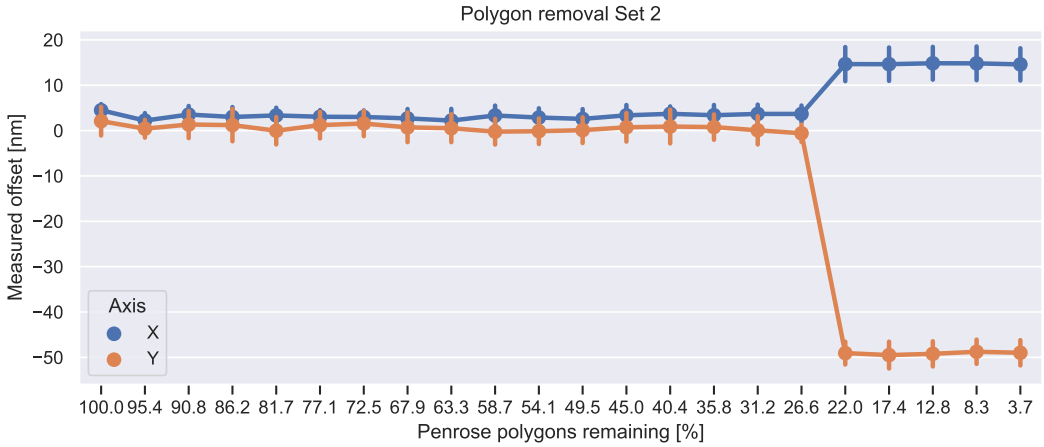


Figure 7.17: Point plot of measured offset from Set 2

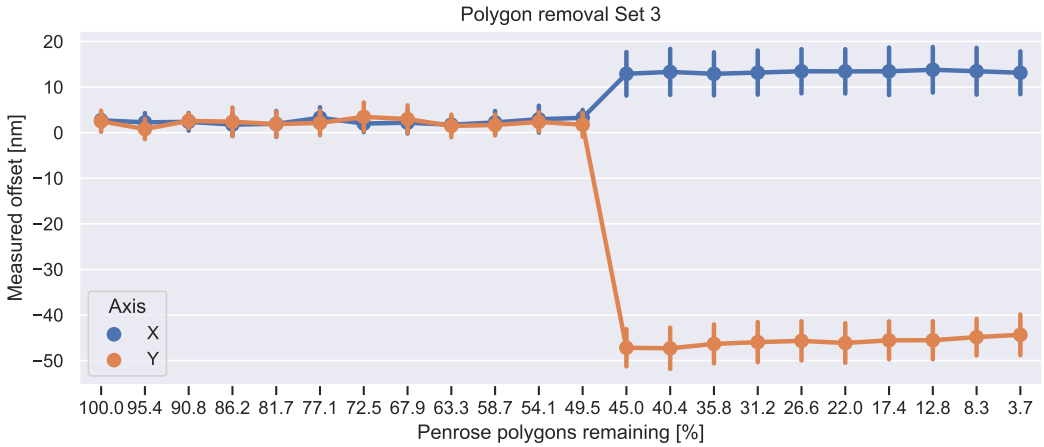


Figure 7.18: Point plot of measured offset from Set 3

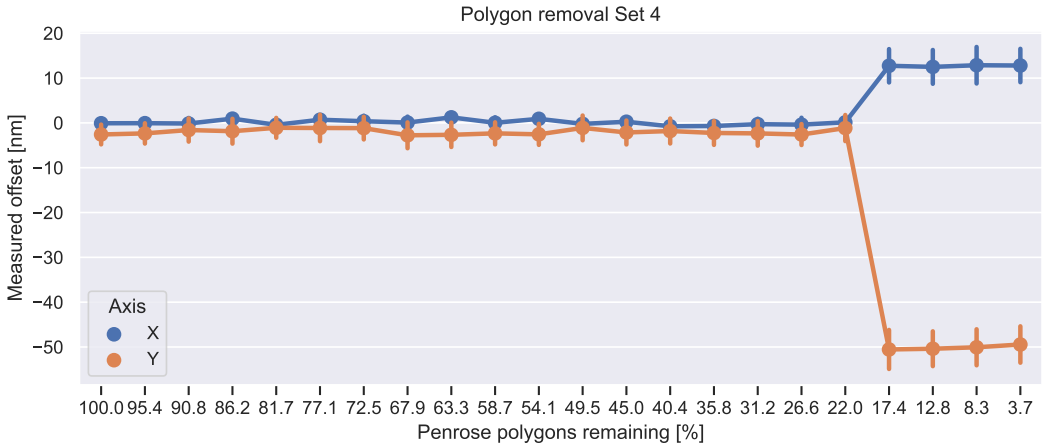


Figure 7.19: Point plot of measured offset from Set 4

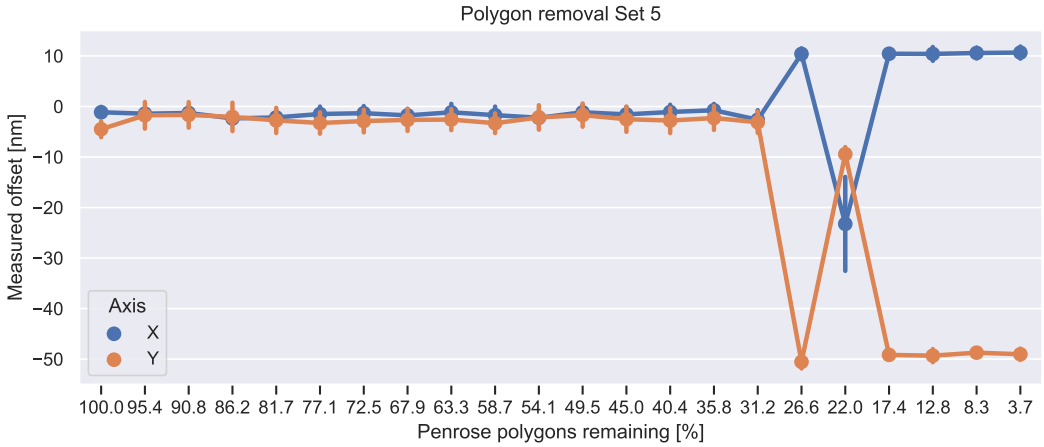


Figure 7.20: Point plot of measured offset from Set 5

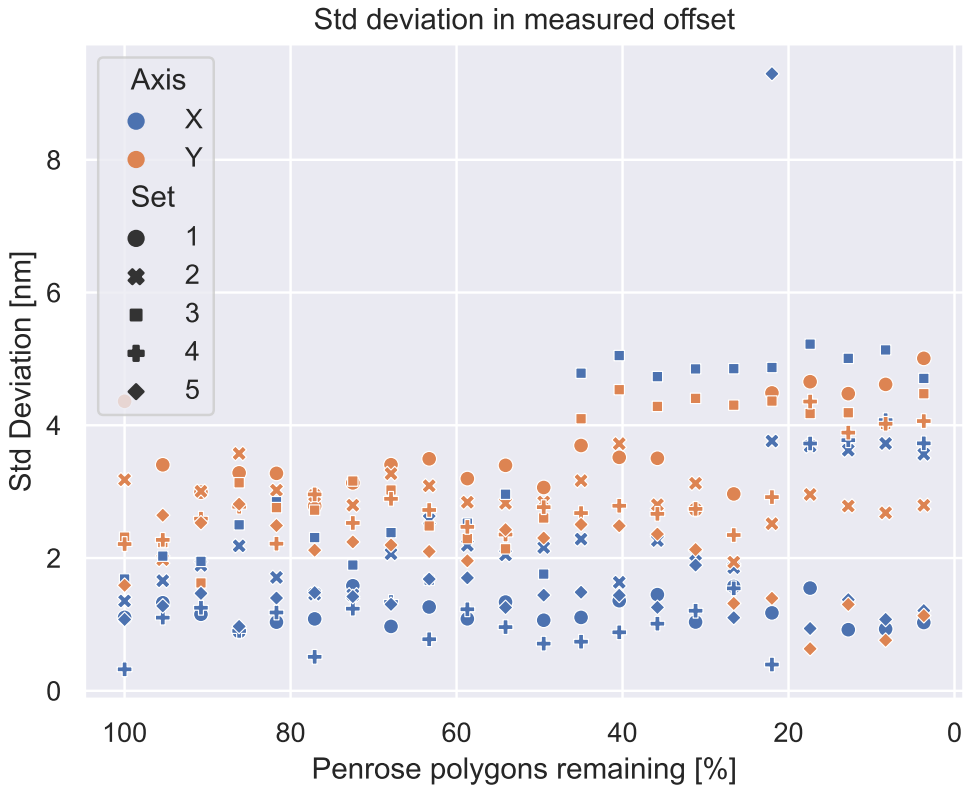


Figure 7.21: Scatter plot of standard deviation's from all measurement sets

It can be seen that with the exception of sets 3, alignment can still be good up until around 20-30% of the pattern remains, with all standard deviations below 4 nm. As alignment falls back to square markers, it becomes more variable with a slightly higher standard deviation in all sets, with the exception of the X-axis in sets 1 and 5. However, more importantly, the mean value in calculated offset in the alignment increases from sub 10 nm in both axes to 15 nm and 50 nm in the X and Y axes respectively.

Set number 3 only shows good alignment until approximately 50% of the pattern remains. Upon closer inspection of the set of Penrose shapes in question in Figure 7.22, set 3 can be compared to a better-performing set (such as 2 and 4) for the 35%-8% remaining marker shape range (Table 7.3). Visual analysis shows that in sets 2 and 4 the larger shapes in the centre remain for longer, comparatively to set 3 where more centre patterns have been removed and more generally only smaller patterns remain.

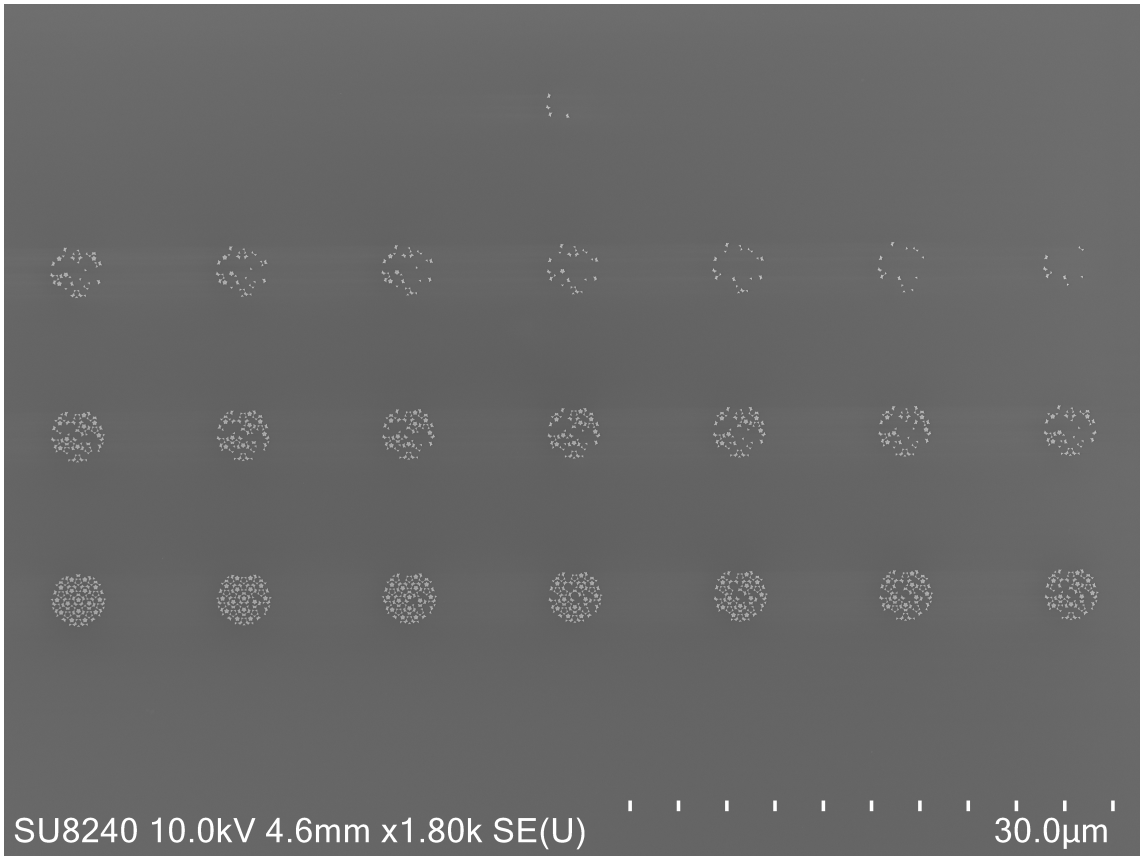
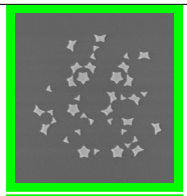
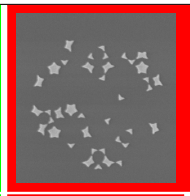
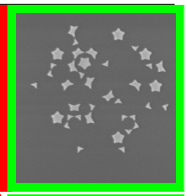
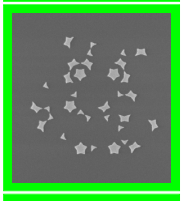
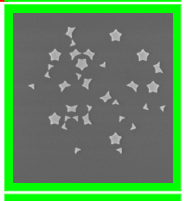
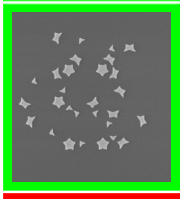
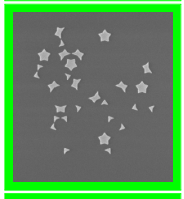
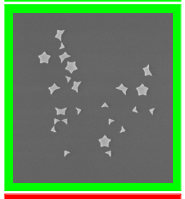
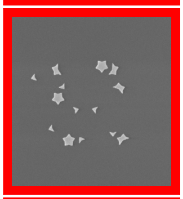
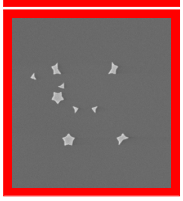
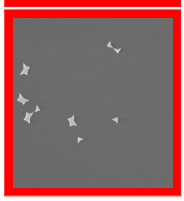


Figure 7.22: Penrose removal set 3 - only shows good alignment until 50% of the pattern remains, comparatively to other sets that show alignment down to 20%

From this experiment, Penrose markers seem to be working as expected in the EBPG5200+ in terms of robustness to defects. However, alignment from Penrose markers should generally be greater than achieved in this study. The issue with the methodology used is the initial alignment of the centre Penrose markers with the corner markers of varying quality is not ideal. As 22 Penrose markers are required to be written in each corner of each cell, with each individual Penrose taking approximately a second to write, it takes approximately a minute and a half to write the corner markers before the centre markers can be written, this does not include any time for stage movements which will also act to increase the time between markers being written. Stage drift in the EBPG5200+ has been measured internally by the JWNC to generally be better than 10 nm/min. However, this is no guarantee and multiple-stage issues have been identified during the experimental period which may be the cause of the increased mean of alignments values.

Due to the effects of stage drift during the initial writing of these patterns, structures to measure nanometer alignments must be written quickly to minimise these effects.

Table 7.3: Penrose removal 35%-8% shape remaining of sets 2, 3, and 4. Green and red boxes indicate marker search success or failure. It can be seen that more shapes have been removed from the centre of set 3 as well as more 'star' features get removed earlier, and only smaller features remain.

	Set 2	Set 3	Set 4
35.8%			
31.2%			
26.6%			
22.0%			
17.4%			
12.8%			
8.3%			

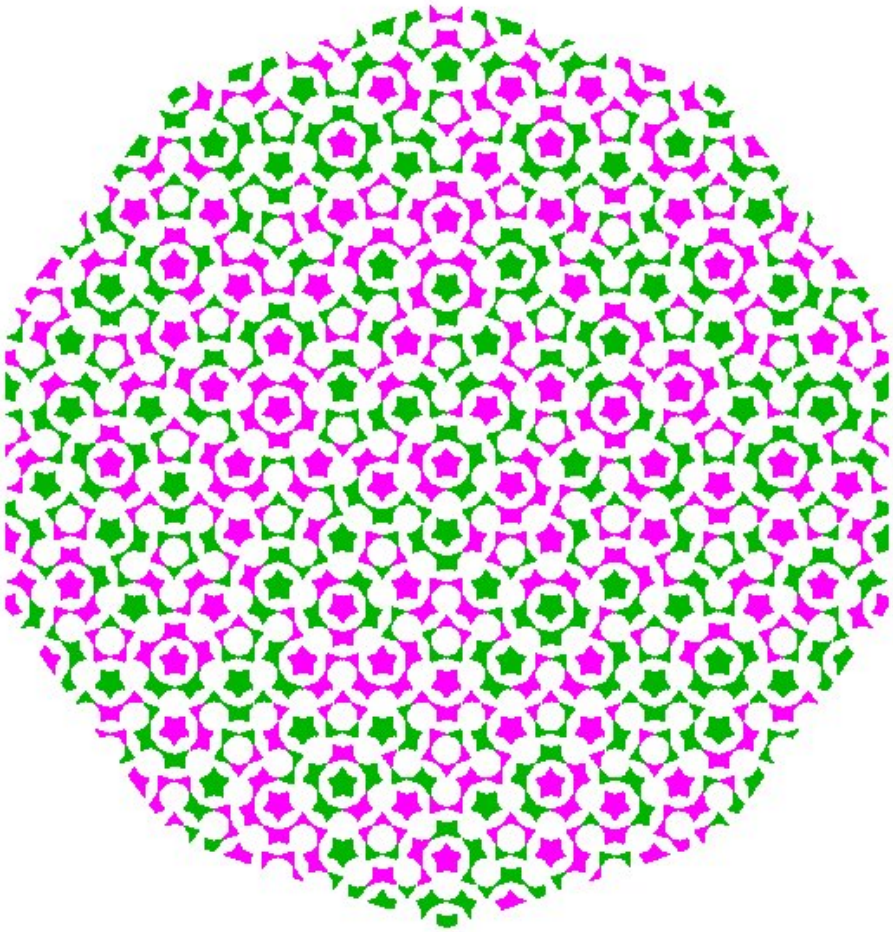
7.4 Split Penrose

The 'Spilt Penrose' pattern can be used to measure nanometer alignment accurately [197]. This consists of a Penrose pattern split in half and superimposed on top of one another, with each half written from a differing alignment map. Calculating the offset between the correlations of these two halves with the image of the split Penrose pattern can give a measure of the alignment accuracy between them. A benefit of this structure is that it acts as a single point vernier, for each structure can obtain a measurement for both the X and Y axes.

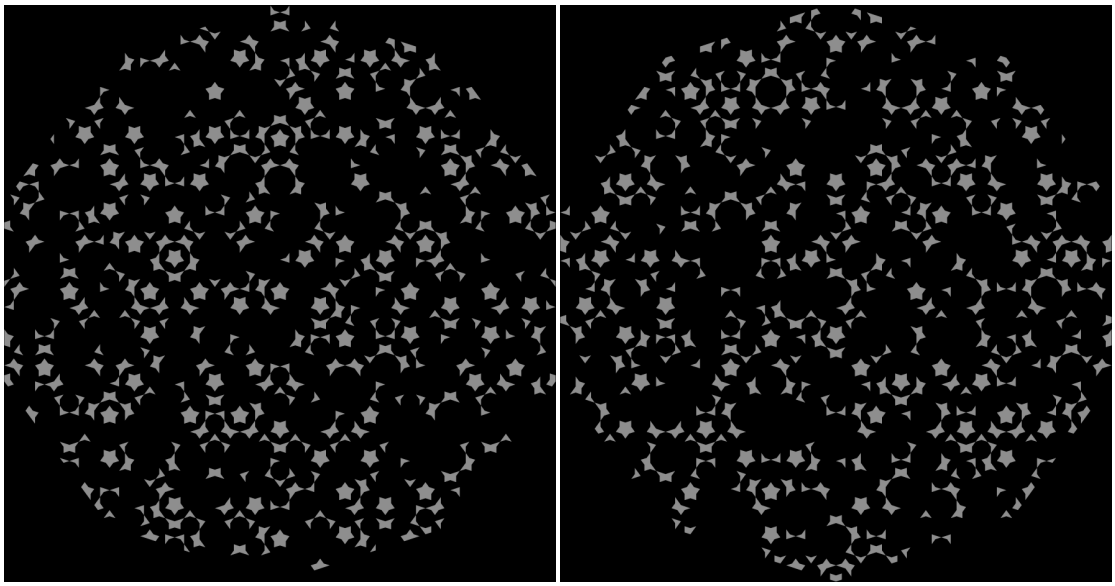
Another benefit to utilising the split Penrose pattern is that it is a null method, effects of stage drift or SEM field distortions are equal across both halves and will cancel out. It has been previously shown in Figure 7.15 that the Penrose pattern will still correlate when at least 50% of the pattern remains, irrespective of which polygons have been removed. So the drop in the number of polygons interrogated can be handled in the correlation searches. An image of the split Penrose pattern can be seen in Figure 7.23.

7.4.1 Experimental design

The fabrication of the Penrose structure has previously been discussed in section 7.2. However, to allow these split Penrose patterns to be fabricated in the same layer as misaligned gratings (discussed later in section 7.5), the process must be slightly altered. The patterns were written in PMMA using the same PMMA bilayer, but both layers are spun at 6000 rpm for a bottom layer thickness of 80 nm and a top layer thickness of 20 nm. Using a beam step size of 1 nm and a 1 nA beam current, the patterns were written with an 840 $\mu C/cm^2$ electron beam dosage. The full process steps for the fabrication of the split Penrose structure are given in Table 7.4.



(a) The split Penrose pattern. The purple half of the structure can be with one alignment map, with the green half pattern being written aligning to a second map.



(b) Correlation template of side A (purple in (a))

(c) Correlation template of side B (green in (a))

Figure 7.23: (a) Split Penrose layout and (b) templates used for correlation of the Penrose halves in. The difference of each image's correlation centre with the full pattern can be used as a measure of their misalignment.

Table 7.4: split Penrose pattern microfabrication steps.

#	Step	Process
1	Sonication	5 mins, in acetone, methanol, IPA, and RO water, then N2 blow dry.
2	O_2 Ash	30 s at 80 W
3	Bake	5 minutes on 180 °C hotplate dehydration.
4	Spin	4% 200K MW Anisole PMMA (AR-P 642.04) at 6000 rpm, 60 s for a 80 nm bottom layer.
5	Bake	3 minutes on 180 °C hotplate PMMA tempering.
6	Spin	1% 950K MW Ethyl-Lactate PMMA (AR-P 679.01) at 6000 rpm, 60 s for a 20 nm top layer.
7	Bake	3 minutes on 180 °C hotplate PMMA tempering.
8	E-Beam	Write Penrose patterns.
9	Develop	23 °C 3:1 MIBK:IPA, 30 s with mild agitation. Stopped in IPA.
10	O_2 Ash	30 s at 80 W.
11	Metalisation	NiCr/Pt (5 nm/35 nm).
12	Lift-off	50 °C acetone bath, 2 hours.
13	Sonication	1 minute in acetone, IPA, and RO water, then N2 blow dry.

The cell layout of the experiment can be seen in Figure 7.24. First, a cell is created with Penrose markers of the new types in the corners (two markers in each corner) of the field according to Table 7.1. Then, the split Penrose structure is fabricated using Table 7.4 with each side of the split Penrose pattern written aligned to alternate corner Penroses, the first side aligned to the left Penrose and the second side aligned to the right.

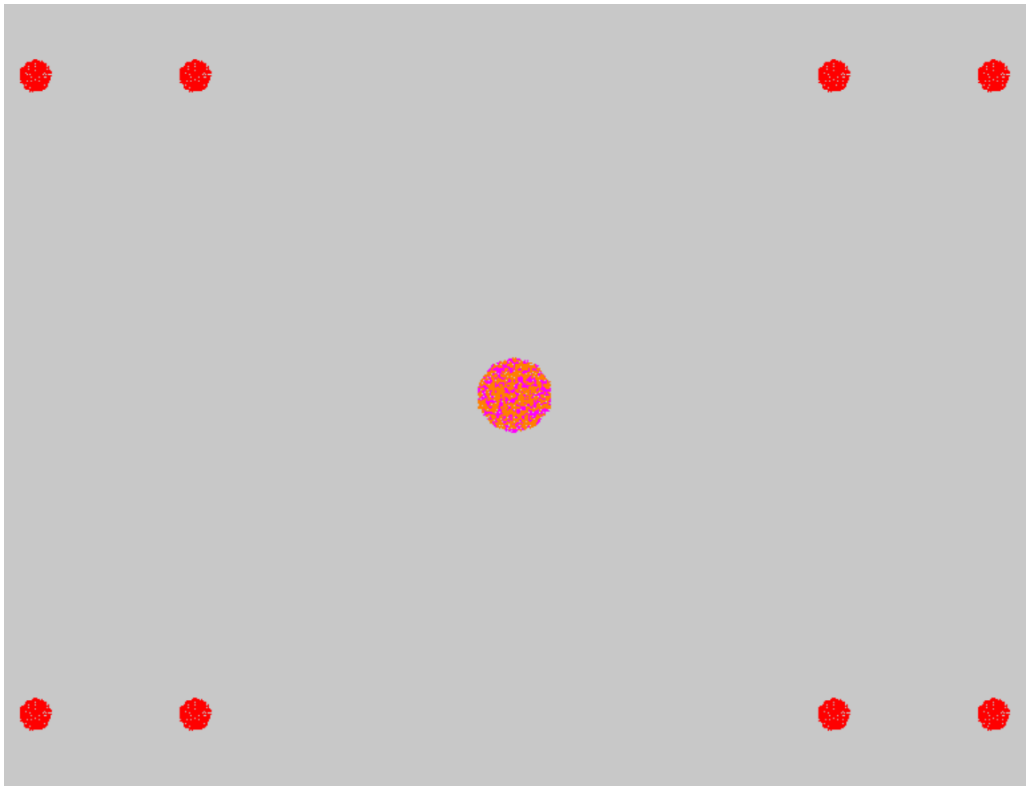


Figure 7.24: Layout of split Penrose cell. Each corner of the cell consists of 2 Penrose markers of a certain type (red), with a Penrose in the centre written in two halves. The first side of the split Penrose (side A - purple in Figure 7.23a) is aligned to the left Penrose in each corner. The second side of the split Penrose is aligned to the right Penrose in each corner (side B - green in Figure 7.23a

As a test of the resolution of this technique, a Penrose (Figure 7.25) was written with the same alignment map (i.e no 'split') and the difference in the correlations of the two halves was measured. This is shown in Figure 7.26. First, the SEM image of the whole pattern and the kernel of each half (not shown) is multiplied by the Hanning window function. The windowed SEM image is then correlated with each Penrose side to produce the correlation result. The centre of each peak in the correlation results can be found through interpolation. The found centres can then be subtracted from each other in each axis to obtain the offset. In this particular example, an offset of 0.63 nm and -0.06 nm can be calculated in the X and Y axes respectively.

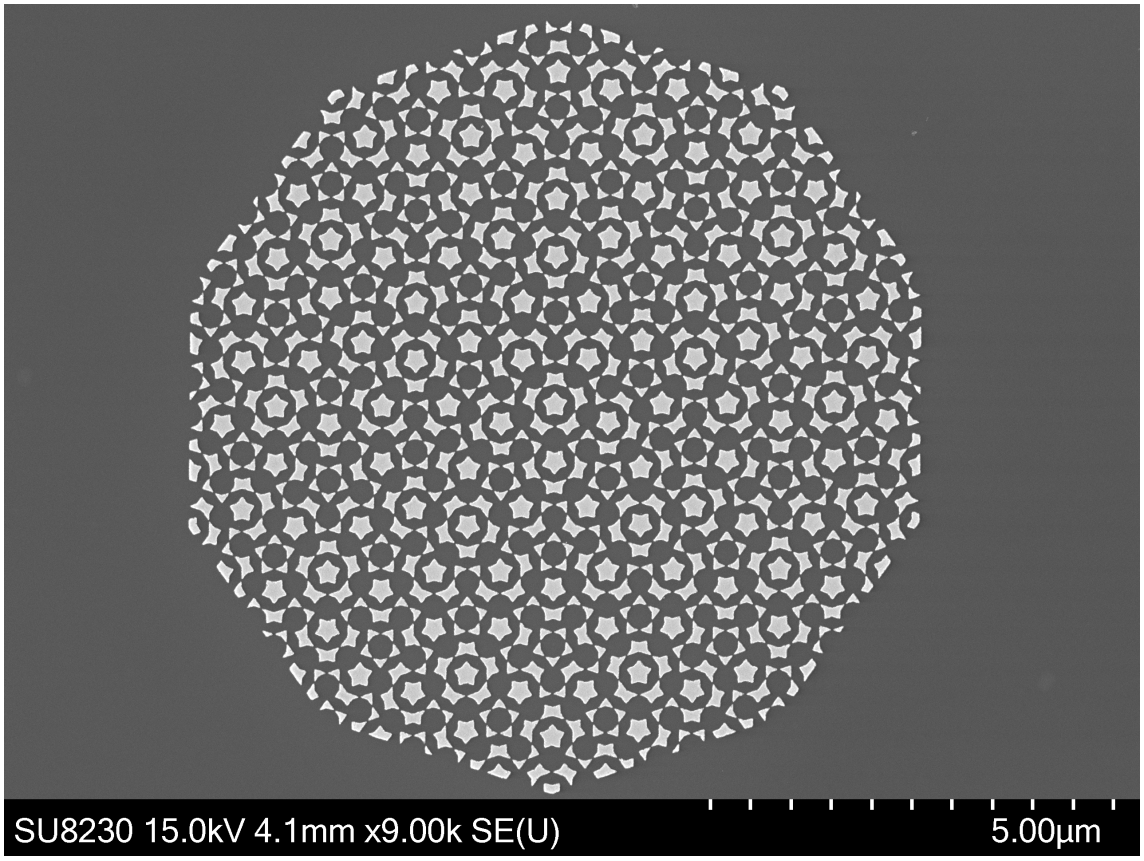


Figure 7.25: Penrose image used for correlation testing of two sides. Two halves have been written in the same alignment map and should show no offset between the halves.

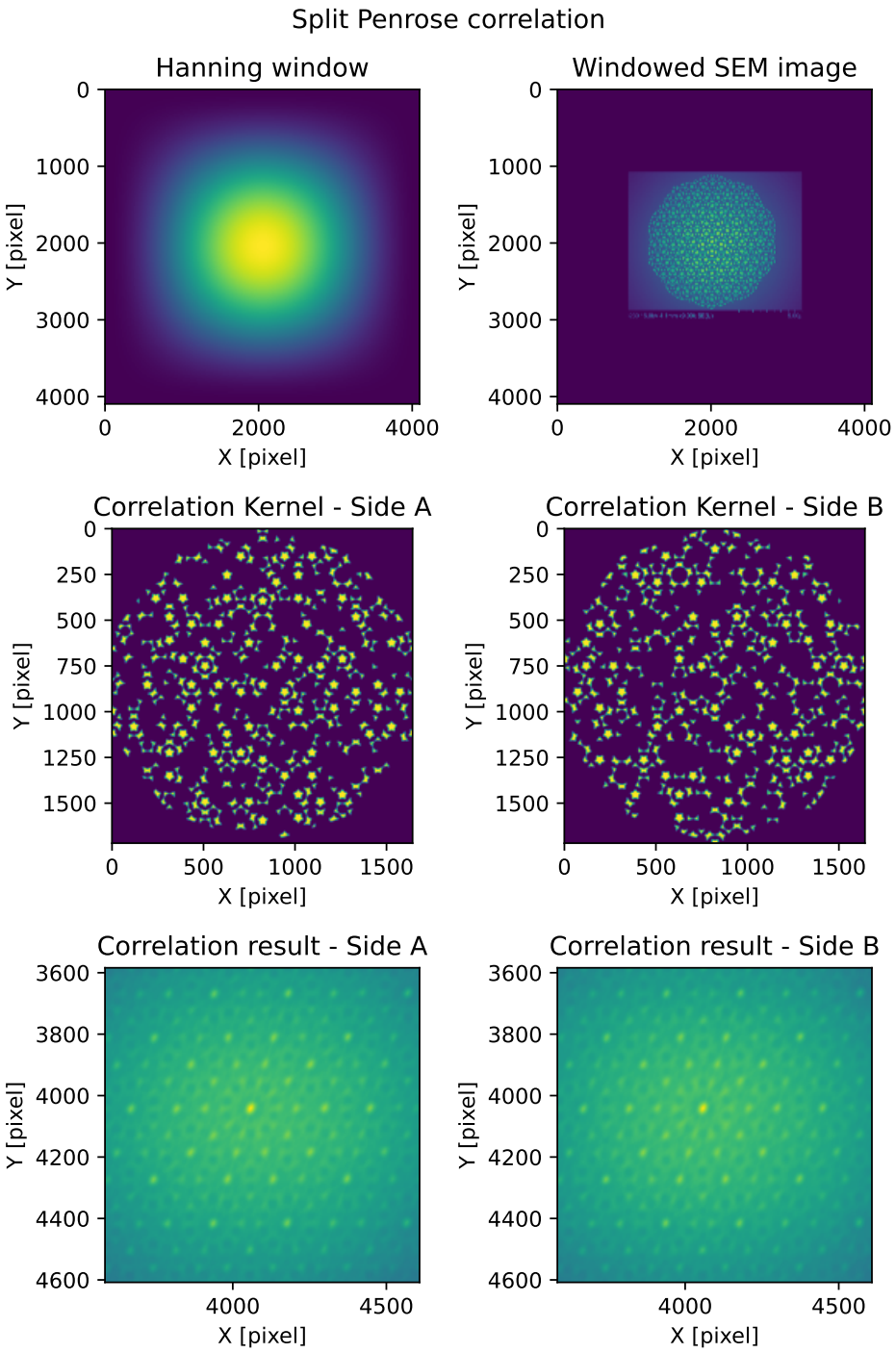


Figure 7.26: Methodology of the split Penrose in Figure 7.25. The SEM image of the whole pattern and the kernel of each half (not shown) is multiplied by the Hanning window function. The windowed SEM image is then correlated with each Penrose side to produce the correlation result. The centre of each peak in the correlation results can be found through interpolation. The found centres can then be subtracted from each other in each axis to obtain the offset. In this particular example, an offset of 0.63 nm and -0.06 nm can be calculated in the X and Y axes respectively.

The test was then repeated on a Penrose where the two sides were aligned to different alignment maps. In this particular example, correlation of the corner Penroses failed (due to poor marker lift-off) and alignment fell back to sets of 20 µm square metalised markers. Figure 7.27 through 7.29 and show a misalignment of the two halves calculated at -10.8 nm and 35.31 nm for the X and Y axes respectively.

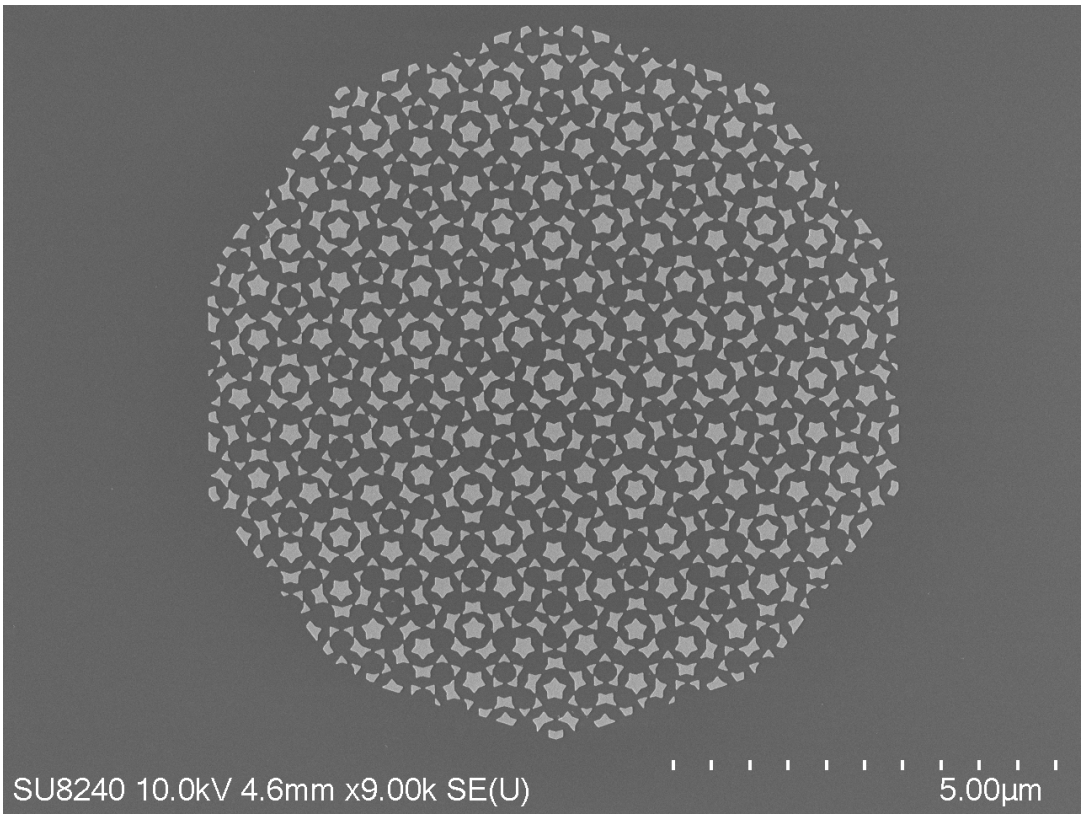


Figure 7.27: Penrose image used for correlation testing of two sides. Two halves have been written with different alignment maps, In this pattern alignment to one set of corner Penrose markers failed, and alignment fell back to global 20 µm square metalised markers. An offset between the two halves is expected.

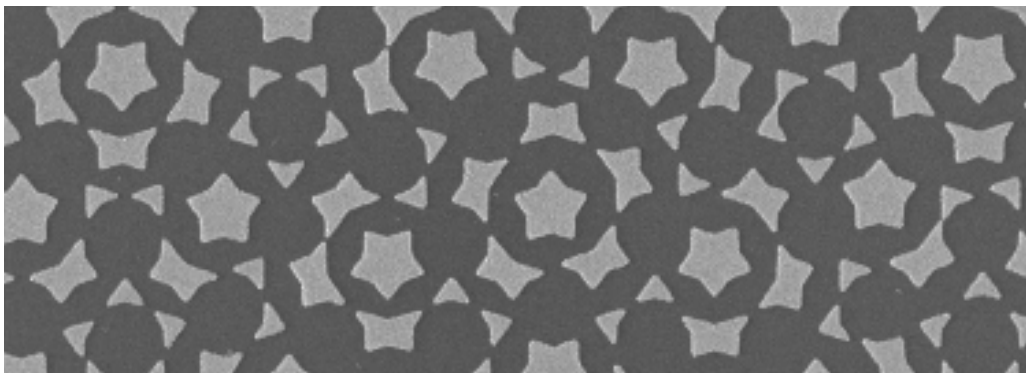


Figure 7.28: Close up of Figure 7.25. Visually, Patterns do not look aligned with each other, it can be seen that the misalignment in Y is larger than X.

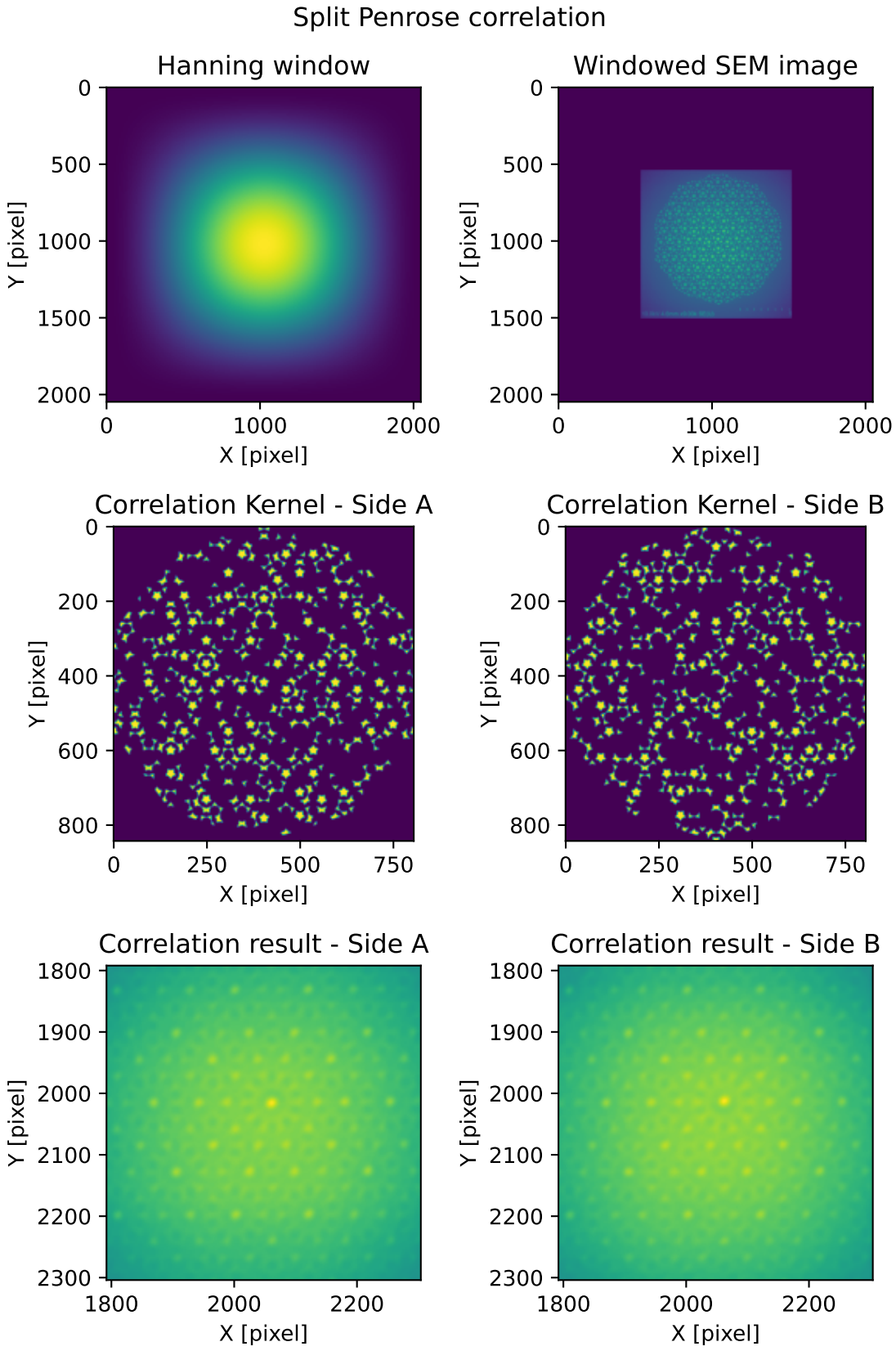


Figure 7.29: Correlation results of Figure 7.27. The difference in peaks of the two correlation result sides show an offset of -10.18 nm and 35.31 nm in the X and Y axes respectively.

To measure the repeatability of the measurement, multiple images of the same split Penrose pattern were captured while moving the pattern around in the SEM field of view, either by moving the SEM stage or by shifting the electron beam, while slightly varying the focus and brightness of the image ever so slightly to simulate movement between cells in the experiment. A total of 44 images were captured with a histogram of the results obtained can be seen in Figure 7.30.

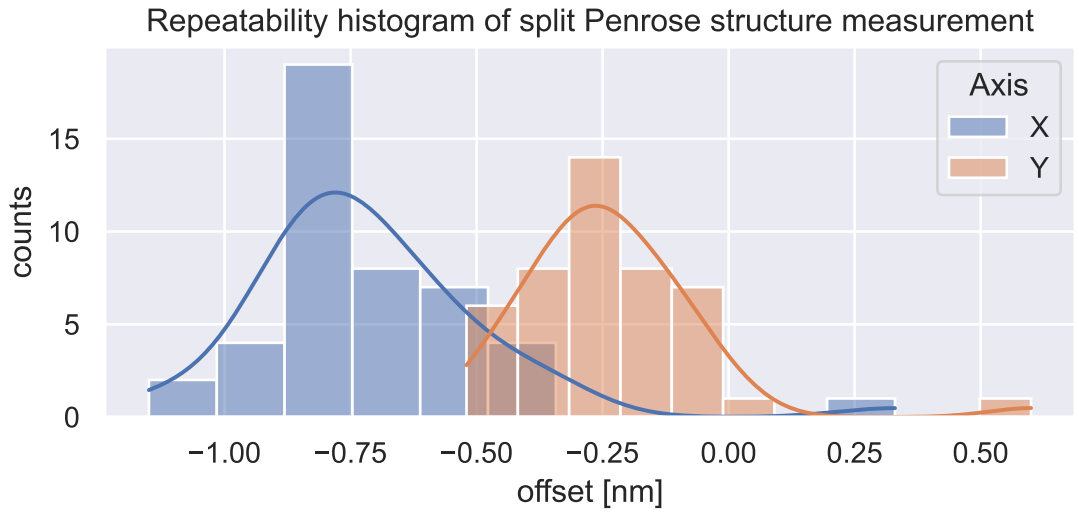


Figure 7.30: Repeatability of the measurement methodology. Both axes show an approximately Gaussian distribution in the measured alignment. The X-axis shows a mean value of -0.71 nm, with a standard deviation of 0.24 nm and a 1.48 nm range. The Y-axis is calculated to have a mean alignment of 0.23 nm, a standard deviation in the measurement of 0.18 nm, and a range of 1.12 nm

Figure 7.30 shows sub-nanometre resolution can be achieved with a standard deviation of 0.24 nm and 0.18 nm for the X and Y axes respectively and an approximately Gaussian distribution in the measurements taken.

7.4.2 Results

SEM images were captured of the split Penrose structure halves being aligned to standard and new Penrose markers. Using the methods set out previously, an alignment value for each image was determined. The spread of calculated alignment for each Penrose type has been displayed in Figure 7.31, and has been divided by axis in Figure 7.32. The distance from perfect alignment (i.e. the Euclidean distance from 0,0 in the spread of measurements) has been displayed as a ridgeline plot split by type in Figure 7.33. Initially looking at the spread of alignment between the Penrose halves in Figure 7.31, it can be seen that all Penrose halve alignment is

well-centred for each Penrose type. All Penrose alignments are better than 2 nm on each axis. Visually, it can be seen that marker type 'Small 8' possibly shows the best centred of the markers investigated.

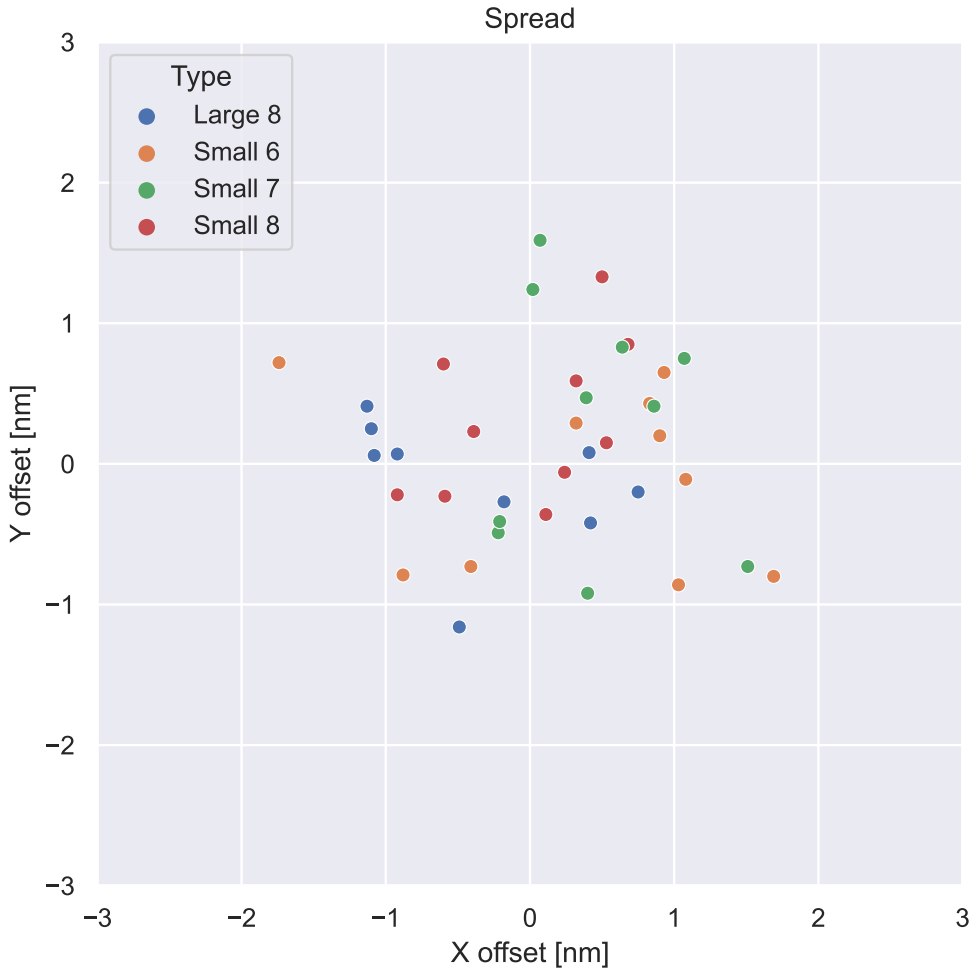


Figure 7.31: Spread of measurements using the split Penrose split by type

Analysis split by axis in Figure 7.32 can give greater insight into the performance of each marker. The standard marker, Large 8, shows mostly sub-nanometer alignment in Y, but a large spread in values in X. Of the new marker types ('Small' marker types), increasing the layer count from 6 to 8 a decrease in the spread of measured alignment can be seen. Small 8 shows all measurements to be sub-nanometre bar one outlier in the Y-Axis. The ridgeline plot in Figure 7.33 can be seen as a good metric for the overall accuracy of the achieved alignment in each cell by plotting the kernel density estimation of each marker type. The Euclidean distance (i.e $\sqrt{X^2 + Y^2}$) can be taken as the absolute distance of each point to 'perfect alignment' which can be considered at coordinate 0,0 in Figure 7.31. The reduction in the spread of values

moving from 6 layers to 8 layers is much clearer.

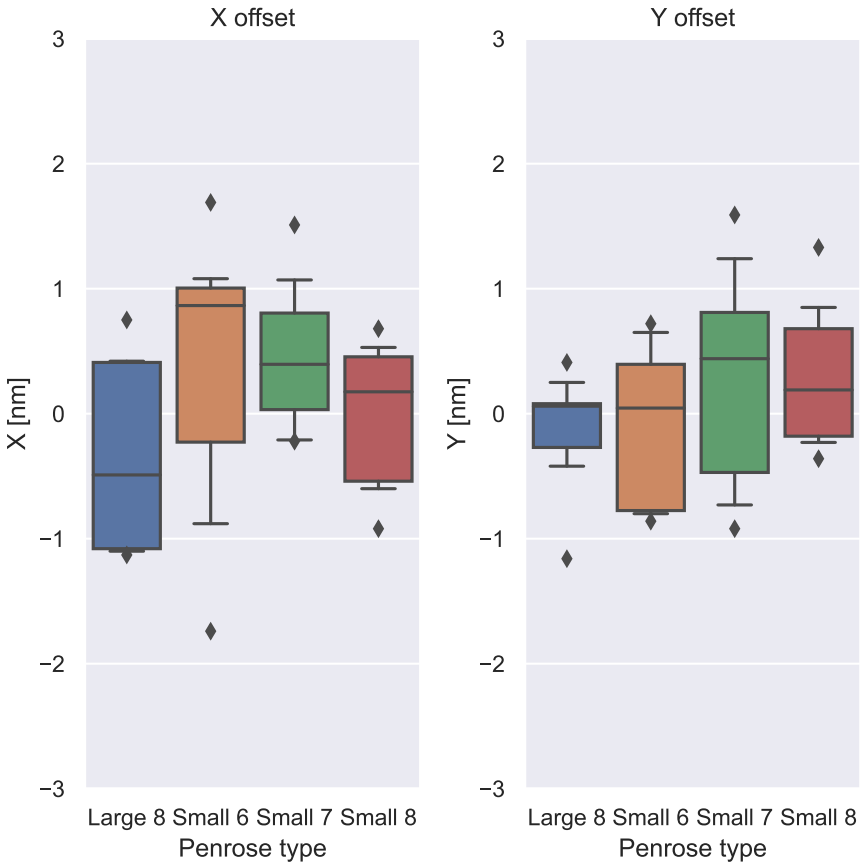


Figure 7.32: Spread of measurements using the split Penrose type and X and Y measurement axis (LHS and RHS respectively).

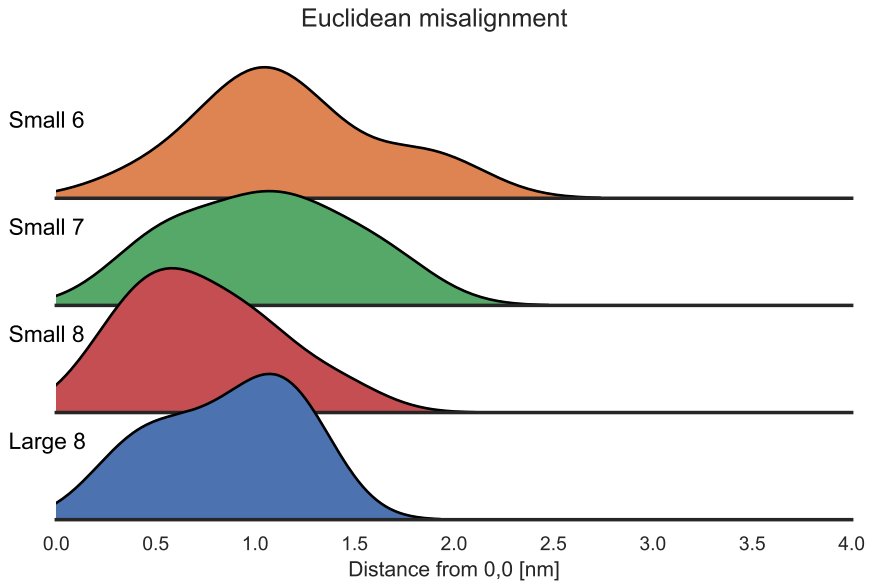


Figure 7.33: Ridgeline plot of Figure 7.31, showing Euclidean distance of each point from centre.

7.5 Misaligned gratings

Another method to measure nanometer alignments accurately is using overlaid and misaligned gratings [141] as discussed earlier in section 3.4.3.

Creating vernier structures using this concept by deliberately offsetting the halves by set amounts (from -10 nm to +10 nm) and analysing the magnitude of the frequency at $\frac{f}{2}$ in the power spectrum each grating should give a magnitude that is proportional to the gratings measured misalignment. Least-squares fitting a 'V'-shaped model of two straight lines with an equal gradient but opposite sign can allow the reading of the minimum of the fit, which can be read as the overall structure alignment accuracy.

The benefit of this method of vernier fabrication is that it can be written in the same EBL step, with the same exposure and resist conditions, but with each half aligned to different markers. Therefore the only variant in the measurand is the set of markers that have been aligned to, as well as any possible stage drift that may have occurred during the writing of the grating, However, with a write time of approximately 20 seconds per half grating, stage drifts should be minimal.

7.5.1 Experimental design

Structures were fabricated on 400 nm silicon nitride coated 400 µm silicon substrates. The gratings were designed with a period of 80 nm. To fabricate such thin gratings in PMMA, one must use thin bi-layer resist to avoid the effects of line width collapse as seen in Figure 7.36. The fabrication steps follow the same steps as the split Penrose (Table 7.4 on page 269), allowing them to be microfabricated on the same layer. The gratings can then be written in the PMMA with a beam step size of 2 nm, a beam current of 1 nA, and an electron dosage of 1764 µC/cm^2. Shape bias and PEC were applied to the pattern design files for better pattern fidelity in the corners of the structures.

The resist was then developed in 3:1 IPA:MIBK for 30 seconds at 23 °C before being stopped in IPA for 30 seconds in IPA. The sample was then deposited with 5 nm nichrome as an adhesion layer before deposition of 35 nm platinum. The sample was then placed in a 50 °C bath of acetone for approximately 2 hours to lift off the metalised features, before 1 minute sonication sequentially in acetone, IPA, and RO water. The sample was then be blow-dried with dry nitrogen.

The layout of the grating can be seen GDSII can be seen in Figure 7.34. The first half of the grating was written on a 160 nm pitch according to one Penrose alignment map. The second half of the grating was also written on a 160 nm pitch, however, it is aligned to a second alignment map but offset from the first grating by 80 nm creating an overall grating structure with an 80 nm pitch. Each row in the second grating had an additional intentional offset ranging from +10 nm to -10 nm in 1 nm increments.

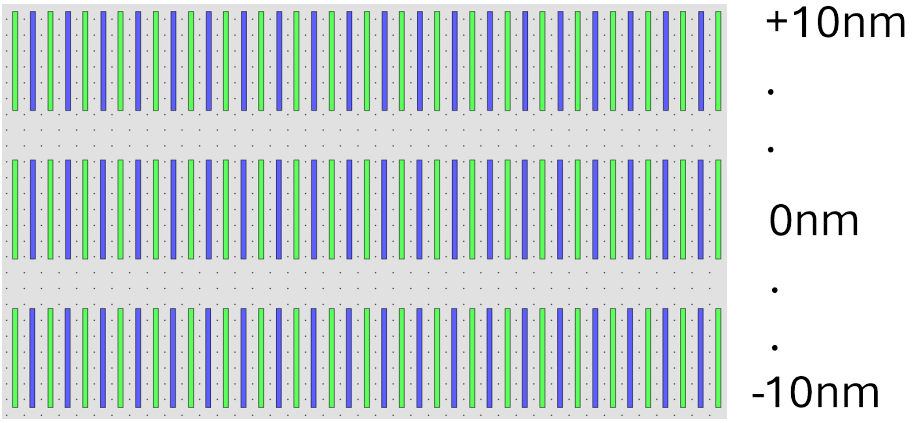


Figure 7.34: Two grating halves. The first half of the grating (green) is written first at a pitch of 160 nm. The second half of the grating (blue) is then written on the same pitch but offset by 80 nm. There is an additional offset in each row of the second grating, ranging from +10 nm to -10 nm in increments of 1 nm.

The cell layout of the experiment is similar to that of the split penrose as described in section 7.4.1 and can be viewed in Figure 7.35. Each cell has sets of misaligned gratings in the centre of the field (blue), one grating for the X-axis (bottom) and one grating rotated 90°for the Y-axis (top), with Penrose markers of the new types in the corners (two markers in each corner). Each side of the grating was written aligning to alternate corner Penroses, the first side aligned to the left Penrose and the second side aligned to the right.

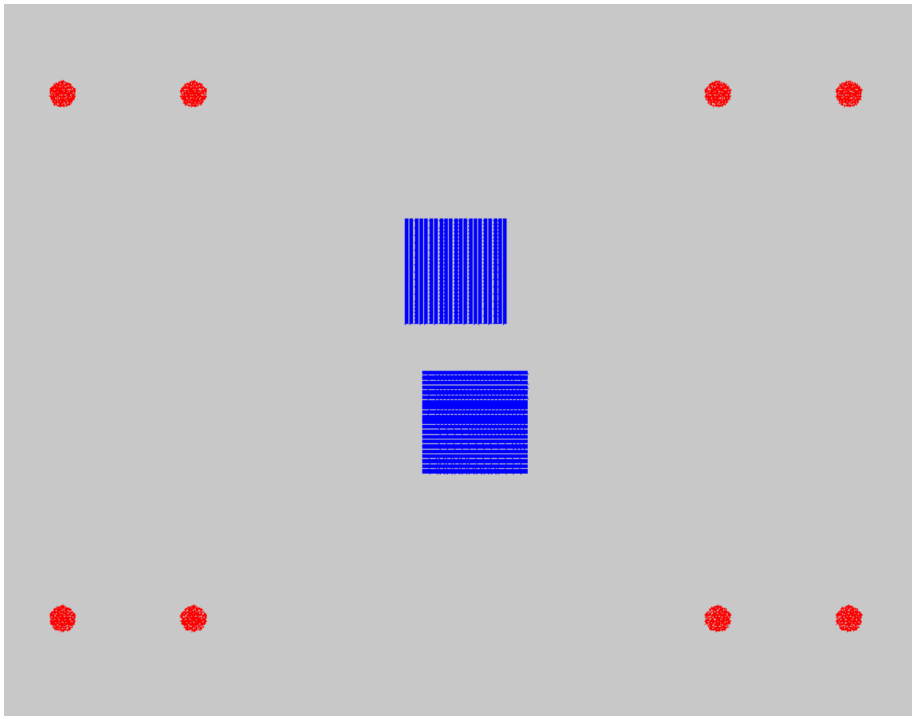


Figure 7.35: Layout of misaligned grating cell. Each corner of the cell consists of 2 Penrose markers of a certain type (red), with two sets of misaligned gratings (blue) in the centre, one for X-axis alignment (bottom), and one for Y-axis alignment (top). The first side of the grating is aligned to the left Penrose in each corner. The second side of the gratings aligned to the right Penrose in each corner.

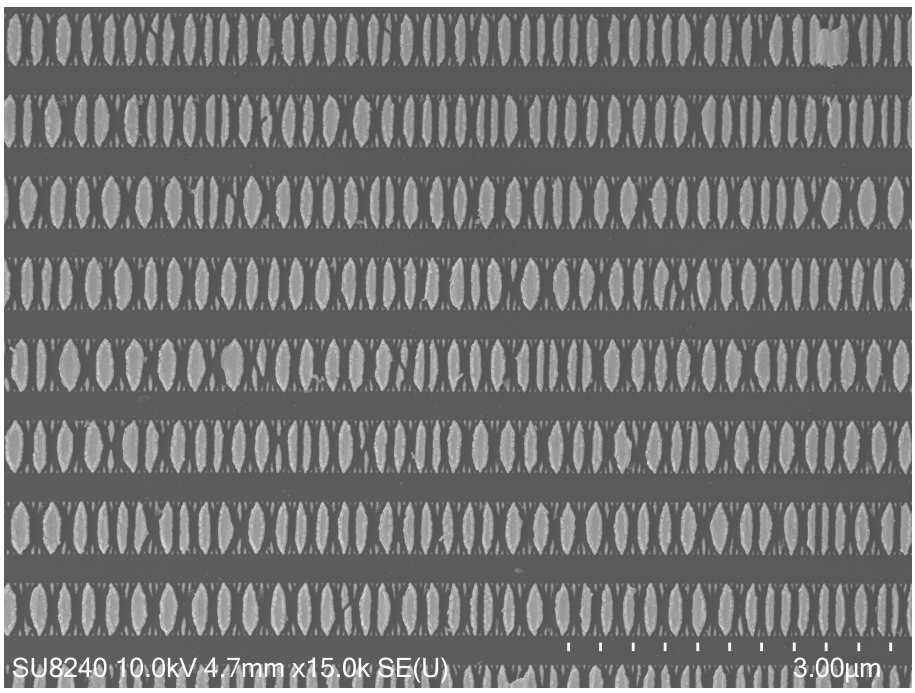


Figure 7.36: A fabricated vernier structure with a designed period of 80 nm showing effects of line-width collapse from PMMA layers having a high aspect ratio.

To first calibrate the ability of the structure to measure alignments in the experiment, the structure was written in a single pass with the same alignment map, a SEM image of which can be seen in Figure 7.37 with higher magnification of the centre grating rods in Figure 7.38. Python scripts were written to automate the measurement of images of the structures. Through image correlation, the structure can be found within the wider SEM image and cropped to the appropriate size. As the height of each grating is known, the structure can then be split up into its individual gratings and saved accordingly, this process flow has been visualised in Figure 7.39.

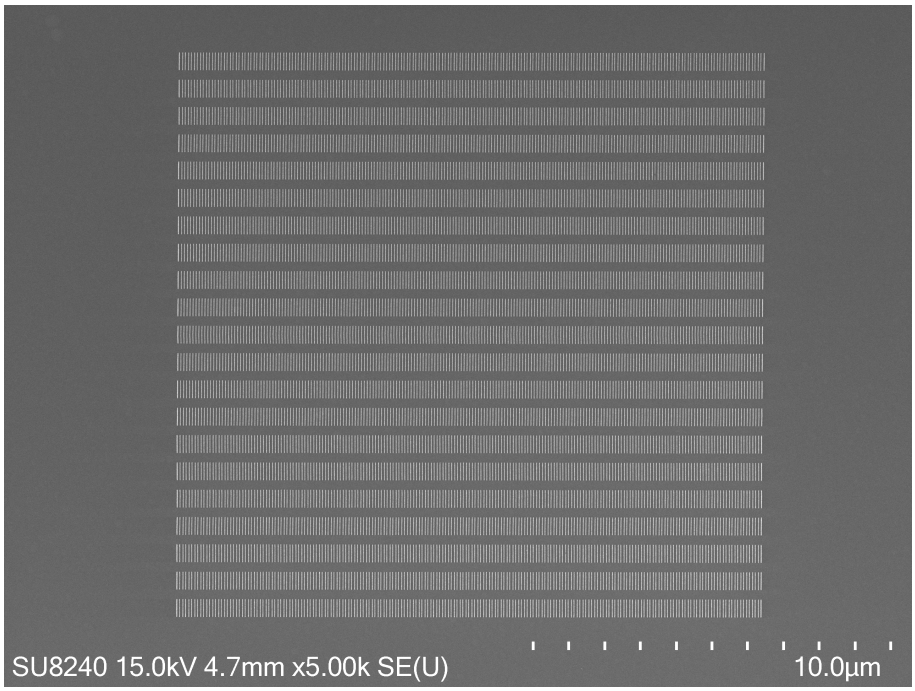


Figure 7.37: A fabricated vernier structure with a designed period of 80 nm with deliberate offsets starting at +10 nm at the top with 1 nm steps going through 0 nm in the centre to -10 nm at the bottom. This particular grating is written in one step as a means to quantify the ultimate resolution of the structure.

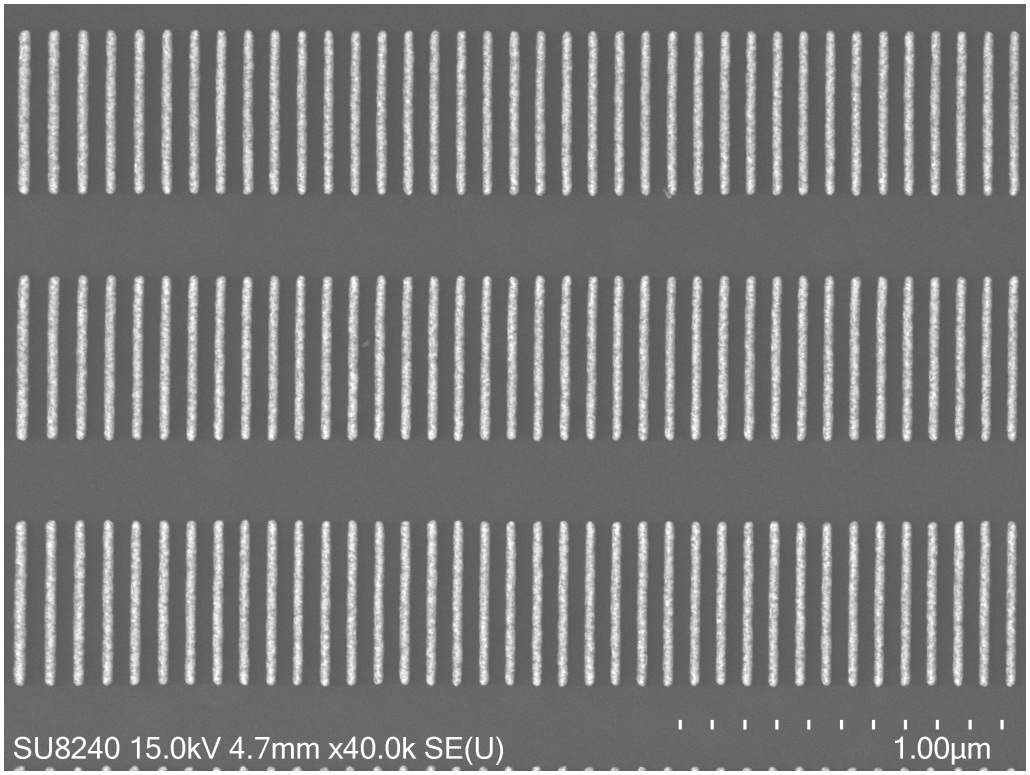


Figure 7.38: Zoom of Figure 7.37 showing top grating with +1 nm designed offset, centre grating with 0 nm designed offset, and bottom grating with -1 nm designed offset

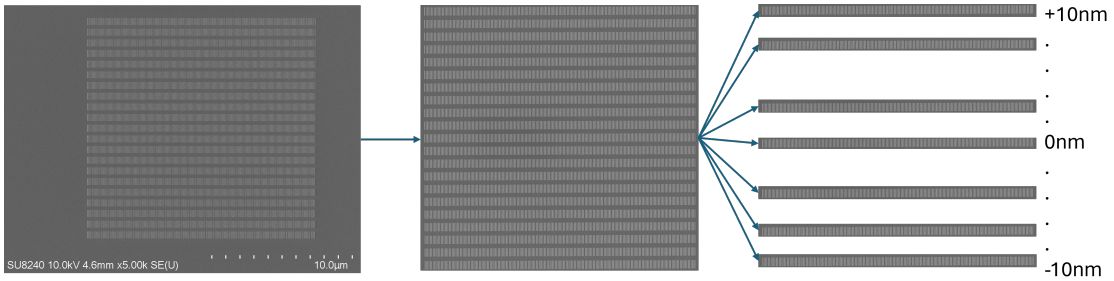
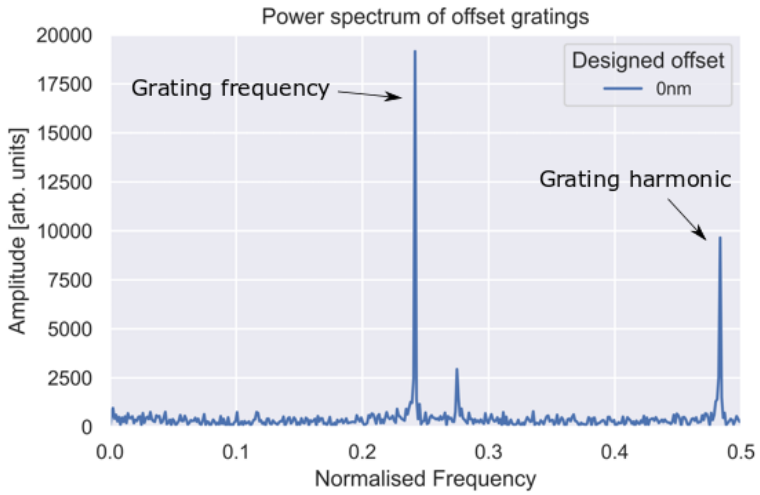


Figure 7.39: The centre of the grating (Middle) is found in the whole SEM image (LHS) through image correlation with a template of the grating. The cropped image is then split up into individual gratings and labelled accordingly (RHS).

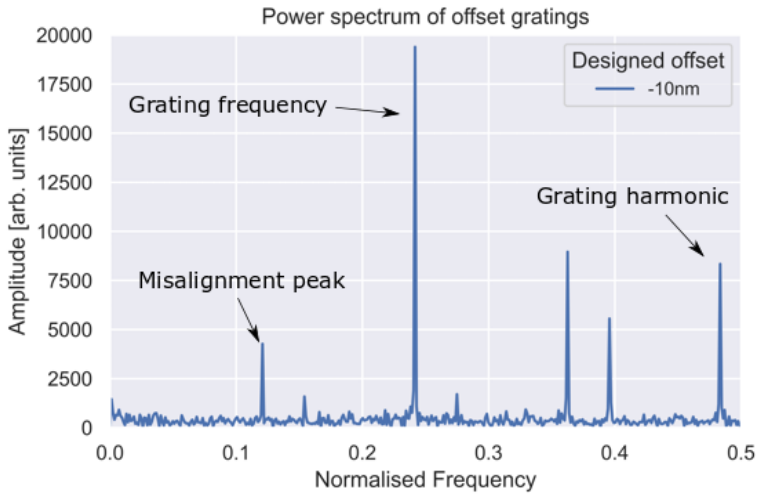
As the individual gratings have been extracted from the overall structure, a line from each individual grating can be extracted and the power spectrum plotted as in Figure 7.40a and 7.40b. It can be seen in Figure 7.40a that we have the main grating frequency spike at 0.242, as well as possibly phase modulation spur secondary peak just below 0.3. The fundamental grating frequency also produces a harmonic at 0.484. Crucially, we see no frequency component at the half frequency of the main grating. Examination of the deliberately offset grating in Figure 7.40b, shows that we now see the component at the half frequency of the main grating at 0.121, as

well as some additional harmonics.

Through peak detection, we can automatically locate the grating frequency (at 0.242 Fs), and search the secondary peak at half this frequency. The peak at this frequency for each offset grating has been plotted in Figure 7.41.



(a) Zero designed offset



(b) 10 nm offset grating

Figure 7.40: Power spectra from two gratings. (a) No designed offset in the grating, and no observed frequency f/2 component. (b) -10 nm designed offset between the grating halves. A component at f/2 proportional to the designed offset is visible.

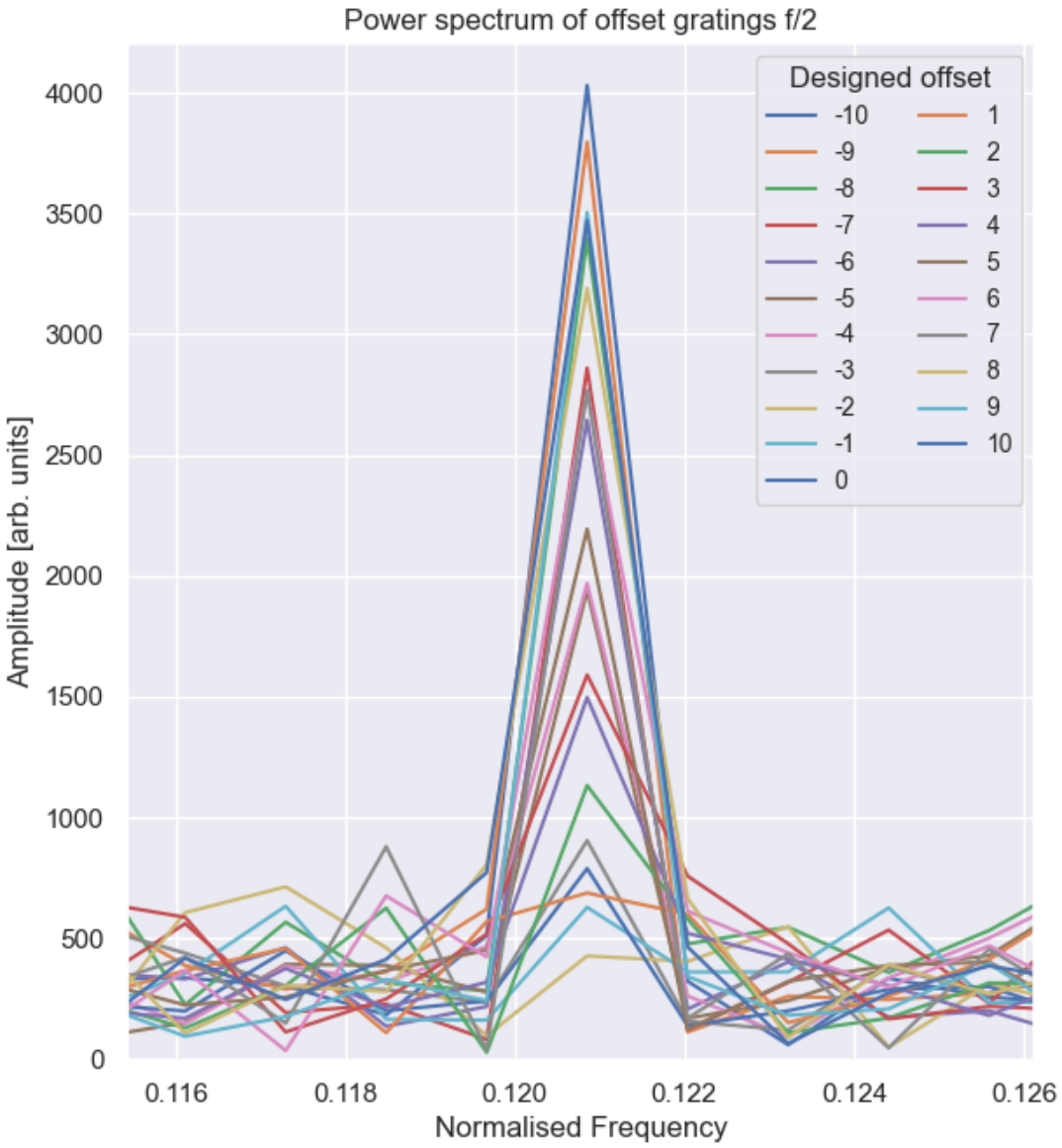


Figure 7.41: All overlaid f/2 peaks from each grating, showing a peak magnitude that is proportional to the level of designed offset.

The peak magnitude of the half-frequency peak of each grating can then be plotted against the designed offset of each grating, before least-squares fitting a V-shaped model to the points. Reading the minimum of the V-fit allows the total misalignment of the two halves in the structure to be read. This is shown in Figure 7.42 to be -0.072 nm. This value can be taken as a systemic error in the measurement protocol. It is believed that the error source arises from drift or charging artefacts in the SEM image during capture [138].

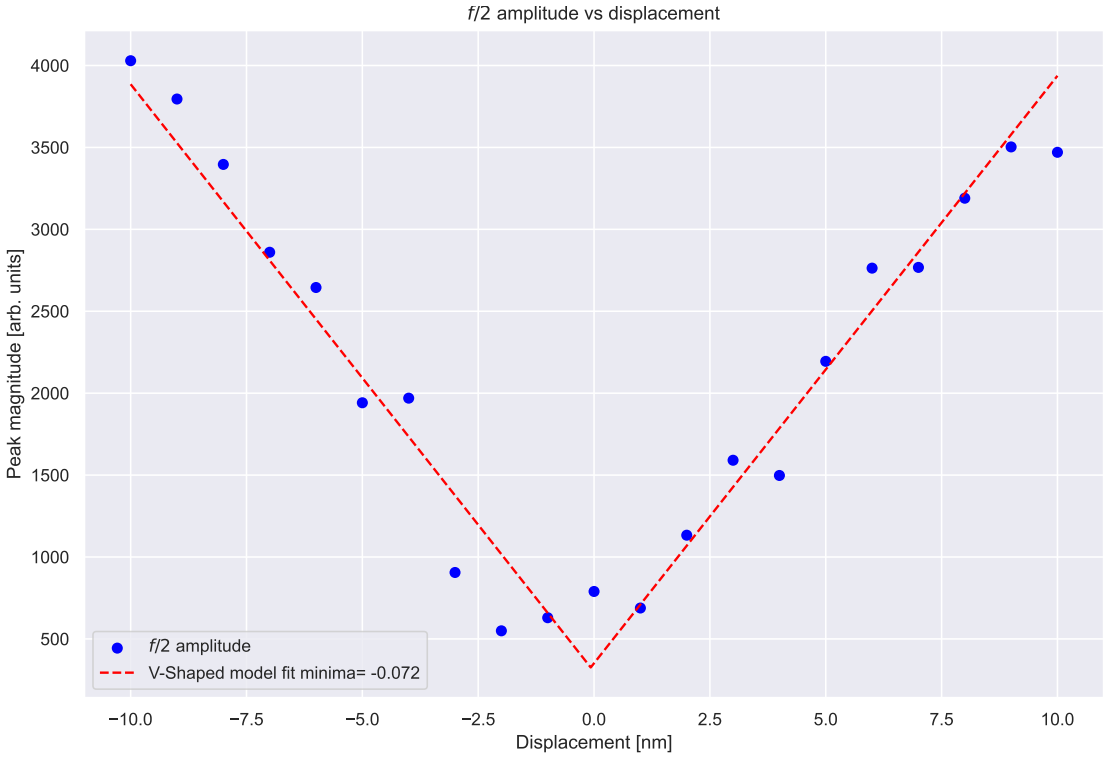


Figure 7.42: V-fit to the plot of peak f/2 magnitudes vs designed offset

To measure the repeatability procedure, utilising a grating structure where the grating halves are aligned to different marker sets, multiple images of the same structure were captured. Before each image capture, focus and image brightness were marginally altered as well as the movement of the structure around in the SEM field of view, either by stage movement or by moving the incident electron beam axis. This attempts to emulate moving between structures, during a measurement collection session on the SEM and introduces a random error into the measurement. A total of 54 images of the same structure were captured. An example V-shaped model fit to one of the images in the dataset can be viewed in Figure 7.43 with a histogram of all V-shaped model minimum in Figure 7.44.

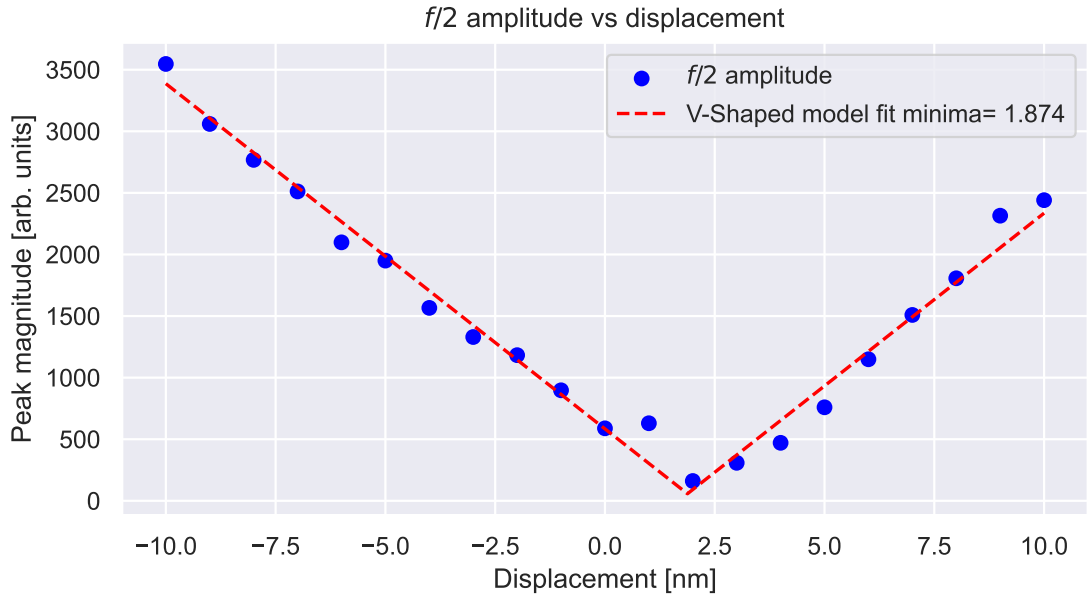


Figure 7.43: V-fit to the plot of peak f/2 magnitudes vs designed offset showing a measured misalignment of the two gratings by 1.87 nm

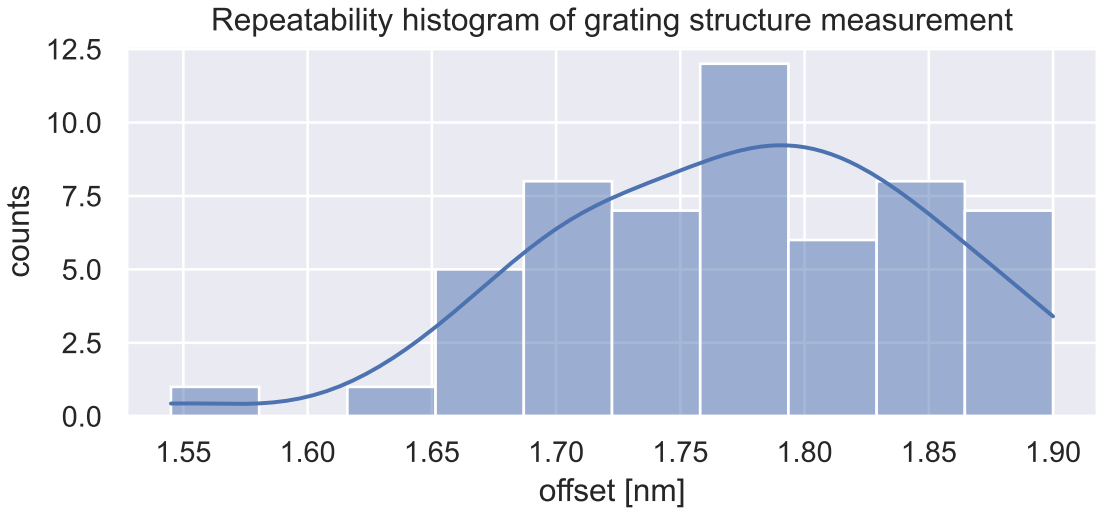


Figure 7.44: Histogram of repeatability measurement showing a mean measurement of 1.774 nm and standard deviation of 0.075 nm and range of 0.355 nm

Figure 7.44 shows that the standard deviation in the calculated alignment of 0.075 nm from the 54 images obtained. This shows there is a high precision utilising this methodology, showing deep sub-nanometre resolution. This measurement of alignment has an approximately halving in the standard deviation compared to the split Penrose technique.

7.5.2 Results

Two SEM images per cell were captured, one for the structure with gratings along the X-axis, and another for the grating structure aligned along the Y-axis, with each half of the grating structures being aligned to separate markers as described previously. These structures were analysed through the method described in the experimental design to provide a measure of alignment in both axes. The spread of the calculated alignments has been presented in Figure 7.45 and is split by marker type used to create the alignment map. It can be seen, with the exception of one value in the X-axis, that all values lie with better than 2 nm alignment accuracy, with 77% of alignments showing sub-nanometre alignment in at least one axis, and 61% of values measuring sub-nanometer in both axes. The spread of alignments is well-centred for all marker types. Alignment values have been broken down by axes in Figure 7.46, and a ridgeline plot of the Euclidean distance of each marker type in Figure 7.47.

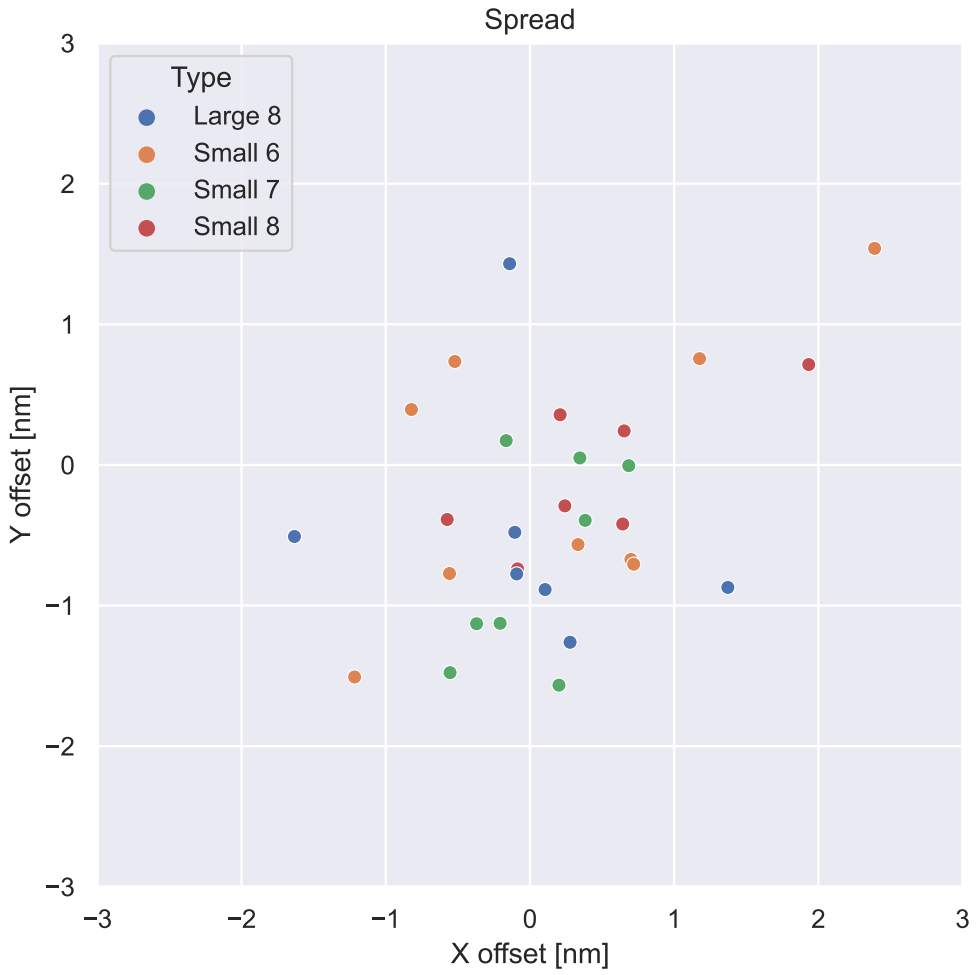


Figure 7.45: Spread of measurements using the misaligned gratings

It can be seen in Figure 7.46 that the distribution of alignments gets narrower as the number of layers increases in the 'Small' marker types, with again, all alignments of type Small 8 achieving sub-nanometer accuracy with the exception of one value in the X-axis. From 7.47 it can also be seen that the density of alignments is nearer to 'perfect' alignment as the number of tiling layers is increased. This aligns with the measurements made utilising the split Penrose technique.

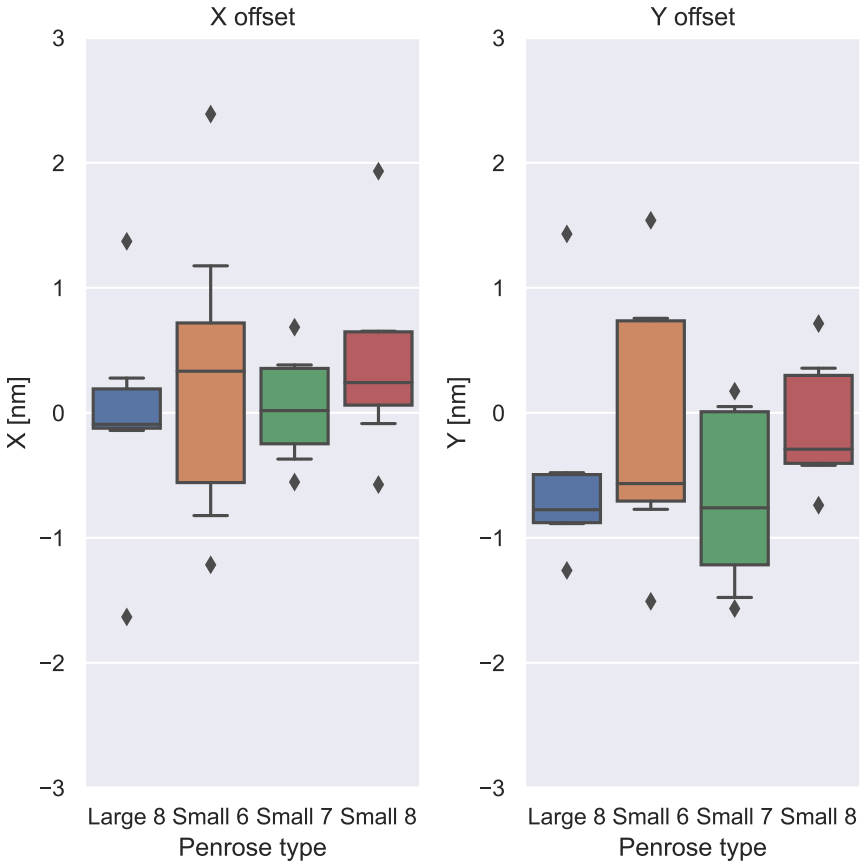


Figure 7.46: Spread of measurements using the misaligned gratings split by type and X and Y measurement axis (LHS and RHS respectively)

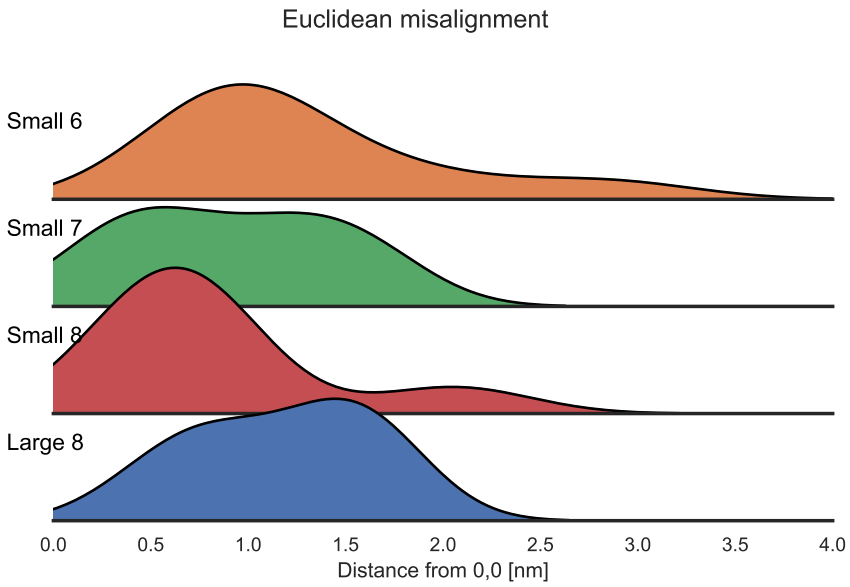


Figure 7.47: Ridgeline plot of Figure 7.45, showing Euclidean distance of each point from centre.

7.6 Discussion

In this chapter, advances in overlay alignment in E-Beam lithography using novel iterations of the Penrose marker have been presented, with the challenges of microfabrication of the markers discussed. An experiment to quantify the process window through the random removal of polygons from the Penrose marker was presented in section 7.3 and shows the large process window of the marker as expected from experimentation by Docherty et al. [140]. However, the experiment showed a need for greater metrology capability of the overlay alignments available from these markers.

Section 7.4 introduced a methodology of the 'split Penrose' technique, where the Penrose structure is written in two halves aligned to two alignment maps. It was shown that by utilising this technique and measuring the same structure multiple times, a standard deviation in the measurement procedure of less than 0.25 nm can be achieved. Through this technique, it has been shown that of the new marker types, the smallest and highest number of layer Penrose markers (Small 8) shows the tightest spread of alignment, with all but one measurement in the Y-axis showing sub-nanometre alignment capability.

An alternative methodology for measuring nanometre alignments based on the concept of deliberately misaligned gratings was discussed in section 7.5. Fabrication of the structures has been presented, with the associated challenges of line width collapse of the features. Automated scripting for analysis of the grating structures has been presented, allowing batch characterisation of SEM images of the structure in a repeatable fashion. A measurement error for the methodology was obtained as a standard deviation of multiple images of the same structure, shown to be 0.075 nm. This methodology can therefore be seen as a high-precision measurement with deep sub-nanometre resolution. Results from utilising the structure to measure new Penrose marker types show the smallest and highest number of layer Penrose marker, Small 8, having the tightest spread of alignment, with all but one measurement in the X-axis showing sub-nanometre accuracy.

Both measurement methodologies are in agreement with one another, with marker type Small 8 showing a higher density spread of alignments nearer to 'perfect' alignment and should be used moving forward to achieve the highest overlay accuracy. However, these structures are near the fabrication limit of the PMMA resist routinely stocked in the JWNC. Higher layer counts would prove difficult to fabricate consistently.

An interesting avenue for further study of these Penrose markers would be to create a 'marker block' of multiple of the smaller marker types per corner of a field, and least squares fit a marker position from multiple separate Penrose markers. This approach has been shown in the literature by Lambert [63] and Thoms et al. [134] to have vast improvements in the available alignments. One could easily place upwards of 15 'small' 4 µm^2 Penrose markers in the same footprint as a 20 µm square marker. This should reduce the effect of markers that may have been subject to damage from either pattern transfer or image capture processes. In fact, one could also de-focus the electron beam during marker search, as done by Thoms et al. [142], to reduce any further damage to the marker block, allowing the same markers to be reused multiple times. It would be interesting to see if the effects of these additional measures could yield even higher alignment capability.

These experiments have effectively quantified the limits of overlay alignment currently achievable using the e-beam lithography tool available in the JWNC. This information can be employed in the design of strain sensors, as will be discussed in chapter 8.

Development of Co-planar Strain Sensors

8.1 Introduction

As discussed in section 2.4, alternate systems of deflection sensing are available, of which tunnel junction strain sensing appears to be an attractive choice due to their low area and high sensitivity. In particular, co-planar junctions seem attractive due to the increased deformation of the barrier as it is located in the axis with high deformation-induced strain. Multiple types of co-planar junctions can be fabricated that would be compatible with strain-sensing element mechanics.

Ramp edge Junctions

Ramp-edge tunnel junctions typically use the edge of a trace of material as the interfacing layer between two electrodes and are more commonly used in superconducting Josephson junctions [198, 199]. The resulting structure can be seen in Figure 8.1. They can be designed by first depositing an electrode material and an insulating cap in a singular deposition. Followed by deposition or growth of the barrier material, and finally deposition of the second junction.

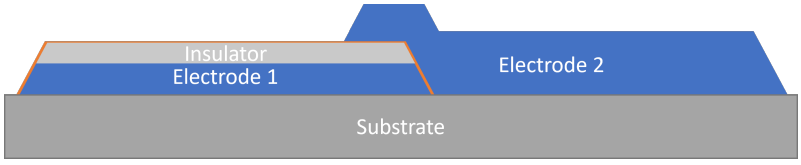


Figure 8.1: Example of ramp-edge tunnel junction (orange shows deposited or grown barrier material)

As there is a single barrier between the electrodes, where the parameters of the barrier can potentially be tuned, this becomes an attractive choice. It allows for the

number of junctions to be placed in series in a controlled manner suitable with batch fabrication requirements. However, such designs cannot be easily fabricated within the JWNC as deposition of insulators that are compatible with TMAH etching are not routinely available.

Crack junctions

Crack junction fabrication relies on designing a point for failure into a wire or connection between two electrodes. Forcing the point of failure to open up or "crack" either by mechanical stress or electron migration allows the creation of a pair of electrodes separated by a tunnelling distance gap. Dubois et al. [200] has shown that crack junction fabrication can be precisely controlled to gap sizes of less than 2 nm. However, the fabrication of such devices can be complex, involving the etching of materials to reveal suspended structures. Such devices also require individual cracking of each junction in a serial nature so is not suitable for batch fabrication needs. Dubois et al. [201] later improved the process so junctions "self-cracked" removing the need for individual cracking by fabricating the electrodes on stressed titanium nitride, which cracked the junction open once relaxed after releasing the suspended structure This has been shown in Figure 8.2. However, the process showed only a yield of 7% of junctions with distances less than 3 nm was possible with such methods. The low yield and variability of this method shows that it is not suited for batch fabrication, and therefore not chosen as a method to go forward with.

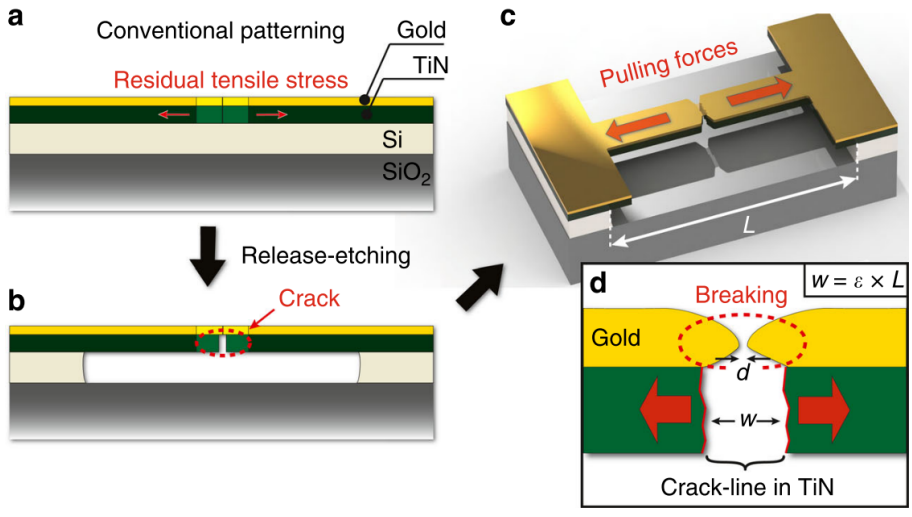


Figure 8.2: Diagram of crack tunnel junction as proposed by Dubois *et al.* (a) gold is deposited on stressed TiN. (b) a bridge structure is release etched, which induces the formation of a crack in the TiN. (c) TiN cantilevers pull apart the structure as the material relaxes. (d) pulling action, w, is determined by the length of the cantilever, L, causing a nanogap between the electrodes, d, to form. (From Dubois et al. [201])

Metal Island Junctions

Metal island tunnel junctions have been regularly reported in the literature for use in single electron devices, a diagram of which is shown in Figure 8.3. Cordan et al. [202] studied the conduction of highly disordered one and two-dimensional arrays of gold nanoislands. It was found that one-dimensional arrays show large tunnel resistances in the gigaohm to teraohm region, this is in part due to the highly disordered nature of the nanoparticles. If even one junction has a separation larger than the tunnelling distance, conductance drops drastically; and consequently, the yield of such usable devices is low. However, two-dimensional metallic island devices increased the yield of usable devices whilst showing relative conductance.

Another study by Pépin et al. [203] showed the temperature effects on the conductance of disordered two-dimensional arrays of metallic islands. Due to the exponential characteristics of the tunnelling effect, such devices show highly non-linear characteristics, especially at low temperatures. In particular, the threshold voltage (due to the coulomb blockade effect) was studied and was shown to increase with temperature as well as inversely with island size. Resistances of their devices were measured in the Mega-ohm ranges, making these device characteristics more favourable than those developed by Cordan et al. [202]. It was also shown that wide arrays of nano-islands are more robust against temperature changes.

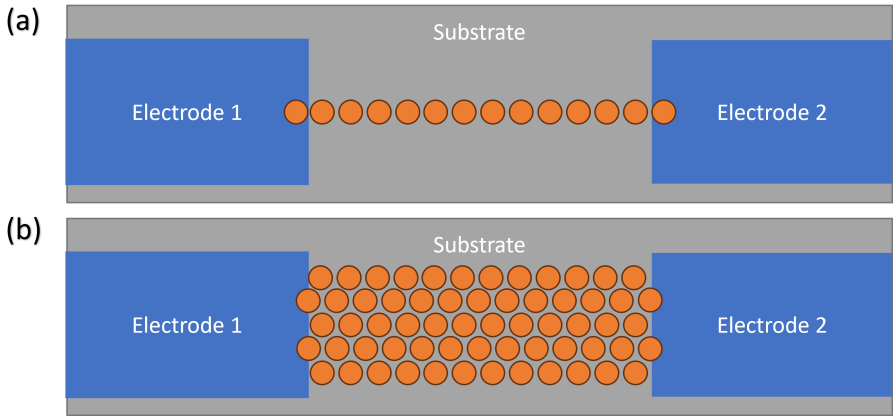


Figure 8.3: Diagram of metal island tunnel junctions - orange circles depict metal island materials. (a) 1D and (b) 2D island chains between the electrodes.

Metal island junctions have been demonstrated to exhibit high sensitivity as strain gauges, as evidenced by Kulkarni et al. [92] and Dukic et al. [93]. Investigating their fabrication using processes compatible with SThM fabrication presents an intriguing avenue for exploration.

Direct Write Junctions

Tunnel junctions can also be created by directly writing a small gap between two electrodes, as shown in Figure 8.4. However, directly writing tunnel junctions in one EBL step pushes the capability limits of many EBL machines. Due to the proximity effect, it is difficult to reliably write feature sizes in the single-digit nanometer region. Manheller et al. [204] created direct write tunnel junctions with 3 nm gaps between electrodes using very low EBL beam currents of 60 pA and accelerating voltages of 50 kV. However, the yield of such devices was relatively low at 55%.

Two-step direct write junctions offer a higher yield than those proposed by Manheller et al. [204]. These types of junctions consist of fabricating one electrode of the junction in one lithography step, then using advanced overlay alignment techniques, fabricating the counter electrode within tunnelling distance from the first. These can be fabricated to single-digit nanometer lengths as demonstrated by Docherty [138].

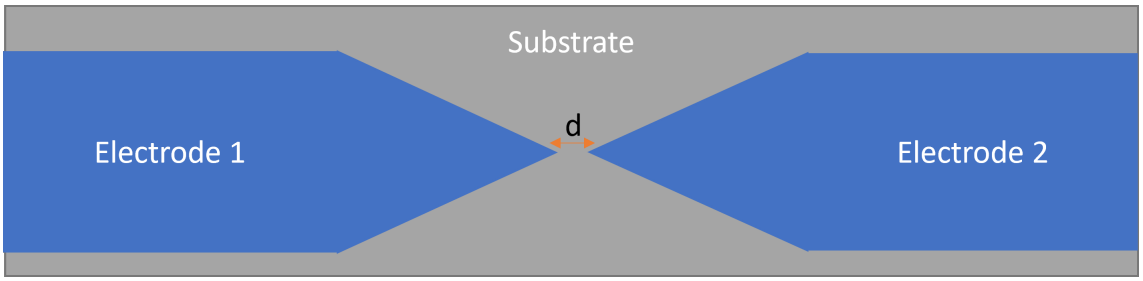


Figure 8.4: Diagram of a direct write tunnel junction. Both electrodes can be written directly within tunnelling distance, d, of each other. However, issues relating to resist limitations and the proximity effect, may necessitate the writing of each electrode in two lithography steps.

8.2 Model

To evaluate the distances required for tunnelling to occur with the required sensitivity in our system, 1D and 2D COMSOL models were created using the Schrödinger equation and electrostatics physics modules with the Schrödinger-Poisson coupling enabled in COMSOL. The Solid Mechanics interface was used to calculate the deformation of the cantilever and gold electrodes in 2-dimensional space for given tip deflections in vacuum. The shortest line between the two electrode boundaries was then calculated and used to set up a 1D Schrödinger-Poisson Metal-Insulator-Metal (MIM) simulation.

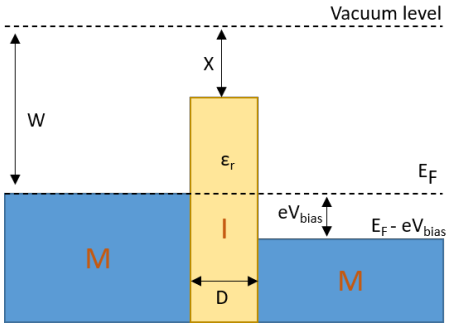


Figure 8.5: Energy diagram for an MIM junction where E_F the fermi energy level, W the metal work function, X, D and ϵ_r the insulating layers electron affinity, width and relative permittivity respectively, and V_{bias} the potential bias applied between the metals

An MIM junction can be modelled as in Figure 8.5, where the potential barrier is equal to the metal work function minus the electron affinity of the barrier. A potential bias can then be applied to one metal electrode and the potential energy in the insulating layer is solved using the bidirectional Schrödinger-Poisson physics coupling.

As the tunnelling probability relies exponentially on the barrier height as well as the barrier length, there will potentially be a large influence of the tunnelling probability through the substrate. With SiN having an electron affinity of 2.1 eV, compared to gold's work function of 5.1 eV, the barrier height will be 3 eV as compared to vacuum's 5.1 eV. This reduction in barrier height through the silicon nitride will be of great significance to the overall tunnelling probability and therefore conductance of the device. Some simple simulations were carried out to check the validity of the model setup. In this case, the transmission coefficient can be a useful parameter of a quantum system and can be expressed as the ratio of the incident electron wave function transferred through the potential barrier (i.e $T = \frac{|\psi_{transmission}|^2}{|\psi_{incident}|^2}$) [205].

Results of a 1D simulation of barrier separation can be seen in Figure 8.6. It shows the exponential relationship between the electrode separation and transmission coefficient. This is to be expected due to the exponential relationship between tunnelling probability and barrier width. Due to the lower barrier height of silicon nitride, it can also be seen that the transmission coefficient with distance varies much stronger for vacuum than it does for silicon nitride.

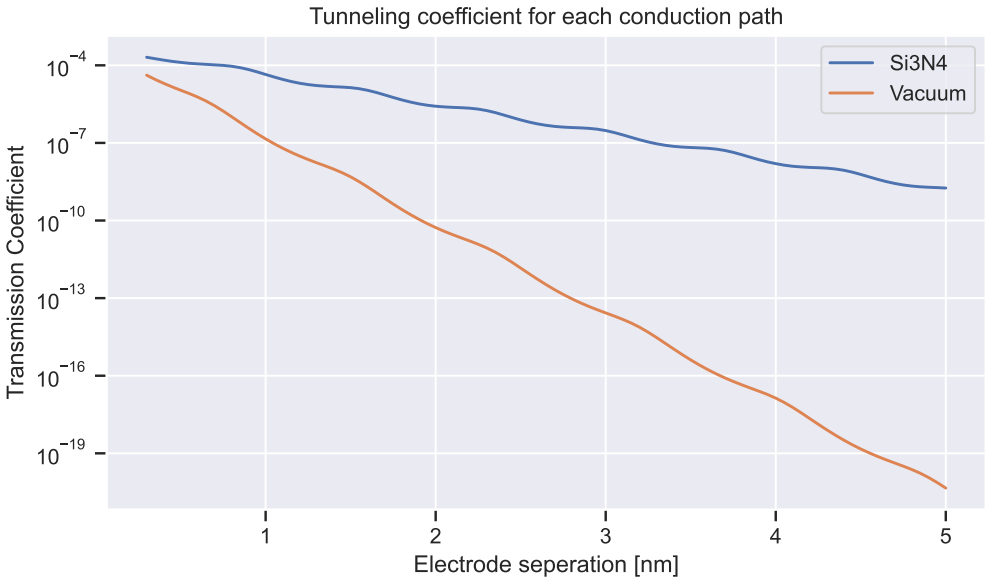


Figure 8.6: Exponential relationship between transmission coefficient and electrode separation through vacuum and silicon nitride.

For small deformations of a cantilever tip, within the elastic limit of a material, it can be assumed that the strain at its base (i.e the change in tunnelling distance of the sensor) will be linear with the free end deflection. Modelling the MIM junction in 2D (Figure 8.7) shows the change in transmission coefficients with respect to given cantilever tip deflections and shows the linear relationship between the transmission coefficient and cantilever deflection, with roughly an order of magnitude increase in sensitivity for positive deflections (inward bending sensor) when tunnelling through vacuum.

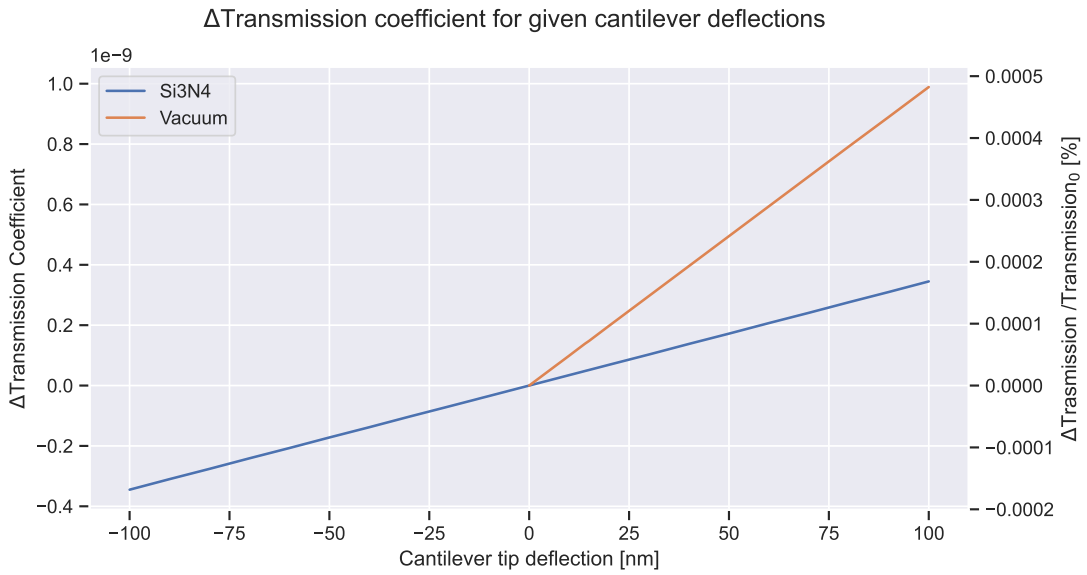


Figure 8.7: Tunneling contribution to Δtransmission coefficient for given tip deflection for 0.5 nm electrode separation and 5 nm electrode metalisation height. Vacuum tunnelling contributions only appear for positive deflections, as the shortest distance between electrodes is through vacuum.

From our model and as seen in Figure 8.7, it can be seen that the deflection of the cantilever causes very slight changes in the transmission coefficient with relatively low changes of less than 0.0005% for large cantilever deflections of 100 nm. This shows that to achieve an appropriate sensitivity of these devices, multiple of these junctions will be required to be placed in series. This adds complications to the fabrication of these elements as well as measurement due to the linear decrease in conductance that occurs when placing junctions in series.

8.3 Design of nano islands

This section looks at the fabrication of a strain sensor similar to that proposed by Kulkarni et al. [92] and Dukic et al. [93]. These devices show high strain sensitivity and are based on electron transport through metallic islands. The deposition of thin films under optimised conditions is known to naturally produce 2D disordered arrays of nano-islands via Volmer-Weber growth mechanisms (as discussed in section 3.3.2) with separations compatible with the tunnel effect [123]. However, the materials and methods used must be compliant with standard SThM probe process steps, in particular the 80 °C TMAH wet etch release step. Discontinuous films of metals and metal alloys that are compliant with the current SThM fabrication process were studied for their suitability as multiple tunnel junction devices (MTJs). This

limits materials that can be deposited via EBPVD in the JWNC to gold, palladium, platinum, and nichrome. During deposition in the EBPVD tool palladium and platinum tend to show quite erratic deposition rate control, making it difficult to deposit ultra-thin layers below their percolation threshold. Therefore, only gold and nichrome were investigated.

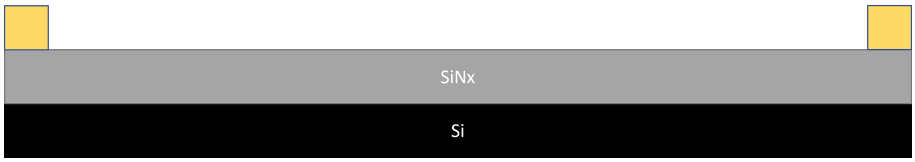
Conduction through thin discontinuous films before the percolation threshold has been extensively studied in the literature [206–210]. While films are still in their discontinuous phase, the conduction mechanics are dominated by the impedance of the inter-island gaps and the geometry of the given islands. Metal islands can be considered small when their dimensions are below 10 nm, this is usually where their thermal energies are lower than their Coulomb potential energies. Inter-island gaps are considered small below 4 nm, approximately the tunnelling path length of electrons.

When small islands and small gaps are present in the device, it is generally accepted that quantum mechanical tunnelling is the main form of conduction [210].

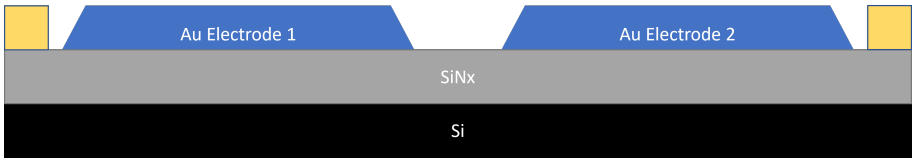
The fabrication of a nanoisland strain sensor may take the form of Figure 8.8. First markers are deposited to allow high accuracy alignment between lithography layers. This is followed by the deposition of electrodes that allow electrical connection to the areas of interest. Nanoislands are then deposited between the electrodes.



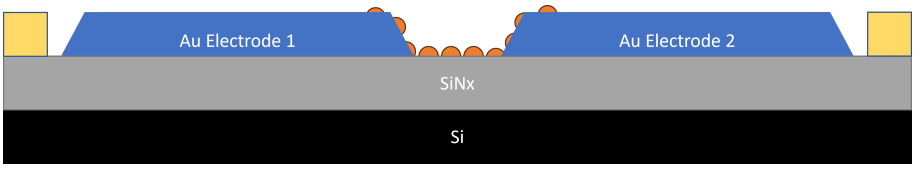
(a) A Silicon substrate with 400 nm SiNx epitaxial layer



(b) substrate markers are deposited for high accuracy pattern alignment



(c) Electrodes are deposited



(d) Deposition of nanoislands between electrodes

Figure 8.8: Fabrication steps of co-planer nanoisland junction device (a) through (d)

8.3.1 Deposition of nano islands

Discontinuous gold

For the creation of metallic nano islands, the electrical properties of gold, in particular its work function of 5 eV, are ideal for quantum tunnelling effects to be observed [211]. As described previously in section 3.3.1, the percolation threshold of deposited metals depends strongly on the bonding strength between the substrate and the deposited material. It has been shown in the literature that gold does not adhere to silicon nitride and easily de-laminates due to its inability to make strong bonds to the surface [212]. An example of such structures can be viewed in Figure 8.9

Due to the ease of de-lamination when deposited straight on silicon nitride, gold on its own cannot be used as nanoislands.

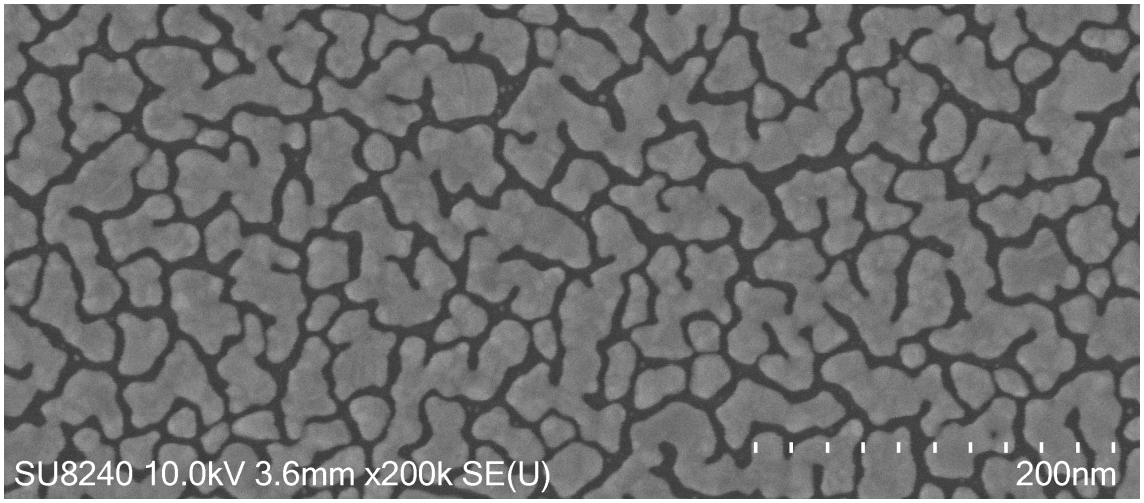


Figure 8.9: Discontinuous 5nm Au film deposited on SiNx.

NiCr/Au core-shell

As discussed in section 3.3.1 Nickel-chromium (nichrome) can act as an adhesion layer between gold and silicon nitride. An experiment was carried out to see if it was possible to anchor gold islands in place with a thin discontinuous layer of NiCr, then grow these gold islands closer together by increasing the gold layer thickness as shown schematically in Figure 8.10. The results are displayed in Figure 8.11 and suggest that such a deposition and technique for growing nanoislands was successful.

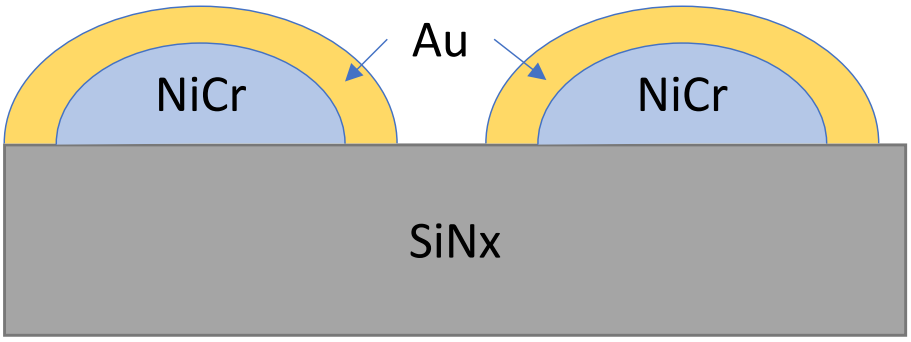


Figure 8.10: NiCr Core, Au Shell nano-particle model as a method to anchor gold to discrete NiCr islands.

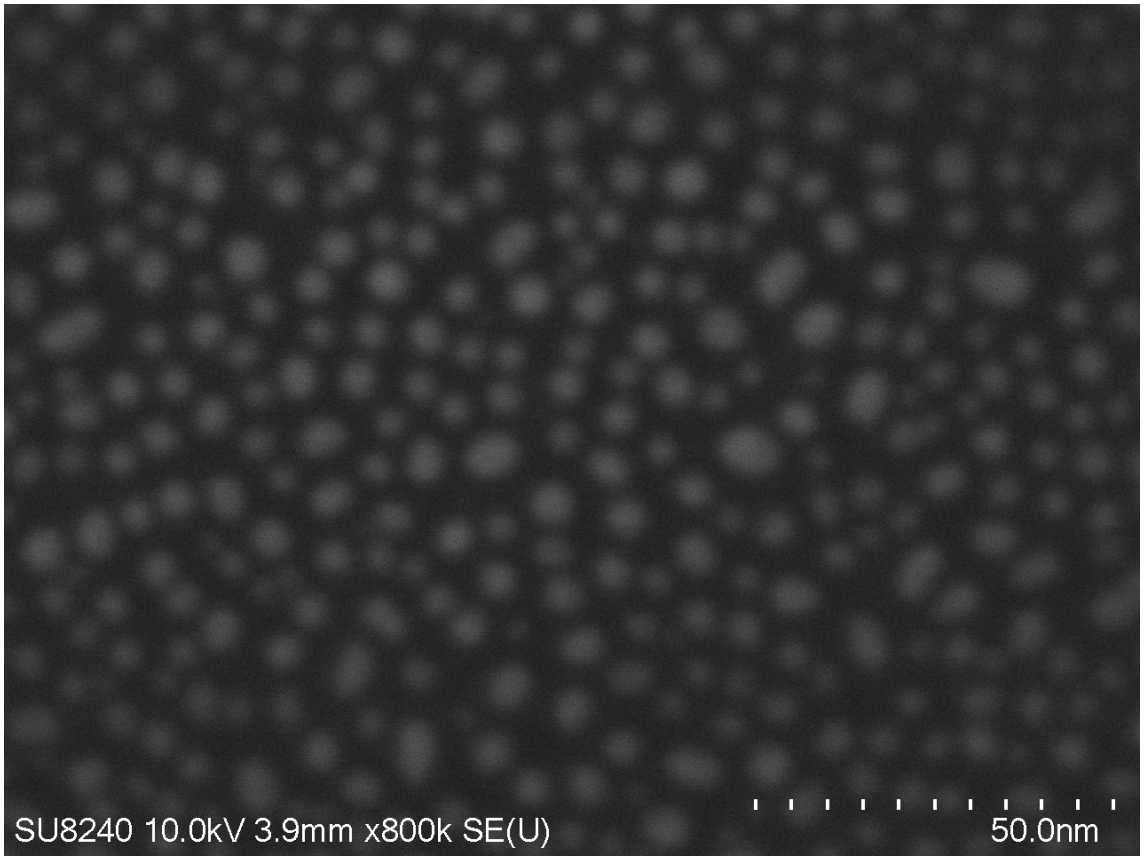


Figure 8.11: SEM images of EBPVD deposition of a layer of discontinuous 0.1 nm NiCr and 0.1 nm Au on SiNx substrate, showing Au anchored to NiCr islands.

From Figure 8.11, it can be seen that sub 10 nm islands and gaps have been deposited on the silicon nitride surface.

An important step for any sensors created for this project is the need for them not to degrade during an SThM probe release etch. This etch is usually carried out in 80 °C TMAH for 3 hours in a silicon micromachining kit. Simulations by Kwak and Kim [213] suggest that the top layer of bimetallic nano islands should stick to the anchor points during thermal dewetting.

To simulate this release process, the sample with deposited NiCr-Au discontinuous film was placed in 80 °C TMAH and left for an hour. The sample was then neutralised in reverse osmosis (RO) water for 10 minutes and dried from methanol with results seen in Figure 8.12. However, discordant to Kwak and Kim [213] simulations, dewetting of the surface during a TMAH release step causes the gold layer to form more energetically favourable larger gold islands. Therefore this technique cannot be utilised as a method to decrease the inter-island distance. It should be noted that the NiCr islands survive such processing and stay in place.

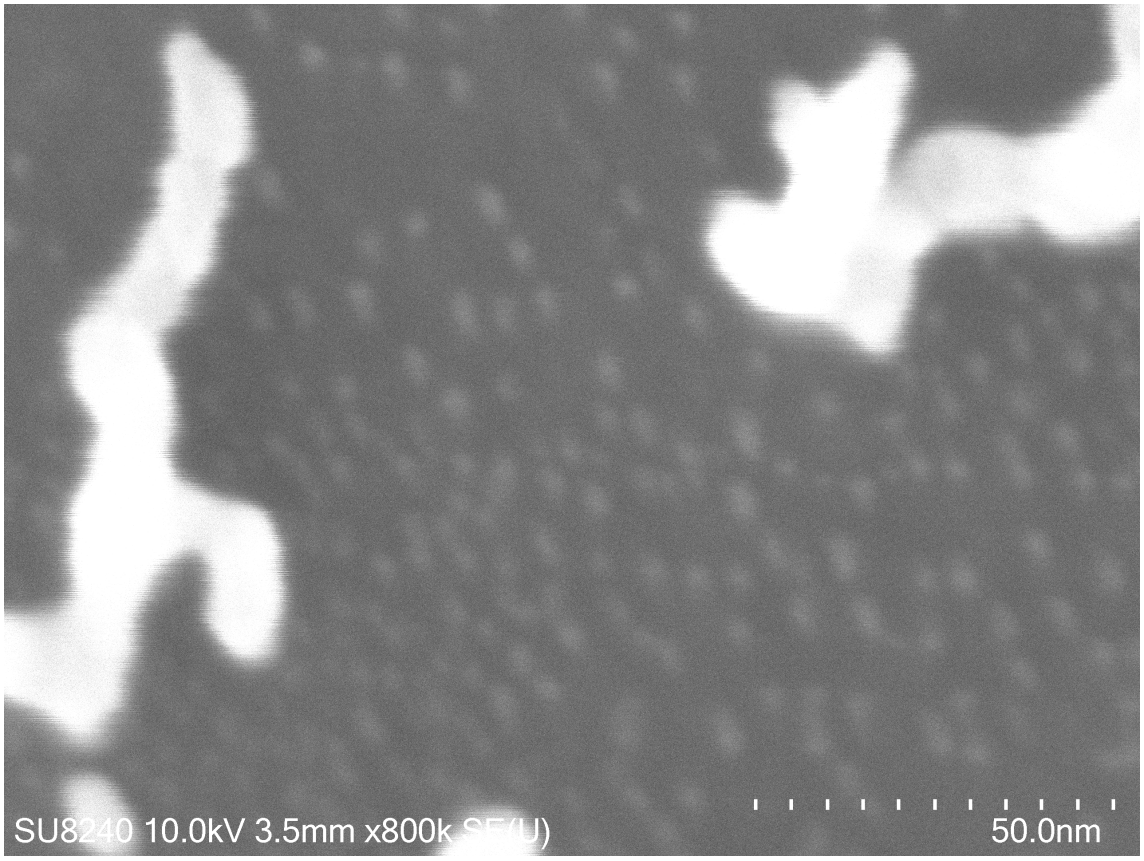


Figure 8.12: Nano-particles after 80 °C TMAH bath to simulate a release etch. The Au islands still de-laminate from the NiCr anchor points, to form larger islands. However, the underlying discontinuous NiCr film survives the simulated etch.

NiCr/Oxide

The observation of NiCr staying in place during the previous experimentation warranted further investigation as a candidate for creating discontinuous thin films. Due to NiCr's increased Cr-O bonding strength compared to the weak Au-O bonding, NiCr deposits on silicon nitride with much greater island density, reaching the percolation threshold at much thinner effective thicknesses. Therefore, highly accurate thickness measurements during deposition are required, as has been described previously in section 3.3.1.

Previous work on thin film NiCr by Avilovas [39] has shown that deposition of low-stress NiCr depends greatly on deposition parameters such as deposition rate and deposition pressure. Therefore, before deposition, a substrate blanked Ti deposition was conducted to lower the chamber pressure. The NiCr target was then run at a high rate (0.4 nm/s) with the substrate blanked to remove oxidation and contamination (i.e. condition the metal target). Finally, the NiCr was run at a lower rate

(0.04 nm/s) to precisely control the deposition thicknesses and decrease the stress of any NiCr islands that form. Figure 8.13 shows highly dense island structures, even when depositing ultra-thin NiCr layers. NiCr could be a suitable candidate if its electrical properties are suitable for tunnelling strain sensing.

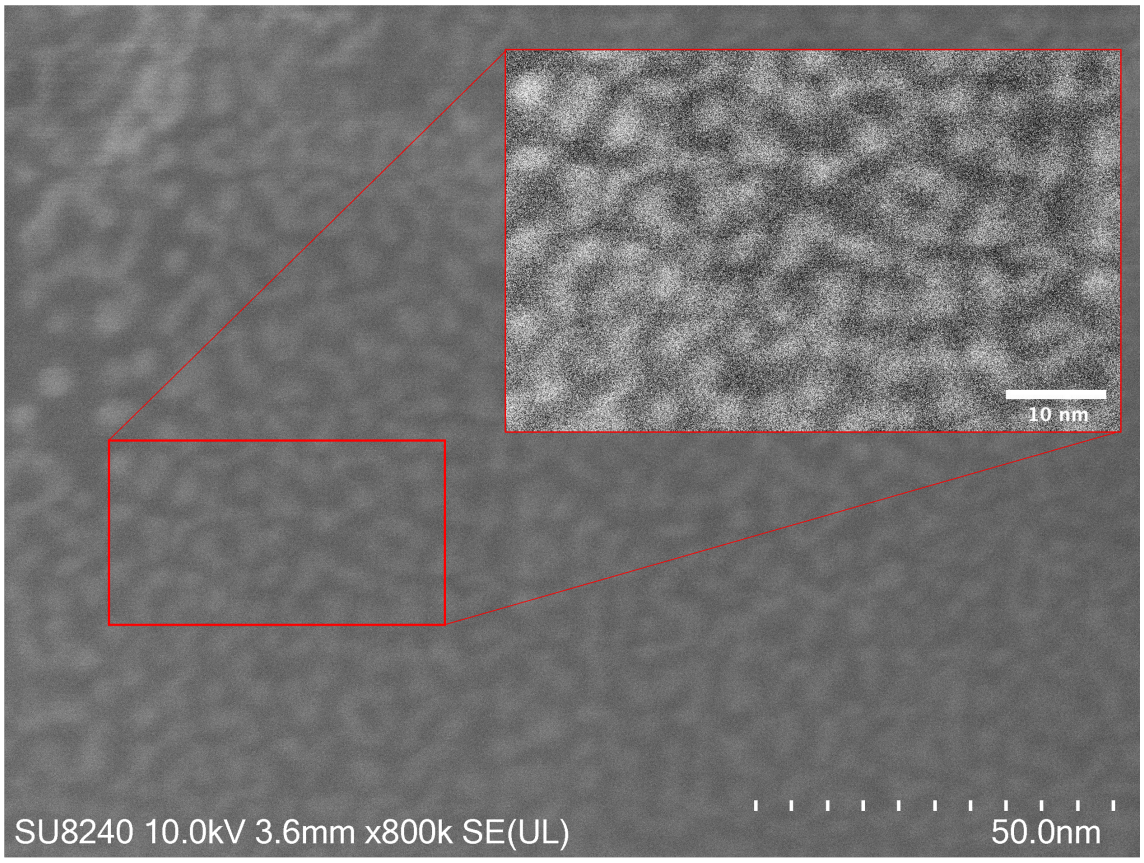


Figure 8.13: Thin discontinuous film deposition of 0.1 nm NiCr layer on SiNx. Red inset shows magnified and digitally enhanced contrast area, making nano islands more visible

From Figure 8.13, sub 5 nm inter-island gaps have been achieved, which is within electron tunnelling distance. However, control of electron transport through the nano-island film can be difficult without appropriate patterning between electrodes.

8.3.2 Electrode design

To provide an electrical connection to the nanoislands and control conduction through the islands, electrodes must be designed with repeatable geometries and electrode separations. Dense lines are known to be difficult to pattern in lithography as defects can cause shorts between the lines. It was decided that in order to relax the requirement of dense lines, one electrode should consist of a flat edge, and the counter electrode patterned as a sharp point in close proximity to the flat edge.

Fabrication of the electrodes is available in Table 8.1. The pattern is then written in the PMMA using EBL, with a beam step size of 1 nm and a beam current of 1 nA. A dose test was carried out to optimise the dosage and electrode separation and is available in Figure 8.14 for electrodes with a designed separation of 50 nm and 100 nm. A SEM image of the fabricated design with a separation width of 50 nm can be viewed in Figure 8.15.

Table 8.1: Electrode microfabrication steps.

#	Step	Process
1	Sonication	5 mins, in acetone, methanol, IPA, and RO water, then N2 blow dry.
2	O_2 Ash	5 mins at 150 W
3	Bake	5 minutes on 180 °C hotplate dehydration.
4	Spin	12% 50K MW Anisole PMMA (AR-P 632.12) at 4000 rpm, 60 s for a 310 nm bottom layer.
5	Bake	3 minutes on 180 °C hotplate PMMA tempering.
6	Spin	4% 200K MW Ethyl-Lactate PMMA (AR-P 649.04) at 4000 rpm, 60 s for a 150 nm top layer.
7	Bake	3 minutes on 180 °C hotplate PMMA tempering.
8	E-Beam	Write electrode patterns.
9	Develop	23 °C 2.5:1 MIBK:IPA, 30s with mild agitation. Stopped in IPA.
10	O_2 Ash	30 s at 80 W.
11	Metalisation	NiCr/Au (5 nm/70 nm).
12	Lift-off	50 °C acetone bath, 2 hours.
13	Sonication	1 min in acetone, IPA, and RO water, then N2 blow dry.

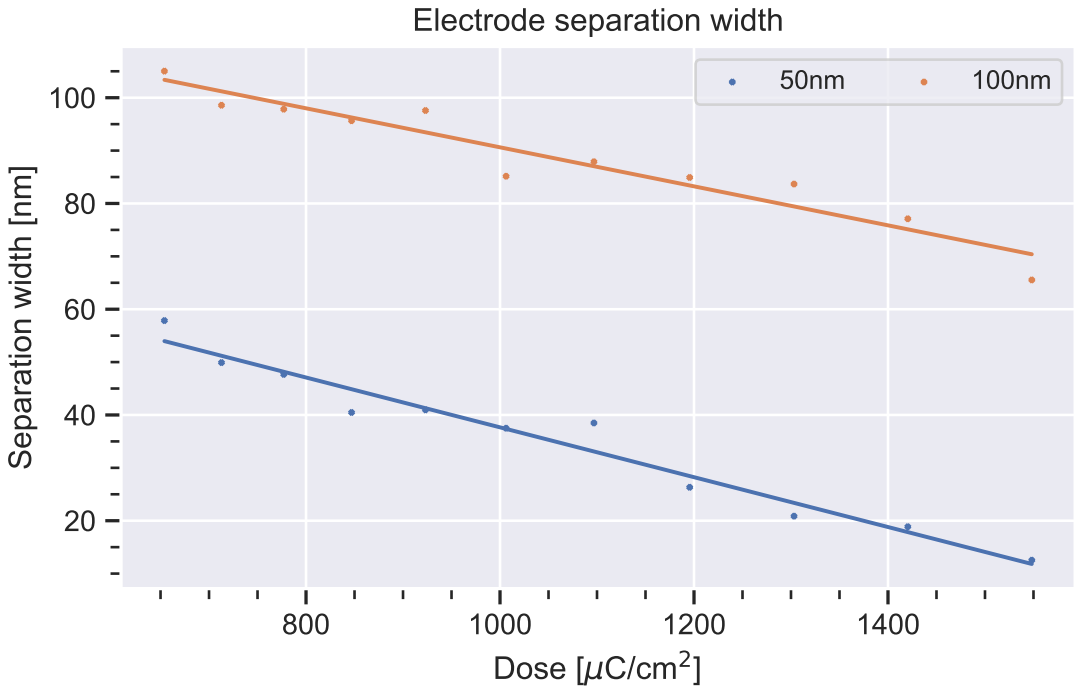


Figure 8.14: Dose test results for electrode separation study, for both 100 nm and 50 nm electrode separations, respectively an electron dosage of approximately 745 µC/cm^2 and 740 µC/cm^2 are required.

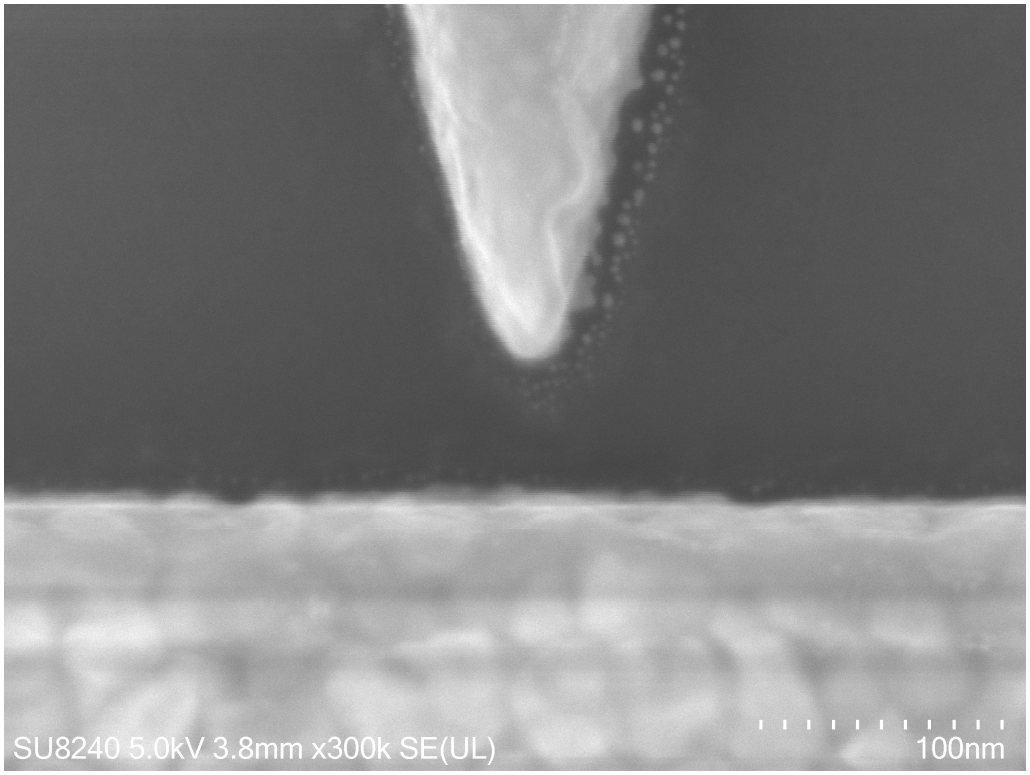


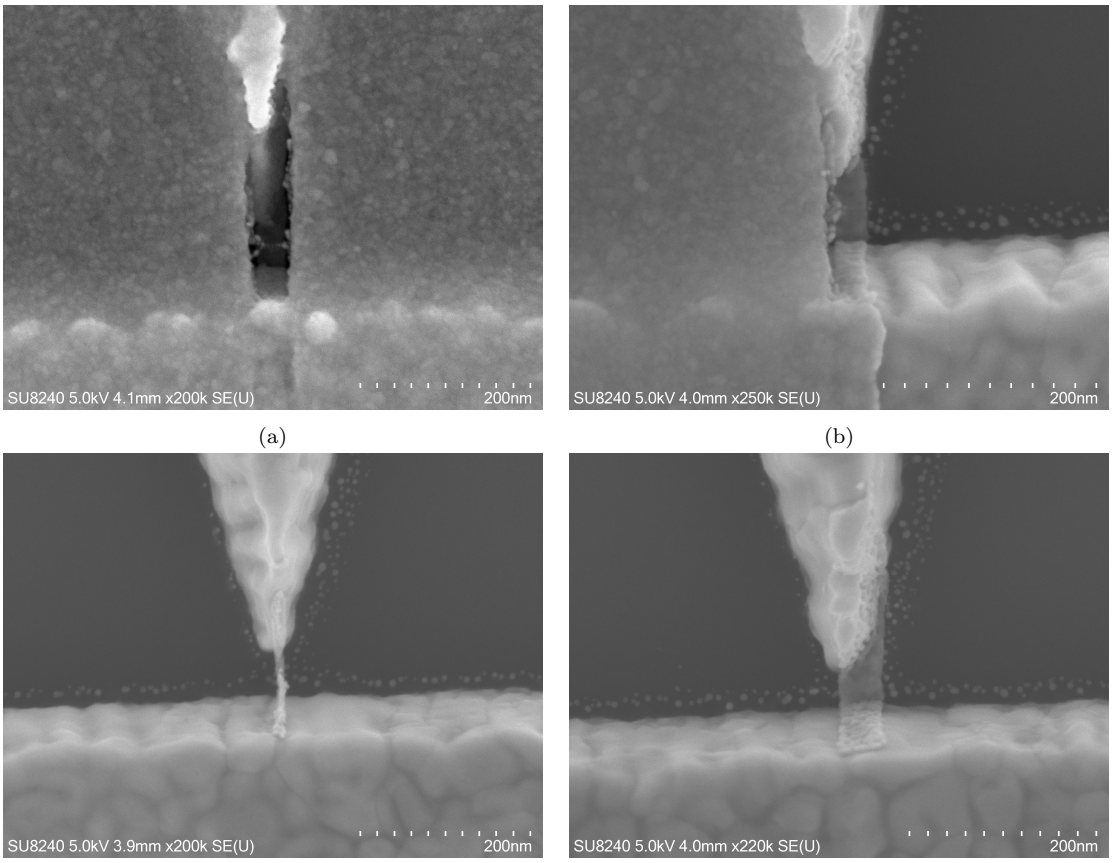
Figure 8.15: SEM image of fabricated 50 nm electrode design. Electrode 1 consists of a flat surface and electrode 2 consists of a sharp point, allowing controllable separation widths with dosage.

8.3.3 Inter-electrode nanoisland metalisation

In a similar fashion to the electrode design, the inter-electrode metal can be patterned utilising EBL with the same process steps as Table 8.1. However, the bi-layer PMMA was altered to a bottom PMMA layer 4% 50k molecular weight dissolved in anisole (Allresist 632.06) spun at 6000 rpm for 60 s to give a layer thickness of 90 nm, and the top layer was 1% 200k molecular weight dissolved in ethyl-lactate spun at 4000 rpm for 60 s giving a layer thickness of 20 nm. Discontinuous metal deposition was achieved through the deposition of 0.1 nm NiCr at a deposition rate of 0.04 nm/s. Ti and NiCr crucibles were evaporated for 50 nm each prior to the shutter opening to condition the chamber and crucibles to reduce contamination of the islands.

Dose tests were carried out to determine suitable line widths to pattern discontinuous NiCr islands between the electrodes. Due to the difficulty in analysing such thin and small metal islands visually, it was decided this could be achieved by depositing continuous films (5 nm/10 nm NiCr/Au) and measuring the line width for given doses. Lift-off of such thin lines next to large electrodes proved difficult

as exposed resist on top of the electrodes caused metal to be deposited on them. Therefore, many dose test sample attempts failed to produce reliable results (Figure 8.16a and 8.16b). Of the devices that were measurable, dose test results show a roughly 600 µC/cm^2 to 800 µC/cm^2 electron dosage for these features (Figure 8.17). This metal flagging was not observed to be a problem going forward in the case of discontinuous films.



(a) (b) (c) (d)

Figure 8.16: SEM imaging of line metallisation dose test. (a) and (b) show failed lift-off due to metal sticking to the electrodes creating a metal membrane, obscuring the view of the line, this proved difficult to reliably measure line width; compared to (c) and (d) where measurement is clearer.

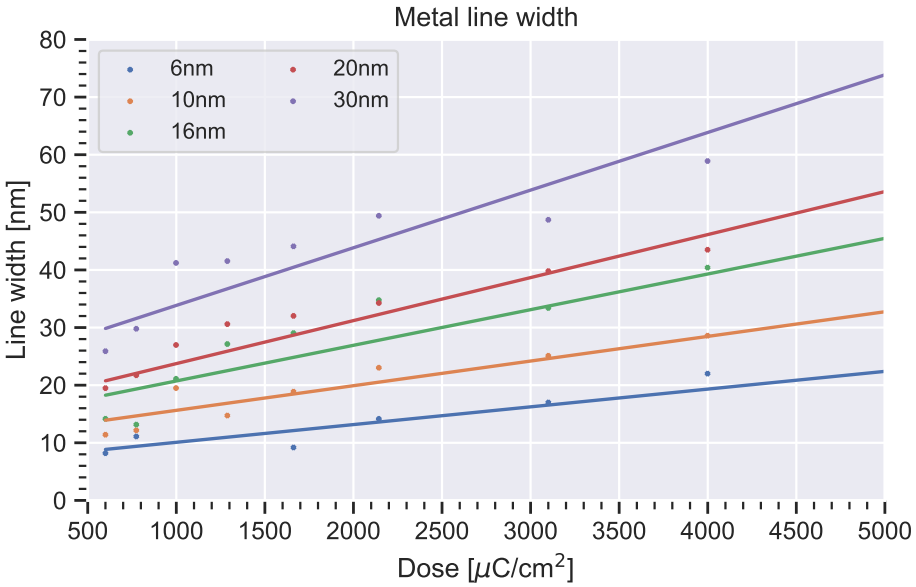


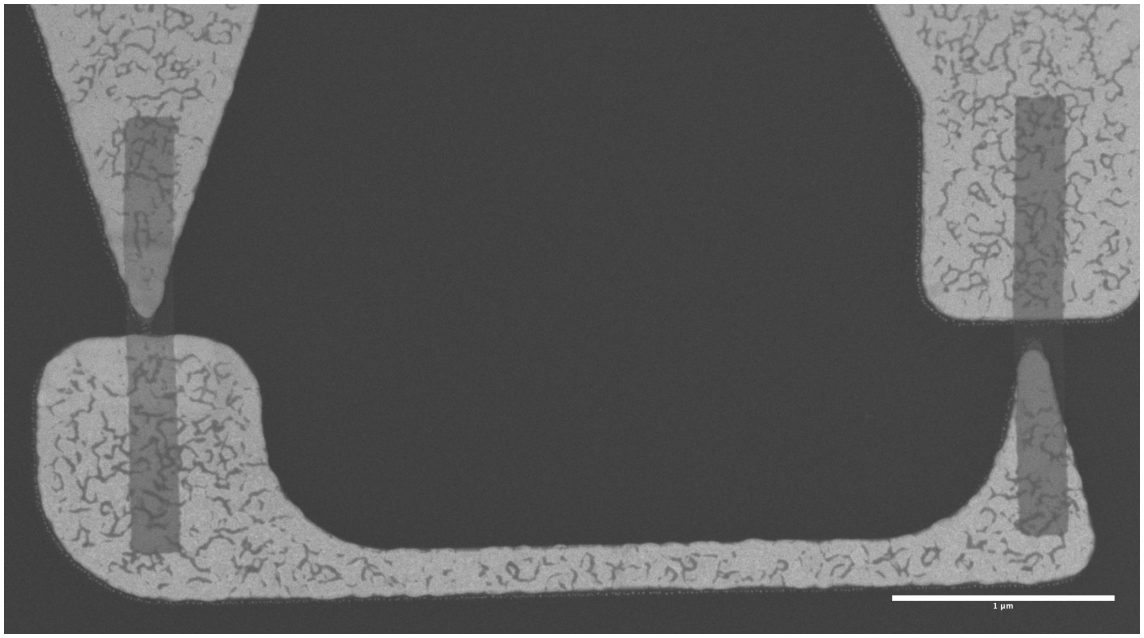
Figure 8.17: Dose test results for thin lines between electrodes.

It should be noted that line widths under 16 nm failed to reach their designed line widths in the dose range. All doses under 600µC/cm^2 failed to pattern appropriately with the chosen recipe. However, lines this thin deposit films only a few islands widths wide and would generally show very high resistances in the gigaohm region [202], and would generally not be practical for measurement. Utilising larger line widths also relaxes the alignment accuracy needed between the sharp tip electrode and the placement of the strip of nanoislands.

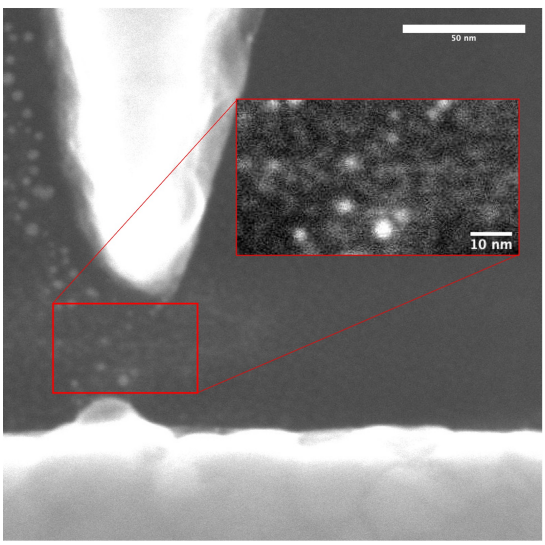
Subsequent metalisation of electrode separations with discontinuous NiCr film can be viewed in Figure 8.18b. These show approximate tunnelling distance gaps between small islands. However, it is difficult to quantify island size and gaps of sub 10 nm features [214]. Backscattered electron (BSE) imaging can give more compositional imaging, showing the differing overall presence of the NiCr thin film in the correct location between the electrodes as in Figure 8.18a. Island sizes and gaps can be more easily distinguished using the SU8240's BSE detector (Figure 8.18c), showing smaller islands and larger gaps compared to SE imaging. However, charging effects results in difficulty in achieving higher magnification images for accurate analysis.

8.3.4 Electrical measurement

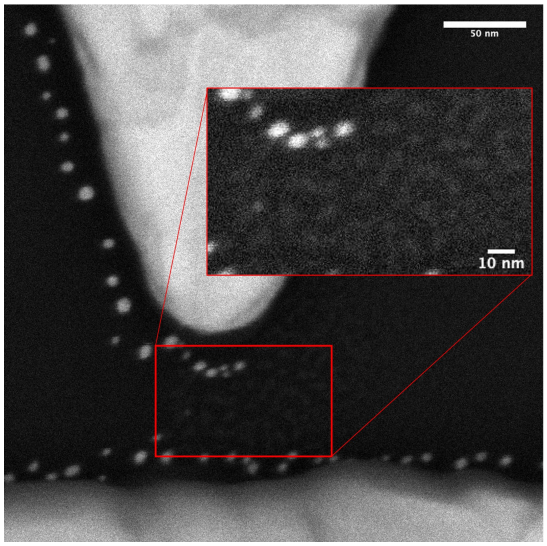
Current-Voltage (IV) curve measurement was carried out through an Agilent 4155C Semiconductor Parameter analyser with micromanipulators connecting to each elec-



(a)



(b)



(c)

Figure 8.18: SEM imaging of inter-electrode metalisation. (a) BSE detector view of the overall device structure with two junctions in series, the NiCr discontinuous film deposition between the electrodes clearly visible (scale bar 1 µm). (b) SE imaging of inter-electrode metalisation. (c) BSE imaging of inter-electrode metalisation, charging effects limit the available magnification for the given setup. Red insets show digitally enhanced contrast and magnified areas of interest. Low contrast NiCr islands become visible. High contrast islands around electrodes are lift-off marks.

trode. Devices were measured up to 100 mV bias across the electrodes. Unfortunately, of the junctions measured, all either instantly measured as a short circuit or open circuit. After electrical measurement, the devices were inspected in the SEM with images seen in Figure 8.19 through 8.24. It can be seen that even devices with larger gaps, such as that in Figure 8.24, show catastrophic failure of the junction.

A plausible rationale for the malfunction of these devices may stem from the potential occurrence of inadvertent direct electrical connection between the electrodes, despite the seemingly successful deposition of nanoislands. Such unintended electrode connectivity could result in the establishment of an electrical path with notably diminished current-carrying capabilities, which may be susceptible to explosive failure from thermal overloading, thereby inducing an open circuit. In such cases, one would expect from multiple junction devices, such as Figure 8.20, that only one junction would blow in such a scenario. However, both junctions have shown extensive failures. This suggests failure of these devices may stem from a high susceptibility to electrostatic discharge, possibly from faults and/or inappropriate grounding of the measurement equipment.

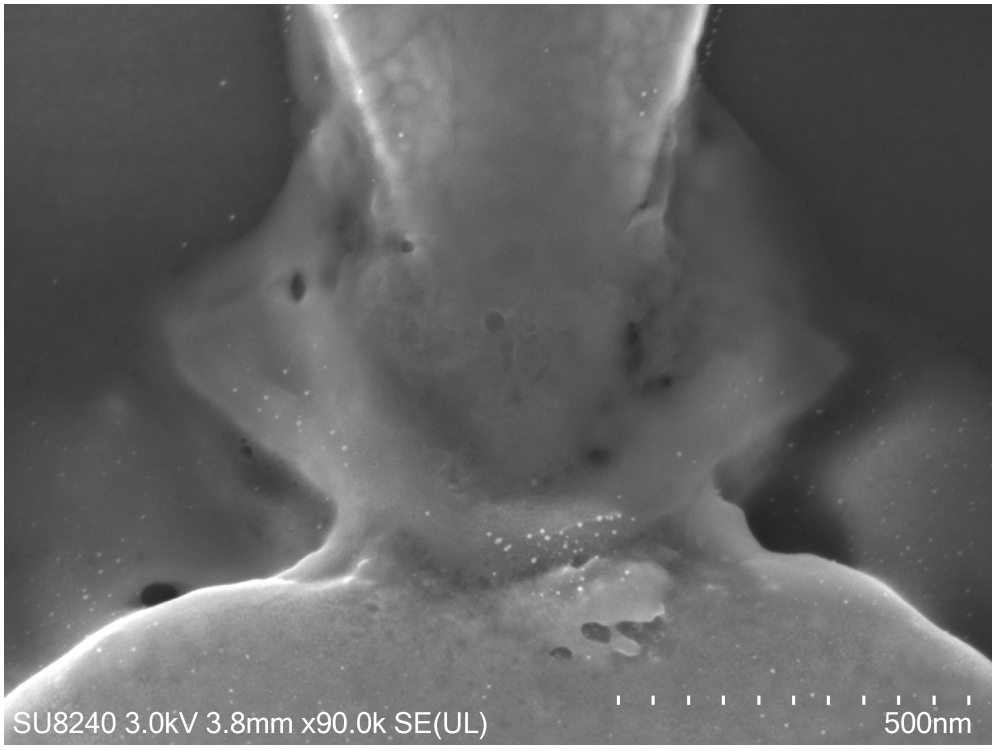


Figure 8.19: Failed device that short circuited.

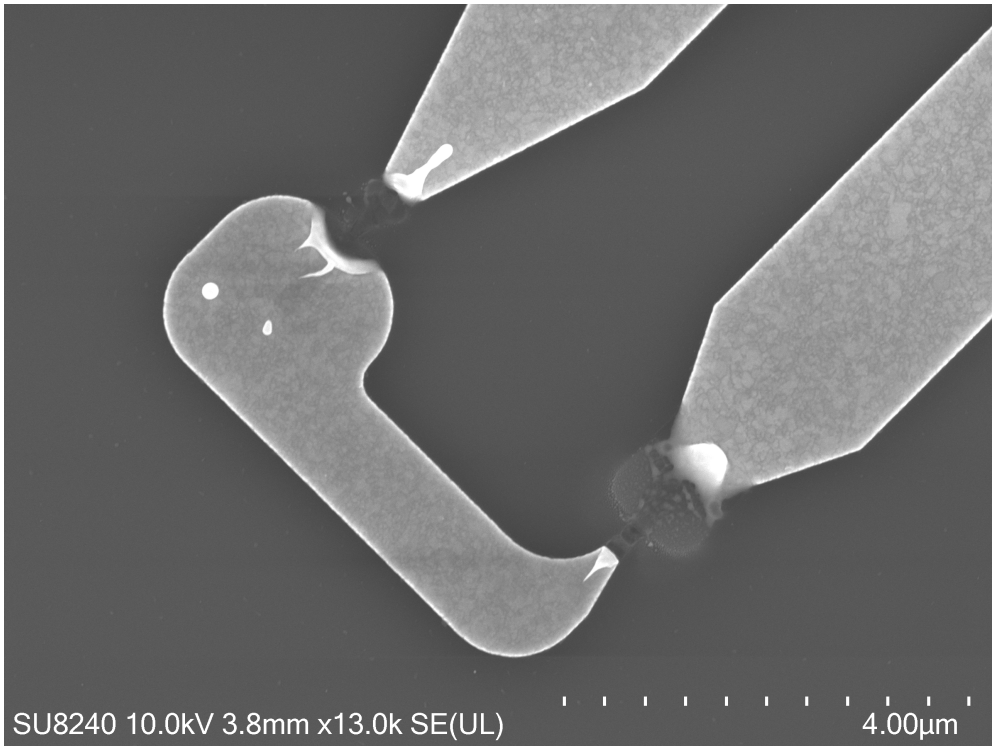


Figure 8.20: Two 50 nm junctions that have failed and blown open circuit

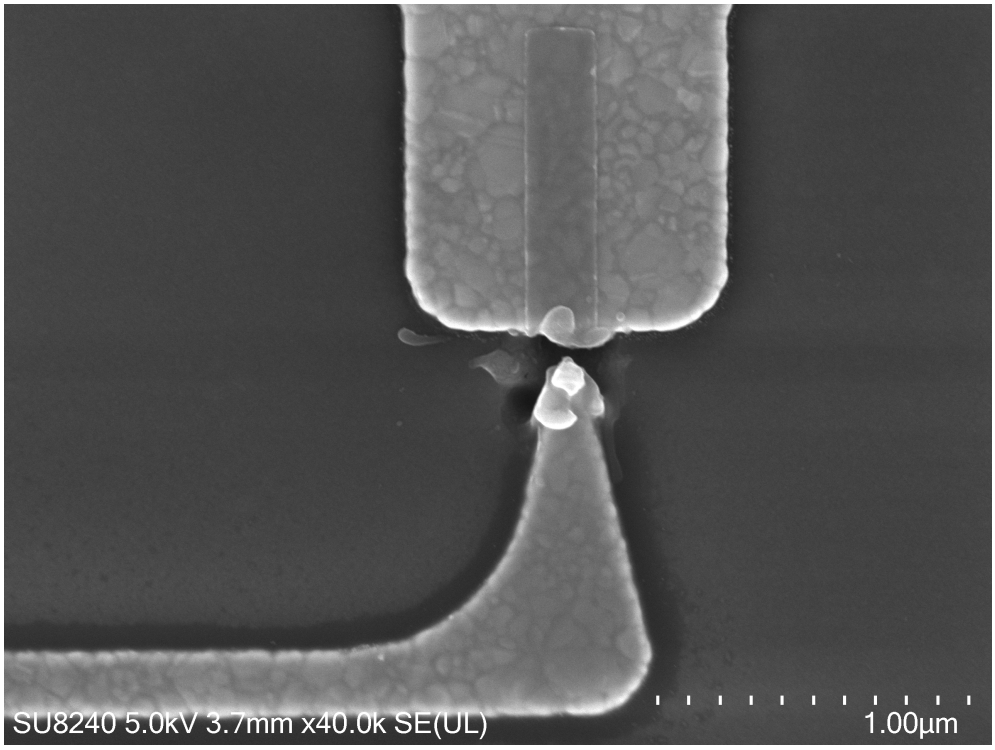


Figure 8.21: Junction that has blown open circuit

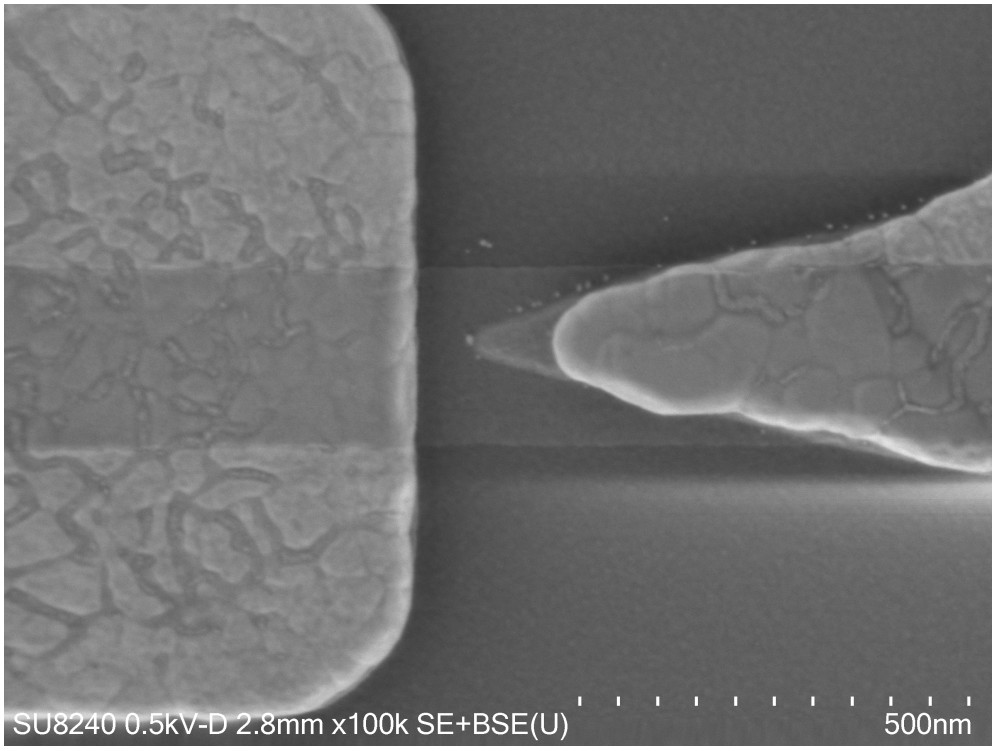


Figure 8.22: Although no visual catastrophic failure has occurred, the gold has dewetted from the sharp electrode point and measures open circuit.

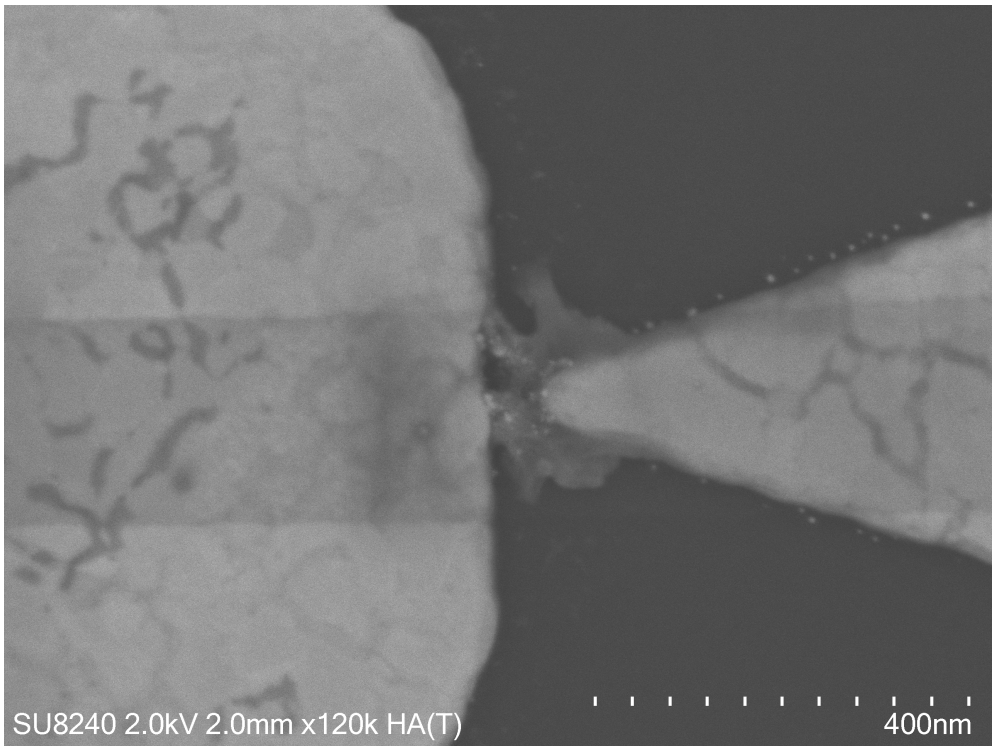


Figure 8.23: 50 nm junction that has become short circuit after measurement.

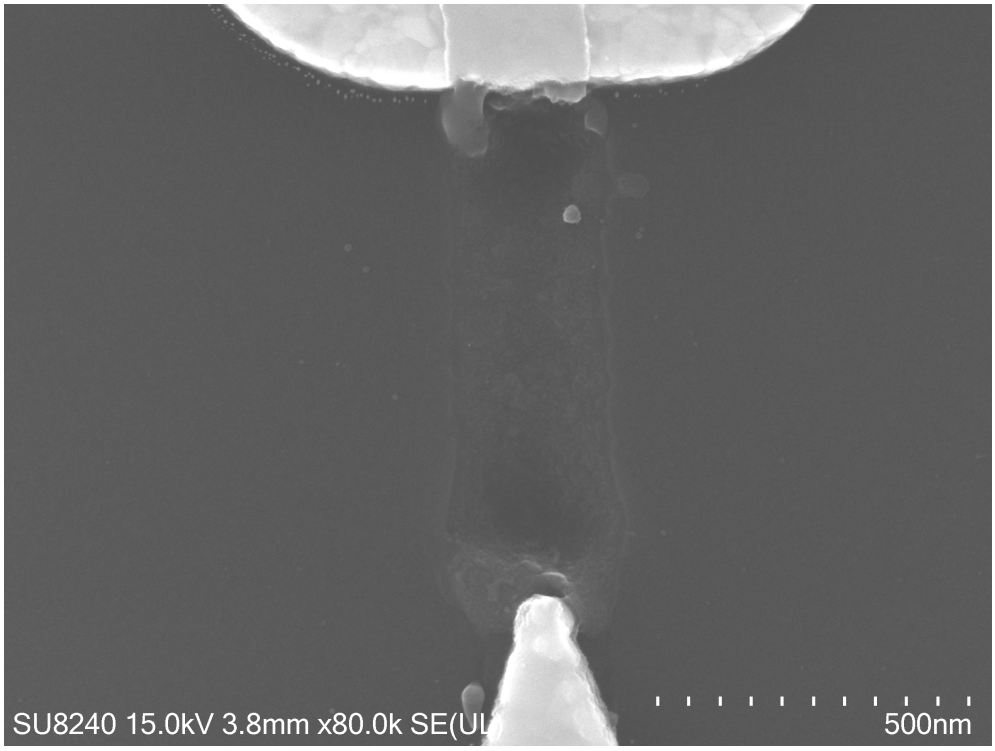


Figure 8.24: Increasing the electrode separation to 750 nm and increasing the deposited NiCr layer thickness also show failure of the device.

8.4 Direct write two-step lithographic ramp-edge junctions

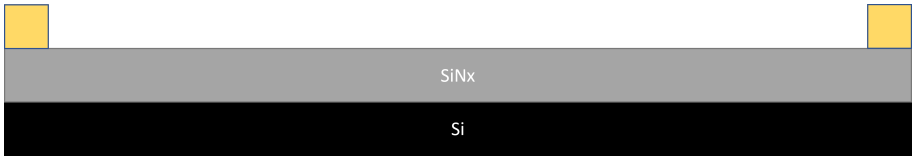
As discussed in section 8.1, ramp-edge style junctions are not routinely available in the JWNC due to the requirement of insulating materials needing to be deposited on top of electrodes. However, the availability of high-accuracy overlay allows the realisation of ramp-edge junctions using a two-step direct write approach similar to that of Docherty et al. [140]. The proposed fabrication steps required to create ramp-edge tunnel junctions using high overlay lithography can be summarised in Figure 8.25.

Starting with a blank Si wafer with 400 nm SiNx epitaxial layer, Penrose markers were first patterned and metalised onto the substrate surface. The first electrode pattern was then written and aligned to these penroses and 55 nm of NiCr deposited. This electrode was then oxidised either naturally or at elevated temperature to form an insulating layer. After this, the second electrode was patterned and deposited atop the first electrode's edge using the high overlay accuracy available from the Penrose markers, thereby establishing a Metal-Insulator-Metal (MIM) junction

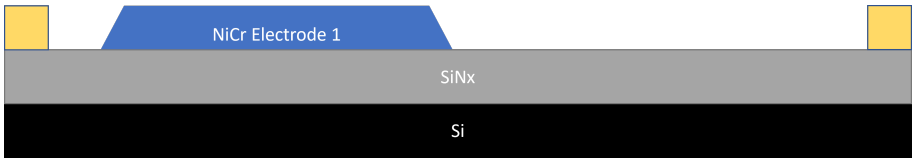
oriented somewhat perpendicular to the substrate surface. Throughout each fabrication step, meticulous precautions were observed to store the samples under vacuum conditions to minimise the extent of natural oxide accumulation to the greatest extent feasible.



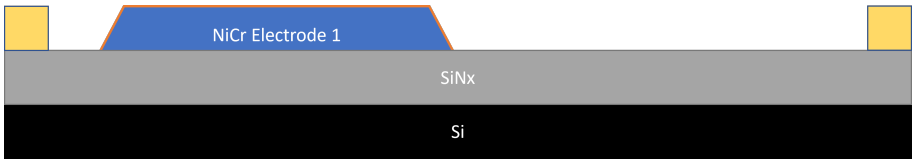
(a) A Silicon substrate with 400 nm SiNx epitaxial layer



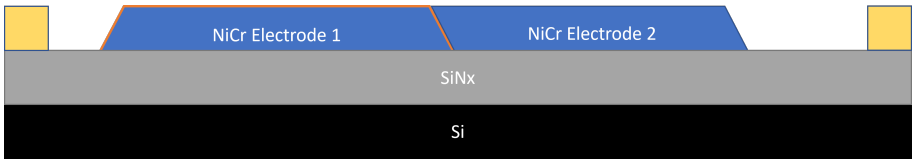
(b) substrate markers are deposited for high accuracy pattern alignment



(c) First electrode is deposited



(d) Oxidation of the first electrode - either naturally or at elevated temperatures



(e) Deposition of the second electrode to create an MIM junction

Figure 8.25: Fabrication steps of co-planer MIM junction (a) through (e)

8.4.1 Electrode design

The electrode design of these sensors follows a similar protocol to that of the nanoisland junctions and is set out in Table 8.2. However, we now utilise high overlay accurate alignment techniques to place the second electrode directly on the metal trace edge of the first electrode, so the electrodes must be written in two steps. We also require long parallel lines to increase the surface area of the junction. Figure 8.26

and 8.27 show the creation of two junctions in series. First, a set of electrodes was deposited with a known separation as in Figure 8.26. This layer was then baked in an oven (Hearus) at an elevated temperature and for various times to control the thickness and parameters of the tunnel barrier (as will be discussed in section 8.4.2), before the deposition of the middle electrode in Figure 8.27.

Table 8.2: Ramp-style MIM junction microfabrication steps.

#	Step	Process
1	Sonication	5 mins, in acetone, methanol, IPA, and RO water, then N2 blow dry.
2	O_2 Ash	5 mins at 150 W
3	Bake	5 minutes on 180 °C hotplate dehydration.
4	Spin	6% 50K MW Anisole PMMA (AR-P 632.06) at 3000 rpm, 60 s for a 140 nm bottom layer.
5	Bake	3 minutes on 180 °C hotplate PMMA tempering.
6	Spin	1% 950K MW Ethyl-Lactate PMMA (AR-P 679.01) at 4000 rpm, 60 s for a 30 nm top layer.
7	Bake	3 minutes on 180 °C hotplate PMMA tempering.
8	E-Beam	Write electrode 1.
9	Develop	23 °C 2.5:1 MIBK:IPA, 30 s with mild agitation. Stopped in IPA.
10	O_2 Ash	30 s at 80 W.
11	Metalisation	NiCr (55 nm).
12	Lift-off	50 °C acetone bath, 2 hours.
13	Sonication	1 min in acetone, IPA, and RO water, then N2 blow dry.
14	O_2 Ash	30 s at 80 W
15	Bake	Oven oxidation of 1st electrode at elevated temperature.
16	Spin	6% 50K MW Anisole PMMA (AR-P 632.06) at 3000 rpm, 60 s for a 140 nm bottom layer.
17	Bake	3 minutes on 180 °C hotplate PMMA tempering.
18	Spin	1% 950K MW Ethyl-Lactate PMMA (AR-P 679.01) at 4000 rpm, 60 s for a 30 nm top layer.
19	Bake	3 minutes on 180 °C hotplate PMMA tempering.
20	E-Beam	Write electrode 2.
21	Develop	23 °C 2.5:1 MIBK:IPA, 30 s with mild agitation. Stopped in IPA.
23	O_2 Ash	30 s at 80 W.
24	Metalisation	NiCr (55 nm).
25	Lift-off	50 °C acetone bath, 2 hours.
26	Sonication	1 min in acetone, IPA, and RO water, then N2 blow dry.

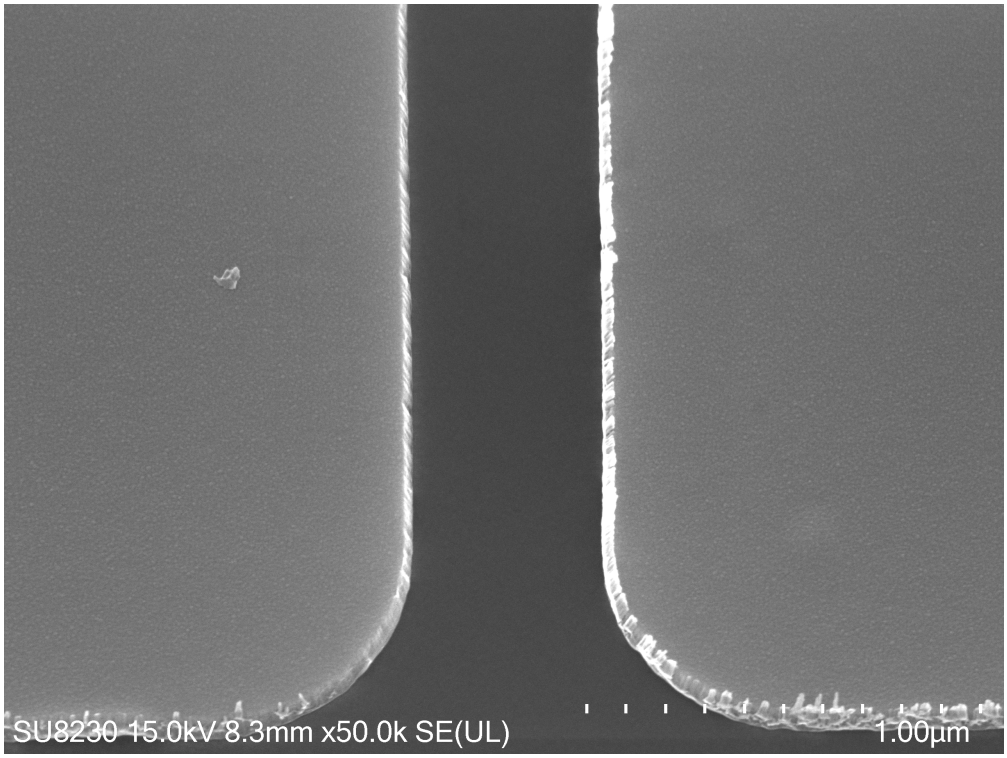


Figure 8.26: Deposition of two electrodes a known distance apart.

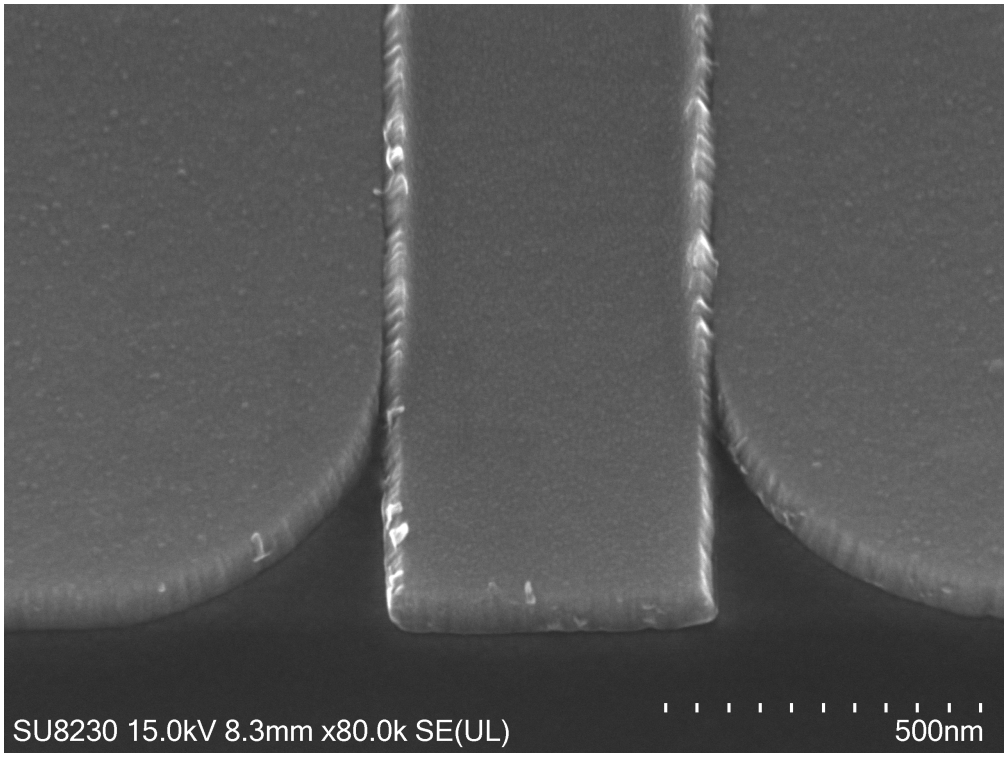


Figure 8.27: Deposition of a centre electrode, allowing for the creation of two junctions at each side.

Better inspection of the junction interface can be acquired through cross-sectional analysis. As such, samples were created with fabricated junctions, they were then cleaved perpendicular to the junction and examined via SEM as seen in Figure 8.28. It can be seen that there is a slight overlap of the electrodes, this is due to the need for increased dosage to clear out the PMMA allowing contact of the electrodes. Figure 8.29 shows from previous experimentation where, although placement is highly accurate, contact of the electrodes has not been made. However, as seen in Figure 8.28, voids under the deposited metal still exist even from higher dosages, making contact inconsistent.

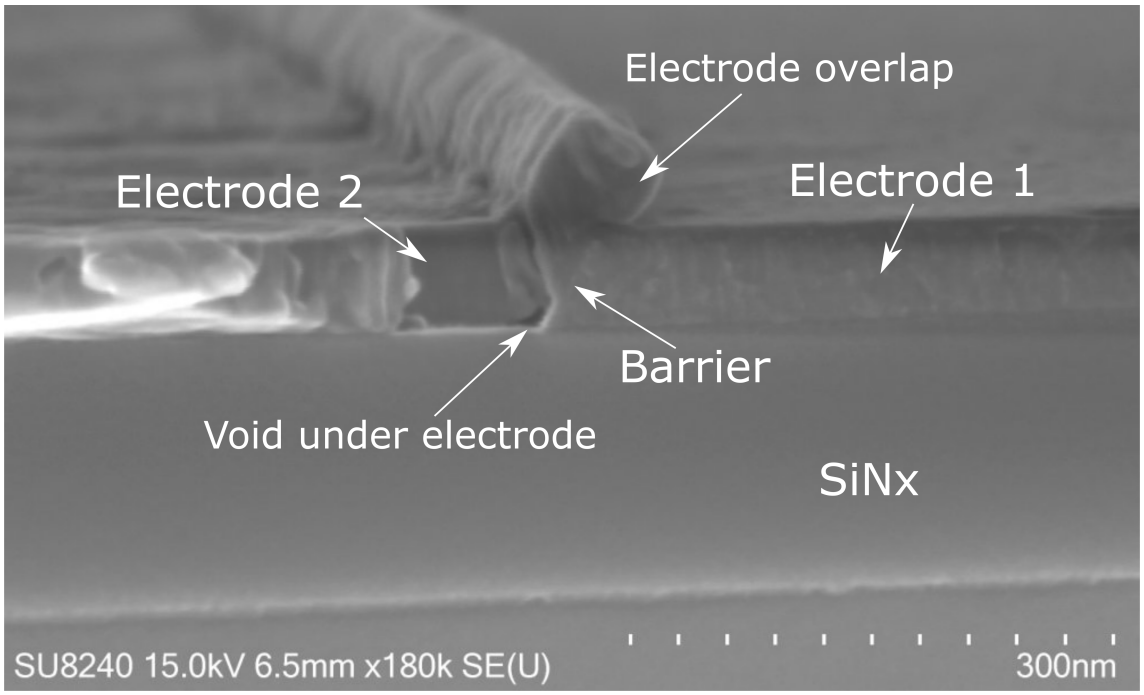


Figure 8.28: Cross sectional SEM image of a single junction. It can be seen that the deposition of the 2nd electrode (LHS) atop the metal edge of the 1st electrode has been successful. However, it should be noted that a void still exists below the deposited 2nd electrode where PMMA failed to clear.

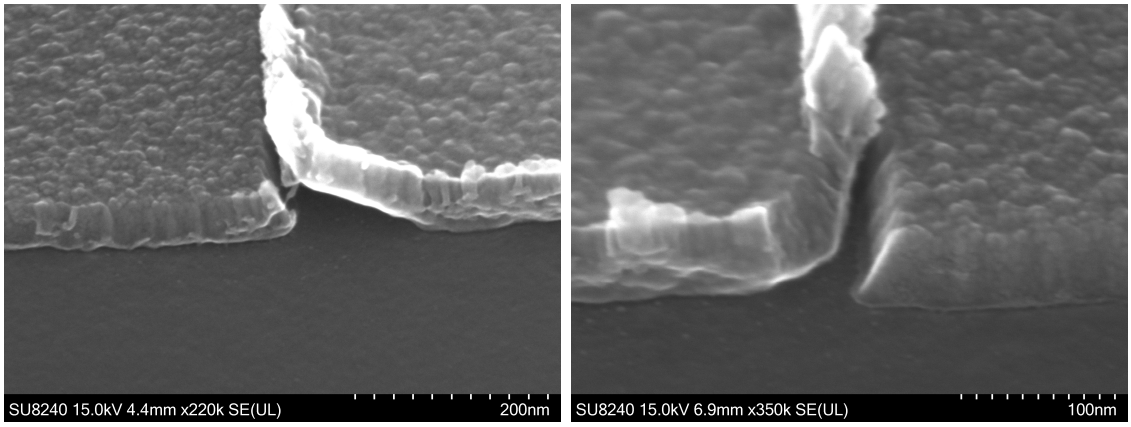


Figure 8.29: SEM image of two single junctions, PMMA consistently fails to clear from the 1st electrode side metal track causing an uncontrollable separation between the two electrodes.

8.4.2 Oxidation of 60/40 NiCr

An important parameter to control in the fabrication of tunnel junction devices is the barrier height and width as the conductance of the junction depends exponentially on these parameters. The oxide growth mechanisms of 60/40 NiCr have not been well studied in the literature. However, low-temperature 80/20 NiCr oxidation mechanisms have been reported in the literature by Wang et al. [215] and 50/50 NiCr by Phuong et al. [216]. Wang et al. [215] had shown that oxide formation up to 200 °C primarily consists an inner layer of Cr_2O_3 with a mix of metal hydroxides, in particular, a temperature-dependent mix of $Ni(OH)_2$ and $Cr(OH)_3$ as an outer layer. At and above 300 °C, a second oxidation phase occurs with the sole formation of a stable Cr_2O_3 layer. Increasing the Cr content in the metal to 50%, studies by Phuong et al. [216] show that the second phase of Cr_2O_3 growth occurs at higher temperatures upwards 350-400°C with scale-like growth and a vast increase in surface roughness. Wang et al. [215] did not report any scale-like growth for their study up to 300 °C.

Attempts to characterise the oxidation growth of NiCr (other than electrically) using SEM were made to study the oxide growth mechanisms of 60/40 NiCr. Devices were created and then cleaved to reveal a cross-section of the junction visible in Figure 8.30. Images were taken using the BSE detector in the SEM, this allows for greater material contrast in the captured compared to SE SEM imaging.

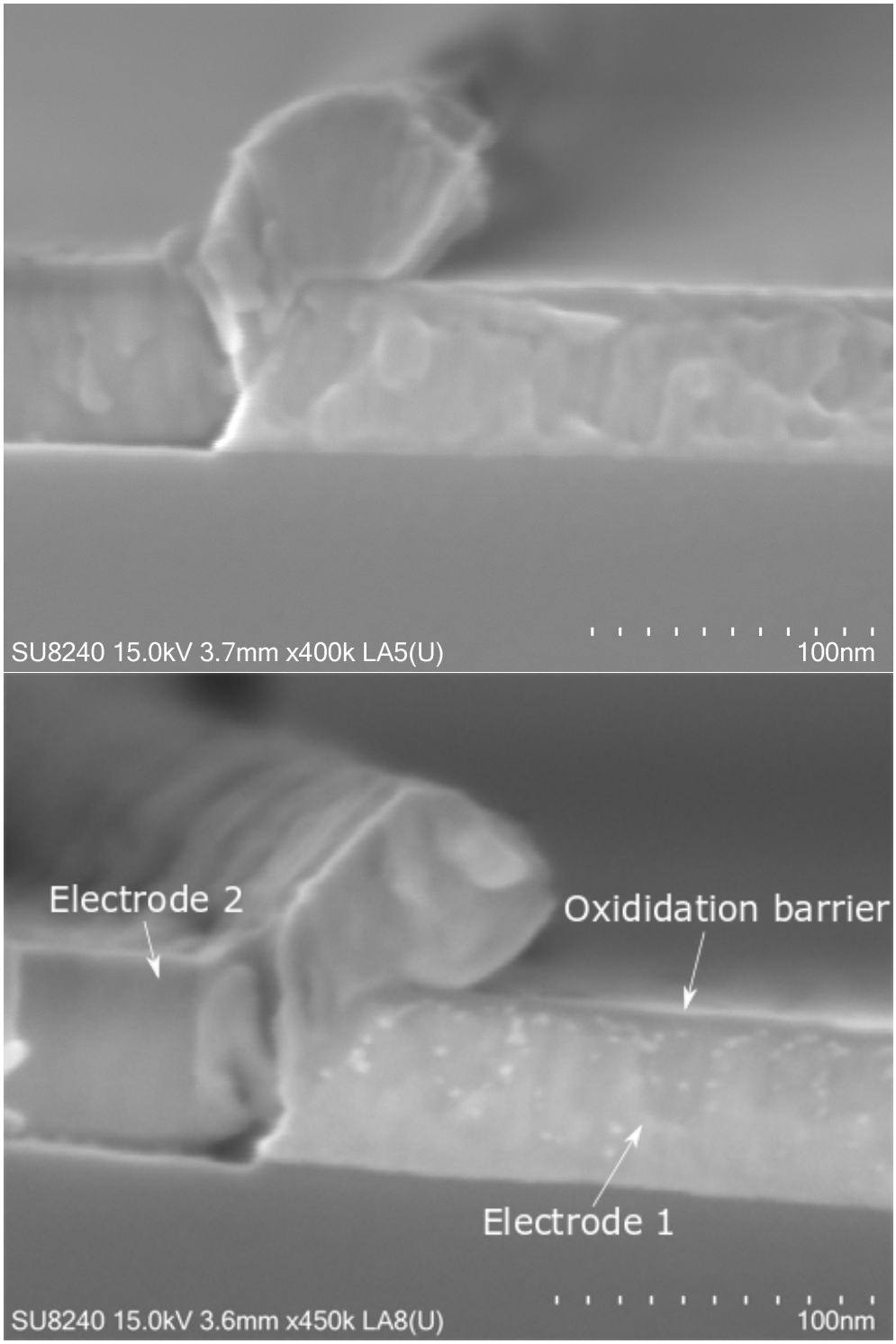


Figure 8.30: SEM image of single junctions. Top image control junction with no grown oxidation. The bottom image shows a slight contrast with a thickness of 3-5 nm atop the first electrode (RHS). This is believed to be the oxide layer after the electrode is subjected to 300 °C temperature for 2 hours.

It is known that oxidation thickness follows parabolic growth with time (parabolic rate law), and exponential growth with temperature (Arrhenius equation). There-

fore, low temperatures and longer oxidation times are favourable to control the oxide thickness precisely. Conversely, oxidation at higher temperatures results in scale-like oxide growth as seen in Figure 8.31 through 8.36 which distorts the definition of the sidewall edge and is therefore not a favourable oxidation process. To avoid this scale formation, oxidation must be kept below 400 °C. Due to the potential of metal contamination of oxidation furnaces within the JWNC, the oxidation bake (step 15 in Table 8.2) was carried out in either an ambient oven for low (below 300 °C) and slow oxidation growth. Higher temperatures were achieved by carrying out oxidation in a rapid thermal annealer (RTA) tool filled with ambient air. However, this tool has an operation time limit, allowing only quick bakes (less than 10 min) to be carried out.

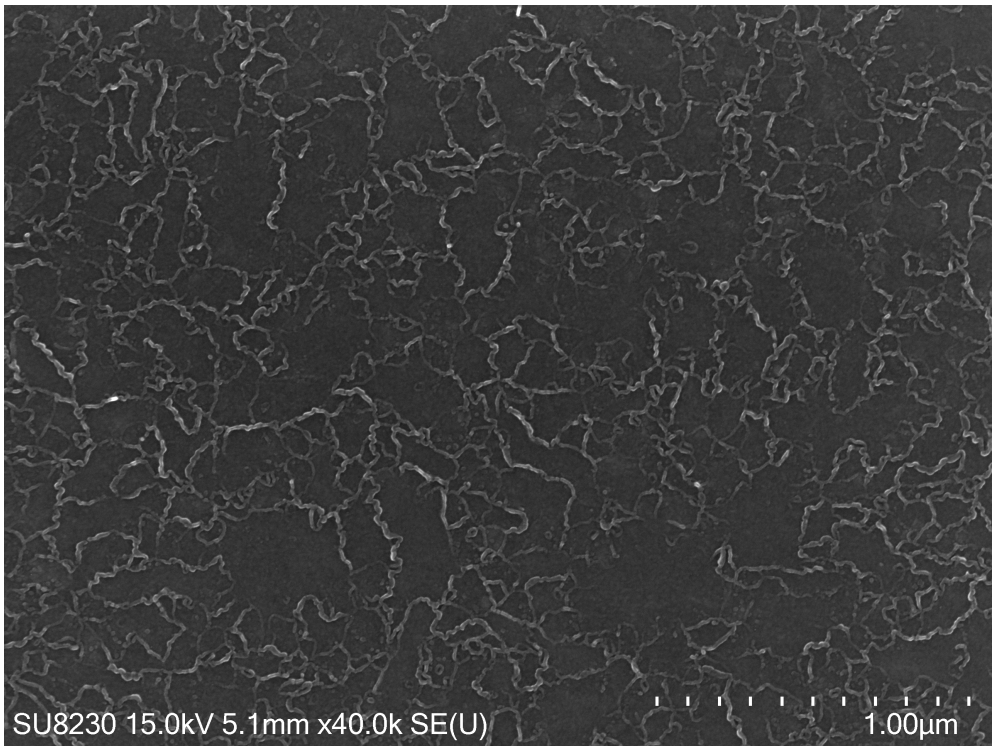


Figure 8.31: SEM image of 500 °C, 10 minute oxidation of NiCr surface. Scale-like growth can be seen on the metal surface, similar to studies by Phuong et al. [216]

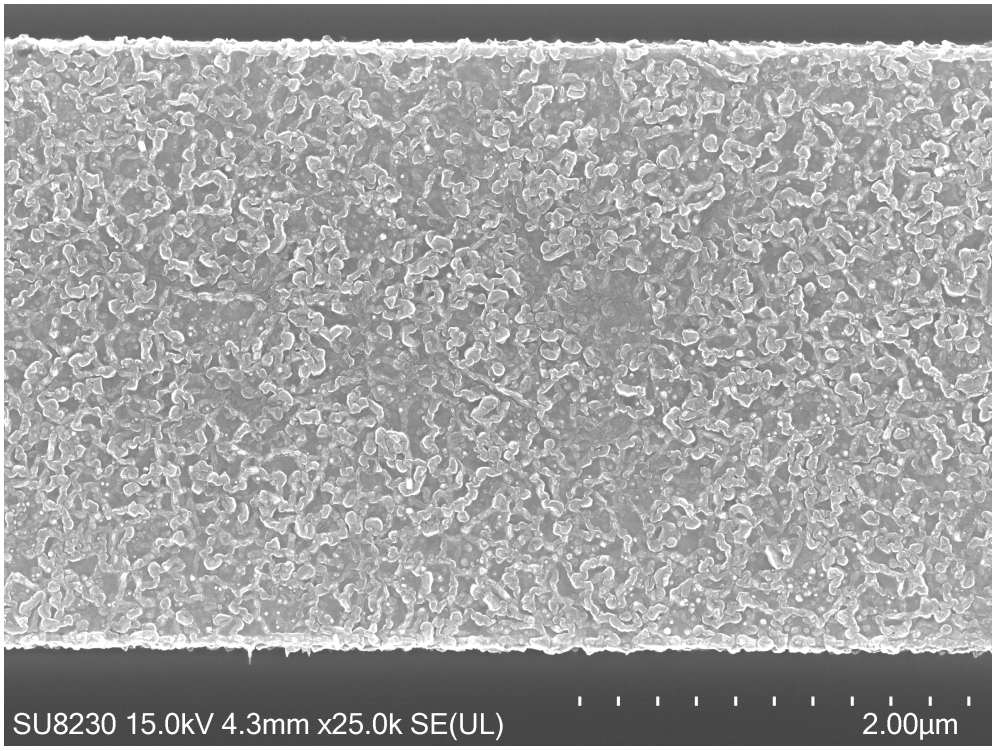


Figure 8.32: SEM image of 700 °C, 10 minute oxidation of NiCr surface. Scale-like growth can be seen on the metal surface, similar to studies by Phuong et al. [216]

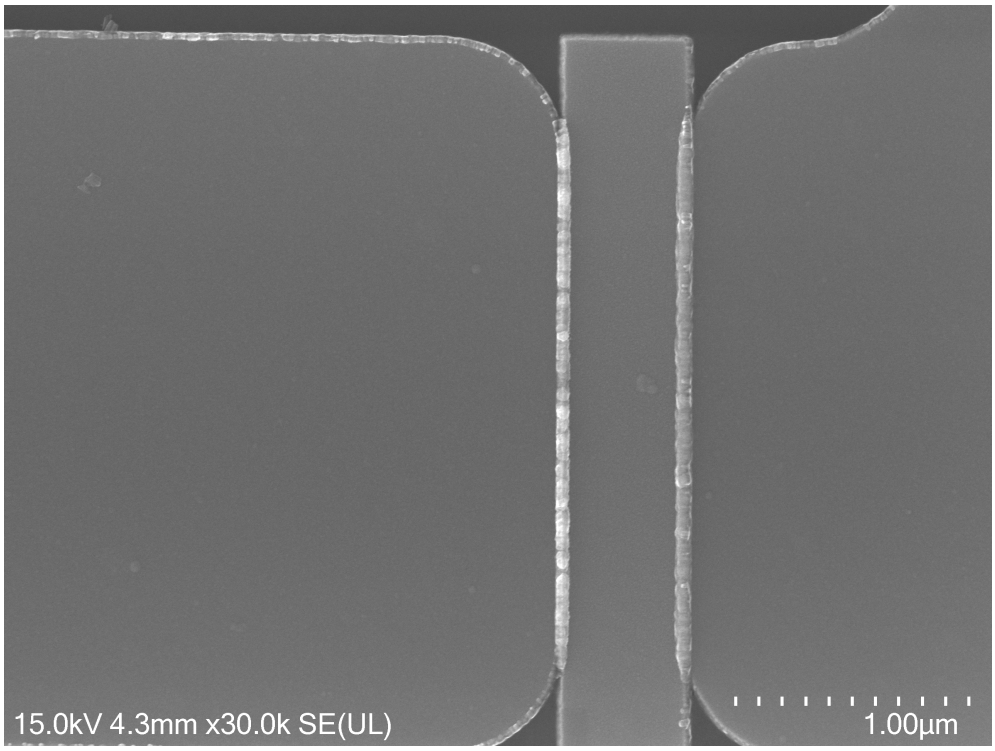


Figure 8.33: SEM SE image of 400 °C, 10 minute oxidation NiCr. LHS/RHS are oxidised electrodes and the centre island show non-oxidised electrode. No scale growth is visible in the SEM image

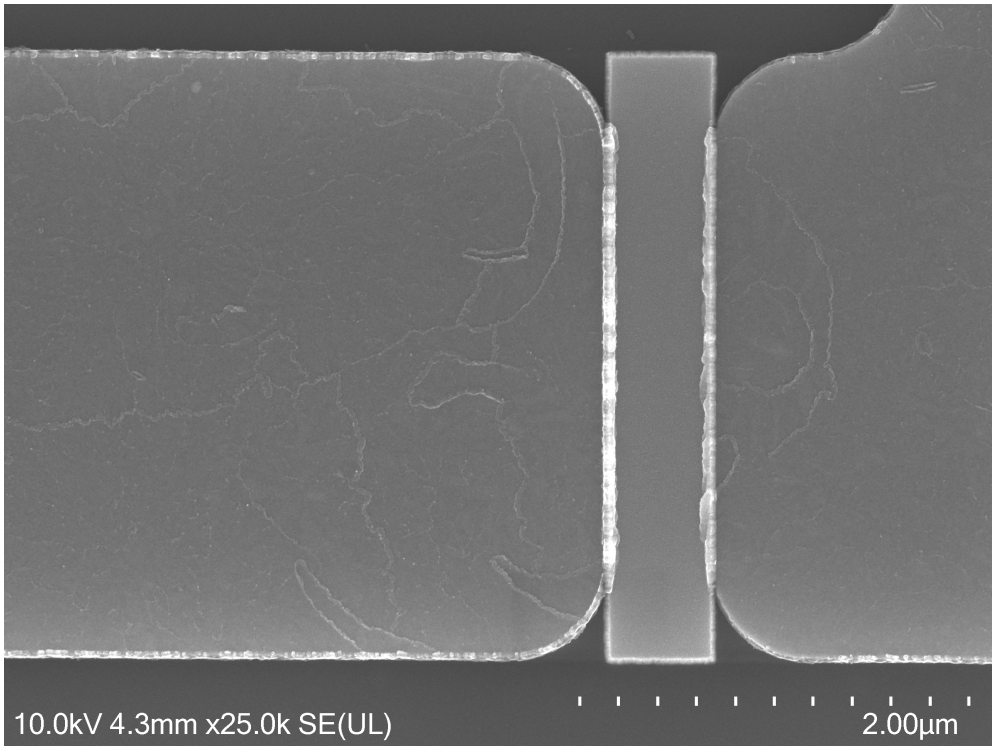


Figure 8.34: SEM SE image of 480 °C, 10 minute oxidation NiCr. LHS/RHS are oxidised electrodes and the centre island show non-oxidised electrode. Slight scale growth is visible in the SEM image

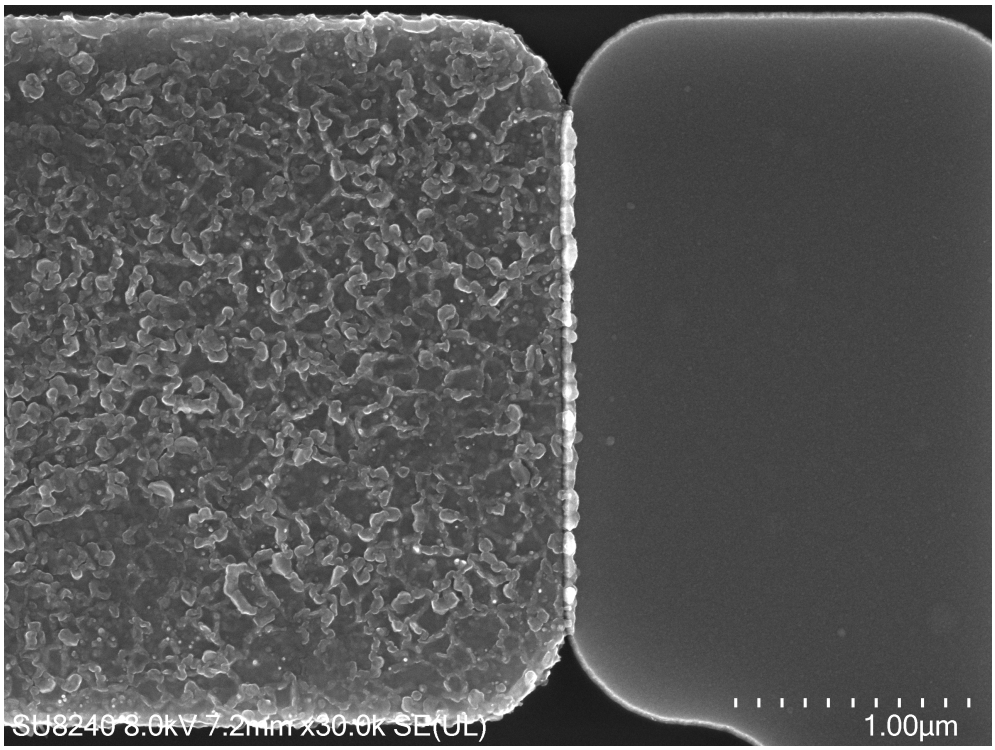


Figure 8.35: SEM SE image of 600 °C, 10 minute oxidation NiCr. LHS are oxidised electrodes and RHS show non-oxidised second electrode

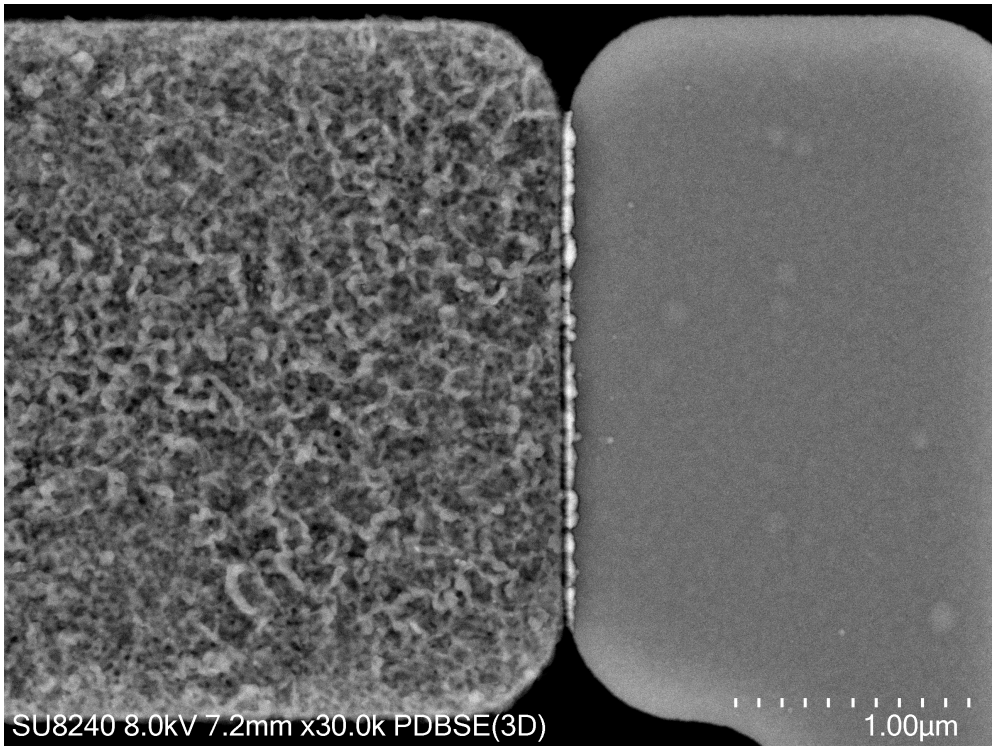


Figure 8.36: SEM BSE image of 600 °C, 10 minute oxidation NiCr. LHS are oxidised electrodes and RHS show non-oxidised second electrode

8.4.3 Electrical measurement

As with the nanoisland junctions, current-voltage (IV) curves of the junctions were taken. A batch of single junction devices was created, varying the oxidation layer growth temperature, while maintaining an oxidation time of 15 minutes for the 1st electrode. IV curves of the single junction devices are visible in Figure 8.37 through 8.40. The tunnelling parameters can be estimated by least squares fitting to the Simmons tunnelling model and provides extraction of the barrier height (Ø) and barrier thickness (S).

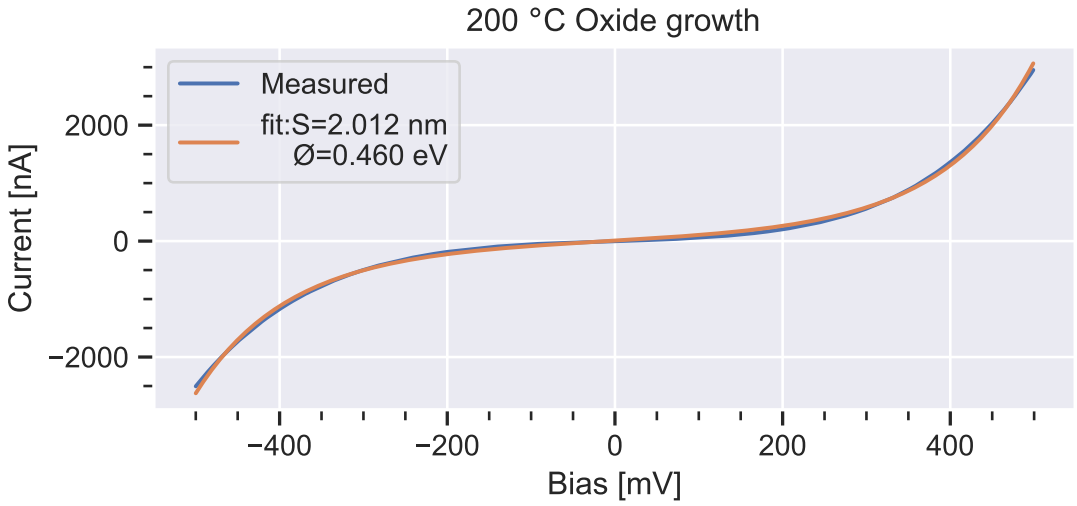


Figure 8.37: IV curve of 200 °C, 15 minute oxidation junction.

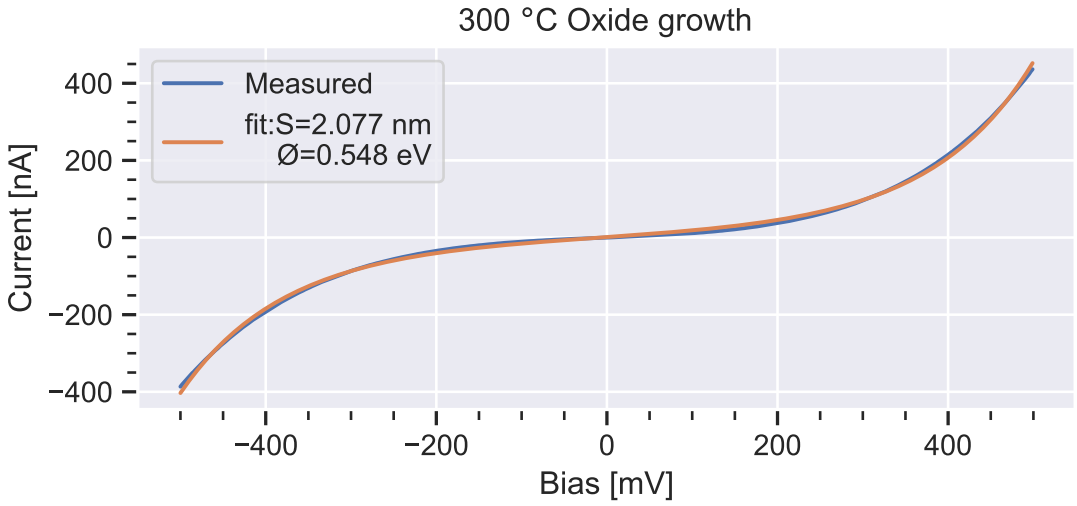


Figure 8.38: IV curve of 300 °C, 15 minute oxidation junction.

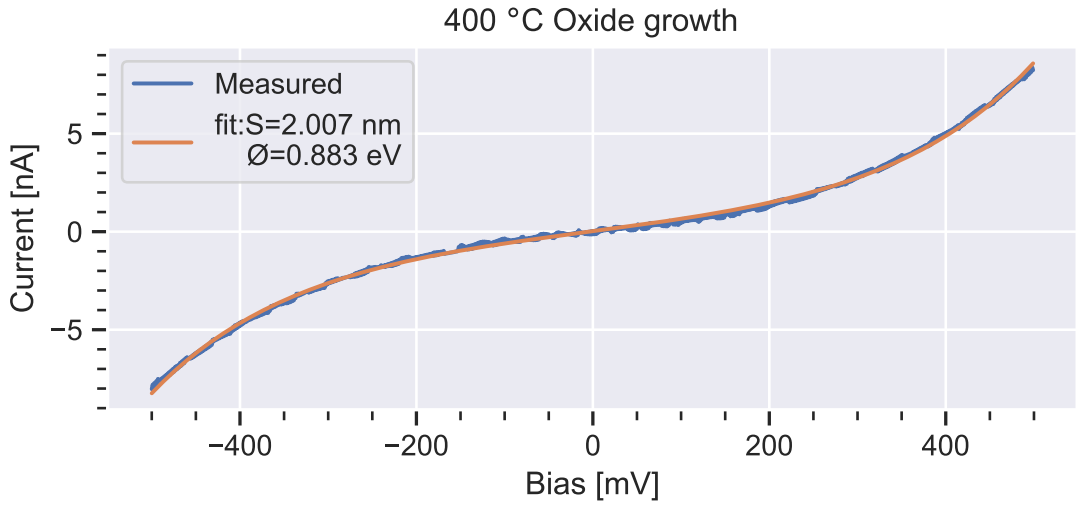


Figure 8.39: IV curve of 400 °C, 15 minute oxidation junction.

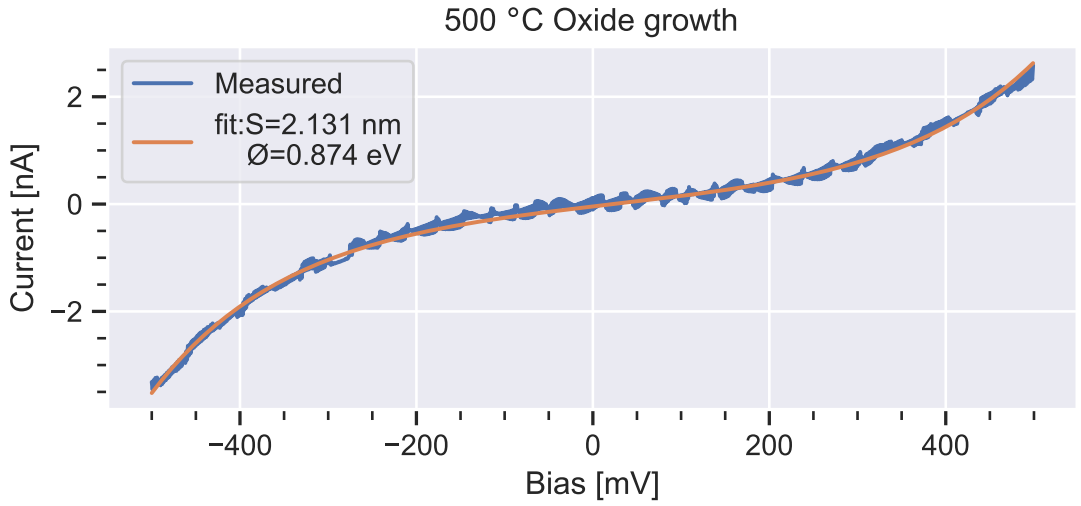


Figure 8.40: IV curve of 500 °C, 15 minute oxidation junction.

From the non-linear relationship of the IV curves in Figure 8.37 through 8.40 and their fits to the Simmons model, it can be seen that electron tunnelling is the primary form of electron transport between the electrodes. Noise in the measurement system is visible for lower current measurements and was difficult to track down, it is assumed that the noise is present from within the SMU itself. Higher oxidation temperatures (400 °C -Figure 8.39 and 500 °C - Figure 8.40) show a large jump in the fitted barrier height. This is consistent with the second oxidation phase visible in the previous SEM images.

Repeatability in the creation of these junctions is also questionable, although the alignment of electrodes has been shown to be within sub-nanometer repeatability in chapter 7, voids between the junctions are present as previously seen in Figure 8.30 on page 320. To test the on-chip repeatability of the device, 11 x two junction devices were created on the same sample, with the oxidation film grown at 250 °C for 1 gour. A table of fitted parameters can be seen in Table 8.3.

Table 8.3: Tabulated results of junction repeatability

Device No.	Barrier fit	
	Width [nm]	Height [eV]
1	1.609	1.301
2	1.621	1.303
3	1.613	1.286
4	Open circuit	
5	1.608	1.347
6	1.632	1.345
7	1.615	1.361
8	Open circuit	
9	1.626	1.337
10	1.666	1.347
11	1.632	1.344

Table 8.3 shows a barrier thickness of 1.625 ± 0.017 nm (mean + σ) and barrier height of 1.30 ± 0.025 eV.

An important factor of any junctions created is that they must survive a silicon release etch. As such, junctions were created at 200 °C with oxidation times of 15 minutes and an hour, before being etched in a silicon micro-machining kit for 45 minutes in 105 °C KOH. Unfortunately, the majority of devices oxidised for 15 minutes failed to show tunnelling characteristics post-silicon etching and yield was low. Devices oxidised for an hour showed better yield in the experiment, a SEM image of a released cantilever beam with a two junction sensor at the base is visible in Figure 8.41. The same junction was measured pre-etching and post-etching, with results for the 15-minute oxidation seen in Figure 8.42 and 8.43 (pre/post etch respectively), and the 1-hour oxidation in Figure 8.44 and 8.45.

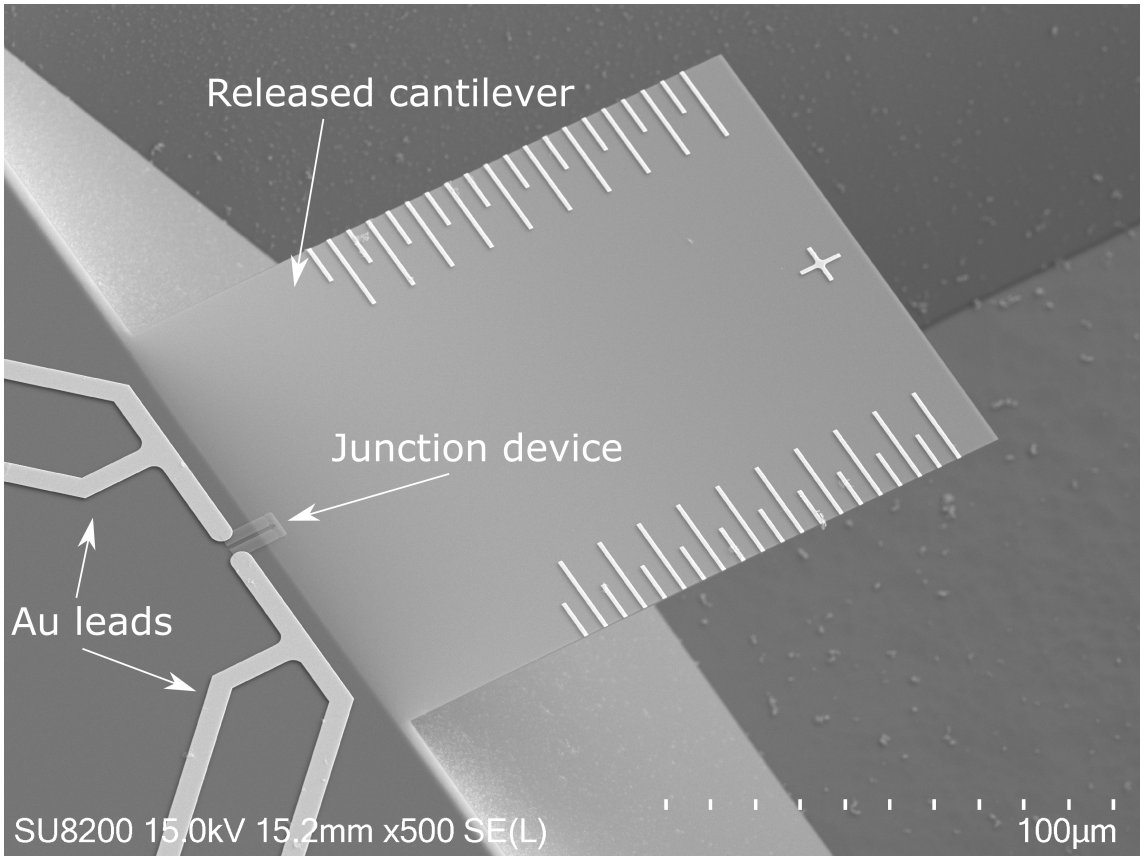


Figure 8.41: Two junction device patterned on a cantilever, and wet-etch released

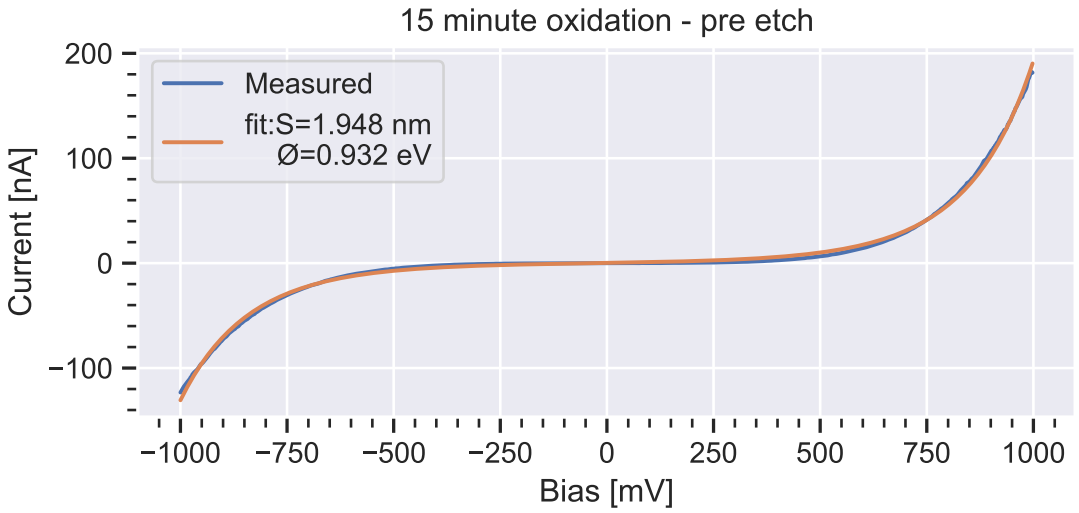


Figure 8.42: 200 °C, 15 minute oxidation, pre-etch measurement

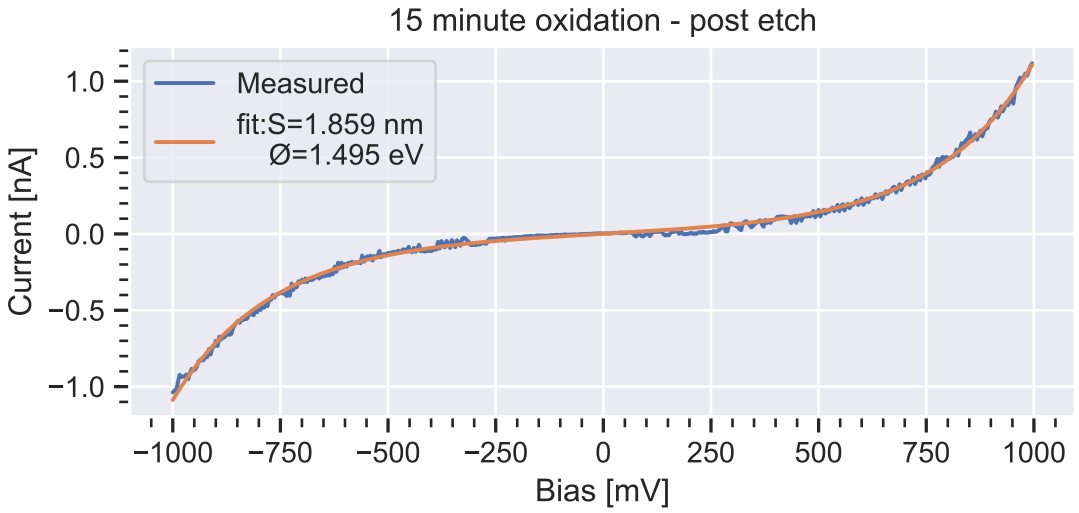


Figure 8.43: 200 °C, 15 minute oxidation, post-etch measurement

As can be observed for the post-etch 15-minute oxidation measurement (Figure 8.43), there is a large increase in the measured barrier height and shows a very small current flow across the junction. A slight asymmetry can be seen between the forward and backward biasing of the electrodes, particularly in Figure 8.42 this is consistent with each electrode having a differing work function. Most likely arising from the annealing of the electrode during oxidation growth.

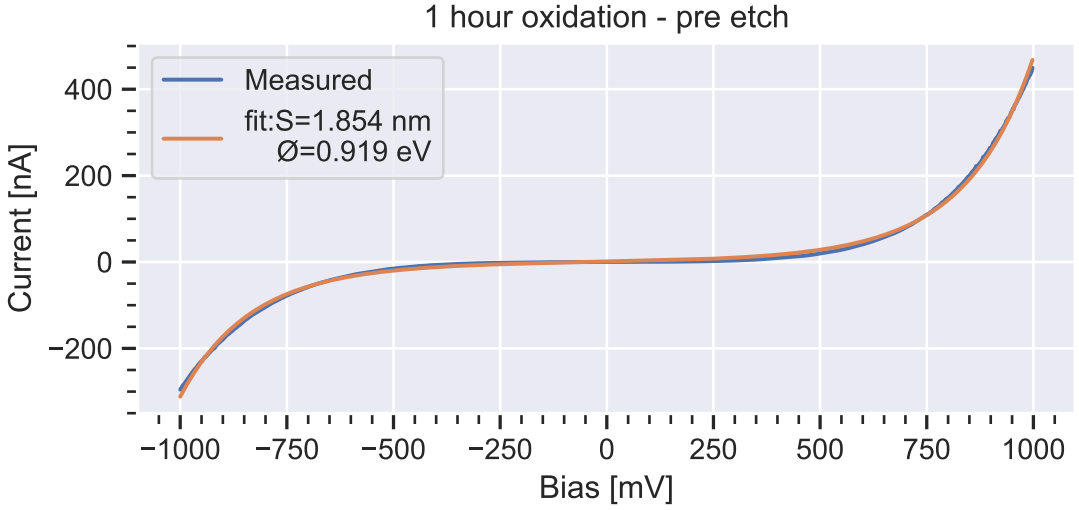


Figure 8.44: 200 °C, 1 hour oxidation, pre-etch measurement

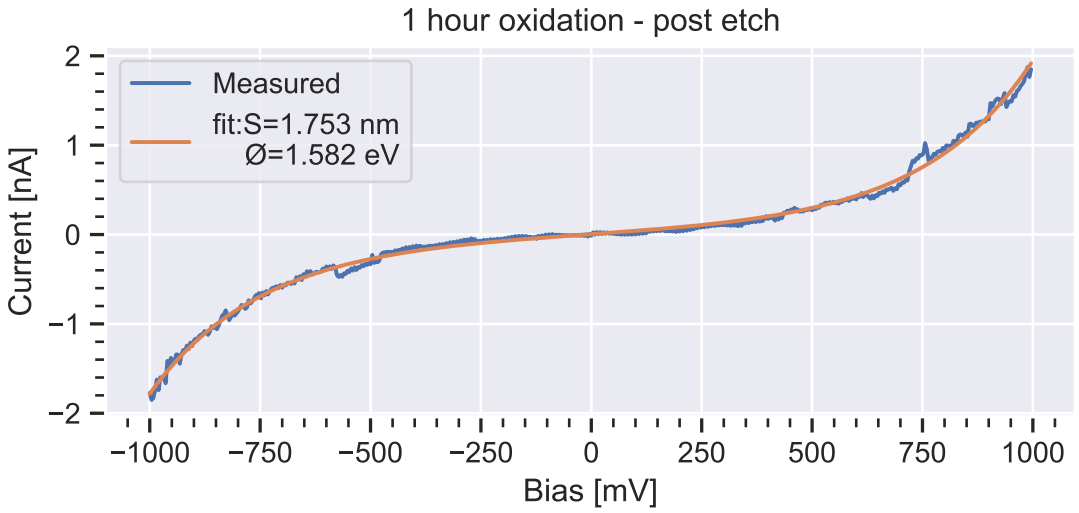


Figure 8.45: 200 °C, 1 hour oxidation, post-etch measurement

The 1-hour oxidised junctions had a larger yield than the 15-minute oxidation junctions. From Figure 8.44 and 8.45, there is a similar increase in the barrier height, with a similar corresponding 100-fold decrease in current flow. It is possible that during the etch, the Cr_2O_3 reacts with the KOH to produce K_2CrO_2, altering the barrier. Although these devices still tunnel post-etch, the conductance between the electrodes has vastly reduced, making accurate measurement difficult.

8.5 Discussion

In this chapter, two strain sensing elements have been explored for their potential application in SThM cantilever deflection sensing. The sensor type based on electron transport through nanoislands proved difficult to measure in this work. Although nanoisland deposition with gaps comparable to tunnelling distances was successful between a set of electrodes, the reason for their failure was most likely due to electrostatic discharge across the small gaps during measurement, but the root cause of this issue was never found in this work.

Ramp-style MIM junctions have also been investigated. As part of this, oxide studies of 60/40 NiCr have been conducted. Utilising high overlay accurate lithography developed in chapter 7, electrodes were successfully placed on the metal edge of one another. Tunnelling parameters of the fabricated junctions have been extracted, but gaining consistency in the obtained results proved difficult, showing a low yield of devices, this is believed to be from voids under the deposited junctions from residual

PMMA. After a release etch, significant alterations to the junctions' tunnelling parameters were observed. This vastly reduced the conductance of the devices, making for very low tunnelling currents for modest voltages across the junctions. Combining this observed reduction in conductance with the need for multiple junctions in series to gain sensitivity made their continued development for integration on the SThM cantilever unfeasible.

Final remarks

9.1 Conclusions

Although well established, low cost and highly effective in the field of AFM, the use of the optical lever laser presents many issues in the repeatability and precision of topographic and thermal measurement through SThM that are rarely acknowledged in the literature. This work has explored avenues of maintaining topographic control of the SThM without the use of the optical lever mechanism. Two approaches have been investigated. Firstly, the utilisation of existing thermal signals as a means of topographic feedback control, and secondly, the incorporation of strain-sensing elements onto the cantilever body.

The first approach takes inspiration from the scanning thermal profiler developed by Williams and Wickramasinghe [67]. Using community-adopted KNT-SThM probes, the existing thermal signal can be used to determine the probe's location in space, such as that of the original STP. Through analysing the change in thermal signals upon tip-sample contact during a probe approach and raster scanning approaches, one can infer the topography of a sample surface to a high precision. The vertical resolution has been shown to be less than 5nm in this work, and it is assumed that this is predominantly limited by the stage used and thermal actuation of the probe. One should note the lack of force measurement when using this technique, as only the point of contact upon an approach is known. However, if using an appropriately accurate stage, and a probe with an accurately known spring constant (e.g. calibrated using techniques described by Avilovas [39]), one can infer the tip-sample force induced by displacing the probe a known distance past the initial contact. With such considerations in the current setup, the errors in topography result in tip-sample forces of around 1-2nN, which fall within those generated by

other AFM imaging techniques such as Tapping mode.

The results presented in chapter 5 demonstrate that this approach is able to handle topographic, material and temperature variability well, with results presented in chapter 6 demonstrating that it can handle changes in scanning environment with little modification to the control loops. However, in situations where the cantilever temperature varies during the scan thermal bend of the probe is still an issue as this causes the 'assumed zero' position of the tip to move in relation to the base of the cantilever. The results presented in section 5.5 suggest that thermal bending does not significantly disrupt the function of the new scanning approach presented in this thesis, however, it is important to be aware of their potential impact. Such thermal bend artefacts are already present in optical lever SThM but can be addressed by modifications to the probe design as set out by Mordue [7].

Focusing on the wider instrumentation developed during this work, the thermal feedback control principles are entirely compatible with any AFM that gives access to the appropriate signals and allows for control of the stage with the laser deactivated. However, due to the probe bandwidth, probe approaches are generally quite slow, causing long scanning times that may show drift artefacts in the acquired scans. It is assumed that much of this drift is associated with thermal expansion of the stage and hardware used to hold the probe during a scan. This could be addressed by employing an improved stage, employing low-expansion materials or by increasing the scan speed. Although this technique had been developed on current-generation KNT-SThM probes, its use opens up opportunities for manufacturing modifications to optimise for thermal design of the probe to improve this bandwidth and speed up imaging, as designing a cantilever for compatibility with an optical lever force system can be disregarded as laser access to the cantilever is no longer required. Having said this, such probe modifications face the same barriers to wide adoption as seen in chapter 8.

When modifying any AFM system, it's important to remember that community-wide adoption of any new type of AFM probe requires access to reproducible and appropriately priced probes. As semiconductor processes and tools are generally quite expensive, batch fabrication of many probes on a wafer allows for a vast reduction in the cost of manufacture per probe, thus reducing the end-user price of a singular probe. However, yield is a significant consideration when designing probes as defects increase the price per probe and can increase the variability between probes. This helps explain that, whilst self-sensing SThM probes have been explored in the literature, such probes and techniques are not generally available commercially.

KNT-SThM probes are well established in the community and available commercially through many distributors. During manufacture, they have the advantage of being lithographically patterning via EBL, providing a lot of flexibility. This offers the possibility to integrate self-sensing into current probe designs, within the limitations of material/process compatibility with the SThM fabrication process, in particular the requirement of a wet release etch in TMAH. As such, tunnel junction strain sensors were fabricated using standard SThM batch fabrication-compatible materials and processes. The integration of such sensors would vastly improve the imaging speed compared to the'thermal feedback' techniques desribed previously as well as allow for accurate measurment of tip-sample forces. Although chapter 8 demonstrated that the technology is feasible, their development in this work shows nothing more than a proof of principle as very high manufacturing tolerances are required. The low consistency in the results from devices fabricated in this work shows that batch fabrication of these sensors would result in a low yield of highly variable probes. This would make such probes very expensive, hindering community adoption. These yield problems could undoubtedly be reduced through systematic process development and optimisation, but it was felt this was more of a commercial endeavour.

9.2 Further work

From the conclusions of this thesis, there are many avenues for further exploration of the work that could be carried out. New probe designs featuring extremely soft and narrow cantilevers could provide for a reduction in the cantilever-sample thermal coupling, improved access to etch trenches, as well as a possible reduction in topographic artefacts arising from the large probe opening angle in current generation KNT probes. An interesting avenue for further exploration follows on from the work carried out in section 5.7, relating to changing the probe angle relative to the sample surface. As laser access to the probe is no longer required, this opens up the possibility of designing cantilevers on a flat wafer (i.e not patterned on a pyramid), and angling the whole probe body toward the sample rather than creating an angled tip. This would enormously simplify the probe microfabrication process, vastly improving yield, decreasing cross-wafer variability, and ultimately, significantly reducing the cost of manufacture making this probe type more accessible. If cantilevers were designed on a flat surface, dry etching can also be used to release cantilevers which would greatly relax the current material and process requirements.

One could also potentially use the improved Penrose alignment developed in this

work to accurately position very small and isolated tip resistors, this would decrease the thermal response time of the probe and increase the sensitivity of measurements as shown by Lambert [63]. Improvements to the feedback electronics to increase the clock rate of the DDS, along with bandwidth improvements to the probe design, could allow for faster probe biasing at higher frequencies. This would enable faster thermal approaches, increasing the pixel capture rate of the control loops, and making the adoption of the technique more viable for the SThM community.

In relation to the fabrication of integrated strain sensors in chapter 8, if the MIM ramp-style junctions could have a passivisation layer deposited over the whole sensor region, the effects of the release etch could potentially be reduced. Again, experimentation with differing resists may provide a better line edge roughness of the first electrode, improving the consistency of the obtained results. Utilising a different resist structure for the second electrode layer may lead to better resist clearing from the ramp edge, again, improving the electrode overlap consistency.

Thermal feedback control flows

The following appendix provides the reader with graphical representations of the control loop through flow diagrams for the topographic control of the SThM, as described in chapter 4.

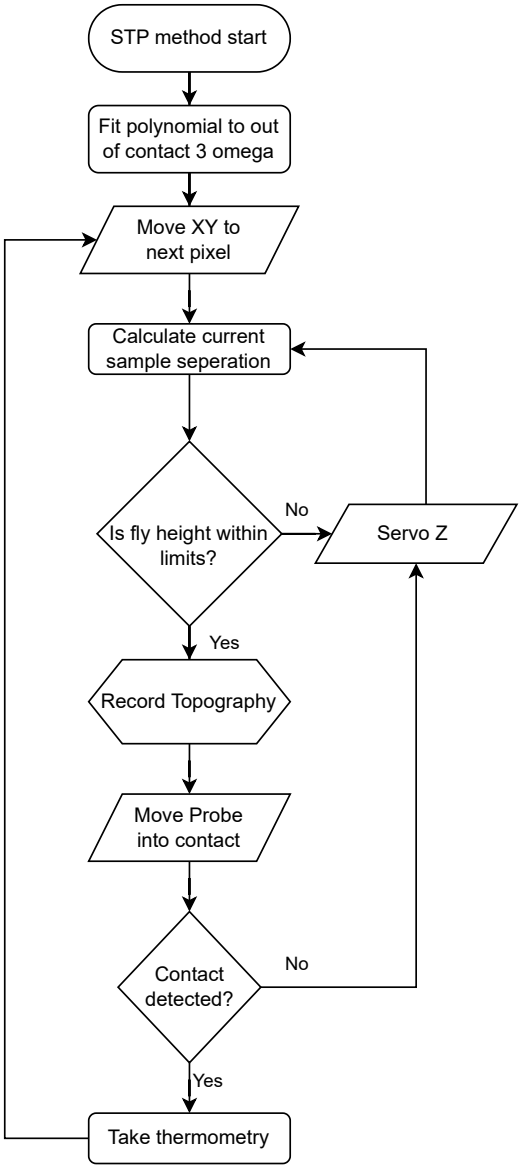


Figure A.1: STP acquisition method

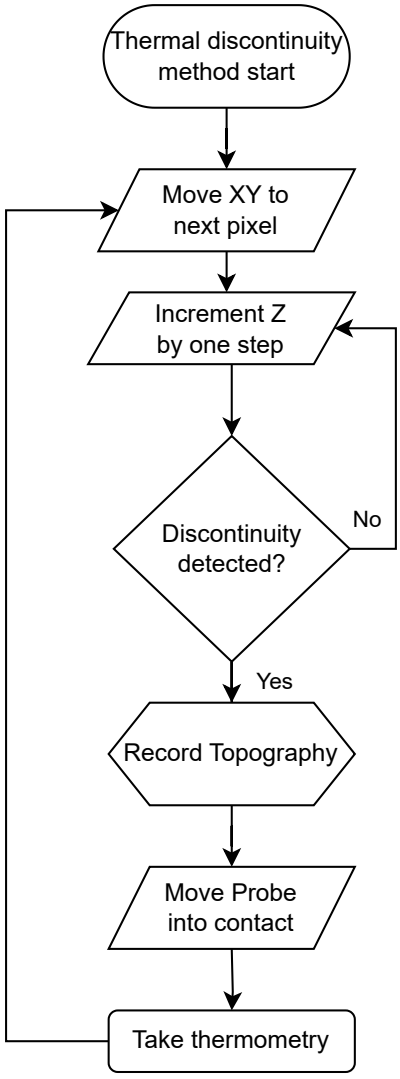


Figure A.2: Thermal discontinuity acquisition method

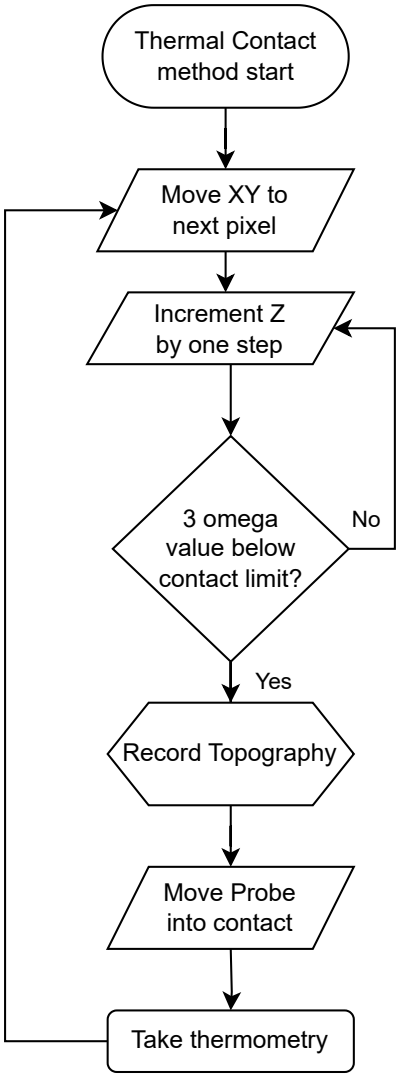


Figure A.3: Contact limit acquisition method

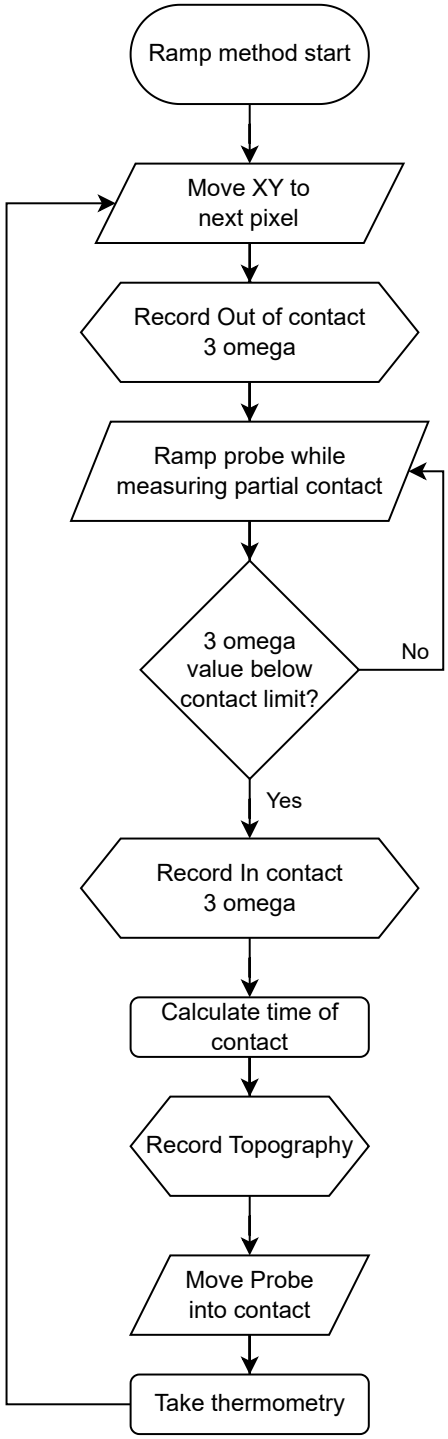


Figure A.4: Ramp through contact acquisition method

List of References

[1] G. Meyer and N. M. Amer, 'Novel optical approach to atomic force microscopy', *Applied Physics Letters*, vol. 53, no. 12, pp. 1045–1047, Sep. 1988. DOI: 10.1063/1.100061.

[2] L. Ramiandrisoa, A. Allard, B. Hay and S. Gomés, 'Uncertainty assessment for measurements performed in the determination of thermal conductivity by scanning thermal microscopy', *Measurement Science and Technology*, vol. 28, no. 11, Oct. 2017. DOI: 10.1088/1361-6501/aa8892.

[3] J. Spiece, C. Evangeli, K. Lulla, A. Robson, B. Robinson and O. Kolosov, 'Improving accuracy of nanothermal measurements via spatially distributed scanning thermal microscope probes', *Journal of Applied Physics*, vol. 124, no. 1, Jul. 2018. DOI: 10.1063/1.5031085.

[4] J. Spièce, 'Quantitative mapping of nanothermal transport via Scanning Thermal Microscopy', Ph.D. dissertation, Lancaster university, Lancaster, Sep. 2018.

[5] F. A. Sandoval, M. Geitner, É. Bertin and L. Bellon, 'Resonance frequency shift of strongly heated micro-cantilevers', *Journal of Applied Physics*, vol. 117, no. 23, Jun. 2015. DOI: 10.1063/1.4922785.

[6] C. W. Mordue, J. M. Weaver and P. S. Dobson, 'Thermal induced deflection in atomic force microscopy cantilevers: analysis & solution', *Measurement Science and Technology*, vol. 34, no. 12, Dec. 2023. DOI: 10.1088/1361-6501/acf061.

[7] C. Mordue, 'Modelling, Quantifying and Attenuating Multi-Material Thermal Bend in Atomic Force Microscopy Cantilevers', Ph.D. dissertation, University of Glasgow, Glasgow, 2022.

[8] M. W. Davidson, 'Ernst Abbe', *Laboratory Medicine*, vol. 40, no. 8, pp. 502–503, Aug. 2009. DOI: 10.1309/lm6yl3shmck6dusm.

[9] E. Abbe, 'On the Theory of the microscope', *Bristol Microscopical society*, Dec. 1874.

[10] M. Jobin and R. Foschia, 'High resolution in interferometric microscopy', in *EMC 2008 14th European Microscopy Congress 1–5 September 2008*, Berlin, Heidelberg: Springer Berlin Heidelberg, 2008, pp. 745–746. DOI: 10.1007/978-3-540-85156-1{_}373.

[11] T. Palucka, *Electron microscopy*, Jan. 2002. [Online]. Available: https://authors.library.caltech.edu/5456/1/hrst.mit.edu/hrs/materials/public/ElecMicr.htm.

[12] M. von Ardenne, 'Das Elektronen-Rastermikroskop. Theoretische Grundlagen', *Zeitschrift für Physik*, vol. 109, pp. 553–572, 1938.

[13] D. H. Shin, E. J. Kirkland and J. Silcox, 'Annular dark field electron microscope images with better than 2 Å resolution at 100 kV', *Applied Physics Letters*, vol. 55, no. 23, pp. 2456–2458, 1989. DOI: 10.1063/1.102297.

[14] M. Tosa, 'Surface Profilometer', in *Compendium of Surface and Interface Analysi*, Springer Singapore, 2018, pp. 679–682. DOI: 10.1007/978-981-10-6156-1{_}110.

[15] G. Binnig and H. Rohrer, 'Scanning Tunneling Microscopy', *Surface Science*, vol. 126, 1983.

[16] MicroscopeMaster, *The Scanning Tunneling Microscope (STM) - The Advantages of Atomic Resolution*, Jan. 2021. [Online]. Available: https://www.microscopemaster.com/scanning-tunneling-microscope.html.

[17] J. Vicary, *A pedant's (Christmas) guide to AFM probe terminology*, Dec. 2016. [Online]. Available: https://www.nunano.com/blog/2016/12/12/a-pedants-christmas-guide-to-afm-probe-terminology.

[18] T. O. Stadelmann, 'Antidot Superlattices in InAs–GaSb Double Heterostructures:Transport Studies', Ph.D. dissertation, 2006, p. 26.

[19] G. Binnig, C. F. Quate and C. Gerber, 'Atomic Force Microscope', *Physical Review Letters*, vol. 56, no. 9, pp. 930–934, 1986.

[20] P. Eaton and P. West, *Atomic Force Microscopy*. Oxford University Press, 2010, pp. 135–137.

[21] M. Dukic, J. D. Adams and G. E. Fantner, 'Piezoresistive AFM cantilevers surpassing standard optical beam deflection in low noise topography imaging', *Scientific Reports*, vol. 5, Nov. 2015. DOI: 10.1038/srep16393.

[22] P. C. Braga and D. Ricci, *Atomic Force Microscopy Biomedical Methods and Applications*. NJ: Humana Totowa, 2004.

[23] M. Vollmer and K.-P. Möllmann, 'Fundamentals of Infrared Thermal Imaging', in *Infrared Thermal Imaging*, John Wiley & Sons, Ltd, 2017, ch. 1, pp. 1–106. DOI: https://doi.org/10.1002/9783527693306.ch1. [Online]. Available: https://onlinelibrary.wiley.com/doi/abs/10.1002/9783527693306.ch1.

[24] M. Planck, *The theory of heat radiation*. Philadelphia: P. Blakiston's Son & Co, 1914.

[25] C. D. Brites et al., 'Thermometry at the nanoscale', *Nanoscale*, vol. 4, no. 16, pp. 4799–4829, Aug. 2012. DOI: 10.1039/c2nr30663h.

[26] M. Farzaneh et al., 'CCD-based thermoreflectance microscopy: Principles and applications', *Journal of Physics D: Applied Physics*, vol. 42, no. 14, 2009. DOI: 10.1088/0022-3727/42/14/143001.

[27] D. Lüerßen, J. A. Hudgings, P. M. Mayer and R. J. Ram, 'Nanoscale Thermoreflectance With 10mK Temperature Resolution Using Stochastic Resonance', in *Semiconductor Thermal Measurement and Management IEEE Twenty First Annual IEEE Symposium*, 2005.

[28] R. B. Wilson, B. A. Apgar, L. W. Martin and D. G. Cahill, 'Thermoreflectance of metal transducers for optical pump-probe studies of thermal properties', *Optics Express*, vol. 20, no. 27, pp. 28 829–28 838, 2012.

[29] Yu Peter Y and M. Cardona, 'Optical Properties II', in *Fundamentals of Semiconductors: Physics and Materials Properties*, Berlin, Heidelberg: Springer Berlin Heidelberg, 2010, pp. 345–426. DOI: 10.1007/978-3-642-00710-1{_}7. [Online]. Available: https://doi.org/10.1007/978-3-642-00710-1_7.

[30] P. W. Epperlein, G. L. Bona and P. Roentgen, 'Local mirror temperatures of red-emitting (Al)GaInP quantum-well laser diodes by Raman scattering and reflectance modulation measurements', *Applied Physics Letters*, vol. 60, no. 6, pp. 680–682, 1992. DOI: 10.1063/1.106563.

[31] M. Ziegler, 'Thermography of Semiconductor Lasers: From Thermal Emission of Semiconductors towards a Novel Analytical Tool for Optoelectronic Devices', Ph.D. dissertation, Humboldt-Universität zu Berlin, Berlin, 2009.

[32] H. Brugger and P. W. Epperlein, 'Mapping of local temperatures on mirrors of GaAs/AlGaAs laser diodes', *Applied Physics Letters*, vol. 56, no. 11, pp. 1049–1051, 1990. DOI: 10.1063/1.102611.

[33] P. J. Hesketh, *BioNanoFluidic MEMS*. Springer, 2008, p. 295.

[34] H. J. Goldsmid, *Introduction to Thermoelectricity*. Berlin, Heidelberg: Springer Berlin Heidelberg, 2016, vol. 121. DOI: 10.1007/978-3-662-49256-7.

[35] J. P. Moore and R. S. Graves, 'Absolute Seebeck coefficient of platinum from 80 to 340 K and the thermal and electrical conductivities of lead from 80 to 400 K', *Journal of Applied Physics*, vol. 44, no. 3, pp. 1174–1178, Mar. 1973. DOI: 10.1063/1.1662324.

[36] J. Priest, 'Temperature and Its Measurement', in *Encyclopedia of Energy*, Elsevier, 2004, pp. 45–54. DOI: 10.1016/B0-12-176480-X/00082-6.

[37] J. Vlcko, 'Thermocouple', in *Encyclopedia of Engineering Geology*, Springer, 2018, pp. 1–2. DOI: 10.1007/978-3-319-12127-7{_}283-1.

[38] Z. Dashevsky, D. Rabinovich, G. Fish, S. Kokolova and A. Lewis, 'Ultrafast response and high sensitivity semiconductor thermocouple', in *Fifteenth International Conference on Thermoelectrics. Proceedings ICT '96*, IEEE, 1996, pp. 321–325. DOI: 10.1109/ICT.1996.553500.

[39] L. Avilovas, 'Micro Electro-Mechanical System Design, Fabrication and Application for Atomic Force Microscopy Probe Elasticity Characterisation', Ph.D. dissertation, University of Glasgow, Glasgow, 2021.

[40] H. Yan and H. Wu, 'Joule Heating and Chip Materials', in *Encyclopedia of Microfluidics and Nanofluidics*, Boston, MA: Springer US, 2008, pp. 886–896. DOI: 10.1007/978-0-387-48998-8{_}758.

[41] D. G. Cahill, 'Thermal conductivity measurement from 30 to 750 K: The 3ω method', *Review of Scientific Instruments*, vol. 61, no. 2, pp. 802–808, 1990. DOI: 10.1063/1.1141498.

[42] D. G. Cahill and R. O. Pohl, 'Thermal conductivity of amorphous solids above the plateau', *Physical Review B*, vol. 35, no. 8, pp. 4067–4073, 1987. DOI: 10.1103/PhysRevB.35.4067.

[43] G. Pernot, A. Metjari, H. Chaynes, M. Weber, M. Isaiev and D. Lacroix, 'Frequency domain analysis of 3ω-scanning thermal microscope probe-Application to tip/surface thermal interface measurements in vacuum environment', *Journal of Applied Physics*, vol. 129, no. 5, Feb. 2021. DOI: 10.1063/5.0020975.

[44] J. Bendtsen, J. Leth and C. Kallesoe, 'A Time-domain Approach to the 3-omega Heat Conductivity Measurement Method', in *2022 Australian and New Zealand Control Conference, ANZCC 2022*, Institute of Electrical and Electronics Engineers Inc., 2022, pp. 249–254. DOI: 10.1109/ANZCC56036.2022.9966983.

[45] M. Dalton et al., 'The 3 omega transient line method for thermal characterization of insulator materials developed for spacecraft thermal control', in *65th International Astronautical Congress*, Toronto, 2014.

[46] H. Wang and M. Sen, 'Analysis of the 3-omega method for thermal conductivity measurement', *International Journal of Heat and Mass Transfer*, vol. 52, no. 7-8, pp. 2102–2109, Mar. 2009. DOI: 10.1016/j.ijheatmasstransfer.2008.10.020.

[47] A. Bontempi, T. P. Nguyen, R. Salut, L. Thiery, D. Teyssieux and P. Vairac, 'Scanning thermal microscopy based on a quartz tuning fork and a microthermocouple in active mode (2ω method)', *Review of Scientific Instruments*, vol. 87, no. 6, Jun. 2016. DOI: 10.1063/1.4952958.

[48] S. Gomès, A. Assy and P. O. Chapuis, 'Scanning thermal microscopy: A review', *Physica Status Solidi (A) Applications and Materials Science*, vol. 212, no. 3, pp. 477–494, 2015. DOI: 10.1002/pssa.201400360.

[49] G. B. Mills, 'Scanning Thermal Microscopy Using Nanofabricated Probes', Ph.D. dissertation, University of Glasgow, Glasgow, Sep. 1999.

[50] K. Kim, J. Chung, G. Hwang, O. Kwon and J. S. Lee, 'Quantitative measurement with scanning thermal microscope by preventing the distortion due to the heat transfer through the air', *ACS Nano*, vol. 5, no. 11, pp. 8700–8709, Nov. 2011. DOI: 10.1021/nn2026325.

[51] K. Luo, Z. Shi, J. Varesi and A. Majumdar, 'Sensor nanofabrication, performance, and conduction mechanisms in scanning thermal microscopy', *Journal of Vacuum Science & Technology B: Microelectronics and Nanometer Structures Processing, Measurement, and Phenomena*, vol. 15, no. 2, pp. 349–360, Mar. 1997. DOI: 10.1116/1.589319.

[52] L. Ramiandrisoa, A. Allard, Y. Joumani, B. Hay and S. Gomés, 'A dark mode in scanning thermal microscopy', *Review of Scientific Instruments*, vol. 88, no. 12, Dec. 2017. DOI: 10.1063/1.5002096.

[53] Y. Ge, Y. Zhang, J. M. R. Weaver, H. Zhou and P. S. Dobson, 'Topography-free sample for thermal spatial response measurement of scanning thermal microscopy', *Journal of Vacuum Science & Technology B, Nanotechnology and Microelectronics: Materials, Processing, Measurement, and Phenomena*, vol. 33, no. 6, Nov. 2015. DOI: 10.1116/1.4933172.

[54] P. Tovee, M. Pumarol, D. Zeze, K. Kjoller and O. Kolosov, 'Nanoscale spatial resolution probes for scanning thermal microscopy of solid state materials', *Journal of Applied Physics*, vol. 112, no. 11, Dec. 2012. DOI: 10.1063/1.4767923.

[55] P. D. Tovee and O. V. Kolosov, 'Mapping nanoscale thermal transfer in-liquid environment - Immersion scanning thermal microscopy', *Nanotechnology*, vol. 24, no. 46, Nov. 2013. DOI: 10.1088/0957-4484/24/46/465706.

[56] A. Assy and S. Gomès, 'Heat transfer at nanoscale contacts investigated with scanning thermal microscopy', *Applied Physics Letters*, vol. 107, no. 4, Jul. 2015. DOI: 10.1063/1.4927653.

[57] J. Juszczyk, M. Wojtol and J. Bodzenta, 'DC experiments in quantitative scanning thermal microscopy', *International Journal of Thermophysics*, vol. 34, no. 4, pp. 620–628, Apr. 2013. DOI: 10.1007/s10765-013-1449-4.

[58] J. Bodzenta, M. Chirtoc and J. Juszczyk, 'Reduced thermal quadrupole heat transport modeling in harmonic and transient regime scanning thermal microscopy using nanofabricated thermal probes', *Journal of Applied Physics*, vol. 116, no. 5, Aug. 2014. DOI: 10.1063/1.4891872.

[59] A. Kaźmierczak-Bałata, J. Juszczyk, D. Trefon-Radziejewska and J. Bodzenta, 'Influence of probe-sample temperature difference on thermal mapping contrast in scanning thermal microscopy imaging', *Journal of Applied Physics*, vol. 121, no. 11, Mar. 2017. DOI: 10.1063/1.4977101.

[60] N. Fleurence, S. Demeyer, A. Allard, S. Douri and B. Hay, 'Quantitative Measurement of Thermal Conductivity by SThM Technique: Measurements, Calibration Protocols and Uncertainty Evaluation', *Nanomaterials*, vol. 13, no. 17, Sep. 2023. DOI: 10.3390/nano13172424.

[61] L. Vera-Londono, A. Ruiz-Clavijo, J. A. Pérez-Taborda and M. Martín-González, 'Nanoscale heat transport analysis by scanning thermal microscopy: from calibration to high-resolution measurements', *Nanoscale Advances*, vol. 4, no. 15, pp. 3194–3211, 2022. DOI: 10.1039/D2NA00287F.

[62] Y. Ge, 'Quantitative measurement using scanning thermal microscopy', Ph.D. dissertation, University of Glasgow, Glasgow, 2016.

[63] R. Lambert, 'Design, Fabrication and Characterisation of Thermally Optimised Novel SThM Probes', Ph.D. dissertation, University of Glasgow, Glasgow, 2020.

[64] Y. Zhang, W. Zhu, F. Hui, M. Lanza, T. Borca-Tasciuc and M. Muñoz Rojo, 'A Review on Principles and Applications of Scanning Thermal Microscopy (SThM)', *Advanced Functional Materials*, vol. 30, no. 18, May 2020. DOI: 10.1002/adfm.201900892.

[65] D. Pierce and P. Brusius, 'Electromigration: A review', *Microelectronics Reliability*, vol. 37, no. 7, pp. 1053–1072, Jul. 1997. DOI: 10.1016/S0026-2714(96)00268-5.

[66] P. S. Ho and T. Kwok, 'Electromigration in metals', *Reports on Progress in Physics*, vol. 52, no. 3, pp. 301–348, Mar. 1989. DOI: 10.1088/0034-4885/52/3/002.

[67] C. C. Williams and H. K. Wickramasinghe, 'Scanning thermal profiler', *Microelectronic Engineering*, vol. 5, no. 1-4, pp. 509–513, Dec. 1986. DOI: 10.1016/0167-9317(86)90084-5.

[68] C. C. Williams and H. K. Wickramasinghe, 'Thermal And Photothermal Imaging On A Sub 100 Nanometer Scale', in *Scanning Microscopy Technologies and Applications*, vol. 0897, SPIE, Jul. 1988, p. 129. DOI: 10.1117/12.944530.

[69] K. Karrai and R. D. Grober, 'Piezo-electric tuning fork tip-sample distance control for near field optical microscopes', *Ultramicroscopy*, vol. 61, pp. 197–205, 1995.

[70] K. Karrai and R. D. Grober, 'Piezoelectric tip-sample distance control for near field optical microscopes', *Applied Physics Letters*, p. 1842, 1995. DOI: 10.1063/1.113340.

[71] H. Edwards, L. Taylor, W. Duncan and A. J. Melmed, 'Fast, high-resolution atomic force microscopy using a quartz tuning fork as actuator and sensor', *Journal of Applied Physics*, vol. 82, no. 3, pp. 980–984, Aug. 1997. DOI: 10.1063/1.365936.

[72] Y. Shiba, T. Ono, K. Minami and M. Esashi, 'Capacitive AFM Probe for High Speed Imaging', *IEEJ Transactions on Sensors and Micromachines*, vol. 118, no. 12, pp. 647–651, 1998.

[73] J. He, W. Zhou, H. Yu, X. He and P. Peng, 'Structural designing of a MEMS capacitive accelerometer for low temperature coefficient and high linearity', *Sensors (Switzerland)*, vol. 18, no. 2, Feb. 2018. DOI: 10.3390/s18020643.

[74] F. Molina-Lopez, T. Kinkeldei, D. Briand, G. Tröster and N. F. De Rooij, 'Theoretical and experimental study of the bending influence on the capacitance of interdigitated micro-electrodes patterned on flexible substrates', *Journal of Applied Physics*, vol. 114, no. 17, Nov. 2013. DOI: 10.1063/1.4829023.

[75] R. Zeiser, T. Fellner and J. Wilde, 'Capacitive strain gauges on flexible polymer substrates for wireless, intelligent systems', *Journal of Sensors and Sensor Systems*, vol. 3, no. 1, pp. 77–86, Apr. 2014. DOI: 10.5194/jsss-3-77-2014.

[76] J.-Y. Wang, C.-F. Hu, C. Hong, W.-S. Su and W. Fang, 'Development of 3D CNTS interdigitated finger electrodes on flexible polymer for bending strain measurement', in *2011 IEEE 24th International Conference on Micro Electro Mechanical Systems*, IEEE, Jan. 2011, pp. 408–411. DOI: 10.1109/MEMSYS.2011.5734448.

[77] A. Rivadeneyra and J. A. López-Villanueva, 'Recent advances in printed capacitive sensors', *Micromachines*, vol. 11, no. 4, Apr. 2020. DOI: 10.3390/MI11040367.

[78] T. Göddenhenrich, H. Lemke, U. Hartmann and C. Heiden, 'Force microscope with capacitive displacement detection', *Journal of Vacuum Science & Technology A: Vacuum, Surfaces, and Films*, vol. 8, no. 1, pp. 383–387, Jan. 1990. DOI: 10.1116/1.576401.

[79] G. Neubauer, S. R. Cohen, G. M. McClelland, D. Horne and C. M. Mate, 'Force microscopy with a bidirectional capacitance sensor', *Review of Scientific Instruments*, vol. 61, no. 9, pp. 2296–2308, 1990. DOI: 10.1063/1.1141354.

[80] M. Ohtsu, K. Minami and M. Esashi, 'Fabrication of packaged thin beam structures by an improved drying method', in *Proceedings of Ninth International Workshop on Micro Electromechanical Systems*, IEEE, 1996, pp. 228–233. DOI: 10.1109/MEMSYS.1996.493985.

[81] J. Li, T. Mattila and V. Vuorinen, 'MEMS Reliability', *Handbook of Silicon Based MEMS Materials and Technologies: Second Edition*, pp. 744–763, Jan. 2015. DOI: 10.1016/B978-0-323-29965-7.00041-5.

[82] H. Ohnishi et al., 'Stability Improvement of Tactile Sensor of Normal and Shear Stresses Using Ni-Cr Thin Film Gauge', *IEEJ Transactions on Sensors and Micromachines*, vol. 129, no. 11, pp. 411–416, 2009.

[83] G. Yang, V. Bailey, G. Lin, W. Tang and J. Keyak, 'Design of microfabricated strain gauge array to monitor bone deformation in vitro and in vivo', in *Proceedings. Fourth IEEE Symposium on Bioinformatics and Bioengineering*, IEEE, 2004, pp. 30–37. DOI: 10.1109/BIBE.2004.1317322.

[84] J. Rölke, 'Nichrome Thin Film Technology and its Application', *ElectroComponent Science and Technology*, vol. 9, no. 1, pp. 51–57, 1981. DOI: 10.1155/APEC.9.51.

[85] I. H. Kazi, P. Wild, T. Moore and M. Sayer, 'Characterization of sputtered nichrome (Ni–Cr 80/20 wt.%) films for strain gauge applications', *Thin Solid Films*, vol. 515, no. 4, pp. 2602–2606, Dec. 2006. DOI: 10.1016/j.tsf.2005.10.077.

[86] M. Tortonese, R. C. Barrett and C. F. Quate, 'Atomic resolution with an atomic force microscope using piezoresistive detection', *Applied Physics Letters*, vol. 62, no. 8, pp. 834–836, Feb. 1993. DOI: 10.1063/1.108593.

[87] A. K. Ghosh, C. Fishman and T. Feng, 'Theory of the electrical and photovoltaic properties of polycrystalline silicon', *Journal of Applied Physics*, vol. 51, no. 1, pp. 446–454, Jan. 1980. DOI: 10.1063/1.327342.

[88] A. Schneider, R. H. Ibbotson, R. J. Dunn and E. Huq, 'Arrays of SU-8 microcantilevers with integrated piezoresistive sensors for parallel AFM applications', *Microelectronic Engineering*, vol. 88, no. 8, pp. 2390–2393, Aug. 2011. DOI: 10.1016/j.mee.2010.11.047.

[89] F. King, J. Shewchun, D. Thompson, H. Barber and W. Pieczonka, 'Polycrystalline silicon resistors for integrated circuits', *Solid-State Electronics*, vol. 16, no. 6, pp. 701–708, Jun. 1973. DOI: 10.1016/0038-1101(73)90113-5.

[90] D. A. B. Miller, *Quantum Mechanics for Scientists and Engineers*. Cambridge: Cambridge University Press, Apr. 2008. DOI: 10.1017/CBO9780511813962.

[91] M. Zheng et al., 'Strain sensors based on chromium nanoparticle arrays', *Nanoscale*, vol. 6, no. 8, pp. 3930–3933, Apr. 2014. DOI: 10.1039/c3nr04135b.

[92] A. Kulkarni et al., 'Monitoring magnetostriction by a quantum tunnelling strain sensor', *Sensors and Actuators A: Physical*, vol. 183, pp. 28–33, Aug. 2012. DOI: 10.1016/j.sna.2012.06.010.

[93] M. Dukic et al., 'Direct-write nanoscale printing of nanogranular tunnelling strain sensors for sub-micrometre cantilevers', *Nature Communications*, vol. 7, no. 1, Sep. 2016. DOI: 10.1038/ncomms12487.

[94] P. J. Koppinen, J. T. Lievonen, M. Ahlskog and I. J. Maasilta, 'Strain sensing with sub-micron sized Al-AlOx-Al tunnel junctions', Jun. 2009. DOI: 10.1063/1.3298582. [Online]. Available: http://arxiv.org/abs/0906.4234%20http://dx.doi.org/10.1063/1.3298582.

[95] S. Franssila, *Introduction to microfabrication*. John Wiley & Sons, 2010, p. 518.

[96] Halbleiter, *Semiconductor Technology from A to Z: Photolithography: Exposition methods*.

[97] C. Valentine, *Lithography basics*, Jun. 2020.

[98] C. Valentine, *Photolithography Exposure Modes*, Jun. 2020.

[99] D. Meyerhofer, 'Characteristics of resist films produced by spinning', *Journal of Applied Physics*, vol. 49, no. 7, pp. 3993–3997, 1978. DOI: 10.1063/1.325357.

[100] N. Takahashi and H. Kikuchi, 'Rayleigh Criterion: The Paradigm of Photolithography Equipment', *Annals of Business Administrative Science*, vol. 16, no. 5, pp. 203–213, Oct. 2017. DOI: 10.7880/abas.0170525a.

[101] M. Rothschild, 'Projection optical lithography', *Materials Today*, vol. 8, no. 2, pp. 18–24, Feb. 2005. DOI: 10.1016/S1369-7021(05)00698-X.

[102] S. Landis, *Lithography*. ISTE Ltd and John Wiley & Sons Inc, Nov. 2010.

[103] V. R. Manfrinato et al., 'Resolution limits of electron-beam lithography toward the atomic scale', *Nano Letters*, vol. 13, no. 4, pp. 1555–1558, Apr. 2013. DOI: 10.1021/nl304715p.

[104] F. E. Camino et al., 'Single-digit nanometer electron-beam lithography with an aberration-corrected scanning transmission electron microscope', *Journal of Visualized Experiments*, vol. 2018, no. 139, Sep. 2018. DOI: 10.3791/58272.

[105] M. Hatzakis, 'Electron Resists for Microcircuit and Mask Production', *Journal of The Electrochemical Society*, vol. 106, pp. 1033–1037, 1969.

[106] V. Sidorkin, A. Grigorescu, H. Salemink and E. v. d. Drift, 'Resist thickness effects on ultra thin HSQ patterning capabilities', *Microelectronic Engineering*, vol. 86, no. 4-6, pp. 749–751, Apr. 2009. DOI: 10.1016/j.mee.2008.12.071.

[107] P. Nealey, M. Stoykovich, K. Yoshimoto and H. Cao, 'Nanolithographic Polymer Structures: Mechanical Properties', *Encyclopedia of Materials: Science and Technology*, pp. 1–9, Jan. 2003. DOI: 10.1016/B0-08-043152-6/01891-X.

[108] S. Alexander et al., 'An atomic-resolution atomic-force microscope implemented using an optical lever', *Journal of Applied Physics*, vol. 65, no. 1, pp. 164–167, 1989. DOI: 10.1063/1.342563.

[109] M. J. Mindeltj and S. R. Pollackt, 'The room temperature oxidation of titanium thin films', *Acta Metallurgica*, vol. 17, no. 12, pp. 1441–1448, 1969.

[110] I. E. Klein, M. Hershkovich and I. A. Goldberg, 'The mechanism of oxidation of thin Ni-Cr films', *Microelectronics Journel*, vol. 19, no. 6, pp. 17–23, 1989.

[111] W. D. Sylwestrowicz, 'Oxidation of Titanium Thin Films', *Journal of the Electrochemical society*, vol. 22, no. 11, p. 1504, Nov. 1975.

[112] S. R. Pollack, 'The Oxidation of Thin Metal Films', *Materials Science and Engineering*, vol. 3, pp. 249–251, 1968.

[113] M. Todeschini, A. Bastos Da Silva Fanta, F. Jensen, J. B. Wagner and A. Han, 'Influence of Ti and Cr Adhesion Layers on Ultrathin Au Films', *ACS Applied Materials and Interfaces*, vol. 9, no. 42, pp. 37 374–37 385, Oct. 2017. DOI: 10.1021/acsami.7b10136.

[114] W. M. Abbott et al., 'Comparison of Metal Adhesion Layers for Au Films in Thermoplasmonic Applications', *ACS Applied Materials and Interfaces*, vol. 12, no. 11, pp. 13 503–13 509, Mar. 2020. DOI: 10.1021/acsami.9b22279.

[115] V. K. Tolpygo, D. R. Clarke and K. S. Murphy, 'Oxidation-induced failure of EB-PVD thermal barrier coatings', Tech. Rep., 2001, pp. 124–131.

[116] A. H. Muggleton and F. A. Howe, 'Crystal oscillator film thickness monitor', *Nuclear Instruments and Methods*, vol. 28, no. 2, pp. 242–244, Aug. 1964. DOI: 10.1016/0029-554X(64)90429-X.

[117] M. Ohring, *Materials Science of Thin Films*, 2nd ed. Academic Press, Jan. 2002, pp. 357–415. DOI: 10.1016/B978-012524975-1/50010-0.

[118] S. R. J. Saunders and J. R. Nicholls, 'Oxidation, hot corrosion and protection of metallic materials', in *Physical Metallurgy*, R. Cahn and P. Haasen, Eds., 4th ed., North Holland, 1996, pp. 1291–1361. DOI: https://doi.org/10.1016/B978-044489875-3/50019-3.

[119] Y. K. Yap and D. Zhang, 'Physical Vapor Deposition', in *Encyclopedia of Nanotechnology*, Dordrecht: Springer Netherlands, 2015, pp. 1–8. DOI: 10.1007/978-94-007-6178-0{_}362-3. [Online]. Available: https://link.springer.com/10.1007/978-94-007-6178-0_362-3.

[120] R. Perez garcia, 'Controlled Deposition of Fullerenes: Effects of Topological nano-Modifications of a Surface on Aggregation and Growth Phenomena', Ph.D. dissertation, 2018. DOI: 10.13140/RG.2.2.31031.78247.

[121] J. A. Venables, T. Spiller and M. Hanbucken, 'Nucleation and growth of thin films', *Rep. Prog. Phys*, vol. 47, pp. 399–459, 1984.

[122] A. Baskaran and P. Smereka, 'Mechanisms of Stranski-Krastanov Growth', Jan. 2011. DOI: 10.1063/1.3679068. [Online]. Available: http://arxiv.org/abs/1101.3775%20http://dx.doi.org/10.1063/1.3679068.

[123] M. Schwartzkopf et al., 'Role of Sputter Deposition Rate in Tailoring Nanogranular Gold Structures on Polymer Surfaces', *ACS Applied Materials and Interfaces*, vol. 9, no. 6, pp. 5629–5637, Feb. 2017. DOI: 10.1021/acsami.6b15172.

[124] A. P. Nayak, M. S. Islam and V. J. Logeeswaran, 'Dry Etching', in *Encyclopedia of Nanotechnology*, B. Bhushan, Ed., Dordrecht: Springer Netherlands, 2012, pp. 587–589. DOI: 10.1007/978-90-481-9751-4{_}353. [Online]. Available: https://doi.org/10.1007/978-90-481-9751-4_353.

[125] D. House and D. Dongqing Li, 'Anisotropic Etching', Tech. Rep., 2008.

[126] M. Elwenspoek and H. Jansen, *Silicon Micromachining*. Cambridge University Press, 2004.

[127] P. Pal, V. Swarnalatha, A. V. N. Rao, A. K. Pandey, H. Tanaka and K. Sato, 'High speed silicon wet anisotropic etching for applications in bulk micromachining: a review', *Micro and Nano Systems Letters*, vol. 9, no. 1, p. 4, Feb. 2021. DOI: 10.1186/s40486-021-00129-0.

[128] Y. Zhang, P. S. Dobson and J. M. Weaver, 'Batch fabricated dual cantilever resistive probe for scanning thermal microscopy', in *Microelectronic Engineering*, vol. 88, Aug. 2011, pp. 2435–2438. DOI: 10.1016/j.mee.2011.02.040.

[129] G. Mills, H. Zhou, A. Midha, L. Donaldson and J. M. Weaver, 'Scanning thermal microscopy using batch fabricated thermocouple probes', *Applied Physics Letters*, vol. 72, no. 22, pp. 2900–2902, 1998. DOI: 10.1063/1.121453.

[130] H. Zhou, A. Midha, G. Mills,) S. Thoms, S. K. Murad and J. M. R. Weaver, 'Generic scanned-probe microscope sensors by combined micromachining and electron-beam lithography', Tech. Rep., 1998.

[131] H. Zhou, G. Mills, B. K. Chong, A. Midha, L. Donaldson and J. M. R. Weaver, 'Recent progress in the functionalization of atomic force microscope probes using electron-beam nanolithography', *J.Vac.Sci.Technol*, 1999.

[132] H. Niedrig, *Physical background of electron backscattering*, 1978. DOI: 10.1002/sca.4950010103.

[133] Raith Nanofabrication, *EBPG Reference Manual*, 2021. [Online]. Available: www.raith.com.

[134] S. Thoms, Y. Zhang and J. M. R. Weaver, 'Improved alignment algorithm for electron beam lithography', *Journal of Vacuum Science \& Technology B, Nanotechnology and Microelectronics: Materials, Processing, Measurement, and Phenomena*, vol. 32, no. 6, 06F509, Nov. 2014. DOI: 10.1116/1.4901015.

[135] R. Dawant, R. Seils, S. Ecoffey, R. Schmid and D. Drouin, 'Hybrid cross correlation and line-scan alignment strategy for CMOS chips electron-beam lithography processing', *Journal of Vacuum Science \& Technology B*, vol. 40, no. 1, p. 012 601, Jan. 2022. DOI: 10.1116/6.0001278.

[136] E. Anderson, D. Ha and Liddle J.A, 'Sub-pixel alignment for direct-write electron beam lithography', *Microelectronic Engineering*, vol. 73-74, pp. 74–79, Jun. 2004. DOI: 10.1016/j.mee.2004.02.019.

[137] B. V. K. V. Kumar and L. Hassebrook, 'Performance measures for correlation filters', *Applied optics*, vol. 29, no. 20, pp. 2997–3006, 1990.

[138] K. E. Docherty, 'Improvements to the alignment process in electron-beam lithography', Ph.D. dissertation, University of Glasgow, Glasgow, 2009.

[139] Roger Penrose, *The Emperor's New Mind: Concerning Computers, Minds and The Laws of Physics*, 1st ed. Oxford University Press, Nov. 1989.

[140] K. E. Docherty, K. A. Lister, J. Romijn and J. M. Weaver, 'High robustness of correlation-based alignment with Penrose patterns to marker damage in electron beam lithography', *Microelectronic Engineering*, vol. 86, no. 4-6, pp. 532–534, Apr. 2009. DOI: 10.1016/j.mee.2008.11.037.

[141] K. E. Docherty, S. Thoms, P. Dobson and J. M. Weaver, 'Improvements to the alignment process in a commercial vector scan electron beam lithography tool', *Microelectronic Engineering*, vol. 85, no. 5-6, pp. 761–763, May 2008. DOI: 10.1016/j.mee.2008.01.081.

[142] S. Thoms, D. S. Macintyre, K. E. Docherty and J. M. Weaver, 'Alignment verification for electron beam lithography', *Microelectronic Engineering*, vol. 123, pp. 9–12, Jul. 2014. DOI: 10.1016/J.MEE.2014.02.005.

[143] L. de Broglie, 'Recherches sur la théorie des quanta (Research on the Theory of Quanta)', Ph.D. dissertation, Paris, 1924.

[144] AZO Materials, *How to Mix Backscattered and Secondary Electron Images*, Jul. 2018.

[145] Oxford-Instruments, *Options and Accessories for Asylum Research MFP-3D AFMs*.

[146] L. Shi, S. Plyasunov, A. Bachtold, P. L. McEuen and A. Majumdar, 'Scanning thermal microscopy of carbon nanotubes using batch-fabricated probes', *Applied Physics Letters*, vol. 77, no. 26, pp. 4295–4297, Dec. 2000. DOI: 10.1063/1.1334658.

[147] A. Assy, 'Development of two techniques for thermal characterization of materials : Scanning Thermal Microscopy (SThM) and 2ω method', Ph.D. dissertation, INSA de Lyon, 2015. [Online]. Available: http://edeea.ec-lyon.fr.

[148] B. Gotsmann and M. A. Lantz, 'Quantized thermal transport across contacts of rough surfaces', *Nature Materials*, vol. 12, no. 1, pp. 59–65, Jan. 2013. DOI: 10.1038/nmat3460.

[149] J. Martinek, P. Klapetek and A. C. Campbell, 'Methods for topography artifacts compensation in scanning thermal microscopy', *Ultramicroscopy*, vol. 155, pp. 55–61, Aug. 2015. DOI: 10.1016/j.ultramic.2015.04.011.

[150] P. Klapetek, J. Martinek, P. Grolich, M. Valtr and N. J. Kaur, 'Graphics cards based topography artefacts simulations in Scanning Thermal Microscopy', *International Journal of Heat and Mass Transfer*, vol. 108, pp. 841–850, 2017. DOI: 10.1016/j.ijheatmasstransfer.2016.12.036.

[151] O. Marti, A. Ruf, M. Hipp, H. Bielefeldt, J. Colchero and J. Mlynek, 'Mechanical and thermal effects of laser irradiation on force microscope cantilevers', *Ultramicroscopy*, vol. 42-44, no. PART 1, pp. 345–350, Jul. 1992. DOI: 10.1016/0304-3991(92)90290-Z.

[152] O. Kučera, 'Self Heating of an Atomic Force Microscope', *Acta Polytechnica*, vol. 50, no. 1, 2010. [Online]. Available: http://ctn.cvut.cz/ap/.

[153] P. Janus et al., 'Novel SThM nanoprobe for thermal properties investigation of micro- and nanoelectronic devices', *Microelectronic Engineering*, vol. 87, no. 5-8, pp. 1370–1374, May 2010. DOI: 10.1016/j.mee.2009.11.178.

[154] C. H. Hsueh, 'Modeling of elastic deformation of multilayers due to residual stresses and external bending', *Journal of Applied Physics*, vol. 91, no. 12, pp. 9652–9656, Jun. 2002. DOI: 10.1063/1.1478137.

[155] S. Timoshenko, 'Analysis of bi-metal thermostats', *Journal of the Optical Society of America*, vol. 11, no. 3, pp. 233–255, 1925.

[156] T. Thundat, R. J. Warmack, G. Y. Chen and D. P. Allison, 'Thermal and ambient-induced deflections of scanning force microscope cantilevers', *Applied Physics Letters*, vol. 64, no. 21, pp. 2894–2896, 1994. DOI: 10.1063/1.111407.

[157] J. Cha, H. Shin and O. Kwon, 'Vacuum null-point scanning thermal microscopy: Simultaneous quantitative nanoscale mapping of undisturbed temperature and thermal resistance', *International Journal of Thermal Sciences*, vol. 172, Feb. 2022. DOI: 10.1016/j.ijthermalsci.2021.107268.

[158] E. Puyoo, S. Grauby, J. M. Rampnoux, E. Rouvìre and S. Dilhaire, 'Scanning thermal microscopy of individual silicon nanowires', *Journal of Applied Physics*, vol. 109, no. 2, Jan. 2011. DOI: 10.1063/1.3524223.

[159] A. Dickman, *Verified Signal Processing Algorithms in MATLAB and C: Advised by Israel Greiss*. Springer International Publishing, Jan. 2022, pp. 1–218. DOI: 10.1007/978-3-030-93363-0.

[160] J. Bodzenta, A. Kaźmierczak-Bałata, M. Lorenc and J. Juszczyk, 'Analysis of possibilities of application of nanofabricated thermal probes to quantitative thermal measurements', *International Journal of Thermophysics*, vol. 31, no. 1, pp. 150–162, Jan. 2010. DOI: 10.1007/s10765-009-0659-2.

[161] L. Kumanchik, T. L. Schmitz and J. R. Pratt, 'An interferometric platform for studying AFM probe deflection', *Precision Engineering*, vol. 35, no. 2, pp. 248–257, 2011. DOI: 10.1016/j.precisioneng.2010.09.013.

[162] J. A. Ivie, 'Charge Transport through Single Molecules with Mechanically Controlled Break Junctions', Ph.D. dissertation, The university of Arizona, Arizona, Sep. 2019. [Online]. Available: http://hdl.handle.net/10150/634218.

[163] Thorlabs, *Technical support private communication*, Jan. 2024.

[164] H. Xue and R. Yang, 'Optimal Cosine Windowed Algorithms For Harmonic Analysis of Power System', *2003 IEEE Power Engineering Society General Meeting (IEEE Cat. No.03CH37491)*, vol. 3, pp. 1548–1552, 2003. DOI: 10.1109/PES.2003.1267385{\}.

[165] D. Nečas and P. Klapetek, 'Gwyddion: an open-source software for SPM data analysis', *Open Physics*, vol. 10, no. 1, pp. 181–188, Feb. 2012. DOI: 10.2478/s11534-011-0096-2.

[166] S. Lefèvre, S. Volz, J. B. Saulnier, C. Fuentes and N. Trannoy, 'Thermal conductivity calibration for hot wire based dc scanning thermal microscopy', *Review of Scientific Instruments*, vol. 74, no. 4, pp. 2418–2423, Apr. 2003. DOI: 10.1063/1.1544078.

[167] M. V. Vitorino, A. Vieira, C. A. Marques and M. S. Rodrigues, 'Direct measurement of the capillary condensation time of a water nanobridge', *Scientific Reports*, vol. 8, no. 1, Dec. 2018. DOI: 10.1038/s41598-018-32021-0.

[168] R. Szoszkiewicz and E. Riedo, 'Nucleation time of nanoscale water bridges', *Physical Review Letters*, vol. 95, no. 13, Sep. 2005. DOI: 10.1103/PhysRevLett.95.135502.

[169] Z. Wei and Y. P. Zhao, 'Growth of liquid bridge in AFM', *Journal of Physics D: Applied Physics*, vol. 40, no. 14, pp. 4368–4375, Jul. 2007. DOI: 10.1088/0022-3727/40/14/036.

[170] USB consortium, 'Universal Serial Bus Specification, Revision 2.0', Tech. Rep., Apr. 2000.

[171] M. Boudaoud, Y. Haddab, Y. Le Gorrec and P. Lutz, 'Study of thermal and acoustic noise interferences in low stiffness AFM cantilevers and characterization of their dynamic properties.', *Review of Scientific Instruments*, vol. 83, no. 1, 2012. DOI: 10.1063/1.3673637{\"{i}}. [Online]. Available: https://hal.science/hal-00672172.

[172] P. Eaton and P. West, 'AFM Image Artefacts', in *Atomic Force Microscopy*, vol. 9780199570454, Oxford University Press, May 2010, pp. 1–256. DOI: 10.1093/acprof:oso/9780199570454.001.0001.

[173] F. Tofani, 'Thermal-AFM under aqueous environment', Ph.D. dissertation, University of Glasgow, Glasgow, 2020.

[174] P. Janus et al., 'Thermal nanometrology using piezoresistive SThM probes with metallic tips', *Ultramicroscopy*, vol. 193, pp. 104–110, Oct. 2018. DOI: 10.1016/j.ultramic.2018.06.016.

[175] C. Canale, B. Torre, D. Ricci and P. C. Braga, 'Recognizing and Avoiding Artifacts in Atomic Force Microscopy Imaging', in *Methods in Molecular Biology*, 2011. [Online]. Available: www.springer.com/series/7651.

[176] Y. Gan, 'Atomic and subnanometer resolution in ambient conditions by atomic force microscopy', *Surface Science Reports*, vol. 64, no. 3, pp. 99–121, Mar. 2009. DOI: 10.1016/j.surfrep.2008.12.001.

[177] H.-J. Butt and M. Jaschke, 'Calculation of thermal noise in atomic force microscopy', *Nanotechnology*, vol. 6, p. 1, 1995.

[178] J. Shen, D. Zhang, F. H. Zhang and Y. Gan, 'AFM tip-sample convolution effects for cylinder protrusions', *Applied Surface Science*, vol. 422, pp. 482–491, Nov. 2017. DOI: 10.1016/j.apsusc.2017.06.053.

[179] H. Ftouni et al., 'Thermal conductivity of silicon nitride membranes is not sensitive to stress', *Physical Review B - Condensed Matter and Materials Physics*, vol. 92, no. 12, Sep. 2015. DOI: 10.1103/PhysRevB.92.125439.

[180] Y. Zhang, W. Zhu and T. Borca-Tasciuc, 'Thermal conductivity measurements of thin films by non-contact scanning thermal microscopy under ambient conditions', *Nanoscale Advances*, vol. 3, no. 3, pp. 692–702, Feb. 2021. DOI: 10.1039/d0na00657b.

[181] P. S. Dobson, G. Mills and J. M. Weaver, 'Microfabricated temperature standard based on Johnson noise measurement for the calibration of micro- and nano-thermometers', *Review of Scientific Instruments*, vol. 76, no. 5, May 2005. DOI: 10.1063/1.1899463.

[182] K. L. Lear and A. N. Al-Omari, 'Progress and issues for high-speed vertical cavity surface emitting lasers', in *Integrated Optoelectronic Devices 2007*, K. D. Choquette and J. K. Guenter, Eds., Feb. 2007. DOI: 10.1117/12.715081.

[183] B. Tell, K. F. Brown-Goebeler, R. E. Leibenguth, F. M. Baez and Y. H. Lee, 'Temperature dependence of GaAs-AlGaAs vertical cavity surface emitting lasers', *Applied Physics Letters*, vol. 60, no. 6, pp. 683–685, Feb. 1992. DOI: 10.1063/1.106536.

[184] F. Jasim, K. Omar, Z. Hassan, F. Z. Jasim, K. Omar and Z. Hassan, 'Temperature effect on VCSEL output performance', Tech. Rep. 11, 2009, pp. 1136–1138. [Online]. Available: https://www.researchgate.net/publication/289357481.

[185] K. Luo, R. W. Herrick, A. Majumdar and P. Petroff, 'Scanning thermal microscopy of a vertical-cavity surface-emitting laser', *Applied Physics Letters*, vol. 71, no. 12, pp. 1604–1606, Sep. 1997. DOI: 10.1063/1.119991.

[186] M. Farzaneh, R. Amatya, D. Lüerßsen, K. J. Greenberg, W. E. Rockwell and J. A. Hudgings, 'Temperature profiling of VCSELs by thermoreflectance microscopy', *IEEE Photonics Technology Letters*, vol. 19, no. 8, pp. 601–603, Apr. 2007. DOI: 10.1109/LPT.2007.894348.

[187] Firecomms, '665nm Multi Mode VCSEL Product specification - RVM665T', Tech. Rep.

[188] M. H. Macdougal, J. Geske, C.-K. Lin, A. E. Bond and P. Daniel Dapkus, 'Thermal Impedance of VCSEL's with AlO-GaAs DBR's', *IEEE Photonics Technology Letters*, vol. 10, no. 1, pp. 15–17, 1998.

[189] O. Svelto, *Principles of Lasers*, 5th ed. New York: Springer New York, 2010. DOI: https://doi.org/10.1007/978-1-4419-1302-9.

[190] F. J. Duarte, 'The Uncertainty Principle in Optics', in *Tunable Laser Optics*, Elsevier, 2003, pp. 45–56. DOI: 10.1016/B978-012222696-0/50050-8.

[191] G. Duggan et al., 'Red vertical cavity surface emitting lasers (VCSELs) for consumer applications', in *Vertical-Cavity Surface-Emitting Lasers XII*, vol. 6908, SPIE, Feb. 2008, 69080G. DOI: 10.1117/12.757779.

[192] K. Kim, W. Jeong, W. Lee and P. Reddy, 'Ultra-high vacuum scanning thermal microscopy for nanometer resolution quantitative thermometry', *ACS Nano*, vol. 6, no. 5, pp. 4248–4257, May 2012. DOI: 10.1021/nn300774n.

[193] P. D. Tovee and O. V. Kolosov, 'Nanoscale resolution immersion scanning thermal microscopy', 2013. [Online]. Available: https://www.researchgate.net/publication/235892630.

[194] L. Aigouy, L. Lalouat, M. Mortier, P. Lw and C. Bergaud, 'A scanning thermal probe microscope that operates in liquids', *Review of Scientific Instruments*, vol. 82, no. 3, Mar. 2011. DOI: 10.1063/1.3567794.

[195] P. S. Dobson, J. M. R. Weaver and G. Mills, 'New Methods for Calibrated Scanning Thermal Microscopy (SThM)', in *2007 IEEE Sensors*, IEEE, 2007, pp. 708–711. DOI: 10.1109/ICSENS.2007.4388498. [Online]. Available: http://ieeexplore.ieee.org/document/4388498/.

[196] F. Gucmann, J. W. Pomeroy and M. Kuball, 'Scanning thermal microscopy for accurate nanoscale device thermography', *Nano Today*, vol. 39, p. 101 206, Aug. 2021. DOI: 10.1016/J.NANTOD.2021.101206.

[197] S. Thoms and P. Reynolds, *Penrose Patterns for Error Measurement in Electron Beam Lithography*, Berlin, Sep. 2023.

[198] J. Yoshida, S. Inoue, H. Sugiyama and T. Nagano, 'Transport processes in ramp-edge-type Josephson junctions', *Physica C*, vol. 335, pp. 226–230, 2000.

[199] M. Hoek, F. Coneri, X. R. Wang and H. Hilgenkamp, 'Ramp-edge junctions between superconducting Nd1.85Ce0.15CuO4 and La1.85Sr0.15CuO4', *Superconductor Science and Technology*, vol. 29, no. 3, Jan. 2016. DOI: 10.1088/0953-2048/29/3/035001.

[200] V. Dubois, F. Niklaus and G. Stemme, 'Design and fabrication of crack-junctions', *Microsystems and Nanoengineering*, vol. 3, 2017. DOI: 10.1038/micronano.2017.42.

[201] V. Dubois et al., 'Massively parallel fabrication of crack-defined gold break junctions featuring sub-3 nm gaps for molecular devices', *Nature Communications*, vol. 9, no. 1, Dec. 2018. DOI: 10.1038/s41467-018-05785-2.

[202] A. S. Cordan, A. Goltzené, Y. Hervé, M. Mejias, C. Vieu and H. Launois, 'Electron transport in metallic dot arrays: Effect of a broad dispersion in the tunnel junction dimensions', *Journal of Applied Physics*, vol. 84, no. 7, pp. 3756–3763, Oct. 1998. DOI: 10.1063/1.368554.

[203] A. Pépin et al., 'Temperature evolution of multiple tunnel junction devices made with disordered two-dimensional arrays of metallic islands', *Applied Physics Letters*, vol. 74, no. 20, pp. 3047–3049, May 1999. DOI: 10.1063/1.124060.

[204] M. Manheller, S. Trellenkamp, R. Waser and S. Karthäuser, 'Reliable fabrication of 3nm gaps between nanoelectrodes by electron-beam lithography', *Nanotechnology*, vol. 23, no. 12, Mar. 2012. DOI: 10.1088/0957-4484/23/12/125302.

[205] S. Ling, J. Sanny and W. Moebs, *University Physics*. Samurai Media Limited, 2017, vol. 3.

[206] G. Dittmer, 'Electrical conduction and electron emission of discontinuous thin films', *Thin Solid Films*, vol. 9, no. 3, pp. 317–328, Mar. 1972. DOI: 10.1016/0040-6090(72)90122-8.

[207] R. D. Kiernan S, 'Tunnelling between Metallic Islands on a Dielectric Substrate', *Proc. Roy. Soc., A*, vol. 33, p. 377, 1962.

[208] C. A. Neugebauer and M. B. Webb, 'Electrical Conduction Mechanism in Ultrathin, Evaporated Metal Films', *Journal of Applied Physics*, vol. 33, no. 1, pp. 74–82, Jan. 1962. DOI: 10.1063/1.1728531.

[209] A. Lassesson, S. A. Brown, J. van Lith and M. Schulze, 'Electrical characterization of gold island films: A route to control of nanoparticle deposition', *Applied Physics Letters*, vol. 93, no. 20, Nov. 2008. DOI: 10.1063/1.3027463.

[210] P. O'connell, 'The Formation of Thin Film Resistors by Ion Implantation of Metal Films', Ph.D. dissertation, 1975.

[211] K. H. Müller and M. M. Yajadda, 'Electron transport in discontinuous gold films and the effect of Coulomb blockade and percolation', *Journal of Applied Physics*, vol. 111, no. 12, Jun. 2012. DOI: 10.1063/1.4729491.

[212] W. Skorupa, P. Knothe and R. Grötzschel, 'Diffusion inhibition against gold of ion beam synthesized buried silicon nitride layers in silicon', *Nuclear Instruments and Methods in Physics Research Section B: Beam Interactions with Materials and Atoms*, vol. 34, no. 4, pp. 523–524, Oct. 1988. DOI: 10.1016/0168-583X(88)90162-0.

[213] T. Kwak and D. Kim, 'Controlling Equilibrium Morphologies of Bimetallic Nanostructures Using Thermal Dewetting via Phase-Field Modeling', *Materials*, vol. 14, no. 21, p. 6697, Nov. 2021. DOI: 10.3390/ma14216697.

[214] S. Thoms and D. S. Macintyre, 'Linewidth metrology for sub-10-nm lithography', *Journal of Vacuum Science \& Technology B, Nanotechnology and Microelectronics: Materials, Processing, Measurement, and Phenomena*, vol. 28, no. 6, C6H6–C6H10, Nov. 2010. DOI: 10.1116/1.3505129.

[215] Z. Wang, C. Carrière, A. Seyeux, S. Zanna, D. Mercier and P. Marcus, 'Thermal stability of surface oxides on nickel alloys (NiCr and NiCrMo) investigated by XPS and ToF-SIMS', *Applied Surface Science*, vol. 576, Feb. 2022. DOI: 10.1016/j.apsusc.2021.151836.

[216] N. M. Phuong, D.-J. Kim, B.-D. Kang and S.-G. Yoon, 'Structural and Electrical Properties of NiCr Thin Films Annealed at Various Temperatures in a Vacuum and a Nitrogen Ambient for π-Type Attenuator Applications', *Journal of The Electrochemical Society*, vol. 153, no. 7, G660, 2006. DOI: 10.1149/1.2202696.